

**Studies in Mechanobiology, Tissue Engineering and
Biomaterials 20**

Gerhard A. Holzapfel
Ray W. Ogden *Editors*

Biomechanics: Trends in Modeling and Simulation

Studies in Mechanobiology, Tissue Engineering and Biomaterials

Volume 20

Series editor

Amit Gefen, Ramat Aviv, Israel

More information about this series at <http://www.springer.com/series/8415>

Gerhard A. Holzapfel · Ray W. Ogden
Editors

Biomechanics: Trends in Modeling and Simulation



Springer

Editors

Gerhard A. Holzapfel
Institute of Biomechanics
Graz University of Technology
Graz
Austria

Ray W. Ogden
School of Mathematics and Statistics
University of Glasgow
Glasgow
UK

and

Faculty of Engineering Science
and Technology
Norwegian University of Science
and Technology (NTNU)
Trondheim
Norway

ISSN 1868-2006 ISSN 1868-2014 (electronic)
Studies in Mechanobiology, Tissue Engineering and Biomaterials
ISBN 978-3-319-41473-7 ISBN 978-3-319-41475-1 (eBook)
DOI 10.1007/978-3-319-41475-1

Library of Congress Control Number: 2016947017

© Springer International Publishing Switzerland 2017

This work is subject to copyright. All rights are reserved by the Publisher, whether the whole or part of the material is concerned, specifically the rights of translation, reprinting, reuse of illustrations, recitation, broadcasting, reproduction on microfilms or in any other physical way, and transmission or information storage and retrieval, electronic adaptation, computer software, or by similar or dissimilar methodology now known or hereafter developed.

The use of general descriptive names, registered names, trademarks, service marks, etc. in this publication does not imply, even in the absence of a specific statement, that such names are exempt from the relevant protective laws and regulations and therefore free for general use.

The publisher, the authors and the editors are safe to assume that the advice and information in this book are believed to be true and accurate at the date of publication. Neither the publisher nor the authors or the editors give a warranty, express or implied, with respect to the material contained herein or for any errors or omissions that may have been made.

Printed on acid-free paper

This Springer imprint is published by Springer Nature
The registered company is Springer International Publishing AG Switzerland

Preface

In September 2014 we ran the sixth Summer School on Biomechanics that we have organized. This one, entitled “Biomechanics: Trends in Modeling and Simulation” was held at Graz University of Technology, Austria, and attended by about 90 Ph.D. students, postdoctoral researchers and university professors from more than 20 countries. We thought that it would be valuable to make the course material more generally available by publishing the lecture notes so as to provide an up-to-date account of some of the topics in the area. As things developed the material in this book in some cases has turned out to be somewhat different from the material that was presented in the Summer School, i.e., it has been updated significantly to account for subsequent developments. In addition, we have included a chapter on mixture theory which was not part of the Summer School. The subject of biomechanics is highly multidisciplinary and the content of the present volume ranges from multiscale continuum mechanics to computational modeling and applications to areas of clinical relevance such as myocardial infarction and vascular stenting.

The combination of modeling and computational methods provides the possibility to simulate multiscale coupled processes as a means to predict (patho)physiological functional interactions. This approach can, for example, provide information of academic, industrial, and clinical relevance that would otherwise not be possible. In the last few years modeling and simulation have significantly advanced our knowledge of the development of pathologies such as atherosclerosis, aneurysms, aortic dissections, and wound healing, and their prognosis. Simulations of clinical applications based on coupled models and powerful computational methods may lead to improved medical device implantations, diagnostics and treatment of tissue disorders, surgical planning and intervention.

This volume comprises seven state-of-the-art chapters on topics of modeling and simulation from the cellular to the tissue level. Chapter “[Mixture Theory for Modeling Biological Tissues: Illustrations from Articular Cartilage](#)” provides an introduction to mixture theory, and its application to articular cartilage with an emphasis on studies that provide validations of theoretical predictions. Particular

attention is given to the theory governing biphasic mixtures consisting of a porous-permeable deformable solid matrix and an interstitial fluid. This chapter also contains a brief overview of the application of mixture theory to solute transport, reactive kinetics, and growth and remodeling. Chapter “[A Bio-chemo-mechanical Model for Cell Contractility, Adhesion, Signaling, and Stress-Fiber Remodeling](#)” focuses on a multi-field approach to modeling the mechanics of cell contractility, adhesion, signaling and stress-fiber remodeling, specifically involving biological, chemical, and mechanical interactions. Particular attention is given to the influence of different flat or patterned substrates or arrays of compliant posts on the contractile behavior of a cell, and the behavior is simulated using a finite element approach.

Chapter “[Nonlinear Continuum Mechanics and Modeling the Elasticity of Soft Biological Tissues with a Focus on Artery Walls](#)” provides a summary of the nonlinear theory of continuum mechanics required for the modeling of the elastic properties of soft biological tissues, with particular reference to the fiber structure of such tissues and the influence of residual stresses. The theory is applied to a prototype problem of the extension and inflation of a fiber-reinforced thick-walled cylindrical tube taking account of fiber dispersion and residual stresses. Chapter “[Microstructure and Mechanics of Human Aortas in Health and Disease](#)” summarizes recent developments aimed at characterizing the microstructure and mechanics of human aortic tissues and also of tissues subject to diseases such as aneurysms and aortic dissection. In particular, a general fiber dispersion model is reviewed and used to capture the differences that have been identified in the microstructure and mechanics of healthy and aneurysmatic aortas. Modeling and simulation of an aortic dissection is provided using the novel phase-field approach. Finally, an aortic clamping simulation is provided for illustration including inelastic phenomena such as stress softening and permanent deformation. Chapter “[Arterial and Atherosclerotic Plaque Biomechanics with Application to Stent Angioplasty Modeling](#)” focuses on the biomechanics of atherosclerotic plaques based on the constitutive theory of tissue anisotropy, remodeling and constitutive damage modeling, including material characterization based on experimental data. Application of the theory is illustrated in the computational simulation of the deployment of a stent during an angioplasty procedure. The main challenges for the future in characterizing the complex atherosclerotic tissue and its modeling are identified.

Chapter “[Biomechanics of Myocardial Ischemia and Infarction](#)” is concerned with the biomechanics of heart disease, in particular myocardial ischemia and infarction. The structure and the mechanical properties of a normal heart are reviewed followed by a discussion of the structure and the mechanical properties of a scar produced by myocardial infarction and its healing post infarction. Analytical and computational models that provide insight into the functional consequences of myocardial infarction are discussed along with potential therapies. Finally, there is discussion of emerging models of wound healing and growth and remodeling in the myocardium. The final chapter discusses a network approach to modeling the fiber structure in tissues, with particular reference to translating the microscopic behavior

to a macroscopic finite element scheme for networks of macromolecular fibers such as collagen. This chapter provides a basic theoretical framework for studying networks with reference to the computational demands in scaling up from the microscopic to the macroscopic level.

We hope that this volume will be useful not only for those who work in the areas of biomechanics and mechanobiology highlighted above but also for those in other areas such as biomedical engineering, biophysics, mechanical and civil engineering, applied mathematics, physiology, and materials science, who might wish to contribute to this developing subject and tackle some of the challenges it faces. Multiscale approaches and multidisciplinary studies bring together scientists with expertise in novel multiscale modeling, computational analysis, and sophisticated experimentation to determine the influence of the interactions of the structures, biology, chemistry, and mechanics at the different scales. Continuing significant advances in experimental techniques, including imaging, computational methods and computer power and multiscale modeling make this a dynamic and rapidly developing subject which offers many challenges for the future. The contents of this book provide a platform for further developments in this exciting subject.

We would like to express our grateful thanks to the lecturers of the Summer School and the contributors to this book and to Ms. Bettina Strametz for her help with the detailed organization of the Summer School. Finally, we would like to thank Silvia Schilgerius, Senior Publishing Editor of Applied Sciences at Springer, for her encouragement to publish this volume.

Graz, Austria/Trondheim, Norway
Glasgow, UK
May 2016

Gerhard A. Holzapfel
Ray W. Ogden

Contents

Mixture Theory for Modeling Biological Tissues: Illustrations from Articular Cartilage.	1
Gerard A. Ateshian	
A Bio-chemo-mechanical Model for Cell Contractility, Adhesion, Signaling, and Stress-Fiber Remodeling	53
Robert M. McMeeking and Vikram S. Deshpande	
Nonlinear Continuum Mechanics and Modeling the Elasticity of Soft Biological Tissues with a Focus on Artery Walls	83
Ray W. Ogden	
Microstructure and Mechanics of Human Aortas in Health and Disease	157
Gerhard A. Holzapfel	
Arterial and Atherosclerotic Plaque Biomechanics with Application to Stent Angioplasty Modeling	193
Brían L. O'Reilly, Claire Conway, J. Patrick McGarry and Peter E. McHugh	
Biomechanics of Myocardial Ischemia and Infarction	233
Colleen M. Witzenburg and Jeffrey W. Holmes	
Fiber-Network Modeling in Biomechanics: Theoretical and Analytical Approaches.	271
Rohit Y. Dhume and Victor H. Barocas	
Author Index	309
Subject Index	311

Mixture Theory for Modeling Biological Tissues: Illustrations from Articular Cartilage

Gerard A. Ateshian

Abstract Mixture theory has been used for modeling hydrated biological tissues for several decades. This chapter reviews the basic foundation of mixture theory as applied to biphasic mixtures consisting of a porous-permeable deformable solid matrix and an interstitial fluid. Canonical problems of permeation, confined compression, and unconfined compression are analyzed from theory and compared to prior experimental measurements on articular cartilage, with an emphasis on studies that provide validations of theoretical predictions. A brief overview is also provided of the application of mixture theory to solute transport, reactive kinetics, and growth and remodeling.

1 Mixture Theory

Continuum modeling of biological tissues poses a number of challenges related to the structure and composition of these tissues, and their temporal evolution as a result of biological and biochemical processes. Most biological tissues are anisotropic and all soft tissues undergo large deformations. Similarly, most biological tissues are porous and permeable, such that interstitial fluid pressurization and flow may contribute significantly to their mechanics. In many cases, mass transport of soluble species within the interstitial fluid plays an important role in the tissue's metabolic response. Electrically neutral and charged solutes, as well as charged molecular species bound to the solid matrix of biological tissues, may also contribute to osmotic and electrical mechanisms, including pressures, potentials, flows, and currents. Growth mechanisms, remodeling, and degradation all involve chemical reactions that alter composition, ultrastructure and properties of these tissues.

Mixture theory provides a continuum framework for modeling all these mechanisms and phenomena within a self-consistent formulation. For example, the solid matrix of a biological tissue may be modeled as a heterogeneous mixture of solid

G.A. Ateshian (✉)
Columbia University, New York, NY, USA
e-mail: ateshian@columbia.edu

constituents, such as collagen, elastin and charged proteoglycans. Porous tissues may be modeled as a mixture of a fluid and a solid, where the fluid itself may consist of a mixture of a solvent and multiple solutes. Chemical reactions among some or all of these constituents may be incorporated to account for growth, remodeling and degradation.

Mixture theory was initially formulated by Truesdell and Toupin (1960) and further extended by a number of theoreticians in the 1960 and 70s (Eringen and Ingram 1965; Bowen 1968, 1976, 1980; Bedford and Drumheller 1983). The theoretical application of mixture theory to biological tissues started in the mid-1970s (Kenyon 1976) and experimental investigations of biological tissues using this theoretical framework began in earnest in the 1980s, most notably in the studies of articular cartilage by Mow, Lai and co-workers (Mow et al. 1980; Mow and Lai 1980; Lai et al. 1981; Armstrong et al. 1984; Mow et al. 1984, 1989; Mak et al. 1987).

One of the principal challenges in the adoption of mixture theory as a modeling framework for biological tissues has been the apparent complexity of its general formulation, especially when alternative traditional modeling frameworks already exist to describe various phenomena under specialized conditions. As noted by Cowin (2011), most papers that use mixture theory have an unusually large number of equations. Indeed, mixture theory has a steep learning curve and a prospective practitioner must balance the burden of its adoption against its potential benefits.

In this chapter, I hope to present the case for the benefits of using mixture theory, by taking the reader through a narrative of the application and extension of this theory to the study of articular cartilage. This chapter neither provides an exhaustive review of mixture theory, nor a complete review of the cartilage mechanics literature. My primary aim is to illustrate how mixture theory encompasses and combines classical continuum mechanics frameworks and how it may extend those frameworks to accommodate challenges specific to biological tissues, and to demonstrate experimental validations of its theoretical predictions.

2 Mass and Momentum Balance

Mixture theory is notoriously intimidating because it requires the formulation of axioms of mass, momentum, and energy balance for each of the mixture constituents, which may then be summed together to produce equivalent formulations for the mixture as a whole. Since mixture constituents may exchange mass, momentum, and energy with each other, the constituent equations include interaction terms unfamiliar to practitioners of classical continuum theories such as solid or fluid mechanics. In a strict sense, the classical theories represent formulations for pure substances (e.g., a fluid consisting of only one substance). Truesdell conjectured that the mixture as a whole should behave as a pure substance; this principle (which may be considered an axiom of mixture theory) places a constraint on the mass, momentum, and energy exchanges between constituents. Some of these constraints may be accepted intuitively while others may seem unfamiliar in the context of classical continuum

mechanics. Importantly, as reviewed by Bedford and Drumheller (1983), the axiom of entropy inequality may only be applied to the mixture as a whole, or else it would overly constrain the formulation of constitutive relations.

As with all continuum theories of heterogeneous substances, mixture theory assumes that all constituents coexist at every point in the continuum. In practice, this mathematical assumption implies that all constituents coexist in a volume sufficiently small to encompass the relevant microstructure; each point in the continuum thus represents the center of mass of that region.

Each constituent in an unconstrained mixture may move independently of other constituents. The motion of constituent α in the mixture is given by $\chi^\alpha(\mathbf{X}^\alpha, t)$, where t is time and \mathbf{X}^α is the position of a material point of constituent α in the reference configuration of that constituent. In the current configuration at time t , an elemental region whose center of mass is $\mathbf{x} = \chi^\alpha(\mathbf{X}^\alpha, t)$ contains material from all constituents α , each of which may have originated from a different location \mathbf{X}^α in its reference configuration.

It is also possible to consider constrained mixtures where different constituents move together in the current configuration. This type of mixture is most commonly used to model solid constituents (Humphrey and Rajagopal 2002). For example, in biological soft tissues such as vascular wall or elastic cartilage, the extracellular matrix may consist of a constrained mixture of collagen and elastin. Constrained mixtures may also be used to model discrete or continuous fiber distributions, where fiber bundles initially oriented in different directions are treated as distinct constituents α of a constrained solid mixture.

The equations of mass and momentum balance are sufficient to address a broad range of analyses in biological tissue mechanics. These general equations are presented below. The energy balance equations are not reviewed in this chapter, as they are only needed for more specialized analyses, such as those arising in bioheat transfer. The entropy inequality is needed to place constraints on constitutive relations for functions of state, such as the stress, mass supply, and dissipative momentum exchange for each mixture constituent. Since the formulation of these constraints is rather involved, only salient relations are summarized here, with proper references to the prior literature provided for more interested readers.

2.1 Mass Balance

The axiom of mass balance for each constituent α of a mixture is given by

$$\frac{D^\alpha \rho^\alpha}{Dt} + \rho^\alpha \text{div} \mathbf{v}^\alpha = \hat{\rho}^\alpha, \quad (1)$$

where ρ^α is the apparent density of constituent α , \mathbf{v}^α is the velocity of that constituent, and $\hat{\rho}^\alpha$ is the apparent mass density supply to constituent α from all other constituents. The apparent density ρ^α owes its name to the fact that it represents the

mass of constituent α per mixture volume (both taken in the current configuration); similarly, $\hat{\rho}^\alpha$ represents the mass supply to constituent α per mixture volume. Sharing the mixture volume as a common denominator makes it possible to sum these parameters over multiple constituents. The operator $D^\alpha(\bullet)/Dt = \partial(\bullet)/\partial t + \text{grad}(\bullet) \cdot \mathbf{v}^\alpha$ represents the material time derivative in the spatial frame, following constituent α .

The mass balance for the mixture has the familiar form of the mass balance relation for a pure substance, i.e.,

$$\frac{D\rho}{Dt} + \rho \text{div} \mathbf{v} = 0, \quad (2)$$

where ρ is the mixture density and \mathbf{v} is the mixture velocity. The operator $D(\bullet)/Dt$ is the familiar material time derivative in the spatial frame, following the mixture. This equation is obtained by taking the summation of Eq. (1) over all α , defining the relationships

$$\rho = \sum_{\alpha} \rho^{\alpha} \quad (3)$$

for the apparent densities, and

$$\mathbf{v} = \frac{1}{\rho} \sum_{\alpha} \rho^{\alpha} \mathbf{v}^{\alpha} \quad (4)$$

for the velocities, and producing the constraint

$$\sum_{\alpha} \hat{\rho}^{\alpha} = 0, \quad (5)$$

in order to satisfy the requirement that the mixture as a whole behaves as a pure substance. The mixture density ρ represents the mass of all constituents per mixture volume. The mixture velocity \mathbf{v} represents the velocity of the center of mass of the elemental region at \mathbf{x} . Equation (5) simply states that any mass gained by some constituent α must be due to mass lost from other constituents in the mixture. It is an intuitively self-evident requirement in a Newtonian mechanics framework.

2.2 Momentum Balance

The axiom of linear momentum balance for each constituent α is given by

$$\rho^{\alpha} \mathbf{a}^{\alpha} = \text{div} \mathbf{T}^{\alpha} + \rho^{\alpha} \mathbf{b}^{\alpha} + \hat{\mathbf{p}}^{\alpha}, \quad (6)$$

where $\mathbf{a}^{\alpha} = D^{\alpha} \mathbf{v}^{\alpha}/Dt$ is the acceleration of constituent α , \mathbf{b}^{α} represents external body forces per mixture volume acting on constituent α , \mathbf{T}^{α} is the apparent stress in constituent α , and $\hat{\mathbf{p}}^{\alpha}$ is the momentum supply to constituent α due to internal

momentum exchanges with all other constituents in the mixture. The apparent stress owes its name to the fact that the associated traction vector \mathbf{t}^α on a plane with unit normal \mathbf{n} , $\mathbf{t}^\alpha = \mathbf{T}^\alpha \cdot \mathbf{n}$, represents the force vector acting on constituent α per mixture area. Sharing the mixture area as a common denominator makes it possible to sum traction vectors and stresses over multiple constituents. The momentum supply $\hat{\mathbf{p}}^\alpha$ is an internal body force that accounts for momentum exchanges among constituents. These momentum exchanges may conserve or dissipate free energy, depending on the presence of frictional interactions.

The momentum balance for the mixture has the familiar form

$$\rho \mathbf{a} = \operatorname{div} \mathbf{T} + \rho \mathbf{b}, \quad (7)$$

where $\mathbf{a} = D\mathbf{v}/Dt$ is the mixture acceleration, and \mathbf{b} is the mixture body force. This form can be obtained by summing Eq. (6) over all constituents, so that the mixture stress \mathbf{T} is given by

$$\mathbf{T} = \sum_{\alpha} \mathbf{T}^\alpha - \rho^\alpha \mathbf{u}^\alpha \otimes \mathbf{u}^\alpha, \quad (8)$$

where $\mathbf{u}^\alpha = \mathbf{v}^\alpha - \mathbf{v}$ is called the diffusion velocity of constituent α . The resulting constraint on the momentum supplies becomes

$$\sum_{\alpha} \hat{\mathbf{p}}^\alpha + \hat{\rho}^\alpha \mathbf{u}^\alpha = \mathbf{0}. \quad (9)$$

In contrast to the mass balance equation, which produces intuitively self-evident relations between the whole mixture and its individual constituents, the momentum balance introduces less evident relations, such as that for the mixture stress \mathbf{T} in Eq. (8) or the constraint of Eq. (9). The unfamiliar term $-\rho^\alpha \mathbf{u}^\alpha \otimes \mathbf{u}^\alpha$ appearing in Eq. (8) arises simply because $\rho \mathbf{a} \neq \sum_{\alpha} \rho^\alpha \mathbf{a}^\alpha$ in a heterogeneous mixture of unconstrained constituents, neither mathematically nor physically. In the special case of a constrained mixture, where $\mathbf{v}^\alpha = \mathbf{v}$, $\forall \alpha$, this term reduces to zero and the mixture stress equals the sum of constituent stresses, which is intuitively more evident; however, the general case accounts for the fact that mixture constituents may have a nonzero diffusion velocity that contributes a rate of change of linear momentum relative to the center of mass. Similarly, in the absence of mass exchanges ($\hat{\rho}^\alpha = 0$, $\forall \alpha$), Eq. (9) indicates that internal momentum exchanges should cancel out, a familiar concept consistent with Newton's third law of action and reaction. However, in the presence of mass exchanges, such as those resulting from chemical reactions between reactants and products, it is necessary to also account for the momentum loss from decreasing reactant mass and momentum gain from increasing product mass.

The axiom of angular momentum balance reduces to $\mathbf{T}^\alpha - (\mathbf{T}^\alpha)^T = \hat{\mathbf{M}}^\alpha$, where $\hat{\mathbf{M}}^\alpha$ is the skew-symmetric tensor whose dual vector represents the internal angular momentum supply to constituent α due to interactions with all other mixture constituents. Assuming that the mixture as a whole models a nonpolar material, the constraint on this angular momentum exchange reduces to $\sum_{\alpha} \hat{\mathbf{M}}^\alpha = \mathbf{0}$. In applications

of mixture theory to biological tissues, it is most common to also assume that $\hat{\mathbf{M}}^\alpha = \mathbf{0}$, $\forall \alpha$, as there is no compelling physical argument for assuming that individual constituents behave as polar materials.

3 Biphasic Theory

A biphasic material is a binary mixture of a solid and a fluid constituent ($\alpha = s$ and $\alpha = f$). Biphasic theory was formulated for the purpose of modeling biological tissues as porous-permeable deformable media. In this theory each constituent is assumed to be intrinsically incompressible, there are no reactions between the solid and fluid ($\hat{\rho}^\alpha = 0$ for $\alpha = s, f$), and isothermal conditions preclude heat flux. Biphasic theory is most appropriate for modeling biological tissues whose interstitial fluid is mobile, such as cartilage (Mansour and Mow 1976; Mow and Mansour 1977), intervertebral disc (Gu et al. 1999), bone (Gailani et al. 2009), cornea (Bryant and McDonnell 1998), or vascular tissue (Harrison and Massaro 1976; Vargas et al. 1979). The mobility of the interstitial fluid may be tested using permeation experiments, which drive fluid through the tissue under the action of a pressure gradient; or using osmotic loading experiments, which drive fluid into or out of the tissue using osmolarity (chemical) gradients (Bayliss et al. 1986; Schneiderman et al. 1986; Bryant and McDonnell 1998; Azeloglu et al. 2008).

Since water is nearly incompressible under physiological stress magnitudes, it is reasonable to idealize the fluid constituent of a biphasic tissue as intrinsically incompressible. The assumption that the solid matrix may be idealized in this manner must be verified experimentally, for example by measuring its volumetric change under the action of a hydrostatic fluid pressure, as reported for articular cartilage for pressures up to 12 MPa (Bachrach et al. 1998).

By definition, when a constituent is intrinsically incompressible, its true density ρ_T^α (mass of constituent α per volume of that constituent) is invariant in space and time. The apparent and true densities are related by the volume fraction φ^α of the constituent (volume of constituent α per mixture volume) according to $\rho^\alpha = \varphi^\alpha \rho_T^\alpha$. In a saturated mixture (a mixture with no voids), volume fractions satisfy the saturation condition

$$\sum_\alpha \varphi^\alpha = 1. \quad (10)$$

For a biphasic mixture ($\alpha = s, f$), the relation for ρ^α may be substituted into the mass balance of Eq. (1) (with $\hat{\rho}^\alpha = 0$) and the resulting relations for the solid and fluid may be summed, then simplified using Eq. (10) to produce

$$\operatorname{div} \left(\sum_\alpha \varphi^\alpha \mathbf{v}^\alpha \right) = 0. \quad (11)$$

This relation may be viewed as a reformulation of the mass balance for the mixture in the special case when all constituents are intrinsically incompressible.

In mixtures that contain a solid constituent it is natural to define the boundaries of the mixture on the solid. Therefore, the summation appearing inside the divergence operator in Eq. (11) may be rewritten as $\varphi^s \mathbf{v}^s + \varphi^f \mathbf{v}^f = \mathbf{v}^s + \mathbf{w}$, where

$$\mathbf{w} = \varphi^f (\mathbf{v}^f - \mathbf{v}^s) \quad (12)$$

is the volumetric flux of fluid relative to the solid (volume of fluid passing through a cross-section of the mixture perpendicular to the flow, per mixture area, and per time).

3.1 Constitutive Assumptions

The functions of state in a biphasic material are the stresses \mathbf{T}^α , the internal momentum supplies $\hat{\mathbf{p}}^\alpha$, and the mixture free-energy density Ψ_r (free energy of solid and fluid in the current configuration, per volume of the mixture in the reference configuration). By restricting our choice of state variables, we decide which material characteristics we would like to model. In biphasic theory we would like to model the solid constituent as an elastic material, therefore, we include the solid deformation gradient \mathbf{F} as a state variable. We also would like to account for frictional interactions resulting from the relative flow between fluid and solid, and therefore, we also include the diffusion velocities \mathbf{u}^α in our list of state variables. However, we are not interested in the frictional interactions within the fluid (viscosity) because these can be shown to be negligible in comparison to frictional interactions between constituents; therefore, we do not select the rate of deformation of the fluid as a state variable. Similarly, we are not interested in modeling reactions between the fluid and solid, therefore, there is no need to include measures of solid and fluid mass content (such as ρ^α) in the list of state variables.

This list of state variables is substituted into the axiom of entropy inequality by expanding the material time derivative of the free energy using the chain rule of differentiation. The assumption of intrinsic incompressibility of the constituents is introduced using the method of Lagrange multipliers (Lai et al. 1991), by adding the product of Eq. (11) with the multiplier p . The resulting expression for the entropy inequality places the following constraints on the constitutive behavior of the mixture (Ateshian and Ricken 2010), i.e.,

$$\Psi_r = \Psi_r (\mathbf{F}), \quad (13)$$

$$\mathbf{T}^s = (-\varphi^s p - \Psi^f) \mathbf{I} + \frac{1}{J} \frac{\partial \Psi_r}{\partial \mathbf{F}} \cdot \mathbf{F}^T, \quad (14)$$

$$\mathbf{T}^f = (-\varphi^f p + \Psi^f) \mathbf{I}, \quad (15)$$

$$\hat{\mathbf{p}}^s = p \operatorname{grad} \varphi^s + \operatorname{grad} \Psi^f + \hat{\mathbf{p}}_d^s, \quad (16)$$

$$\hat{\mathbf{p}}^f = p \operatorname{grad} \varphi^f - \operatorname{grad} \Psi^f + \hat{\mathbf{p}}_d^f, \quad (17)$$

$$\sum_{\alpha} \hat{\mathbf{p}}_d^{\alpha} \cdot \mathbf{u}^{\alpha} \leq 0, \quad (18)$$

where Ψ^f is the free-energy density in the fluid (free energy per volume in the current configuration) and $\hat{\mathbf{p}}_d^{\alpha}(\mathbf{F}, \mathbf{u}^s, \mathbf{u}^f)$ is the dissipative part of the internal momentum supply to constituent α . The expression of Eq. (18) is called the dissipation inequality (Coleman and Noll 1963), as it represents the dissipation of free energy due to frictional interactions between the mixture constituents.

Equation (13) shows that the mixture free energy density only depends on the solid deformation. Equations (14) and (15) provide the general relations between constituent stresses and free-energy densities, which require functional expressions for both Ψ_r and Ψ^f . Conveniently, the dependence on Ψ^f goes away when we sum the solid and fluid stresses and make use of the saturation condition in Eq. (10),

$$\mathbf{T}^I \equiv \sum_{\alpha} \mathbf{T}^{\alpha} = -p\mathbf{I} + \frac{1}{J} \frac{\partial \Psi_r}{\partial \mathbf{F}} \cdot \mathbf{F}^T, \quad (19)$$

where \mathbf{T}^I is called the inner part of the mixture stress. Thus, only a formulation for Ψ_r is needed to evaluate the constitutive relation for the mixture stress. This expression also shows that the scalar multiplier p in the isotropic stress contribution, $-p\mathbf{I}$, represents the pressure in the interstitial fluid, since the remaining term only depends on the solid deformation. The convenience of using \mathbf{T}^I instead of \mathbf{T}^s implies that the mixture linear momentum balance in Eq. (7) is a more convenient alternative to the solid linear momentum balance in Eq. (6). Substituting the relations of Eqs. (15) and (17) into the fluid linear momentum balance in Eq. (6) produces

$$\rho^f \mathbf{a}^f = -\varphi^f \operatorname{grad} p + \rho^f \mathbf{b}^f + \hat{\mathbf{p}}_d^f, \quad (20)$$

which conveniently does not include Ψ^f either. Therefore, this reduced form of the fluid linear momentum balance may be used, together with the mixture momentum balance, to solve problems in the biphasic theory. Alternatively, we may assume constitutively that $\Psi^f = 0$ on the basis that the free energy in the fluid is already represented by the pressure p , as a proxy to free energy resulting from dilatation. In that case, we recover the earlier biphasic theory formulation of Mow and co-workers (Mow et al. 1980; Holmes 1985).

Similarly, summing Eqs. (16) and (17) and making use of Eq. (9) in the absence of mass exchanges, along with Eq. (10), produces

$$\sum_{\alpha} \hat{\mathbf{p}}^{\alpha} = \sum_{\alpha} \hat{\mathbf{p}}_d^{\alpha} = \mathbf{0}. \quad (21)$$

This relation shows that the dissipative part of internal momentum supplies satisfy the same constraint as the more general term. Combining the dissipation inequality of Eq. (18) with the constraint of Eq. (21) shows that the general form for $\hat{\mathbf{p}}_d^\alpha$ is (Lai et al. 1991; Ateshian 2007)

$$\mathbf{p}_d^\alpha = \sum_{\beta \neq \alpha} \mathbf{f}^{\alpha\beta} \cdot (\mathbf{u}^\beta - \mathbf{u}^\alpha), \quad (22)$$

where $\mathbf{f}^{\alpha\beta}$ ($\alpha, \beta = s, f$) are second-order tensors called frictional drag coefficients (Mow et al. 1980; Lai et al. 1991), which satisfy $\mathbf{f}^{\beta\alpha} = \mathbf{f}^{\alpha\beta}$.

For a biphasic mixture these relations reduce to $\hat{\mathbf{p}}_d^f = -\hat{\mathbf{p}}_d^s = \mathbf{f}^{fs} \cdot (\mathbf{v}^s - \mathbf{v}^f)$, where \mathbf{f}^{fs} is a function of $(\mathbf{F}, \mathbf{u}^s, \mathbf{u}^f)$ in general; thus, the dissipative (frictional) momentum exchange between fluid and solid is proportional to the relative velocity between these constituents. Substituting this expression into the fluid momentum balance in Eq. (20) produces the relation classically described as Darcy's law,

$$\mathbf{w} = -\mathbf{k} \cdot [\text{grad} p + \rho_T^f (\mathbf{a}^f - \mathbf{b}^f)], \quad (23)$$

where

$$\mathbf{k} = (\varphi^f)^2 (\mathbf{f}^{fs})^{-1} \quad (24)$$

is called the hydraulic permeability tensor. The relation of Eq. (23) relates the relative fluid flux to its driving forces, namely, the gradient in fluid pressure and the difference of inertia and body forces. In general, the permeability tensor \mathbf{k} may depend on the state variables $(\mathbf{F}, \mathbf{u}^s, \mathbf{u}^f)$; in a strict sense, Darcy's law is recovered when \mathbf{k} is constant. Darcy's law was originally formulated as a phenomenological relation in porous media; mixture theory shows that it derives from the momentum balance for the fluid constituent.

In practice, problems in biphasic theory may be solved by adopting several additional simplifications applicable to biological tissues. First, inertial effects are typically neglected relative to other terms in the linear momentum balance, since they are relevant mostly in wave propagation problems, where the assumption of intrinsic incompressibility of the constituents would not be valid; thus, acceleration terms involving \mathbf{a}^α are dropped out of those equations. Second, the diffusive terms $-\rho^\alpha \mathbf{u}^\alpha \otimes \mathbf{u}^\alpha$ in Eq. (8) for the mixture stress are typically neglected in comparison to the stresses \mathbf{T}^α , as may be verified from an order of magnitude analysis using typical stress, diffusive velocity, and apparent density magnitudes expected to arise in biological tissues; thus, the mixture stress and its inner part are assumed to be the same, $\mathbf{T} \approx \mathbf{T}^I$. Finally, external body forces \mathbf{b}^α (typically representing gravity) are only relevant in specific applications. Consequently, the most common usage of biphasic theory employs the simplified expressions

$$\text{div} \mathbf{T} = \mathbf{0}, \quad (25)$$

for the mixture momentum balance,

$$\operatorname{div}(\mathbf{v}^s + \mathbf{w}) = 0, \quad (26)$$

for the mixture mass balance, and

$$\mathbf{w} = -\mathbf{k} \cdot \operatorname{grad} p, \quad (27)$$

for the fluid momentum balance (Darcy's law).

The expression for \mathbf{T} is approximated by \mathbf{T}^l in Eq. (19), which may be rewritten as

$$\mathbf{T} = -p\mathbf{I} + \mathbf{T}^e, \quad (28)$$

where

$$\mathbf{T}^e = \frac{1}{J} \frac{\partial \Psi_r}{\partial \mathbf{F}} \cdot \mathbf{F}^T \quad (29)$$

is the stress resulting from solid matrix strain. This equation requires the formulation of a constitutive relation for $\Psi_r(\mathbf{F})$. A constitutive relation is also needed to describe the dependence of \mathbf{k} on \mathbf{F} (its dependence on \mathbf{u}^s and \mathbf{u}^f is neglected in practice). The solid deformation gradient is uniquely related to the solid displacement \mathbf{u} via $\mathbf{F} = \mathbf{I} + \operatorname{Grad} \mathbf{u}$, where $\operatorname{Grad} \mathbf{u} = \partial \mathbf{u} / \partial \mathbf{X}^s$ and \mathbf{I} is the identity tensor. The solid velocity is also uniquely related to the displacement via $\mathbf{v}^s = D^s \mathbf{u} / Dt$. Therefore, the unknowns in a biphasic analysis are \mathbf{u} and p , which may be solved from Eqs. (25) and (26), using the relation of Eq. (27).

Many biological tissues undergo large deformations under normal physiological conditions. Similarly, the solid matrix of many biological tissues exhibits anisotropy, such that the constitutive relations for $\Psi_r(\mathbf{F})$ and $\mathbf{k}(\mathbf{F})$ need to account for physiologically relevant material symmetries. Therefore, it is often necessary to solve these biphasic equations using numerical schemes, such as the finite element method (Spilker et al. 1992; Maas et al. 2012), that facilitate the solution of the resulting nonlinear equations.

Nevertheless, much insight may be gained into the response of biphasic materials by obtaining analytical solutions under infinitesimal strains and rotations, assuming that the solid matrix is isotropic. Under these conditions, the deformation gradient simplifies to $\mathbf{F} \approx \mathbf{I} + \boldsymbol{\epsilon}$, where $\boldsymbol{\epsilon} = (\operatorname{grad} \mathbf{u} + \operatorname{grad}^T \mathbf{u}) / 2$ is the infinitesimal strain tensor and $\boldsymbol{\omega} = (\operatorname{grad} \mathbf{u} - \operatorname{grad}^T \mathbf{u}) / 2$ is related to the infinitesimal rotation tensor, with $\operatorname{grad} \mathbf{u} = \partial \mathbf{u} / \partial \mathbf{x}$ representing the spatial gradient of the solid displacement. Under infinitesimal strains and the constraint of frame invariance, the relation of (29) simplifies to $\mathbf{T}^e = \partial \Psi_r / \partial \boldsymbol{\epsilon}$. The solid matrix may thus be modeled using Hooke's law for isotropic elastic solids, i.e.,

$$\Psi_r(\boldsymbol{\epsilon}) = \frac{\lambda_s}{2} (\operatorname{tr} \boldsymbol{\epsilon})^2 + \mu_s \operatorname{str} \boldsymbol{\epsilon}^2, \quad (30)$$

where the material constants λ_s and μ_s are the Lamé coefficients for the solid. It follows from this relation that

$$\mathbf{T} = -p\mathbf{I} + \lambda_s(\text{tr}\boldsymbol{\epsilon})\mathbf{I} + 2\mu_s\boldsymbol{\epsilon}. \quad (31)$$

The simplest model for permeability assumes that it is isotropic and strain independent,

$$\mathbf{k} = k\mathbf{I}, \quad (32)$$

where k is a scalar material constant.

3.2 Boundary Conditions

Boundary conditions are formulated by satisfying axioms of mass, momentum, and energy balance across interfaces in the mixture. Interfaces could represent external boundaries of the mixture, or they may separate two regions of interest within the mixture with a surface Γ . If this interface Γ is an idealization of a material surface (such as a thin membrane idealized as a mathematical surface), the interface conditions need to allow for mass, momentum, or energy jumps across that surface (e.g., surface tension in the membrane embodies a momentum jump). The boundary conditions presented here apply to immaterial interfaces, such as boundaries of a biphasic tissue with its surrounding environment, or boundaries between adjacent elements in a finite element mesh of a biphasic material.

3.2.1 Mass Balance

Since there are two sides across an interface Γ , we may denote them with $+$ and $-$. The outward unit normal to the $+$ side is \mathbf{n}_+ and that of the $-$ side is \mathbf{n}_- , such that $\mathbf{n}_- = -\mathbf{n}_+$. Assuming that each constituent is intrinsically incompressible and that there are no reactions exchanging mass at the interface, the axiom of mass balance for constituent α across Γ requires that

$$\varphi_+^\alpha (\mathbf{v}_+^\alpha - \mathbf{v}_\Gamma) \cdot \mathbf{n}_+ + \varphi_-^\alpha (\mathbf{v}_-^\alpha - \mathbf{v}_\Gamma) \cdot \mathbf{n}_- = 0, \quad (33)$$

where the subscripts $+$ and $-$ represent quantities on either side of the interface and \mathbf{v}_Γ is the velocity of the interface Γ (Eringen and Ingram 1965; Ateshian 2007). This expression summarizes the requirement that the volumetric flux of constituent α normal to the interface must be continuous across Γ . For convenience, let us define $\mathbf{n} \equiv \mathbf{n}_+$ and $\llbracket f \rrbracket \equiv f_+ - f_-$ for any argument f , so that Eq. (33) may be rewritten in a less cluttered form as

$$\llbracket \varphi^\alpha (\mathbf{v}^\alpha - \mathbf{v}_\Gamma) \rrbracket \cdot \mathbf{n} = 0. \quad (34)$$

In a biphasic material, the interface Γ is typically defined to follow the motion of the solid matrix, since the boundaries of a biphasic tissue are those of the solid. In those cases we let $\mathbf{v}_\Gamma \cdot \mathbf{n} = \mathbf{v}^s \cdot \mathbf{n}$ and we may examine boundary conditions for three typical situations: At the interface between a biphasic material and a pure fluid ($\varphi^s = 0$ and $\varphi^f = 1$), the jump condition of Eq. (33) as applied to $\alpha = f$ produces $\varphi^f (\mathbf{v}^f - \mathbf{v}^s) \cdot \mathbf{n} = (\mathbf{v} - \mathbf{v}^s) \cdot \mathbf{n}$, where \mathbf{v} is the velocity of the pure fluid. This expression may be rearranged as

$$(\mathbf{v}^s + \mathbf{w}) \cdot \mathbf{n} = \mathbf{v} \cdot \mathbf{n}. \quad (35)$$

At the interface between two biphasic materials, the jump condition for the fluid reduces to $[\![\varphi^f (\mathbf{v}^f - \mathbf{v}^s)]\!] \cdot \mathbf{n} = 0$, indicating that the volumetric fluid flux across the boundary is continuous, which may be rewritten as

$$[\![\mathbf{w}]\!] \cdot \mathbf{n} = 0. \quad (36)$$

In this case, since $\mathbf{v}_\Gamma \cdot \mathbf{n}$ is the same on both sides of Γ , it also follows that the normal component of the solid velocity must be continuous across Γ ,

$$[\![\mathbf{v}^s]\!] \cdot \mathbf{n} = 0. \quad (37)$$

Finally, at the interface of a biphasic material and a pure solid ($\varphi^s = 1$ and $\varphi^f = 0$), Eq. (34) applied to $\alpha = f$ reduces to $\varphi^f (\mathbf{v}^f - \mathbf{v}^s) \cdot \mathbf{n} = 0$, implying that the fluid on the biphasic side may not flow across the interface Γ ; equivalently,

$$\mathbf{w} \cdot \mathbf{n} = 0. \quad (38)$$

Note that there is no requirement imposed by the mass balance condition on tangential components of the constituent velocities. Jump conditions on tangential components may only be prescribed using constitutive assumptions. For example, the tangential jump condition for the solid velocity between two adherent biphasic materials (a constitutive assumption) requires that $(\mathbf{I} - \mathbf{n} \otimes \mathbf{n}) \cdot [\![\mathbf{v}^s]\!] = \mathbf{0}$. This assumption, combined with the mass balance jump condition of Eq. (37), produces $[\![\mathbf{v}^s]\!] = \mathbf{0}$ in the case of adhesive biphasic interfaces.

3.2.2 Momentum and Energy Balance

For an immaterial interface Γ , the jump condition on the momentum balance for the mixture reduces to (Eringen and Ingram 1965; Ateshian 2007)

$$[\![\mathbf{T}]\!] \cdot \mathbf{n} = \mathbf{0}. \quad (39)$$

This condition is equivalent to requiring that the mixture traction vector, $\mathbf{t} = \mathbf{T} \cdot \mathbf{n}$, be continuous across Γ . Letting \mathbf{T} be given by the expression of Eq. (28), we may

also write $\mathbf{t} = -p\mathbf{n} + \mathbf{t}^e$, where $\mathbf{t}^e = \mathbf{T}^e \cdot \mathbf{n}$ is the traction resulting from the solid matrix strain.

The jump conditions for the momentum balance of the solid and fluid constituents involve the jump in internal momentum supply to these constituents. Similar to the expressions of Eqs. (16) and (17), these momentum jumps may not be defined uniquely without further constitutive assumptions. Therefore, to complete the set of boundary conditions, we must turn to the jump condition derived from the energy balance for the fluid constituents (Ateshian 2007), which reduces to $[\tilde{\mu}^f] = 0$, where $\tilde{\mu}^f$ is the mechano-electrochemical potential of the fluid (in units of energy per mass). In the case of a biphasic material, the fluid is a pure substance (e.g., water) which is electrically neutral, implying that its chemical and electrical potentials are constants that may be set to zero with no loss of generality. In this case, $\tilde{\mu}^f = p/\rho_T^f$ and the jump condition arising from the fluid energy balance reduces to

$$[p] = 0, \quad (40)$$

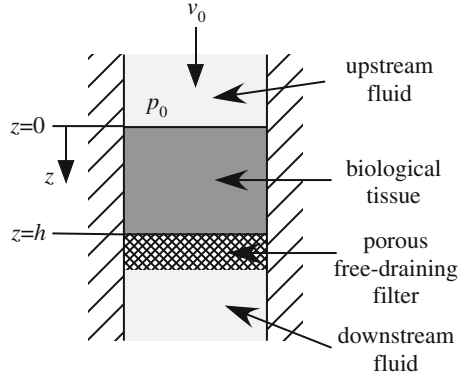
since ρ_T^f is invariant for intrinsically incompressible constituents. This jump condition implies that the interstitial fluid pressure p of a biphasic material is continuous across the interface Γ . If there is no fluid on either side of Γ , the jump condition of Eq. (40) does not apply.

3.3 Permeation

Permeation is a canonical problem for biphasic materials, since it analyzes the transport of interstitial fluid through the porous solid matrix and provides a direct measure of the hydraulic permeability k . Permeation experiments are typically performed on a disk of tissue constrained within a tube with a rigid impermeable inner wall (Fig. 1). The tissue specimen is placed against a free-draining rigid porous filter downstream of the flow. Optionally, the specimen is clamped upstream as well, using another similar filter, to a predetermined compressive strain. Either a known fluid pressure is prescribed upstream (e.g., using a column of fluid), or a known fluid velocity (e.g., using a syringe pump). Permeation experiments are notoriously challenging because of the risk of leakage around the tissue specimen, which may confound the true measurement of the tissue permeability. Another common challenge is that these types of experiments may take a long time to equilibrate to a steady-state response; therefore, premature termination of the experiment may produce an unreliable measure of k .

An analytical solution to the permeation problem may help identify the conditions that alleviate some of these challenges, and may assist in interpreting the results. For a permeation problem along the z -direction as shown in Fig. 1, a cylindrical coordinate system is adopted. For the one-dimensional axisymmetric conditions of this configuration, the only nonzero components of the displacement and fluid flux vectors, \mathbf{u} and \mathbf{w} , are u_z and w_z , respectively, and the dependent variables are only functions of z and t . Under these conditions, the mass balance in Eq. (26) reduces to

Fig. 1 Permeation through a biological tissue



$$\frac{\partial}{\partial z} \left(\frac{\partial u_z}{\partial t} + w_z \right) = 0. \quad (41)$$

The fluid momentum balance in Eq. (27) simplifies to

$$w_z = -k \frac{\partial p}{\partial z}, \quad (42)$$

and the mixture momentum in Eq. (25), combined with the constitutive relation in Eq. (31), produces

$$-\frac{\partial p}{\partial z} + H_A \frac{\partial^2 u_z}{\partial z^2} = 0, \quad (43)$$

where $H_A = \lambda_s + 2\mu_s$ is the aggregate modulus. Upstream, at $z = 0$, the boundary conditions reduce to

$$\frac{\partial u_z}{\partial t} + w_z \Big|_{z=0} = v_a(t), \quad p(0, t) = p_a(t), \quad T_{zz}^e(0, t) = H_A \frac{\partial u_z}{\partial z} \Big|_{z=0} = 0, \quad (44)$$

where $v_a(t)$ is the flow velocity upstream of the tissue sample and $p_a(t)$ is the upstream pressure (Fig. 1). Downstream, at $z = h$, boundary conditions reduce to

$$\begin{aligned} u_z(h, t) &= 0, & \frac{\partial u_z}{\partial t} + w_z \Big|_{z=h} &= v_a(t), \\ p(z, t) &= 0, & T_{zz}^e(h, t) &= H_A \frac{\partial u_z}{\partial z} \Big|_{z=h} = \sigma_a(t), \end{aligned} \quad (45)$$

where σ_a is the normal traction component between the tissue sample and the porous filter. Here, we have made implicit use of the equation of continuity of mass for the fluid entering and leaving the biphasic tissue, by requiring that the upstream and downstream fluid velocities both be given by v_a . We also assume that because

the porous filter is free-draining, the downstream pressure is equal to zero, representing atmospheric pressure. It should be appreciated that if v_a is known a priori, the upstream pressure p_a and downstream traction σ_a can be determined a posteriori upon completion of the analysis. Integrating the mass balance in Eq. (41) with respect to z , and using the boundary condition either at $z = 0$ or at $z = h$, produces

$$w_z = v_a(t) - \frac{\partial u_z}{\partial t}. \quad (46)$$

By eliminating $\partial p / \partial z$ from Eqs. (42) and (43) and using (46), we find that

$$H_A k \frac{\partial^2 u_z}{\partial z^2} - \frac{\partial u_z}{\partial t} + v_a(t) = 0. \quad (47)$$

This is a partial differential equation in the unknown $u_z(z, t)$ alone. Once solved, the fluid pressure can be obtained from the integration of Eq. (43) with respect to z , making use of the boundary condition of Eq. (45),

$$p(z, t) = H_A \left(\frac{\partial u_z}{\partial z} \Big|_z - \frac{\partial u_z}{\partial z} \Big|_{z=h} \right). \quad (48)$$

3.3.1 Steady-State Permeation

The steady-state response may be obtained from these equations by letting $\partial u_z / \partial t = 0$ and $v_a = v_0 = \text{constant}$. The mathematical steps leading to the solution are left to the reader. The solution for the steady-state axial displacement is given by

$$u_z(z) = \frac{v_0 h^2}{2 H_A k} \left(1 - \frac{z^2}{h^2} \right), \quad (49)$$

whereas that for the fluid pressure is

$$p(z) = \frac{v_0 h}{k} \left(1 - \frac{z}{h} \right). \quad (50)$$

Since the pressure varies linearly with z , it can be concluded that the pressure gradient is uniform through the thickness of the tissue sample at steady state. From this expression, it is now possible to determine the upstream fluid pressure at $z = 0$,

$$p_0 = \frac{v_0 h}{k}. \quad (51)$$

From an experimental perspective this is an important result because it shows that the permeability can be determined from the measurement of p_0 and the knowledge of v_0 and h , using $k = v_0 h / p_0$. This result can also be substituted into the solution for

u_z in Eq. (49) to express the solid matrix displacement as a function of the upstream fluid pressure p_0 ,

$$\frac{u_z(z)}{h} = \frac{p_0}{2H_A} \left(1 - \frac{z^2}{h^2} \right). \quad (52)$$

The normal traction at the interface between the tissue and the porous filter is then found to equal the upstream pressure in magnitude, $\sigma_a = -p_0$. The normal strain in the axial z -direction is obtained from the slope of the displacement, and is found to vary linearly through the depth, i.e.,

$$\varepsilon_{zz} = \frac{du_z}{dz} = -\frac{v_0}{H_A k} z = -\frac{p_0}{H_A} \frac{z}{h}. \quad (53)$$

The results of this steady-state permeation problem show that the pressure decreases linearly from p_0 upstream to 0 downstream (Fig. 2a). The magnitude of the upstream pressure is directly proportional to the fluid perfusion velocity and sample thickness, and inversely proportional to the permeability. As the fluid flows through the tissue, a drag-induced compaction occurs, as indicated by the displacement profile (Fig. 2b). As a result, the height or thickness of the sample is reduced by a magnitude of $p_0 h / 2H_A$. This compaction is nonuniform, with the axial normal strain starting at zero upstream, where the fluid pressure is highest, and increasing linearly in magnitude with depth, achieving its highest value at the interface with the porous filter, where the fluid pressure is smallest (Fig. 2c). The maximum strain, which is compressive, is given by $-p_0 / H_A$; clearly, for the above small strain solution to remain valid, the upstream pressure p_0 must remain small relative to the tissue aggregate modulus H_A .

When the axial normal strain (or, more strictly, the dilatation) changes in magnitude as shown in Fig. 2c, the assumption that the permeability remains constant may not necessarily be valid experimentally and the above solution may need to be

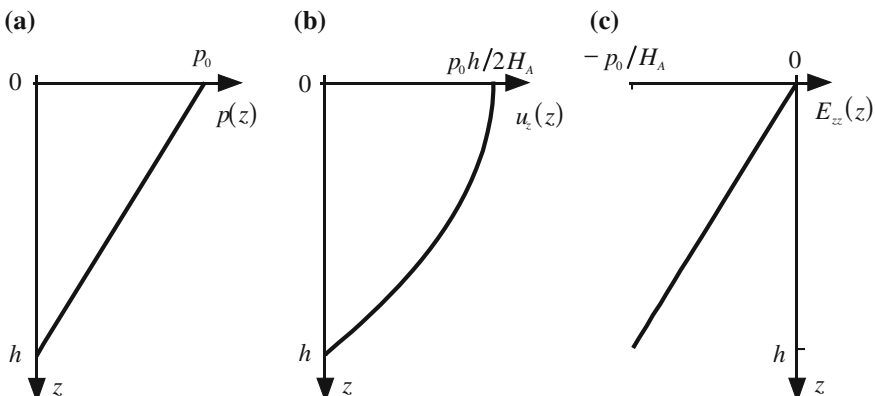


Fig. 2 Solution of steady-state permeation analysis, presented as a function of the depth coordinate z

reevaluated using a strain-dependent permeability function. However, it is of interest that the above solution is in agreement with Darcy's law, as long as the permeability is assumed constant, considering that Darcy's law does not address the deformation of porous materials.

As a practical matter, in permeation experiments, the tissue sample needs to fit tightly within the side wall of the test chamber to avoid compromising side leakage. This is sometimes achieved by osmotically swelling the sample after it has been placed in the test chamber, but more frequently a clamping strain is applied onto the sample via a second rigid porous filter placed upstream. (Oversizing the tissue sample relative to the diameter of the chamber and press-fitting it in place is generally a less successful option, whereas, the use of glue should be avoided due to seepage into the tissue.) The analysis of a clamped sample would be similar to the above, although the boundary conditions for the displacement function would be different.

As a final remark, the expression of Eq. (51) can be rewritten as

$$\frac{p_0}{H_A} = \frac{v_0}{H_A k / h}, \quad (54)$$

from which it can be construed that just as H_A may represent a characteristic measure of the stress in the tissue, so is $H_A k / h$ a characteristic measure of the interstitial fluid velocity. For example, in articular cartilage, typical values of $H_A \sim 0.5 \text{ MPa}$, $k \sim 10^{-3} \text{ mm}^4/\text{N}\cdot\text{s}$, and $h \sim 2 \text{ mm}$ produce a characteristic velocity of $0.25 \mu\text{m}/\text{s}$. If the perfusion velocity is much smaller than this characteristic value, the upstream pressure acting upon the tissue sample will be negligible compared to H_A . Conversely, if v_0 approaches this characteristic value, then p_0 becomes nonnegligible relative to the aggregate modulus. Such analyses are helpful when designing an experimental apparatus and deciding upon the full scale range of the instrumentation, such as pressure transducers or syringe pumps. Since v_0 is the convective velocity of the interstitial fluid whereas $H_A k / h$ is its characteristic diffusive velocity through the mixture, the ratio of these two quantities is the nondimensional Peclet number for interstitial fluid flow through the tissue, i.e.,

$$P_e^w = \frac{v_0 h}{H_A k}. \quad (55)$$

Usually, the Peclet number is invoked for transport of solutes in a solution (as the ratio of convective to diffusive velocities) or for heat transfer (as the ratio of forced convection to heat conduction). Here, we see that it is also applicable to fluid transport in porous media. Since $P_e^w = p_0 / H_A$ in this problem, and since we already explained that p_0 should remain small compared to H_A in order to keep the compressive strains small, it follows that P_e^w should also remain small compared to unity. In practice, $P_e^w \lesssim 0.2$ is acceptable.

3.3.2 Transient Permeation

Permeation experiments on many biological tissues typically require a long time to achieve the steady-state response described in the previous section, because of the very low permeability of these tissues. To estimate the length of time required to achieve steady state, it is necessary to solve for the transient response of $u_z(z, t)$, either in response to a step increase in the perfusion velocity, $v_a(t) = v_0 H(t)$, or a step increase in upstream fluid pressure, $p_a(t) = p_0 H(t)$. The mathematical details for deriving the transient solutions for these two cases are not provided here, though they are readily solved by standard methods for linear second-order partial differential equations with constant coefficients.

When the velocity is prescribed upstream, the solution for $u_z(z, t)$ is

$$\frac{u_z(z, t)}{h} = P_e^w \left[\frac{1}{2} \left(1 - \frac{z^2}{h^2} \right) + \frac{2}{\pi^3} \sum_{n=1}^{\infty} \frac{(-1)^n}{(n - \frac{1}{2})^3} \cos \left[\left(n - \frac{1}{2} \right) \pi \frac{z}{h} \right] e^{-\left(n - \frac{1}{2} \right)^2 \pi^2 \frac{t}{\tau}} \right], \quad (56)$$

where the Peclet number P_e^w is given in Eq. (55) and

$$\tau = h^2 / H_A k \quad (57)$$

may be called the gel time constant. The axial normal strain is then given by $\varepsilon_{zz} = \partial u_z / \partial z$, and the fluid pressure may be obtained from Eq. (48). In particular, the upstream pressure at $z = 0$ is given by

$$\frac{p_a(t)}{H_A} = \frac{p(0, t)}{H_A} = P_e^w \left[1 - \frac{2}{\pi^2} \sum_{n=1}^{\infty} \frac{1}{(n - \frac{1}{2})^2} e^{-\left(n - \frac{1}{2} \right)^2 \pi^2 \frac{t}{\tau}} \right]. \quad (58)$$

Since the exponential term in these expressions will decay to zero as time increases to infinity, it is easy to see that these equations reduce to the steady-state solutions presented in the previous section. The complete transient response of the upstream fluid pressure $p_a(t)$, normalized by its steady-state value, is plotted in Fig. 3a as a function of normalized time. The pressure is found to increase monotonically with time.

Let us address the question that first motivated this analysis: How long will it take for the response to reach a steady state after initiation of the experiment? The easiest way to address this question is to analyze the solution for the upstream pressure in Eq. (58), since this pressure is typically measured in a permeation experiment where $v_a(t)$ is prescribed. Initially, at $t = 0$, this pressure is equal to zero. The steady-state solution for the upstream pressure is $p_a(t \rightarrow \infty) / H_A = P_e^w$; in theory, according to the solution, it will take an infinite amount of time to reach this steady-state value. In practice however, we would be satisfied to stop the experiment after this upstream pressure has reached perhaps 95% of its steady-state value. The characteristic time

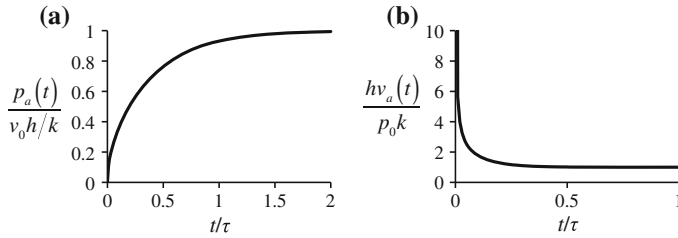


Fig. 3 **a** Transient response of the upstream pressure $p_a(t)$ in a permeation experiment under a prescribed fluid velocity $v_a(t) = v_0 H(t)$. **b** Transient response of the fluid velocity $v_a(t)$ across the tissue sample in a permeation experiment with a prescribed upstream fluid pressure $p_a(t) = p_0 H(t)$. The gel time constant τ is given in Eq. (57)

constant for the increase in pressure can be deduced by looking at the first two terms of the infinite series in Eq. (58). The time constants for these exponential functions are given by

$$\tau_1 = \frac{4}{\pi^2} \tau, \quad \tau_2 = \frac{4}{9\pi^2} \tau. \quad (59)$$

Since τ_2 is nine times smaller than τ_1 , the response is clearly dominated by τ_1 . A simple numerical calculation shows that the solution has reached 95 % of its steady-state value when

$$0.95 \approx 1 - \frac{8}{\pi^2} e^{-\frac{\pi^2}{4} \frac{t}{\tau}} \quad \text{or} \quad t_{0.95} \approx \tau. \quad (60)$$

This calculation shows that the gel time constant τ provides a good estimate of the time required to nearly reach steady state. In Sect. 3.3.1 typical values of H_A , k and h were suggested for articular cartilage. Using these values, we find $t_{0.95} \approx 8000 \text{ s} \approx 2 \text{ h } 13 \text{ m}$, which confirms that permeation experiments can be time-consuming. Since the time constant is proportional to h^2 , this time may be reduced by a factor of four if the specimen thickness is halved.

When the fluid pressure is prescribed upstream, the solution for $u_z(z, t)$ is

$$\frac{u_z(z, t)}{h} = \frac{p_0}{2H_A} \left(1 - \frac{z^2}{h^2} - \frac{4}{\pi^2} \sum_{n=1}^{\infty} \frac{1}{n^2} \left[1 - (-1)^n \cos \frac{n\pi z}{h} \right] e^{-n^2 \pi^2 \frac{t}{\tau}} \right), \quad (61)$$

and the resulting fluid velocity across the tissue sample is

$$\frac{h}{p_0 k} v_a(t) = 1 + 2 \sum_{n=1}^{\infty} e^{-n^2 \pi^2 \frac{t}{\tau}}. \quad (62)$$

Interestingly, we find that the initial velocity at $t = 0^+$ is infinite, but eventually reduces to $p_0 k / h$ (Fig. 3b). This infinite value (which occurs because inertial effects are neglected) arises from the fact that the initial fluid pressure $p(z, 0^+)$ increases to

p_0 instantaneously throughout the tissue thickness, $0 \leq z < h$, except at the downstream porous filter ($z = h$) where the pressure must be zero according to the downstream boundary condition. Therefore, for an infinitesimal amount of time, there exists an infinite pressure gradient $\text{grad} p$ at $z = h$ that produces an infinite fluid flux $w_z = -k \text{ grad} p$ at a fixed boundary where $\partial u_z / \partial t = 0$.

The dominant time constant in the exponential decay of $v_a(t)$ corresponds to $n = 1$ in Eq. (62), and is given by $\tau_1 = \tau/\pi^2$. This value is four times smaller than in the permeation problem with a prescribed upstream velocity, Eq. (59). Therefore, it is more expedient to perform experiments with a prescribed upstream pressure than a prescribed upstream velocity, as is also evident from a comparison of transient responses in Fig. 3a, b.

3.3.3 Experimental Validations of Permeation

Permeation experiments have been reported for a number of connective soft tissues such as articular cartilage (Mansour and Mow 1976), intervertebral disc (Gu et al. 1999), and ligament (Weiss and Maakestad 2006), as well as for vascular tissue (Harrison and Massaro 1976; Vargas et al. 1979) and hydrogels, such as alginate and agarose (Albro et al. 2007, 2010). Since these experiments aimed to characterize the hydraulic permeability k of these tissues, they all focused on analyzing the steady-state response to a prescribed fluid pressure or velocity. By varying the clamping strain across the tissue specimen, they reported the strain-dependent characteristic of k , typically exhibiting an exponential decrease with increasing compressive strain magnitude. Therefore, other than confirming that these tissues were permeable to their interstitial fluid, these studies did not provide direct validations of the biphasic theory from permeation analyses.

Since limited experimental data have been published for transient permeation, we provide an experimental data set obtained from the permeation study of Albro et al. (2010) on agarose hydrogels. A disk of Type VII agarose (9 % w/v, 1.5 mm thick) was clamped at 15 % compressive strain and subjected to an upstream fluid pressure of $p_0 = 7.4 \text{ kPa}$ using a fluid column. The volumetric flow rate of fluid transporting across the gel was determined using time-lapse photography of the fluid meniscus formed in a capillary tube connected to the downstream side of the flow chamber. Experimental results reported in Fig. 4 show that the fluid flux decreased with time, consistent with the theoretical prediction reported in Fig. 3b. The permeability extracted from the steady-state fluid flux using Eq. (51) was $k = 3.4 \times 10^{-3} \text{ mm}^4/\text{N} \cdot \text{s}$. The aggregate modulus was then obtained from a single-parameter fit of the transient response, producing $H_A = 35 \text{ kPa}$. For comparison purposes, direct measurements of H_A for the same type and concentration of agarose exhibited a strong dependence on compressive strain, decreasing exponentially from $203 \pm 8 \text{ kPa}$ in the limit of 0 % compression, down to $58 \pm 0 \text{ kPa}$ at 15 % compression. Therefore, under a clamping strain of 15 %, the best-fit value for H_A obtained from the permeation analysis was reasonably consistent with direct measurements, especially when we recall that permeation produces a nonuniform compressive strain

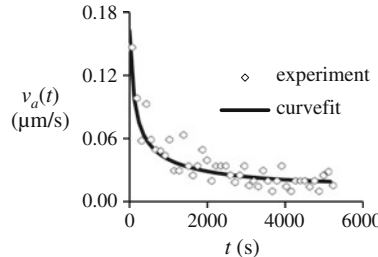


Fig. 4 Experimental results and theoretical curve fit of the fluid flux, using $v_a(t)$ in Eq. (62), in a permeation experiment performed on an agarose disk with $h = 1.5$ mm, under a prescribed fluid pressure $p_0 = 7.4$ kPa. Unpublished raw data is from the study reported by Albro et al. (2010)

distribution within the tissue sample as shown in Eq. (53) and Fig. 2. Thus, assuming linear superposition of the clamping strain and permeation response, the actual compressive strain within the sample at steady state ranged from 15 % upstream to approximately 28 % downstream.

3.4 Confined Compression

Confined compression problems represent some of the simplest problems for which closed-form solutions exist in the biphasic theory. The basic assumption of a confined compression problem is that the kinematics of the solid and fluid constituents are entirely one-dimensional. Typically, a cylindrical tissue sample of radius r_0 and thickness h is placed within a chamber of equal diameter, whose side wall is rigid and impermeable. The bottom of the chamber may be either rigid impermeable or rigid porous and the specimen is loaded with a rigid free-draining porous indenter of diameter equal to that of the chamber, save for a clearance to avoid interference. The free-draining nature of the loading indenter and, optionally, the bottom of the chamber, is necessary to allow fluid to exude from the tissue as it is being compressed (Fig. 5). If these pathways were not provided, the biphasic theory would predict no deformation of the tissue sample since each of the constituents is assumed intrinsically incompressible and the confined nature of the loading would prevent any change in tissue volume. For practical purposes, tissue confinement can only be maintained under axial compression, since tensile loading would reduce the diameter of the cylindrical sample as its lateral surface recedes from the side wall of the chamber, thereby violating the assumption of one-dimensional kinematics. Thus one-dimensional problems of this kind are always understood to be confined *compression*.

If a prescribed static load is applied onto the indenter, the sample will deform under this steady load as the fluid exudes from the tissue. This time-dependent response is known as creep. Conversely, if the deformation of the tissue is prescribed at the

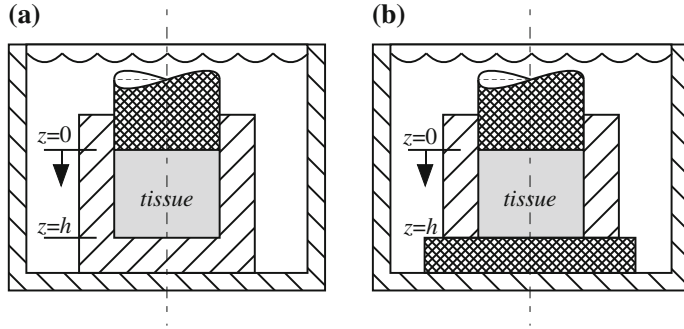


Fig. 5 Confined compression testing configuration. The cylindrical tissue sample is placed in a chamber with rigid impermeable side wall and loaded by a free-draining rigid porous indenter. **a** the bottom of the chamber is rigid impermeable; **b** the bottom of the chamber is free-draining rigid porous

indenter, the reaction force exerted on the indenter by the tissue will rise as long as the deformation is increased, then will relax when the deformation is maintained constant. This time-dependent response is called stress relaxation. Creep and stress relaxation confined compression are easy to implement experimentally and are often used to characterize the material properties of biological tissues which can be modeled with the biphasic theory. Clearly, the loading or deformation prescribed at the indenter can be of a much more general nature than creep or stress relaxation; another popular testing configuration is to prescribe a sinusoidal displacement or load at the indenter and to analyze the response of the tissue under steady state. This dynamic loading, which can yield the frequency response of the tissue, may also be used to extract its material properties.

We assume that the cylindrical tissue sample is homogeneous. The governing equations for a one-dimensional problem are analyzed in cylindrical coordinates, as performed in the permeation analysis presented in Sect. 3.3. Therefore, the governing equations are the same as those presented in Eqs. (41)–(43). For the configuration of Fig. 5a, the boundary conditions at $z = h$ are

$$\left. \frac{\partial u_z}{\partial t} \right|_{z=h} = 0, \quad w_z(z = h, t) = 0, \quad (63)$$

indicating that the solid velocity and relative fluid flux in the axial direction are equal to zero at the bottom of the chamber at all times. These boundary conditions imply that $v_a(t) = 0$ in Eq. (47). Since the displacement of the tissue at the bottom of the chamber is constrained, one of the boundary conditions for this partial differential equation is

$$u_z(z = h, t) = 0. \quad (64)$$

Under the loading indenter, either the displacement or the applied traction may be prescribed. For a displacement-control experiment,

$$u_z(z = 0, t) = u_a(t), \quad (65)$$

where $u_a(t)$ is the prescribed displacement. For a load-control experiment, $T_{zz}(z = 0, t) = \sigma_a(t)$, where $T_{zz} = -p + H_A \partial u_z / \partial z$ is the total axial normal stress and $\sigma_a(t)$ is the prescribed traction, related to the applied load $W(t)$ (assumed positive in compression) through $\sigma_a(t) = -W(t) / \pi r_0^2$. Because the loading indenter is free-draining, the pressure of the interstitial fluid at the top surface of the tissue sample is equal to the pressure of the fluid in the bathing solution. This is taken to be zero gauge pressure,

$$p(z = 0, t) = 0, \quad (66)$$

and thus the load-control boundary condition reduces to

$$H_A \frac{\partial u_z}{\partial z} \Big|_{z=0} = \sigma_a(t). \quad (67)$$

Once the solution for $u_z(z, t)$ has been obtained, the interstitial pressure throughout the tissue sample can be obtained from Eq. (48), which represents the difference in elastic stress between the location where the pressure is sought and the surface under the indenter. Typically, the initial condition on $u_z(z, t)$ is that the sample has no deformation at the beginning of the experiment, $u_z(z, t = 0) = 0$.

3.4.1 Creep

In the creep problem, a step load is applied onto the tissue and maintained constant as the tissue undergoes creep deformation. For this load-control case, the applied traction may be specified as

$$\sigma_a(t) = \sigma_0 H(t), \quad (68)$$

where $\sigma_0 = -W_0 / \pi r_0^2$ is the constant traction corresponding to the constant applied load W_0 , and $H(t)$ is the Heaviside unit step function. For this set of equations, the solution for $u_z(z, t)$ is given by

$$\begin{aligned} \frac{u_z(z, t)}{h} &= \frac{\sigma_0}{H_A} \left\{ \frac{z}{h} - 1 \frac{(-1)^n}{(n - \frac{1}{2})^2} \right. \\ &\quad \left. + \frac{2}{\pi^2} \sum_{n=1}^{\infty} \frac{(-1)^n}{(n - \frac{1}{2})^2} \sin \left[\left(n - \frac{1}{2} \right) \pi \left(\frac{z}{h} - 1 \right) \right] e^{-\left(n - \frac{1}{2}\right)^2 \pi^2 \frac{t}{h}} \right\}. \end{aligned} \quad (69)$$

The axial normal strain is then obtained from $\varepsilon_{zz} = \partial u_z / \partial z$ and the interstitial fluid pressure may be evaluated from Eq. (48) as $p = H_A [\varepsilon_{zz}(z, t) - \varepsilon_{zz}(0, t)]$.

In particular, at $z = h$, the fluid pressure is given by

$$\frac{p(h, t)}{H_A} = \frac{\sigma_0}{H_A} \frac{2}{\pi} \sum_{n=1}^{\infty} \frac{(-1)^n}{n - \frac{1}{2}} e^{-(n-\frac{1}{2})^2 \pi^2 \frac{t}{\tau}}. \quad (70)$$

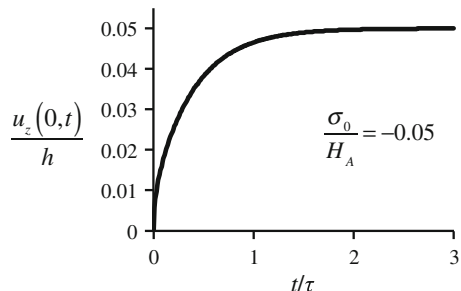
Finally, the relative fluid flux may be evaluated from Eq. (46) as $w_z = -\partial u_z / \partial t$.

Recall from Sect. 3.3.1 that $H_A k / h = h/\tau$ is a measure of the characteristic velocity of diffusive fluid flow within the biphasic matrix. We also note from the exponent of the exponential function in the solution for the displacement that τ is also a characteristic measure of the temporal response for creep problems. The typical creep deformation response of confined compression is shown in Fig. 6, where it can be observed that equilibrium is nearly reached at approximately two and half times the gel time constant.

The axial normal strain distribution is shown as a function of z and various times t in Fig. 7a. It is apparent from this result that there exists a boundary layer near the surface at early times, where the normal strain rapidly varies from the value of σ_0/H_A immediately under the porous indenter, to zero outside of the boundary layer. However, as time progresses, the strain becomes more uniform with depth until it reaches the constant value of σ_0/H_A throughout the tissue at equilibrium. A boundary layer is also observed in the spatial distribution of the interstitial fluid pressure at early times (Fig. 7b). At the porous indenter the pressure is equal to zero but at early times this pressure rapidly rises to the value of σ_0 outside of the boundary layer. Over time, however, the pressure begins to decrease throughout the tissue until it reaches the uniform value of zero at equilibrium.

The fluid flux, which is proportional to the gradient in pressure, is greatest at early times and at the interface with the free-draining porous indenter and reduces to a uniform value of zero at equilibrium. It can be noted that, instantaneously upon loading, the relative fluid flux is infinite at the interface with the porous filter. However, immediately after that instant the relative fluid flux assumes finite values. The equilibrium response for the creep problem can also be determined by taking the limit of the solutions above as $t \rightarrow \infty$, which reduces all the exponential terms to zero, i.e.,

Fig. 6 Creep deformation at the surface of a biphasic tissue under confined compression



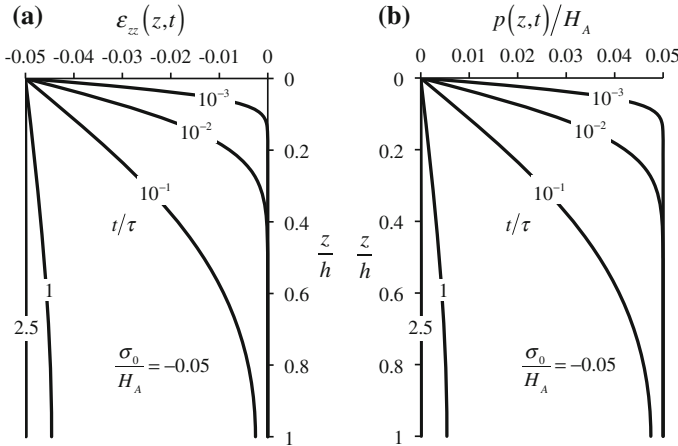


Fig. 7 **a** Axial normal strain $\varepsilon_{zz}(z, t)$ and **b** interstitial fluid pressure $p(z, t)$ in confined compression creep, as a function of the axial coordinate z/h , at various times t/τ

$$\begin{aligned} \lim_{t \rightarrow \infty} \frac{u_z(z, t)}{h} &= \frac{\sigma_0}{H_A} \left(\frac{z}{h} - 1 \right), & \lim_{t \rightarrow \infty} \varepsilon_{zz}(z, t) &= \frac{\sigma_0}{H_A}, \\ \lim_{t \rightarrow \infty} \frac{p(z, t)}{H_A} &= 0, & \lim_{t \rightarrow \infty} \frac{w_z(z, t)}{H_A k/h} &= 0. \end{aligned} \quad (71)$$

We find that the deformation is linear through the depth at equilibrium, the axial normal strain is uniform, and the interstitial fluid pressure and relative fluid flux reduce to zero. At equilibrium, a linear isotropic biphasic material behaves like a linear isotropic compressible elastic material.

One note of caution when interpreting these results is the need to distinguish between the observed responses described above and the assumed responses of the tissue under physiological loading conditions. Most generally, soft hydrated biological tissues do not get loaded *in situ* via a porous indenter, therefore the boundary layers in the strain, interstitial fluid pressure, and relative fluid flux observed in confined compression are generally not physiologic. This is of particular importance when live tissue explants are tested to monitor their biosynthetic response to confined compression. Any biosynthetic activity observed near the interface with the rigid porous indenter should be viewed as being specific to this choice of testing configuration and not necessarily representative of the biosynthetic response of the tissue *in vivo*.

3.4.2 Stress Relaxation

In the stress-relaxation problem the indenter displacement is prescribed to increase linearly in time and then kept constant until the tissue's load response reaches equilibrium, i.e.,

$$u_a(t) = \begin{cases} v_0 t & t < t_0, \\ v_0 t_0 & t \geq t_0, \end{cases} \quad (72)$$

where v_0 is the indenter velocity during the ramp loading. For these equations, the solution for $u_z(z, t)$ is

$$\frac{u_z(z, t)}{h} = -P_e^w \begin{cases} \left(\frac{z}{h} - 1\right) \frac{t}{\tau} \\ + \frac{2}{\pi^3} \sum_{n=1}^{\infty} \frac{(-1)^n}{n^3} \sin[n\pi(\frac{z}{h} - 1)] \left(1 - e^{-n^2\pi^2 \frac{t}{\tau}}\right) & t < t_0, \\ \left(\frac{z}{h} - 1\right) \frac{t_0}{\tau} \\ + \frac{2}{\pi^3} \sum_{n=1}^{\infty} \frac{(-1)^n}{n^3} \sin[n\pi(\frac{z}{h} - 1)] e^{-n^2\pi^2 \frac{t_0}{\tau}} \left(e^{n^2\pi^2 \frac{t_0}{\tau}} - 1\right) t \geq t_0, \end{cases} \quad (73)$$

where P_e^w is given in Eq. (55) and τ in Eq. (57). The axial normal strain $\varepsilon_{zz} = \partial u_z / \partial z$ may be evaluated from this solution, along with the interstitial fluid pressure p and fluid flux w_z . In particular, at $z = h$, the fluid pressure is

$$\frac{p(h, t)}{H_A} = P_e^w \begin{cases} \frac{4}{\pi^2} \sum_{n=1}^{\infty} \frac{1}{(2n-1)^2} \left(1 - e^{-(2n-1)^2\pi^2 \frac{t}{\tau}}\right) & t < t_0, \\ \frac{4}{\pi^2} \sum_{n=1}^{\infty} \frac{1}{(2n-1)^2} \left(e^{-(2n-1)^2\pi^2 \frac{t-t_0}{\tau}} - e^{-(2n-1)^2\pi^2 \frac{t_0}{\tau}}\right) t \geq t_0. \end{cases} \quad (74)$$

To evaluate the stress-relaxation response, the axial normal stress can be evaluated at the interface with the porous indenter, $\sigma_a(t) = T_{zz}(0, t) = -p(0, t) + H_A \partial u_z / \partial z$,

$$\frac{\sigma_a(t)}{H_A} = -P_e^w \begin{cases} \frac{t}{\tau} + \frac{2}{\pi^2} \sum_{n=1}^{\infty} \frac{1}{n^2} \left(1 - e^{-n^2\pi^2 \frac{t}{\tau}}\right) & t < t_0, \\ \frac{t_0}{\tau} + \frac{2}{\pi^2} \sum_{n=1}^{\infty} \frac{1}{n^2} \left(e^{-n^2\pi^2 \frac{t-t_0}{\tau}} - e^{-n^2\pi^2 \frac{t_0}{\tau}}\right) t \geq t_0. \end{cases} \quad (75)$$

The solution of Eq. (75) is presented for a representative case in Fig. 8a, with $t_0/\tau = 0.25$ and $P_e^w = 0.2$, such that the equilibrium compressive strain has the

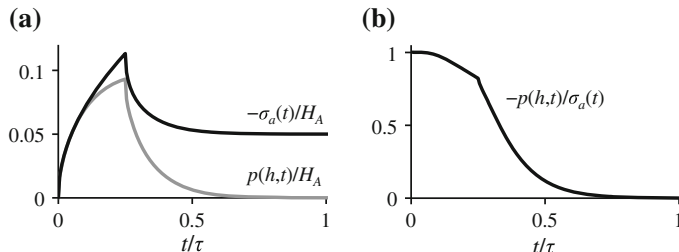


Fig. 8 Confined compression stress-relaxation responses showing **a** the normal compressive traction $-\sigma_a(t)$ and interstitial fluid pressure at $z = h$, and **b** the interstitial fluid load support $-p(h, t) / \sigma_a(t)$, when $t_0/\tau = 0.25$ and $P_e^w = 0.2$

magnitude $v_0 t_0 / h = 0.05$. During the ramp phase, the axial normal stress increases nonlinearly with time. At the end of the ramp, the stress relaxes to an equilibrium value. The interstitial fluid pressure at the bottom of the chamber ($z = h$) similarly rises during the ramp phase, then relaxes down to zero. By taking the ratio of the fluid pressure to the total normal stress $\sigma_a(t)$, the interstitial fluid load support can be evaluated as shown in Fig. 8b. Initially, at $t = 0^+$, the fluid load support is 100% immediately upon application of tissue deformation. This occurs because the fluid has not yet had time to escape and the mixture acts as an incompressible fluid (or solid) with uniform pressure and zero deformation. As time progresses however, fluid exudes from the tissue and the interstitial fluid pressure and fluid load support start decreasing with time. The strain profile through the depth of the tissue follows a similar history to the creep response, with tissue compaction (increased strain) occurring initially near the interface with the porous indenter and slowly progressing to a uniform strain distribution at equilibrium. The fluid flux is also initially confined to a narrow boundary layer near the porous indenter. As in the case of the creep response, the equilibrium stress-relaxation response can be obtained by taking the limit of the above solutions as $t \rightarrow \infty$. We find that the resulting expressions have the same form as in the creep problem,

$$\begin{aligned} \lim_{t \rightarrow \infty} \frac{u_z(z, t)}{h} &= \left(\frac{z}{h} - 1 \right) \frac{V_0 t_0}{h}, & \lim_{t \rightarrow \infty} \varepsilon_{zz}(z, t) &= -\frac{V_0 t_0}{h}, \\ \lim_{t \rightarrow \infty} \frac{p(z, t)}{H_A} &= 0, & \lim_{t \rightarrow \infty} \frac{w_z(z, t)}{H_A k / h} &= 0. \end{aligned} \quad (76)$$

If we compare the exponents of the exponential responses in creep and stress relaxation, the time constant of the dominant term (corresponding to $n = 1$) is four times greater in the creep problem than in the stress-relaxation problem. This means that equilibrium is reached more slowly in creep than in stress relaxation, which is also evident when comparing the responses of Figs. 6 and 8. When designing an experiment for testing biological tissue samples in confined compression, the shorter duration of the stress-relaxation test may be considered beneficial, particularly when attempting to minimize tissue degradation over long periods of testing.

3.4.3 Dynamic Loading

A frequent alternative to creep and stress-relaxation testing is dynamic loading in confined compression. This testing configuration typically consists of prescribing a sinusoidal load or displacement on the indenter and measuring the resulting response. To get the complete time-dependent response for this kind of loading, we let

$$\sigma_a(t) = \sigma_0 + \sigma_1 \sin \omega t, \quad (77)$$

where σ_0 is a tare stress, σ_1 is the amplitude and ω is the angular frequency of the dynamic stress. This problem is simply the superposition of the creep solution of Sect. 3.4.1 with the solution to the sinusoidal loading problem,

$$\sigma_a(t) = \sigma_1 \sin \omega t, \quad (78)$$

so we only need to solve the latter problem to complete the solution. The applied traction must remain compressive at all times to ensure that the porous indenter does not lift off from the tissue; this constraint can be easily satisfied by having $|\sigma_1| \leq |\sigma_0|$. The remaining boundary conditions are the same as those of the creep problem described in Sect. 3.4.1.

The solution for the transient response under this dynamic loading configuration is (Soltz and Ateshian 2000b)

$$\frac{u_z(z, t)}{h} = 2 \frac{\sigma_1}{H_A} \sum_{n=1}^{\infty} \frac{(-1)^{n-1}}{\omega^2 \tau^2 + \alpha_n^4} \sin \left[\alpha_n \left(\frac{z}{h} - 1 \right) \right] \times \left(\alpha_n^2 \sin \omega t - \omega \tau \cos \omega t + \omega \tau e^{-\alpha_n^2 t / \tau} \right), \quad (79)$$

where $\alpha_n = (n - 1/2) \pi$. Plots of the transient displacement and corresponding fluid pressure from this solution are presented in Sect. 3.4.4 below, where the solution is compared to experimental measurements.

As a special case, it is also possible to get the steady-state response of the tissue to dynamic loading by assuming that the general solution at steady state has the form $u_z(z, t) = u_z^d(z, \omega) e^{i\omega t}$, where $i = \sqrt{-1}$ is the pure imaginary number. The boundary conditions of Eqs. (64)–(67) have a similar form, with $\sigma_a(t) = \sigma_1 e^{i\omega t}$. It follows that the solution for $u_z^d(z, \omega)$ is given by

$$\frac{u_z^d(z, \omega)}{h} = \frac{\sigma_1}{H_A} \frac{\sinh \sqrt{i\omega\tau} \left(\frac{z}{h} - 1 \right)}{\sqrt{i\omega\tau} \cosh \sqrt{i\omega\tau}}. \quad (80)$$

The terms in the above expressions have been grouped such as to be nondimensional, e.g., u_z^d/h , σ_1/H_A , or $\omega\tau$. The solutions for the fluid pressure and relative fluid flux can be similarly obtained.

The expression of Eq. (80) is a complex number whose magnitude represents the amplitude of the response and whose argument is the phase angle. For example, the amplitude and phase of the displacement response at the interface with the porous indenter are shown in Fig. 9 as a function of the loading frequency $f = \omega/2\pi$. At very low frequencies, $f \ll \tau^{-1}$, the displacement is effectively in phase with the applied load and its amplitude (given by the engineering strain measure u_z^d/h) is equal to $|\sigma_1|/H_A$. (The figure shows a phase angle of π since the displacement u_z is positive when the prescribed compressive traction σ_1 is negative, given our choice of coordinate direction in Fig. 5a.) The load and displacement are in phase because at very low frequencies there is plenty of time for the fluid to flow through the

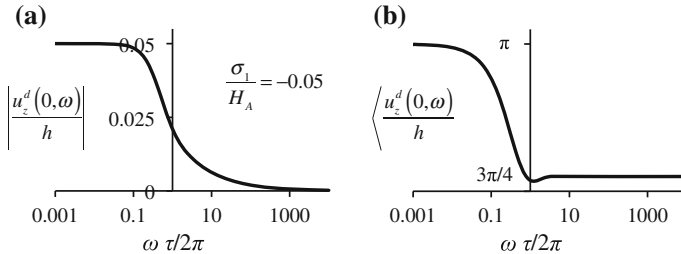


Fig. 9 **a** Amplitude and **b** phase angle for dynamic confined compression under load control, with $\sigma_1/H_A = -0.05$

tissue matrix and there is negligible drag between the two constituents. The tissue behaves elastically with a modulus of H_A . At very high frequencies, $f \gg \tau^{-1}$, the displacement is effectively $\pi/4$ out of phase with the applied load and the amplitude of the deformation becomes negligible. This is because there is very little time for the fluid to flow through the matrix as the load alternates back and forth; with negligible exchange of fluid with the external environment the tissue acts as an incompressible medium which cannot undergo any deformation in a rigid confining chamber; its dynamic modulus theoretically tends to infinity as the frequency is increased. For intermediate frequencies, $f \approx \tau^{-1}$, the tissue response is markedly viscoelastic, with nonnegligible relative fluid flow and biphasic drag forces and a dynamic modulus greater than H_A .

The interstitial fluid pressure can also be evaluated with this approach, producing

$$\frac{p^d(z, \omega)}{H_A} = \frac{\sigma_1}{H_A} \frac{\cosh \sqrt{i\omega\tau} \left(\frac{z}{h} - 1\right) - \cosh \sqrt{i\omega\tau}}{\cosh \sqrt{i\omega\tau}}. \quad (81)$$

3.4.4 Experimental Validation of Confined Compression

The biphasic theory was introduced in two papers by Mow and colleagues (Mow and Lai 1980; Mow et al. 1980). These papers provided theoretical solutions for confined compression creep and stress relaxation. Experimental results on bovine and human articular cartilage were also reported for these testing configurations. In the creep experiments, an initial jump was observed in the displacement response which did not agree with theory (Fig. 6) and was attributed to the lack of full initial confinement of the specimen within the test chamber (Mow et al. 1980; Armstrong and Mow 1982). In stress relaxation, a successful comparison of theory with experimental results on human knee cartilage was reported by Holmes et al. (1985) (Fig. 10), who extended the theory to account for strain-dependent permeability as motivated by earlier experimental findings (Mansour and Mow 1976; Mow and Mansour 1977; Lai et al. 1981). These results established that biphasic theory could successfully fit

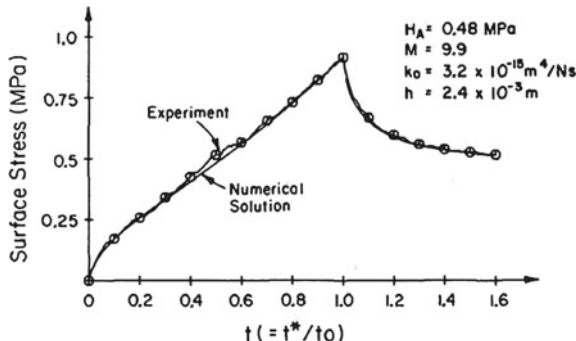


Fig. 10 Comparison of biphasic theory and experimental measurements in confined compression stress relaxation, as reported by Holmes et al. (1985) (reproduced with permission). The permeability was modeled to depend on the solid matrix dilatation $I^s = \text{tr} \epsilon$ according to $k = k_0 e^{M I^s}$, where k_0 is the hydraulic permeability in the limit of zero strain and M is a material parameter governing the dependence on the strain

the response of articular cartilage in confined compression stress relaxation, which was a necessary condition for validating the theoretical framework.

Since articular cartilage is a soft tissue that may undergo large deformations in situ, finite deformation frameworks were subsequently formulated for biphasic theory to account for large strains (Holmes and Mow 1990; Kwan et al. 1990). Ateshian et al. (1997) performed stress-relaxation, creep and dynamic loading experiments in confined compression on bovine articular cartilage to investigate the theoretical framework proposed by Holmes and Mow (1990). In their studies, stress-relaxation experiments were first performed to curve fit the material properties of the tested specimen as follows: Samples were compressed using five consecutive ramp-and-hold displacement profiles that each compressed the sample by 10% of its initial thickness, producing five stress-relaxation responses to a final compressive strain of 50% (Fig. 11). The elastic properties of the solid matrix were fitted from the equilibrium responses of these five steps (Fig. 11b). Then, the hydraulic permeability material constants from a strain-dependent model were fitted to the transient response (Fig. 11a).

To validate this model and material properties obtained from fitting the stress-relaxation responses, a creep test was also performed on the same specimens, followed by dynamic loading at a frequency of 0.005 Hz. The fitted parameters from the stress-relaxation response were used to predict the specimen deformation under creep and dynamic loading under the same loading conditions. In this series of studies, no initial jump was observed in the creep response upon the application of the step load, because an initial tare load was prescribed on the specimen to ensure full confinement (Ateshian et al. 1997). Very good agreement was observed between experimental results and theoretical prediction (Fig. 12), providing strong support toward the validation of the theoretical framework. The ability to predict outcomes

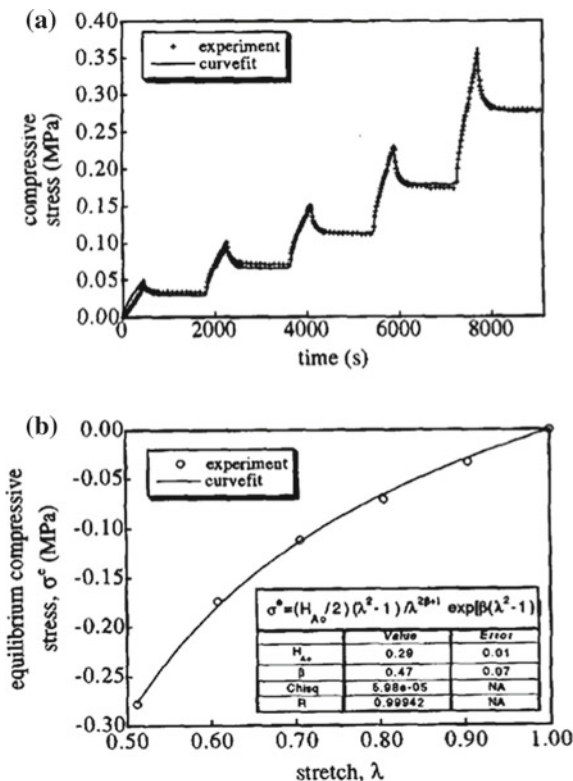


Fig. 11 Experimental stress responses and theoretical curve fit of confined compression stress relaxation on bovine articular cartilage, as reported by Ateshian et al. (1997) (reproduced with permission). **a** Complete transient response for five consecutive ramp-and-hold compression profiles that each compressed the sample by 10% of its initial thickness. **b** Equilibrium stress-stretch response from the end of each compression step. The elastic properties H_{A0} and β of the solid matrix were obtained from fitting the equilibrium response. The hydraulic permeability parameters k_0 and M were obtained from fitting the transient response

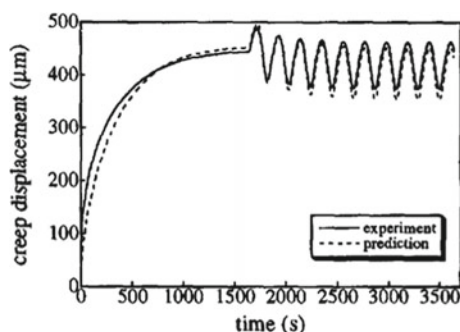


Fig. 12 Experimental displacement response of bovine cartilage plug under confined compression creep and dynamic loading (*solid curve*), and prediction of the response from biphasic theory (Holmes and Mow 1990) using material constants fitted to the stress-relaxation response (Fig. 11). Reproduced from Ateshian et al. 1997 (with permission)

of an experiment that did not inform the model represents a sufficient step in the validation of a theoretical framework.

In addition to predicting the deformation and stresses in the solid matrix, the biphasic theory can also predict responses for the interstitial fluid pressure and flux. As seen in Sect. 3.3.3, which reviewed experimental validations of biphasic permeation, there is a dearth of experimental studies that report the transient response for interstitial fluid flux within cartilage. However, starting with the work of Oloyede and Broom (1991, 1993), experimental measurements of the interstitial fluid pressure within cartilage have been reported. In the studies by Soltz and Ateshian (1998, 2000b), interstitial fluid pressure was measured in bovine articular cartilage at the interface of the tissue sample and bottom of the confining chamber ($z = h$ in Fig. 5a), in creep and stress relaxation (Soltz and Ateshian 1998) and dynamic loading (Soltz and Ateshian 2000b). The biphasic theory was used to extract H_A and k by curve fitting the tissue deformation at $z = 0$ (using Eq. (69) in creep and Eq. (80) for dynamic loading experiments) or the stress response of Eq. (75) in stress relaxation. The fluid interstitial pressure was then predicted from the theory, using Eq. (70) for creep, Eq. (81) for dynamic loading, and Eq. (74) for stress relaxation, using these values of H_A and k . Very good agreement was obtained between the predicted and measured interstitial fluid pressure in these studies (Fig. 13), validating the ability of

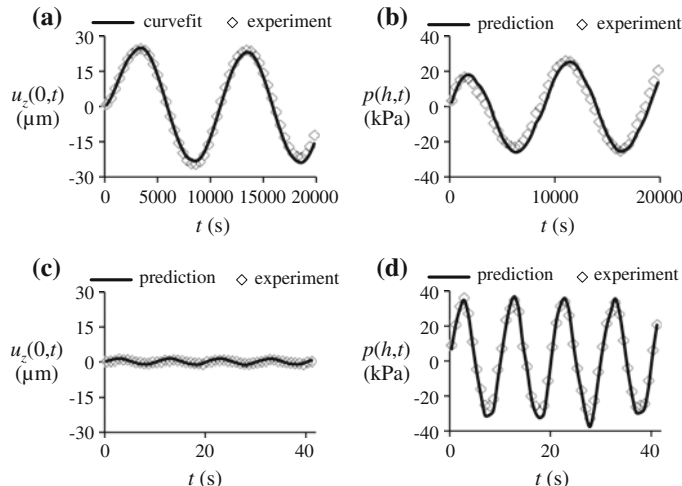


Fig. 13 Experimental and theoretical responses of bovine articular cartilage under confined compression dynamic loading, using data from the study of Soltz and Ateshian (2000b). **a** Experimental deformation and curve fit of the tissue deformation $u_z(0, t)$ to Eq. (79), under the action of a dynamic compressive stress with $\sigma_1 = -33 \text{ kPa}$ and frequency $f = 10^{-4} \text{ Hz}$, superposed over a static tare stress of $\sigma_0 = -130 \text{ kPa}$; the fitted values are $H_A = 0.54 \text{ MPa}$ and $k = 1.6 \times 10^{-4} \text{ mm}^4/\text{N} \cdot \text{s}$. **b** Experimental response and prediction of the fluid pressure $p(h, t)$ for the same specimen, using the values of H_A and k from the curve fit in (a). **c** Experimental response and prediction of $u_z(0, t)$ for the same specimen at a loading frequency of 0.1 Hz , using properties from (a). **d** Experimental response and prediction of $p(h, t)$ for the conditions described in (c)

the biphasic theory to predict the transient response of the interstitial fluid pressure in confined compression.

3.5 Unconfined Compression

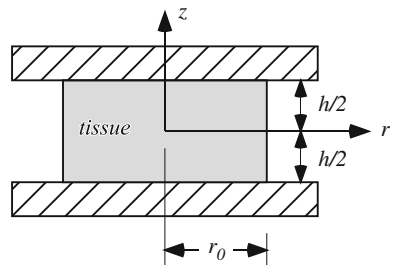
Unconfined compression is a testing configuration that subjects a cylindrical tissue sample to compressive strains in the axial direction and tensile strains in the radial and circumferential directions. Since many soft biological tissues have a fibrillar solid matrix that resists tension with much greater stiffness than compression, we may extend the constitutive model of Eq. (31) to include the contribution of fibrils that may only sustain tensile loading,

$$\mathbf{T}^e = \lambda_s (\text{tr}\boldsymbol{\epsilon}) \mathbf{I} + 2\mu_s \boldsymbol{\epsilon} + \xi \sum_{i=1}^m H(\varepsilon_n^{(i)}) \mathbf{n}^{(i)} \otimes \mathbf{n}^{(i)}, \quad (82)$$

where ξ is the tensile modulus of each fibril bundle, m is the number of fibril bundles, $\mathbf{n}^{(i)}$ is a unit vector along the direction of the i th fibril bundle, $\varepsilon_n^{(i)}$ is the normal strain component along that bundle, $\varepsilon_n^{(i)} = \mathbf{n}^{(i)} \cdot \boldsymbol{\epsilon} \cdot \mathbf{n}^{(i)}$, and $H(\bullet)$ is the Heaviside unit step function, which limits the contribution of the i th fibril bundle to loading configurations that produce a positive normal strain, $\varepsilon_n^{(i)} > 0$.

In the following analysis of unconfined compression the tissue is assumed to be homogeneous and the loading platens are assumed frictionless. For the constitutive model of Eq. (82), the governing equations for this problem can be reduced from the general equations using cylindrical coordinates (r, θ, z) under axisymmetric conditions (zero circumferential displacement and fluid flux, and no dependence of the remaining displacement components and fluid pressure on θ). For simplicity, we assume that there are only three fibril bundles ($m = 3$), each oriented along one of the coordinate directions, such that the fibril directions $\mathbf{n}^{(i)}$ coincide with the basis vectors of this cylindrical coordinate system (see Fig. 14).

Fig. 14 Geometry of unconfined compression problem



We now make the following simplifying assumptions which anticipate the final solution, in order to reduce the number of equations. These assumptions must be consistent with the boundary conditions for this problem, which are described in greater detail below. Because of the frictionless platens we expect the radial displacement u_r to be independent of the axial coordinate z since no bulging of the specimen is expected under these conditions ($\partial u_r / \partial z = 0$). Since the shear strain is given by $\varepsilon_{rz} = (\partial u_r / \partial z + \partial u_z / \partial r) / 2$ and is directly proportional to the shear stress, and since the shear traction is zero on the top and bottom surfaces as well as the lateral boundary, this suggests that we should also assume $\partial u_z / \partial r = 0$ everywhere within the tissue sample. The loading platens are impermeable so that the fluid flux normal to the platens must be zero, $w_z = 0$. This constraint implies that the pressure gradient along z is zero at the top and bottom surfaces, and we assume it is zero throughout the sample. Combining all these assumptions we get $u_r = u_r(r, t)$, $u_\theta = 0$, $u_z = u_z(z, t)$, $p = p(r, t)$, $w_r = w_r(r, t)$, $w_\theta = 0$ and $w_z = 0$. Finally, we anticipate from the nature of this problem that the axial normal strain ε_{zz} is compressive, whereas the radial and circumferential normal strains, ε_{rr} and $\varepsilon_{\theta\theta}$ respectively, are tensile. Thus, only fibril bundles in the latter two directions contribute to the stress response according to Eq. (82). Substituting these relations into the component form of Eqs. (26) and (27), and the radial and axial components of Eq. (25) respectively, we now get

$$\frac{1}{r} \frac{\partial}{\partial r} \left[r \left(\frac{\partial u_r}{\partial t} + w_r \right) \right] + \frac{\partial}{\partial t} \frac{\partial u_z}{\partial z} = 0, \quad (83)$$

$$w_r = -k \frac{\partial p}{\partial r}, \quad (84)$$

$$-\frac{\partial p}{\partial r} + H_{+A} \frac{\partial}{\partial r} \left(\frac{1}{r} \frac{\partial}{\partial r} (r u_r) \right) = 0, \quad (85)$$

$$\frac{\partial^2 u_z}{\partial z^2} = 0, \quad (86)$$

where $H_{+A} = H_A + \xi$ combines the stiffnesses of fibrils and ground matrix in this fibril-reinforced model. Integrating the last of these relations with respect to z , we get $\partial u_z / \partial z = \varepsilon(t)$, where $\varepsilon(t)$ is the axial normal strain ε_{zz} in the cylindrical specimen, which is found to be only a function of time in this problem. Substituting this result into Eq. (83) and integrating the resulting equation with respect to r yields

$$r \left(\frac{\partial u_r}{\partial t} + w_r \right) = -\dot{\varepsilon}(t) \frac{r^2}{2} + v(t), \quad (87)$$

where $v(t)$ is an integration function. Evaluating this equation at $r = 0$ shows that $v(t) = 0$ in this problem. Using Eq. (84), the above relation now reduces to

$$\frac{\partial p}{\partial r} = \frac{1}{k} \left[\frac{\partial u_r}{\partial t} + \dot{\varepsilon}(t) \frac{r}{2} \right], \quad (88)$$

which can be substituted into Eq. (85) to yield a partial differential equation in the dependent variable $u_r(r, t)$,

$$\frac{\partial}{\partial r} \left(\frac{1}{r} \frac{\partial}{\partial r} (r u_r) \right) - \frac{1}{H_{+A} k} \frac{\partial u_r}{\partial t} = \frac{1}{H_{+A} k} \dot{\varepsilon}(t) \frac{r}{2}. \quad (89)$$

The boundary conditions for this problem must be formulated at all the boundaries of the cylindrical tissue sample: at $r = 0$ and $r = r_0$ (where r_0 is the specimen radius), and at $z = \pm h/2$. Because of axisymmetry, there is no radial displacement or fluid flux at $r = 0$ and the axial displacement is symmetric relative to the z -axis. These conditions lead to the relations

$$u_r(0, t) = 0, \quad T_{rz}^e(0, t) = 0, \quad \left. \frac{\partial p}{\partial r} \right|_{r=0} = 0. \quad (90)$$

The condition $T_{rz}^e = 0$ is satisfied automatically throughout the cylindrical specimen based on the assumptions summarized above; the condition $\partial p / \partial r = 0$ is satisfied automatically at $r = 0$ according to Eq. (88) as long as $u_r(0, t) = 0$. At the radial edge of the sample the total traction is zero, both in the normal and shear directions, and the fluid pressure must be ambient,

$$\begin{aligned} T_{rr}^e(r_0, t) &= H_{+A} \left. \frac{\partial u_r}{\partial r} \right|_{r=r_0} + \lambda_s \left[\frac{u_r(r_0, t)}{r_0} + \varepsilon(t) \right] = 0, \\ T_{rz}^e(r_0, t) &= 0, \\ p(r_0, t) &= 0. \end{aligned} \quad (91)$$

At the top and bottom surfaces ($z = \pm h/2$), the shear traction T_{rz}^e is equal to zero because of the assumption of frictionless contact, and the normal fluid flux must be zero because the loading platens are impermeable, thus $\partial p / \partial z = 0$; these boundary conditions are satisfied automatically based on our prior assumptions. For load control experiments the integrated normal traction component at the top and bottom surfaces must be equal to the applied load, whereas for displacement-control experiments the axial displacement is prescribed,

$$\begin{cases} 2\pi \int_0^{r_0} r (-p + T_{zz}^e) dr = W(t) & \text{load control} \\ u_z = \pm \frac{1}{2} u_a(t) & \text{displacement control} \end{cases} \quad \text{at } z = \pm \frac{h}{2}. \quad (92)$$

The interstitial fluid pressure is obtained by integrating $\partial p / \partial r$ in Eq. (85) and making use of the boundary condition on p in Eq. (91),

$$p(r, t) = -H_{+A} \left(\frac{\partial u_r}{\partial r} + \frac{u_r}{r} \right) \Big|_{r=r_0}. \quad (93)$$

The total normal load at the platens is then given by Eq. (92), $W(t) = W^p(t) + W^e(t)$, where

$$W^p(t) = -2\pi \int_0^{r_0} rp(r, t) dr, \quad W^e(t) = 2\pi \int_0^{r_0} r T_{zz}^e(r, t) dr. \quad (94)$$

Here, $W^p(t)$ is the component of the total axial load contributed by the interstitial fluid pressure and $W^e(t)$ is the component contributed by the effective stress. Using the above results, these expressions reduce to

$$W^p(t) = -\pi r_0^2 \left[\lambda_s \varepsilon(t) + (H_{+A} + \lambda_s) \frac{u_r}{r} \Big|_{r=r_0} \right], \quad (95)$$

$$W^e(t) = \pi r_0^2 \left[H_A \varepsilon(t) + 2\lambda_s \frac{u_r}{r} \Big|_{r=r_0} \right], \quad (96)$$

$$W(t) = \pi r_0^2 (H_A - \lambda_s) \left[\varepsilon(t) - \frac{H_{+A} - \lambda_s}{H_A - \lambda_s} \frac{u_r}{r} \Big|_{r=r_0} \right]. \quad (97)$$

Note that the boundary condition of Eq. (91) was used to eliminate $\partial u_r / \partial r|_{r=r_0}$ from the right-hand side.

3.5.1 Instantaneous and Equilibrium Responses

For an unconfined compression stress-relaxation problem where the axial strain is prescribed as a step function, let $\varepsilon(t) = \varepsilon_0 H(t)$, where $\varepsilon_0 \leq 0$. The instantaneous response at $t = 0^+$ may be obtained by recognizing that $p(r, 0^+)$ is uniform (thus $w_r(r, 0^+) = 0$) over the range $0 \leq r < r_0$, and $u_r(r, 0^+)$ is a linear function of r over that range. In that case, it can be shown that the instantaneous response is given by

$$\lim_{t \rightarrow 0^+} \frac{u_r(r, t)}{r_0} = -\frac{\varepsilon_0 r}{2r_0}. \quad (98)$$

It follows from this solution that

$$W^p(0^+) = \pi r_0^2 (H_{+A} - \lambda_s) \frac{\varepsilon_0}{2}, \quad W(0^+) = \pi r_0^2 (2H_A + H_{+A} - 3\lambda_s) \frac{\varepsilon_0}{2}, \quad (99)$$

so that the instantaneous fluid load support is given by

$$\frac{W^p(0^+)}{W(0^+)} = \frac{H_{+A} - \lambda_s}{2H_A + H_{+A} - 3\lambda_s} = \frac{2\mu_s + \xi}{6\mu_s + \xi}, \quad (100)$$

and the instantaneous (dynamic) unconfined compression modulus is

$$E_Y^{0^+} = \frac{W(0^+)}{\pi r_0^2 \varepsilon_0} = 3\mu_s + \frac{1}{2}\xi, \quad (101)$$

whereas the instantaneous effective Poisson's ratio is given by

$$\nu^{0^+} = \lim_{t \rightarrow 0^+} -\frac{\varepsilon_{rr}}{\varepsilon_{zz}} = \lim_{t \rightarrow 0^+} -\frac{1}{\varepsilon_0} \frac{\partial u_r}{\partial r} = \frac{1}{2}, \quad (102)$$

consistent with this instantaneous isochoric deformation. These results show that the instantaneous stiffness of the tissue is significantly influenced by the fibril modulus ξ : In the absence of fibrils ($\xi = 0$), the fluid load support in Eq. (100) reduces to $W^p(0^+) / W(0^+) = 1/3$ and the effective unconfined compression modulus reduces to $E_Y^{0^+} = 3\mu_s$; however, as ξ increases to values much greater than the ground matrix shear modulus μ_s , the fluid load support approaches unity,

$$\lim_{\xi/\mu_s \rightarrow \infty} \frac{W^p(0^+)}{W(0^+)} = 1, \quad (103)$$

and $E_Y^{0^+}$ increases in proportion to $\xi/2$. Thus, a relatively stiff fibril matrix has the effect of enhancing fluid pressurization and interstitial fluid load support under instantaneous loading; as a result of this fluid pressurization, the effective compressive modulus is nearly proportional to the tensile stiffness of the fibrils. This counterintuitive result implies that a hydrated biological tissue that is typically loaded in compression, such as articular cartilage, may resist compressive loads more effectively by having a fibril-reinforced solid matrix, even though fibrils may only sustain tension.

Similarly, the equilibrium response as $t \rightarrow \infty$ is obtained by setting time derivatives to zero, recognizing that $p = 0$ and u_r is similarly a linear function of r , thus

$$\lim_{t \rightarrow \infty} \frac{u_r(r, t)}{r_0} = -\frac{\lambda_s}{H_{+A} + \lambda_s} \varepsilon_0 \frac{r}{r_0}. \quad (104)$$

The effective equilibrium Young's modulus in unconfined compression is

$$E_{-Y} = \lim_{t \rightarrow \infty} \frac{W(t)}{\pi r_0^2 \varepsilon_0} = H_A - \frac{2\lambda_s^2}{H_{+A} + \lambda_s}, \quad (105)$$

and the corresponding effective equilibrium Poisson's ratio is

$$\nu_- = \lim_{t \rightarrow \infty} -\frac{\varepsilon_{rr}}{\varepsilon_{zz}} = \lim_{t \rightarrow \infty} -\frac{1}{\varepsilon_0} \frac{\partial u_r}{\partial r} = \frac{\lambda_s}{H_{+A} + \lambda_s}. \quad (106)$$

Since the fibrils may only sustain tension, the results presented here are specific to unconfined compression. In particular, it may be noted from these last equations that $E_{-Y} \rightarrow H_A$ and $\nu_- \rightarrow 0$ as $\xi/\lambda_s \rightarrow \infty$; thus, in compression, Young's modulus behaves as the confined compression modulus H_A as the fibrils become very stiff, consistent with the finding that the effective Poisson's ratio tends to zero, implying little lateral expansion under compression.

3.5.2 Transient Response

The transient solution for $u_r(r, t)$ may be obtained by the method of Laplace transforms and is given by

$$\frac{u_r(r, t)}{r_0} = \varepsilon_0 \left[\frac{1 - \eta}{2\eta - 1} \frac{r}{r_0} + \sum_{n=1}^{\infty} \frac{J_1\left(\gamma_n \frac{r}{r_0}\right)}{\gamma_n J_0(\gamma_n) (2\eta - 1 - \eta^2 \gamma_n^2)} e^{-\gamma_n^2 t/\tau} \right], \quad (107)$$

where $\eta = H_{+A}/(H_{+A} - \lambda_s)$ and the gel time constant for this problem is given by

$$\tau = r_0^2/H_{+A}k. \quad (108)$$

Here, γ_n 's are the roots of

$$\eta \gamma_n J_0(\gamma_n) - J_1(\gamma_n) = 0, \quad (109)$$

where J_0 and J_1 are Bessel functions of the first kind, of order 0 and 1, respectively ($\gamma_n > 0$). The fluid pressure may then be obtained from Eq. (93) using

$$\frac{\partial u_r}{\partial r} = \varepsilon_0 \left[\frac{1 - \eta}{2\eta - 1} + \sum_{n=1}^{\infty} \frac{\gamma_n J_0\left(\gamma_n \frac{r}{r_0}\right) - \frac{r_0}{r} J_1\left(\gamma_n \frac{r}{r_0}\right)}{\gamma_n J_0(\gamma_n) (2\eta - 1 - \eta^2 \gamma_n^2)} e^{-\gamma_n^2 t/\tau} \right], \quad (110)$$

and the fluid load support, evaluated from Eqs. (95)–(97), reduces to

$$\frac{W^p(t)}{W(t)} = \frac{(2\eta - 1) \sum_{n=1}^{\infty} \frac{J_1(\gamma_n)}{\gamma_n J_0(\gamma_n) (2\eta - 1 - \eta^2 \gamma_n^2)} e^{-\gamma_n^2 t/\tau}}{\eta \zeta - 1 + \frac{1 - \eta}{2\eta - 1} + \sum_{n=1}^{\infty} \frac{J_1(\gamma_n)}{\gamma_n J_0(\gamma_n) (2\eta - 1 - \eta^2 \gamma_n^2)} e^{-\gamma_n^2 t/\tau}}, \quad (111)$$

where $\zeta = 1 - H_A/H_{+A}$.

A typical response for the time-dependent radial displacement $u_r(r, t)$ is presented in Fig. 15a as a function of time, for the case where $\eta = 9/8$ (or equivalently, $H_{+A} = 9\lambda_s$). The corresponding spatial distribution of the displacement is presented

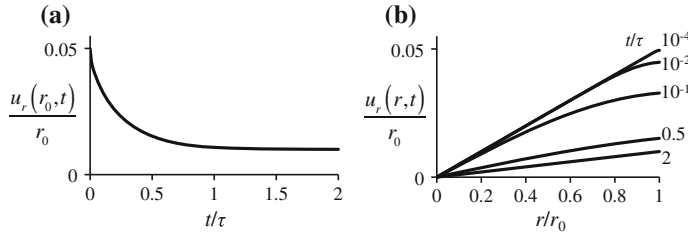


Fig. 15 Radial displacement in unconfined compression stress relaxation under an applied step strain $\varepsilon_0 = -0.1$, with $H_{+A} = 9\lambda_s$, using Eq. (107). **a** Time-dependent radial displacement at $r = r_0$. **b** Radial displacement along r , at selected time points t/τ

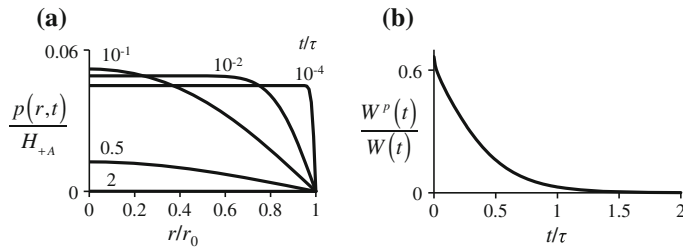


Fig. 16 **a** Spatial distribution of interstitial fluid pressure in unconfined compression stress relaxation, at selected time points t/τ ; and **b** interstitial fluid load support as a function of time when $H_A = 3\lambda_s$

in Fig. 15b at selected time points. Immediately upon loading (represented by the very short time response $t/\tau = 10^{-4}$), an instantaneous lateral expansion of the cylindrical specimen occurs, which varies linearly from 0 to r_0 as predicted by Eq. (98), after which the radial displacement slowly recoils to its equilibrium value with increasing time.

The interstitial pressure for the same case is presented in Fig. 16a. The instantaneous response of the pressure is a homogeneous distribution whose magnitude is given by $-W^P(0^+)/\pi r_0^2$ in Eq. (99) (which evaluates to $4\varepsilon_0/9H_{+A}$ in this example), except at the boundary $r = r_0$ where the pressure reduces to zero. Over time the pressure becomes inhomogeneous and decreases toward zero, though it is noteworthy that the pressure near the center of the cylindrical specimen temporarily rises above its instantaneous response before dropping down. The corresponding fluid load support is given in Fig. 16b as a function of time, when $\zeta = 2/3$ (or equivalently, $H_A = 3\lambda_s$), showing an initial jump, then a slow decrease toward zero as equilibrium is reached. For the choices of η and ζ selected in this example, Eq. (100) predicts that the initial peak fluid load support is $2/3$.

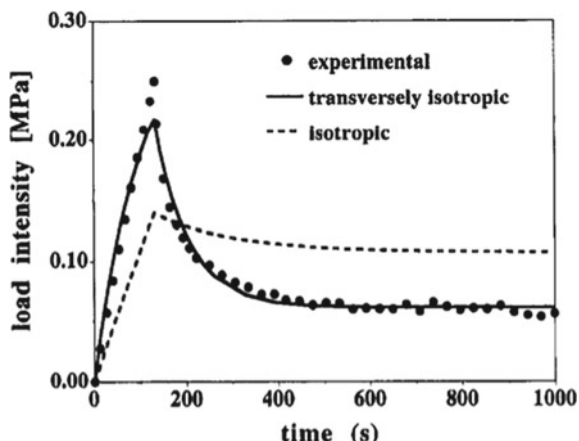
3.5.3 Experimental Validation of Unconfined Compression

The analytical solution for unconfined compression presented in the previous sections was first formulated by Armstrong et al. (1984) for the case $\xi = 0$ (no fibrils). In their original study, these authors did not report experimental measurements to corroborate their theoretical predictions. In fact, Brown and Singerman (1986) reported poor agreement between their measurements on epiphyseal (growth plate) cartilage and the unconfined stress-relaxation response of Armstrong et al. (1984). In those years, the root cause for this poor agreement remained uncertain. Eventually, starting in the late 1990s, a hypothesis emerged that could explain this discrepancy.

Cohen et al. (1998) proposed that the unconfined compression response should account for the known disparity between the tensile and compressive properties of the solid matrix of cartilage. Experimental studies had long demonstrated that articular cartilage is much stiffer in tension than compression (Kempson et al. 1968; Armstrong and Mow 1982; Akizuki et al. 1986), as its solid matrix consists of fibrillar (type II) collagen that can resist tension, and aggregating proteoglycans (aggrecans) that can resist compression (Maroudas 1976). To account for this disparity in the context of classical solid mechanics, they modeled the solid matrix of articular cartilage as a transversely isotropic elastic material. The stress-strain response in the axial direction employed the compressive modulus, whereas that in the transverse plane of isotropy employed the tensile modulus. They provided an analytical solution for unconfined compression stress relaxation, similar to that of Eq. (107), that better fitted the experimental response of bovine epiphyseal cartilage (Fig. 17).

Bursać et al. (1999) raised concerns about the use of a transversely isotropic model to model articular cartilage, as this approach would produce inconsistent results between confined and unconfined compression. In the same year, Soulhat et al. (1999) and Li et al. (1999, 2000) proposed to model the solid matrix of biphasic cartilage in unconfined compression using a fibril-network reinforced material.

Fig. 17 Experimental response and theoretical curve fits for unconfined compression stress relaxation of bovine epiphyseal cartilage, as reported by Cohen et al. (1998) (reproduced with permission). Using a transversely isotropic model for the solid matrix of cartilage produced significantly better fits than the isotropic model



In their approach, collagen fibrils were modeled using linear or nonlinear springs that could only sustain tension, as shown in Sect. 3.5. They demonstrated good curve fits of the stress-relaxation response of articular cartilage, under single or multiple ramp-and-hold displacement profiles. Their formulation did not exhibit the limitation raised in the study of Bursać et al. (1999).

Soltz and Ateshian (2000a) adopted the Conewise Linear Elasticity (CLE) framework, formulated earlier by Curnier et al. (1995) for modeling elastic solids that exhibit different behaviors in tension and compression, to model the solid matrix of biphasic cartilage. They performed confined and unconfined compression and torsion experiments on bovine articular cartilage disks to extract their compressive, tensile and shear properties, as well as axial and radial permeability coefficients. They also measured the interstitial fluid pressure at the center of the disk in unconfined compression stress relaxation, and compared these measurements to predictions from this biphasic-CLE model. These results showed very good agreement between theory and experiments (Fig. 18), providing strong support for the validation of biphasic theory in a framework that accounts for the tension-compression nonlinearity of articular cartilage. Further validation using interstitial fluid pressure measurements in unconfined compression was also reported subsequently in the study of Park et al. (2003), who showed that the peak magnitude of interstitial fluid load support in unconfined compression approached 100 % as the ratio of tensile to compressive moduli of the solid matrix increased, consistent with Eqs. (100) and (103).

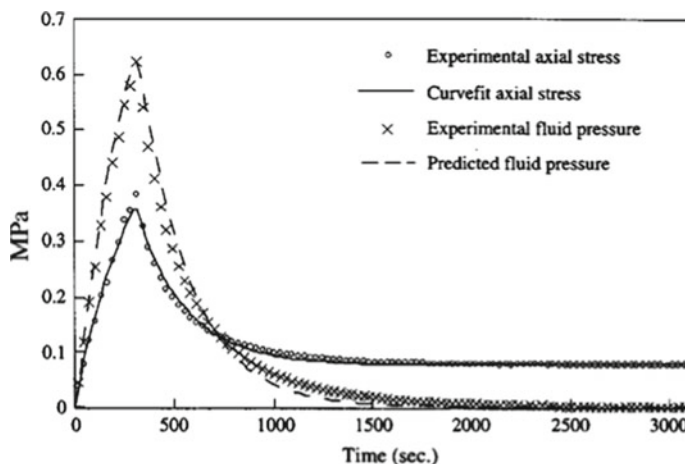
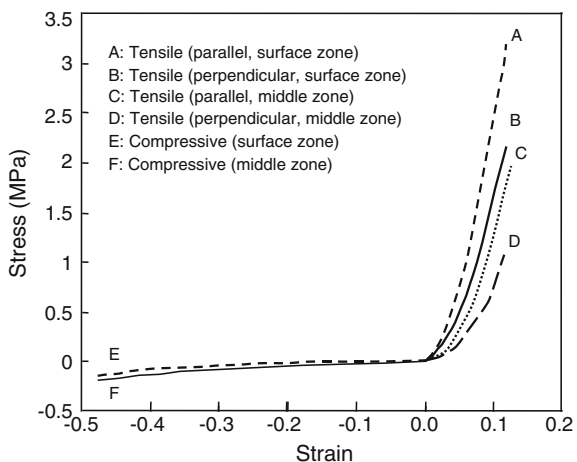


Fig. 18 Experimental and theoretical responses for unconfined compression stress relaxation of a bovine articular cartilage disk, as reported by Soltz and Ateshian (2000a) (reproduced with permission). The transient axial stress response was fitted to extract material parameters for the biphasic-CLE model adopted in that study. The interstitial fluid pressure was measured at the bottom center of the disk, showing very good agreement with the fluid pressure predicted from the model using the fitted material parameters

Fig. 19 Equilibrium stress-strain responses for representative human shoulder cartilage samples tested in tension and compression, as reported by Huang et al. (2005) (reproduced with permission). Specimens tested in tension were harvested in the plane tangential to the articular surface, parallel or perpendicular to the local split-line direction



At the time of these studies, all tensile measurements of cartilage properties had been performed using specimens harvested parallel to the articular surface, whereas compressive properties had been measured on disks harvested with their axis normal to the articular surface. Thus, tensile and compressive moduli reported in the prior literature were not measured along the same direction, raising the possibility that cartilage could be linear elastic (having the same moduli in tension and compression across the strain origin) but highly anisotropic (accounting for the larger moduli parallel to the surface and smaller moduli perpendicular to the surface). This issue was first resolved by Jurvelin et al. (2003), who reported that the compressive modulus of human knee cartilage was statistically different, but of comparable magnitude, when measured on disks harvested with their axis perpendicular (~ 1.2 MPa) or parallel (~ 0.8 MPa) to the articular surface. Similar findings were subsequently reported by Wang et al. (2003) and Chahine et al. (2004), who measured the compressive and tensile properties of bovine articular cartilage cubes tested along three orthogonal directions. Evidence of the large disparity between tensile and compressive properties of articular cartilage is shown in the stress-strain responses reported by Huang et al. (2005) for human shoulder cartilage (Fig. 19). Today, based on the preponderance of evidence reviewed here, a fiber-reinforced elastic solid matrix is considered the preferred modeling approach for articular cartilage.

4 Other Related Mixture Models

This chapter focused on a review of a biphasic mixture of intrinsically incompressible solid and fluid constituents, with a review of selected studies that validated the model against experimental measurements, mostly in articular cartilage. Since biphasic theory provides a framework for modeling the solid matrix stresses and

interstitial fluid flow within a porous deformable material, many of the validation studies employed measurements of the interstitial fluid pressure or flux in response to mechanical loading to provide direct evidence in support of theoretical predictions. Fundamentally, mixture theory recovers the classical equations of elasticity theory in the limit when the fluid pressure is set to zero. In the limit when the porous solid matrix is rigid, it also recovers Darcy's law, a well-attested phenomenological relation for flow through porous media. Therefore, the validation studies reported here effectively demonstrate that the theory can also predict the coupling between solid matrix deformation and interstitial fluid pressurization.

4.1 Modeling Solutes in Mixtures

Mixture theory has also been extended to include solute transport within the interstitial fluid of a solid-fluid mixture. Extending the theory to incorporate solutes is relatively straightforward, based on the governing equations covered in Sect. 2. When solutes are included, the list of state variables must be extended to include the solute apparent density $\rho_r^\alpha = J\rho^\alpha$ (mass of solute α per volume of the mixture in the reference configuration). The dependence of the mixture free energy Ψ_r on solute density is then embodied in the chemical potential $\mu^\alpha = \partial\Psi_r/\partial\rho_r^\alpha$. If solutes and the solid matrix are electrically charged, an electric potential ψ may arise if it is assumed that the mixture must satisfy the electroneutrality condition (much like the pressure p arises from the assumption that the mixture constituents are intrinsically incompressible). The fluid pressure p , electrical potential ψ , and chemical potential μ^α may then be combined into a single scalar variable $\tilde{\mu}^\alpha$ called the mechano-electrochemical potential. Then, according to the momentum equations, solvent and solute fluxes are driven by gradients in $\tilde{\mu}^\alpha$, as well as inertia and body forces, and resisted by dissipative momentum exchanges $\hat{\mathbf{p}}_d^\alpha$ similar to the presentation in Sect. 3.1 and Eq. (20).

The first extension of biphasic theory to include solutes was presented by Lai et al. (1991), who modeled cartilage as a triphasic mixture consisting of a charged porous deformable solid matrix, and an interstitial fluid consisting of a neutral solvent (water) and two monovalent counterions from a dissolved salt (such as Na^+ and Cl^-). These authors showed that mixture theory could reproduce Fick's law of diffusion in the limit of a free fluid solution, which arises from the momentum balance for the solute. It could also reproduce Donnan's law to predict the osmotic swelling pressure arising from soluble charge segregation between the triphasic mixture and its surrounding fluid environment. More generally, in addition to permeation, diffusion and barophoresis, electrokinetic phenomena could also be recovered from triphasic theory, such as electrophoresis, electro-osmosis, and streaming potentials and currents (Gu et al. 1993; Lai et al. 2000). The triphasic formulation was later extended by Gu et al. (1998) to include any number of electrolytes. These formulations demonstrated that mixture theory provides the foundation for modeling a wide range of phenomena encountered in biological tissues and cells.

Mixture theory provides a fundamental framework that accounts for interactions among all mixture constituents. Consequently, when classical phenomenological relations emerge from the mixture equations, such as Darcy's law and Fick's law, we may discover (or rediscover) terms that were neglected in these earlier formulations. Mauck et al. (2003) formulated a mixture framework for a neutral solute in a porous deformable hydrated solid matrix. While mixture theory accounts for frictional drag tensors $f^{\alpha\beta}$ between every pair of constituents, the earlier triphasic (Lai et al. 1991) and multi-electrolyte (Gu et al. 1998) models opted to neglect the friction between solutes and the solid matrix, arguably because the resulting expressions were sufficient to reproduce Darcy's law and Fick's law. By keeping the frictional drag between solute and solid, Mauck et al. (2003) showed that the resulting momentum equations for the solute could differentiate between solute diffusivity within a free fluid versus the diffusivity within the mixture (inclusive of the solid matrix). While experiments had long attested that these diffusivities could be different (depending on the molecular size of the solute relative to the pore structure of the solid) (Deen 1987), most models of solute transport within porous media simply employed Fick's phenomenological law with an adjusted value of the solute diffusivity.

Mauck et al. (2003) showed that the mixture formulation could predict phenomena resulting from the interaction of solid matrix deformation and solute transport that were not anticipated by the phenomenological relations. Most notably, they found that dynamic loading of a disk of tissue, or hydrogel, submerged in a bath containing a solute, would increase the solute concentration far above that predicted from Fick's law. A series of subsequent experimental studies validated these predictions in agarose and articular cartilage (Albro et al. 2008, 2010, 2011; Chahine et al. 2009), providing further confidence that mixture theory is a sound framework for extending classical formulations (Fig. 20). Similarly, using basic principles from

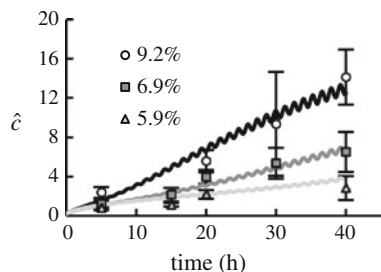


Fig. 20 Experimental results (symbols) and theoretical predictions (solid curves) for the uptake of 70 kDa dextran into agarose disks of various concentrations (see legend) in response to dynamic unconfined compression ($\pm 5\%$ strain amplitude at 1 Hz, superimposed on a 15% compressive strain offset, Albro et al. 2008) for 40 h. \hat{c} is the ratio of average dextran concentration in the dynamically loaded disk to the average concentration achieved at steady state in the absence of loading; it represents the enhancement ratio resulting from dynamic loading. Theoretical predictions were obtained by independently measuring the mechanical and transport properties of this agarose-dextran system and using them in the mixture model formulated by Mauck et al. (2003). Reproduced from the study by Albro et al. (2010) (with permission)

mixture theory and physical chemistry, Mauck et al. (2003) proposed a formulation for solute partitioning between the pore space in the mixture and a surrounding solution, which could account for solid matrix deformation and incomplete volume recovery in response to osmotic loading. This formulation was later found to accurately predict the response of hydrogels and chondrocytes to osmotic loading using a variety of osmolytes (Ateshian et al. 2006; Albro et al. 2007, 2009).

4.2 Constrained Solid Mixtures

As shown by Humphrey and Rajagopal (2002), mixture theory may also be used to model the solid matrix of biological tissues that have heterogeneous constituents, such as mixtures of collagen, elastin, and smooth muscle cells, as found in the aortic wall. When these constituents are physically bound together, it may be assumed that the solid mixture is constrained such that all solid constituents α share the same velocity $\mathbf{v}^\alpha \equiv \mathbf{v}^s$. It is noteworthy that this assumption simplifies the formulation of the mixture governing equations, since the diffusion velocity \mathbf{u}^α and dissipative momentum supply $\hat{\mathbf{p}}_d^\alpha$ (Sect. 2.2) reduce to zero in the case of such mixtures. Moreover, it may be assumed that each solid constituent in the mixture has a different reference configuration \mathbf{X}^α (Ateshian and Ricken 2010; Wan et al. 2010), even though all constituents share the same current configuration \mathbf{x} , which makes it possible to model the evolution of residual stresses in growing tissues.

In hindsight, another model commonly adopted in the biomechanics of soft biological tissues implicitly describes constrained solid mixtures whose constituents all share the same reference configuration. Notably, Lanir's approach for modeling soft tissues using continuous fiber distributions (Lanir 1979, 1983) relies on the superposition of fiber bundles that may contribute to the tissue response only if their normal strain is tensile, as illustrated in Eq. (82). In his approach, which has been widely followed in the biomechanics literature, only fiber bundles that are in tension contribute to the response; thus, each fiber bundle may be viewed as a mixture constituent, even while the number of constituents in the mixture varies with the state of loading. Yet, all fibril bundles share the same reference and current configuration, satisfying the assumption of a constrained solid mixture.

4.3 Growth and Remodeling

As shown in the mass balance equation (1) for each constituent, mixture theory allows mass exchanges, thus chemical reactions, between its constituents. Reactions that add or remove mass from the solid matrix of a biological tissue may describe growth and remodeling. An elegant demonstration of this basic concept was presented by Cowin and Hegedus (1976), who modeled interstitial growth and remodeling of bone in response to mechanical loading using a mass supply term for the solid matrix,

which depended on the state of strain. The supply of mass to the solid matrix came from implicit soluble constituents available in the trabecular pore space. Modeling growth using mixture theory has since been reprised by many authors, as reviewed by Ambrosi et al. (2011) and Ateshian and Humphrey (2012), and is currently an active topic of investigation.

It is intriguing that the theory of reactive mixtures may also be used to model classical phenomena such as viscoelasticity, where the viscous behavior results from bonds that break in response to loading, and reform in a stress-free state (Ateshian 2015). Other related phenomena, such as damage mechanics, may thus be similarly modeled, where bonds break permanently in response to loading. A main advantage of this approach is that bond mass densities are observable variables whose temporal evolution is governed by the equation of mass balance. Since the evolving composition of a material may be measured experimentally, reactive mixture models may be validated directly against such measurements.

5 Summary

Mixture theory is an elegant continuum mechanics framework that is well suited for modeling biological tissues. While many biomechanics investigators have opted to use this framework since its introduction in the 1960s, it is fair to state that some of its earliest and most determined proponents were Van C. Mow and W. Michael Lai,¹ who applied it to the modeling of articular cartilage, and worked over several decades in an effort to validate and extend this framework to accommodate the complexities of biological tissues. With their biphasic theory, they applied mixture theory to model biological tissues as deformable porous media.

Porous media had already been successfully modeled using earlier theories, first proposed by Fillunger, then Terzaghi, as reviewed in the captivating historical perspective of Boer (1996), subsequently advanced by Biot (1941) as consolidation theory, and recast as poroelasticity theory by Rice and Cleary (1976). Indeed, Bowen (1980) and Mow and Lai (1980) pointed out the equivalence of their approaches to Biot's earlier work. However, despite its elegance, the poroelasticity framework did not provide the foundations for extending the theory to multiple constituents, nor mass exchanges among the constituents. By using mixture theory, Lai et al. (1991) showed that biphasic theory could be systematically extended to triphasic theory, which laid the foundations for many subsequent developments, as partially reviewed in Sect. 4.

Many other investigators have independently demonstrated the value of mixture theory for modeling complex phenomena in biological tissues, as also partially reviewed above. Because theoretical frameworks are critically dependent on constitutive assumptions, there is no unique formulation of mixture theory for a given combination of fluid and solid constituents. Consequently, I felt that an exhaustive

¹Mow and Lai were this author's doctoral advisors and mentors, starting in 1986.

review and comparison of mixture models in biological tissues was beyond the scope of this chapter. The modeling approach reviewed here provides the foundation of the framework and I have found useful in my own investigations and applications to biological tissues. In collaboration with Jeffrey Weiss, Steve Maas and other colleagues, we have strived to provide finite element computational tools (Maas et al. 2012) that implement biphasic and multiphasic theories (Ateshian et al. 2011, 2013), including contact mechanics (Ateshian et al. 2010, 2012) and chemical reactions (Ateshian et al. 2014), to facilitate the dissemination of this framework within the biomechanics community.

Acknowledgments I would like to thank the many former and current doctoral students and fellows who labored with me over the years, performing experiments and validating the mixture models used in our investigations of biological tissues: Dr. Huiqun (Laura) Wang, Dr. William H. Warden, Dr. Michael A. Soltz, Prof. Robert L. Mauck, Prof. Chun-Yuh (Charles) Huang, Dr. Changbin Wang, Dr. Ramaswamy Krishnan, Prof. Seonghun Park, Prof. Ines M. Basalo, Prof. Nadeen O. Chahine, Dr. Michael B. Albro, Dr. Matteo M. Caligaris, Dr. Clare Canal-Guterl, Dr. Sevan R. Oungoulian, Dr. Alexander D. Cigan, Mr. Robert J. Nims, Mr. Brian K. Jones, Mr. Chieh Hou, and Ms. Krista M. Durney. I would also like to thank Dr. Albro for providing the experimental data appearing in Fig. 4, and Mr. Brandon K. Zimmerman for re-analyzing older data sets to produce Fig. 13.

References

- Akizuki, S., Mow, V.C., Müller, F., Pita, J.C., Howell, D.S., Manicourt, D.H.: Tensile properties of human knee joint cartilage: I. Influence of ionic conditions, weight bearing, and fibrillation on the tensile modulus. *J. Orthop. Res.* **4**, 379–392 (1986)
- Albro, M.B., Chahine, N.O., Caligaris, M., Wei, V.I., Likhitpanichkul, M., Ng, K.W., Hung, C.T., Ateshian, G.A.: Osmotic loading of spherical gels: a biomimetic study of hindered transport in the cell protoplasm. *J. Biomech. Eng.* **129**, 503–510 (2007)
- Albro, M.B., Chahine, N.O., Li, R., Yeager, K., Hung, C.T., Ateshian, G.A.: Dynamic loading of deformable porous media can induce active solute transport. *J. Biomech.* **41**, 3152–3157 (2008)
- Albro, M.B., Petersen, L.E., Li, R., Hung, C.T., Ateshian, G.A.: Influence of the partitioning of osmolytes by the cytoplasm on the passive response of cells to osmotic loading. *Biophys. J.* **97**, 2886–2893 (2009)
- Albro, M.B., Li, R., Banerjee, R.E., Hung, C.T., Ateshian, G.A.: Validation of theoretical framework explaining active solute uptake in dynamically loaded porous media. *J. Biomech.* **43**, 2267–2273 (2010)
- Albro, M.B., Banerjee, R.E., Li, R., Oungoulian, S.R., Chen, B., del Palomar, A.P., Hung, C.T., Ateshian, G.A.: Dynamic loading of immature epiphyseal cartilage pumps nutrients out of vascular canals. *J. Biomech.* **44**, 1654–1659 (2011)
- Ambrosi, D., Ateshian, G.A., Arruda, E.M., Cowin, S.C., Dumais, J., Goriely, A., Holzapfel, G.A., Humphrey, J.D., Kemkemer, R., Kuhl, E., Olberding, J.E., Taber, L.A., Garikipati, K.: Perspectives on biological growth and remodeling. *J. Mech. Phys. Solids* **59**, 863–883 (2011)
- Armstrong, C.G., Lai, W.M., Mow, V.C.: An analysis to unconfined compression of articular cartilage. *J. Biomech. Eng.* **106**, 165–173 (1984)
- Armstrong, C.G., Mow, V.C.: Variations in the intrinsic mechanical properties of human articular cartilage with age, degeneration, and water content. *J. Bone Joint Surg. Am.* **64**, 88–94 (1982)
- Ateshian, G.A.: On the theory of reactive mixtures for modeling biological growth. *Biomech. Model. Mechanobiol.* **6**, 423–445 (2007)

- Ateshian, G.A.: Viscoelasticity using reactive constrained solid mixtures. *J. Biomech.* **48**, 941–947 (2015)
- Ateshian, G.A., Humphrey, J.D.: Continuum mixture models of biological growth and remodeling: past successes and future opportunities. *Annu. Rev. Biomed. Eng.* **14**, 97–111 (2012)
- Ateshian, G.A., Ricken, T.: Multigenerational interstitial growth of biological tissues. *Biomech. Model. Mechanobiol.* **9**, 689–702 (2010)
- Ateshian, G.A., Warden, W.H., Kim, J.J., Grelsamer, R.P., Mow, V.C.: Finite deformation biphasic material properties of bovine articular cartilage from confined compression experiments. *J. Biomech.* **30**, 1157–1164 (1997)
- Ateshian, G.A., Likhitpanichkul, M., Hung, C.T.: A mixture theory analysis for passive transport in osmotic loading of cells. *J. Biomech.* **39**, 464–475 (2006)
- Ateshian, G.A., Maas, S., Weiss, J.A.: Finite element algorithm for frictionless contact of porous permeable media under finite deformation and sliding. *J. Biomech. Eng.* **132**(061), 006 (2010)
- Ateshian, G.A., Albro, M.B., Maas, S., Weiss, J.A.: Finite element implementation of mechanochemical phenomena in neutral deformable porous media under finite deformation. *J. Biomech. Eng.* **133**(081), 005 (2011)
- Ateshian, G.A., Maas, S., Weiss, J.A.: Solute transport across a contact interface in deformable porous media. *J. Biomech.* **45**, 1023–1027 (2012)
- Ateshian, G.A., Maas, S., Weiss, J.A.: Multiphasic finite element framework for modeling hydrated mixtures with multiple neutral and charged solutes. *J. Biomech. Eng.* **135**(111), 001 (2013)
- Ateshian, G.A., Nims, R.J., Maas, S., Weiss, J.A.: Computational modeling of chemical reactions and interstitial growth and remodeling involving charged solutes and solid-bound molecules. *Biomech. Model. Mechanobiol.* **13**, 1105–1120 (2014)
- Azeloglu, E.U., Albro, M.B., Thimmappa, V.A., Ateshian, G.A., Costa, K.D.: Heterogeneous transmural proteoglycan distribution provides a mechanism for regulating residual stresses in the aorta. *Am. J. Physiol. Heart Circ. Physiol.* **294**, H1197–1205 (2008)
- Bachrach, N.M., Mow, V.C., Guilak, F.: Incompressibility of the solid matrix of articular cartilage under high hydrostatic pressures. *J. Biomech.* **31**, 445–451 (1998)
- Bayliss, M.T., Urban, J.P., Johnstone, B., Holm, S.: In vitro method for measuring synthesis rates in the intervertebral disc. *J. Orthop. Res.* **4**, 10–17 (1986)
- Bedford, A., Drumheller, D.S.: Recent advances theories of immiscible and structured mixtures. *Int. J. Eng. Sci.* **21**, 863–960 (1983)
- Biot, M.A.: General theory of three-dimensional consolidation. *J. Appl. Phys.* **12**, 155–164 (1941)
- Boer, R.D.: Highlights in the historical development of the porous media theory: toward a consistent macroscopic theory. *Appl. Mech. Rev.* **49**, 201–262 (1996)
- Bowen, R.M.: Thermochemistry of reacting materials. *J. Chem. Phys.* **49**, 1625–1637 (1968)
- Bowen, R.M.: Theory of mixtures. In: Eringen, A.C. (ed.) *Continuum Physics*, vol. III, pp. 1–127. Academic Press, New York (1976)
- Bowen, R.M.: Incompressible porous media models by use of theory of mixture. *Int. J. Eng. Sci.* **18**, 1129–1148 (1980)
- Brown, T.D., Singerman, R.J.: Experimental determination of the linear biphasic constitutive coefficients of human fetal proximal femoral chondroepiphysis. *J. Biomech.* **19**, 597–605 (1986)
- Bryant, M.R., McDonnell, P.J.: A triphasic analysis of corneal swelling and hydration control. *J. Biomech. Eng.* **120**, 370–381 (1998)
- Bursać, P.M., Obitz, T.W., Eisenberg, S.R., Stamenović, D.: Confined and unconfined stress relaxation of cartilage: appropriateness of a transversely isotropic analysis. *J. Biomech.* **32**, 1125–1130 (1999)
- Chahine, N.O., Wang, C.C.B., Hung, C.T., Ateshian, G.A.: Anisotropic strain-dependent material properties of bovine articular cartilage in the transitional range from tension to compression. *J. Biomech.* **37**, 1251–1261 (2004)
- Chahine, N.O., Albro, M.B., Lima, E.G., Wei, V.I., Dubois, C.R., Hung, C.T., Ateshian, G.A.: Effect of dynamic loading on the transport of solutes into agarose hydrogels. *Biophys. J.* **97**, 968–975 (2009)

- Cohen, B., Lai, W.M., Mow, V.C.: A transversely isotropic biphasic model for unconfined compression of growth plate and chondroepiphysis. *J. Biomech. Eng.* **120**, 491–496 (1998)
- Coleman, B.D., Noll, W.: The thermodynamics of elastic materials with heat conduction and viscosity. *Arch. Ration. Mech. Anal.* **13**, 167–178 (1963)
- Cowin, S.C.: The specific growth rates of tissues: a review and a re-evaluation. *J. Biomech. Eng.* **133**(041), 001 (2011)
- Cowin, S.C., Hegedus, D.H.: Bone remodelling I: theory of adaptive elasticity. *J. Elasticity* **6**, 313–326 (1976)
- Curnier, A., He, Q.-C., Zysset, P.: Conewise linear elastic materials. *J. Elast.* **37**, 1–38 (1995)
- Deen, W.: Hindered transport of large molecules in liquid-filled pores. *AIChE J* **33**, 1409–1425 (1987)
- Eringen, A., Ingram, J.: Continuum theory of chemically reacting media - 1. *Int. J. Eng. Sci.* **3**, 197–212 (1965)
- Gailani, G., Benalla, M., Mahamud, R., Cowin, S.C., Cardoso, L.: Experimental determination of the permeability in the lacunar-canalicular porosity of bone. *J. Biomech. Eng.* **131**(101), 007 (2009)
- Gu, W.Y., Lai, W.M., Mow, V.C.: Transport of fluid and ions through a porous-permeable charged-hydrated tissue, and streaming potential data on normal bovine articular cartilage. *J. Biomech.* **26**, 709–723 (1993)
- Gu, W.Y., Lai, W.M., Mow, V.C.: A mixture theory for charged-hydrated soft tissues containing multi-electrolytes: Passive transport and swelling behaviors. *J. Biomech. Eng.* **120**, 169–180 (1998)
- Gu, W.Y., Mao, X.G., Foster, R.J., Weidenbaum, M., Mow, V.C., Rawlins, B.A.: The anisotropic hydraulic permeability of human lumbar anulus fibrosus. influence of age, degeneration, direction, and water content. *Spine (Phila Pa 1976)* **24**, 2449–2455 (1999)
- Harrison, R.G., Massaro, T.A.: Water flux through porcine aortic tissue due to a hydrostatic pressure gradient. *Atherosclerosis* **24**, 363–367 (1976)
- Holmes, M.: A theoretical analysis for determining the nonlinear hydraulic permeability of a soft tissue from a permeation experiment. *Bull. Math. Biol.* **47**, 669–683 (1985)
- Holmes, M.H., Mow, V.C.: The nonlinear characteristics of soft gels and hydrated connective tissues in ultrafiltration. *J. Biomech.* **23**, 1145–1156 (1990)
- Holmes, M.H., Lai, W.M., Mow, V.C.: Singular perturbation analysis of the nonlinear, flow-dependent compressive stress relaxation behavior of articular cartilage. *J. Biomech. Eng.* **107**, 206–218 (1985)
- Huang, C.-Y., Stankiewicz, A., Ateshian, G.A., Mow, V.C.: Anisotropy, inhomogeneity, and tension-compression nonlinearity of human glenohumeral cartilage in finite deformation. *J. Biomech.* **38**, 799–809 (2005)
- Humphrey, J.D., Rajagopal, K.R.: A constrained mixture model for growth and remodeling of soft tissues. *Math. Model. Meth. Appl. Sci.* **12**, 407–430 (2002)
- Jurvelin, J., Buschmann, M., Hunziker, E.: Mechanical anisotropy of the human knee articular cartilage in compression. *Proc Inst Mech Eng Part H: J Eng Med* **217**, 215–219 (2003)
- Kempson, G.E., Freeman, M.A., Swanson, S.A.: Tensile properties of articular cartilage. *Nature* **220**, 1127–1128 (1968)
- Kenyon, D.E.: Transient filtration in a porous elastic cylinder. *J. Appl. Mech.* **43**, 594–598 (1976)
- Kwan, M.K., Lai, W.M., Mow, V.C.: A finite deformation theory for cartilage and other soft hydrated connective tissues-I. Equilib. *Results J. Biomech.* **23**, 145–155 (1990)
- Lai, W.M., Mow, V.C., Roth, V.: Effects of nonlinear strain-dependent permeability and rate of compression on the stress behavior of articular cartilage. *J. Biomech. Eng.* **103**, 61–66 (1981)
- Lai, W.M., Hou, J.S., Mow, V.C.: A triphasic theory for the swelling and deformation behaviors of articular cartilage. *J. Biomech. Eng.* **113**, 245–258 (1991)
- Lai, W.M., Mow, V.C., Sun, D.D., Ateshian, G.A.: On the electric potentials inside a charged soft hydrated biological tissue: Streaming potential versus diffusion potential. *J. Biomech. Eng.* **122**, 336–346 (2000)

- Lanir, Y.: A structural theory for the homogeneous biaxial stress-strain relationships in flat collagenous tissues. *J. Biomech.* **12**, 423–436 (1979)
- Lanir, Y.: Constitutive equations for fibrous connective tissues. *J. Biomech.* **16**, 1–12 (1983)
- Li, L.P., Soulhat, J., Buschmann, M.D., Shirazi-Adl, A.: Nonlinear analysis of cartilage in unconfined ramp compression using a fibril reinforced poroelastic model. *Clin. Biomech. (Bristol, Avon)* **14**, 673–682 (1999)
- Li, L.P., Buschmann, M.D., Shirazi-Adl, A.: A fibril reinforced nonhomogeneous poroelastic model for articular cartilage: Inhomogeneous response in unconfined compression. *J. Biomech.* **33**, 1533–1541 (2000)
- Maas, S.A., Ellis, B.J., Ateshian, G.A., Weiss, J.A.: FEBio: Finite elements for biomechanics. *J. Biomech. Eng.* **134**(011), 005 (2012)
- Mak, A.F., Lai, W.M., Mow, V.C.: Biphasic indentation of articular cartilage-I. *Theor. Anal. J. Biomech.* **20**, 703–714 (1987)
- Mansour, J.M., Mow, V.C.: The permeability of articular cartilage under compressive strain and at high pressures. *J. Bone Joint Surg. Am.* **58**, 509–516 (1976)
- Maroudas, A.I.: Balance between swelling pressure and collagen tension in normal and degenerate cartilage. *Nature* **260**, 808–809 (1976)
- Mauck, R.L., Hung, C.T., Ateshian, G.A.: Modeling of neutral solute transport in a dynamically loaded porous permeable gel: implications for articular cartilage biosynthesis and tissue engineering. *J. Biomech. Eng.* **125**, 602–614 (2003)
- Mow, V.C., Lai, W.M.: Recent developments in synovial joint biomechanics. *SIAM Rev.* **22**, 275–317 (1980)
- Mow, V.C., Mansour, J.M.: The nonlinear interaction between cartilage deformation and interstitial fluid flow. *J. Biomech.* **10**, 31–39 (1977)
- Mow, V.C., Kuei, S.C., Lai, W.M., Armstrong, C.: Biphasic creep and stress relaxation of articular cartilage in compression: theory and experiments. *J. Biomech. Eng.* **102**, 73–84 (1980)
- Mow, V.C., Holmes, M.H., Lai, W.M.: Fluid transport and mechanical properties of articular cartilage: a review. *J. Biomech.* **17**, 377–394 (1984)
- Mow, V.C., Gibbs, M.C., Lai, W.M., Zhu, W.B., Athanasiou, K.A.: Biphasic indentation of articular cartilage-II. A numerical algorithm and an experimental study. *J. Biomech.* **22**, 853–861 (1989)
- Oloyede, A., Broom, N.: Is classical consolidation theory applicable to articular cartilage deformation? *Clin. Biomech. (Bristol, Avon)* **6**, 206–212 (1991)
- Oloyede, A., Broom, N.: Stress-sharing between the fluid and solid components of articular cartilage under varying rates of compression. *Connect. Tissue Res.* **30**, 127–141 (1993)
- Park, S., Krishnan, R., Nicoll, S.B., Ateshian, G.A.: Cartilage interstitial fluid load support in unconfined compression. *J. Biomech.* **36**, 1785–1796 (2003)
- Rice, J.R., Cleary, M.P.: Some basic stress diffusion solutions for fluid-saturated elastic porous media with compressible constituents. *Rev. Geophys. Space Phys.* **14**, 227–241 (1976)
- Schneiderman, R., Keret, D., Maroudas, A.: Effects of mechanical and osmotic pressure on the rate of glycosaminoglycan synthesis in the human adult femoral head cartilage: an in vitro study. *J. Orthop. Res.* **4**, 393–408 (1986)
- Soltz, M.A., Ateshian, G.A.: Experimental verification and theoretical prediction of cartilage interstitial fluid pressurization at an impermeable contact interface in confined compression. *J. Biomed.* **31**, 927–934 (1998)
- Soltz, M.A., Ateshian, G.A.: A conewise linear elasticity mixture model for the analysis of tension-compression nonlinearity in articular cartilage. *J. Biomed. Eng.* **122**, 576–586 (2000a)
- Soltz, M.A., Ateshian, G.A.: Interstitial fluid pressurization during confined compression cyclical loading of articular cartilage. *Ann. Biomed. Eng.* **28**, 150–159 (2000b)
- Soulhat, J., Buschmann, M.D., Shirazi-Adl, A.: A fibril-network-reinforced biphasic model of cartilage in unconfined compression. *J. Biomed. Eng.* **121**, 340–347 (1999)
- Spilker, R.L., de Almeida, E.S., Donzelli, P.S.: Finite element methods for the biomechanics of soft hydrated tissues: nonlinear analysis and adaptive control of meshes. *Crit. Rev. Biomed. Eng.* **20**, 279–313 (1992)

- Truesdell, C., Toupin, R.A.: The classical field theories. In: Flügge, S. (ed.) Encyclopedia of Physics, III(1), pp. 226–793. Springer, Berlin (1960)
- Vargas, C.B., Vargas, F.F., Pribyl, J.G., Blackshear, P.L.: Hydraulic conductivity of the endothelial and outer layers of the rabbit aorta. *Am. J. Physiol.* **236**, H53–H60 (1979)
- Wan, W., Hansen, L., Gleason Jr., R.L.: A 3-D constrained mixture model for mechanically mediated vascular growth and remodeling. *Biomech. Model. Mechanobiol.* **9**, 403–419 (2010)
- Wang, C.C.B., Chahine, N.O., Hung, C.T., Ateshian, G.A.: Optical determination of anisotropic material properties of bovine articular cartilage in compression. *J. Biomech.* **36**, 339–353 (2003)
- Weiss, J.A., Maakestad, B.J.: Permeability of human medial collateral ligament in compression transverse to the collagen fiber direction. *J. Biomech.* **39**, 276–283 (2006)

A Bio-chemo-mechanical Model for Cell Contractility, Adhesion, Signaling, and Stress-Fiber Remodeling

Robert M. McMeeking and Vikram S. Deshpande

Abstract A bio-chemo-mechanical model is described that targets contractility, adhesion, signaling, and cytoskeleton formation and remodeling, where the effort in the case of the last phenomena is focused on actomyosin stress-fibers. The contractility of the cell is driven by the stress-fibers, which also determine much of the active and passive mechanics that characterize the cell's mechanical behavior. The stress-fibers attach to adhesion proteins that connect the cell to an extracellular matrix or to a substrate, and apply contractile force through them. This in turn generates signals that can trigger cytoskeleton formation and remodeling. The signals can also arise from external sources such as nervous impulses and biochemical changes to the cell's surroundings. The model is installed as a user element in a finite element code and used to simulate cell behavior in vitro, such as contraction on a compliant, smooth, flat substrate, or on a bed of compliant posts. Interactions with patterned substrates are also modeled, such as where cells have a limited area to which they can adhere, or where the cells interact with grooves. The results of these simulations are very encouraging as they are largely consistent with observed cell behavior.

1 Introduction

About 10 years ago we became interested in the biomechanics of eukaryotic cells, mainly due to the experiments of Chen and coworkers (Tan et al. 2003), where cells are placed on a bed of small compliant posts and, adhering to them, contract and cause bending of the posts. The post deflections can be measured, and as a result the forces being applied by the cell, typically on the scale of tens of nanonewtons, can

R.M. McMeeking (✉)
University of California, Santa Barbara, CA, USA
e-mail: rmcm@engineering.ucsb.edu

R.M. McMeeking
University of Aberdeen, Aberdeen, UK

V.S. Deshpande
University of Cambridge, Cambridge, UK

be quantified. Many interesting phenomena emerge from such experiments, such as how cells interact with posts of various levels of stiffness, and with differing numbers of posts. These phenomena are paralleled by equivalent observations of cells on compliant, smooth, flat substrates, or on patterned substrates consisting of topography (say grooves) or limited segments to which the cell can adhere. We developed a bio-chemo-mechanical model for the cell contractility, its adhesion to its substrate whether smooth or post-like, the relevant biochemical signaling that goes on inside the cell, and the consequent activity within the cell such as cytoskeleton formation and remodeling. Our purpose in developing the model was to aid in the development of a deeper understanding of the cell behavior being observed in the experiments, and to support the development of further experimental activity. In addition, we hope that our model can be applied to situations where cell mechanics, contractility, and adhesion are known to be important in biology and medicine, such as cell motility, wound healing, development, and embryology, the behavior of stem cells, and in diseases such as cancer, congestive heart failure and cardiac recovery after infarctions where forces and stiffness are known to be relevant parameters. This hope is as yet unrealized, but we aim to continue to develop our model to bring it to a state of readiness where it may yet play such a role.

The purpose of this article is to summarize the model, originally presented in Deshpande et al. (2006, 2007), and to describe some results obtained with it. In doing so, we will describe the results of some experiments on the mechanobiology of cells that we have been able to simulate. However, we do not intend this paper to be a comprehensive review of the behavior of cells in a mechanical setting, or of their active mechanical behavior. We only describe experiments that have either guided our thinking in the development of our models or that we have simulated with some degree of success. Similarly, we will not review the broad category of models for the mechanobiology of cells and will focus only on our own work to provide a summary of it. Furthermore, much of the biochemistry that is a background to our work, and some of the mechanics, is described in the textbook of Alberts et al. (2008).

We note also that the model we describe is one currently in transition. There are certain elements of it that have a high degree of phenomenology built in to them, and our current view is that some of this should be replaced by model features that possess a more fundamental treatment of the chemistry and physics. In fact, one of us is a co-author of a recent paper that puts forward some of the ideas and treatments that bring a more fundamental approach to some aspects of the chemistry and physics of the cell behavior than has previously been embedded in our model. This paper, Vigliotti et al. (2015b), addresses the response of cells under cyclic straining *in vitro* on flat substrates and within 3-dimensional synthetic extracellular matrices. As a result of this new treatment, the complex and subtle differences in behavior in the relevant experiments have been rationalized, whereas the previous version was only able to simulate the results of the experiments to a low level of fidelity. Therefore, the more fundamental treatments embedded in the new version of the model, and their success in their ability to model the situation described, encourage us that they have value that can be exploited to simulate further important phenomena in the mechanobiology of cells. This development may suggest that summarizing the prior

features of the model in the current article is pointless; however, many aspects of the model remain the same, and the phenomenological treatments that are used in many cases give the same results as would arise from the new, more fundamental treatment. Furthermore, at this turning point a retrospective assessment of where we are has value and is briefly summarized in this paper.

2 Relevant Cell Features

The behavior of the cell that is described by the model arises from stress-fibers, long fibrils that consist of actin protein chains entangled by myosin molecular motors. These fibrils, described in further detail by Alberts et al. (2008), are one component of the cell cytoskeleton. In addition to the stress-fibers, in the cytoskeleton there are intermediate filaments and microtubules, also fibrillar elements. However, we focus on the stress-fibers as they are the source of cell contractility, and therefore mechanically provide one of the most important contributions to the cell active behavior. The cytoskeleton lives within a lipid cell membrane that surrounds the cell, and within a hydrous cytosol that has protein monomers for the fibrillar elements of the cytoskeleton dissolved in it. In addition, there are other elements within the cell such as the endoplasmic reticulum, the mitochondria and the golgi body that all play roles in the biochemistry of the cell. For example, the mitochondria generate ATP, the fuel for many processes that take place within the cell, including the contractility driven by the myosin motors. Central to the cell is the nucleus where its DNA is stored and gene transcription takes place. All these features are described in more detail by Alberts et al. (2008).

An illustration of the geometry of stress-fibers is shown in Fig. 1, where they have been visualized in vitro by proteins that attach to them and cause fluorescence. In the left-hand image the stress-fibers can be seen and in the right-hand image the bright

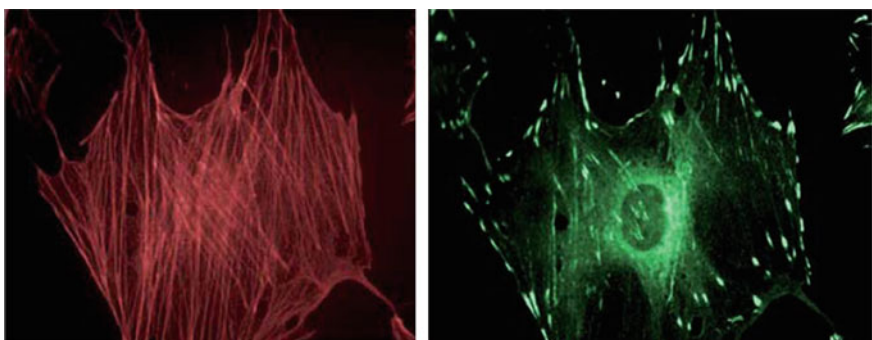


Fig. 1 A cell treated to enable visualization of stress-fibers (*left*) and focal adhesions. In the *right-hand image* image the nucleus is also visible

short streaks are focal adhesions. The latter consist of a plaque of various proteins inside the cell membrane and adjacent to it. One protein within the plaque, integrin, is transmembrane and attaches to ligands outside the cell. This anchors the focal adhesion either to the extracellular matrix or, *in vitro*, to a substrate that has been treated to present ligands. The other end of the integrin molecule attaches to the focal adhesion plaque, which in turn attaches to the end of one or more stress-fibers. There are usually multiple integrins associated with a given focal adhesion; indeed a focal adhesion is defined to be an attachment that encompasses many integrin proteins.

In vitro, a substrate can be treated with materials, such as fibronectin, that present ligands favored by integrins for attachment. This can be done on a flat stiff surface, and a cell in a nutrient bath adjacent to this surface will spontaneously adhere. However, the most interesting results are obtained when the substrate is compliant so that the cell is capable of deforming the substrate by its contractile apparatus. Experiments on such surfaces have shown that many types of cells are indeed contractile, and respond both biochemically and mechanically to the stiffness of the substrate, e.g., by growing a more profuse cytoskeleton that is more powerful in contraction when the stiffness is at a favorable level. The most easily quantifiable experiments in terms of mechanics are those involving cells on posts, since it is straightforward to measure the forces applied to the posts by the cells. An illustration of this set up, developed by Tan et al. (2003), is shown in Fig. 2 which is a top view of a smooth muscle cell adhered to PDMS posts having fibronectin on their tips. The posts are 3 μm in diameter and tens of μm long, and it can be seen that the cell is capable of bending the posts, having done so by contracting. The results of an experiment visualizing the actin in the cell and showing arrows that indicate the forces applied is illustrated in Fig. 3. A temporal graph of the magnitudes of the forces applied to posts by a smooth muscle cell is given in Fig. 4. In the relevant experiment by Tan et al. (2003) the cell was at first down regulated so that it was relatively inactive, a state it was in at time zero in Fig. 4.

Fig. 2 A smooth muscle cell adhered to PDMS posts whose tips are coated with fibronectin. The cell has contracted, and as a result deflected the posts. The scale marker is 10 μm . Results from Tan et al. (2003)

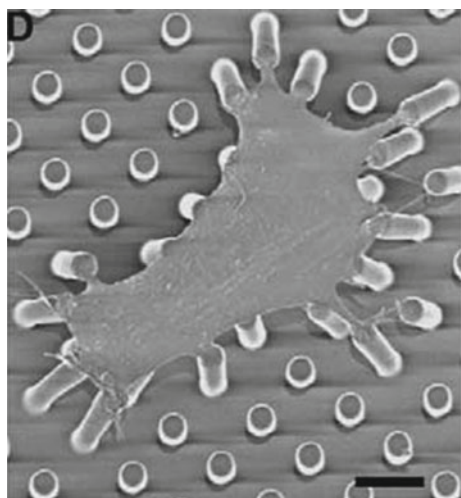


Fig. 3 A cell imaged for actin (green) with arrows showing the magnitude and direction of force applied to the tip of the relevant post. The arrow at bottom right is a scale indicator whose length equals 20 nN

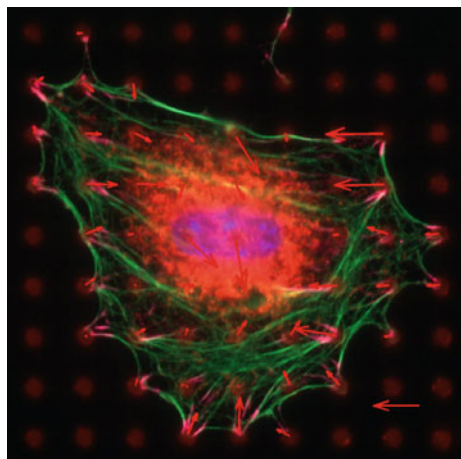
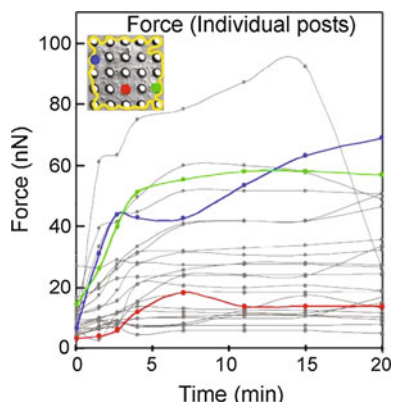


Fig. 4 Force magnitudes applied to 25 posts by a smooth muscle cell. Shown as a function of time elapsed after up-regulation of the cell. Results from Tan et al. (2003)



The cell was then stimulated biochemically at time zero, with the result that it remodeled its cytoskeleton, and in doing so increased the forces generated by its contractile machinery. In this case, the post is attached to approximately 25 posts, and it can be seen that the forces applied rise as high as 100 nN and take approximately 5 min to mature. We note that some aspects of the behavior of cells on posts are influenced by the fact that only discrete areas are available for the cell to adhere to, and that the tips of the posts are all in the same plane. Therefore, the distribution of actin and the degree of contractility may be influenced by the synthetic setting that the cell is placed in. However, almost all of the phenomena observed in cells on posts are reflected by the behavior of cells in other settings, such as in 3-dimensional gels. Furthermore, we judge the response of cells on posts to be a valid set of results for guiding the development of a model and for verifying and validating it.

The significance of focal adhesions is illustrated in the results of experiments carried out by Théry et al. (2006), who formed patterned, flat, surfaces by coating

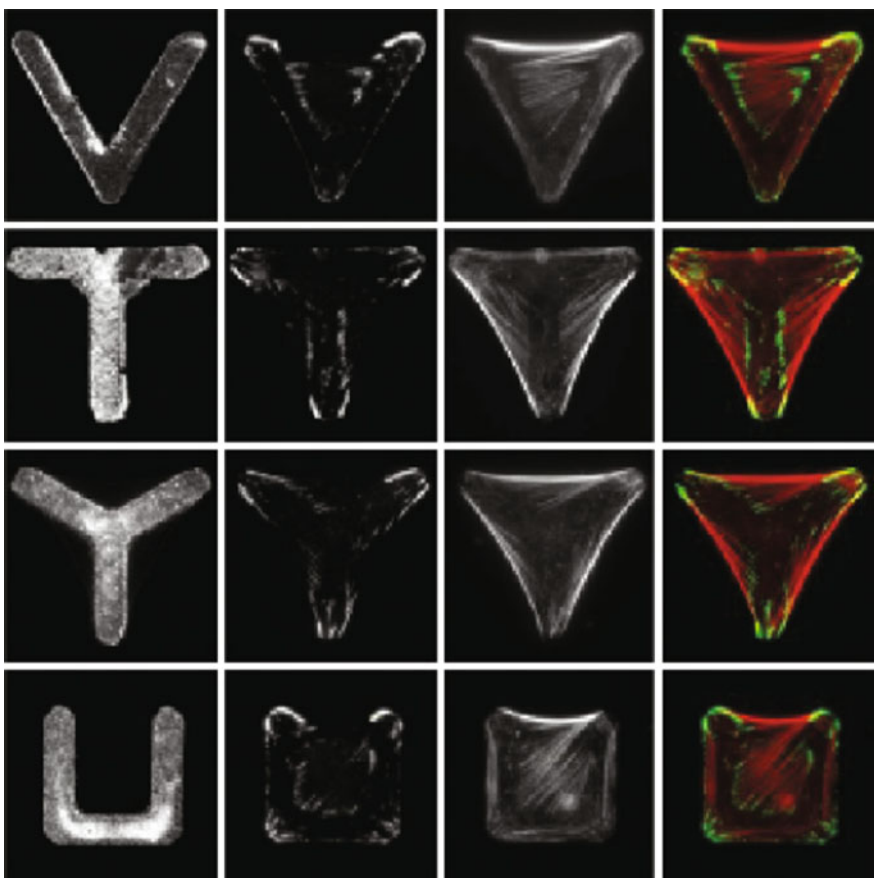


Fig. 5 Cells on fibronectin patterns stained to allow visualization of fibronectin (*left column*), vinculin (*second column from the left*) and actin (*second column from the right*). Vinculin is a protein present in focal adhesion complexes. The *column on the right* is a merger of the other three columns. Results from Théry et al. (2006)

fibronectin in shapes of the letters of the alphabet on a stiff substrate. They then allowed cells to adhere to the fibronectin, with results shown in Fig. 5. In these images it can be seen that the cells extend to cover almost the convex hull of the fibronectin patterns, but the cells adhere directly only to the fibronectin, as vinculin, a focal adhesion protein, is visible only where there is fibronectin available for the adhesion to bind to. Furthermore, the focal adhesions are clustered around the edges of the fibronectin patterns with highest curvature. The focal adhesions are providing the means by which the cells anchor themselves to the substrate, which they do so by binding to the fibronectin, which is an extracellular matrix protein. This illustrates the role of the focal adhesions, or focal complexes, as they can connect the cells to

the adjacent extracellular matrix, thereby enabling cells to perform their functions in conjunction with nearby cells of like type.

We note that in the images of Fig. 5 there are significant areas of the cells that are not adhered directly to the fibronectin, as there are large areas where vinculin is absent. We see, therefore, that the focal adhesions form around the perimeter of the available ligands, and that actin stress-fibers are strung from one set of focal adhesions to another. Although this behavior is not universal *in vivo*, it is a notable aspect of the role that focal adhesions play. We note also that that there are pronounced amounts of actin visible along the unadhered edges of the cells, and that these edges are concave outwards due to contractility of the cell cytoskeleton.

3 The Model

As noted above, our model focuses on the cytoskeleton and the adhesions, but has a rudimentary representation of other features of the cell, captured by background elasticity. We use isotropic, linear infinitesimal strain elasticity, but this could be replaced by something more complicated such as viscoelasticity or nonlinear large strain elasticity. Indeed, in some versions of our model applied to some simulations, the latter is what is used for the background mechanical behavior. The stress-fiber model consists of three elements. The first is a signal that initiates the processes of interest; it could be generated by a nervous impulse, or it could be the outcome of a feedback loop that involves forces being applied to proteins within the cell. An example of the latter is that focal adhesions are known to generate signals when forces are applied to them. In the initial version of the model, the signal is very simple, given by

$$C = e^{-t_i/\theta}, \quad (1)$$

where t_i is the time elapsed since initiation of the signal and θ is its decay time. Therefore the signal rises to unity very rapidly and decays to zero as time elapses thereafter. This behavior is designed to simulate the concentration of signaling proteins and ions, with an example of the latter being Ca^{++} . The signal is applied simultaneously everywhere in the cell; in later versions of the model developed by Pathak et al. (2011) we have used reaction-diffusion equations to simulate signals, including the release of signaling proteins from their sources as the signal initiates, the downstream activation of further signaling proteins and the accompanying ions such as calcium. We have found that in many settings the simple signal in Eq.(1) applied simultaneously everywhere in the cell is an adequately accurate representation of the deeper complexities of the signaling process.

The second element of the model is the chemical kinetics of stress-fiber polymerization and depolymerization. This is stated as

$$\frac{d\eta}{dt} = (1 - \eta) \frac{\bar{k}_f C}{\theta} - \left(1 - \frac{T}{nT_{\max}}\right) \eta \frac{\bar{k}_b}{\theta}, \quad (2)$$

where at a material point in the cell η is a scaled concentration of stress-fibers emanating from that point in a given orientation, t is time, \bar{k}_f/θ is the forward rate constant for the polymerization reaction, \bar{k}_b/θ is the reverse, i.e., depolymerization rate constant, T is the tension in the stress-fiber and T_{\max} is a cell phenotype dependent constant. We note that the signal is embedded in the forward reaction term in Eq. (2), and therefore sets off the process of polymerization of stress-fibers from actin and myosin proteins. Furthermore, ηT_{\max} is the isometric tension in a stress-fiber at concentration η . The presence of the stress-fiber tension in the depolymerization term of Eq. (2) makes the process mechanosensitive. If the tension T reaches the isometric level, ηT_{\max} , depolymerization is eliminated and a stable stress-fiber can be retained. In the absence of the term in parenthesis containing the stress-fiber tension the signal in Eq. (2), which decays to zero after its initial rise, would simply initiate polymerization that would lead to depolymerization that would sweep away the stress-fiber. Therefore, in our model stress-fibers can only be formed where they can sustain isometric tension at some level of stress-fiber concentration, which means that they must be constrained in some way to a foundation that can sustain the tension applied to it. This foundation is considered to be focal adhesions that connect the stress-fibers to the extracellular matrix or to a substrate to which the cell is affixed. In the earliest version of the model, these focal adhesions form spontaneously on demand so that they are always available to support stress-fibers that are able to attach to them. As noted above, η is a scaled concentration equal to the number passing through unit area divided by the maximum possible number that can do so. Its value is therefore limited to $0 \leq \eta \leq 1$.

The third element of our model is a constitutive law for the stress-fiber contraction, given by

$$\frac{T}{T_{\max}} = \begin{cases} 0 & \dot{\varepsilon}/\dot{\varepsilon}_0 < -\eta/\bar{k}_v, \\ \eta + \bar{k}_v \frac{\dot{\varepsilon}}{\dot{\varepsilon}_0} & -\eta/\bar{k}_v \leq \dot{\varepsilon}/\dot{\varepsilon}_0 \leq 0, \\ \eta & \dot{\varepsilon}/\dot{\varepsilon}_0 > 0, \end{cases} \quad (3)$$

where \bar{k}_v is a rate constant or viscosity parameter, $\dot{\varepsilon}$ is the strain-rate of the stress-fiber (positive in extension) and $\dot{\varepsilon}_0$ is a material constant. The model in Eq. (3) is justified by Hill (1938) muscle kinetics and is a simplified version of it, approximated into three linear segments instead of the usual nonlinear function. Such justification relies on the fact that the proteins in stress-fibers (myosin II and actin) are identical to those present in the sarcomeres of skeletal muscle, and therefore will possess the same dynamic constitutive response. Furthermore, stress-fiber shrinkage is a somewhat slow process, and therefore the original Hill (1938) model is assumed to be an adequate representation of their constitutive behavior.

The equations above are homogenized into a 2-dimensional or 3-dimensional formulation through the construction of a representative volume element (RVE) that is used to compute the stress. We will summarize the 2-dimensional case as it is simpler and is valid for a spread cell whose thickness is very small compared to its other dimensions. A 3-dimensional formulation is given in papers such as that by

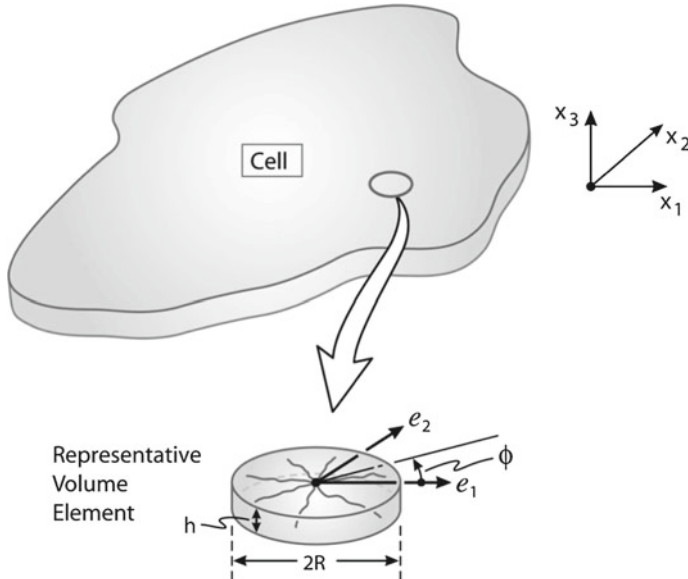


Fig. 6 A spread cell and a representative volume element (RVE) extracted from it. The layout of the cytoskeleton is represented by stress-fibers emanating from the *center* of the *disk* in all orientations within the plane of the flat cell, which has uniform thickness h . The density of stress-fibers passing through unit area at the perimeter of the RVE is a function of position, ϕ , around the perimeter. Similarly the concentration and distribution of stress-fibers at one point in the cell can be very different from those elsewhere in the cell

Ronan et al. (2012) and Dowling et al. (2012). For the 2-dimensional formulation we consider the disk shaped region shown in Fig. 6, sometimes known as a microdisk or micropill. The layout of the cytoskeleton is represented by stress-fibers emanating from the center of the disk in all orientations within the plane of the flat cell, which has uniform thickness h . The density of stress-fibers passing through unit area at the perimeter of the RVE is a function of position, ϕ , around the perimeter. Similarly the concentration of stress-fibers at one point in the cell can be very different from that elsewhere in the cell. We first compute the stress-fiber tension at ϕ according to Eq. (3) and convert it to a stress by use of

$$\sigma(\phi) = \frac{2T(\phi)}{\pi Rh}, \quad (4)$$

where R is the radius of the RVE as shown in Fig. 6. A plane stress tensor at the material point centered within the RVE is then given by

$$\begin{bmatrix} \sigma_{11} & \sigma_{12} \\ \sigma_{12} & \sigma_{22} \end{bmatrix} = \frac{1}{\pi} \int_{-\pi/2}^{\pi/2} \begin{bmatrix} \sigma(\phi) \cos^2 \phi & \frac{1}{2}\sigma(\phi) \sin 2\phi \\ \frac{1}{2}\sigma(\phi) \sin 2\phi & \sigma(\phi) \sin^2 \phi \end{bmatrix} d\phi. \quad (5)$$

Note that in this formulation we have assumed that the rigid rotation of the RVE associated with the deformation is negligible and therefore no adjustment of the stress components into the current configuration is used. In our paper Deshpande et al. (2007) this adjustment is given to provide a more general case and is used throughout our numerical computations. To the stress deduced from Eq. (5) are added components to represent other elements of the cell acting in parallel to the stress-fiber cytoskeleton. For example, linear or nonlinear continuum elasticity is used to represent microtubules, intermediate filaments (i.e., other elements of the cytoskeleton are modeled as passive elements), the plasma membrane, the nucleus and other organelles within the cell. The total Cauchy stress in the cell is therefore

$$\Sigma_{ij} = \sigma_{ij} + \sigma_{ij}^A, \quad (6)$$

where σ_{ij}^A is the stress added in the manner described above. Note that the stress σ_{ij}^A is usually derived from uniform mechanical properties within the cell such as the elasticities, and therefore does not recognize spatial heterogeneities within the cell. However, in some of our 3D computations, with a more elaborate stress tensor than is given in Eq. (5), organelles such as the nucleus are identified explicitly as separate regions of the cell and given their own mechanical properties.

We have developed user materials for finite element codes such as the Abaqus software (2013) that encompass all the phenomena and formulations summarized in Eqs. (1)–(6), thereby enabling us to undertake fairly elaborate computations. Similarly, 3-dimensional user elements have been developed for the same purpose, and have been used in papers such as Ronan et al. (2012) and Dowling et al. (2012).

4 Results

The model described above has been used to simulate a number of phenomena in the response of cells to their mechanical environment. In one case, a spread cell is attached to 121 compliant microposts that are represented as springs in a square array in the numerical simulations. The cell is down regulated so that its stress-fiber cytoskeleton is minimal and its contractile stress negligible. It is then stimulated by a signal, so that stress-fibers polymerize, attach to posts through focal adhesion connections, and, by contracting, pull on the posts. The results for post deflection magnitudes, or equivalently the magnitude of forces applied to posts, are shown in Fig. 7 as a function of time elapsed after stimulation. Since the problem has twofold symmetry results for one quarter of the system are shown in Fig. 7, i.e., for the 25 posts in a given quarter that displace. Material and cell parameters can be identified to quantify the forces generated and applied to the posts by the cell activity. This will not be pursued here, but instead we will simply draw the reader's attention to Fig. 4, which displays the equivalent experimental results of Tan et al. (2003) for a cell on 25 posts. The similarities between the results of the simulation in Fig. 7 and

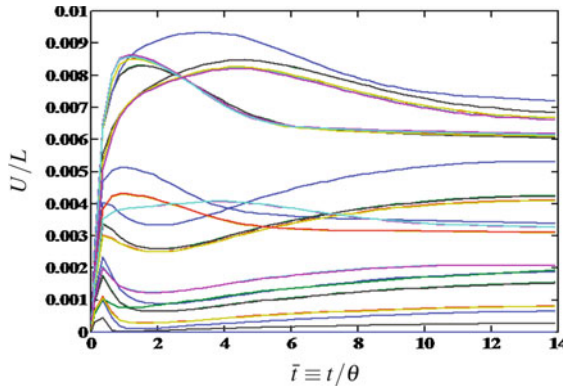


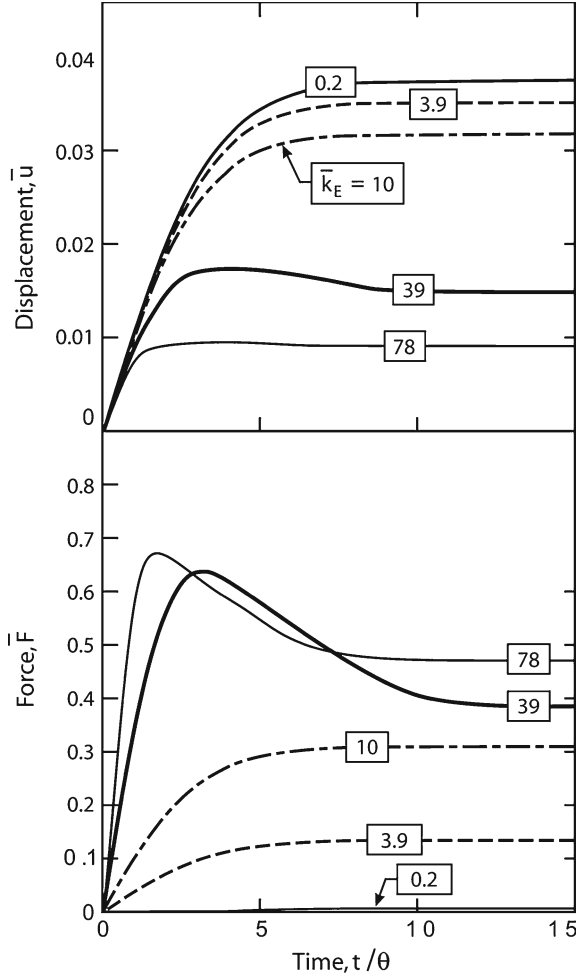
Fig. 7 Simulation results for the displacement of the tips of posts to which a contractile cell is attached. The cell is at first quiescent, but is then stimulated, polymerizing a stress-fiber cytoskeleton that attaches to posts via focal adhesions, and, by pulling on the posts through contractility, displaces the tips of the posts by a magnitude U . The length of the posts is L and the result are shown as a function of time elapsed after stimulation

those for the experiments in Fig. 4 are clear. Given that a 100 nN force would deflect a post tip by 1 % of its length, and that the signal relaxation time, θ , is approximately 1 min, the equivalency between the two sets of results is very close. Furthermore the experimental observation that posts around the perimeter of the cell experience greater force and displacement magnitudes than posts in the interior of the cell is present also in the results of the simulation.

4.1 Influence of Substrate Stiffness on Cell Response

Having shown that the model simulates well the response of cells adhered to micro-posts, we now investigate the influence of post stiffness on the cell's behavior. The motivation behind this step is the experimental observation of Lo et al. (2000), Discher et al. (2005) and others that cells generate a prominent cytoskeleton and apply relatively high contractile forces to a substrate when that substrate is stiff, but when the substrate is compliant the cytoskeleton is less well developed and the contractile forces are lower. The relevant simulations, described by Deshpande et al. (2006), are carried out for a square, spread cell that is attached to posts at each of its corners, and are implemented for an initially quiescent cell that is stimulated by a signal at time zero. As with the simulation for the cell on 121 posts, it then builds a cytoskeleton, attaches stress-fibers to posts via focal adhesions, and, by contracting the stress-fibers, pulls on the posts. Results for the post deflections and forces applied to the posts are shown in Fig. 8. The lower of the diagrams in Fig. 8 demonstrates that stiffer posts lead to higher forces being applied to the posts. The nonmonotonic response observed for the higher stiffness posts is a result of the interplay among the various

Fig. 8 Simulation results for the post deflections and forces applied to corner posts by a square, spread cell. The post deflections are normalized by $50 \mu\text{m}$ which is the edge length of the cell, and the force applied to the post is normalized by 17.5nN , which is the largest force the stress-fibers can exert on a post. The signal decay time, θ , is 720s . The number in the box over each curve is the normalized stiffness of the posts, where the normalization factor is $0.35 \text{nN}/\mu\text{m}$



time constants in the model, details of which for these computations are given in Deshpande et al. (2006). Note that the post displacements follow the opposite trend and are larger for the more compliant posts. Thus the model does not yield cell behavior that conforms to homeostasis for the post deflections, i.e., the cell deformations do not seek a fixed value of the final post deflections that is independent of the post stiffness.

The source of the behavior summarized in Fig. 8 is the interaction of the post stiffness with the depolymerization of stress-fibers. A stress-fiber attached to a stiff post and pulling on it will not be able to shrink rapidly and, from Eq. (3), will generate a high tension before the post has deflected very much. As a result T in Eq. (2) will remain close to ηT_{\max} and there will not be much depolymerization. That which does occur will cease when ηT_{\max} reaches a value equal to T , and the stress-fiber

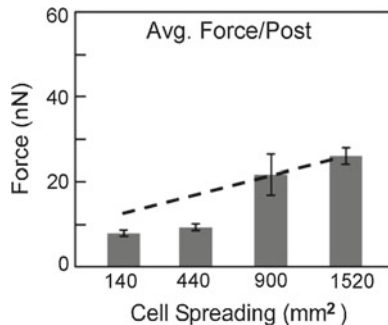
network will be stabilized in isometric condition at a relatively high value of η . Thus, the stress-fiber cytoskeleton network will be relatively profuse. In turn, Eq. (3) tells us that with a relatively high value of η , the force applied by the stress-fiber to the post will be high. In contrast, when a stress-fiber is attached to a compliant post and pulls on it, the stress-fiber will be able to shrink relatively rapidly as the post deflects significantly. As a result T in Eq.(2) will fall significantly below ηT_{\max} allowing a great deal of depolymerization. Thus ηT_{\max} will equate with T at a relatively low value of η , leaving an isometric network of stress-fibers that is not very well developed. Furthermore, the result from Eq. (3) indicates that when η is low, the isometric force generated by the stress-fiber is small, and thus the force applied to the post is relatively low. These observations regarding the extent of cytoskeleton development and the level of forces applied to the substrate are consistent with experimental observations, such as those made by Lo et al. (2000) and Discher et al. (2005).

4.2 *Influence of the Number of Posts to Which a Cell Is Attached*

Tan et al. (2003) carried out an experiment to investigate the behavior of smooth muscle cells when allowed to adhere to a limited number of posts. They coated fibronectin on a limited number of posts and attached cells to them where the posts elsewhere had no fibronectin, and were thus unattractive for attachment by the cells. In this way Tan et al. (2003) were able to adhere the cells to square arrays of 4, 9, 16, and 25 posts. In fact, the plot shown in Fig. 4 depicts the forces generated when the cell is attached to 25 posts. From the post deflections, Tan et al. (2003) computed the average magnitude of the forces applied to the posts, and obtained the surprising result that this value rose with the number of posts. These results are shown in Fig. 9. The reason why these results are surprising lies in the observation in Figs. 4 and 7 that the magnitude of the force applied to perimeter posts is larger, sometimes much larger, than the magnitude applied to interior posts. Thus as one introduces more interior posts by increasing the number in a square array, i.e., going from zero, to 1, 4 to 9 interior posts as the total number of posts is taken from 4 to 25, the force per post should fall if the force applied to the perimeter posts retains its magnitude as the number of posts increases. The experimental results indicate that this trend is not occurring, and that the magnitude of the forces being applied to the perimeter posts must be rising as the number of posts increases.

We have simulated this situation by placing our model cells on different numbers of posts in square arrays, going as high as 21 by 21 posts, and initiating stress-fiber polymerization by imposing a signal. The results are obtained in nondimensional form, and we have fitted one set of them to the experimental data by forcing agreement with the experimental result for the largest number of posts in Fig. 9. Although Fig. 9 is not a linear plot on the abscissa, it happens that our four results when plotted on Fig. 9 fall in a straight line, which is the dashed one shown in that figure. It can be

Fig. 9 Average magnitude of the force applied by a smooth muscle cell to posts as a function of the size of the cell. The *four bar graphs* correspond from left to right to cells on 4, 9, 16, and 25 posts. The *dashed line* is a result of one of our simulations fitted to the result for the largest cell



seen that our model correctly predicts the scaling of the average force per post as the number of posts is increased. This behavior comes about in our model because a cell sitting on many posts senses a stiff environment, whereas a cell attached to only a few posts is in a compliant one. Therefore the cell responds with the same trend that is seen when it interacts with stiff posts as opposed to the same number of compliant post; the force magnitudes applied to the posts rise as the environment stiffens. Thus, in the stiff environment where the cell is sitting on many posts it responds by generating a high force per post, whereas in the compliant situation of being on a few posts causes the cell to generate lower forces per post.

As noted above, we carried out our calculations for a very large number of posts in a square array, up to 441. By that stage in some of our simulations for stiffer posts the average magnitude of the forces applied to the posts is falling as the number of posts is increased. This is an indication that the effect referred to above is occurring; namely as more interior posts are introduced, the force per post is diluted because the interior posts experience lower forces than the perimeter posts. To investigate this situation, we consider experiments by Yan et al. (2007) for fibroblasts where much smaller posts are used, so that many more can be placed under a cell of a given size. We find that our simulations for this case agree with the data, which now see a reduction in force per post as the number of posts is increased. Both the experimental data and the results of the simulations are published in McGarry et al. (2009).

4.3 Cells Subject to Cyclic Stretch

Certain types of cells in the body are subject to stretching and shortening in a cyclic manner; a prominent example is the vascular endothelial cell that lines arteries. Since an artery's diameter expands and contracts with the cardiac cycle, these cells are subject to cyclic stretch at a frequency of approximately 1 Hz. An experimental observation is that *in vivo* stress-fibers align transverse to the direction of stretch, and therefore align with the blood flow direction in the artery (Zhao et al. 1995). It should be noted that fluid shear stress from the flowing blood also influences the stress-fiber

orientation, but we will confine ourselves to the case where stretch dominates the resulting morphology. This situation can be reproduced *in vitro* by placing a cell on a flexible flat substrate and imposing a strain cycle on it, an experiment that has been carried out by several research groups. Results from some of these efforts are summarized in the paper by Wei et al. (2008), and the experimental setup for one of them, carried out by Kaunas et al. (2005), is depicted in Fig. 10. As indicated in that graphic, in this case uniaxial strain in the plane of the substrate is imposed on the cell, so that $\varepsilon_{22} = 0$. The amplitude of ε_{11} during cycling is varied from zero to 10 %. Images of the cells after 6 h of cycling at 1 Hz are shown in Fig. 11, which is taken from Kaunas et al. (2005). In the case of isometric strain imposed on the cell, i.e., $\varepsilon_{11} = 0$, the distribution of stress-fibers is essentially isotropic at the end of the experiment after steady state conditions have set in, with equal numbers found in any orientation within the plane of the cell. At $\varepsilon_{11} = 10\%$ the stress-fibers at the end of the experiment in steady state are almost all aligned in the direction of zero strain, i.e., parallel to the x_2 -axis. Results from simulations carried out with our bio-chemo-mechanical model are shown in Fig. 12. The graphs show the development of stress-fiber polymerization with time during uniaxial cyclic stretch at 1 Hz, with the degree of polymerization shown in different orientations relative to the direction of cyclic stretch which is at 0°. It can be seen that by 6 h the cell is in steady state, and that 10 % straining produces a greater degree of stress-fiber alignment than 3 %. A polar plot showing the stress-fiber orientations after 6 h is also shown in Fig. 12, which brings out clearly the greater degree of alignment in the case of the larger

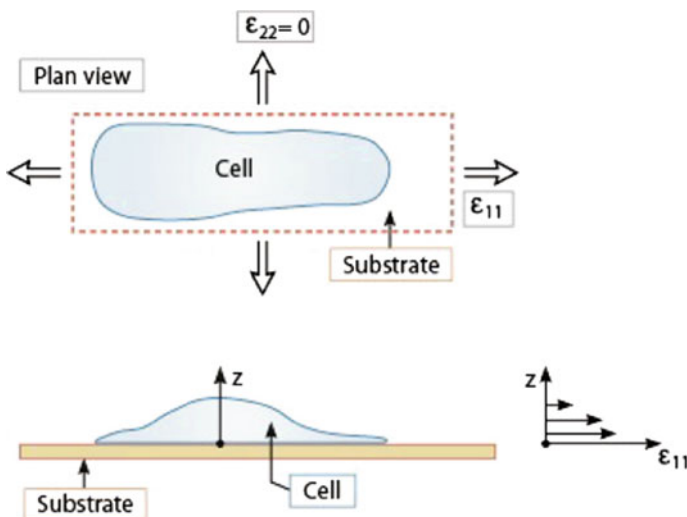


Fig. 10 Experimental setup for the *in vitro* strain cycling of cells attached to flexible substrates. The strain cycle imposed on the substrate is also experienced by the base of the cell where it adheres to the substrate

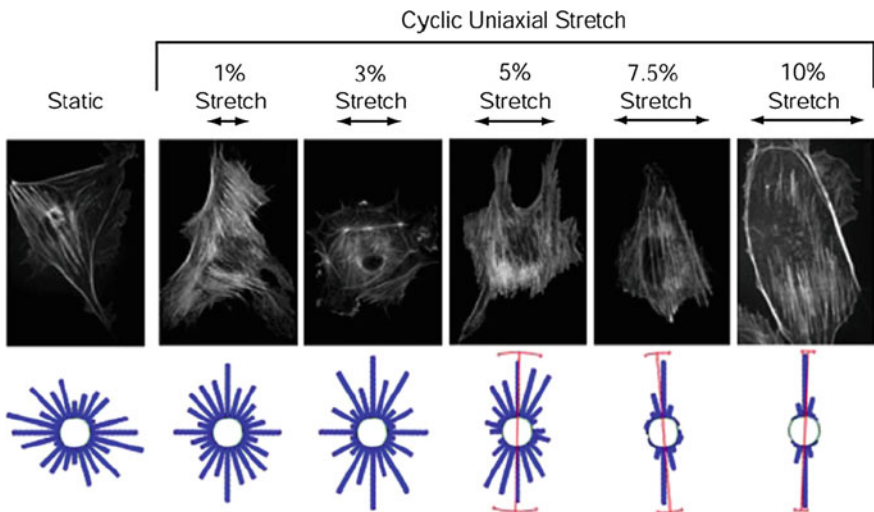
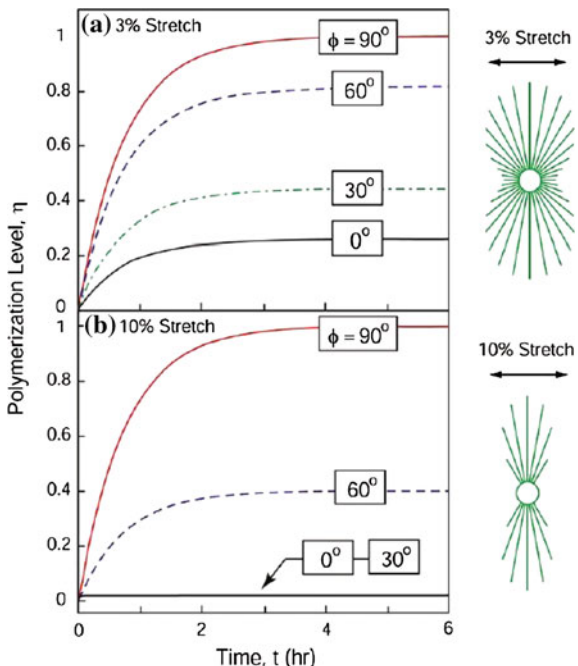


Fig. 11 Cells that have been subjected to uniaxial cyclic straining in vitro for 6 h at 1 Hz. The cells have been stained to visualize the stress-fibers, with an increased degree of alignment associated with an increased magnitude of cyclic stretch. Results from Kaunas et al. (2005)

Fig. 12 Degree of polymerization of stress-fibers as a function of time during cyclic stretch at 1 Hz as simulated using the bio-chemo-mechanical model. The results are shown for various orientations relative to the cyclic stretch direction which is at 0° . Greater alignment is achieved at 10 % straining than at 3 % and the alignment is then transverse to the direction of cyclic stretch



strain. It is also clear that the stress-fibers tend to align in the nonstretching direction, just as is observed in the experiments.

In our model the phenomenon of alignment of the stress-fibers arises from the tendency for them to polymerize and depolymerize. First we note that a signal is initiated at the beginning of the stretching stage of the strain cycle, consistent with the fact that focal adhesions generate signals when tension increments are applied to them. Since the decay time for the signal is rather long compared to the period of cycling, one signal has hardly decayed before the subsequent one replaces it. As a consequence one may regard the simulations as ones in which the signal is permanently on at its maximum strength. This feature drives continued polymerization in all orientations within the cell at all times during the simulations. The different results at different orientations therefore depend solely on how depolymerization is occurring. Because isometric behavior induces a large tension in the stress-fibers, and because such a tension precludes significant depolymerization, many stress-fibers form and are preserved in the isometric, nonstretching direction in all cases. In contrast, the shortening stage of the cyclic straining leads to a lower tension in the stress-fibers, allowing depolymerization to occur. It should be noted that the stretching stage of the strain cycle is associated with a high tension in the stress-fibers so that significant depolymerization does not then occur. However, the depolymerization associated with the stage of shortening is sufficient to reduce the stress-fibers in the shortening direction, leading to the results depicted in Fig. 12.

4.4 Cells on Patterned Substrates

As noted above in Sect. 2, Théry et al. (2006) formed patterns of fibronectin in shapes of letters of the alphabet and allowed cells to adhere to them, with results that are illustrated in Fig. 5. The features of these results have been described already in Sect. 2, and will not be repeated here. To simulate these results, it was found necessary to develop a more detailed model of focal adhesions, including their growth that is coupled to the development of the stress-fiber network. For this development, described in Deshpande et al. (2008), emphasis is placed on the role of integrins. These proteins are transmembrane elements that are capable of connecting the focal adhesion plaque to ligands external to the cell, and therefore binding the cell to the extracellular matrix or to a substrate in vitro. The focal adhesion plaque is a complex aggregate of proteins, including vinculin, and attaches to stress-fibers to make the connection between the adhesion and the cytoskeleton. It is vinculin that is visualized in Fig. 5 to provide the images of the locations of the focal adhesions.

4.4.1 Focal Adhesion Model

The integrin protein has two configurations, a bent state and a straight one as shown in Fig. 13, where the gray patches at the bottom of the molecules represent the membrane

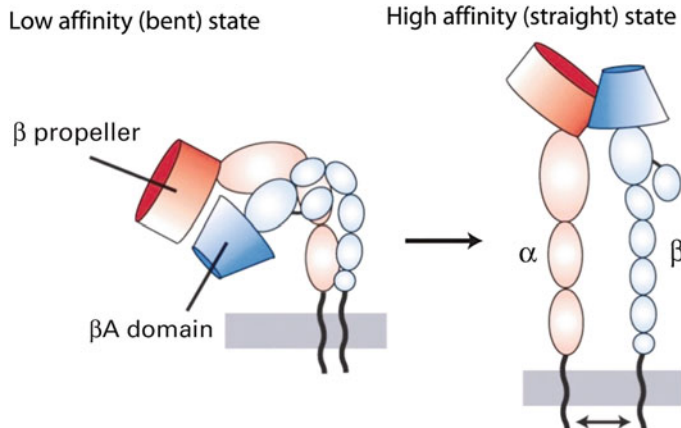


Fig. 13 The integrin protein shown in its two configurations, the bent and straight states. The gray patch at the bottom represents the membrane, in which the integrin sits

in which the integrin is embedded. In the straight configuration the integrin can bind to the focal adhesion plaque and to extracellular ligands, and therefore becomes immobilized. In the bent state, interactions among the complexes of the protein preclude it from binding to any other entity. Furthermore, its embedment in the membrane involves only physical bonds, so that the bent integrin is free to move around on the membrane surface of the cell. In the bent state the energy of the protein is low, whereas it is high when the integrin is straight. However, the difference in energy between the two states is relatively low and thermal activation is capable of spontaneously converting one to another. We therefore assume thermodynamic equilibrium between integrins in the straight and bent states. The chemical potential of the bent integrins is given as

$$\chi_L = \mu_L + kT \ln \left(\frac{\xi_L}{\xi_R} \right), \quad (7)$$

where μ_L is the standard chemical potential or enthalpy of the protein, k is Boltzmann's constant for the molecule, T is the absolute temperature, ξ_L is the number of integrins per unit area of the membrane, and ξ_R is a reference datum for such concentration. The chemical potential for the straight, bound integrins is

$$\chi_H = \mu_H + kT \ln \left(\frac{\xi_H}{\xi_R} \right) + \Phi(\Delta) - F\Delta, \quad (8)$$

where χ_H , μ_H , and ξ_H have definitions analogous to those for the bent integrins, Δ is the distance between the integrin and an extracellular ligand with which it is interacting, Φ is the internal energy of that interaction and therefore a function of Δ , and $F = d\Phi/d\Delta$ is the force of attraction between the integrin and the extracellular

ligand. Thus the combination $\Phi(\Delta) - F\Delta$ is the potential energy of the load applied to the integrin, and installs mechanosensitivity in the chemical potential of the integrin. The description of the mechanosensitive term in Eq. (8) given above is confined to a one-dimensional picture that is adequate for flat, spread cells. In that case, the integrin and the ligand to which it is attracted lie in the same plane and the parameter Δ is the distance within that plane between the integrin and the ligand. The function Φ is zero when $\Delta = 0$, with that state representing a perfect placement of the integrin and the ligand in regard to their attraction to each other. The function Φ increases monotonically with Δ and has a smooth minimum at $\Delta = 0$. For example, a quadratic dependence of Φ on Δ is a reasonable model adjacent to $\Delta = 0$. For larger values of Δ the function Φ approaches an asymptote as the interaction between the integrin and the ligand becomes insensitive to increasing distance between them. The asymptotic value of Φ at large values of Δ , when averaged over many integrins, is analogous to a surface energy as it represents the work that must be done to create a large separation between the integrins and the ligands to which they are attracted. Furthermore, the force attracting the integrin to a ligand is zero when they are well separated. We note that the function Φ is such that $\Phi(\Delta) - F\Delta \leq 0$ when the magnitude of Δ is less than a critical value. Beyond that value, $\Phi(\Delta) - F\Delta \geq 0$, and $\Phi(\Delta) - F\Delta = 0$ only when $\Delta = 0$, and at the critical separation where $\Phi(\Delta) - F\Delta$ changes sign. In addition, there are complications when a given integrand is interacting with multiple ligands. Details of these and other aspects of the model are given in Deshpande et al. (2008) but will not be described here as they are not essential to an understanding of the mechanosensitive behavior that Eq. (8) induces.

We note that $\mu_H > \mu_L$. Therefore in the absence of any displacement of the integrin relative to a ligand to which it is bound, i.e., $\Delta = 0$, the equilibrium condition $\chi_H = \chi_L$ requires exponentially more low affinity, bent integrins than straight ones. However, if $\Delta \neq 0$, but lies below the critical level so that $\Phi(\Delta) - F\Delta \leq 0$, equilibrium will demand an increased number of straight integrins, so that the formation of focal adhesions is favored by the application of force to them. Such behavior is observed in experiments, e.g., Chen et al. (2003). In contrast, if the integrin is pulled strongly away from its favored ligand, $\Phi(\Delta) - F\Delta \geq 0$ and equilibrium will encourage the focal adhesion to disintegrate.

In our model, equilibrium between the low and high affinity integrins is augmented by a trafficking equation that moves the mobile, low affinity integrins on the membrane by diffusional mass transport. Details of the mass transport equations are given in the paper by Deshpande et al. (2008), and some enhancements are presented by Pathak et al. (2011), but this aspect of the model will not be detailed here.

4.4.2 Results from the Simulations for Cells on Patterned Substrates

The resulting focal adhesion formulation, coupled to the cytoskeleton model summarized in Eqs. (1)–(6), is used to simulate the cell behavior depicted in Fig. 5, with results, developed by Pathak et al. (2008), summarized in Figs. 14 and 15.

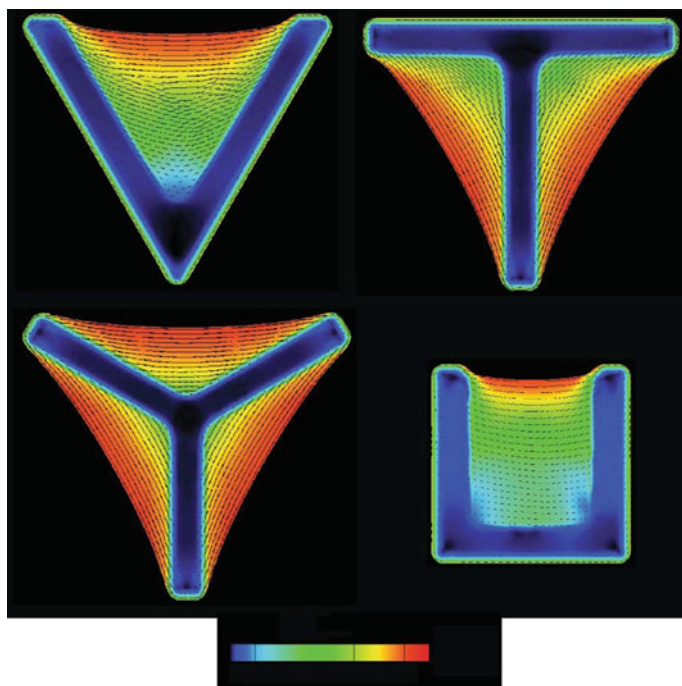


Fig. 14 Distribution of actin resulting from simulations of cells placed on fibronectin patterns. The shape in *blue* is the fibronectin patch while the cell is depicted by the color contour plot representing the concentration and orientation of stress-fibers. *Red* indicates a high concentration of stress-fibers while *blue* depicts a low concentration. The orientation of the stress-fibers is shown by the *dashed lines* in the color contour plot

As with many of our simulations, the process of development of the cytoskeleton is initiated by a signal from a condition in which the cell is down regulated, without a significant cytoskeleton and lacking adhesions. The integrins are initially distributed uniformly on the cell membrane and are predominantly low affinity bent ones, with a few straight ones in equilibrium with the bent type. After the signal is initiated, polymerization of the stress-fibers begins and evolves into an isometric steady state, with the resulting structure stabilized by the tension retained within the contractile stress-fibers. This tension in the stress-fibers is transduced to the straight integrins that bind to the stress-fibers. The force applied to the integrins encourages the formation of an ever-increasing concentration of straight ones, which are converted from the bent type. The resulting depletion of the mobile, bent type of integrin induces their diffusion on the membrane in an attempt to equalize their distribution. This has the effect of bringing a fresh supply of low affinity integrins to the locations where force is being applied to the straight ones, and enables further conversion of bent ones to the straight configuration, binding them to the stress-fibers and permitting continued growth of the focal adhesion cluster. This process continues to steady state.

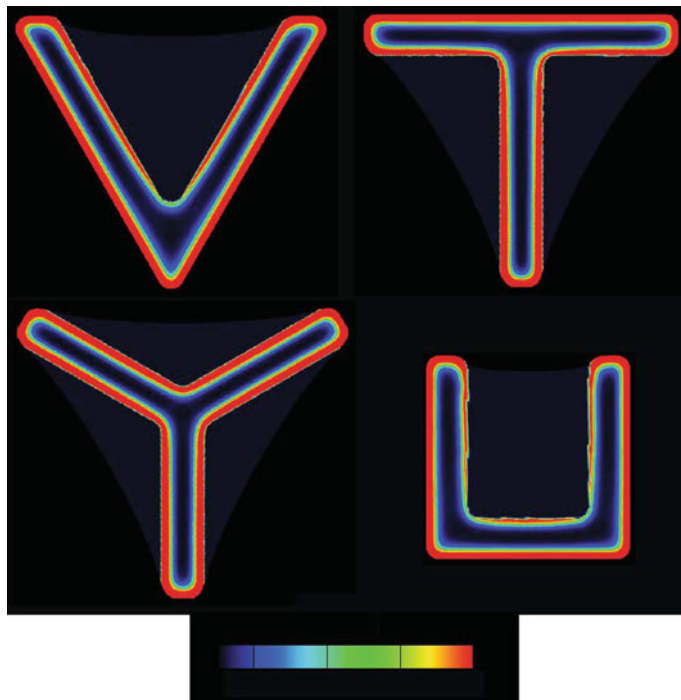


Fig. 15 Distribution of focal adhesions resulting from simulations of cells placed on fibronectin patterns. The focal adhesions are the *red zone* and outline the perimeter of the fibronectin patch

As noted above, the outcomes are shown in Figs. 14 and 15, with the former depicting the distribution of actin, i.e., the stress-fibers, and the latter giving the concentration of high affinity, bound integrins, i.e., the focal adhesions. These results should be compared with Fig. 5, which shows the experimental observations of the same features. The following characteristics can be observed in both the experimental results and the outcomes of the simulations. The actin concentration is highest adjacent to the unadhered edges of the cell, i.e., in each case the cell has extended beyond the fibronectin patch to almost cover its convex hull, so that there are regions where the cell is not adhered to the substrate below it—it is at the edges of these zones that the actin concentration is greatest. The stress-fibers are aligned parallel to the nearby edge of the cell, and contractility has deformed the unadhered edge of the cell into a concave outward configuration. The curvature of these edges in the simulations agrees with that in the experiments. In both the simulations and the experiments, the focal adhesions are formed around the perimeter of the fibronectin patch, with low concentrations of bound integrins in the interior of the patch. In the experiments the focal adhesions are largely confined to the high curvature edges of the fibronectin patch, but in the simulations the focal adhesions have extended to such an extent that they completely surround the fibronectin patch. This discrepancy is the

only major deficiency in the results of our simulations. However, it should be noted that during the transient process of developing the results shown in Fig. 15 the focal adhesions first appear at the high curvature edges of the fibronectin patch. Unfortunately they continue to grow until they completely surround the patch. This outcome suggests that we have too many integrins present in our simulations, providing an almost inexhaustible supply of components for the formation of focal adhesions. We believe, therefore, that if we reduced the initial supply of integrins in our simulations the growth of focal adhesions would terminate before completely surrounding the fibronectin patch. In steady state this would leave the focal adhesions clustered near the high curvature edges of the fibronectin patch, consistent with the experimental observations.

4.5 Cells Adhered to Elastic Substrates

We have simulated the interaction of cells with flat, compliant substrates using a 3-dimensional extension of the model. The results of these computations are reported in Ronan et al. (2014), and an example of these is shown in Fig. 16. This figure is a color contour plot for cells adhered to elastic substrates. The upper one is a cell on a relatively stiff substrate, while the lower one sits on a more compliant substrate; however, in both cases the elastic stiffness of the substrate is low enough that the contractile tractions generated by the cell are able to distort the substrate. The red color in the contour plots indicates a high concentration of stress-fibers while the blue depicts a low concentration. It can be seen that the stiff substrate induces the cell

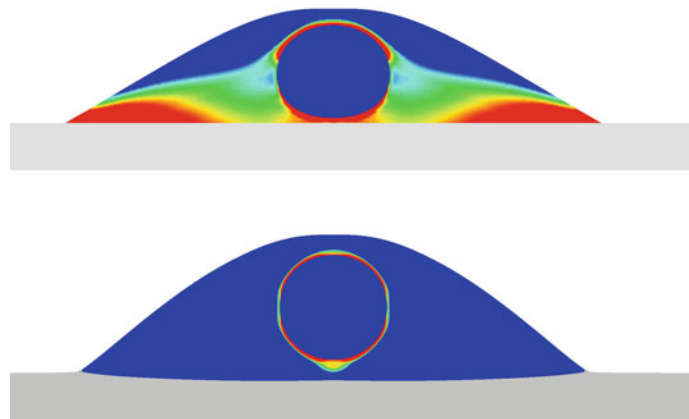


Fig. 16 A cell on a stiff elastic substrate (*upper*) and one on a compliant elastic substrate (*lower*). The colors represent the concentration of stress-fibers with *red* being the highest level and *blue* being low. The cell has a nucleus, which is the central feature in *blue* in each case surrounded by a small concentration of stress-fibers

to generate a profuse stress-fiber cytoskeleton while the more compliant substrate does not. Furthermore, the tractions applied to the stiff substrate are much higher in magnitude than those applied to the compliant substrate, a feature that correlates with the degree of stress-fiber development. Furthermore, results of Ronan et al. (2014) not depicted here show that the focal adhesion at the edge of the cell on the stiff substrate is much larger than that at the edge of the cell on the compliant substrate. These outcomes of the model in which a stiff substrate induces a greater degree of cytoskeleton polymerization, higher contractile tractions and larger focal adhesions are consistent with experimental observations, such as those of Engler et al. (2006). We note also that the contractility of the cytoskeleton of the cell on the stiff substrate applies a higher pressure to the nucleus of that cell than when the cell is on a compliant substrate. This raises the possibility of the mechanics of the cell playing a role in the biochemistry and genetic regulatory mechanisms that take place in the nucleus.

4.6 Cells Subject to Shearing Deformations

The 3-dimensional formulation of the cell model has also been used to study the response of chondrocyte cells being sheared, where these results are fully described in the paper by Dowling et al. (2012). A schematic of the experimental setup is shown in Fig. 17 with a simulated cell shown being deformed by the probe. The cell is adhered to the substrate and the concentration of stress-fibers within it at the stage of the simulation depicted is shown as a color contour plot with the red color

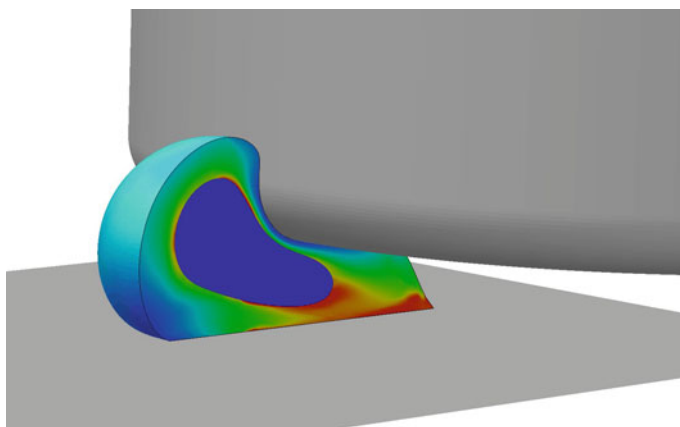


Fig. 17 A cell being sheared by a probe being moved horizontally relative to the substrate to which the cell is adhered. The colors in the cell represent the concentration of stress-fibers, which remodel during deformation of the cell. *Red* indicates a high concentration of stress-fibers while *blue* depicts a low concentration

indicating a high concentration of stress-fibers and the blue showing a low one. By comparing Figs. 16 and 17 one can see that during the deformation the cell experiences remodeling of its stress-fiber network, since initially, prior to deformation, the cell's stress-fiber network was somewhat similar to that depicted in Fig. 16, and therefore symmetric about the nucleus. Comparison of the simulation results with experimental observations by Dowling et al. (2012) indicates that the remodeling predicted by the simulation is similar to that which occurs in the cell during the shearing experiment.

In both the experiments and the simulations the load-deflection curve during shearing is obtained, with all results shown in Fig. 18. The upper plots in the figure, marked 'Untreated cells', are for active cells that are contractile and remodel. It can be seen that the simulation agrees very well with the experimental results. To emphasize the importance of the active contractility and the remodeling that occurs in the cell, shearing was also carried out for a cell treated with cytochalasin D, which disrupts the stress-fiber network and reduces its contractility. The lower plots in Fig. 18 are for such cells, and it can be seen that the behavior is not just quantitatively but qualitatively different from that of active cells. In fact the response of the cells treated with cytochalasin D can be simulated using a passive, nonlinear elastic model that stiffens slightly during deformation. Such a model is inadequate for simulating the active cells, as the shape of their load-deflection curve contrasts with that for treated cells in that the active cells exhibit stiff response followed by a reduction in tangent stiffness. The initial stiff response is caused by the active remodeling, and is thus absent from the behavior of the cells treated with cytochalasin D. These results, as

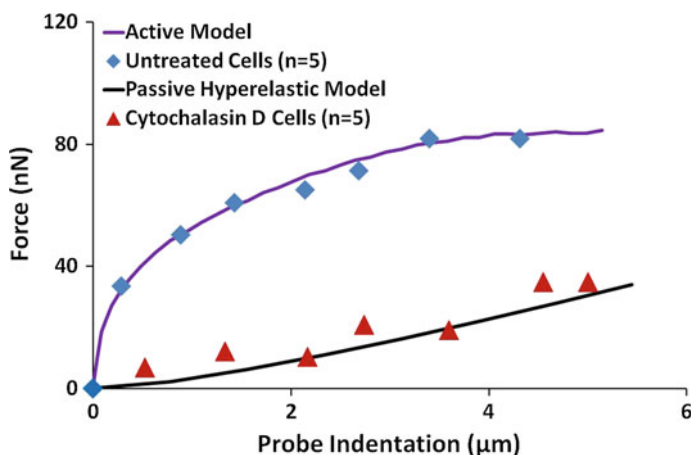


Fig. 18 Graph of the force versus displacement curve for cells subject to shearing deformation by a probe. The blue data points are experimental results for a cell in an active state while the red data points are experimental results for a down-regulated cell. The full lines are the results of simulations, with the upper plot representing an active cell modeled by our coupled stress-fiber and focal adhesion formulations. The lower plot is obtained using a passive nonlinear elastic model. Results from Dowling et al. (2012)

well as confirming the validity of our model, emphasize the importance of capturing the active contractility and cytoskeleton remodeling that take place in cells in normal conditions.

We note that we have obtained equivalent results for cells subject to compression (Ronan et al. 2012), those being aspirated by pipetting (Reynolds et al. 2014), and for those interacting with arrays of microposts (McGarry et al. 2009; Ronan et al. 2013). We have also considered the role of contractility in regulating cell–cell junctions (Ronan et al. 2015).

4.7 Cells on Grooved Substrates

Lamers et al. (2010) have studied the behavior of osteoblasts adhered to grooved substrates. The width of the grooves, which in most cases were flat bottomed with flat, square cross-sectioned ridges, ranged from 10 nm to 2 μ m. In addition, the study encompassed flat, ungrooved substrates. Lamers et al. (2010) found increasing alignment of the cells as the pitch of the grooves increased. Of most interest to us is the degree of alignment of the stress-fibers. In the case of the narrowest grooves the distribution of orientations of the stress-fibers was indistinguishable from that observed on the flat, ungrooved substrate, and therefore was essentially isotropic. On the widest grooves, the stress-fibers aligned themselves so that none was more than 10° away from being parallel to the grooves. Examples of osteoblasts from these experiments on grooves having pitches of 150 and 10 nm are shown in Fig. 19. The contrasting alignment of the stress-fibers is visible.

We have modeled this behavior, with results reported in Vigliotti et al. (2015a). For this study we utilized reaction-diffusion equations to represent signaling in the cell, according to Pathak et al. (2011). These simulations involved a 1-dimensional geometry across a groove, but permitted formation of stress-fibers in any orientation

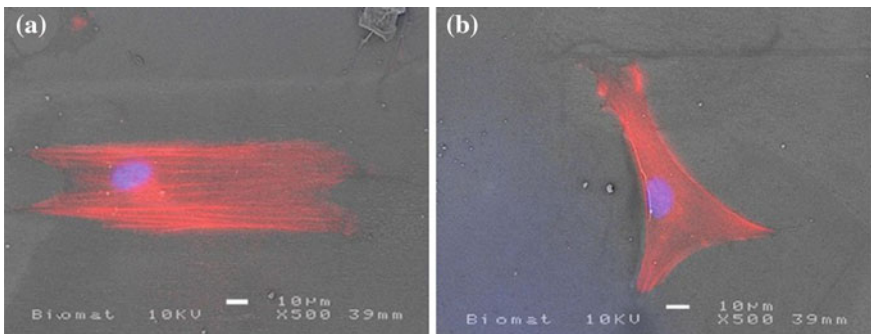


Fig. 19 Osteoblasts on grooved substrates. In one case, **a**, the pitch of the grooves is 150 nm, and in the other case, **b**, it is 10 nm

in the plane of the peaks of the grooves. As with many of our simulations, the process of developing the stress-fibers is commenced with the initiation of a signal. However, in this case, the signal emanates from the focal adhesions, which are confined to the tops of the groove ridges where adhesion ligands are to be found. Due to the time it takes for the reaction-diffusion equation to transmit the signal over the well of the groove, the signal then initiates stress-fiber polymerization on a nonsynchronous basis within the cell, with it commencing later over the well of the groove than on the tops of the ridges. The development of the stress-fiber network is further complicated by the fact that, after its initial period of activity, the signal dies away as the signaling proteins and ions are mopped up by the cell, implicitly being sequestered in the reticulum, returned to the focal adhesions, or pumped out through the cell membrane. As a consequence, the possibility arises that the signal will die before it can completely cross the well of the groove. If the diffusion distances are great enough, that is what happens, the case in point being the grooves with the widest pitches. In that case, due to the absence of a signal over the center of the well, stress-fibers cannot form there, and instead are confined to the tops of the grooves; inevitably there are many more aligned with the grooves than transverse to them. In contrast, when the grooves are narrow, the signal successfully crosses the groove well, and there can be many stress-fibers aligned transverse to the grooving direction.

This situation is reflected in the results shown in Fig. 20, which depicts the concentration of stress-fibers across the grooves as a function of groove pitch. In the case of narrow grooves, stress-fibers are to be found above the well of the groove, whereas for the widest grooves no stress-fibers are found there. As noted above, this

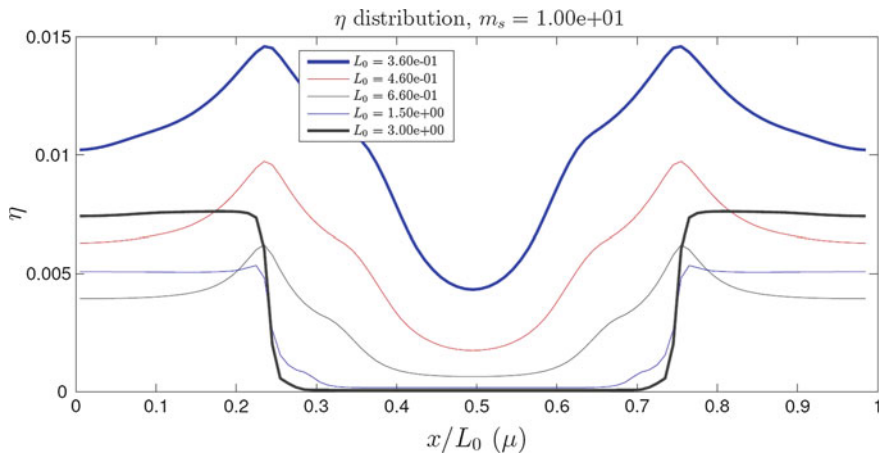


Fig. 20 Simulation results for the concentration of stress-fibers for osteoblasts adhered to a grooved substrate. The scaling is such that the graph at the *top* is for narrow grooves and that at the *bottom*, i.e., the *heavy dark line*, is for a wide groove. In the case of the wide groove there are no stress-fibers above the well of the groove, and stress-fibers are only found on the ridges of the grooving. When the grooves are narrower stress-fibers succeed in being polymerized across the wells of the grooves

result translates into alignment of the stress-fibers with the grooves when the pitch of the grooves is wide, and a lack of alignment for narrow grooves. It is found that, statistically, the simulations are in agreement with the experimental results of Lamers et al. (2010) in regard to the degree of alignment of the stress-fibers.

5 Discussion

We have provided a concise description of our bio-chemo-mechanical models for stress-fiber contractility, cytoskeleton development and remodeling, the formation of focal adhesions, and the mechanics associated with these phenomena. In addition, we have described our simplistic representation of a cell signal, and given references to work where a more realistic signal model, based on reaction-diffusion equations for the signaling proteins and ions, can be found. We have illustrated how our model captures many of the observed features of mechanosensitivity in cells, and we believe that this validates and justifies our model. We note that the examples given in this chapter are all focused on single cells; however, we have exercised the model to simulate interactions between cells (Ronan et al. 2015), and in work by Legant et al. (2009) that we have not reviewed here we have successfully applied the model to tissues composed of many cells, and obtained satisfactory results.

Despite our success with the model described here, we are not entirely satisfied with it. Some of the features, such as the mechanosensitivity present in Eq. (2), though justifiable, are somewhat phenomenological and rather ad hoc. Furthermore, to capture some additional effects beyond those summarized in connection with the examples described in the present chapter it has been necessary to modify and extend the model, with the updates described by Vigliotti et al. (2015b). We expect to see further enhancements and improvements to the model in the coming years, to endow it with greater versatility and relevance to problems of mechanobiology.

References

- Abaqus: Abaqus 6.13 Analysis User's Guide, Simulia, Dassault Systèmes Simulia Corp., (2013). www.simulia.com
- Alberts, B., Johnson, A., Lewis, J., Raff, M., Roberts, K., Walter, P.: Molecular Biology of the Cell, 5th edn. Garland Science, New York (2008)
- Chen, C.S., Alonso, J.L., Ostuni, E., Whitesides, G.M., Ingber, D.E.: Cell shape provides global control of focal adhesion assembly. *Biochem. Biophys. Res. Commun.* **307**, 355–361 (2003)
- Deshpande, V.S., McMeeking, R.M., Evans, A.G.: A bio-chemo-mechanical model for cell contractility. *Proc. Natl. Acad. Sci. USA* **103**, 14015–14020 (2006)
- Deshpande, V.S., McMeeking, R.M., Evans, A.G.: A model for the contractility of the cytoskeleton including the effects of stress-fibre formation and dissociation. *Proc. R. Soc. Lond. A* **463**, 787–815 (2007)

- Deshpande, V.S., Mrksich, M., McMeeking, R.M., Evans, A.G.: A bio-mechanical model for coupling cell contractility with focal adhesion formation. *J. Mech. Phys. Solids* **56**, 1484–1510 (2008)
- Discher, D.E., Janmey, P., Wang, Y.-L.: Tissue cells feel and respond to the stiffness of their substrate. *Science* **310**, 1139–1143 (2005)
- Dowling, E.P., Ronan, W., Ofek, G., Deshpande, V.S., McMeeking, R.M., Athanasiou, A.K., McGarry, J.P.: The effect of remodeling and contractility of the actin cytoskeleton on the shear resistance of single cells. *J. R. Soc. Interface* **9**, 3469–3479 (2012)
- Engler, A.J., Sen, S., Sweeney, H.L., Discher, D.E.: Matrix elasticity directs stem cell lineage specification. *Cell* **126**, 677–689 (2006)
- Hill, A.V.: The heat of shortening and the dynamic constants of muscle. *Proc. R. Soc. Lond. B* **126**, 136–195 (1938)
- Kaunas, R., Nguyen, P., Usami, S., Chien, S.: Cooperative effects of Rho and mechanical stretch on stress fiber organization. *Proc. Natl. Acad. Sci. USA* **102**, 15895–15900 (2005)
- Lamers, E., Walboomers, X.F., Domanski, M., te Riet, J., van Delft, F.C.M.J.M., Luttge, R., Winnebust, L.A.J.A., Gardeniers, H.J.G.E., Jansen, J.A.: The influence of nanoscale grooved substrates on osteoblast behavior and extracellular matrix deposition. *Biomaterials* **31**, 3307–3316 (2010)
- Legant, W.R., Pathak, A., Yang, M.T., Deshpande, V.S., McMeeking, R.M., Chen, C.S.: Microfabricated tissue to measure and manipulate cellular forces in 3d tissues. *Proc. Natl. Acad. Sci. USA* **106**, 10097–10102 (2009)
- Lo, C.-M., Wang, H.-B., Dembo, M., Wang, Y.-L.: Cell movement is guided by the rigidity of the substrate. *Biophys. J.* **79**, 144–152 (2000)
- McGarry, J.P., Fu, J., Yang, M.T., Chen, C.S., McMeeking, R.M., Evans, A.G., Deshpande, V.S.: Simulation of the contractile response of cells on an array of micro-posts. *Philos. T. Roy. Soc. A* **367**, 3477–3497 (2009)
- Pathak, A., Deshpande, V.S., McMeeking, R.M., Evans, A.G.: The simulation of stress fibre and focal adhesion development in cells on patterned substrates. *J. R. Soc. Interface* **5**, 507–524 (2008)
- Pathak, A., McMeeking, R.M., Evans, A.G., Deshpande, V.S.: An analysis of the cooperative mechano-sensitive feedback between intracellular signaling, focal adhesion development and stress fiber contractility. *J. Appl. Mech.* **78**(041001), 1–12 (2011)
- Reynolds, N.H., Ronan, W., Dowling, E.P., Owens, P., McMeeking, R.M., McGarry, J.P.: On the role of the actin cytoskeleton and nucleus in the biomechanical response of spread cells. *Biomaterials* **35**, 4015–4025 (2014)
- Ronan, W., Deshpande, V.S., McMeeking, R.M., McGarry, J.P.: Numerical investigation of the active role of the actin cytoskeleton in the compression resistance of cells. *J. Mech. Behav. Biomed. Mater.* **14**, 143–157 (2012)
- Ronan, W., Pathak, A., Deshpande, V.S., McMeeking, R.M., McGarry, J.P.: Simulation of the mechanical response of cells on micropost substrates. *J. Biomech. Eng.* **135**(101012), 1–10 (2013)
- Ronan, W., Deshpande, V.S., McMeeking, R.M., McGarry, J.P.: Cellular contractility and substrate elasticity: a numerical investigation of the actin cytoskeleton and cell adhesion. *Biomech. Model. Mechanobiol.* **13**, 417–435 (2014)
- Ronan, W., McMeeking, R.M., Chen, C.S., McGarry, J.P., Deshpande, V.S.: Cooperative contractility: the role of stress fibres in the regulation of cell-cell junctions. *J. Biomech.* **48**, 520–528 (2015)
- Tan, J.L., Tien, J., Pirone, D.M., Gray, D.S., Bhadriraju, K., Chen, C.S.: Cells lying on a bed of microneedles: an approach to isolate mechanical force. *Proc. Natl. Acad. Sci. USA* **100**, 1484–1489 (2003)
- Théry, M., Pépin, A., Dressaire, E., Chen, Y., Bornens, M.: Cell distribution of stress fibres in response to the geometry of the adhesive environment. *Cell Motil. Cytoskeleton* **63**, 341–355 (2006)
- Vigliotti, A., McMeeking, R.M., Deshpande, V.S.: Simulation of the cytoskeletal response of cells on grooved or patterned substrates. *J. R. Soc. Interface* **12**, 20141320 (2015a)

- Vigliotti, A., Ronan, W., Deshpande, V.S.: A thermodynamically-motivated model for stress-fiber reorganization. *Biomech. Model. Mechanobiol.* (2015b). doi:[10.1007/s10237-015-0722-9](https://doi.org/10.1007/s10237-015-0722-9)
- Wei, Z., Deshpande, V.S., McMeeking, R.M., Evans, A.G.: Analysis and interpretation of stress fiber organization in cells subject to cyclic stretch. *J. Biomech. Eng.* **130**(013009), 1–9 (2008)
- Yan, M.T., Sniadecki, N.J., Chen, C.S.: Geometric considerations of micro- to nanoscale elastomeric post arrays to study cellular traction forces. *Adv. Mater.* **19**, 3119–3123 (2007)
- Zhao, S., Suciu, A., Ziegler, T., Moore, J.E., Bürki, E., Meister, J.-J., Brunner, H.R.: Synergistic effects of fluid shear stress and cyclic circumferential stretch on vascular endothelial cell morphology and cytoskeleton. *Arterioscler. Thromb. Vasc. Biol.* **15**, 1781–1786 (1995)

Nonlinear Continuum Mechanics and Modeling the Elasticity of Soft Biological Tissues with a Focus on Artery Walls

Ray W. Ogden

Abstract This chapter provides a detailed summary of the background from the nonlinear theory of continuum mechanics that is required in the modeling of the elastic properties of soft biological tissues. In particular, it highlights methods for including the fibrous structure of such tissues within the constitutive description of the material properties at the macroscopic level. Of particular relevance in this connection are the so-called preferred directions associated with fibers and the structure tensors and associated deformation invariants that are needed for taking these fibers and their dispersed directions into consideration. These are incorporated into the material models and the effect of fiber structure on the material response is then illustrated with several basic examples. Generalizations of structure tensors are also used for including within the theory the important residual stresses that are evident in unloaded tissues such as arteries and the myocardium, and the influence of residual stresses on the material response is illustrated by considering the extension and inflation of a thick-walled circular cylindrical tube.

1 Introduction

This chapter is based on lectures given at the Summer School on ‘Biomechanics: Trends in Modeling and Simulation’ in Graz, Austria, in September 2014, but includes additional material that was not presented in the lectures. Effective modeling of the mechanics of soft biological tissues, such as the layered walls of arteries, the myocardium and skin, requires a sophisticated application of the nonlinear theory of continuum mechanics. Within the structure of these tissues a key component is the protein collagen, which endows the material with anisotropic properties because of its significant stiffness relative to the surrounding material within which it is embedded. We refer to the surrounding (less stiff) material as the *matrix*, which, depending on the tissue under consideration, includes elastin fibers, proteoglycans, and smooth

R.W. Ogden (✉)
University of Glasgow, Glasgow, UK
e-mail: raymond.ogden@glasgow.ac.uk

muscle cells, for example. Tissues have a naturally fibrous structure, which has a strong influence on their mechanical response. Thus, from the mechanical perspective, it is important to be able to understand the influence of the fiber structure on the overall mechanical response of the composite materials of which the fibers are constituents, and nonlinear continuum mechanics provides the vehicle for analyzing this response.

Consider, for example, a length of artery, which may be idealized as a circular cylindrical tube, as illustrated in Fig. 1. Typically, in the simplest terms, an artery contains two families of collagen fibers that are helically arranged and symmetrically disposed relative to its axis, with the fiber directions locally lying within the tangent plane, i.e., they have no radial component. Suppose that each family makes an angle φ with the circumferential direction. Of course, the picture is much more complex than we have indicated here—for example, there is dispersion of the fiber directions within each family, there is in general a small radial component of each fiber direction and the arrangement is different within each layer of an artery wall. These matters will concern us later in the chapter, but for our initial illustration we consider the simple situation depicted in Fig. 1.

This enables us to provide a simple illustration of the influence of fiber orientation on the mechanical response of an artery. This is the content of Fig. 2, which shows how the pressure in a circular cylindrical tube depends on its radial expansion (as measured by the circumferential stretch—the ratio of inner deformed radius to undeformed radius) for different fiber orientations in the absence of axial extension. The curves shown, which exhibit highly nonlinear behavior, are characteristic of those for arteries found in the literature and are based on a model of these characteristics (see, for example, Holzapfel et al. 2000). The response becomes stiffer as the fiber directions become closer to circumferential than axial, which reflects the high stiffness of collagen fibers. The shapes are also very similar to those obtained in uniaxial tests on, for example, strip samples of different artery wall layers (see, for example, Holzapfel et al. 2005). There is a soft ‘toe’ region where the wavy collagen fibers provide little

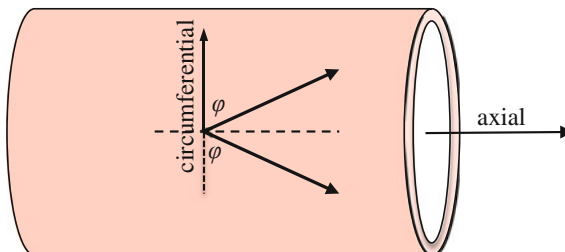


Fig. 1 Depiction of an undeformed artery as a thin-walled circular cylindrical tube with two symmetrically and helically arranged families of (collagen) fibers locally lying in the tangent plane and with directions making angles φ with the circumferential direction. The two symmetrically arranged arrows indicate the directions of the tangents to the fibers at a general point

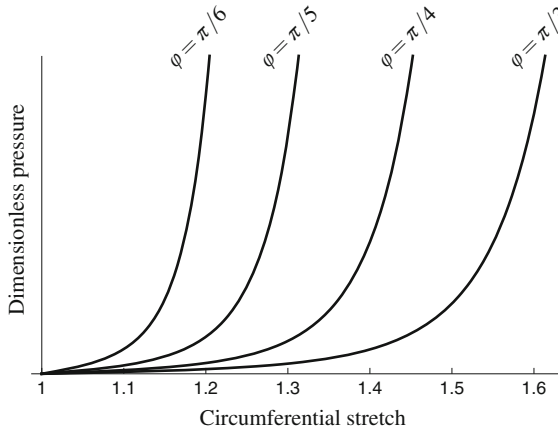


Fig. 2 Representative curves of (dimensionless) pressure versus circumferential stretch on inflation of an artery without axial extension for several values of the angle φ shown in Fig. 1. The curves highlight both the nonlinearity of the material response and the significant effect of fiber orientation. The response is much stiffer for fibers oriented more toward the circumferential direction than the axial direction

if any resistance to tension, which is borne by the soft matrix, followed by rapid stiffening as they reach their natural lengths.

We are concerned here with the elastic response of arteries, but the framework of the nonlinear theory of elasticity underpins the basic elastic response of all soft fibrous materials and is a starting point for more general continuum theories. Our aim is to describe the elastic behavior of these materials by the construction of constitutive laws, informed by data from experimental tests. The fiber directions within a tissue endow the material locally with so-called *preferred directions*, as a result of which the mechanical response of the material is anisotropic.

From the point of view of modeling the elastic properties of tissues the complications associated with the fibrous structure are well known and have been the subject of many publications, and for an extensive list of references we refer to Holzapfel et al. (2000), Gasser et al. (2006) and Holzapfel and Ogden (2010), for example. Another issue, which increases the complication, is the existence of residual stresses in unloaded tissue exemplified by the residual stress in artery walls, as evidenced by the so-called opening angle test (Vaishnav and Vossoughi 1983; Chuong and Fung 1986). In this, a short ring of excised artery (and therefore unloaded radially and axially) when cut radially springs open significantly into a sector, thereby demonstrating the existence of residual stress in the intact state. A two-dimensional idealized version of this experimental test, in which a circular ring of artery springs open into the sector of a circular ring, is illustrated in Fig. 3.

Thus, both residual stresses and the tissue structure need to be accounted for in the development of constitutive laws for soft biological tissues, and this is the concern of this chapter as we develop nonlinearly elastic constitutive laws for these materials,

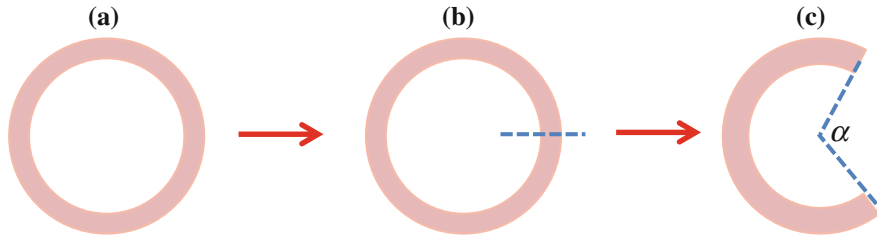


Fig. 3 A ring of artery (a) is cut radially (b) and deforms into a sector of a circular ring (c) with the opening angle α , thus demonstrating that in the unloaded configuration (a) there exist (radial and circumferential) residual stresses relief of which results in configuration (c)

with a focus on their passive and time-independent response. For general background on the mechanics of tissues we refer to the classical text of Fung (1993) and for detailed discussion of the mechanical properties of arteries and, more generally cardiovascular solid mechanics, the works of Humphrey (1995, 2002) should be consulted. For developments in the continuum description of arterial wall mechanics we refer to Holzapfel et al. (2000, 2015), Gasser et al. (2006), and Holzapfel and Ogden (2010) and references therein, while for the myocardium we cite Holzapfel and Ogden (2009a). See also the collections of papers in the edited volumes by Holzapfel and Ogden (2003, 2006, 2009b).

In Sect. 2, we provide a description of the kinematics of deformation, introduce a number of stress tensors and derive the equations governing equilibrium, while in Sect. 3 we focus on general aspects of the constitutive law of an elastic material based on a strain-energy function and the associated stress tensors. More comprehensive treatments of the nonlinear theory of elasticity can be found in, for example, standard texts such as Ogden (1997, 2003a), and Holzapfel (2000) and the collection of articles in Fu and Ogden (2001). Particular attention is paid here to the role of structure tensors and invariants associated with preferred directions in the development of the strain-energy function for different material symmetries. The notion of a structure tensor is also used to include residual stress in the constitutive law of an elastic material.

In Sect. 4 the theory for fiber-reinforced materials, with two fiber families (and without residual stress), is then applied in a basic application to homogeneous deformations, in particular to the problem of pure homogeneous strain of a thin sheet of material, a setup that is often used in experiments for helping to characterize the mechanical properties of fibrous materials. The general results are illustrated for a special choice of constitutive law which has a role, in various modified forms, throughout the chapter.

This is followed, in Sect. 5, by an application of the theory to a key boundary-value problem involving a nonhomogeneous deformation relevant to the behavior of arteries, namely that of the extension and inflation of a thick-walled elastic tube reinforced symmetrically with two families of fibers. The corresponding thin-walled approximation is derived and used for illustration of the pressure and axial load response of a tube. The difference between the response with and without fibers and

the effect of different fiber orientations is highlighted by applying the material model from Sect. 4. The effect of residual stress is then illustrated by a further application to the problem of extension and inflation of a thick-walled elastic tube in Sect. 5.3, and a particular form of the residual stress is chosen along with simple constitutive laws, enabling explicit expressions to be obtained for the pressure and axial load applied to achieve a prescribed axial extension and inflation of the tube. For purposes of numerical calculation and graphical illustration, a range of particular values of the parameters of the problem is selected, leading to comparative plots of the pressure and axial load for a residually stressed tube, with and without fiber reinforcement.

The model strain-energy function fits data for the overall response of an artery, and it also fits well the data for the medial layer, but it does less well for the intimal and adventitial layers. One possible explanation for this is that rather than being perfectly aligned the fibers are dispersed in their orientations, and this is more evident in the adventitia than in the media, for example. Therefore, to take account of fiber dispersion the model was modified by Gasser et al. (2006). In Sect. 6 is described the model based on fiber dispersion, which is accounted for via a so-called *generalized structure tensor* and associated generalized invariants. In particular, for three dimensions a rotationally symmetric dispersion is considered which involves just a single dispersion parameter as a measure of the degree of dispersion. A two-dimensional counterpart of this is also examined.

For the rotationally symmetric model a π -periodic von Mises distribution is used to quantify the dispersion, and with the same general structure the model strain-energy function from the previous sections is modified to accommodate the dispersion. This extended model is applied to the extension–inflation problem to illustrate the significant difference that inclusion of dispersion makes. Then, using the model and data relating to the adventitia of a human iliac artery, the problem of the nonhomogeneous uniaxial extension of strips from the circumferential and axial directions is examined using a finite element calculation, further highlighting the significant influence of dispersion.

However, it has been found in the recent extensive series of experiments of Schriefl et al. (2012) on separate intimal, medial, and adventitial layers of human thoracic and abdominal aortas and common iliac arteries that the fiber dispersion does not possess rotational symmetry in three dimensions. The dispersion was found to be essentially symmetric in the circumferential/axial plane (in-plane) but has a small radial component (out-of-plane). To accommodate these new data the rotationally symmetric model of Gasser et al. (2006) has therefore been adapted in Holzapfel et al. (2015) by developing new generalized structure tensors and generalized invariants. This work is described in Sect. 6.4. In particular, this modification uses a bivariate von Mises distribution to characterize the in-plane and out-of-plane dispersions involving two dispersion parameters, one in-plane and one out-of-plane, as distinct from the single dispersion parameter associated with a rotationally symmetric dispersion.

Within the same general structure as for the previous models, the strain-energy function has been modified merely by updating the definitions of the generalized invariants. Based on a set of data obtained from histology and imaging, values of the dispersion parameters and mean fiber orientations were exemplified in Schriefl

et al. (2012), and, with these values, the corresponding material parameters were determined in Holzapfel et al. (2015) by fitting data from uniaxial tension tests on circumferential and axial specimens of an adventitial layer of a human non-atherosclerotic abdominal aorta. Following Holzapfel et al. (2015) this complete set of parameters is used finally in a finite element simulation of a nonhomogeneous uniaxial extension test on this adventitial layer. Some concluding remarks form the content of Sect. 7.

In Holzapfel et al. (2015) we have provided a brief review of dispersion models, which are based on two main approaches, namely the angular integration (AI) approach pioneered by Lanir (1983), and the generalized structure tensor (GST) approach due to Gasser et al. (2006). We focus on the GST approach in this chapter and refer the reader to Holzapfel et al. (2015) for pointers to the literature.

2 Fundamentals of Continuum Mechanics

Here we summarize the key notation used for describing the kinematics associated with continuum deformation, followed by a brief account of the stress tensors used to describe the stress within a deformed material and the associated equilibrium equations. We do not analyze (time-dependent) motion in this chapter. For more details of the background for this section we refer to Ogden (1997) and Holzapfel (2000), for example.

2.1 The Geometry of Deformation

As is usual in continuum mechanics, we consider a material body which, when unloaded (i.e., when not subject to either surface tractions or body forces) occupies a *reference configuration*, which we denote by \mathcal{B}_r , the boundary of which is denoted $\partial\mathcal{B}_r$. Let an arbitrary point of \mathcal{B}_r be labeled by its position vector \mathbf{X} . After deformation the body occupies the *deformed configuration*, denoted \mathcal{B} , which has boundary $\partial\mathcal{B}$. The material point \mathbf{X} is then taken to the new position vector \mathbf{x} in \mathcal{B} , as depicted in Fig. 4.

Mathematically, the deformation is described by the *deformation function* χ , which is a one-to-one, onto mapping from \mathcal{B}_r to \mathcal{B} . Thus, we write

$$\mathbf{x} = \chi(\mathbf{X}) \quad \text{for all } \mathbf{X} \in \mathcal{B}_r, \tag{1}$$

and, without further comment, χ is assumed to possess sufficient regularity for the analysis in this chapter.

In standard notation the second-order tensor \mathbf{F} , the so-called *deformation gradient tensor*, denotes the gradient of $\mathbf{x} = \chi(\mathbf{X})$, explicitly

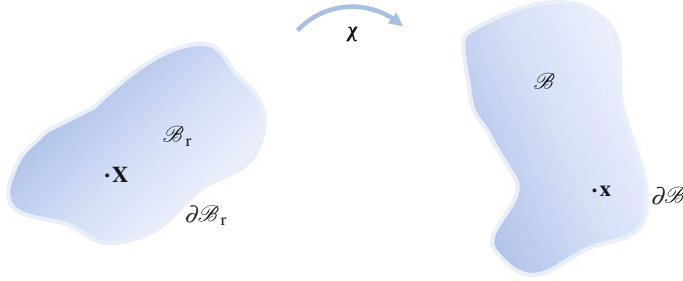


Fig. 4 On the *left-hand side* is depicted a body in its (unloaded) reference configuration \mathcal{B}_r , which has boundary $\partial\mathcal{B}_r$. As a result of the deformation χ the body occupies the deformed configuration \mathcal{B} , which has boundary $\partial\mathcal{B}$, as depicted on the *right-hand side*

$$\mathbf{F} = \text{Grad } \mathbf{x} = \text{Grad } \chi(\mathbf{X}), \quad (2)$$

where Grad denotes the gradient with respect to \mathbf{X} , as distinct from the gradient grad with respect to \mathbf{x} . Likewise Div and div denote the divergence operators with respect to \mathbf{X} and \mathbf{x} , respectively. We shall also use the notations $(\bullet)^T$ and $\text{tr}(\bullet)$, respectively, to denote the transpose and trace of a second-order tensor (\bullet) . With reference to a rectangular Cartesian coordinate system, we write the components of \mathbf{F} as $F_{i\alpha} = \partial x_i / \partial X_\alpha$, where x_i and X_α , $i, \alpha \in \{1, 2, 3\}$, are the components of \mathbf{x} and \mathbf{X} , respectively, Greek and Roman indices being associated with \mathcal{B}_r and \mathcal{B} , respectively.

We use the standard notation J for the determinant $\det \mathbf{F}$ of \mathbf{F} and, by convention, this is taken to be positive, i.e.,

$$J \equiv \det \mathbf{F} > 0, \quad (3)$$

which is clearly satisfied when \mathcal{B} coincides with \mathcal{B}_r since then $\mathbf{x} = \mathbf{X}$, $\mathbf{F} = \mathbf{I}_r$, the identity tensor in \mathcal{B}_r , and $\det \mathbf{F} = 1$. The physical interpretation of J is that it represents the local ratio of an infinitesimal volume element dv in \mathcal{B} to the corresponding volume element dV in \mathcal{B}_r based on \mathbf{X} in \mathcal{B}_r , i.e., $dv = J dV$.

Thus, for an isochoric (volume preserving) deformation $J = 1$, while for an incompressible material the constraint

$$J \equiv \det \mathbf{F} = 1 \quad (4)$$

must be satisfied at each \mathbf{X} in \mathcal{B}_r . This constraint is important here since many soft biological tissues, including artery walls, can be treated as incompressible.

We now define an important kinematical quantity known as the *stretch* $\lambda(\mathbf{M})$ in the direction of a unit vector \mathbf{M} based at \mathbf{X} in \mathcal{B}_r . Let dS be the length of an infinitesimal line element of material lying along the direction \mathbf{M} in \mathcal{B}_r . Under the deformation this becomes the infinitesimal line element $\mathbf{F}\mathbf{M}dS$ based at \mathbf{x} in \mathcal{B} , which has length $|\mathbf{F}\mathbf{M}|dS$. Thus, the ratio of deformed to undeformed length of the line element is

$|\mathbf{F}\mathbf{M}|$, which defines the stretch in the direction \mathbf{M} :

$$\lambda(\mathbf{M}) = |\mathbf{F}\mathbf{M}| = [(\mathbf{F}^T \mathbf{F}\mathbf{M}) \cdot \mathbf{M}]^{1/2}. \quad (5)$$

The product $\mathbf{F}^T \mathbf{F}$ in (5) defines the *right Cauchy–Green deformation tensor*, denoted \mathbf{C} , which has Cartesian components $C_{\alpha\beta} = F_{p\alpha} F_{p\beta}$, where the usual Einstein summation convention is used for repeated indices. Since $C_{\alpha\beta}$ has two Greek indices it is associated with \mathcal{B}_r , and \mathbf{C} is referred to as a Lagrangian tensor. This distinguishes it from its Eulerian counterpart, the *left Cauchy–Green deformation tensor* $\mathbf{B} = \mathbf{F}\mathbf{F}^T$, which has Cartesian components $B_{ij} = F_{i\alpha} F_{j\alpha}$ and is associated with \mathcal{B} . For future reference we record here the definitions

$$\mathbf{B} = \mathbf{F}\mathbf{F}^T, \quad \mathbf{C} = \mathbf{F}^T \mathbf{F}. \quad (6)$$

Scalar quantities known as the *principal invariants* of \mathbf{B} (the same as those of \mathbf{C}) are the coefficients I_1, I_2, I_3 in the identity

$$\mathbf{B}^3 - I_1 \mathbf{B}^2 + I_2 \mathbf{B} - I_3 \mathbf{I} = \mathbf{O}, \quad (7)$$

where \mathbf{O} is the zero tensor and \mathbf{I} the identity tensor in \mathcal{B} . This is the Cayley–Hamilton theorem, and I_1, I_2, I_3 are defined by

$$I_1 = \text{tr}(\mathbf{B}), \quad I_2 = \frac{1}{2}[I_1^2 - \text{tr}(\mathbf{B}^2)], \quad I_3 = \det \mathbf{B} \equiv J^2. \quad (8)$$

Since $I_3 = J^2$, we see that for an incompressible material $I_3 = 1$. Furthermore, for a plane strain deformation $I_2 = I_1$ and then, for an incompressible material, (7) factorizes as

$$(\mathbf{B} - \mathbf{I})[\mathbf{B}^2 - (I_1 - 1)\mathbf{B} + \mathbf{I}] = \mathbf{O}, \quad (9)$$

thus yielding the two-dimensional (plane strain) version of the Cayley–Hamilton theorem for an incompressible material, namely

$$\mathbf{B}^2 - (I_1 - 1)\mathbf{B} + \mathbf{I} = \mathbf{O}, \quad (10)$$

wherein the tensors are now two-dimensional.

Valuable further analysis of the local deformation governed by \mathbf{F} is provided by the *polar decomposition theorem*, which enables \mathbf{F} to be expressed in the two forms

$$\mathbf{F} = \mathbf{R}\mathbf{U} = \mathbf{V}\mathbf{R}, \quad (11)$$

each of which is uniquely defined. Here, \mathbf{R} is a proper orthogonal tensor, which represents a rotation, and \mathbf{U} and \mathbf{V} are positive definite and symmetric tensors, termed the *right* and *left stretch tensors*, respectively. Their symmetry allows us to introduce the spectral decompositions

$$\mathbf{U} = \sum_{i=1}^3 \lambda_i \mathbf{u}^{(i)} \otimes \mathbf{u}^{(i)}, \quad \mathbf{V} = \sum_{i=1}^3 \lambda_i \mathbf{v}^{(i)} \otimes \mathbf{v}^{(i)}, \quad (12)$$

where $\lambda_i > 0$, $i \in \{1, 2, 3\}$, are the *principal stretches*, $\mathbf{u}^{(i)}$ and $\mathbf{v}^{(i)}$ are the (unit) eigenvectors of \mathbf{U} and \mathbf{V} , respectively, and \otimes denotes the tensor product: $\mathbf{u}^{(i)}$ and $\mathbf{v}^{(i)}$ are referred to as the *Lagrangian principal axes* and *Eulerian principal axes*, respectively. By taking $\mathbf{M} = \mathbf{u}^{(i)}$ in the definition (5) of stretch, we see that $\lambda(\mathbf{u}^{(i)}) = \lambda_i$, the principal stretch corresponding to $\mathbf{u}^{(i)}$.

The connections

$$\mathbf{C} = \mathbf{U}^2, \quad \mathbf{B} = \mathbf{V}^2 \quad (13)$$

are also recorded here for later reference. These each have eigenvalues $\lambda_1^2, \lambda_2^2, \lambda_3^2$, and their principal invariants I_1, I_2, I_3 defined by (8) may now be expressed in terms of the principal stretches as

$$I_1 = \lambda_1^2 + \lambda_2^2 + \lambda_3^2, \quad I_2 = \lambda_2^2 \lambda_3^2 + \lambda_3^2 \lambda_1^2 + \lambda_1^2 \lambda_2^2, \quad I_3 = \lambda_1^2 \lambda_2^2 \lambda_3^2. \quad (14)$$

Note that these are symmetric functions of $\lambda_1, \lambda_2, \lambda_3$.

Finally in this section we note that from (3), (11) and (12) we may express J in the alternative forms

$$J = \det \mathbf{F} = \det \mathbf{U} = \det \mathbf{V} = \lambda_1 \lambda_2 \lambda_3. \quad (15)$$

In particular, for an incompressible material, the principal stretches satisfy the constraint

$$\lambda_1 \lambda_2 \lambda_3 = 1. \quad (16)$$

2.2 Stress and Equilibrium

While deformation is essentially concerned with geometry, the forces acting on a body that cause the deformation and changes in geometry are described in terms of stresses, and this section therefore introduces the notion of stress and its representation in terms of tensors. For this purpose we consider an arbitrary subdomain of \mathcal{B}_r , denoted \mathcal{D}_r , and its deformed counterpart \mathcal{D} in \mathcal{B} . Let $\partial \mathcal{D}_r$ and $\partial \mathcal{D}$ be the boundaries of \mathcal{D}_r and \mathcal{D} , respectively. An element of area dA on $\partial \mathcal{D}_r$ with unit outward normal \mathbf{N} is deformed into the area da on $\partial \mathcal{D}$ with unit normal \mathbf{n} , as depicted in Fig. 5.

According to Cauchy's stress theorem, the surface force acting on the area da due to its contact with the surrounding material depends linearly on the normal \mathbf{n} and may be written as $\sigma^T \mathbf{n} da$, where σ is the *Cauchy stress tensor* (a second-order tensor). If the deformation results from the combined action of surface tractions on $\partial \mathcal{B}$ and a body force \mathbf{b} per unit mass then for equilibrium of the domain \mathcal{D} the total force on it must vanish, i.e.,

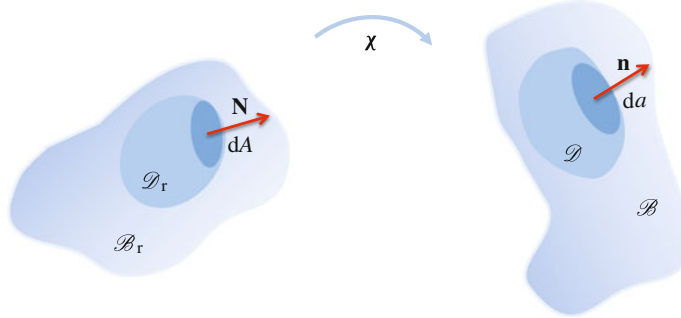


Fig. 5 An area element dA with unit outward normal \mathbf{N} on the boundary $\partial\mathcal{D}_r$ of the reference domain $\mathcal{D}_r \subset \mathcal{B}_r$ deforms into the area element da with unit outward normal \mathbf{n} on the boundary $\partial\mathcal{D}$ of the domain $\mathcal{D} \subset \mathcal{B}$ under the deformation χ

$$\int_{\partial\mathcal{D}} \boldsymbol{\sigma}^T \mathbf{n} da + \int_{\mathcal{D}} \rho \mathbf{b} dv \equiv \int_{\mathcal{D}} (\operatorname{div} \boldsymbol{\sigma} + \rho \mathbf{b}) dv = \mathbf{0}, \quad (17)$$

where ρ is the mass density per unit volume in \mathcal{D} , dv is an element of volume in \mathcal{D} , and the divergence theorem has been applied to the surface integral to obtain the volume integral on the right-hand side.

Assuming that the integrand on the right-hand side of (17) is continuous the arbitrariness of \mathcal{D} allows us to deduce the standard local form of the equilibrium equation, namely

$$\operatorname{div} \boldsymbol{\sigma} + \rho \mathbf{b} = \mathbf{0}. \quad (18)$$

If there are no intrinsic couple stresses in the material then symmetry of $\boldsymbol{\sigma}$ follows from the equilibrium of the moments of the forces acting on \mathcal{D} , so that $\boldsymbol{\sigma}^T = \boldsymbol{\sigma}$, and the transpose on $\boldsymbol{\sigma}$ is no longer needed.

The equilibrium equation (18) is Eulerian in nature since \mathbf{x} is the independent variable. The equation may also be expressed in Lagrangian form, with \mathbf{X} as the independent variable, by using the standard kinematic identity $\operatorname{Div}(J\mathbf{F}^{-1}) = \mathbf{0}$ and the definition

$$\mathbf{S} = J\mathbf{F}^{-1}\boldsymbol{\sigma} \quad (19)$$

of the so-called *nominal stress tensor*, which leads to the connection $\operatorname{Div} \mathbf{S} = J \operatorname{div} \boldsymbol{\sigma}$. By defining the mass density ρ_r per unit reference volume, invoking conservation of mass $\rho_r dV = \rho dv$ and recalling that $dv = JdV$, we obtain the connection

$$\rho_r = J\rho, \quad (20)$$

and hence the equilibrium equation (18) can be expressed in the equivalent form as

$$\operatorname{Div} \mathbf{S} + \rho_r \mathbf{b} = \mathbf{0}. \quad (21)$$

The transpose \mathbf{S}^T of \mathbf{S} is known as the *first Piola–Kirchhoff stress tensor*. For an isochoric deformation ($J = 1$) we have $\rho = \rho_r$, which becomes an identity for an incompressible material.

Note that, unlike $\boldsymbol{\sigma}$, \mathbf{S} is not in general symmetric but it follows from (19) and the symmetry of $\boldsymbol{\sigma}$ that

$$\mathbf{S}^T \mathbf{F}^T = \mathbf{F} \mathbf{S}. \quad (22)$$

Another stress tensor that is often used, particularly in the computational mechanics community, is the *second Piola–Kirchhoff stress tensor*, here denoted \mathbf{P} . It is symmetric and defined here for later reference through its connections with $\boldsymbol{\sigma}$ and \mathbf{S} , namely

$$\mathbf{P} = J \mathbf{F}^{-1} \boldsymbol{\sigma} \mathbf{F}^{-T} = \mathbf{S} \mathbf{F}^{-T}, \quad (23)$$

where $\mathbf{F}^{-T} = (\mathbf{F}^{-1})^T = (\mathbf{F}^T)^{-1}$.

2.2.1 Residual Stress

At this point we introduce the notion of *residual stress*. Here we adopt the definition of Hoger (1985) that residual stress is a stress distribution that exists in the reference configuration \mathcal{B}_r in the absence of loads, either surface tractions or body forces, and should be distinguished from other types of initial stresses (often referred to as prestresses) that are associated with loads. We denote the residual (Cauchy) stress by $\boldsymbol{\tau}$ and assume that there are no intrinsic couple stresses in \mathcal{B}_r , so that $\boldsymbol{\tau}$ is symmetric: $\boldsymbol{\tau}^T = \boldsymbol{\tau}$. The equilibrium equation that must be satisfied by $\boldsymbol{\tau}$ is, from (21) with $\mathbf{b} = \mathbf{0}$,

$$\operatorname{Div} \boldsymbol{\tau} = \mathbf{0} \quad \text{in } \mathcal{B}_r. \quad (24)$$

Since there are no surface tractions, $\boldsymbol{\tau}$ must also satisfy the boundary condition

$$\boldsymbol{\tau} \mathbf{N} = \mathbf{0} \quad \text{on } \partial \mathcal{B}_r. \quad (25)$$

It is worth emphasizing at this point that residual stresses are necessarily nonuniform and a material with residual stress is itself inhomogeneous. This follows from the identity $\operatorname{Div}(\boldsymbol{\tau} \otimes \mathbf{X}) = (\operatorname{Div} \boldsymbol{\tau}) \otimes \mathbf{X} + \boldsymbol{\tau}$, the use of (24), application of the divergence theorem and then (25), which leads to

$$\int_{\mathcal{B}_r} \boldsymbol{\tau} dV = \mathbf{O}. \quad (26)$$

Clearly, a nontrivial $\boldsymbol{\tau}$ cannot be uniform, and the character of the inhomogeneity depends on the geometry of the considered material body.

3 Constitutive Theory

In this section we focus on the characterization of the elastic behavior of solids based on the existence of a *strain-energy function*. Materials which possess a strain-energy function are referred to as *hyperelastic*. First, by considering the virtual work of the forces acting on the body, we motivate the introduction of a strain-energy function. We then examine its general properties and its functional dependence for particular classes of material symmetry through the use of invariants. We also show how residual stress can affect the material response by its inclusion in the argument of the strain-energy function.

3.1 The Elastic Strain-Energy Function

Consider the work done by the forces acting on the region \mathcal{D} in a virtual displacement, i.e., a small increment in \mathbf{x} , which we denote by $\dot{\mathbf{x}}$. This work is

$$\int_{\partial\mathcal{D}} (\boldsymbol{\sigma} \mathbf{n}) \cdot \dot{\mathbf{x}} \, da + \int_{\mathcal{D}} \rho \mathbf{b} \cdot \dot{\mathbf{x}} \, dv = \int_{\mathcal{D}} \text{tr}(\boldsymbol{\sigma} \text{grad } \dot{\mathbf{x}}) \, dv, \quad (27)$$

where the right-hand side has been obtained by an application of the divergence theorem and use of the equilibrium equation (18). By means of the connections (19) and $dv = JdV$ this may also be written

$$\int_{\mathcal{D}_r} \text{tr}(\mathbf{S} \dot{\mathbf{F}}) \, dV, \quad (28)$$

where $\dot{\mathbf{F}} = \text{Grad } \dot{\mathbf{x}}$. The work done is converted into stored elastic energy if there exists a scalar function $W(\mathbf{F})$ such that

$$\dot{W} = \text{tr}(\mathbf{S} \dot{\mathbf{F}}), \quad (29)$$

in which case (28) represents the virtual change in the total elastic energy stored in \mathcal{D}_r . We assume that a strain-energy function $W(\mathbf{F})$ exists, defined per unit volume in \mathcal{D}_r . If the material is inhomogeneous then W also depends separately on \mathbf{X} , but for a homogeneous material the dependence on \mathbf{X} is through $\mathbf{F}(\mathbf{X})$ alone.

Because of (29) the nominal stress is considered to be *work conjugate* to the deformation gradient. If there are no constraints on \mathbf{F} then, since $\dot{\mathbf{F}}$ is arbitrary, we obtain the stress deformation relation

$$\mathbf{S} = \frac{\partial W}{\partial \mathbf{F}}, \quad (30)$$

or, in index notation,

$$S_{\alpha i} = \frac{\partial W}{\partial F_{i\alpha}}, \quad (31)$$

the latter defining the convention used here for the order of the indices when differentiating with respect to $F_{i\alpha}$.

If \mathbf{F} is subject to a constraint then its components are no longer independent and $\dot{\mathbf{F}}$ is not arbitrary so that (30) requires modification. In the case of the incompressibility constraint, for example, (30) is replaced by

$$\mathbf{S} = \frac{\partial W}{\partial \mathbf{F}} - p \mathbf{F}^{-1}, \quad \det \mathbf{F} = 1, \quad (32)$$

where p is a Lagrange multiplier associated with the constraint.

The corresponding Cauchy stress tensor is then obtained from (19) as

$$\boldsymbol{\sigma} = J^{-1} \mathbf{F} \frac{\partial W}{\partial \mathbf{F}}, \quad \boldsymbol{\sigma} = \mathbf{F} \frac{\partial W}{\partial \mathbf{F}} - p \mathbf{I}, \quad (33)$$

for unconstrained and incompressible materials, respectively, with $J = \det \mathbf{F} = 1$ in the latter, where \mathbf{I} is again the identity tensor in \mathcal{B} .

Let us take the strain energy to be measured from \mathcal{B}_r , where $\mathbf{F} = \mathbf{I}_r$, the identity tensor in \mathcal{B}_r . This imposes the condition

$$W(\mathbf{I}_r) = 0. \quad (34)$$

If the configuration \mathcal{B}_r is stress free then we have

$$\frac{\partial W}{\partial \mathbf{F}}(\mathbf{I}_r) = \mathbf{O}, \quad \frac{\partial W}{\partial \mathbf{F}}(\mathbf{I}_r) - p^{(r)} \mathbf{I}_r = \mathbf{O}, \quad (35)$$

for unconstrained and incompressible materials, respectively, where $p^{(r)}$ is the specialization of the Lagrange multiplier p to \mathcal{B}_r . The reference configuration \mathcal{B}_r is sometimes referred to as a *natural configuration* if the conditions (34) and (35)₁ (or (35)₂) hold simultaneously.

If \mathcal{B}_r is not stress free, but supports a residual stress $\boldsymbol{\tau}$ then (35) does not hold and \mathcal{B}_r is referred to as a *residually stressed configuration*. In this case W , still measured from \mathcal{B}_r , depends on $\boldsymbol{\tau}$ as well as \mathbf{F} . We therefore include $\boldsymbol{\tau}$ explicitly in the arguments of W and write

$$W = W(\mathbf{F}, \boldsymbol{\tau}). \quad (36)$$

We emphasize that $\boldsymbol{\tau}$, being inhomogeneous, depends on \mathbf{X} , and therefore the material itself is also inhomogeneous if it is residually stressed.

The formulas (30)–(33) are unaffected by the presence of $\boldsymbol{\tau}$ but we now include the dependence on $\boldsymbol{\tau}$ and write

$$\mathbf{S} = \frac{\partial W}{\partial \mathbf{F}}(\mathbf{F}, \boldsymbol{\tau}), \quad \boldsymbol{\sigma} = J^{-1}\mathbf{FS} = J^{-1}\mathbf{F} \frac{\partial W}{\partial \mathbf{F}}(\mathbf{F}, \boldsymbol{\tau}) \quad (37)$$

for an unconstrained material, and

$$\mathbf{S} = \frac{\partial W}{\partial \mathbf{F}}(\mathbf{F}, \boldsymbol{\tau}) - p\mathbf{F}^{-1}, \quad \boldsymbol{\sigma} = \mathbf{FS} = \mathbf{F} \frac{\partial W}{\partial \mathbf{F}}(\mathbf{F}, \boldsymbol{\tau}) - p\mathbf{I} \quad (38)$$

for an incompressible material.

In \mathcal{B}_r there is no distinction between different stress tensors and each one must reduce to the residual stress, in which case

$$\boldsymbol{\tau} = \frac{\partial W}{\partial \mathbf{F}}(\mathbf{I}_r, \boldsymbol{\tau}), \quad \boldsymbol{\tau} = \frac{\partial W}{\partial \mathbf{F}}(\mathbf{I}_r, \boldsymbol{\tau}) - p^{(r)}\mathbf{I}_r, \quad (39)$$

for an unconstrained and incompressible material, respectively, where again \mathbf{I}_r is the identity tensor in \mathcal{B}_r and $p^{(r)}$ represents the value of p in \mathcal{B}_r (see, for example, Shams et al. 2011). These equations can be thought of as conditions providing either constraints on the residual stress for a given strain-energy function or constraints on the properties of the strain-energy function for a known residual stress. Some specializations of these conditions will be seen in later sections. These are particular constraints that apply for a residually stressed material and should be respected when specific models are constructed. Forms of W should also be consistent with data obtained from experimental tests that elicit the elastic properties of materials they aim to model. Other constraints may arise from basic physical and mathematical considerations, but we do not address these here. However, a key constraint, which should always be adopted, arises from the notion of *objectivity*, otherwise referred to as *material frame indifference*, which we discuss in the following.

3.2 The Principle of Objectivity

For a residually stressed material a general strain-energy function must satisfy the conditions (39), but it is not as yet subject to any other restrictions. At each \mathbf{X} it depends on \mathbf{F} and $\boldsymbol{\tau}$ in an otherwise general way. However, not all candidates for $W(\mathbf{F}, \boldsymbol{\tau})$ are admissible, and, importantly, after deformation W should be unaffected by any superimposed rigid body transformation. Such a transformation has the form $\mathbf{x}^* = \mathbf{Qx} + \mathbf{c}$, where, since we are not considering time dependence, \mathbf{Q} is an arbitrary constant rotation tensor and \mathbf{c} is an arbitrary constant vector. The deformation gradient $\mathbf{F}^* = \text{Grad } \mathbf{x}^*$ associated with this new deformation is then given by $\mathbf{F}^* = \mathbf{QF}$. Noting that $\boldsymbol{\tau}$ is defined in the reference configuration and is not therefore affected by the rotation in \mathcal{B} , the requirement imposed on W is that it must be invariant under this transformation, i.e.,

$$W(\mathbf{QF}, \boldsymbol{\tau}) = W(\mathbf{F}, \boldsymbol{\tau}) \quad (40)$$

for arbitrary proper orthogonal \mathbf{Q} and for any deformation gradient \mathbf{F} .

This restriction on W is referred to as the *principle of objectivity*, or just *objectivity* for brevity, and from now on we regard W as objective.

From the polar decomposition (11)₁ we obtain $\mathbf{Q}\mathbf{F} = \mathbf{Q}\mathbf{R}\mathbf{U}$ and then by choosing $\mathbf{Q} = \mathbf{R}^T$, Eq. (40) yields $W(\mathbf{F}, \boldsymbol{\tau}) = W(\mathbf{U}, \boldsymbol{\tau})$, which shows that W is independent of the rotational part \mathbf{R} of the deformation gradient and depends on \mathbf{F} only through the stretch tensor \mathbf{U} . Equivalently, since $\mathbf{C} = \mathbf{U}^2$, we can regard W as a function of \mathbf{C} and $\boldsymbol{\tau}$. Each of \mathbf{C} and $\boldsymbol{\tau}$ is a Lagrangian tensor, unaffected by a rotation in \mathcal{B} , and therefore any function of these two tensors is necessarily objective. In particular, without changing the notation for W on changing its argument, we write the strain-energy function as

$$W(\mathbf{C}, \boldsymbol{\tau}), \quad (41)$$

which automatically accommodates the required objectivity.

From this form of W we obtain the second Piola–Kirchhoff stress tensor

$$\mathbf{P} = 2 \frac{\partial W}{\partial \mathbf{C}}, \quad \mathbf{P} = 2 \frac{\partial W}{\partial \mathbf{C}} - p \mathbf{C}^{-1} \quad (42)$$

for unconstrained and incompressible materials, respectively. We remark that \mathbf{P} and $\mathbf{C}/2$ are therefore work conjugate stress and deformation tensors. In this case the incompressibility constraint is $I_3 = \det \mathbf{C} = 1$.

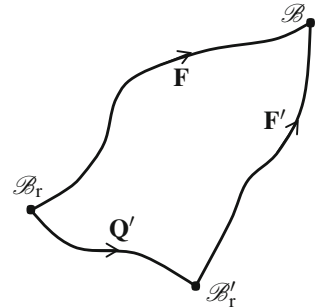
3.3 Material Symmetry (with no Residual Stress)

Objectivity applies irrespective of the material properties, but other restrictions arise that depend on the character of the material considered, and, in particular, the material may possess some intrinsic symmetry in its reference configuration. In order to examine such symmetry we consider $\boldsymbol{\tau} = \mathbf{O}$ since nonzero residual stresses complicate the arguments. For discussion of symmetry considerations in the presence of residual stress we refer to Hoger (1985) and Ogden (2003b).

If the material response is the same with respect to different reference configurations then this implies that the material has an intrinsic symmetry, and the transformation between the reference configurations is then known as a *symmetry transformation*.

To be specific, consider two reference configurations, denoted \mathcal{B}_r and \mathcal{B}'_r , and let a typical material point in these configurations have position vectors \mathbf{X} and \mathbf{X}' , respectively. Suppose the transformation (deformation) from \mathcal{B}_r to \mathcal{B}'_r has the deformation gradient $\mathbf{Q}' = \text{Grad } \mathbf{X}'$, which should be distinguished from the rotation \mathbf{Q} in \mathcal{B} . Then the deformation gradients of \mathcal{B} relative to \mathcal{B}_r and \mathcal{B}'_r , respectively, are \mathbf{F} and $\mathbf{F}' = \mathbf{F}\mathbf{Q}'^{-1}$, as depicted in Fig. 6. In components the latter reads $\partial x_i / \partial X'_\alpha = (\partial x_i / \partial X_\beta)(\partial X_\beta / \partial X'_\alpha)$.

Fig. 6 Depiction of the reference configurations \mathcal{B}_r and \mathcal{B}'_r and the deformed configuration \mathcal{B} connected by the deformation gradients \mathbf{F} , \mathbf{F}' and \mathbf{Q}' , with $\mathbf{F} = \mathbf{F}'\mathbf{Q}'$ in the space of deformation gradients



The right Cauchy–Green tensor relative to \mathcal{B}_r is \mathbf{C} , and that relative to \mathcal{B}'_r is $\mathbf{C}' = \mathbf{F}'^T \mathbf{F}' = \mathbf{Q}'^{-T} \mathbf{C} \mathbf{Q}'^{-1}$. If the material properties, as characterized by the strain-energy function W , are independent of this change of reference configuration then we must have, for the given \mathbf{Q}' ,

$$W(\mathbf{Q}'^{-T} \mathbf{C} \mathbf{Q}'^{-1}) = W(\mathbf{C}) \quad (43)$$

for all right Cauchy–Green deformation tensors \mathbf{C} , where the argument $\boldsymbol{\tau} = \mathbf{O}$ has been omitted from W . Such a \mathbf{Q}' identifies a symmetry of the material in the original reference configuration \mathcal{B}_r .

The set of all such changes of reference configuration for which (43) holds, i.e., the set of \mathbf{Q}' satisfying (43) for all right Cauchy–Green deformation tensors \mathbf{C} , forms a group of transformations, called the *symmetry group of the material relative to the reference configuration \mathcal{B}_r* . In this chapter we consider only symmetries for which the \mathbf{Q}' 's are proper orthogonal transformations, so that $\mathbf{Q}'^{-1} = \mathbf{Q}'^T$. It should be emphasized that the rotation \mathbf{Q}' is applied in \mathcal{B}_r , whereas \mathbf{Q} is applied in \mathcal{B} . The two rotations are entirely independent. We now consider the consequences of (43) for some particular classes of symmetry groups.

3.3.1 Isotropy

With the restriction to proper orthogonal transformations, Eq. (43) becomes

$$W(\mathbf{Q}' \mathbf{C} \mathbf{Q}'^T) = W(\mathbf{C}). \quad (44)$$

An *isotropic elastic material* is one for which the symmetry group is the full *proper orthogonal group*, i.e., (44) holds for arbitrary proper orthogonal \mathbf{Q}' . Equation (44) implies that W is an *isotropic function* of \mathbf{C} . This means, in particular, that W depends on \mathbf{C} through just three scalar deformation variables, which typically are taken to be the three principal invariants I_1, I_2, I_3 defined in (8) in terms of the left Cauchy–Green tensor \mathbf{B} . For convenience we now repeat them here in terms of \mathbf{C} :

$$I_1 = \text{tr } \mathbf{C}, \quad I_2 = \frac{1}{2}[I_1^2 - \text{tr}(\mathbf{C}^2)], \quad I_3 = \det \mathbf{C}. \quad (45)$$

We now write $W = W(I_1, I_2, I_3)$, and from (30) the nominal stress is given by

$$\mathbf{S} = \frac{\partial W}{\partial \mathbf{F}} = \sum_{i=1}^3 W_i \frac{\partial I_i}{\partial \mathbf{F}}, \quad (46)$$

where we have used the shorthand notation $W_i = \partial W / \partial I_i$, $i = 1, 2, 3$. All the information about material properties is contained in the coefficients W_i , $i = 1, 2, 3$, while the derivatives $\partial I_i / \partial \mathbf{F}$ are purely kinematic quantities. The latter can be calculated simply from (45) as

$$\frac{\partial I_1}{\partial \mathbf{F}} = 2\mathbf{F}^T, \quad \frac{\partial I_2}{\partial \mathbf{F}} = 2(I_1\mathbf{F}^T - \mathbf{C}\mathbf{F}^T), \quad \frac{\partial I_3}{\partial \mathbf{F}} = 2I_3\mathbf{F}^{-1}, \quad (47)$$

and an expanded expression for \mathbf{S} then follows from (46). The corresponding Cauchy stress tensor $\boldsymbol{\sigma} = J^{-1}\mathbf{FS}$ is then given by

$$J\boldsymbol{\sigma} = 2W_1\mathbf{B} + 2W_2(I_1\mathbf{B} - \mathbf{B}^2) + 2I_3W_3\mathbf{I}. \quad (48)$$

For an incompressible material $I_3 \equiv 1$, W depends only on I_1 and I_2 and, instead of (48), we have

$$\boldsymbol{\sigma} = 2W_1\mathbf{B} + 2W_2(I_1\mathbf{B} - \mathbf{B}^2) - p\mathbf{I}, \quad (49)$$

where p is the Lagrange multiplier (an arbitrary hydrostatic pressure) appearing in (33)₂.

Since, by (14), I_1, I_2, I_3 are symmetric functions of the stretches, we can also think of W as a symmetric function of the stretches and write $W = W(\lambda_1, \lambda_2, \lambda_3)$, and it follows that

$$\lambda_i \frac{\partial W}{\partial \lambda_i} = 2\lambda_i^2 W_1 + 2\lambda_i^2 (I_1 - \lambda_i^2) W_2 + 2I_3 W_3, \quad i = 1, 2, 3. \quad (50)$$

By (48) $\boldsymbol{\sigma}$ has the same principal axes as \mathbf{B} . Thus, (50) represents the principal components of (48) and enables the principal Cauchy stresses, denoted σ_i , $i = 1, 2, 3$, to be identified as

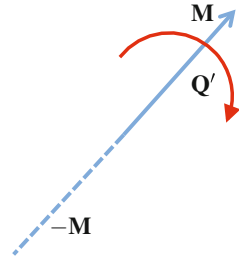
$$\sigma_i = J^{-1}\lambda_i \frac{\partial W}{\partial \lambda_i}, \quad i = 1, 2, 3, \quad (51)$$

for an unconstrained material. For an incompressible material this is replaced by

$$\sigma_i = \lambda_i \frac{\partial W}{\partial \lambda_i} - p, \quad i = 1, 2, 3, \quad (52)$$

which correspond to the eigenvalues of Eq. (49).

Fig. 7 Transverse isotropy with preferred direction \mathbf{M} in the reference configuration. The material properties are independent of rotations \mathbf{Q}' about \mathbf{M} and reversal of the direction of \mathbf{M} : $\mathbf{M} \rightarrow -\mathbf{M}$



3.3.2 One Preferred Direction (Transverse Isotropy)

If there is a single preferred direction in the material in its reference configuration, as in the case of a fiber-reinforced material with a single family of (locally) aligned fibers, then we identify that direction by the unit vector \mathbf{M} in \mathcal{B}_r , which in general depends on the point \mathbf{X} . Such a material is said to be *transversely isotropic* with direction of transverse isotropy \mathbf{M} . In the plane transverse to \mathbf{M} the material response is isotropic.

The material properties are invariant with respect to an arbitrary rotation about the direction \mathbf{M} and to reversal of \mathbf{M} , i.e., to rotations \mathbf{Q}' such that $\mathbf{Q}'\mathbf{M} = \pm\mathbf{M}$, as depicted in Fig. 7.

From the mathematical point of view the strain-energy function must satisfy (44) for all such \mathbf{Q}' . Thus, W depends on \mathbf{M} as well as \mathbf{C} and we may regard W as a function of both \mathbf{M} and \mathbf{C} , but since material properties are treated as independent of the sense of \mathbf{M} we can consider the \mathbf{M} dependence to be through the tensor product $\mathbf{M} \otimes \mathbf{M}$ and write $W(\mathbf{C}, \mathbf{M} \otimes \mathbf{M})$ instead of just $W(\mathbf{C})$, and note that $\mathbf{M} \otimes \mathbf{M}$ is unaffected by reversal of \mathbf{M} . In general, \mathbf{M} depends on \mathbf{X} , in which case the material is inhomogeneous. This is left implicit in $W(\mathbf{C}, \mathbf{M} \otimes \mathbf{M})$ since material symmetry is a local property.

It follows that transverse isotropy may be characterized by W being an *isotropic function* of the two symmetric tensors \mathbf{C} and $\mathbf{M} \otimes \mathbf{M}$ (Liu 1982); for general background on transverse isotropy and more generally on the theory of invariants we refer to Spencer (1971, 1972, 1984). Noting that $\mathbf{Q}'\mathbf{M} = \mathbf{M}\mathbf{Q}'^T$, the symmetry requirement is then

$$W(\mathbf{Q}'\mathbf{C}\mathbf{Q}'^T, \mathbf{Q}'\mathbf{M} \otimes \mathbf{Q}'\mathbf{M}) = W(\mathbf{C}, \mathbf{M} \otimes \mathbf{M}) \quad (53)$$

for all orthogonal \mathbf{Q}' . In this case there is no difference whether we restrict attention to *proper* orthogonal \mathbf{Q}' or consider all orthogonal \mathbf{Q}' since we may replace \mathbf{Q}' by $-\mathbf{Q}'$ in (53) without changing its consequences. Similarly in Eq. (44). The tensor $\mathbf{M} \otimes \mathbf{M}$ is referred to as a *structure tensor*.

The symmetry (53) is equivalent to W being a function of five independent invariants for an unconstrained material in three dimensions. These are, for example, the three isotropic invariants I_1, I_2, I_3 defined in (45) and two invariants that depend on \mathbf{M} and \mathbf{C} , these usually being denoted I_4 and I_5 . The choice of I_4 and I_5 is not unique

but, typically, they are defined by

$$I_4 = \mathbf{M} \cdot (\mathbf{C}\mathbf{M}), \quad I_5 = \mathbf{M} \cdot (\mathbf{C}^2\mathbf{M}). \quad (54)$$

Note that in terms of the stretch $\lambda(\mathbf{M})$ defined in (5), $I_4 = \lambda(\mathbf{M})^2$, the square of the stretch in the direction \mathbf{M} . The invariant I_5 does not have a similar simple interpretation, and we refer to Merodio and Ogden (2002) for discussion of a related invariant which does have a direct physical interpretation.

Then, by expanding out the formula (30) based on the invariants I_1, \dots, I_5 , similarly to that in the isotropic case, and using again the derivatives (47), supplemented by the derivatives

$$\frac{\partial I_4}{\partial \mathbf{F}} = 2\mathbf{M} \otimes \mathbf{FM}, \quad \frac{\partial I_5}{\partial \mathbf{F}} = 2(\mathbf{M} \otimes \mathbf{BFM} + \mathbf{CM} \otimes \mathbf{FM}), \quad (55)$$

we obtain an expression for the nominal stress tensor \mathbf{S} , which we do not write here. The corresponding Cauchy stress tensor $\boldsymbol{\sigma} = J^{-1}\mathbf{FS}$ for a transversely isotropic material is then given by

$$J\boldsymbol{\sigma} = 2W_1\mathbf{B} + 2W_2(I_1\mathbf{B} - \mathbf{B}^2) + 2I_3W_3\mathbf{I} + 2W_4\mathbf{m} \otimes \mathbf{m} + 2W_5(\mathbf{m} \otimes \mathbf{Bm} + \mathbf{Bm} \otimes \mathbf{m}), \quad (56)$$

where $\mathbf{m} = \mathbf{FM}$ is the ‘push forward’ of \mathbf{M} from \mathcal{B}_t to \mathcal{B} and now $W_i = \partial W / \partial I_i$, $i = 1, \dots, 5$, with $W = W(I_1, I_2, I_3, I_4, I_5)$. This recovers the formula (48) for an isotropic material when $W_4 = W_5 = 0$.

For an incompressible material $I_3 \equiv 1$, so only the four independent invariants I_1, I_2, I_4, I_5 are required in W to characterize the material, with $W = W(I_1, I_2, I_4, I_5)$ in general. Then, instead of (56), we have

$$\boldsymbol{\sigma} = 2W_1\mathbf{B} + 2W_2(I_1\mathbf{B} - \mathbf{B}^2) + 2W_4\mathbf{m} \otimes \mathbf{m} + 2W_5(\mathbf{m} \otimes \mathbf{Bm} + \mathbf{Bm} \otimes \mathbf{m}) - p\mathbf{I}. \quad (57)$$

Plane Strain

If attention is restricted to plane strain deformations, for example, then the number of independent invariants is reduced. In particular, for plane strain with \mathbf{M} in the considered plane the connections

$$I_2 = I_1 + I_3 - 1, \quad I_5 = (I_1 - 1)I_4 - I_3 \quad (58)$$

may be deduced (Merodio and Ogden 2002, 2003), and only three independent invariants remain, which we can take as I_1, I_3 and I_4 , for example. In the incompressible case just two invariants remain, namely I_1 and I_4 , and we define the plane strain specialization of W , denoted \hat{W} , by

$$\hat{W}(I_1, I_4) = W(I_1, I_2, I_4, I_5) \quad \text{with} \quad I_2 = I_1, \quad I_5 = (I_1 - 1)I_4 - 1. \quad (59)$$

For plane strain $\mathbf{m} = \mathbf{F}\mathbf{M}$ lies in the considered plane, and if we identify planar second-order tensors with a superposed hat $\hat{\cdot}$ then the plane strain version of Cauchy stress, denoted $\hat{\sigma}$, becomes simply

$$\hat{\sigma} = 2\hat{W}_1\hat{\mathbf{B}} + 2\hat{W}_4\mathbf{m} \otimes \mathbf{m} - \hat{p}\hat{\mathbf{I}}, \quad (60)$$

where $\hat{W}_1 = \partial\hat{W}/\partial I_1$ and $\hat{W}_4 = \partial\hat{W}/\partial I_4$ and \hat{p} is an adjusted form of p that includes various derivatives of W that contribute only hydrostatic terms to $\hat{\sigma}$.

3.4 A General Invariant Formulation

As we have seen, both isotropy and transverse isotropy can be formulated in terms of invariants. More generally, suppose that there are N independent invariants associated with \mathbf{C} and the material structure. Let these be denoted by I_1, I_2, \dots, I_N . They depend on \mathbf{C} and the material structure but not otherwise on the properties of the material, i.e., not on the particular form of W . Thus, we can write $W = W(I_1, I_2, \dots, I_N)$, and for an unconstrained material the nominal and Cauchy stress tensors can be expanded as

$$\mathbf{S} = \sum_{i=1}^N W_i \frac{\partial I_i}{\partial \mathbf{F}}, \quad \boldsymbol{\sigma} = J^{-1} \mathbf{F} \sum_{i=1}^N W_i \frac{\partial I_i}{\partial \mathbf{F}}, \quad (61)$$

where we have extended the notation W_i to $i = 1, 2, \dots, N$. The corresponding expressions for an incompressible material are

$$\mathbf{S} = \sum_{i=1, i \neq 3}^N W_i \frac{\partial I_i}{\partial \mathbf{F}} - p \mathbf{F}^{-1}, \quad \boldsymbol{\sigma} = \mathbf{F} \sum_{i=1, i \neq 3}^N W_i \frac{\partial I_i}{\partial \mathbf{F}} - p \mathbf{I}. \quad (62)$$

In general, the derivatives W_i depend on the material properties through the strain-energy function W , but, independently of that, apart from the case of isotropy, some information about the material structure is also contained within the derivatives $\partial I_i/\partial \mathbf{F}$, as for a transversely isotropic material for which $\partial I_4/\partial \mathbf{F}$ and $\partial I_5/\partial \mathbf{F}$ depend on the structure through \mathbf{M} .

In the remainder of this section we apply the above first to a material with two preferred directions and second to a material with a general residual stress but no preferred directions.

3.4.1 Two Preferred Directions and the Special Case of Orthotropy

Consider the situation in which there are two preferred directions in the reference configuration \mathcal{B}_r of the material, identified by the unit vectors \mathbf{M} and \mathbf{M}' with associated structure tensors $\mathbf{M} \otimes \mathbf{M}$ and $\mathbf{M}' \otimes \mathbf{M}'$. The strain-energy function now depends on \mathbf{C} , $\mathbf{M} \otimes \mathbf{M}$ and $\mathbf{M}' \otimes \mathbf{M}'$, and we write $W(\mathbf{C}, \mathbf{M} \otimes \mathbf{M}, \mathbf{M}' \otimes \mathbf{M}')$. Similarly to the transversely isotropic model, W is an isotropic function of its three arguments, i.e., it must satisfy

$$W(\mathbf{Q}'\mathbf{C}\mathbf{Q}'^T, \mathbf{Q}'\mathbf{M} \otimes \mathbf{Q}'\mathbf{M}, \mathbf{Q}'\mathbf{M}' \otimes \mathbf{Q}'\mathbf{M}') = W(\mathbf{C}, \mathbf{M} \otimes \mathbf{M}, \mathbf{M}' \otimes \mathbf{M}') \quad (63)$$

for arbitrary orthogonal \mathbf{Q}' and for any right Cauchy–Green tensor \mathbf{C} .

This means that W can be expressed in terms of invariants of the three tensors and their combinations. For an unconstrained material this requires eight independent invariants. These are the invariants I_1, \dots, I_5 associated with \mathbf{C} and $\mathbf{M} \otimes \mathbf{M}$, but additionally the invariants combining \mathbf{C} and $\mathbf{M}' \otimes \mathbf{M}'$, denoted I_6, I_7 , analogously to I_4, I_5 , and defined by

$$I_6 = \mathbf{M}' \cdot (\mathbf{C}\mathbf{M}'), \quad I_7 = \mathbf{M}' \cdot (\mathbf{C}^2\mathbf{M}'). \quad (64)$$

Finally, there is the invariant $[\mathbf{M} \cdot (\mathbf{C}\mathbf{M}')] \mathbf{M} \cdot \mathbf{M}'$ that involves all three tensors when $\mathbf{M} \cdot \mathbf{M}' \neq 0$. However, it is more convenient in the analysis to use $\mathbf{M} \cdot (\mathbf{C}\mathbf{M}')$ without the geometric factor, and we denote this by I_8 . Thus,

$$I_8 = \mathbf{M} \cdot (\mathbf{C}\mathbf{M}'), \quad (65)$$

which is not strictly invariant since it changes sign if either \mathbf{M} or \mathbf{M}' is reversed. An alternative, which is invariant, is to use I_8^2 rather than I_8 itself, and in any case the strain-energy function should depend on I_8 through I_8^2 . In fact, for the special case in which $\mathbf{M} \cdot \mathbf{M}' = 0$, I_8^2 is not needed since it depends on the other invariants and is given by (Merodio and Ogden 2006)

$$I_8^2 = I_2 + I_5 + I_7 + I_4I_6 - I_1(I_4 + I_6). \quad (66)$$

To form expressions for the stress tensors we require the derivatives of I_6 , I_7 and I_8 with respect to \mathbf{F} in addition to those given in (47) and (55) for I_1, \dots, I_5 . These are

$$\frac{\partial I_6}{\partial \mathbf{F}} = 2\mathbf{M}' \otimes \mathbf{F}\mathbf{M}', \quad \frac{\partial I_7}{\partial \mathbf{F}} = 2(\mathbf{M}' \otimes \mathbf{BFM}' + \mathbf{CM}' \otimes \mathbf{FM}'), \quad (67)$$

and

$$\frac{\partial I_8}{\partial \mathbf{F}} = \mathbf{M} \otimes \mathbf{FM}' + \mathbf{M}' \otimes \mathbf{FM}. \quad (68)$$

These enable the Cauchy stress tensor $\boldsymbol{\sigma}$ for an unconstrained material to be given via

$$J\sigma = 2W_1\mathbf{B} + 2W_2(I_1\mathbf{B} - \mathbf{B}^2) + 2I_3W_3\mathbf{I} + 2W_4\mathbf{m} \otimes \mathbf{m} + 2W_5(\mathbf{m} \otimes \mathbf{Bm} + \mathbf{Bm} \otimes \mathbf{m}) \\ + 2W_6\mathbf{m}' \otimes \mathbf{m}' + 2W_7(\mathbf{m}' \otimes \mathbf{Bm}' + \mathbf{Bm}' \otimes \mathbf{m}') + W_8(\mathbf{m} \otimes \mathbf{m}' + \mathbf{m}' \otimes \mathbf{m}), \quad (69)$$

where $\mathbf{m} = \mathbf{FM}$ and $\mathbf{m}' = \mathbf{FM}'$ and the notation $W_i = \partial W / \partial I_i$ now applies for $i = 1, \dots, 8$.

For an incompressible material the list of invariants reduces by one to $I_1, I_2, I_4, \dots, I_8$ and the Cauchy stress is given by

$$\sigma = 2W_1\mathbf{B} + 2W_2(I_1\mathbf{B} - \mathbf{B}^2) - p\mathbf{I} + 2W_4\mathbf{m} \otimes \mathbf{m} + 2W_5(\mathbf{m} \otimes \mathbf{Bm} + \mathbf{Bm} \otimes \mathbf{m}) \\ + 2W_6\mathbf{m}' \otimes \mathbf{m}' + 2W_7(\mathbf{m}' \otimes \mathbf{Bm}' + \mathbf{Bm}' \otimes \mathbf{m}') + W_8(\mathbf{m} \otimes \mathbf{m}' + \mathbf{m}' \otimes \mathbf{m}), \quad (70)$$

the notation $W_i = \partial W / \partial I_i$ now applying for $i = 1, 2, 4, \dots, 8$.

In general, the material response associated with two preferred directions is not *orthotropic*, orthotropy being characterized locally by the existence of three mutually orthogonal planes of symmetry in the reference configuration of the material. There are two situations in which the response is orthotropic. The first situation arises in the special case in which the two directions are orthogonal and the second for which the preferred directions are mechanically equivalent (Spencer 1972).

In the second case, for example, the material properties are unaffected by interchange of \mathbf{M} and \mathbf{M}' , which implies that

$$W(I_1, I_2, I_3, I_4, I_5, I_6, I_7, I_8) = W(I_1, I_2, I_3, I_6, I_7, I_4, I_5, I_8). \quad (71)$$

Plane Strain

As for the case of transverse isotropy, the number of independent invariants is reduced for plane strain, and we have the connections given in (58) together with

$$I_7 = (I_1 - 1)I_6 - I_3, \quad I_8^2 = I_4I_6 - I_3|\mathbf{M} \times \mathbf{M}'|^2, \quad (72)$$

and there are only four independent invariants, such as I_1, I_3, I_4, I_6 . In the incompressible case we summarize the connections between the invariants as

$$I_2 = I_1, \quad I_5 = (I_1 - 1)I_4 - 1, \quad I_7 = (I_1 - 1)I_6 - 1, \quad I_8^2 = I_4I_6 - |\mathbf{M} \times \mathbf{M}'|^2, \quad (73)$$

and the strain-energy function depends on just three invariants: $W \rightarrow \hat{W}(I_1, I_4, I_6)$, and the (planar) Cauchy stress has the form

$$\hat{\sigma} = 2\hat{W}_1\hat{\mathbf{B}} + 2\hat{W}_4\mathbf{m} \otimes \mathbf{m} + 2\hat{W}_6\mathbf{m}' \otimes \mathbf{m}' - \hat{p}\hat{\mathbf{I}}, \quad (74)$$

which generalizes the formula (60). Note that when $\mathbf{M} \cdot \mathbf{M}' = 0$, $I_8^2 = I_4I_6 - 1$, which is a special case of the three-dimensional formula (66).

3.4.2 Invariant Formulation with Residual Stress

We now consider the residual stress τ within the invariant framework of Sect. 3.4. First, we note that since τ is symmetric it can be written in spectral form as

$$\tau = \sum_{i=1}^3 \tau_i \mathbf{M}_i \otimes \mathbf{M}_i, \quad (75)$$

where τ_i , $i = 1, 2, 3$, are its eigenvalues and \mathbf{M}_i , $i = 1, 2, 3$, are the corresponding eigenvectors. Each $\mathbf{M}_i \otimes \mathbf{M}_i$, $i = 1, 2, 3$, can be considered as a structure tensor, although they are not all independent since they satisfy

$$\sum_{i=1}^3 \mathbf{M}_i \otimes \mathbf{M}_i = \mathbf{I}_r. \quad (76)$$

Thus, τ can be thought of as a generalized structure tensor, and we shall consider the combined invariants of the two tensors \mathbf{C} and τ , and without any other structure in the material. Thus, generalizing the condition (53), the strain-energy function of a residually stressed material must satisfy

$$W(\mathbf{Q}'\mathbf{C}\mathbf{Q}'^T, \mathbf{Q}'\tau\mathbf{Q}'^T) = W(\mathbf{C}, \tau) \quad (77)$$

for all orthogonal \mathbf{Q}' . Note that we are using the notation W for the strain-energy function irrespective of its arguments.

Since $\text{Div } \tau = \mathbf{0}$ in \mathcal{B}_r and $\tau \mathbf{N} = \mathbf{0}$ on $\partial\mathcal{B}_r$ it is easy to show that τ cannot be purely isotropic (i.e., a hydrostatic stress); for a proof, see, for example, Ogden (2003b). Thus, the response of a residually stressed material relative to \mathcal{B}_r is necessarily anisotropic and the effect of τ on the response is similar to, but more complex than, that of a single preferred direction. In particular, the condition (77) implies that W can be expressed in terms of invariants, in fact only 10 independent invariants in general, as discussed in Shams et al. (2011) and more generally, for a residually stressed transversely isotropic elastic material with 18 invariants, as derived by Hoger (1993) and used in the context of wave propagation by Ogden and Singh (2011).

Here we adopt the notation K_1, K_2, K_3 for the isotropic invariants, i.e.,

$$K_1 = \text{tr } \mathbf{C}, \quad K_2 = \frac{1}{2}[(\text{tr } \mathbf{C})^2 - \text{tr } (\mathbf{C}^2)], \quad K_3 = \det \mathbf{C} \quad (78)$$

instead of I_1, I_2, I_3 so as avoid a conflict with the notations for the remaining invariants with the notations I_4, I_5, \dots for the other invariants considered heretofore. The three invariants of τ , since they do not depend on \mathbf{C} , are collected conveniently as

$$K_4 \equiv \left\{ \text{tr } \tau, \frac{1}{2}[(\text{tr } \tau)^2 - \text{tr } (\tau^2)], \det \tau \right\}, \quad (79)$$

and the set of independent invariants involving the combination of \mathbf{C} and $\boldsymbol{\tau}$ is taken to be

$$K_5 = \text{tr}(\boldsymbol{\tau}\mathbf{C}), \quad K_6 = \text{tr}(\boldsymbol{\tau}\mathbf{C}^2), \quad K_7 = \text{tr}(\boldsymbol{\tau}^2\mathbf{C}), \quad K_8 = \text{tr}(\boldsymbol{\tau}^2\mathbf{C}^2). \quad (80)$$

For a residually stressed material we therefore consider the strain-energy function $W = W(K_1, K_2, K_3, K_4, K_5, K_6, K_7, K_8)$, K_4 consisting of three separate invariants in general.

For an incompressible material, since $K_3 = 1$, nine independent invariants are required in general. For the specialization to plane strain with a planar residual stress the number of independent invariants is reduced, as was illustrated, for example, in Sect. 3.4.1 for two preferred directions. We refer to Merodio et al. (2013) for details.

Note that when evaluated in the reference configuration \mathcal{B}_r the invariants that depend on \mathbf{C} reduce to

$$K_1 = K_2 = 3, \quad K_3 = 1, \quad K_5 = K_6 = \text{tr } \boldsymbol{\tau}, \quad K_7 = K_8 = \text{tr}(\boldsymbol{\tau}^2). \quad (81)$$

Stress Tensors

With the considered set of invariants the expanded expressions for the stress tensors given in (61) become

$$\mathbf{S} = \sum_{i \in \mathcal{I}} W_i \frac{\partial K_i}{\partial \mathbf{F}}, \quad \boldsymbol{\sigma} = J^{-1} \mathbf{F} \mathbf{S}, \quad (82)$$

for an unconstrained material, where \mathcal{I} is the index set $\{1, 2, 3, 5, 6, 7, 8\}$, while for an incompressible material (62) reads

$$\mathbf{S} = \sum_{i \in \mathcal{I}} W_i \frac{\partial K_i}{\partial \mathbf{F}} - p \mathbf{F}^{-1}, \quad \boldsymbol{\sigma} = \mathbf{F} \mathbf{S}, \quad (83)$$

in which case the index set reduces to $\{1, 2, 5, 6, 7, 8\}$. Note that the derivative of K_4 with respect to \mathbf{F} vanishes and so is not included in the above expressions, although K_4 is included in the arguments of W . We emphasize here that in this section W_i stands for $\partial W / \partial K_i$ as distinct from $\partial W / \partial I_i$ used earlier. At this point we do not include both residual stress and structure associated with preferred directions.

In addition to the expressions $\partial K_i / \partial \mathbf{F}$ given by (47) for $i = 1, 2, 3$ with I_i replaced by K_i , we require the corresponding expressions for $i = 5, 6, 7, 8$. Similarly to the derivatives of I_4 and I_5 in (55), these are easily obtained as

$$\frac{\partial K_5}{\partial \mathbf{F}} = 2\boldsymbol{\tau}\mathbf{F}^T, \quad \frac{\partial K_6}{\partial \mathbf{F}} = 2(\boldsymbol{\tau}\mathbf{C}\mathbf{F}^T + \mathbf{C}\boldsymbol{\tau}\mathbf{F}^T), \quad (84)$$

$$\frac{\partial K_7}{\partial \mathbf{F}} = 2\boldsymbol{\tau}^2\mathbf{F}^T, \quad \frac{\partial K_8}{\partial \mathbf{F}} = 2(\boldsymbol{\tau}^2\mathbf{C}\mathbf{F}^T + \mathbf{C}\boldsymbol{\tau}^2\mathbf{F}^T). \quad (85)$$

Using these in (82) we obtain the expanded Cauchy stress via

$$\begin{aligned} J\sigma = & 2W_1\mathbf{B} + 2W_2(I_1\mathbf{B} - \mathbf{B}^2) + 2I_3W_3\mathbf{I} + 2W_5\boldsymbol{\Sigma} + 2W_6(\boldsymbol{\Sigma}\mathbf{B} + \mathbf{B}\boldsymbol{\Sigma}) \\ & + 2W_7\boldsymbol{\Sigma}\mathbf{B}^{-1}\boldsymbol{\Sigma} + 2W_8(\boldsymbol{\Sigma}\mathbf{B}^{-1}\boldsymbol{\Sigma}\mathbf{B} + \mathbf{B}\boldsymbol{\Sigma}\mathbf{B}^{-1}\boldsymbol{\Sigma}), \end{aligned} \quad (86)$$

where we have introduced the notation $\boldsymbol{\Sigma} = \mathbf{F}\boldsymbol{\tau}\mathbf{F}^T$. This is the Eulerian counterpart of the Lagrangian residual stress tensor $\boldsymbol{\tau}$ and represents the push forward of $\boldsymbol{\tau}$ from \mathcal{B}_r to \mathcal{B} .

For an incompressible material we obtain similarly, from (83),

$$\begin{aligned} \sigma = & 2W_1\mathbf{B} + 2W_2(I_1\mathbf{B} - \mathbf{B}^2) + 2W_5\boldsymbol{\Sigma} + 2W_6(\boldsymbol{\Sigma}\mathbf{B} + \mathbf{B}\boldsymbol{\Sigma}) \\ & + 2W_7\boldsymbol{\Sigma}\mathbf{B}^{-1}\boldsymbol{\Sigma} + 2W_8(\boldsymbol{\Sigma}\mathbf{B}^{-1}\boldsymbol{\Sigma}\mathbf{B} + \mathbf{B}\boldsymbol{\Sigma}\mathbf{B}^{-1}\boldsymbol{\Sigma}) - p\mathbf{I}. \end{aligned} \quad (87)$$

When evaluated in \mathcal{B}_r Eqs. (86) and (87) reduce to

$$\boldsymbol{\tau} = 2(W_1 + 2W_2 + W_3)\mathbf{I}_r + 2(W_5 + 2W_6)\boldsymbol{\tau} + 2(W_7 + 2W_8)\boldsymbol{\tau}^2 \quad (88)$$

and

$$\boldsymbol{\tau} = (2W_1 + 4W_2 - p^{(r)})\mathbf{I}_r + 2(W_5 + 2W_6)\boldsymbol{\tau} + 2(W_7 + 2W_8)\boldsymbol{\tau}^2, \quad (89)$$

respectively, wherein each W_i , $i \in \mathcal{I}$, is evaluated for the invariants given in \mathcal{B}_r by (81). These are the specializations of the general formulas in (39) to the present circumstances.

From (88) and (89) we deduce that in \mathcal{B}_r the conditions

$$W_1 + 2W_2 + W_3 = 0, \quad 2(W_5 + 2W_6) = 1, \quad W_7 + 2W_8 = 0 \quad (90)$$

and

$$2W_1 + 4W_2 - p^{(r)} = 0, \quad 2(W_5 + 2W_6) = 1, \quad W_7 + 2W_8 = 0, \quad (91)$$

must hold for an unconstrained and incompressible material, respectively, as derived by Shams et al. (2011).

Plane Strain

In the plane strain specialization, for example, in the (1, 2) plane with the residual stress having only the in-plane components τ_{11} , τ_{22} , τ_{12} and \mathbf{C} having nonzero components C_{11} , C_{22} , C_{12} , $C_{33} = 1$, considerable simplification is achieved and only the invariants K_1 , K_3 , K_4 , K_5 remain independent. They are given by

$$K_1 = C_{11} + C_{22} + 1, \quad K_3 = C_{11}C_{22} - C_{12}^2, \quad K_4 = \{\tau_{11} + \tau_{22}, \tau_{11}\tau_{22} - \tau_{12}^2, 0\}, \quad (92)$$

$$K_5 = C_{11}\tau_{11} + C_{22}\tau_{22} + 2C_{12}\tau_{12}, \quad (93)$$

and in terms of these the other invariants are given by

$$K_2 = K_1 + K_3 - 1, \quad K_6 = (K_1 - 1)K_5 - K_3(\tau_{11} + \tau_{22}), \quad (94)$$

$$K_7 = (\tau_{11} + \tau_{22})K_5 - (K_1 - 1)(\tau_{11}\tau_{22} - \tau_{12}^2), \quad (95)$$

$$K_8 = (K_1 - 1)K_7 - K_3[(\tau_{11} + \tau_{22})^2 - 2(\tau_{11}\tau_{22} - \tau_{12}^2)]. \quad (96)$$

Similarly to the plane strain cases considered in Sects. 3.3.2 and 3.4.1 the planar Cauchy stress $\hat{\sigma}$ is given in a simple form via

$$J\hat{\sigma} = 2\hat{W}_1\hat{\mathbf{B}} + 2K_3\hat{W}_3\hat{\mathbf{I}} + 2\hat{W}_5\hat{\Sigma}, \quad (97)$$

where $\hat{W}(K_1, K_3, K_4, K_5)$ is obtained from $W(K_1, K_2, K_3, K_4, K_5, K_6, K_7, K_8)$ with the specializations (92)–(96) and, as before, the hats refer to the plane specialization. For an incompressible material the details were given by Merodio et al. (2013) and in the above the invariants specialize with $K_3 = 1$, \hat{W} depends on just K_1, K_4, K_5 , and the plane Cauchy stress has the form

$$\hat{\sigma} = 2\hat{W}_1\hat{\mathbf{B}} + 2\hat{W}_5\hat{\Sigma} - \hat{p}\hat{\mathbf{I}}. \quad (98)$$

The latter formulation has been used in Merodio et al. (2013) in the analysis of the azimuthal shear deformation of a residually stressed circular cylindrical tube.

4 The Role of Homogeneous Deformations

For the experimental determination of the elastic properties of soft biological tissues homogeneous deformations play a key role. Theoretically they are exact deformations for which the deformation gradient \mathbf{F} is independent of position \mathbf{X} , but experimentally a uniform \mathbf{F} is only achievable approximately. Provided the tissue specimens are selected appropriately and the experiments are carefully conducted then the approximation can be considered sufficiently good to allow certain tissue properties to be elicited. In this connection homogeneous deformations have been discussed extensively for isotropic, transversely isotropic and orthotropic fiber-reinforced materials in the literature, and we refer to, for example, Ogden (2003b, 2009, 2015) and Holzapfel and Ogden (2009c) and references therein for details.

Rather than repeating full details here, we shall consider only the case of the homogeneous biaxial deformation of a thin rectangular sheet of material loaded in tension in the plane of the sheet. The sheet is assumed to contain two preferred directions that represent two families of parallel fibers, the two families being disposed symmetrically to the axes of biaxial tension, which are parallel to the sheet edges. This deformation is an example of a so-called *pure homogeneous strain*, which is defined in terms of rectangular Cartesian coordinates (X_1, X_2, X_3) and (x_1, x_2, x_3) in the reference and deformed configurations, respectively, by

$$x_1 = \lambda_1 X_1, \quad x_2 = \lambda_2 X_2, \quad x_3 = \lambda_3 X_3, \quad (99)$$

where the principal stretches $\lambda_1, \lambda_2, \lambda_3$ are constants, i.e., independent of (X_1, X_2, X_3) .

With respect to these coordinates \mathbf{F} and \mathbf{C} have diagonal forms $\text{diag}[\lambda_1, \lambda_2, \lambda_3]$ and $\text{diag}[\lambda_1^2, \lambda_2^2, \lambda_3^2]$, respectively, and for an incompressible material the constraint (16) must be satisfied. For convenience of reference in this section we repeat this here:

$$\lambda_1 \lambda_2 \lambda_3 = 1. \quad (100)$$

Note that for a homogeneous deformation there can be no residual stress.

4.1 Application to Fiber-Reinforced Materials

We now suppose that the preferred directions in the reference configuration, denoted \mathbf{M} and \mathbf{M}' , are given by

$$\mathbf{M} = \cos \varphi \mathbf{e}_1 + \sin \varphi \mathbf{e}_2, \quad \mathbf{M}' = \cos \varphi \mathbf{e}_1 - \sin \varphi \mathbf{e}_2, \quad (101)$$

where φ is a constant angle, as depicted in Fig. 8, and $\mathbf{e}_1, \mathbf{e}_2$ denote the in-plane Cartesian coordinate directions. The directions \mathbf{M} and \mathbf{M}' deform into the vectors \mathbf{m} and \mathbf{m}' , which are given by

$$\mathbf{m} = \lambda_1 \cos \varphi \mathbf{e}_1 + \lambda_2 \sin \varphi \mathbf{e}_2, \quad \mathbf{m}' = \lambda_1 \cos \varphi \mathbf{e}_1 - \lambda_2 \sin \varphi \mathbf{e}_2. \quad (102)$$

In terms of the principal stretches the invariants defined in (45), or (14), (54), (64) and (65) are, for an incompressible material,

$$I_1 = \lambda_1^2 + \lambda_2^2 + \lambda_1^{-2} \lambda_2^{-2}, \quad I_2 = \lambda_1^{-2} + \lambda_2^{-2} + \lambda_1^2 \lambda_2^2, \quad (103)$$

where (100) has been used to replace λ_3 in terms of λ_1 and λ_2 ,

$$I_4 = I_6 = \lambda_1^2 \cos^2 \varphi + \lambda_2^2 \sin^2 \varphi, \quad I_5 = I_7 = \lambda_1^4 \cos^2 \varphi + \lambda_2^4 \sin^2 \varphi, \quad (104)$$

and

$$I_8 = \lambda_1^2 \cos^2 \varphi - \lambda_2^2 \sin^2 \varphi. \quad (105)$$

In this situation, on applying the general formula (70) for the Cauchy stress tensor σ , it can be seen that the components σ_{13} and σ_{23} are zero and the other components are given by

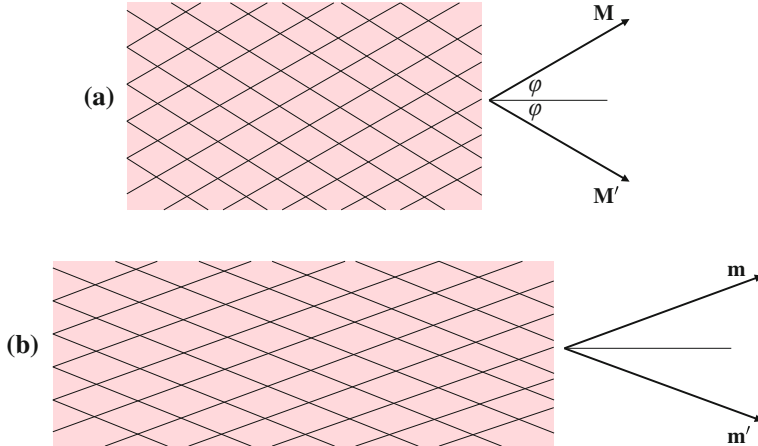


Fig. 8 Pure homogeneous strain of a thin sheet of material in the $(1, 2)$ plane with two in-plane symmetrically disposed families of fibers with directions \mathbf{M} and \mathbf{M}' in the reference configuration (a), and \mathbf{m} and \mathbf{m}' in the deformed configuration (b)

$$\begin{aligned}\sigma_{11} = & 2W_1\lambda_1^2 + 2W_2(I_1\lambda_1^2 - \lambda_1^4) + 2(W_4 + W_6 + W_8)\lambda_1^2 \cos^2 \varphi \\ & + 4(W_5 + W_7)\lambda_1^4 \cos^2 \varphi - p,\end{aligned}\quad (106)$$

$$\begin{aligned}\sigma_{22} = & 2W_1\lambda_2^2 + 2W_2(I_1\lambda_2^2 - \lambda_2^4) + 2(W_4 + W_6 - W_8)\lambda_2^2 \sin^2 \varphi \\ & + 4(W_5 + W_7)\lambda_2^4 \sin^2 \varphi - p,\end{aligned}\quad (107)$$

$$\sigma_{12} = 2[W_4 - W_6 + (W_5 - W_7)(\lambda_1^2 + \lambda_2^2)]\lambda_1\lambda_2 \sin \varphi \cos \varphi, \quad (108)$$

$$\sigma_{33} = 2W_1\lambda_3^2 + 2W_2(I_1\lambda_3^2 - \lambda_3^4) - p. \quad (109)$$

Clearly, the invariants in this case depend on just the two independent stretches λ_1 and λ_2 and the angle φ and it is therefore convenient to reduce the dependence of W on the seven invariants to dependence on these three quantities by means of the notation $\tilde{W}(\lambda_1, \lambda_2, \varphi)$, which is defined by

$$\tilde{W}(\lambda_1, \lambda_2, \varphi) = W(I_1, I_2, I_4, I_5, I_6, I_7, I_8), \quad (110)$$

where $I_1, I_2, I_4, \dots, I_8$ are given by (103)–(105). Note that φ is a material property, not a deformation variable. For an isotropic material W depends on I_1 and I_2 only and in this case \tilde{W} is symmetric in λ_1 and λ_2 , but otherwise \tilde{W} is not symmetric except in the particular case $\varphi = \pi/4$. It is then easy to obtain the simple formulas

$$\sigma_{11} - \sigma_{33} = \lambda_1 \frac{\partial \tilde{W}}{\partial \lambda_1}, \quad \sigma_{22} - \sigma_{33} = \lambda_2 \frac{\partial \tilde{W}}{\partial \lambda_2}. \quad (111)$$

There is no corresponding simple formula for σ_{12} , which is not in general zero and hence, unlike σ_{33} , the normal stresses σ_{11} and σ_{22} are not in general principal stresses. However, there are particular circumstances in which they are principal stresses. First, if $\varphi = 0$ or $\pi/2$ the two preferred directions coincide and the material is transversely isotropic; second, if the two families of fibers have the same elastic properties and then, for the specific deformation considered here, since $I_4 = I_6$ and $I_5 = I_7$, $W_4 = W_6$ and $W_5 = W_7$ and $\sigma_{12} = 0$. In this second case the material is *orthotropic*, as indicated in Sect. 3.4.1, and the axes of orthotropy coincide with the Cartesian axes.

We emphasize at this point that, except in the case of incompressible isotropic materials, biaxial tests provide only limited information about tissue elastic properties, but they are nevertheless very useful since experimental setups in which more than two deformation components can be varied independently and the associated stress components measured are rare. Indeed, for an incompressible material there are seven constitutive functions $W_1, W_2, W_4, \dots, W_8$ that are required to be known in order to fully characterize material properties and at present it is not possible experimentally to distinguish the effects on the material behavior of all the different invariants and constitutive functions. As a result it is usual to specialize the dependence of the strain-energy function to a limited number of invariants that are able to capture the essence of the elastic behavior of tissues.

For the latter purpose strain-energy functions restricted to the invariants I_1, I_4 and I_6 are often considered and typically these have the general form

$$W(I_1, I_4, I_6) = W_{\text{iso}}(I_1) + W_{\text{aniso}}(I_4, I_6), \quad (112)$$

more particularly with the symmetry $W_{\text{aniso}}(I_4, I_6) = W_{\text{aniso}}(I_6, I_4)$, reflecting the fact that the two families of fibers have the same elastic properties. This decouples the isotropic part W_{iso} , which models the matrix, from the contributions of the collagen fibers embedded in the matrix and modeled by the anisotropic part W_{aniso} . A particular strain-energy function of this form has a neo-Hookean isotropic part

$$W_{\text{iso}}(I_1) = \frac{1}{2}\mu(I_1 - 3), \quad (113)$$

where $\mu (>0)$ is the shear modulus of the matrix in its reference configuration, and Fung-type exponentials associated with the fiber elasticity, namely

$$W_{\text{aniso}}(I_4, I_6) = \frac{k_1}{2k_2}\{\exp[k_2(I_4 - 1)^2] + \exp[k_2(I_6 - 1)^2] - 2\}, \quad (114)$$

where k_1 (with the dimension of stress) and k_2 (dimensionless) are material constants. In this case $\sigma_{12} = 0$ and the other stress components are given by

$$\sigma_{11} = \mu\lambda_1^2 + 4k_1(I_4 - 1)\exp[k_2(I_4 - 1)^2]\lambda_1^2\cos^2\varphi - p, \quad (115)$$

$$\sigma_{22} = \mu\lambda_2^2 + 4k_1(I_4 - 1)\exp[k_2(I_4 - 1)^2]\lambda_2^2\sin^2\varphi - p, \quad (116)$$

and $\sigma_{33} = \mu\lambda_3^2 - p$. On setting $\sigma_{33} = 0$ and eliminating p and λ_3 , we then obtain

$$\sigma_{11} = \mu(\lambda_1^2 - \lambda_1^{-2}\lambda_2^{-2}) + 4k_1(I_4 - 1) \exp[k_2(I_4 - 1)^2] \lambda_1^2 \cos^2 \varphi, \quad (117)$$

$$\sigma_{22} = \mu(\lambda_2^2 - \lambda_1^{-2}\lambda_2^{-2}) + 4k_1(I_4 - 1) \exp[k_2(I_4 - 1)^2] \lambda_2^2 \sin^2 \varphi, \quad (118)$$

equations for the in-plane stress components σ_{11} and σ_{22} in terms of the independent stretches λ_1 and λ_2 , I_4 being given by Eq. (104)₁.

To illustrate these formulas and, in particular, their dependence on the fiber angle we plot the dimensionless stress components $\bar{\sigma}_{11} = \sigma_{11}/\mu$ and $\bar{\sigma}_{22} = \sigma_{22}/\mu$ as functions of λ_1 for a fixed value of λ_2 in Figs. 9 and 10, respectively. Results are shown for the representative values $\lambda_2 = 1$ with $\bar{k}_1 = k_1/\mu = 1$ and $k_2 = 1$. Clearly, as is apparent from Fig. 9, the response becomes stiffer as the fiber become closer to the direction of the applied tension σ_{11} .

Fig. 9 Plot of the dimensionless stress $\bar{\sigma}_{11} = \sigma_{11}/\mu$ against λ_1 based on Eq. (117) for $\lambda_2 = 1$, dimensionless parameter values $\bar{k}_1 = k_1/\mu = 1$ and $k_2 = 1$ and the indicated values of the fiber angle φ together with the unmarked curve for $\varphi = \pi/2$ (which has the softest response)

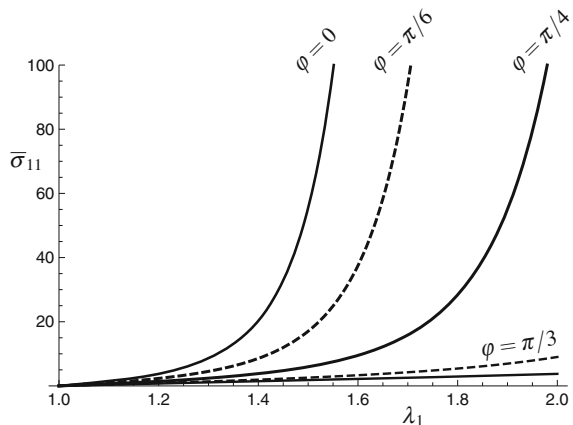
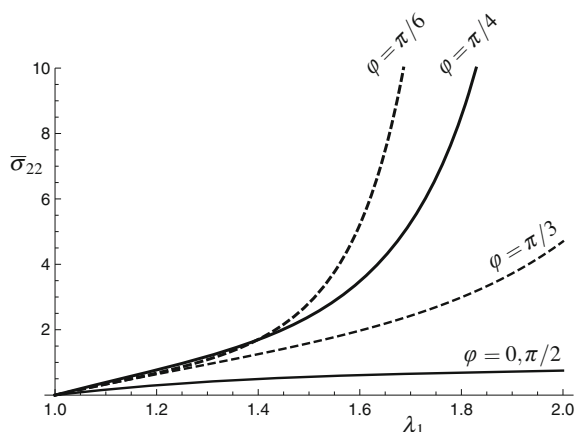


Fig. 10 Plot of the dimensionless stress $\bar{\sigma}_{22} = \sigma_{22}/\mu$ against λ_1 based on Eq. (118) for $\lambda_2 = 1$, dimensionless parameter values $\bar{k}_1 = k_1/\mu = 1$ and $k_2 = 1$ and the indicated values of the fiber angle φ



In Fig. 10 the behavior of the lateral stress is illustrated, also as a function of the active stretch λ_1 . These show a similar stiffening trend to that in Fig. 9 although there is some overlap of the curves for different values of φ . The curves for $\varphi = 0$ and $\varphi = \pi/2$ are identical since the anisotropic term vanishes, with $\varphi = 0$ and $I_4 = 1$, respectively, because we have chosen $\lambda_2 = 1$.

5 Extension and Inflation of an Artery

We now consider the elastic deformation of an artery, which is modeled as a thick-walled circular cylindrical tube. In particular, we restrict attention to the extension and inflation of an artery in which there are two symmetrically and helically arranged families of fibers with the two families having the same elastic properties. We obtain general expressions for the pressure and axial load on the artery in terms of the radial and axial stretches. As a special case, and as a first approximation, we examine the specialization of the results to a thin-walled (or membrane) tube. A membrane does not support residual stresses and in order to consider the effect of residual stresses on the elastic behavior of the tube we then return to consideration of the thick-walled model.

5.1 Geometry and Deformation

We consider first a thick-walled circular cylindrical tube with reference geometry defined in cylindrical polar coordinates R, Θ, Z by

$$0 < A \leq R \leq B, \quad 0 \leq \Theta \leq 2\pi, \quad 0 \leq Z \leq L, \quad (119)$$

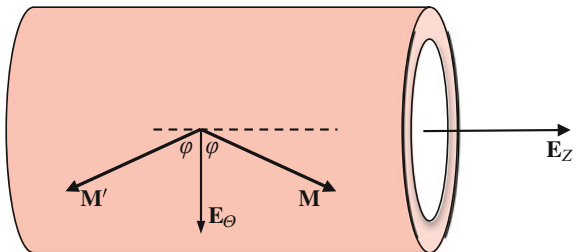
where A and $B > A$ are the inner and outer radii of the tube and L is its length. We consider that the unit tangents to the two families of continuously distributed fibers are given by

$$\mathbf{M} = \cos \varphi \mathbf{E}_\Theta + \sin \varphi \mathbf{E}_Z, \quad \mathbf{M}' = \cos \varphi \mathbf{E}_\Theta - \sin \varphi \mathbf{E}_Z, \quad (120)$$

locally with respect to unit basis vectors \mathbf{E}_Θ and \mathbf{E}_Z , as shown in Fig. 11, and symmetric with respect to the tube axis. In general we may take φ to depend on R , but in order to maintain radial symmetry we assume that it is independent of Θ and Z .

A particular significance of the prior consideration of the biaxial deformation in Sect. 4 is that locally (at each radius R) the deformation of the tube is biaxial and several of the formulas in Sect. 4.1 carry over to the present situation. Indeed, if the plane sheet shown in Fig. 8a is folded to form a cylinder then the straight lines (fiber directions) in the sheet become helices in the thin-walled cylinder so formed. The difference is that here the tube has a finite thickness and there is dependence on R .

Fig. 11 Unit vectors \mathbf{M} and \mathbf{M}' lying in the (Θ, Z) plane at radial distance R from the tube axis in the reference configuration and locally tangent to the two helically arranged families of fibers



It is generally considered that the material of artery walls is incompressible, and we therefore adopt the incompressibility assumption. Then, subject to the circular cylindrical shape being maintained during deformation (which requires the application of an appropriate internal pressure and axial load), the deformation of the tube can be described by the equations

$$r^2 = a^2 + \lambda_z^{-1}(R^2 - A^2), \quad \theta = \Theta, \quad z = \lambda_z Z, \quad (121)$$

where r, θ, z are cylindrical polar coordinates in the deformed configuration, λ_z is the constant (independent of R) axial stretch of the tube and a is its internal radius in the deformed configuration. The external deformed radius, denoted b , is given by

$$b^2 = a^2 + \lambda_z^{-1}(B^2 - A^2). \quad (122)$$

An advantage of the deformation defined in (121) is that, as is the case for homogeneous biaxial deformation, the principal axes of deformation do not rotate, which means that the radial, azimuthal, and axial directions are principal directions of the deformation. We denote by $\lambda_r, \lambda_\theta, \lambda_z$ the corresponding principal stretches, the first two of which are given by

$$\lambda_r = \lambda^{-1}\lambda_z^{-1}, \quad \lambda_\theta = \frac{r}{R}, \quad (123)$$

λ_r having been obtained from the incompressibility constraint, written here as

$$\lambda_r \lambda_\theta \lambda_z = 1. \quad (124)$$

We now adopt the notations

$$\lambda_a = a/A, \quad \lambda_b = b/B \quad (125)$$

for the values of λ_θ at $r = a$ and $r = b$, respectively, and we note that by expressing (121)₁ in terms of λ_θ we obtain

$$\lambda_a^2 \lambda_z - 1 = \frac{R^2}{A^2} (\lambda_\theta^2 \lambda_z - 1) = \frac{B^2}{A^2} (\lambda_b^2 \lambda_z - 1). \quad (126)$$

One implication of these connections is that the sign of $\lambda_\theta^2 \lambda_z - 1$ is independent of R , and, in particular, if $\lambda_\theta^2 \lambda_z - 1 = 0$ at one radius then this holds for all $R \in [A, B]$, so that λ_θ is independent of R and the deformation is homogeneous.

5.2 Stresses and Loads

Circular symmetry is maintained during the considered deformation, and because the two fiber families are symmetrically disposed and have the same elastic properties the (Cauchy) stresses required to maintain the deformation are the normal stresses in the r, θ, z directions, which we denote by $\sigma_{rr}, \sigma_{\theta\theta}$ and σ_{zz} . These are principal stresses, similarly to the situation for the homogeneous biaxial deformation discussed in Sect. 4.1. This means that the elastic response is orthotropic and the axes of orthotropy coincide with the cylindrical polar axes locally. For each radius R the considered deformation has the form of a pure homogeneous strain and hence the strain-energy function can be written as $\tilde{W}(\lambda_\theta, \lambda_z, \varphi)$, as in (110), except that λ_1 and λ_2 are replaced by λ_θ and λ_z , respectively.

Thus, similarly to (111), the principal stress differences take the forms

$$\sigma_{\theta\theta} - \sigma_{rr} = \lambda_\theta \frac{\partial \tilde{W}}{\partial \lambda_\theta}, \quad \sigma_{zz} - \sigma_{rr} = \lambda_z \frac{\partial \tilde{W}}{\partial \lambda_z}, \quad (127)$$

with the indices 1, 2, 3 corresponding to θ, z, r , respectively, and we emphasize that in general $\tilde{W}(\lambda_\theta, \lambda_z, \varphi) \neq \tilde{W}(\lambda_z, \lambda_\theta, \varphi)$.

The required invariants are

$$I_1 = \lambda_\theta^2 + \lambda_z^2 + \lambda_\theta^{-2} \lambda_z^{-2}, \quad I_2 = \lambda_\theta^{-2} + \lambda_z^{-2} + \lambda_\theta^2 \lambda_z^2, \quad (128)$$

$$I_4 = I_6 = \lambda_\theta^2 \cos^2 \varphi + \lambda_z^2 \sin^2 \varphi, \quad I_5 = I_7 = \lambda_\theta^4 \cos^2 \varphi + \lambda_z^4 \sin^2 \varphi, \quad (129)$$

$$I_8 = \lambda_\theta^2 \cos^2 \varphi - \lambda_z^2 \sin^2 \varphi, \quad (130)$$

which, with the identifications $\lambda_1 \leftrightarrow \lambda_\theta$ and $\lambda_2 \leftrightarrow \lambda_z$, can be seen to be the same as (103)–(105). In general, λ_θ depends on R so all the invariants also depend on R , as do the stress components $\sigma_{rr}, \sigma_{\theta\theta}$ and σ_{zz} .

We now apply the equilibrium equation (20) with body force $\mathbf{b} = \mathbf{0}$, which, by virtue of the radial symmetry (no dependence on θ or z), reduces to the radial equation

$$\frac{d\sigma_{rr}}{dr} + \frac{1}{r} (\sigma_{rr} - \sigma_{\theta\theta}) = 0. \quad (131)$$

Integration of this equation requires boundary conditions on the interior and exterior boundaries $r = a$ and $r = b$, and we assume that there is an internal pressure P (≥ 0) on $r = a$ but no traction on $r = b$. Thus, we set

$$\sigma_{rr} = \begin{cases} -P & \text{on } r = a \\ 0 & \text{on } r = b. \end{cases} \quad (132)$$

In order to maintain the deformation axial loads on the ends of the tube are needed in addition to the pressure P on $r = a$. At any cross section of the tube the resultant axial load, which is independent of z , is denoted N and given by

$$N = 2\pi \int_a^b \sigma_{zz} r dr. \quad (133)$$

On integration of (131) and use of (127)₁ and the boundary condition (132)₂ we obtain

$$\sigma_{rr} = - \int_r^b \lambda_\theta \frac{\partial \tilde{W}}{\partial \lambda_\theta} \frac{dr}{r}, \quad (134)$$

and then, on application of the boundary condition (132)₁, it follows that

$$P = \int_a^b \lambda_\theta \frac{\partial \tilde{W}}{\partial \lambda_\theta} \frac{dr}{r}. \quad (135)$$

For given A and B , noting that from (122) b depends on a and λ_z , Eq.(135) yields an expression for the P that is required to achieve the deformed internal radius a for any given λ_z .

On use of the expressions in (127) and the equilibrium equation (131) it is straightforward to show that N can be recast in the form

$$N = \pi \int_a^b \left(2\lambda_z \frac{\partial \tilde{W}}{\partial \lambda_z} - \lambda_\theta \frac{\partial \tilde{W}}{\partial \lambda_\theta} \right) r dr + \pi \int_a^b \frac{d}{dr}(r^2 \sigma_{rr}) dr. \quad (136)$$

Integration of the latter term and application of the boundary conditions (132) leads to

$$N = \pi \int_a^b \left(2\lambda_z \frac{\partial \tilde{W}}{\partial \lambda_z} - \lambda_\theta \frac{\partial \tilde{W}}{\partial \lambda_\theta} \right) r dr + \pi a^2 P. \quad (137)$$

Thus, N consists of two parts: the load that is applied on the ends between $r = a$ and $r = b$ and the contribution $\pi a^2 P$ of the pressure on the end area πa^2 of a tube with closed ends. The difference $N - \pi a^2 P$, which is the integral expression here, is known as the *reduced axial load*, and for this we adopt the notation $F = N - \pi a^2 P$.

5.2.1 Inclusion of Residual Stress

If residual stresses are included in the tube then some of the formulas in the previous section are essentially unchanged, as we now show. An axial residual stress is not compatible with the tube being circular cylindrical and a deformation independent of Θ and Z , so we restrict attention to radial and circumferential residual stresses, which we denote by τ_{RR} and $\tau_{\Theta\Theta}$. They satisfy the radial equation of equilibrium

$$\frac{d\tau_{RR}}{dR} + \frac{1}{R}(\tau_{RR} - \tau_{\Theta\Theta}) = 0, \quad (138)$$

which is associated with the boundary conditions

$$\tau_{RR} = 0 \quad \text{on } R = A \text{ and } B, \quad (139)$$

these being the specializations of (24) and (25), respectively, to the present geometry.

The invariants $I_1, I_2, I_4, I_5, I_6, I_7, I_8$ are again given by (128)–(130), the invariants K_4 in (79) reduce to just $\tau_{RR} + \tau_{\Theta\Theta}$ and $\tau_{RR}\tau_{\Theta\Theta}$, and

$$K_5 = \lambda_\theta^{-2}\lambda_z^{-2}\tau_{RR} + \lambda_\theta^2\tau_{\Theta\Theta}, \quad K_6 = \lambda_\theta^{-4}\lambda_z^{-4}\tau_{RR} + \lambda_\theta^4\tau_{\Theta\Theta}, \quad (140)$$

$$K_7 = \lambda_\theta^{-2}\lambda_z^{-2}\tau_{RR}^2 + \lambda_\theta^2\tau_{\Theta\Theta}^2, \quad K_8 = \lambda_\theta^{-4}\lambda_z^{-4}\tau_{RR}^2 + \lambda_\theta^4\tau_{\Theta\Theta}^2. \quad (141)$$

The strain-energy function can then be written in the form

$$\tilde{W}(\lambda_\theta, \lambda_z, \varphi, \tau_{RR} + \tau_{\Theta\Theta}, \tau_{RR}\tau_{\Theta\Theta}), \quad (142)$$

which is as in Sect. 5.2 except that $\tau_{RR} + \tau_{\Theta\Theta}$ and $\tau_{RR}\tau_{\Theta\Theta}$ are now included. With this change accounted for, the formulas for the Cauchy stress differences have exactly the same form as in (127), and likewise the formulas for P and N are given by (135) and (137). Only the content of \tilde{W} is different.

5.2.2 The Thin-Walled Approximation

As a first approximation arteries can be considered to be thin-walled tubes, which can be treated on the basis of membrane theory. Membranes do not support through-thickness stresses and, in particular, this means that $\sigma_{rr} = 0$ and there can be no residual stress. However, the membrane approximation does allow us to obtain (for general \tilde{W}) simple expressions for the pressure and axial load that do not involve integrals. The analysis is as follows. Introduce the small parameter $\varepsilon = (B - A)/A$, so the reference wall thickness $B - A$ is small compared with the inner radius A , and linearize (122) in ε to obtain, using the definitions $\lambda_a = a/A$, $\lambda_b = b/B$, the approximation

$$\lambda_b = \lambda_a - \varepsilon\lambda_a^{-1}\lambda_z^{-1}(\lambda^2\lambda_z - 1), \quad (143)$$

where, to first order in ε, λ , the membrane azimuthal stretch, can be chosen to be in $[\lambda_b, \lambda_a]$.

To the first order in ε , on application of the mean value theorem to Eq.(135) and use of (143), we obtain an approximation for P , namely

$$P = \varepsilon \lambda^{-1} \lambda_z^{-1} \frac{\partial \tilde{W}}{\partial \lambda}(\lambda, \lambda_z, \varphi). \quad (144)$$

Similarly, an approximation for the reduced axial load can be obtained from (137), which yields

$$F = \varepsilon \pi A^2 \lambda_z^{-1} \left[2\lambda_z \frac{\partial \tilde{W}}{\partial \lambda_z}(\lambda, \lambda_z, \varphi) - \lambda \frac{\partial \tilde{W}}{\partial \lambda}(\lambda, \lambda_z, \varphi) \right]. \quad (145)$$

Results for P and F in the case of a thick-walled tube will be illustrated in the following with and without residual stress, and also for the membrane approximation. In each case the results will be based on model constitutive equations, i.e., on special choices of \tilde{W} , which we discuss in the following section.

5.3 Constitutive Laws

We now illustrate the preceding theory by considering specific material models. In Sect. 5.3.1 we consider a strain-energy function for a fibrous material without residual stress, while in Sect. 5.3.2 we extend this to account for residual stress. This is followed by an illustration in which residual stresses and fiber reinforcement are combined.

5.3.1 Fiber Model

The fiber model is of the form (112) with (113) and (114). Thus, $\tilde{W}(\lambda_\theta, \lambda_z, \varphi)$ is given by

$$\begin{aligned} \tilde{W}(\lambda_\theta, \lambda_z, \varphi) &= \frac{1}{2} \mu (\lambda_\theta^2 + \lambda_z^2 + \lambda_\theta^{-2} \lambda_z^{-2} - 3) \\ &\quad + \frac{k_1}{k_2} \{ \exp[k_2(\lambda_\theta^2 \cos^2 \varphi + \lambda_z^2 \sin^2 \varphi - 1)^2] - 1 \}, \end{aligned} \quad (146)$$

and hence

$$\begin{aligned} \lambda_\theta \frac{\partial \tilde{W}}{\partial \lambda_\theta} &= \mu(\lambda_\theta^2 - \lambda_\theta^{-2}\lambda_z^{-2}) + 4k_1(\lambda_\theta^2 \cos^2 \varphi + \lambda_z^2 \sin^2 \varphi - 1)\lambda_\theta^2 \cos^2 \varphi \\ &\times \exp[k_2(\lambda_\theta^2 \cos^2 \varphi + \lambda_z^2 \sin^2 \varphi - 1)^2], \end{aligned} \quad (147)$$

and

$$\begin{aligned} \lambda_z \frac{\partial \tilde{W}}{\partial \lambda_z} &= \mu(\lambda_z^2 - \lambda_\theta^{-2}\lambda_z^{-2}) + 4k_1(\lambda_\theta^2 \cos^2 \varphi + \lambda_z^2 \sin^2 \varphi - 1)\lambda_z^2 \sin^2 \varphi \\ &\times \exp[k_2(\lambda_\theta^2 \cos^2 \varphi + \lambda_z^2 \sin^2 \varphi - 1)^2]. \end{aligned} \quad (148)$$

This is applied first for a membrane tube and then for a thick-walled tube. In Fig. 12a, with $\lambda_z = 1$, the dimensionless pressure $P^* = P/\mu\varepsilon$ is plotted against λ for the model with four values of the fiber angle φ and for representative values of the material constants. Results for $\lambda_z > 1$ are qualitatively similar to those for $\lambda_z = 1$ and are not therefore plotted separately. For $\lambda_z < 1$, in the absence of internal pressure, the tube becomes unstable and this case is not therefore considered here. Figure 12a illustrates the strong dependence on fiber orientation. In particular, as the fibers approach the circumferential direction (decreasing φ) the pressure required to reach a given circumferential stretch increases, i.e., the fibers have a stronger restraining effect on inflation. In Fig. 12b the corresponding plots for a thick-walled tube are shown for comparison, with $\eta = 1.4$ and the same values of the material constants and for representative fiber angles. Qualitatively, these are very similar, but, of course, larger pressures are required to achieve the same level of inflation as for a membrane tube, although the dimensionless pressure is lower because of the different scaling used. The pressure curves exhibit qualitatively the typical response of artery walls. Note that the character of the curves in Fig. 12 is very similar to that evident for $\bar{\sigma}_{11}$ shown in Fig. 9 for the homogeneous deformation of a sheet.

For the thin-walled tube, the corresponding reduced axial load F is plotted against λ in Fig. 13a in the dimensionless form $F^* = F/(\pi A^2 \mu\varepsilon)$, also for $\lambda_z = 1$ and four values of the fiber angle φ . For the larger values of φ , i.e., for fibers closer to the axial direction than the circumferential direction, there is initially, as λ increases from 1 under pressure, a tendency for the pressure to shorten the tube and an increasing positive (tensile) value of F is required in order to maintain $\lambda_z = 1$. Then, as inflation continues, F reaches a maximum and then becomes negative, so the trend is reversed and the tube would elongate in the absence of the axial load. When the fibers are aligned closer to the circumferential direction, on the other hand, F becomes negative as soon as inflation begins and then decreases rapidly. Such ‘switching’ in response has been noted previously, both for isotropic materials (Haughton and Ogden 1979) and for a Fung-type model (Holzapfel and Gasser 2001). Some corresponding plots for a thick-walled tube are also shown in Fig. 13b for comparison. These are broadly similar.

Clearly, the membrane approximation gives a good qualitative picture of the pressure and axial load versus stretch behavior. However, the membrane approximation cannot account for the through-thickness stress distribution in artery walls and is

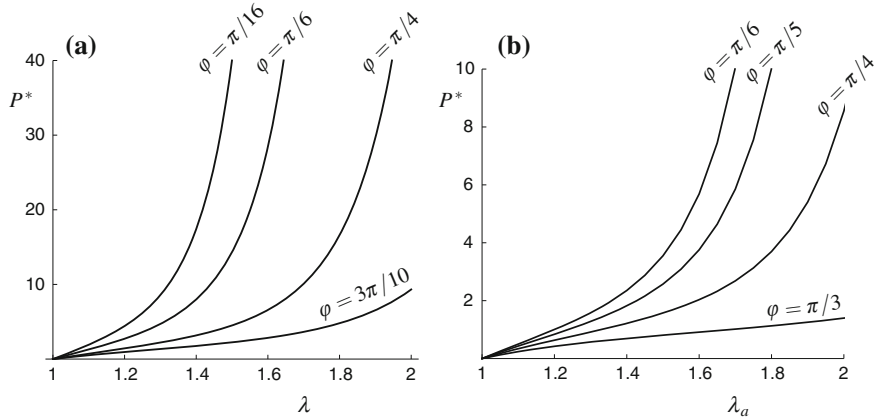


Fig. 12 **a** Plots of the dimensionless pressure $P^* = P/\mu\varepsilon$ versus the azimuthal stretch λ for the membrane approximate Eq. (144) for the strain-energy function given by (146) with $k_1/\mu = 1$, $k_2 = 1$ and $\varphi = \pi/16, \pi/6, \pi/4, 3\pi/10$. **b** Plots of $P^* = P/[\mu(\eta - 1)]$ versus the stretch λ_a , where $\eta = B/A = 1.4$ for a thick-walled tube based on Eq. (135), the same strain-energy function and material parameters and $\varphi = \pi/6, \pi/5, \pi/4, \pi/3$

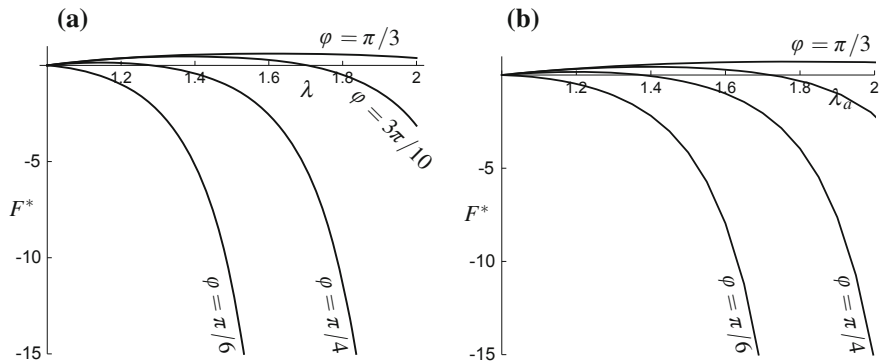


Fig. 13 **a** Plots of the dimensionless reduced axial load $F^* = F/(\pi A^2 \mu\varepsilon)$ versus the azimuthal stretch λ based on Eq. (145) with $k_1/\mu = 1$, $k_2 = 1$ and the values $\varphi = \pi/3, 3\pi/10, \pi/4, \pi/6$. **b** Plots of $F^* = (N - \pi a^2 P)/[\pi A^2 \mu(\eta - 1)]$ versus λ_a for the thick-walled case based on Eq. (137) with $\eta = 1.4$ and for the same values of the material constants, and $\varphi = \pi/3, \pi/4, \pi/6$

not able to support the residual stresses that have an important influence on the mechanical response of arteries. See, for example, the papers by Holzapfel et al. (2000), Ogden and Schulze-Bauer (2000) and Ogden (2003b) and references therein for detailed discussion of these features. In the following, therefore, we consider a thick-walled tube with residual stress.

5.3.2 Residual Stress Model

In order to illustrate the influence of residual stress on the material response we now specialize both the form of the residual stress and the strain-energy function. First, we choose a simple form of τ_{RR} satisfying the boundary conditions (139) and then use (138) to determine $\tau_{\Theta\Theta}$. Specifically, we take

$$\tau_{RR} = \alpha(R - A)(R - B), \quad (149)$$

where $\alpha (>0)$ is a constant, and obtain

$$\tau_{\Theta\Theta} = \alpha[3R^2 - 2(A + B)R + AB]. \quad (150)$$

Plots of τ_{RR} and $\tau_{\Theta\Theta}$ are shown in Fig. 14 for $\alpha = 1$. Since dependence on α is linear, curves for other values are obtained by appropriate scaling.

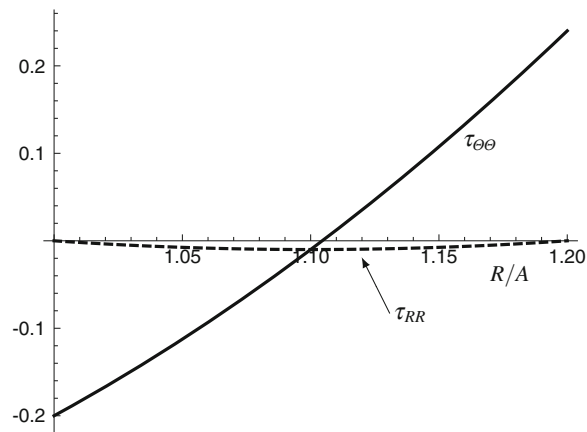
The characteristics of τ_{RR} and $\tau_{\Theta\Theta}$ shown in Fig. 14 are very similar to those obtained for a single layer from the so-called ‘opening angle’ method (Ogden 2003b) or from the assumption that the circumferential stress at a typical physiological pressure is uniform (Ogden and Schulze-Bauer 2000).

Recalling the constitutive law of a residually stressed material discussed in Sect. 3.4.2, we now specialize the strain-energy function to include the influence of residual stress with dependence only on the invariants K_1 , K_4 and K_5 and without dependence on fibers. Then $W = W(K_1, K_4, K_5)$ and from (87) the expression for the Cauchy stress reduces to

$$\sigma = 2W_1\mathbf{B} + 2W_5\boldsymbol{\Sigma} - p\mathbf{I}, \quad (151)$$

and the restrictions (91) reduce to

Fig. 14 Residual stresses τ_{RR} (dashed curve) and $\tau_{\Theta\Theta}$ (continuous curve) plotted for $\alpha = 1$ based on Eqs. (149) and (150) as functions of R/A for $B/A = 1.2$, a typical value for artery walls



$$2W_1 - p^{(r)} = 0, \quad 2W_5 = 1 \quad (152)$$

in \mathcal{B}_r . Consistently with (152) we now consider the prototype model strain-energy function given by

$$W = \frac{1}{2}\mu(K_1 - 3) + \frac{1}{2}(K_5 - \text{tr } \tau), \quad (153)$$

so that $W = 0$ in \mathcal{B}_r and (152) is satisfied with $p^{(r)} = \mu$, where $\mu (>0)$ is a constant.

For the considered problem the strain-energy function (142), on omission of φ , becomes

$$\begin{aligned} \tilde{W}(\lambda_\theta, \lambda_z, \tau_{RR}, \tau_{\Theta\Theta}) &= \frac{1}{2}\mu(\lambda_\theta^2 + \lambda_z^2 + \lambda_\theta^{-2}\lambda_z^{-2} - 3) \\ &\quad + \frac{1}{2}[\lambda_\theta^{-2}\lambda_z^{-2}\tau_{RR} + \lambda_\theta^2\tau_{\Theta\Theta} - (\tau_{RR} + \tau_{\Theta\Theta})], \end{aligned} \quad (154)$$

and the stress differences (127) specialize to

$$\sigma_{\theta\theta} - \sigma_{rr} = \lambda_\theta \frac{\partial \tilde{W}}{\partial \lambda_\theta} = \mu(\lambda_\theta^2 - \lambda_\theta^{-2}\lambda_z^{-2}) + \lambda_\theta^2\tau_{\Theta\Theta} - \lambda_\theta^{-2}\lambda_z^{-2}\tau_{RR}, \quad (155)$$

and

$$\sigma_{zz} - \sigma_{rr} = \lambda_z \frac{\partial \tilde{W}}{\partial \lambda_z} = \mu(\lambda_z^2 - \lambda_\theta^{-2}\lambda_z^{-2}) - \lambda_\theta^{-2}\lambda_z^{-2}\tau_{RR}. \quad (156)$$

The next step is to evaluate the integrals in the expressions for the pressure P and the reduced axial load $F = N - \pi a^2 P$ from the integrals in (135) and (137). This requires the expressions

$$\begin{aligned} \lambda_\theta \frac{\partial \tilde{W}}{\partial \lambda_\theta} &= (\mu + \alpha AB)(\lambda_\theta^2 - \lambda_\theta^{-2}\lambda_z^{-2}) - \alpha(A + B)R(2\lambda_\theta^2 - \lambda_\theta^{-2}\lambda_z^{-2}) \\ &\quad + \alpha R^2(3\lambda_\theta^2 - \lambda_\theta^{-2}\lambda_z^{-2}), \end{aligned} \quad (157)$$

$$\begin{aligned} 2\lambda_z \frac{\partial \tilde{W}}{\partial \lambda_z} - \lambda_\theta \frac{\partial \tilde{W}}{\partial \lambda_\theta} &= 2\mu\lambda_z^2 - (\mu + \alpha AB)(\lambda_\theta^2 + \lambda_\theta^{-2}\lambda_z^{-2}) \\ &\quad + \alpha(A + B)R(2\lambda_\theta^2 + \lambda_\theta^{-2}\lambda_z^{-2}) - \alpha R^2(3\lambda_\theta^2 + \lambda_\theta^{-2}\lambda_z^{-2}), \end{aligned} \quad (158)$$

which are obtained by substituting for the expressions (149) and (150) into (155) and (156).

The integrals are evaluated, with the help of the definition $\lambda_\theta = r/R$, using the radial part (121)₁ of the deformation in the form $r^2 - \lambda_z^{-1/2} R^2 = c$, where the notation $c = a^2 - \lambda_z^{-1} A^2 = b^2 - \lambda_z^{-1} B^2$ has been introduced for brevity. The resulting expressions for P and F , after some manipulation, are obtained as

$$\begin{aligned} P &= (\mu + \alpha AB) \lambda_z^{-1} \log \left(\frac{aB}{Ab} \right) + \frac{1}{2} \mu c \lambda_z^{-2} \frac{B^2 - A^2}{a^2 b^2} + 2\alpha c \log \left(\frac{b}{a} \right) \\ &\quad - \frac{3}{2} \alpha \sqrt{c} (A + B) \lambda_z^{-1/2} \left[\tan^{-1} \left(\frac{\lambda_z^{1/2} \sqrt{c}}{A} \right) - \tan^{-1} \left(\frac{\lambda_z^{1/2} \sqrt{c}}{B} \right) \right] \end{aligned} \quad (159)$$

and

$$\begin{aligned} F &= \pi \mu (B^2 - A^2) (\lambda_z - \lambda_z^{-2}) + \pi c \left\{ (\mu + \alpha AB) \lambda_z^{-1} \log \left(\frac{bA}{aB} \right) - \alpha c \log \left(\frac{b}{a} \right) \right. \\ &\quad \left. + \alpha \sqrt{c} (A + B) \lambda_z^{-1/2} \left[\tan^{-1} \left(\frac{B}{\lambda_z^{1/2} \sqrt{c}} \right) - \tan^{-1} \left(\frac{A}{\lambda_z^{1/2} \sqrt{c}} \right) \right] \right\}. \end{aligned} \quad (160)$$

In the case $\lambda_z = 1$ these formulas were given in Ogden (2015).

For numerical purposes we now nondimensionalize all the quantities in the above two equations but restricted to the case $\lambda_z = 1$.

First, we set $P^* = P/\mu$ and $F^* = F/(\pi A^2 \mu)$, which are different from the nondimensionalizations used for the membrane model in Sect. 5.2.2. We also introduce the notations

$$\eta = \frac{B}{A}, \quad \alpha^* = \frac{\alpha A^2}{\mu}, \quad (161)$$

and, as a measure of the radial inflation,

$$e = \frac{\sqrt{c}}{A} \equiv \sqrt{\lambda_a^2 - 1}. \quad (162)$$

The connections

$$\frac{b^2}{a^2} = \frac{\eta^2 + e^2}{1 + e^2}, \quad \lambda_b^2 = 1 + \eta^{-2} e^2 \quad (163)$$

then follow and hence P^* and F^* can be written

$$\begin{aligned} P^* &= \frac{1}{2} (1 + \alpha^* \eta) \log \left[\frac{(1 + e^2) \eta^2}{\eta^2 + e^2} \right] + \alpha^* e^2 \log \left(\frac{\eta^2 + e^2}{1 + e^2} \right) \\ &\quad + \frac{1}{2} \frac{(\eta^2 - 1) e^2}{(\eta^2 + e^2)(1 + e^2)} - \frac{3}{2} \alpha^* (1 + \eta) e \tan^{-1} \left[\frac{(\eta - 1)e}{\eta + e^2} \right], \end{aligned} \quad (164)$$

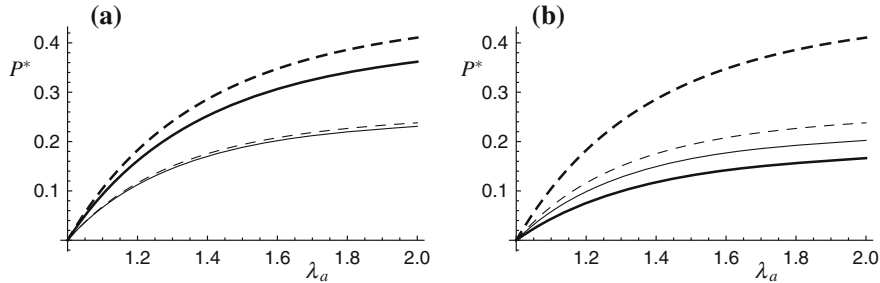


Fig. 15 Plots of $P^* = P/\mu$ versus λ_a based on Eq. (164) for **a** $\alpha^* = 2$ and **b** $\alpha^* = 10$ with $\eta = 1.3, 1.6$ in each case (*continuous curves*)—thin for $\eta = 1.3$ and thick for $\eta = 1.6$. Also shown are the corresponding curves without residual stress ($\alpha^* = 0$ —*dashed* for $\eta = 1.3$, *thick dashed* for $\eta = 1.6$)

$$\begin{aligned} F^* = & -\frac{1}{2}(1 + \alpha^*\eta)e^2 \log \left[\frac{(1 + e^2)\eta^2}{\eta^2 + e^2} \right] - \frac{1}{2}\alpha^*e^4 \log \left(\frac{\eta^2 + e^2}{1 + e^2} \right) \\ & + \alpha^*(1 + \eta)e^3 \tan^{-1} \left[\frac{(\eta - 1)e}{\eta + e^2} \right]. \end{aligned} \quad (165)$$

Illustrative plots of P^* versus λ_a are shown in Fig. 15a, b for a residual stress with $\alpha^* = 2$ and $\alpha^* = 10$, respectively, and compared with corresponding plots without residual stress. In each case we choose $\eta = 1.3$ and $\eta = 1.6$. For thin-walled tubes with η between 1 and about 1.2 the effect of residual stress is small. For larger values of η and α^* it becomes more significant. Note that for larger α^* and/or larger values of η the negative value of the final term in (164) becomes significant and causes a reduction in the pressure. In particular, by comparing Fig. 15a, b we see that the pressure is larger for $\eta = 1.6$ than for $\eta = 1.3$ in Fig. 15a but the reverse is true in Fig. 15b. The effect of residual stress is to reduce the pressure required to achieve a given level of inflation compared with the case without residual stress. Moreover, if the residual stress has a very large magnitude the pressure becomes negative, which is unrealistic. Note: there is a typo in the sign of the final term in the corresponding expressions for P and P^* in Ogden (2015).

Plots of F^* are illustrated in Fig. 16a, b for $\alpha^* = 2$ and $\alpha^* = 10$, respectively, and compared with corresponding results without residual stress. The character of F^* changes because of the competing effects of the positive and negative terms in (165). As Fig. 16a shows, for $\alpha^* = 2$, F^* is negative for the considered values of η and increases in magnitude as η increases (only curves for $\eta = 1.3$ and $\eta = 1.6$ are shown). In this case F^* is slightly less negative than in the absence of residual stress. The tube has a tendency to elongate under pressure. But for larger α^* , F^* turns from negative to positive for the thicker walled tubes, exemplified by $\eta = 2$ in Fig. 16b, in which case the tube has a tendency to shorten under pressure.

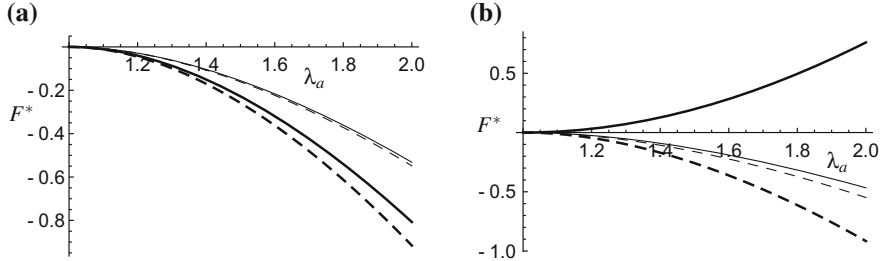


Fig. 16 Plots of $F^* = F/(\pi A^2 \mu)$ versus λ_a based on Eq. (165) for **a** $\alpha^* = 2$ with $\eta = 1.3, 1.6$ (continuous curves)—thin for $\eta = 1.3$ and thick for $\eta = 1.6$, and **b** $\alpha^* = 10$, with $\eta = 1.3, 2$ (continuous curves)—thin for $\eta = 1.3$ and thick for $\eta = 2$. Also shown are the corresponding curves without residual stress $\alpha^* = 0$: **a** dashed for $\eta = 1.3$, thick dashed for $\eta = 1.6$; **b** dashed for $\eta = 1.3$, thick dashed for $\eta = 2$

With both fibers and residual stress included in the strain-energy function we combine (146) and (154) to obtain

$$\begin{aligned} \tilde{W}(\lambda_\theta, \lambda_z, \varphi, \tau_{RR}, \tau_{\Theta\Theta}) &= \frac{1}{2}\mu(\lambda_\theta^2 + \lambda_z^2 + \lambda_\theta^{-2}\lambda_z^{-2} - 3) \\ &+ \frac{k_1}{k_2}\{\exp[k_2(\lambda_\theta^2 \cos^2 \varphi + \lambda_z^2 \sin^2 \varphi - 1)^2] - 1\} \\ &+ \frac{1}{2}[\lambda_\theta^{-2}\lambda_z^{-2}\tau_{RR} + \lambda_\theta^2\tau_{\Theta\Theta} - (\tau_{RR} + \tau_{\Theta\Theta})], \end{aligned} \quad (166)$$

and the associated

$$\begin{aligned} \lambda_\theta \frac{\partial \tilde{W}}{\partial \lambda_\theta} &= \mu(\lambda_\theta^2 - \lambda_\theta^{-2}\lambda_z^{-2}) + 4k_1(\lambda_\theta^2 \cos^2 \varphi + \lambda_z^2 \sin^2 \varphi - 1)\lambda_\theta^2 \cos^2 \varphi \\ &\times \exp[k_2(\lambda_\theta^2 \cos^2 \varphi + \lambda_z^2 \sin^2 \varphi - 1)^2] + \lambda_\theta^2\tau_{\Theta\Theta} - \lambda_\theta^{-2}\lambda_z^{-2}\tau_{RR}, \end{aligned} \quad (167)$$

$$\begin{aligned} \lambda_z \frac{\partial \tilde{W}}{\partial \lambda_z} &= \mu(\lambda_z^2 - \lambda_\theta^{-2}\lambda_z^{-2}) + 4k_1(\lambda_\theta^2 \cos^2 \varphi + \lambda_z^2 \sin^2 \varphi - 1)\lambda_z^2 \sin^2 \varphi \\ &\times \exp[k_2(\lambda_\theta^2 \cos^2 \varphi + \lambda_z^2 \sin^2 \varphi - 1)^2] - \lambda_\theta^{-2}\lambda_z^{-2}\tau_{RR}. \end{aligned} \quad (168)$$

Based on the general formulas (135) and (137) we now exemplify the characters of P^* and F^* . First, in Fig. 17, $P^* = P/[\mu(\eta - 1)]$ is plotted for the representative parameter values $\alpha^* = 2$, $\eta = 1.4$, $k_1/\mu = k_2 = 1$, and for four values of φ , as indicated in the figure caption. For comparison, curves are also shown for $\alpha^* = 0$ (no residual stress) in order to illustrate the effect of residual stress. The residual stress has a significant effect on P^* only for fiber directions relatively close to the axial direction, as illustrated for $\varphi = \pi/3$ in Fig. 17a, in which case the presence of residual stress requires a significantly larger value of P^* to achieve a given level

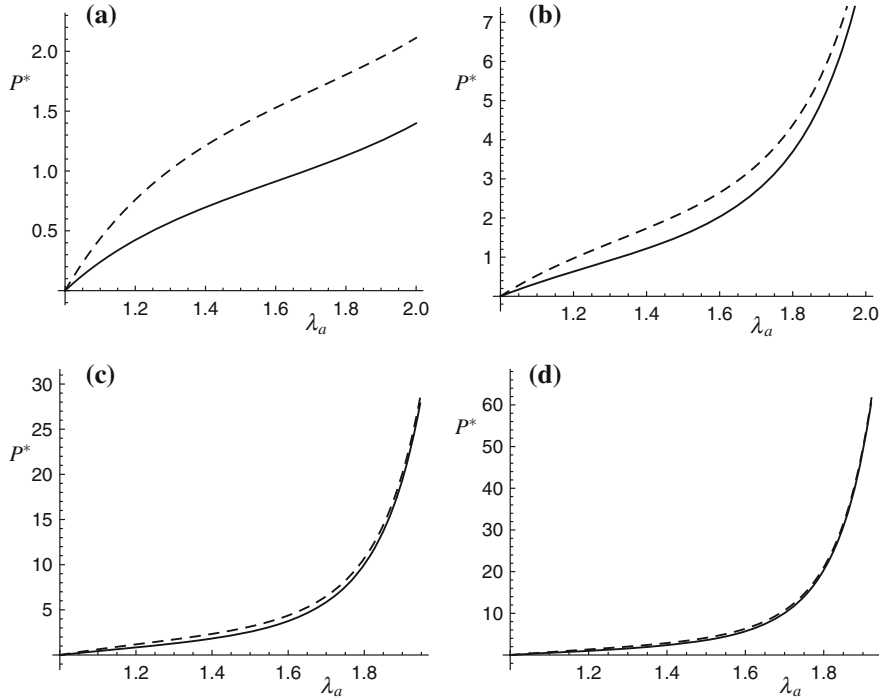


Fig. 17 Plots of $P^* = P/[\mu(\eta - 1)]$ versus λ_a based on (135) with (167) and parameters $\alpha^* = 2$, $\eta = 1.4$, $k_1/\mu = k_2 = 1$ for **a** $\varphi = \pi/3$, **b** $\varphi = \pi/4$, **c** $\varphi = \pi/5$, **d** $\varphi = \pi/6$ (dashed curves), and corresponding plots for $\alpha^* = 0$ (continuous curves)

of inflation than in the absence of residual stress. As the fiber direction approaches circumferential the residual stress has a smaller and smaller influence. The pattern is very similar for larger values of α^* and details are not therefore included here.

In Fig. 18a, b representative plots of $F^* = F/[\pi A^2 \mu(\eta - 1)]$ are shown for the same parameter values as for P^* . In Fig. 18c and d corresponding plots are shown for $\alpha^* = 20$ in order to illustrate that larger values of α^* have only a marginal effect on the character of the curves. In each case the curves are compared with those obtained in the absence of residual stress. For smaller values of φ there is only very little difference between the curves with and without residual stress, and as for P^* it is only for fiber directions close to axial that the residual stress has a significant effect. While the residual stress has the effect of increasing the value of P^* required to achieve a given inflation it reduces the magnitude of F^* .

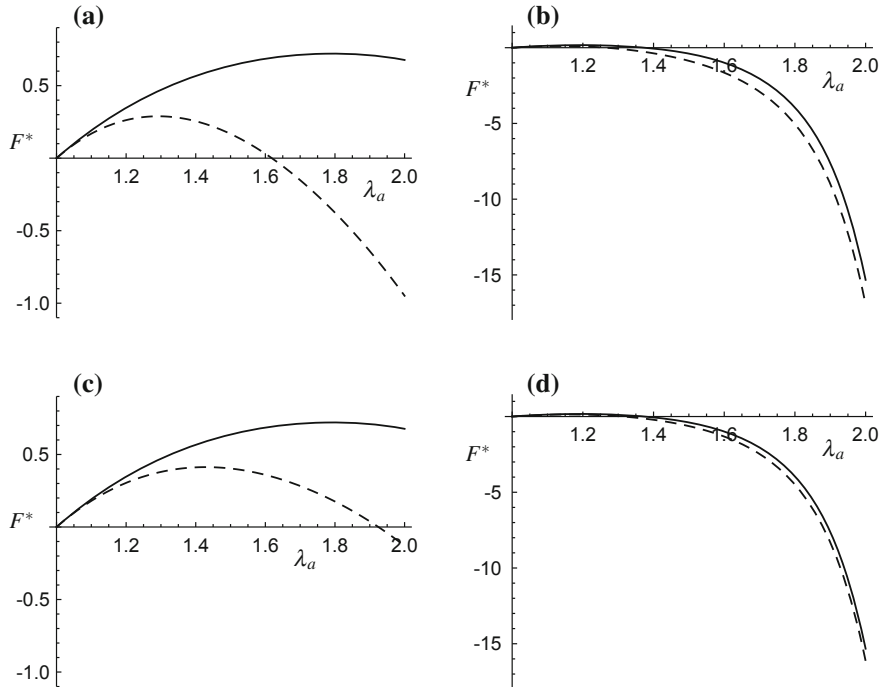


Fig. 18 Plots of $F^* = F/[\pi A^2 \mu(\eta - 1)]$ versus λ_a based on (137) with (167) and (168) and parameters $\eta = 1.4$, $k_1/\mu = k_2 = 1$ for **a** $\varphi = \pi/3$, **b** $\varphi = \pi/4$, with $\alpha^* = 2$, and **c** $\varphi = \pi/3$, **d** $\varphi = \pi/4$, with $\alpha^* = 20$ (dashed curves), and corresponding plots for $\alpha^* = 0$ (continuous curves)

6 The Effect of Fiber Dispersion

The model discussed in the preceding section assumes that all fibers within a given family are oriented in the same direction. This is patently not the case for actual arteries. There is dispersion in the orientations of collagen fibers within each family, as exemplified by histological data from human coronary and brain arteries obtained by Canham et al. (1989), Finlay et al. (1995, 1998). In particular, it was found that there is wider dispersion in the intimal and adventitial layers than in the medial layer. This is reflected in uniaxial test data obtained for the separate layers of aged human coronary arteries by Holzapfel et al. (2005). Mean data for such tests on strip specimens from the circumferential and axial directions of intimal, adventitial and medial layers are illustrated in Fig. 19. In the media, where the mean fiber direction is closer to the circumferential direction than the axial direction, the uniaxial response is stiffest in the circumferential direction, while for the intima and adventitia the reverse is the case.

The model discussed in Sect. 5.3.1 gives a good representation of the data for the media (and also for the intact, layer-unseparated artery, which behaves very similarly

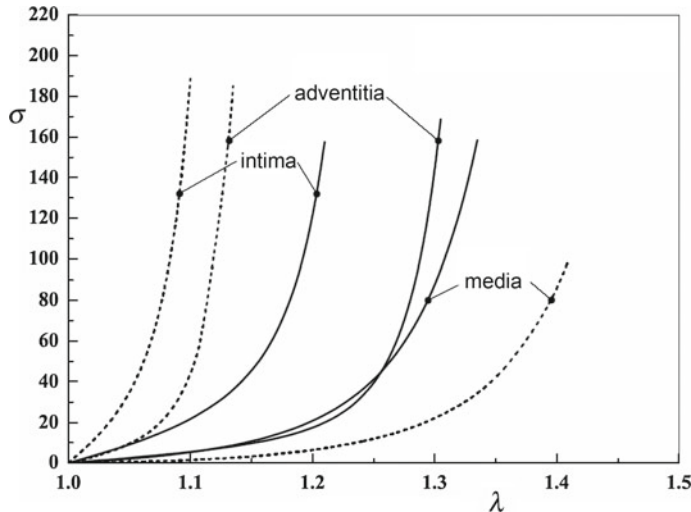


Fig. 19 Plots of the uniaxial Cauchy stress σ (kPa) versus the stretch λ based on mean data for intimal, medial, and adventitial strips from uniaxial tension experiments on aged human coronary arteries (Holzapfel et al. 2005). The tests were performed on strips from the circumferential direction (*continuous curves*) and axial direction (*dashed curves*). Based on Holzapfel et al. (2005), Fig. 7, with permission

to the media), but not of the data for the intima or adventitia. In Gasser et al. (2006) this difference was attributed to the greater level of dispersion in the latter two layers and led to the development of a model based on a so-called *generalized structure tensor*, which takes account of the dispersion and generalizes the model in Sect. 5.3.1. This is discussed in the following.

6.1 A Model of Fiber Dispersion in Three Dimensions

Consider a fiber dispersion with a general fiber direction \mathbf{N} within the dispersion referred to spherical polar angles Θ and Φ in the reference configuration, as depicted in Fig. 20 with respect to rectangular Cartesian basis vectors $\mathbf{e}_1, \mathbf{e}_2, \mathbf{e}_3$. Thus, we have

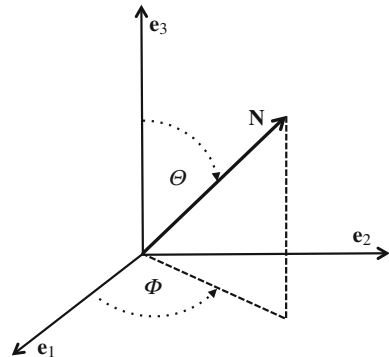
$$\mathbf{N}(\Theta, \Phi) = \sin \Theta \cos \Phi \mathbf{e}_1 + \sin \Theta \sin \Phi \mathbf{e}_2 + \cos \Theta \mathbf{e}_3, \quad (169)$$

where $\Theta \in [0, \pi]$ and $\Phi \in [0, 2\pi]$.

It is assumed that the fiber orientations in the reference configuration are distributed according to an *orientation density function* (or probability density function), which we denote by $\rho = \rho(\Theta, \Phi)$, and it is also assumed that this is unaffected by reversal of \mathbf{N} , so that $\rho(\pi - \Theta, \pi + \Phi) \equiv \rho(\Theta, \Phi)$.

The density is normalized according to

Fig. 20 Unit vector \mathbf{N} representing the orientation of a fiber within a dispersion in the reference configuration in terms of spherical polar angles Θ and Φ relative to background rectangular Cartesian axes $\mathbf{e}_1, \mathbf{e}_2, \mathbf{e}_3$



$$\frac{1}{4\pi} \int_{\Omega} \rho(\Theta, \Phi) d\Omega = 1, \quad (170)$$

where Ω is the unit sphere $\{(\Theta, \Phi) \mid \Theta \in [0, \pi], \Phi \in [0, 2\pi]\}$, and the proportion of fibers within the solid angle $d\Omega = \sin \Theta d\Theta d\Phi$ is $\rho(\Theta, \Phi)d\Omega$.

If there is no dispersion and all fibers in a family are aligned in the direction \mathbf{M} then the structure tensor $\mathbf{M} \otimes \mathbf{M}$ can be used to construct the invariants I_4 and I_5 , as in Sect. 3.3.2. This notion of a structure tensor is now generalized to form a *generalized structure tensor*, denoted \mathbf{H} , which is an average of $\mathbf{N} \otimes \mathbf{N}$ weighted by $\rho(\Theta, \Phi)$ over the unit sphere, i.e., it is defined by

$$\mathbf{H} = \frac{1}{4\pi} \int_{\Omega} \rho(\Theta, \Phi) \mathbf{N} \otimes \mathbf{N} d\Omega. \quad (171)$$

Clearly, \mathbf{H} is symmetric, and because \mathbf{N} is a unit vector it follows from (170) and (171) that

$$\text{tr } \mathbf{H} = 1. \quad (172)$$

Thus, in three dimensions \mathbf{H} has five independent components in general, and when the expression (171) is expanded using (169) the five components of \mathbf{H} with respect to the Cartesian basis $\mathbf{e}_1, \mathbf{e}_2, \mathbf{e}_3$ are

$$H_{11} = \frac{1}{4\pi} \int_{\Omega} \rho \sin^3 \Theta \cos^2 \Phi d\Theta d\Phi, \quad (173)$$

$$H_{22} = \frac{1}{4\pi} \int_{\Omega} \rho \sin^3 \Theta \sin^2 \Phi d\Theta d\Phi, \quad (174)$$

$$H_{12} = \frac{1}{4\pi} \int_{\Omega} \rho \sin^3 \Theta \sin \Phi \cos \Phi d\Theta d\Phi, \quad (175)$$

$$H_{23} = \frac{1}{4\pi} \int_{\Omega} \rho \sin^2 \Theta \cos \Theta \sin \Phi \cos \Phi d\Theta d\Phi, \quad (176)$$

$$H_{13} = \frac{1}{4\pi} \int_{\Omega} \rho \sin^2 \Theta \cos \Theta \cos \Phi d\Theta d\Phi, \quad (177)$$

with $H_{ij} = H_{ji}$, $i, j \in \{1, 2, 3\}$, and from (172) we also have $H_{33} = 1 - H_{11} - H_{22}$.

6.1.1 Fiber Dispersion with Rotational Symmetry

In Gasser et al. (2006) the focus was on the special case in which ρ is independent of ϕ , and we therefore omit the dependence of ϕ and write $\rho = \rho(\theta)$. Then, the fiber dispersion has rotational symmetry about the direction \mathbf{e}_3 , and the normalization condition (170) reduces to

$$\frac{1}{2} \int_0^\pi \rho(\theta) \sin \theta d\theta = 1. \quad (178)$$

This dispersion is sometimes referred to as a *transversely isotropic dispersion*, and in this case \mathbf{e}_3 is the mean fiber direction.

Now there is only one independent component of \mathbf{H} , and its components can be written compactly as

$$H_{11} = H_{22} = \kappa, \quad H_{33} = 1 - 2\kappa, \quad H_{ij} = 0, \quad i \neq j, \quad (179)$$

where κ , which is a measure of dispersion, is defined by

$$\kappa = \frac{1}{4} \int_0^\pi \rho(\theta) \sin^3 \theta d\theta. \quad (180)$$

This allows the tensor \mathbf{H} to be represented in the form

$$\mathbf{H} = \kappa \mathbf{I}_r + (1 - 3\kappa) \mathbf{M} \otimes \mathbf{M}, \quad (181)$$

where \mathbf{I}_r is again the identity tensor in \mathcal{B}_r and \mathbf{M} is a unit vector denoting the mean fiber direction, which, in terms of the considered Cartesian axes, is $\mathbf{M} = \mathbf{e}_3$. More generally, without specifying the axes, (181) represents a rotationally symmetric distribution about the mean direction \mathbf{M} .

In general κ must lie in the interval $[0, 1/2]$. The limiting value $\kappa = 0$ corresponds to the case where all fibers are aligned and there is no dispersion, in which case $\mathbf{H} = \mathbf{M} \otimes \mathbf{M}$ (ρ being a delta function). The intermediate value $\kappa = 1/3$ corresponds to an isotropic fiber dispersion, i.e., the fibers are dispersed uniformly in all directions in three dimensions, $\rho = 1$ and $\mathbf{H} = \mathbf{I}_r/3$. For the upper limit $\kappa = 1/2$ the fiber dispersion is isotropic in two dimensions in the plane normal to \mathbf{M} (and ρ is again a delta function). We note that in some circumstances values of κ in the range $(1/3, 1/2]$ lead to unphysical results, as pointed out in Holzapfel and Ogden (2010); see also Melnik et al. (2015).

Dispersion Represented as a von Mises Distribution

The fiber dispersion can be measured approximately by imaging histological samples and represented using a probability density function. In particular, it has been found reasonable to represent $\rho(\Theta)$ by a π -periodic von Mises distribution (Gasser et al. 2006; Holzapfel et al. 2015) based on the exponential function $\exp[\cos(2\Theta)]$. Here we write it in the form

$$\rho(\Theta) = 4 \sqrt{\frac{b}{2\pi}} \frac{\exp(2b \cos^2 \Theta)}{\operatorname{erfi}(\sqrt{2b})}, \quad (182)$$

which is symmetrical about $\Theta = 0$ and the constant factor is needed to satisfy the normalization (178), where erfi is the imaginary error function related to the standard error function erf by $\operatorname{erfi}(x) = -i\operatorname{erf}(ix)$, erf being defined by

$$\operatorname{erf}(x) = \frac{2}{\sqrt{\pi}} \int_0^x \exp(-u^2) du, \quad (183)$$

and b is the so-called *concentration parameter*. Plots of $\rho(\Theta)$ versus Θ are shown in Fig. 21 for several values of b , with larger values of b giving a more concentrated distribution about $\Theta = 0$, tending to a delta function as $b \rightarrow \infty$, in which case there is no dispersion. For ease of viewing $\rho(\Theta)$ is plotted for the range $\Theta \in [-\pi/2, \pi/2]$ instead of $[0, \pi]$.

The integral in (180) can be evaluated explicitly to give κ as a function of b in the form

$$\kappa = \frac{1}{2} + \frac{1}{8b} - \frac{1}{4} \sqrt{\frac{2}{\pi b}} \frac{\exp(2b)}{\operatorname{erfi}(\sqrt{2b})}, \quad (184)$$

and Fig. 22 provides a plot of this function. This shows, in particular, that $\kappa \rightarrow 0$ as $b \rightarrow \infty$ and the isotropic case corresponds to $b = 0$ and $\kappa = 1/3$.

Fig. 21 Plot of $\rho(\Theta)$ versus Θ for the von Mises distribution (182) for $b = 2, 5, 8$, the dashed, continuous and thick dashed curves, respectively

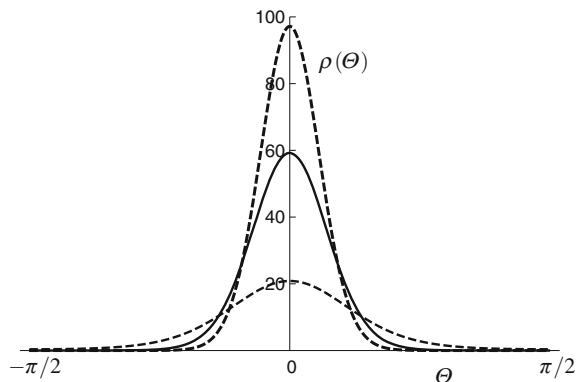
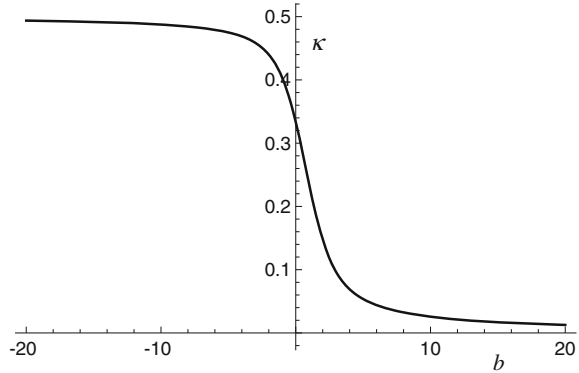


Fig. 22 Plot of the dispersion parameter κ as a function of the concentration parameter b based on the formula (184)



Generalized Invariants

Let us now recall the definition of the invariants I_4 and I_5 given in (54). These may equivalently be written as

$$I_4 = \text{tr}(\mathbf{CM} \otimes \mathbf{M}), \quad I_5 = \text{tr}(\mathbf{C}^2\mathbf{M} \otimes \mathbf{M}). \quad (185)$$

These motivate the introduction of *generalized invariants*, which we denote by I_4^* and I_5^* , based on the generalized structure tensor \mathbf{H} in (181). These are defined by

$$I_4^* = \text{tr}(\mathbf{CH}), \quad I_5^* = \text{tr}(\mathbf{C}^2\mathbf{H}), \quad (186)$$

and from (181) and (45) it follows that

$$I_4^* = \kappa I_1 + (1 - 3\kappa)I_4, \quad I_5^* = \kappa(I_1^2 - 2I_2) + (1 - 3\kappa)I_5, \quad (187)$$

in which we have used the definitions (185) with \mathbf{M} now being the mean fiber direction. Thus, for the considered rotationally symmetric fiber dispersion the generalized invariants I_4^* and I_5^* are combinations of isotropic and transversely isotropic invariants, weighted with respect to the dispersion parameter κ . Implicit in this consideration is that at a given point \mathbf{X} in \mathcal{B}_r the deformation gradient \mathbf{F} applies to each fiber in the dispersion at \mathbf{X} .

The generalized invariants do not, of course, capture complete information about the dispersion. Further information on the structure can be obtained by considering higher order structure tensors, an example of which is the fourth-order structure tensor \mathcal{H} with components given by

$$\mathcal{H}_{ijkl} = \frac{1}{4\pi} \int_0^\pi \rho(\Theta) \int_0^{2\pi} N_i N_j N_k N_l \sin \Theta d\Theta d\Phi, \quad (188)$$

which has complete i, j, k, l symmetry and satisfies (in the summation convention)

$$\mathcal{H}_{iijj} = 1, \quad \mathcal{H}_{11jj} = \mathcal{H}_{22jj} = \kappa, \quad \mathcal{H}_{33jj} = 1 - 2\kappa, \quad (189)$$

and also introduces an additional dispersion parameter, denoted κ_1 and defined by

$$\kappa_1 = \frac{1}{4} \int_0^\pi \rho(\Theta) \sin^5 \Theta d\Theta. \quad (190)$$

The only nonzero components of \mathcal{H} are

$$\mathcal{H}_{1111} = \mathcal{H}_{2222} = 3\mathcal{H}_{1122} = \frac{3}{4}\kappa_1, \quad \mathcal{H}_{1133} = \mathcal{H}_{2233} = \kappa - \kappa_1 \quad (191)$$

and

$$\mathcal{H}_{3333} = 1 - 4\kappa + 2\kappa_1. \quad (192)$$

Clearly, additional generalized invariants based on \mathcal{H} and involving κ_1 can be constructed; indeed, extension to higher order structure tensors would introduce yet more dispersion parameters. However, for our purposes it suffices to restrict attention to \mathbf{H} and its associated generalized invariants.

6.1.2 A Strain-Energy Function for a Rotationally Symmetric Dispersion

In Sect. 3.3.2, for an incompressible material with a single preferred direction \mathbf{M} , we considered the strain-energy function to depend on the invariants I_1, I_2, I_4, I_5 : $W(I_1, I_2, I_4, I_5)$. In view of the dependence noted in (187) this can be considered to remain the case when there is a rotationally symmetric fiber dispersion with the proviso concerning higher order generalized structure tensors mentioned above, except that \mathbf{M} in the definitions in (185) is now the mean fiber direction.

Thus, to account for the dispersion in the strain-energy function of an incompressible elastic material with a single rotationally symmetric dispersion it suffices to replace I_4 and I_5 by I_4^* and I_5^* , and we write the strain-energy function as $W^*(I_1, I_2, I_4^*, I_5^*)$, which depends on κ as well as (I_1, I_2, I_4, I_5) .

The Cauchy stress is then calculated from (57) with the help of (187) as

$$\boldsymbol{\sigma} = 2W_1^*\mathbf{B} + 2W_2^*(I_1\mathbf{B} - \mathbf{B}^2) + 2W_4^*\mathbf{h} + 2W_5^*(\mathbf{B}\mathbf{h} + \mathbf{h}\mathbf{B}) - p\mathbf{I}, \quad (193)$$

where $W_1^* = \partial W^*/\partial I_1$, $W_2^* = \partial W^*/\partial I_2$, $W_4^* = \partial W^*/\partial I_4^*$, $W_5^* = \partial W^*/\partial I_5^*$ and $\mathbf{h} = \mathbf{F}\mathbf{H}\mathbf{F}^T$, the latter being the push forward of \mathbf{H} to \mathcal{B} . Thus, compared with (57) the role of $\mathbf{m} \otimes \mathbf{m}$ is taken by \mathbf{h} . For a material with two families of dispersed fibers with mean fiber directions \mathbf{M} and \mathbf{M}' additional invariants $I_6 = \mathbf{M}' \cdot (\mathbf{C}\mathbf{M}')$, $I_7 = \mathbf{M}' \cdot (\mathbf{C}^2\mathbf{M}')$ and $I_8 = \mathbf{M} \cdot (\mathbf{C}\mathbf{M}')$ can be defined as in (64) and (65) with the new interpretation of \mathbf{M} and \mathbf{M}' , and an expression for the Cauchy stress formed, extending (193).

However, it is sufficient in what follows to restrict attention to the dependence of W on I_1, I_4, I_6 instead of $I_1, I_2, I_4, I_5, I_6, I_7, I_8$ in order to capture the effect of two fiber families. For this purpose we introduce the notation $W^*(I_1, I_4^*, I_6^*) = W(I_1, I_4, I_6)$, where, analogously to (187),

$$I_6^* = \kappa' I_1 + (1 - 3\kappa') I_6, \quad (194)$$

with $I_6^* = \text{tr}(\mathbf{CH}')$ and $\mathbf{H}' = \kappa' \mathbf{I}_r + (1 - 3\kappa') \mathbf{M}' \otimes \mathbf{M}'$, κ' being the dispersion parameter associated with \mathbf{M}' .

The Cauchy stress then has the form

$$\boldsymbol{\sigma} = 2W_1^* \mathbf{B} + 2W_4^* \mathbf{h} + 2W_6^* \mathbf{h}' - p \mathbf{I}, \quad (195)$$

where $\mathbf{h}' = \mathbf{F} \mathbf{H}' \mathbf{F}^T$.

We now recall the strain-energy function with the structure given by (112) in terms of I_1, I_4, I_6 , i.e.,

$$W = W_{\text{iso}}(I_1) + W_{\text{aniso}}(I_4, I_6), \quad (196)$$

and extend this to account for fiber dispersion by writing

$$W^* = W_{\text{iso}}^*(I_1) + W_{\text{aniso}}^*(I_4^*, I_6^*), \quad (197)$$

where $W_{\text{iso}}^*(I_1)$ characterizes the properties of the isotropic matrix in which the fibers are embedded and $W_{\text{aniso}}^*(I_4^*, I_6^*)$ characterizes the properties of the fiber dispersions.

As in (113) the isotropic part is taken to have the neo-Hookean form

$$W_{\text{iso}}^* = \frac{1}{2}\mu(I_1 - 3) \quad (198)$$

with the shear modulus $\mu (> 0)$. The anisotropic part of (197) is now

$$W_{\text{aniso}}^* = \frac{k_1}{2k_2} \sum_{i=4,6} \{\exp[k_2(I_i^* - 1)^2] - 1\}, \quad (199)$$

which is obtained from (114) by replacing I_4 and I_6 by I_4^* and I_6^* , respectively. In particular, we note that when $\kappa' = \kappa$ the two families of dispersed fibers have the same elastic properties. The material constants $k_1 (> 0)$ and $k_2 (> 0)$ have the same interpretation as in (114).

The strain-energy function (197) with (198) and (199) was introduced by Gasser et al. (2006), and, in particular, we note that the anisotropic contribution (199) involves the isotropic invariant I_1 as well as the anisotropic ones I_4 and I_6 . We also note that it was assumed in Gasser et al. (2006) that the anisotropic term in I_4^* only contributes to the energy and the stress if $I_4 > 1$ and similarly the term in I_6^* only contributes to the energy and the stress if $I_6 > 1$, i.e., if the mean fiber direction is extended in one or other family of fibers. In the case when there is no dispersion

this is because it is assumed that individual fibers cannot support compression. When there is dispersion, on the other hand, that the mean fiber direction is extended does not in general mean that all fibers in a dispersion are extended and those that are compressed should therefore be omitted from contributing to the energy and stress if it is again assumed that compressed fibers do not support compression. Whether this is the case or not is open to debate since closely packed fibers may well support some compression. Equally, if, for example, $I_4 \leq 1$ then this does not in general mean that all fibers in the dispersed family are under compression, so to omit the contribution of the I_4^* term may not then be appropriate. See the discussion in Holzapfel and Ogden (2015) and Melnik et al. (2015), for example. This is an issue that requires further investigation.

6.2 Fiber Dispersion in Two Dimensions

In two-dimensional problems such as for plane strain or plane stress it is appropriate to consider planar dispersions, and toward the analysis of such dispersions we confine attention to the plane defined by the unit basis vectors \mathbf{e}_1 and \mathbf{e}_2 . We follow the analysis in Ogden (2009) and Holzapfel and Ogden (2010) but with different notation. Let the direction of a general fiber lying in this plane be represented by the unit vector \mathbf{N} in the reference configuration, where

$$\mathbf{N} = \cos \Theta \mathbf{e}_1 + \sin \Theta \mathbf{e}_2. \quad (200)$$

Suppose that the fiber dispersion is symmetric about \mathbf{e}_1 , which is then the mean fiber direction. The orientation density ρ then depends only on Θ and satisfies $\rho(-\Theta) = \rho(\Theta)$.

The counterpart of the three-dimensional normalization in the considered two dimensions is

$$\frac{1}{\pi} \int_{-\pi/2}^{\pi/2} \rho(\Theta) d\Theta = 1, \quad (201)$$

and the (two-dimensional) generalized structure tensor is defined by

$$\hat{\mathbf{H}} = \frac{1}{\pi} \int_{-\pi/2}^{\pi/2} \rho(\Theta) \mathbf{N} \otimes \mathbf{N} d\Theta, \quad (202)$$

where the hat is used to indicate the two-dimensional restriction. The only nonzero components of $\hat{\mathbf{H}}$ are \hat{H}_{11} and \hat{H}_{22} , which satisfy $\hat{H}_{11} + \hat{H}_{22} = 1$, where

$$\hat{H}_{22} = \frac{1}{\pi} \int_{-\pi/2}^{\pi/2} \rho(\Theta) \sin^2 \Theta d\Theta. \quad (203)$$

Let us introduce the notation $\hat{H}_{22} = \kappa$ as a characteristic parameter of the dispersion, similarly to the three-dimensional situation. Then $\hat{\mathbf{H}}$ can be expanded in the form

$$\hat{\mathbf{H}} = \kappa \hat{\mathbf{I}}_r + (1 - 2\kappa) \mathbf{e}_1 \otimes \mathbf{e}_1, \quad (204)$$

where $\hat{\mathbf{I}}_r$ is the two-dimensional identity in the reference configuration of the considered plane.

More generally, if \mathbf{M} is the mean fiber direction in the plane and the dispersion is symmetric about \mathbf{M} then (204) generalizes slightly to

$$\hat{\mathbf{H}} = \kappa \hat{\mathbf{I}}_r + (1 - 2\kappa) \mathbf{M} \otimes \mathbf{M}. \quad (205)$$

By way of illustration we now apply this to the case of plane strain for an incompressible material. In respect of a single preferred direction, we recall the plane strain connections $I_2 = I_1$ and $I_5 = (I_1 - 1)I_4 - 1$ given in (59) and the expression

$$\hat{\boldsymbol{\sigma}} = 2\hat{W}_1 \hat{\mathbf{B}} + 2\hat{W}_4 \mathbf{m} \otimes \mathbf{m} - \hat{p} \hat{\mathbf{I}} \quad (206)$$

from (60) for the planar Cauchy stress, where $\hat{W} = \hat{W}(I_1, I_4)$.

Similarly to the three-dimensional model considered in the preceding section we accommodate the dispersion by replacing I_4 by $I_4^* = \text{tr}(\mathbf{C}\hat{\mathbf{H}})$, which in this case is given by

$$I_4^* = \kappa(I_1 - 1) + (1 - 2\kappa)I_4, \quad (207)$$

with $\hat{W}^*(I_1, I_4^*) = \hat{W}(I_1, I_4)$. A short calculation then leads to the planar Cauchy stress

$$\hat{\boldsymbol{\sigma}} = 2\hat{W}_1^* \hat{\mathbf{B}} + 2\hat{W}_4^* \hat{\mathbf{h}} - \hat{p} \hat{\mathbf{I}}, \quad (208)$$

where $\hat{\mathbf{h}} = \mathbf{F}\hat{\mathbf{H}}\mathbf{F}^T$, and, analogously to (195), if there are two fiber families with mean fiber directions \mathbf{M} and \mathbf{M}' in the plane, corresponding generalized invariants I_4^* and I_6^* and dispersion parameters κ and κ' , (208) extends to

$$\hat{\boldsymbol{\sigma}} = 2\hat{W}_1^* \hat{\mathbf{B}} + 2\hat{W}_4^* \hat{\mathbf{h}} + 2\hat{W}_6^* \hat{\mathbf{h}}' - \hat{p} \hat{\mathbf{I}}, \quad (209)$$

where $\hat{W}^* = \hat{W}^*(I_1, I_4^*, I_6^*)$,

$$\hat{\mathbf{h}}' = \mathbf{F}[\kappa' \hat{\mathbf{I}}_r + (1 - 2\kappa') \mathbf{M}' \otimes \mathbf{M}'] \mathbf{F}^T, \quad (210)$$

and $I_6^* = \kappa'(I_1 - 1) + (1 - 2\kappa')I_6$.

6.3 The Influence of Fiber Dispersion on the Response of an Artery

Again we denote the mean orientations of the two fiber families by \mathbf{M} and \mathbf{M}' and we assume that each dispersion is rotationally symmetric about its mean direction with the same dispersion parameter κ . We take the mean fiber directions to be symmetrically disposed, making equal angles φ with the circumferential direction and to lie in the tangential (Θ , Z) plane locally, as illustrated in Fig. 23. Hence,

$$\mathbf{M} = \cos \varphi \mathbf{E}_\Theta + \sin \varphi \mathbf{E}_Z, \quad \mathbf{M}' = -\cos \varphi \mathbf{E}_\Theta + \sin \varphi \mathbf{E}_Z. \quad (211)$$

Note that with respect to Fig. 11 the sense of \mathbf{M}' has been reversed here.

Then, for the deformation described in Sect. 5.1 we again have

$$I_1 = \lambda_\theta^2 + \lambda_z^2 + \lambda_\theta^{-2} \lambda_z^{-2}, \quad I_4 = I_6 = \lambda_\theta^2 \cos^2 \varphi + \lambda_z^2 \sin^2 \varphi, \quad (212)$$

and the invariants I_4^* and I_6^* are

$$I_4^* = I_6^* = \kappa I_1 + (1 - 3\kappa) I_4. \quad (213)$$

We again adopt the strain-energy function (197) with (198) and (199), which, under the present assumptions, specializes to

$$W^* = \frac{1}{2} \mu (I_1 - 3) + \frac{k_1}{k_2} \{\exp[k_2(I_4^* - 1)^2] - 1\}. \quad (214)$$

In order to illustrate the effect of the fiber dispersion it suffices to consider the membrane equations for P and F given by (144) and (145), respectively, but now with the strain-energy function \tilde{W} in (146) replaced by \tilde{W}^* obtained from (214) as

Fig. 23 Mean fiber directions \mathbf{M} and \mathbf{M}' locally in (Θ, Z) planes at radial location R through the tube wall, with an indication of the rotationally symmetric fiber dispersions about \mathbf{M} and \mathbf{M}'

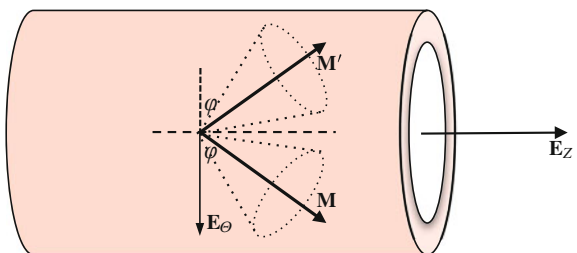
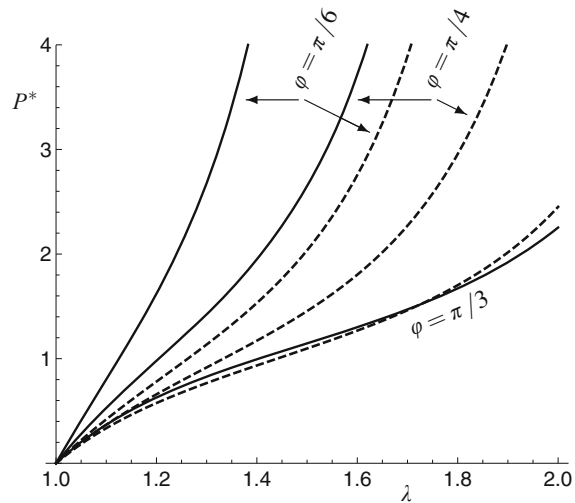


Fig. 24 Plot of the dimensionless pressure $P^* = P/\mu\varepsilon$ against λ for the strain-energy function (215) with $\lambda_z = 1$, material parameters $k_1/\mu = 1$, $k_2 = 1$ and dispersion parameters $\kappa = 0.2$ (dashed curves) and $\kappa = 0$ (continuous curves—no dispersion), and angles $\varphi = \pi/6, \pi/4, \pi/3$, based on the thin-wall approximation (144)



$$\begin{aligned} \tilde{W}^*(\lambda_\theta, \lambda_z, \varphi, \kappa) &= \frac{1}{2}\mu(\lambda_\theta^2 + \lambda_z^2 + \lambda_\theta^{-2}\lambda_z^{-2} - 3) \\ &\quad + \frac{k_1}{k_2} [\exp\{k_2[\kappa(\lambda_\theta^2 + \lambda_z^2 + \lambda_\theta^{-2}\lambda_z^{-2}) \\ &\quad + (1 - 3\kappa)(\lambda_\theta^2 \cos^2 \varphi + \lambda_z^2 \sin^2 \varphi) - 1]^2\} - 1]. \end{aligned} \quad (215)$$

In Fig. 24 the dimensionless pressure $P^* = P/\mu\varepsilon$ is plotted as a function of λ for the representative axial stretch $\lambda_z = 1$, dispersion parameter $\kappa = 0.2$ and material parameters $k_1/\mu = k_2 = 1$, with the three different values of the mean fiber angle $\varphi = \pi/6, \pi/4, \pi/3$. These are the dashed curves in the figure and are compared with corresponding results in the absence of dispersion (the continuous curves). The latter are the same as the curves in Fig. 12a but the vertical scale has been reduced here in order to highlight the significant difference that dispersion makes to the pressure response for $\varphi = \pi/6, \pi/4$, in particular for mean fiber directions relatively close to circumferential.

When the mean fiber direction is closer to axial the effect of dispersion is considerably reduced. For larger values of κ our calculations show that the response becomes less stiff and as κ approaches $1/3$ (the isotropic case) the three dispersion curves merge. The chosen values of λ_z , k_1/μ and k_2 serve to illustrate the main features of the pressure response in the presence of dispersed fibers, and results for other values of these parameters are qualitatively similar. Examples with different parameter values corresponding to fitting to arterial wall data can be found in Gasser et al. (2006) and Ogden (2009) in which P and/or P^* is plotted against λ for fixed λ_z or for $F = 0$ and against λ_z for $F = 0$.

Next, in Fig. 25, corresponding plots of the dimensionless reduced axial load $F^* = F/(\pi A^2 \mu \varepsilon)$ as a function of λ are illustrated for the same parameters as in

Fig. 25 Plot of the dimensionless reduced axial load $F^* = F/(\pi A^2 \mu \epsilon)$ against λ for the strain-energy function (215) with $\lambda_z = 1$, material parameters $k_1/\mu = 1$, $k_2 = 1$ and dispersion parameters $\kappa = 0.2$ (dashed curves) and $\kappa = 0$ (continuous curves—no dispersion), and angles $\varphi = \pi/6, \pi/4, \pi/3$, based on the thin-wall approximation (145)

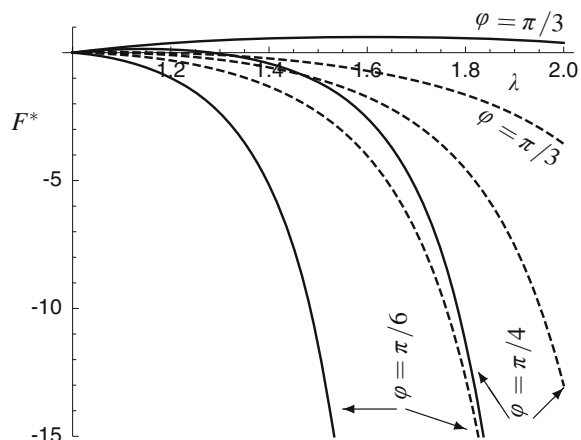


Fig. 24. In this case the dispersion has a significant effect for all values of φ , and, in particular, for $\varphi = \pi/3$, F^* changes from positive to negative as a result of dispersion for the considered range of values of λ .

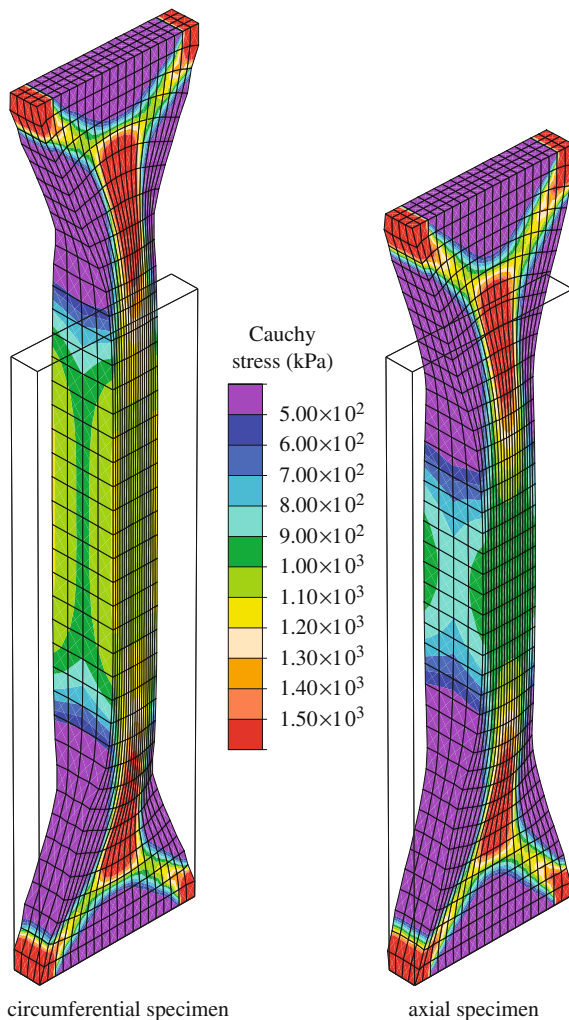
As a final example in this section we illustrate the influence of fiber dispersion on circumferential and axial strips subjected to uniaxial tensile load with the ends of the strips constrained so that the resulting deformations and stress distributions are nonuniform. Based on data relating to an iliac adventitia, finite element results were presented in Gasser et al. (2006) for a uniaxial tension of 1 N, with material parameter $\mu = 7.64$ kPa for the soft (neo-Hookean) matrix and $k_1 = 996.6$ kPa, $k_2 = 524.6$. Here we show a small selection of their results, for full details of which we refer to Gasser et al. (2006).

In Fig. 26 we show the distribution of the component of Cauchy stress in the direction of the applied load for the case of no fiber dispersion ($\kappa = 0$) with fibers oriented at an angle $\varphi = 49.98^\circ$ relative to the circumferential direction. Clearly, the circumferential specimen, shown on the left of the figure, extends more than the axial specimen because the stiff fibers are oriented closer to the axial than the circumferential direction. For each specimen there is a significant lateral contraction in the width of the specimens caused by rotation of the fibers, which tends to squeeze the material in the width. This is accompanied by an expansion in the thickness direction in which the stretch is, by incompressibility, $\lambda_3 = \lambda_1^{-1} \lambda_2^{-1} > 1$, although this is less evident near the ends of the specimens because of the end constraints.

Figure 27 shows the corresponding results for a case with fiber dispersion and dispersion parameter $\kappa = 0.226$ and mean fiber angle $\varphi = 49.98^\circ$. In this case the thickness is approximately constant and the uniaxial response is stiffer. Clearly, the dispersion has a significant effect on the response.

Fig. 26 Finite element computation showing the component of the Cauchy stress distribution in the direction of the applied load for a uniaxial tensile load of 1 N applied to strips in the circumferential and axial directions with no fiber dispersion ($\kappa = 0$).

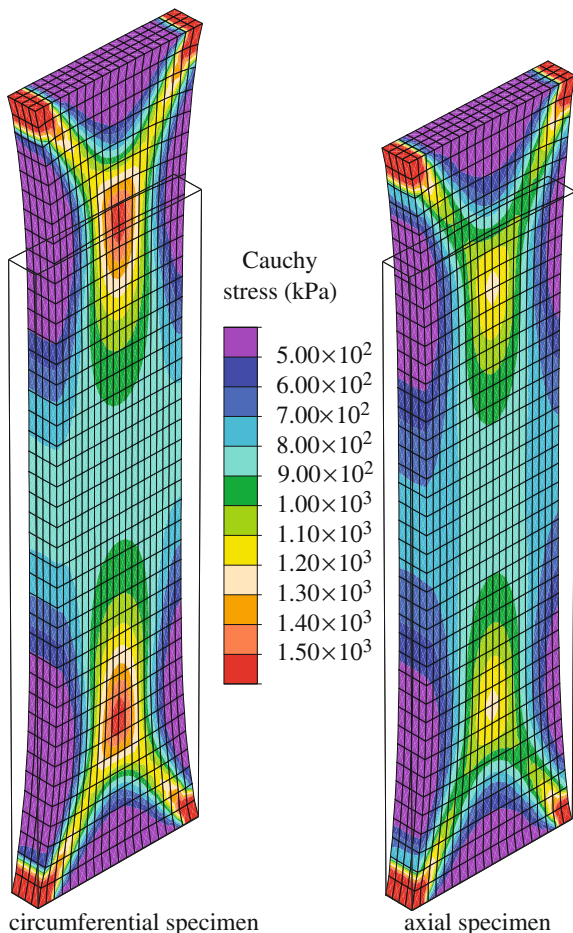
Reproduced from Fig. 9 of Gasser et al. (2006) with permission



6.4 Nonsymmetric Fiber Dispersion

Recent extensive experiments of Schriefl et al. (2012) have characterized the in-plane (circumferential–axial) dispersion of collagen fibers in the intima, media, and adventitia of human non-atherosclerotic thoracic and abdominal aortas and common iliac arteries. They also measured out-of-plane (radial) fiber angles for each layer and found that the out-of-plane dispersions are similar at all anatomic locations for each layer. In particular, they determined that for each (three-dimensional) dispersion the mean fiber angle was very close to tangential, and that the out-of-plane component was very small. These results show that it is inappropriate to adopt rotationally

Fig. 27 Finite element computation showing the component of the Cauchy stress distribution in the direction of the applied load for a uniaxial tensile load of 1 N applied to strips in the circumferential and axial directions with fiber dispersion parameter $\kappa = 0.226$. Reproduced from Fig. 12 of Gasser et al. (2006) with permission



symmetric dispersions for the two fiber families with mean fiber direction in the circumferential–axial plane. The purpose of this section, therefore, it to provide a modification of the rotationally symmetric dispersion model that takes account of these new results. Our analysis here is based on the recent paper by Holzapfel et al. (2015), but for consistency with the previous sections herein some of the notation has been changed.

With reference to Fig. 20 we again assume that a general fiber direction \mathbf{N} within a dispersion is given by (169), which we repeat here for ease of reference as

$$\mathbf{N}(\Theta, \Phi) = \sin \Theta \cos \Phi \mathbf{e}_1 + \sin \Theta \sin \Phi \mathbf{e}_2 + \cos \Theta \mathbf{e}_3, \quad (216)$$

with $\Theta \in [0, \pi]$, $\Phi \in [0, 2\pi]$, and, locally, for a circular cylinder, $\mathbf{e}_1, \mathbf{e}_2$ defining the tangential plane of a cylindrical coordinate system, \mathbf{e}_1 being the circumferential direction and \mathbf{e}_2 the axial direction. Thus, \mathbf{e}_3 is the outward radial direction.

We again adopt the notation $\rho(\Theta, \Phi)$ for the fiber orientation density, and this is normalized according to (170). The requirement that ρ is independent of the sense of \mathbf{N} again gives $\rho(\pi - \Theta, \pi + \Phi) = \rho(\Theta, \Phi)$. The experimental results of Schriebl et al. (2012) suggest two additional symmetries, the in-plane symmetry $\rho(\Theta, \pi + \Phi) = \rho(\Theta, \Phi)$, and the out-of-plane symmetry $\rho(\pi - \Theta, \Phi) = \rho(\Theta, \Phi)$, as a result of which we can now focus on the ranges of values $\Theta \in [0, \pi/2]$ and $\Phi \in [0, \pi]$.

Again we assume that the material properties are independent of the sense of \mathbf{N} , so that the strain-energy function depends on \mathbf{N} via the tensor product $\mathbf{N} \otimes \mathbf{N}$, as in Sect. 6.1, through the (symmetric) generalized structure tensor \mathbf{H} defined in (171), which, in view of the symmetries mentioned above, we now write as

$$\mathbf{H} = \frac{1}{\pi} \int_{\Omega'} \rho(\Theta, \Phi) \mathbf{N} \otimes \mathbf{N} \sin \Theta d\Theta d\Phi, \quad (217)$$

where $\Omega' = \{(\Theta, \Phi) \mid \Theta \in [0, \pi/2], \Phi \in [0, \pi]\}$.

With reference to the basis $\mathbf{e}_1, \mathbf{e}_2, \mathbf{e}_3$ we denote the components of \mathbf{H} by $H_{ij} = H_{ji}$, so that (in the summation convention) $\mathbf{H} = H_{ij} \mathbf{e}_i \otimes \mathbf{e}_j$. However, the symmetries of ρ identified above ensure that $H_{13} = H_{23} = 0$. In view of the restriction (172) there remain only three independent components of \mathbf{H} . Thus, we consider

$$H_{11}, \quad H_{22}, \quad H_{12}, \quad \text{with} \quad H_{33} = 1 - H_{11} - H_{22}. \quad (218)$$

It was found in Schriebl et al. (2012) that the in-plane and out-of-plane dispersions are essentially independent, which means that $\rho(\Theta, \Phi)$ can be decoupled as

$$\rho(\Theta, \Phi) = \rho_{\text{op}}(\Theta) \rho_{\text{ip}}(\Phi), \quad (219)$$

where $\rho_{\text{op}}(\Theta)$ and $\rho_{\text{ip}}(\Phi)$ are the out-of-plane and in-plane fiber orientation densities, respectively. The symmetries discussed above then impose the conditions

$$\rho_{\text{op}}(\pi - \Theta) = \rho_{\text{op}}(\Theta), \quad \rho_{\text{ip}}(\pi + \Phi) = \rho_{\text{ip}}(\Phi). \quad (220)$$

As a result, with the symmetries accounted for, the normalization (170) gives

$$\frac{1}{\pi} \int_0^{\pi/2} \rho_{\text{op}}(\Theta) \sin \Theta d\Theta \int_0^\pi \rho_{\text{ip}}(\Phi) d\Phi = 1. \quad (221)$$

Clearly, the out-of-plane dispersion has rotational symmetry, and guided therefore by the normalization (178) in the case of rotational symmetry, we assume that $\rho_{\text{op}}(\Theta)$ is normalized according to

$$\int_0^{\pi/2} \rho_{\text{op}}(\Theta) \sin \Theta d\Theta = 1, \quad (222)$$

which leaves the normalization of $\rho_{\text{ip}}(\Phi)$ in the form

$$\frac{1}{\pi} \int_0^\pi \rho_{\text{ip}}(\Phi) d\Phi = 1. \quad (223)$$

Analogously to the dispersion parameter κ defined in (180) we now define the out-of-plane dispersion parameter κ_{op} by

$$\kappa_{\text{op}} = \frac{1}{2} \int_0^{\pi/2} \rho_{\text{op}}(\Theta) \sin^3 \Theta d\Theta, \quad (224)$$

which lies in the range of values

$$0 \leq \kappa_{\text{op}} \leq 1/2, \quad (225)$$

as discussed in Sect. 6.1.1 in respect of κ . Thus, in particular, $\kappa_{\text{op}} = 1/3$ corresponds to an isotropic dispersion with $\rho_{\text{op}} = 1$.

Note that (223) is automatically satisfied if $\rho_{\text{ip}}(\Phi) \equiv 1$, which corresponds to in-plane isotropy, in which case $H_{12} = 0$, $H_{11} = H_{22} = \kappa_{\text{op}}$, and $H_{33} = 1 - 2\kappa_{\text{op}}$, so that the dispersion is rotationally symmetric with mean fiber direction \mathbf{e}_3 . Three-dimensional isotropy arises if $\rho_{\text{op}}(\Theta) = \rho_{\text{ip}}(\Phi) = 1$ and $\kappa_{\text{op}} = 1/3$.

Having considered the out-of-plane dispersion in terms of κ_{op} , we now discuss the in-plane dispersion. From the definitions (217), (226) and (227) with Eq. (219) the components of \mathbf{H} are calculated simply as

$$H_{ij} = 2\kappa_{\text{op}} \bar{\kappa}_{ij}, \quad i, j \in \{1, 2\}, \quad H_{11} + H_{22} = 2\kappa_{\text{op}}, \quad H_{33} = 1 - 2\kappa_{\text{op}}, \quad (226)$$

where $\bar{\kappa}_{11}$, $\bar{\kappa}_{22}$ and $\bar{\kappa}_{12}$ are given by

$$\bar{\kappa}_{11} = \frac{1}{\pi} \int_0^\pi \rho_{\text{ip}}(\Phi) \cos^2 \Phi d\Phi, \quad \bar{\kappa}_{22} = \frac{1}{\pi} \int_0^\pi \rho_{\text{ip}}(\Phi) \sin^2 \Phi d\Phi, \quad (227)$$

$$\bar{\kappa}_{12} = \frac{1}{\pi} \int_0^\pi \rho_{\text{ip}}(\Phi) \sin \Phi \cos \Phi d\Phi. \quad (228)$$

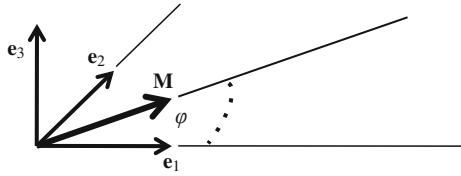
It follows from (223) that

$$\bar{\kappa}_{11} + \bar{\kappa}_{22} = 1. \quad (229)$$

Note that in the case of in-plane isotropy, $\rho_{\text{ip}}(\Phi) \equiv 1$, it follows that $\bar{\kappa}_{12} = 0$ and $\bar{\kappa}_{11} = \bar{\kappa}_{22} = 1/2$.

If the mean in-plane fiber direction coincides with \mathbf{e}_1 or \mathbf{e}_2 then we also have $\bar{\kappa}_{12} = 0$. We then consider a mean in-plane fiber direction \mathbf{M} , as depicted in Fig. 28, with

Fig. 28 Schematic of the in-plane mean fiber direction $\mathbf{M} = \cos \varphi \mathbf{e}_1 + \sin \varphi \mathbf{e}_2$, with in-plane unit vectors \mathbf{e}_1 (circumferential) and \mathbf{e}_2 (axial) and plane normal \mathbf{e}_3



the dispersion symmetric about \mathbf{M} , which is a unit vector given by $\mathbf{M} = \cos \varphi \mathbf{e}_1 + \sin \varphi \mathbf{e}_2$, φ being the angle between \mathbf{M} and the circumferential direction \mathbf{e}_1 . With respect to axes aligned with $\mathbf{e}'_1 = \mathbf{M}$ and $\mathbf{e}'_2 = -\sin \varphi \mathbf{e}_1 + \cos \varphi \mathbf{e}_2$, we denote the dispersion parameters by $\bar{\kappa}'_{ij}$ and in this case also $\bar{\kappa}'_{12} = 0$. In such a case we drop the bars and use the notation κ_{11} and κ_{22} , noting that $\kappa_{11} + \kappa_{22} = 1$.

Then, the dispersion components $\bar{\kappa}_{ij}$ are related to κ_{ij} , $i, j \in \{1, 2\}$, and the angle φ by

$$\bar{\kappa}_{11} = \kappa_{11} \cos^2 \varphi + \kappa_{22} \sin^2 \varphi, \quad \bar{\kappa}_{12} = (\kappa_{11} - \kappa_{22}) \sin \varphi \cos \varphi, \quad (230)$$

with $\bar{\kappa}_{22}$ given by (229), and hence

$$\tan 2\varphi = \frac{2\bar{\kappa}_{12}}{\bar{\kappa}_{11} - \bar{\kappa}_{22}}. \quad (231)$$

Note that

$$(\bar{\kappa}_{11} - \bar{\kappa}_{22})^2 + 4\bar{\kappa}_{12}^2 = (\kappa_{11} - \kappa_{22})^2 \quad (232)$$

is an invariant, i.e., independent of φ . Clearly then, given the angle φ , there is only one independent in-plane dispersion parameter. We take this to be κ_{22} , which we denote by κ_{ip} henceforth.

Now let us refer the structure tensor \mathbf{H} to the axes $\mathbf{e}'_1, \mathbf{e}'_2$ identified above, along with $\mathbf{e}'_3 = \mathbf{e}_3$, and let H'_{ij} be the corresponding components of \mathbf{H} , where

$$H'_{11} = 2\kappa_{op}(1 - \kappa_{ip}), \quad H'_{22} = 2\kappa_{op}\kappa_{ip}, \quad H'_{33} = 1 - 2\kappa_{op} \quad (233)$$

and $H'_{ij} = 0$, $i \neq j$. By using the identity $\mathbf{e}'_1 \otimes \mathbf{e}'_1 + \mathbf{e}'_2 \otimes \mathbf{e}'_2 + \mathbf{e}'_3 \otimes \mathbf{e}'_3 = \mathbf{I}_r$, the spectral form of \mathbf{H} , i.e.,

$$\mathbf{H} = H'_{11}\mathbf{e}'_1 \otimes \mathbf{e}'_1 + H'_{22}\mathbf{e}'_2 \otimes \mathbf{e}'_2 + H'_{33}\mathbf{e}'_3 \otimes \mathbf{e}'_3, \quad (234)$$

can be rewritten as

$$\mathbf{H} = 2\kappa_{op}\kappa_{ip}\mathbf{I}_r + 2\kappa_{op}(1 - 2\kappa_{ip})\mathbf{M} \otimes \mathbf{M} + (1 - 2\kappa_{op} - 2\kappa_{op}\kappa_{ip})\mathbf{M}_n \otimes \mathbf{M}_n, \quad (235)$$

where the unit vector \mathbf{M}_n is now used in place of \mathbf{e}_3 . This is the generalized structure tensor associated with a fiber dispersion that has a single in-plane mean direction

\mathbf{M} , and because of the considered symmetries \mathbf{M} is also the mean direction of the three-dimensional dispersion.

We emphasize that \mathbf{H} involves just two independent dispersion parameters, κ_{op} and κ_{ip} , and κ_{op} can be calculated when ρ_{op} is prescribed, while $\bar{\kappa}_{11}$, $\bar{\kappa}_{22}$ and $\bar{\kappa}_{12}$ can be determined from a given form of ρ_{ip} . The latter lead to the angle φ via (231). The calculations are exemplified in the following section by considering ρ_{op} and ρ_{ip} to be von Mises distributions.

Special Cases

It is worthwhile at this point to identify the values of κ_{op} and κ_{ip} for which the structure tensor (235) reduces to the particular structure tensors considered previously. First, by taking $\kappa_{\text{ip}} = 1/2$, we obtain

$$\mathbf{H} = \kappa_{\text{op}} \mathbf{I}_r + (1 - 3\kappa_{\text{op}}) \mathbf{M}_n \otimes \mathbf{M}_n, \quad (236)$$

which is the structure tensor of a rotationally symmetric dispersion with mean fiber direction \mathbf{M}_n . Alternatively, we may obtain

$$\mathbf{H} = \kappa \mathbf{I}_r + (1 - 3\kappa) \mathbf{M} \otimes \mathbf{M} \quad (237)$$

by setting $\kappa = 2\kappa_{\text{op}}\kappa_{\text{ip}} = 1 - 2\kappa_{\text{op}}$, which is the structure tensor of a rotationally symmetric dispersion with mean fiber direction \mathbf{M} . If there is no dispersion then by taking $\kappa_{\text{op}} = 0$ and $\kappa = 0$, respectively, in these two cases we obtain $\mathbf{H} = \mathbf{M}_n \otimes \mathbf{M}_n$ and $\mathbf{H} = \mathbf{M} \otimes \mathbf{M}$. The structure tensor for an isotropic dispersion of fibers is obtained by taking either $\kappa_{\text{op}} = 1/3$ in (236) or $\kappa = 1/3$ in (237).

The structure tensor $\hat{\mathbf{H}}$ for a two-dimensional dispersion given in (205) is obtained from (235) by setting $\kappa_{\text{op}} = 1/2$ and $\kappa_{\text{ip}} = \kappa$, and noting that the in-plane identity is given by $\hat{\mathbf{I}}_r = \mathbf{I}_r - \mathbf{M}_n \otimes \mathbf{M}_n$. Then, with $\kappa = 1/2$, we obtain the structure tensor for an isotropic in-plane dispersion, namely $\hat{\mathbf{H}} = \hat{\mathbf{I}}_r/2$.

6.4.1 Describing Dispersions in Terms of von Mises Distributions

We consider π -periodic von Mises distributions that account for the symmetries identified at the beginning of Sect. 6.4. For general details of von Mises distributions we refer to Fisher et al. (1987). We begin by representing the out-of-plane orientation density $\rho_{\text{op}}(\Theta)$ as a von Mises distribution of the form

$$\rho_{\text{op}}(\Theta) = 4 \sqrt{\frac{b}{2\pi}} \frac{\exp(-2b \cos^2 \Theta)}{\operatorname{erf}(\sqrt{2b})}. \quad (238)$$

This can be obtained from the $\rho(\Theta)$ given in (182) in Sect. 6.1.1 by replacing b by $-b$ and leads to the closed-form expression for κ_{op} given by

$$\kappa_{\text{op}} = \frac{1}{2} - \frac{1}{8b} + \frac{1}{4} \sqrt{\frac{2}{\pi b}} \frac{\exp(-2b)}{\text{erf}(\sqrt{2b})}, \quad (239)$$

which has the character shown in Fig. 22 as for κ in (184) but with b and $-b$ interchanged.

For $\rho_{\text{ip}}(\Phi)$ we consider the von Mises distribution

$$\rho_{\text{ip}}(\Phi) = \frac{\exp(-a \cos 2\Phi)}{I_0(a)}, \quad (240)$$

which has a different normalization from $\rho_{\text{op}}(\Theta)$, where the constant a is again a concentration parameter, while $I_0(a)$ is the modified Bessel function of the first kind of order 0 defined by

$$I_0(x) = \frac{1}{\pi} \int_0^\pi \exp(x \cos \alpha) d\alpha. \quad (241)$$

The distribution (240) is slightly different from that used in Holzapfel et al. (2015) and is chosen to have its maximum at the center $\Phi = \pi/2$ of the integration interval. The forms of the curves of $\rho_{\text{ip}}(\Phi)$ for different values of a are, apart from the different scale, identical to those shown in Fig. 21. When $a \rightarrow \infty$, $\rho_{\text{ip}}(\Phi)$ becomes a delta function.

It is instructive to visualize the dispersion in three dimensions by plotting $\rho(\Theta, \Phi)\mathbf{N} = \rho_{\text{op}}(\Theta)\rho_{\text{ip}}(\Phi)\mathbf{N}$. Thus, Fig. 29 shows this for the different cases of dispersions considered, as described in the figure caption.

Since the distribution (240) is symmetric about $\Phi = 0$ it follows from the definition (228) that $\bar{\kappa}_{12} = 0$, and from (227), on dropping the bars, that κ_{11} and κ_{22} can be obtained in the closed forms

$$\kappa_{11} = \frac{1}{2} - \frac{I_1(a)}{2I_0(a)}, \quad \kappa_{22} = \kappa_{\text{ip}} = \frac{1}{2} + \frac{I_1(a)}{2I_0(a)}, \quad (242)$$

where

$$I_1(x) = \frac{1}{\pi} \int_0^\pi \exp(x \cos \alpha) \cos \alpha d\alpha \quad (243)$$

is the modified Bessel function of the first kind of order 1. Note that the expressions for κ_{11} and κ_{22} are reversed compared with those given in Holzapfel et al. (2015) because of the different form of $\rho_{\text{ip}}(\Phi)$ adopted here. Each of κ_{11} and κ_{22} lies in the range $[0, 1]$ subject to $\kappa_{11} + \kappa_{22} = 1$ and plots of them as functions of a are shown in Fig. 30. The character of κ_{22} is very similar to that of κ shown in Fig. 22 although the range of values is different.

If κ_{11} and κ_{22} are the dispersion parameters corresponding to a mean fiber direction at an angle φ to the \mathbf{e}_1 direction (see Fig. 28) then the dispersion parameters $\bar{\kappa}_{11}$, $\bar{\kappa}_{22}$ and $\bar{\kappa}_{12}$ are given by (229) and (230).

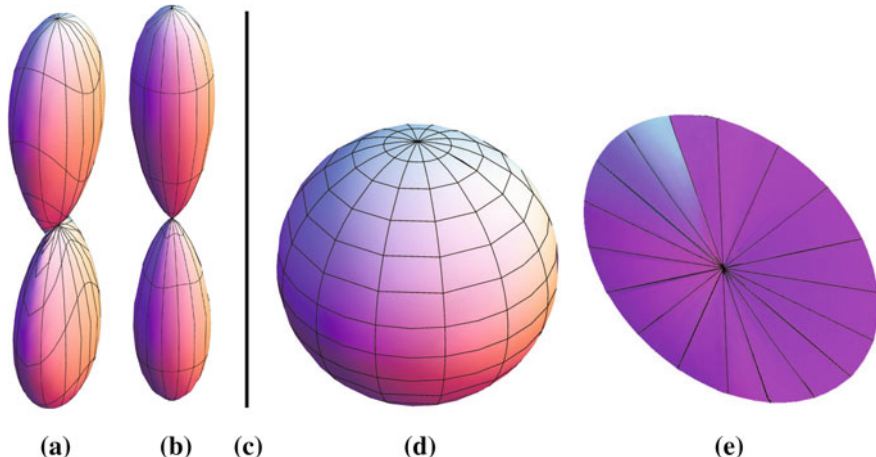
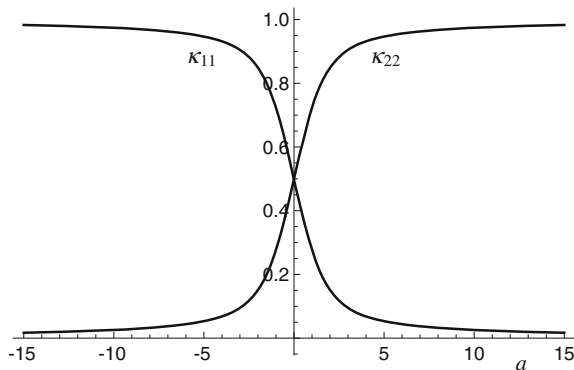


Fig. 29 Visualization of the fiber dispersion defined by $\rho(\Theta, \Phi)\mathbf{N} = \rho_{\text{op}}(\Theta)\rho_{\text{ip}}(\Phi)\mathbf{N}$ based on the von Mises distributions (238) and (240). The plots have been scaled differently and represent **a** a nonrotationally symmetric dispersion, **b** a rotationally symmetric dispersion, **c** perfectly aligned fibers, **d** a 3D isotropic dispersion and **e** a planar dispersion. The planar isotropic case corresponds to a circle in **e**. Except for case **c** the distance from the center to the surface represents the probability of finding a fiber in the direction \mathbf{N} . Reproduced from Fig. 6 of Holzapfel et al. (2015) with permission

Fig. 30 Plots of κ_{11} and κ_{22} versus a based on the formulas in (242)



6.4.2 Consideration of Data from Schriefl et al. (2012)

We now illustrate the results from Schriefl et al. (2012) by considering the angular dispersion data from a single adventitial specimen of a human non-atherosclerotic abdominal aorta which were included in the average data set in Fig. 5 of their paper. In Fig. 31 we show the data as a probability density for the out-of-plane dispersion together with a curve obtained by fitting $\rho_{\text{op}}(\Theta)$ obtained from (238) to the data for which the concentration parameter was found to be $b = 19.44$. Incidentally, the

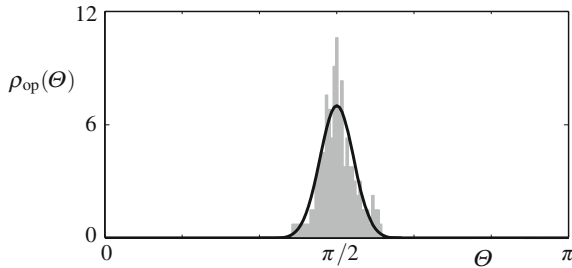
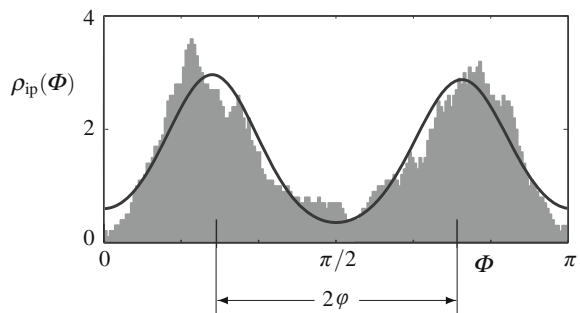


Fig. 31 Representative set of out-of-plane fiber angular dispersion data from Schriebl et al. (2012) and the fit to these data with the orientation density function (238) with concentration parameter $b = 19.44$ and with $\rho_{op}(\Theta)$ plotted against Θ . Based on Fig. 5b in Holzapfel et al. (2015), with permission

Fig. 32 Representative set of in-plane fiber angular dispersion data from Schriebl et al. (2012) and the fit to these data with the orientation density function (240) with concentration parameter $a = 2.54$ and angle $\varphi = 47.99^\circ$ and with $\rho_{ip}(\Phi)$ plotted against Φ . Based on Fig. 5a in Holzapfel et al. (2015), with permission



vertical scale shown in the corresponding figure (Fig. 5b) in Holzapfel et al. (2015) is incorrect, and Fig. 31 corrects this.

In Fig. 32 we show the data of the in-plane bimodal dispersion, the data being fitted by the curve shown using $\rho_{ip}(\Phi)$ from (240) with Φ replaced by $\Phi + \varphi$ and $\Phi - \varphi$ together, φ being determined as $\varphi = 47.99^\circ$, and the concentration parameter as $a = 2.54$.

Note that the data shown in Figs. 31 and 32 are centered on $\Theta = \pi/2$ rather than the $\Theta = 0$ used in Holzapfel et al. (2015).

From the formulas (239) and (242)₂ with the values of b and a above we then obtain the corresponding values of κ_{op} and κ_{ip} as $\kappa_{op} = 0.494$ and $\kappa_{ip} = 0.885$. Note that in Holzapfel et al. (2015) the value of κ_{op} was 0.493 and, because we are using a slightly different version of ρ_{ip} here κ_{ip} in Holzapfel et al. (2015) was 0.116, whereas the value of κ_{11} here is 0.115.

6.4.3 An Extended Constitutive Law

We recall the generalized structure tensor defined in (235) as

$$\mathbf{H} = 2\kappa_{op}\kappa_{ip}\mathbf{I}_r + 2\kappa_{op}(1 - 2\kappa_{ip})\mathbf{M} \otimes \mathbf{M} + (1 - 2\kappa_{op} - 2\kappa_{op}\kappa_{ip})\mathbf{M}_n \otimes \mathbf{M}_n, \quad (244)$$

for a single family of dispersed fibers. We now consider a second family with mean fiber direction \mathbf{M}' and the same material properties with structure tensor

$$\mathbf{H}' = 2\kappa_{op}\kappa_{ip}\mathbf{I}_r + 2\kappa_{op}(1 - 2\kappa_{ip})\mathbf{M}' \otimes \mathbf{M}' + (1 - 2\kappa_{op} - 2\kappa_{op}\kappa_{ip})\mathbf{M}_n \otimes \mathbf{M}_n, \quad (245)$$

\mathbf{M} and \mathbf{M}' lying in the $(\mathbf{e}_1, \mathbf{e}_2)$ plane and symmetrically arranged with respect to the axes, and $\mathbf{M}_n = \mathbf{e}_3$ normal to that plane, as depicted in Fig. 33. Thus,

$$\mathbf{M} = \cos \varphi \mathbf{e}_1 + \sin \varphi \mathbf{e}_2, \quad \mathbf{M}' = \cos \varphi \mathbf{e}_1 - \sin \varphi \mathbf{e}_2. \quad (246)$$

Note, with reference to Fig. 11, that \mathbf{e}_1 and \mathbf{e}_2 may be identified with \mathbf{E}_Θ and \mathbf{E}_Z , respectively.

The associated generalized invariants are denoted I_4^* and I_6^* , generalizing the definitions used in (186)₁ and (194), the latter with $\kappa' = \kappa$, and given by

$$I_4^* = \text{tr}(\mathbf{CH}) = 2\kappa_{op}\kappa_{ip}I_1 + 2\kappa_{op}(1 - 2\kappa_{ip})I_4 + (1 - 2\kappa_{op} - 2\kappa_{op}\kappa_{ip})I_n, \quad (247)$$

$$I_6^* = \text{tr}(\mathbf{CH}') = 2\kappa_{op}\kappa_{ip}I_1 + 2\kappa_{op}(1 - 2\kappa_{ip})I_6 + (1 - 2\kappa_{op} - 2\kappa_{op}\kappa_{ip})I_n, \quad (248)$$

where $I_n = \mathbf{M}_n \cdot (\mathbf{CM}_n)$

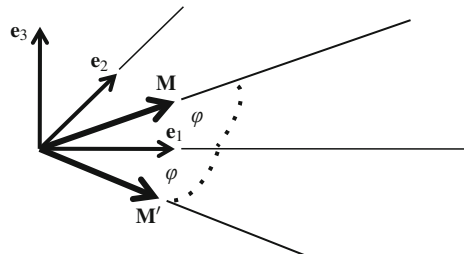
Note, by considering the (orthogonal) unit bisectors of \mathbf{M} and \mathbf{M}' , namely $\mathbf{e}_1 = (\mathbf{M} + \mathbf{M}')/2 \cos \varphi$ and $\mathbf{e}_2 = (\mathbf{M} - \mathbf{M}')/2 \sin \varphi$, where 2φ is the angle between \mathbf{M} and \mathbf{M}' , and using the identity

$$\mathbf{e}_1 \otimes \mathbf{e}_1 + \mathbf{e}_2 \otimes \mathbf{e}_2 + \mathbf{e}_3 \otimes \mathbf{e}_3 = \mathbf{I}_r, \quad (249)$$

we obtain

$$I_n = I_1 - \frac{I_4 + I_6 - 2I_8 \cos 2\varphi}{\sin^2 2\varphi}, \quad (250)$$

Fig. 33 Schematic of the in-plane mean fiber directions
 $\mathbf{M} = \cos \varphi \mathbf{e}_1 + \sin \varphi \mathbf{e}_2$ and
 $\mathbf{M}' = \cos \varphi \mathbf{e}_1 - \sin \varphi \mathbf{e}_2$,
with in-plane unit vectors \mathbf{e}_1 (circumferential) and \mathbf{e}_2 (axial) and plane normal \mathbf{e}_3



where I_8 is defined by (65). Thus, I_n is in general an independent invariant, i.e., independent of I_1, I_4, I_6 , except in the special case in which \mathbf{M} and \mathbf{M}' are themselves orthogonal, and the above reduces to $I_n = I_1 - (I_4 + I_6)$.

Now, instead of treating W as a function of just I_1, I_4, I_6 we append the invariant I_n , which appears only in I_4^* and I_6^* , and consider $W(I_1, I_4, I_6, I_n) = W^*(I_1, I_4^*, I_6^*)$. Recalling the connections (23) and the formula (42)₂, the second Piola–Kirchhoff stress tensor \mathbf{P} is then given by

$$\mathbf{P} = 2 \frac{\partial W}{\partial \mathbf{C}} - p \mathbf{C}^{-1} = 2(W_1 \mathbf{I}_r + W_4 \mathbf{M} \otimes \mathbf{M} + W_6 \mathbf{M}' \otimes \mathbf{M}' + W_n \mathbf{M}_n \otimes \mathbf{M}_n) - p \mathbf{C}^{-1}, \quad (251)$$

and the Cauchy stress tensor is obtained from $\boldsymbol{\sigma} = \mathbf{F} \mathbf{P} \mathbf{F}^T$. When expressed in terms of $W^*(I_1, I_4^*, I_6^*)$ it can then be shown that the Cauchy stress is given by

$$\boldsymbol{\sigma} = -p \mathbf{I} + 2W_1^* \mathbf{B} + 2W_4^* \mathbf{h} + 2W_6^* \mathbf{h}', \quad (252)$$

the same formula as in (195), where $\mathbf{h} = \mathbf{F} \mathbf{H} \mathbf{F}^T$ and $\mathbf{h}' = \mathbf{F} \mathbf{H}' \mathbf{F}^T$, but \mathbf{H} and \mathbf{H}' are now given by (244) and (245). Hence

$$\mathbf{h} = 2\kappa_{op}\kappa_{ip}\mathbf{B} + 2\kappa_{op}(1 - 2\kappa_{ip})\mathbf{m} \otimes \mathbf{m} + (1 - 2\kappa_{op} - 2\kappa_{op}\kappa_{ip})\mathbf{m}_n \otimes \mathbf{m}_n, \quad (253)$$

$$\mathbf{h}' = 2\kappa_{op}\kappa_{ip}\mathbf{B} + 2\kappa_{op}(1 - 2\kappa_{ip})\mathbf{m}' \otimes \mathbf{m}' + (1 - 2\kappa_{op} - 2\kappa_{op}\kappa_{ip})\mathbf{m}_n \otimes \mathbf{m}_n, \quad (254)$$

with $\mathbf{m} = \mathbf{F} \mathbf{M}$, $\mathbf{m}' = \mathbf{F} \mathbf{M}'$, $\mathbf{m}_n = \mathbf{F} \mathbf{M}_n$.

We now extend the decomposition of the strain-energy function given in (197) to the present situation by writing it as

$$W^*(I_1, I_4^*, I_6^*) = W_{iso}^*(I_1) + W_{aniso}^*(I_4^*, I_6^*), \quad (255)$$

but now with I_4^* and I_6^* given by (247) and (248). With this change, as in (198) and (199), we take

$$W_{iso}^* = \frac{1}{2}\mu(I_1 - 3) \quad (256)$$

and

$$W_{aniso}^* = \frac{k_1}{2k_2} \sum_{i=4,6} \{\exp[k_2(I_i^* - 1)^2] - 1\}. \quad (257)$$

Following Holzapfel et al. (2000), we make the common assumption that the fibers do not resist any compression and are only active in tension. In this respect the invariants I_4 and I_6 act as switches between fiber compression and tension so that W_{aniso}^* only contributes to the strain energy if either $I_4 > 1$ or $I_6 > 1$. Thus, if one or both of these conditions is not satisfied then the corresponding part of W_{aniso}^* is omitted. If neither condition is satisfied then the tissue response is purely isotropic.

For discussion of subtle points regarding the choice of switching criteria, we refer to Holzapfel and Ogden (2015).

6.4.4 Material Parameter Identification

For the particular data considered in Sect. 6.4.2 the dispersion parameters κ_{op} and κ_{ip} and the angle φ , and hence the mean fiber directions \mathbf{M} and \mathbf{M}' , were determined on the basis of histology and imaging. Thus, for the model (255) with (256) and (257), it remains to determine the material parameters μ , k_1 and k_2 . In Holzapfel et al. (2015) they were determined by fitting the model to uniaxial data.

To review this we first refer to the definition of pure homogeneous strain in (99) in terms of the principal stretches $\lambda_1, \lambda_2, \lambda_3$, which satisfy the incompressibility constraint $\lambda_1\lambda_2\lambda_3 = 1$, in which context \mathbf{M} and \mathbf{M}' were given by (101), the same formulas as in (246). Correspondingly, \mathbf{m} and \mathbf{m}' are given by (102) and $\mathbf{m}_n = \lambda_3\mathbf{M}_n = \lambda_3\mathbf{e}_3$.

From (103) and (104)₁, the invariants I_1, I_4, I_6 are given by

$$I_1 = \lambda_1^2 + \lambda_2^2 + \lambda_3^2, \quad I_4 = I_6 = \lambda_1^2 \cos^2 \varphi + \lambda_2^2 \sin^2 \varphi, \quad (258)$$

while $I_n = \lambda_3^2$.

The nonzero components of \mathbf{h} and \mathbf{h}' are calculated as

$$h_{11} = h'_{11} = 2\kappa_{\text{op}}[\kappa_{\text{ip}} + (1 - 2\kappa_{\text{ip}})\cos^2 \varphi]\lambda_1^2, \quad (259)$$

$$h_{22} = h'_{22} = 2\kappa_{\text{op}}[\kappa_{\text{ip}} + (1 - 2\kappa_{\text{ip}})\sin^2 \varphi]\lambda_2^2, \quad (260)$$

$$h_{33} = h'_{33} = (1 - 2\kappa_{\text{op}})\lambda_3^2, \quad (261)$$

$$h_{12} = -h'_{12} = 2\kappa_{\text{op}}(1 - 2\kappa_{\text{ip}})\lambda_1\lambda_2 \sin \varphi \cos \varphi, \quad (262)$$

and hence I_4^* and I_6^* can be written simply as

$$I_4^* = I_6^* = h_{11} + h_{22} + h_{33}. \quad (263)$$

The nonzero components of the Cauchy stress tensor are obtained from (252) as

$$\sigma_{11} = \mu\lambda_1^2 + 4k_1(I_4^* - 1)\exp[k_2(I_4^* - 1)^2]h_{11} - p, \quad (264)$$

$$\sigma_{22} = \mu\lambda_2^2 + 4k_1(I_4^* - 1)\exp[k_2(I_4^* - 1)^2]h_{22} - p, \quad (265)$$

$$\sigma_{33} = \mu\lambda_3^2 + 4k_1(I_4^* - 1)\exp[k_2(I_4^* - 1)^2]h_{33} - p. \quad (266)$$

On specializing to the case of simple tension with $\sigma_{22} = \sigma_{33} = 0$, elimination of p from (264)–(266) leaves two equations, namely the incompressibility condition $\lambda_1\lambda_2\lambda_3 = 1$ and the implicit equation $\sigma_{22} - \sigma_{33} = 0$, which determine λ_2 and λ_3 in terms of λ_1 , so that σ_{11} can be expressed in terms of λ_1 , the material parameters μ, k_1 and k_2 and the structural parameters $\kappa_{\text{ip}}, \kappa_{\text{op}}$ and φ . To determine the material

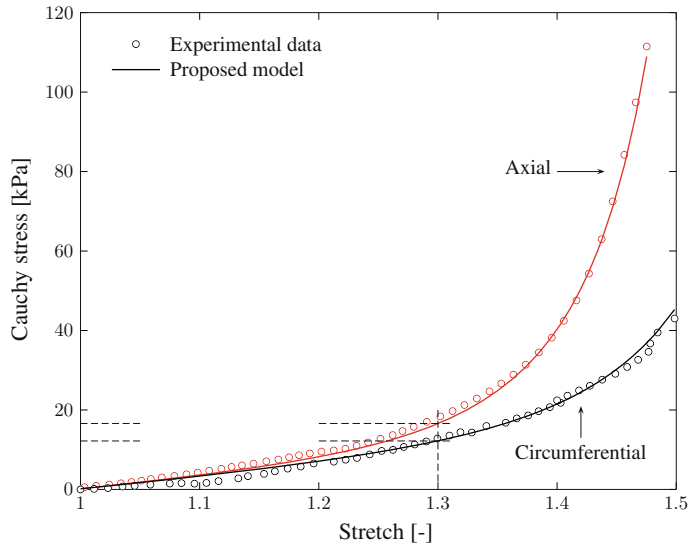


Fig. 34 Fitting of the model (255)–(257) to the results of uniaxial tension tests. The Cauchy stresses at a stretch of 1.3 are 16.6 kPa (axial) and 12.2 kPa (circumferential) and are identified here for reference to values determined in a finite element simulation of a uniaxial tension test illustrated in Fig. 35. Reproduced from Fig. 8 of Holzapfel et al. (2015) with permission

parameters, the values of the structural parameters given in Sect. 6.4.2 are used in conjunction with (unpublished) experimental data from uniaxial tension tests performed in the Graz lab on an adventitial layer of a human non-atherosclerotic abdominal aorta cut along the axial and circumferential directions. Following Holzapfel et al. (2015), and bearing in mind the different definitions of ρ_{op} and ρ_{ip} herein, we use the values $\varphi = \pm 47.99^\circ$, $\kappa_{op} = 0.493$, $\kappa_{ip} = 0.116$ for this exercise.

Full details of the fitting procedure are given in Holzapfel et al. (2015) wherein the material parameters $\mu = 10.07$ kPa, $k_1 = 5.89$ kPa, $k_2 = 21.62$ (dimensionless) were obtained, giving an excellent fit to the data, as shown in Fig. 34.

6.4.5 Application to the Extension of Adventitial Strips

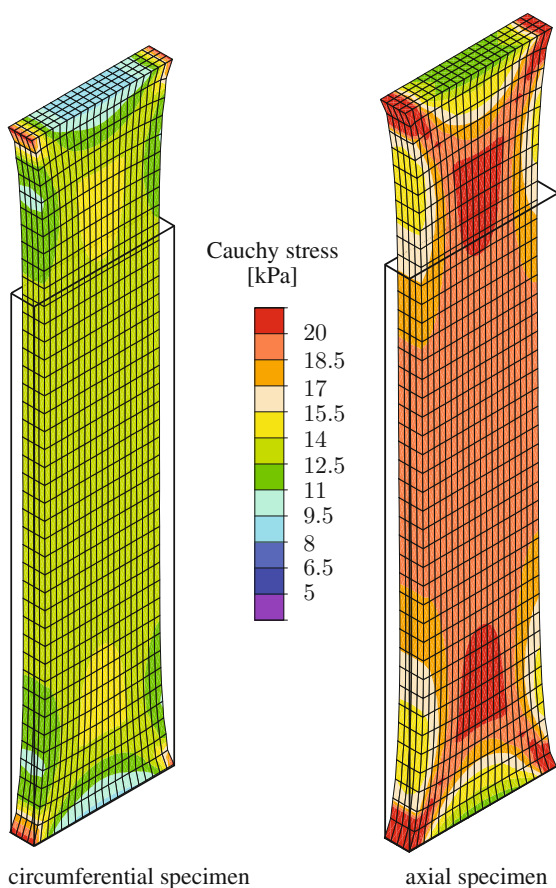
In this section we illustrate the results of a finite element implementation of the constitutive model (255)–(257) in which uniaxial extension tests related to the aforementioned experiments on strips in the circumferential and axial directions of an adventitial layer of a human non-atherosclerotic abdominal aorta are simulated. For the implementation each strip was assumed to have initial length, width and thickness of 10.0, 3.0 and 0.5 mm, respectively, and was subjected to a stretch of 1.3. The ends of each strip were fixed as if in the mounting of a testing machine and

were not allowed to deform, as a result of which the deformation of each strip was nonhomogeneous.

We adopt the material parameters determined in Holzapfel et al. (2015) and take them to be uniform over each strip. The two considered fiber families with symmetric dispersions and mean fiber directions are assumed to make angles φ of $\pm 47.99^\circ$ with the circumferential direction, as indicated in Fig. 33, with dispersion parameters $\kappa_{ip} = 0.116$ and $\kappa_{op} = 0.493$. The implementation, details of which are described in Holzapfel et al. (2015), was performed using the finite element analysis program FEAP (2013). Specifically, numerical results were obtained for the distribution of Cauchy stress component in the direction of the applied stretch for each nonhomogeneous extension, which was fixed at a stretch of 1.3.

The results are illustrated in Fig. 35 for both circumferential and axial specimens. For both specimens the Cauchy stresses were found to be within the range of values determined from the experimental results in Fig. 34. In fact, in the center of each

Fig. 35 Finite element results for circumferential and axial specimens based on data from an adventitia, subjected to a stretch of 1.3. The distribution of the component of the Cauchy stress in the direction of the applied stretch is shown in each case. The undeformed (initial) configuration is indicated by *solid lines*. Reproduced from Fig. 11 of Holzapfel et al. (2015) with permission



specimen the values of the Cauchy stress in the direction of the applied stretch were found to be marginally higher than the stresses at the same value (1.3) of the (homogeneous) stretch noted in Fig. 34. This difference is attributed to the effect of the boundary constraints on the ends.

7 Concluding Remarks

This chapter was in part aimed at illustrating the general value of using nonlinear continuum mechanics as a mathematical modeling framework for describing and predicting the mechanical, in particular the elastic, properties of fibrous soft biological tissues. The approach adopted here is based on the notion of structure tensors, which are used to characterize fiber directions within the tissues. In the present context the starting point was the paper by Holzapfel et al. (2000), which incorporated the fibrous structure into constitutive models of tissues. As more experimental evidence, and more structural information, became available this allowed us to build up the level of complexity of the model, first by incorporating dispersion into the model (Gasser et al. 2006). On the basis of imaging and histology more detailed information on the angular fiber dispersion was revealed in the work of Schriegl et al. (2012), which determined, in particular, various structural parameters, showing that the dispersion is not rotationally symmetric, and these new findings were incorporated into the recent model of Holzapfel et al. (2015). The fact that the structure tensor approach can also be used to incorporate residual stresses into the constitutive theory has also been highlighted. The problem of extension and inflation of an artery, treated simply as a circular cylindrical tube, has been considered throughout the chapter as an example application of the models to a prototype boundary-value problem.

The modeling allows us to define strain-energy functions from which the stress and the elasticity tensors can be computed, and these form the basis for implementing the model within a finite element framework, although this is not the concern of the present chapter. Expressions for the elasticity tensors have not been included here but can be found in, for example, Holzapfel et al. (2015). For a more detailed discussion we refer to Holzapfel (2000). Nevertheless, some examples of the results produced by finite element computations have been illustrated in Sect. 6.

For artery walls many more data are needed to determine finer details of the collagen fiber structure, in particular the dispersion of collagen fibers, and the inelastic behavior of the tissues in both health and disease in order to inform further development of the modeling process. This applies also to a range of other soft biological tissues, in particular those for which the experimental and modeling activities have not thus far been so extensive. *In vivo* data are really needed as a basis for constructing more realistic models of tissue and organ mechanics.

References

- Canham, P.B., Finlay, H.M., Dixon, J.G., Boughner, D.R., Chen, A.: Measurements from light and polarised light microscopy of human coronary arteries fixed at distending pressure. *Cardiovasc. Res.* **23**, 973–982 (1989)
- Chuong, C.J., Fung, Y.C.: Residual stress in arteries. In: Schmid-Schönbein, G.W., Woo, S.L.-Y., Zweifach, B.W. (eds.) *Frontiers in Biomechanics*, pp. 117–129. Springer, New York (1986)
- FEAP. A finite element analysis program, Version 8.4, User manual. University of California at Berkeley, California (2013)
- Finlay, H.M., McCullough, L., Canham, P.B.: Three-dimensional collagen organization of human brain arteries at different transmural pressures. *J. Vasc. Res.* **32**, 301–312 (1995)
- Finlay, H.M., Whittaker, P., Canham, P.B.: Collagen organization in the branching region of human brain arteries. *Stroke* **29**, 1595–1601 (1998)
- Fisher, N.I., Lewis, T.L., Embleton, B.J.J.: *Statistical Analysis of Spherical Data*. Cambridge University Press, Cambridge (1987)
- Fu, Y.B., Ogden, R.W.: *Nonlinear Elasticity: Theory and Applications*. Cambridge University Press, Cambridge (2001)
- Fung, Y.C.: *Biomechanics: Mechanical Properties of Living Tissue*, 2nd edn. Springer, New York (1993)
- Gasser, T.C., Ogden, R.W., Holzapfel, G.A.: Hyperelastic modelling of arterial layers with distributed collagen fibre orientations. *J. R. Soc. Interface* **3**, 15–35 (2006)
- Haughton, D.M., Ogden, R.W.: Bifurcation of inflated circular cylinders of elastic material under axial loading - I. Membrane theory for thin-walled tubes. *J. Mech. Phys. Solids* **27**, 179–212 (1979)
- Hoger, A.: On the residual stress possible in an elastic body with material symmetry. *Arch. Rational Mech. Anal.* **88**, 271–290 (1985)
- Hoger, A.: The constitutive equation for finite deformations of a transversely isotropic hyperelastic material with residual stress. *J. Elast.* **33**, 107–118 (1993)
- Holzapfel, G.A.: *Nonlinear Solid Mechanics. A Continuum Approach for Engineering*. Wiley, Chichester (2000)
- Holzapfel, G.A., Gasser, T.C.: A viscoelastic model for fiber-reinforced materials at finite strains: continuum basis, computational aspects and applications. *Comput. Meth. Appl. Mech. Eng.* **190**, 4379–4403 (2001)
- Holzapfel, G.A., Ogden, R.W. (eds.): *Biomechanics of Soft Tissue in Cardiovascular Systems. CISM Courses and Lectures*, vol. 441. Springer, Wien (2003)
- Holzapfel, G.A., Ogden, R.W. (eds.): *Proceedings of the IUTAM Symposium on Mechanics of Biological Tissue, Graz 2004*. Springer, Heidelberg (2006)
- Holzapfel, G.A., Ogden, R.W.: Constitutive modelling of passive myocardium. A structurally-based framework for material characterization. *Philos. Trans. R. Soc. Lond. A* **367**, 3445–3475 (2009a)
- Holzapfel, G.A., Ogden, R.W. (eds.): *Biomechanical Modelling at the Molecular, Cellular and Tissue Levels. CISM Courses and Lectures*, vol. 508. Springer, Wien (2009b)
- Holzapfel, G.A., Ogden, R.W.: On planar biaxial tests for anisotropic nonlinearly elastic solids. A continuum mechanical framework. *Math. Mech. Solids* **14**, 474–489 (2009c)
- Holzapfel, G.A., Ogden, R.W.: Constitutive modelling of arteries. *Proc. R. Soc. Lond. A* **466**, 1551–1596 (2010)
- Holzapfel, G.A., Ogden, R.W.: On the tension-compression switch in soft fibrous solids. *Eur. J. Mech. A/Solids* **49**, 561–569 (2015)
- Holzapfel, G.A., Gasser, T.C., Ogden, R.W.: A new constitutive framework for arterial wall mechanics and a comparative study of material models. *J. Elast.* **61**, 1–48 (2000)
- Holzapfel, G.A., Sommer, G., Gasser, T.C., Regitnig, P.: Determination of the layer-specific mechanical properties of human coronary arteries with non-atherosclerotic intimal thickening, and related constitutive modelling. *Am. J. Physiol. Heart Circ. Physiol.* **289**, H2048–H2058 (2005)

- Holzapfel, G.A., Niestrawska, J., Ogden, R.W., Reinisch, A.J., Schriefl, A.J.: Modelling non-symmetric collagen fibre dispersion in arterial walls. *J. R. Soc. Interface* **12**, 0188 (2015)
- Humphrey, J.D.: Mechanics of the arterial wall: review and directions. *Crit. Rev. Biomed. Eng.* **23**, 1–162 (1995)
- Humphrey, J.D.: *Cardiovascular Solid Mechanics. Cells, Tissues, and Organs*. Springer, New York (2002)
- Lanir, Y.: Constitutive equations for fibrous connective tissues. *J. Biomech.* **16**, 1–12 (1983)
- Liu, I.-S.: On representations of anisotropic invariants. *Int. J. Eng. Sci.* **20**, 1099–1109 (1982)
- Melnik, A.V., Borja Da Rocha, H., Goriely, A.: On the modeling of fiber dispersion in fiber-reinforced elastic materials. *Int. J. Non-Linear Mech.* **75**, 92–106 (2015)
- Merodio, J., Ogden, R.W.: Material instabilities in fiber-reinforced nonlinearly elastic solids under plane deformation. *Arch. Mech.* **54**, 525–552 (2002)
- Merodio, J., Ogden, R.W.: Instabilities and loss of ellipticity in fiber-reinforced compressible nonlinearly elastic solids under plane deformation. *Int. J. Solids Struct.* **40**, 4707–4727 (2003)
- Merodio, J., Ogden, R.W.: The influence of the invariant I_8 on the stress-deformation and ellipticity characteristics of doubly fiber-reinforced nonlinearly elastic solids. *Int. J. Non-Linear Mech.* **41**, 556–563 (2006)
- Merodio, J., Ogden, R.W., Rodríguez, J.: The influence of residual stress on finite deformation elastic response. *Int. J. Non-Linear Mech.* **56**, 43–49 (2013)
- Ogden, R.W.: *Non-linear Elastic Deformations*. Dover, New York (1997)
- Ogden, R.W.: Nonlinear Elasticity with Application to Material Modelling. Centre of Excellence for Advanced Materials and Structures. Lecture Notes, vol. 6. IPPT, PAN, Warsaw (2003a)
- Ogden, R.W.: Nonlinear elasticity, anisotropy and residual stresses in soft tissue. In: Holzapfel, G.A., Ogden, R.W. (eds.) *Biomechanics of Soft Tissue in Cardiovascular Systems*. CISM Courses and Lectures Series, vol. 441, pp. 65–108. Springer, Wien (2003b)
- Ogden, R.W.: Anisotropy and nonlinear elasticity in arterial wall mechanics. In: Holzapfel, G.A., Ogden, R.W. (eds.) *Biomechanical Modelling at the Molecular, Cellular and Tissue Levels*. CISM Courses and Lectures Series, vol. 508, pp. 179–258. Springer, Wien (2009)
- Ogden, R.W.: Nonlinear elasticity with application to soft fibre-reinforced materials. In: Dorfmann, L., Ogden, R.W. (eds.) *Nonlinear Mechanics of Soft Fibrous Materials*. CISM Courses and Lectures Series, vol. 559, pp. 1–48. Springer, Wien (2015)
- Ogden, R.W., Schulze-Bauer, C.A.J.: Phenomenological and structural aspects of the mechanical response of arteries. In: Casey, J., Bao, G. (eds.) *Mechanics in Biology*. AMD-Vol. 242/BED-Vol. 46. ASME, New York (2000)
- Ogden, R.W., Singh, B.: Propagation of waves in an incompressible transversely isotropic elastic solid with initial stress: Biot revisited. *J. Mech. Mater. Struct.* **6**, 453–477 (2011)
- Schriefl, A.J., Zeindlinger, G., Pierce, D.M., Reginig, P., Holzapfel, G.A.: Determination of the layer-specific distributed collagen fiber orientations in human thoracic and abdominal aortas and common iliac arteries. *J. R. Soc. Interface* **9**, 1275–1286 (2012)
- Shams, M., Destrade, M., Ogden, R.W.: Initial stresses in elastic solids: constitutive laws and acoustoelasticity. *Wave Motion* **48**, 552–567 (2011)
- Spencer, A.J.M.: Theory of invariants. In: Eringen, A.C. (ed.) *Continuum Physics*, vol. 1. Academic Press, New York (1971)
- Spencer, A.J.M.: *Deformations of Fibre-Reinforced Materials*. Oxford University Press, Oxford (1972)
- Spencer, A.J.M.: Constitutive theory for strongly anisotropic solids. In: Spencer, A.J.M. (ed.) *Continuum Theory of the Mechanics of Fibre-Reinforced Composites*. CISM Courses and Lectures Series, vol. 282, pp. 1–32. Springer, Wien (1984)
- Vaishnav, R.N., Vossoughi, J.: Estimation of residual strains in aortic segments. In: Hall, C.W. (ed.) *Biomedical Engineering II: Recent Developments*, pp. 330–333. Pergamon Press, New York (1983)

Microstructure and Mechanics of Human Aortas in Health and Disease

Gerhard A. Holzapfel

Abstract Human aortas are three-layered fibrous composites assembled by a ground matrix and embedded families of dispersed collagen fibers. The microstructural arrangement of the collagen fibers alters due to diseases such as aneurysms. We review a general dispersion model that is required to describe the mechanical response of a variety of collagenous tissues such as aortic walls considering three structural and three material parameters. The dispersion model is used to capture the remarkable differences in the microstructure and mechanics of healthy and aneurysmatic aortas. Related modeling/simulation of an aortic dissection is provided using the recently developed phase-field approach. An energy-based anisotropic failure criterion is used to numerically simulate the evolution of the crack phase-field in a simple shear test. Model parameters are provided and numerical results agree favorably with the experimental findings. Finally, an aortic clamping simulation is described by considering the individual aortic layers, residual stresses, nonsymmetric blood pressure after clamping, patient-specific data and damage-induced inelastic phenomena, i.e., stress softening and permanent deformations.

1 Introduction

The human aorta is an elastic blood vessel which is composed of three distinguishable layers, the intima (tunica intima), the media (tunica media), and the adventitia (tunica externa). In healthy young individuals, the intima is very thin but in old individuals the intima makes a significant contribution to the solid mechanical properties of the aortic wall. In each individual aortic layer, two collagen fiber families are present, and they are helically and almost symmetrically arranged with respect to the vessel

G.A. Holzapfel (✉)
Graz University of Technology, 8010 Graz, Austria
e-mail: holzapfel@tugraz.at

G.A. Holzapfel
Norwegian University of Science and Technology (NTNU),
7491 Trondheim, Norway

axis. In some cases a third and sometimes a fourth collagen family is present in the intima in axial and circumferential directions. This structural arrangement is different in muscular arteries and veins where there is a transition from the helical arrangement to two nearly orthogonal fiber families aligned in the circumferential and axial directions. The material properties of the aorta depend on the network structure of elastin and collagen. Changes in the structural components lead to an alteration of the mechanical aortic response, and play a key role in the pathogenesis of aneurysms.

This book chapter deals with the biomechanics and the related modeling and simulation of aortic walls by considering the collagen microstructure. We focus attention on (i) the aortic wall with nonatherosclerotic intimal thickening, (ii) the structural and mechanical changes that occur during disease progression such as in an aneurysm, (iii) modeling and simulation aspects of aortic dissections, and (iv) the modeling of stress softening and permanent deformations in aortic walls. In Sect. 2 we start by reviewing a recently proposed nonsymmetric collagen fiber dispersion model for arterial walls that is able to capture the significantly different fiber dispersions present in the tangential plane and out-of-plane. This is accommodated with a bivariate von Mises distribution that is used to capture the continuous fiber dispersion throughout the entire thickness, which serves for the construction of a structure tensor. Explicit expressions for the constitutive model are provided which includes several existing dispersion models as special cases such as rotationally symmetric dispersion, perfect collagen alignment, 3D isotropic fiber dispersion, and planar (isotropic) fiber dispersion; two special cases are discussed in this chapter. It should be noted that the general dispersion model reviewed here is needed for describing the mechanical response of a variety of collagenous tissues including cartilage.

In Sect. 3 we continue to provide microstructural and mechanical data for human abdominal aortas and abdominal aortic aneurysms which are then analyzed and compared. Second-harmonic generation imaging after optical clearing is used to identify the collagen microstructure and biaxial stretching tests are performed to identify the related mechanics. The dispersion model is then used to provide two independent dispersion parameters, the angle between the mean fiber direction and the circumferential direction, and the (three) related material parameters. The remarkable differences identified between healthy and diseased tissues are briefly discussed.

The first part of Sect. 4 focuses on the mechanics of aortic dissection providing recently published experimental data obtained from shear tests using aneurysmatic specimens from different thoracic aortas. Data indicate that the ‘in-plane’ shear behavior is significantly different to the ‘out-of-plane’ shear behavior; ultimate shear stresses and the corresponding amounts of shear are also provided. The next part of Sect. 4 deals with failure modeling in aortic dissection using a recently developed phase-field approach. We introduce the deformation map and the crack phase-field at finite strains, and use a regularized crack surface by employing a length-scale parameter which relaxes the sharp crack into a diffusive one. Subsequently, the governing equations of the multifield problem are provided. A special case of the dispersion model from Sect. 2 (perfect collagen alignment) is used as a constitutive descriptor, and the evolution of the crack phase-field is based on an energy-based

anisotropic failure criterion. The final part of Sect. 4 summarizes the finite element formulation by providing the discrete residual vectors and the element matrices for the two subproblems, and it shows the operator-splitting algorithm used to solve the multifield problem composed of a mechanical predictor step and a crack evolution step. Finally, with the phase-field approach simple shear fracture tests are simulated, and elastic and crack phase-field parameters for anisotropic failure are provided.

Section 5 reviews a recently proposed pseudoelastic damage model capturing specific features including anisotropy, nonlinearity, and damage-induced inelastic phenomena (in particular stress softening and permanent deformations) as they occur in cardiovascular treatments such as arterial clamping and balloon angioplasty. From the damage model explicit forms of the stress tensor are derived and material and damage parameters are specified for one sample obtained from intimal strips of a thoracic human aorta. Finite element results (from Abaqus/Standard) of the aortic clamping process are also presented taking account of the three aortic layers, residual stresses, nonsymmetric blood pressure after clamping, and patient-specific data. Section 6 provides some concluding remarks.

2 A Model of Nonsymmetric Collagen Fiber Dispersion

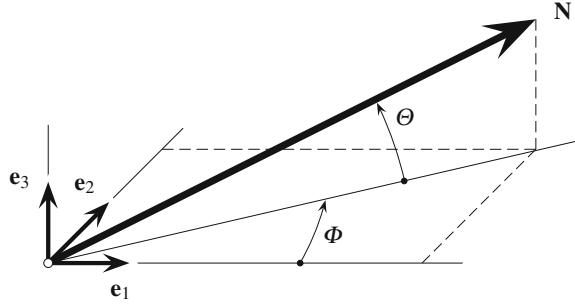
In arterial layers the collagen fiber orientations are nonsymmetrically distributed and their accommodation in a constitutive model can be achieved by (i) a generalized structure tensor (GST) that incorporates a measure of fiber dispersion, or (ii) an angular integration approach in which the strain energy of a single fiber is considered as a function of the fiber stretch, and integrated over a unit sphere to obtain the total free-energy function of the fibers. We follow here the GST approach and summarize a model to capture nonsymmetric fiber dispersion recently proposed by Holzapfel et al. (2015).

2.1 A Measure for In-Plane and Out-of-Plane Fiber Dispersion

A general fiber direction is described by a coordinate system which is characterized by the unit rectangular Cartesian basis vectors $\mathbf{e}_1, \mathbf{e}_2, \mathbf{e}_3$ (see Fig. 1), with the unit vector \mathbf{N} representing a general fiber direction in the (unloaded) reference configuration, defined by the two angles $\Phi \in [0, 2\pi]$ and $\Theta \in [-\pi/2, \pi/2]$. For a circular cylinder \mathbf{e}_1 is taken to be the circumferential direction and \mathbf{e}_3 the radial direction, therefore we refer to Φ and Θ as the in-plane and out-of-plane angles, respectively.

The in-plane and out-of-plane collagen fiber orientations are modeled with a bivariate von Mises distribution $\rho(\Theta, \Phi) = \rho_{ip}(\Phi)\rho_{op}(\Theta)$ for the probability density

Fig. 1 Unit vector \mathbf{N} representing a general fiber direction defined by the angles Φ , Θ with respect to rectangular Cartesian unit basis vectors \mathbf{e}_1 , \mathbf{e}_2 , \mathbf{e}_3 (Holzapfel et al. 2015)



ρ of \mathbf{N} (in-plane and out-of-plane dispersions are essentially independent, see Schriefl et al. 2012), with the particular choice

$$\rho_{\text{ip}}(\Phi) = \frac{\exp[a \cos 2(\Phi \pm \alpha)]}{I_0(a)}, \quad \rho_{\text{op}}(\Theta) = 2\sqrt{\frac{2b}{\pi}} \frac{\exp[b(\cos 2\Theta - 1)]}{\text{erf}(\sqrt{2b})}, \quad (1)$$

where $\rho_{\text{ip}}(\Phi) = \rho_{\text{ip}}(\Phi + \pi)$ and $\rho_{\text{op}}(\Theta) = \rho_{\text{op}}(-\Theta)$ describe the in-plane and out-of-plane dispersions, respectively, a and b are (constant) concentration parameters, $I_0(a)$ is the modified Bessel function of the first kind of order 0 and α is the angle between the mean fiber direction and the circumferential direction \mathbf{e}_1 .

We introduce an in-plane dispersion κ_{ip} (tangential plane of the artery) and an out-of-plane dispersion κ_{op} that turns out to be dependent on the state of disease (Niestrawska et al. 2016). Thus,

$$\kappa_{\text{ip}} = \frac{1}{2} - \frac{I_1(a)}{2I_0(a)}, \quad \kappa_{\text{op}} = \frac{1}{2} - \frac{1}{8b} + \frac{1}{4}\sqrt{\frac{2}{\pi b}} \frac{\exp(-2b)}{\text{erf}(\sqrt{2b})}, \quad (2)$$

where $I_1(a)$ is the modified Bessel function of the first kind of order 1, while $0 \leq \kappa_{\text{ip}} \leq 1$ and $0 \leq \kappa_{\text{op}} \leq 1/2$.

2.2 Constitutive Model

The in-plane and out-of-plane fiber dispersion parameters are now used in structure tensors, one for each fiber family, which we incorporate into the constitutive model. We denote the deformation gradient by \mathbf{F} , the right Cauchy–Green tensor by $\mathbf{C} = \mathbf{F}^T \mathbf{F}$, the Green–Lagrange strain tensor by $\mathbf{E} = (\mathbf{C} - \mathbf{I})/2$ (Holzapfel 2000), and introduce two symmetric fiber families with the (in-plane) mean fiber directions \mathbf{M}_4 and \mathbf{M}_6 according to

$$\mathbf{M}_4 = \cos \alpha \mathbf{e}_1 + \sin \alpha \mathbf{e}_2, \quad \mathbf{M}_6 = \cos \alpha \mathbf{e}_1 - \sin \alpha \mathbf{e}_2, \quad (3)$$

where \mathbf{M}_4 and \mathbf{M}_6 make an angle α with the circumferential direction \mathbf{e}_1 . Furthermore, we introduce the invariants I_1 , I_4 , I_6 , and I_n as

$$I_1 = \text{tr}\mathbf{C}, \quad I_i = \mathbf{C} : \mathbf{M}_i \otimes \mathbf{M}_i, \quad i = 4, 6, \quad I_n = \mathbf{C} : \mathbf{M}_n \otimes \mathbf{M}_n, \quad (4)$$

where \mathbf{M}_n is a unit out-of-plane vector shown in Fig. 2.

Additionally, we introduce two generalized structure tensors \mathbf{H}_4 and \mathbf{H}_6 which describe the material behavior, i.e.,

$$\mathbf{H}_i = A\mathbf{I} + B\mathbf{M}_i \otimes \mathbf{M}_i + (1 - 3A - B)\mathbf{M}_n \otimes \mathbf{M}_n, \quad i = 4, 6, \quad (5)$$

where the constants A and B are

$$A = 2\kappa_{\text{op}}\kappa_{\text{ip}}, \quad B = 2\kappa_{\text{op}}(1 - 2\kappa_{\text{ip}}). \quad (6)$$

The structure tensors \mathbf{H}_i are then incorporated into a decoupled free-energy function Ψ per unit reference volume according to

$$\Psi = \Psi_g(\mathbf{C}) + \sum_{i=4,6} \Psi_{fi}(\mathbf{C}, \mathbf{H}_i) + p\mathbf{I}, \quad (7)$$

where p represents the Lagrange multiplier which enforces incompressibility and \mathbf{I} is the second-order unit tensor. The function Ψ_g represents the ground matrix, i.e.,

$$\Psi_g(\mathbf{C}) = \frac{c}{2}(I_1 - 3), \quad (8)$$

where c is a parameter, and Ψ_{fi} the contribution of the two fiber families to Ψ , i.e.,

$$\Psi_{fi}(\mathbf{C}, \mathbf{H}_i) = \frac{k_1}{2k_2} \left\{ \exp[k_2(I_i^* - 1)^2] - 1 \right\}, \quad i = 4, 6, \quad (9)$$

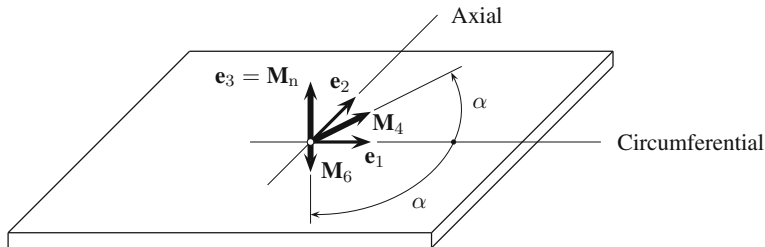


Fig. 2 Sample with two symmetric fiber families with mean fiber directions \mathbf{M}_4 and \mathbf{M}_6 , each making an angle α with the circumferential direction \mathbf{e}_1 . The normal direction to the plane is \mathbf{M}_n (Holzapfel et al. 2015)

with the stress-like parameter $k_1 > 0$, the dimensionless parameter $k_2 > 0$, and the generalized invariants I_i^* defined by

$$I_i^* = \text{tr}(\mathbf{H}_i \mathbf{C}) = AI_1 + BI_i + (1 - 3A - B)I_n, \quad i = 4, 6, \quad (10)$$

which includes the mean fiber directions \mathbf{M}_i in terms of I_i and the two dispersion parameters κ_{ip} and κ_{op} in terms of A and B .

The resulting constitutive model contains three structural parameters (κ_{ip} , κ_{op} , α) to be determined by structural analysis, and three material parameters (c , k_1 , k_2) to be determined by mechanical data.

2.3 Two Special Cases of the Constitutive Model

As one special case we consider transversely isotropic dispersion about \mathbf{M} for which $A = \kappa$ and $B = 1 - 3\kappa$ in (6), where $\kappa \in [0, 1/3]$ is a single dispersion parameter and \mathbf{M} is located in the $(\mathbf{e}_1, \mathbf{e}_2)$ plane according to Fig. 2. Hence, Eq. (5) reduces to one structure tensor of the form

$$\mathbf{H} = \kappa \mathbf{I} + (1 - 3\kappa) \mathbf{M} \otimes \mathbf{M}, \quad (11)$$

as proposed by Gasser et al. (2006).

Another special case which is of interest for this chapter is the one where all collagen fibers are perfectly aligned in the in-plane direction of \mathbf{M} (no dispersion in either plane), which corresponds to $A = 0$ and $B = 1$ in (6), and Eq. (5) reduces to

$$\mathbf{H} = \mathbf{M} \otimes \mathbf{M}, \quad (12)$$

as proposed by Holzapfel et al. (2000), the HGO model. For the case $a = b = 0$ the dispersion is isotropic in each plane, and $\kappa_{\text{ip}} = 1/2$ and $\kappa_{\text{op}} = 1/3$.

The constitutive model (9) with (10) includes several other special cases which are discussed in detail in Holzapfel et al. (2015).

3 Microstructure and Mechanics of Abdominal Aortas

One goal of this section is to provide a novel parameter set for the constitutive model as introduced in the previous section. The parameters consist of microstructural 3D collagen orientation and dispersion which are linked to mechanical parameters. Values for the parameters are reported as medians and interquartile ranges, and are based on tissue samples from 17 human abdominal aortas (AA) and samples from 11 abdominal aortic aneurysms (AAA). The collagen microstructure of all samples was examined by analyzing data obtained from second-harmonic generation (SHG)

imaging after optical clearing according to the protocol documented in Schriefl et al. (2013), while the mechanical investigation was performed using biaxial stretching tests. It is important to note that SHG imaging yields a continuous distribution of the collagen fabric throughout the thickness without destroying the tissue. The results highlight remarkable differences between healthy (AA) and diseased (AAA) tissues and the need to incorporate the significantly different AAA wall structure into the constitutive model.

3.1 Data for Healthy Abdominal Aortas

Seventeen human abdominal aortas with nonatherosclerotic intimal thickening (63 ± 11 (SD) yr, range 45–84), were harvested as intact tubes within 24 h of death and stored in 0.9 % physiological saline solution at 4 °C until testing. Small samples were acquired for SHG imaging and mechanical testing according to the protocol detailed in Niestrawska et al. (2016).

The layers displayed a highly organized structure both in the tangential plane and through the thickness of the aortic wall. Figure 3a shows representative SHG images of one AA sample; the three images (top) display in-plane sections of the ‘carpet-like’ structure in the intima (I), two families of fibers in the media (M) and wavy and thicker fiber bundles in the adventitia (A), while the image below displays the structure through the thickness ((I) on the left). The intensity plot of Fig. 3b depicts the collagen fiber orientation and dispersion through the aortic wall.

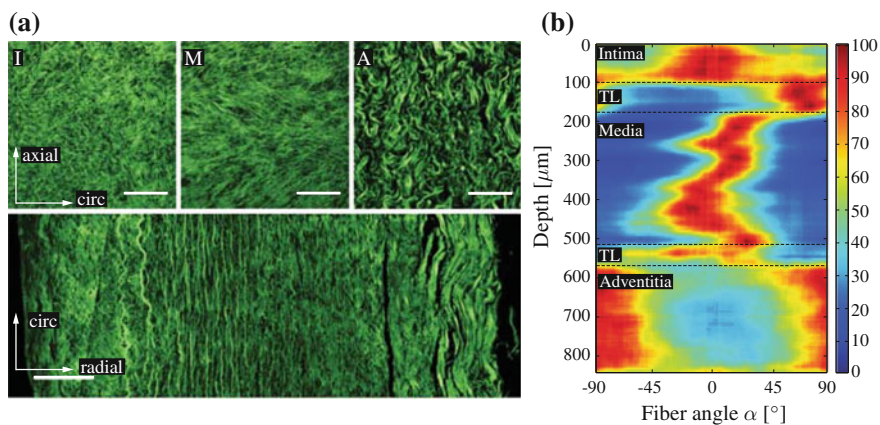


Fig. 3 Representative structure of a healthy abdominal aorta: **a** three SHG images (top) show in-plane sections of the intima (I), media (M) and adventitia (A), while the image below shows a view through the thickness, scale bar is 100 μm ; **b** intensity plot shows collagen structure through the depth of the wall (TL = transition layer): dark red depicts preferred fiber directions, blue relates to no distinguished orientations (Niestrawska et al. 2016)

A fiber angle of 0° denotes the circumferential direction, whereas 90° denotes the axial direction. Dark red depicts preferred fiber directions, whereas blue shows no distinguished orientations. In the intensity plot the (I) shows a strong dispersion around the circumferential direction that is followed by a transition layer (TL) (rapid orientation change of collagen fibers toward the axial direction), which then changes back to the circumferential direction in the (M). The images show two counter-rotating fiber families around the circumferential direction. Another TL in the region of the membrana elastica externa is reached displaying the transition of thinner media collagen to thicker wavy collagen fiber bundles in the (A), appearing in two fiber families and being oriented more toward the axial direction.

The structural parameters κ_{ip} , κ_{op} , and α for the abdominal aorta samples were averaged over the thickness of the separate layers. Together with the material parameters c , k_1 , and k_2 they are summarized in Table 1. In-plane fibers were slightly more aligned in the media ($\kappa_{ip} = 0.208 \pm 0.090$) when compared with the intima; there was no significant difference between the alignment in the media compared with the adventitia. The out-of-plane dispersion κ_{op} was rather low in all three healthy layers. The median of R^2 for c , k_1 , and k_2 was 0.95, 0.98, 0.95, and 0.96 for the intima, media, adventitia, and the intact AA wall, respectively. The intima showed a relatively short toe region with a rapid stiffening at a low stretch, as also documented in Weisbecker et al. (2012), whereas the adventitia was rather compliant ($c = 3.77$, $k_1 = 0.36$), which stiffened at higher stretches, displaying a significantly higher k_2 value in comparison with the media and the intact wall ($k_2 = 45.88$). With the structural parameters fixed the material model was fitted to mechanical experimental data, giving a very good fit although there are only three material parameters.

3.2 Data for Abdominal Aortic Aneurysms

An abdominal aortic aneurysm (AAA) is a localized and irreversible dilation of the aorta, as described by, e.g., Vorp (2007) and Humphrey and Taylor (2008). Continuous AAA growth may lead to wall rupture, an event frequently related to mortality and life threatening morbidity if not addressed (Fleming et al. 2005). The underlying pathogenesis has not yet been fully clarified (Humphrey and Holzapfel 2012).

Eleven wall samples from AAAs (69 ± 8 (SD) yr; range 53–76) were harvested from open aneurysm repair and stored in Dulbecco's Modified Eagle's Medium at 4°C until testing. Except for one sample, specific layers within the AAA wall could not be identified unlike for healthy AA walls, and even in samples without obvious atherosclerotic alterations the structure was remarkably different from those obtained from AAs. A substantial variability in fiber architecture, fiber diameter, and waviness could be identified, even within the same AAA sample. In general, samples showed a degenerated luminal layer, calcification and sometimes small fat cells, and a deposition of aggregated parallel collagen sheets oriented more toward the circumferential direction. Also cystic medial degeneration could be seen, including

Table 1 Medians and interquartile ranges of the structural parameters (κ_{ip} , κ_{op} , α) and the material parameters (c , k_1 , k_2) with coefficient of determination (R^2) for intima, media, adventitia and intact wall of the abdominal aortas determined from SHG images and biaxial stretching tests

	Intima		Media		Adventitia		Intact Wall	
	Median	[Q1; Q3]	Median	[Q1; Q3]	Median	[Q1; Q3]	Median	[Q1; Q3]
κ_{ip}	0.261 (n = 7)	[0.214; 0.283] (n = 17)	0.208 (n = 17)	[0.165; 0.255] (n = 16)	0.232 (n = 17)	[0.192; 0.282] (n = 7)	0.237 (n = 7)	[0.212; 0.287]
κ_{op}	0.484 (n = 17)	[0.468; 0.488] (n = 17)	0.487 (n = 17)	[0.481; 0.489] (n = 17)	0.466 (n = 17)	[0.459; 0.479] (n = 17)	0.479 (n = 17)	[0.473; 0.482]
α	3.25° (n = 7)	[1.09; 6.13] (n = 17)	6.91° (n = 17)	[5.269; 9.715] (n = 16)	77.53° (n = 16)	[67.04; 84.02] (n = 7)	24.46° (n = 7)	[22.45; 30.18]
c	33.86 (n = 4)	[6.88; 98.76] (n = 9)	16.08 (n = 9)	[10.34; 30.52] (n = 9)	3.77 (n = 9)	[2.18; 4.97] (n = 9)	11.59 (n = 7)	[4.13; 19.93]
k_1	7.79 (n = 4)	[4.90; 55.00] (n = 9)	11.68 (n = 9)	[2.32; 22.81] (n = 9)	0.36 (n = 9)	[0.06; 1.70] (n = 7)	2.66 (n = 7)	[1.15; 11.64]
k_2	139.1 (n = 4)	[41.95; 243.31] (n = 9)	7.18 (n = 9)	[2.94; 22.78] (n = 9)	45.88 (n = 9)	[21.10; 69.85] (n = 9)	19.25 (n = 7)	[9.93; 26.06]
R^2	0.95	[0.93; 0.98]	0.98	[0.07; 0.99]	0.95	[0.84; 0.97]	0.96	[0.94; 0.97]

The parameters c and k_1 are provided in [kPa], while all others are dimensionless; n indicates the number of samples

larger adipocytes. For the structural analysis only those images were considered which did *not* show calcification or lipid adipocytes.

Figure 4a displays the only sample (AAA-6) with a microarchitecture comparable to a healthy wall. The intensity plot on the side shows a rather isotropic structure for the intima until a depth of about 400 μm , while the media shows straight collagen fibers resulting in high and narrow intensities, while the collagen fibers in the abluminal layers lost their waviness and exhibited rather straight and thick struts of collagen. Figure 4b shows two patches taken from adjacent locations of sample AAA-4 and displays an intact abluminal layer (AL) similar to a healthy adventitia layer, while no media was visible in this sample. The upper left image (LL-1) (where (LL) stands for

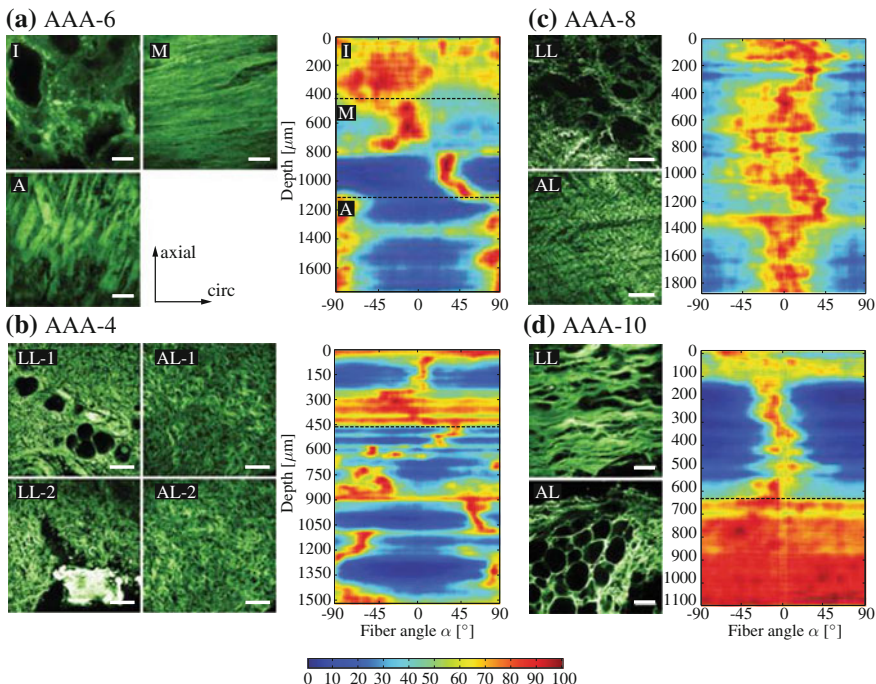


Fig. 4 SHG images and intensity plots for AAA samples: **a** layered structure (I: intima, M: Media, A: Adventitia), the only AAA sample to exhibit a layer-specific character. The intensity plot shows three distinct layers—a rather calcified (I), two fiber families in (M) and (A); **b** structure of luminal layer (LL) and abluminal layer (AL) of two patches taken from adjacent locations ($-1, -2$) displaying differences. The lower left image (LL-2) shows wavy collagen fibers and calcification. The first 450 μm in the intensity plot shows a highly disturbed structure followed by an adventitia-like structure with two alternating fiber families; **c** collagen structure in (LL) and (AL). The intensity plot shows collagen preferably oriented toward the circumferential direction throughout the wall; **d** ruptured sample exhibiting a (LL) with a highly oriented collagen structure and a significant number of adipocytes toward the (AL) side. The intensity plot shows a collagen structure highly oriented toward the circumferential direction followed by a rather isotropic (AL). All intensity plots start at the top with the (LL). Scale bar is 100 μm (Niestrawska et al. 2016)

Table 2 Medians and interquartile ranges of the structural parameters (κ_{ip} , κ_{op} , α) and the material parameters (c , k_1 , k_2) with coefficient of determination (R^2), referring to the material parameters, for AAA walls determined from SHG images and biaxial stretching tests; n indicates the number of samples

	κ_{ip}	κ_{op}	α	c (kPa)	k_1 (kPa)	k_2 (-)	R^2
Median	0.229	0.438	13.97	1.58	2.84	57.17	0.94
[Q1; Q3]	[0.209; 0.268]	[0.409; 0.455]	[9.998; 22.85]	[0.57; 2.56]	[0.92; 5.49]	[28.54; 100.07]	[0.90; 0.98]
n	11	11	11	10	10	10	-

luminal layer) shows bright ‘stains’ representing a degenerated collagen structure, and the lower left image (LL-2) displays an adjacent region in the same luminal layer exhibiting a different structure with wavy collagen fibers and calcification. The first 450 μm in the intensity plot indicates a disturbed structure merging into two alternating fiber families. Figure 4c shows the (AL) of sample AAA-8 with thickened collagen struts, still wavy but oriented more toward the circumferential direction, while toward the (LL) the fibers became thinner, merging into a disturbed collagen structure. The intensity plot on the side shows fibers preferably oriented toward the circumferential direction throughout the wall. Figure 4d shows a ruptured sample with a significant amount of cystic medial degeneration, infiltrated with adiposities in the (AL), preceded by a highly organized collagen structure in the (LL) oriented more toward the circumferential direction. The (AL) is rather isotropic as can be seen from the intensity plot.

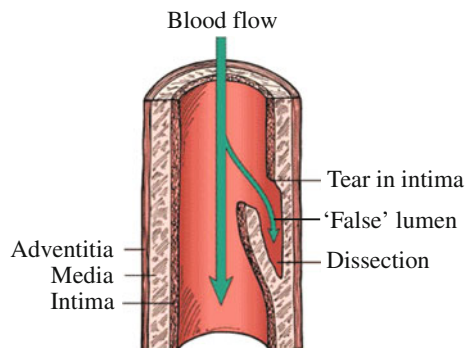
The medians and interquartile ranges of the structural and material parameters for the AAA walls are summarized in Table 2. All AAA samples with the exception of one, which was ruptured, showed a similarly high alignment of collagen fibers with a median of $\kappa_{\text{ip}} = 0.229$, and the in-plane dispersion did not show any statistical difference with respect to intact AA walls, compare with Table 1. However, the out-of-plane dispersion was significantly higher in AAA samples in comparison with the healthy AA samples (lower dispersion parameter κ_{op} for AAA walls). Finally, when compared with intact AA walls, AAA samples showed a statistically smaller angle α , see Table 1. The parameter c for AAA walls was significantly lower in comparison to AA walls. However, the dimensionless parameter k_2 with 57.17, resembling the exponential stiffening of the loading curves due to the collagen fibers, was significantly higher than for AA walls ($k_2 = 19.25$). Interestingly, by comparing the adventitia of AAs with AAA tissue the k_2 value was not significantly different between the two groups, however, AAA tissue differed significantly in both the c value and the k_1 value with respect to the adventitia of AAs.

4 Mechanics, Modeling, and Simulation of Aortic Dissection

Aortic dissection is a severe vascular pathology which may occur spontaneously or nonspontaneously as a result of trauma. The annual occurrence of aortic dissection is about 5–30 cases per million of the population (Davies et al. 2002; Knipp et al. 2007); however, the mortality rate during the first 24–48 h is high if patients are not treated appropriately.

Frequently, an aortic dissection initiates from an intimal tear (Thubrikar et al. 1999) or from a perforation of the intima caused by intramural hemorrhage and hematoma formation (Khan and Nair 2002). This kind of intimal defect may continue propagating along the radial direction to the media, and may cause a delamination of the media or delaminate the media from the adventitia. One clinical consequence

Fig. 5 Aortic dissection: the intima of the aorta tears, and the tear spreads into the media or between the media and adventitia creating a ‘false lumen’ (Holzapfel 2009)



may be the creation of a ‘false lumen’, which affects the hemodynamics and changes the stress distribution of the underlying wall. The false lumen narrows the true lumen and decreases oxygen supply from the blood to the tissues. As a result, the mechanical properties and the structural stability of the local aortic wall may also alter. Most factors contributing to the initiation of dissection are trauma-related; other predisposing factors can be pathological changes due to hypertension and atherosclerosis (Pratt and Curci 2010), but also inherited diseases such as Marfan syndrome and Ehlers–Danlos syndrome may lead to a ruined aortic wall. For a schematic sketch of an aortic dissection, see Fig. 5.

Aortic dissection is fatal when running to the adventitial side causing an acute rupture of the wall which is relatively rare (Criado 2011). Biomechanically, a dissection is primarily attributed to intralamellar failure of the main load-bearing microstructural components within the wall, i.e., elastin and collagen fibers (Pal et al. 2014). For a recent review of the key advances in the mechanical characterization of tissue dissection in health and disease from the experimental and modeling point of view, also focusing on the microstructure and morphology of dissected tissues, see Tong et al. (2016). It is important to better understand the intrinsic mechanism in propagating a dissection through an aortic tissue, which is basically a biomechanical process. In this section, we briefly discuss the mechanical strength of aortic tissues undergoing a dissection, then the related continuum modeling and finally we propose a novel approach to simulate 3D aortic dissection using the finite element method.

4.1 Mechanics of Aortic Dissection

Biomechanical data of aortic dissections have the potential to provide more insight and to be helpful in related surgical treatments. Compared to healthy aortic tissues, aneurysmal aortic dissections are rarely studied from the biomechanical point of view. Using the same experimental protocol as Sommer et al. (2008) (peeling tests), it seems

that the first study was conducted by Pasta et al. (2012) who quantified/compared the dissection properties of nonaneurysmal with aneurysmal human ascending thoracic aortas with bicuspid/tricuspid aortic valve morphology. The results indicate that aneurysmal tissues have a significantly lower delamination strength than tissues from nonaneurysmal thoracic aortas. During peeling tests, as performed by Pasta et al. (2012), rupture of elastin and collagen fibers is mainly caused by tensile stresses. Consequently, peeling tests provide little information about the role of shear stresses in the formation of aortic dissection.

The recent study of Sommer et al. (2016) developed a novel biomechanically based approach for characterizing dissection pattern of tissues and failure modes in response to shear deformation in different orientations. All tests were conducted with an extension rate of 1.0 mm/min. Figure 6a, b shows the ‘in-plane’ shear stress versus the amount of shear behavior for 9 successfully tested aneurysmatic specimens (obtained

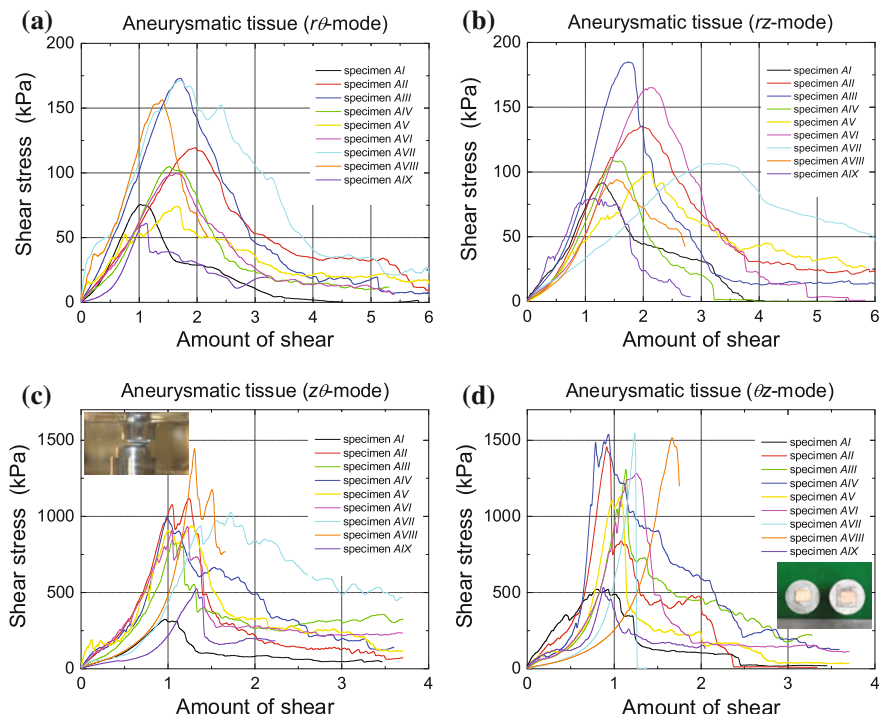


Fig. 6 Cauchy shear stress versus amount of shear relationship during shear tests of 9 aneurysmatic specimens from different thoracic aortas: **a, b** ‘in-plane’ shear behavior in the circumferential ($r\theta$ -mode) and longitudinal (rz -mode) directions of the aorta; **c, d** ‘out-of-plane’ shear behavior in the circumferential ($z\theta$ -mode) and longitudinal (θz -mode) directions of the aorta. The photographs show a specimen subjected to simple shear loading and ruptured into two parts (modified from Sommer et al. 2016)

Table 3 Ultimate shear stress τ^u and corresponding amount of shear γ^u for 9 aneurysmatic specimens (from different thoracic aortas) subjected to ‘in-plane’ shear in the circumferential ($r\theta$ -mode) and longitudinal (rz -mode) directions of the aorta, and ‘out-of-plane’ shear in the circumferential ($z\theta$ -mode) and longitudinal (θz -mode) directions of the aorta

Specimen	‘In-plane’ shear				‘Out-of-plane’ shear			
	$\tau_{r\theta}^u$ (kPa)	$\gamma_{r\theta}^u$ (-)	τ_{rz}^u (kPa)	γ_{rz}^u (-)	$\tau_{z\theta}^u$ (kPa)	$\gamma_{z\theta}^u$ (-)	$\tau_{\theta z}^u$ (kPa)	$\gamma_{\theta z}^u$ (-)
I	76	1.02	92	1.30	325	0.97	528	0.94
II	120	1.97	135	1.98	1122	1.24	1467	0.92
III	105	1.53	109	1.49	860	1.05	1349	1.14
IV	173	1.71	185	1.74	1011	0.99	1563	0.79
V	74	1.63	100	2.12	946	1.27	1138	1.08
VI	100	1.63	165	2.13	947	1.23	1292	1.26
VII	173	1.73	106	3.14	1035	1.74	1565	1.24
VIII	157	1.40	94	1.55	1479	1.31	1529	1.67
IX	61	1.12	80	1.15	533	1.33	548	0.88
Mean	115	1.53	118	1.84	918	1.24	1221	1.10
SD	41	0.28	34	0.56	313	0.22	388	0.25

from different thoracic aortas) in the circumferential ($r\theta$ -mode) and longitudinal (rz -mode) directions of the aorta, while Fig. 6c, d shows the corresponding results of the ‘out-of-plane’ shear tests in the circumferential ($z\theta$ -mode) and longitudinal (θz -mode) directions. In Table 3 ultimate shear stresses and corresponding amount of shear values of the aneurysmatic tissues are listed.

Interestingly, in comparison with ‘in-plane’ shear tests, ‘out-of-plane’ shear tests exhibited much higher ultimate shear stress values (about a factor of 10!). Consequently, aortic tissues indicate a much higher resistance to rupture under ‘out-of-plane’ shear loading than under ‘in-plane’ shear loading. Most tissue specimens (except VII and VIII) revealed higher ultimate shear stresses in the longitudinal direction when compared with the circumferential direction under ‘in-plane’ shear loading, while all specimens showed higher ultimate stresses in the longitudinal direction with respect to the circumferential direction under ‘out-of-plane’ shear loading (Table 3). Hence, all shear tests showed significant anisotropic failure properties. Recently Haslach Jr. et al. (2015) also performed shear tests on rectangular aortic wall blocks observing that interstitial fluid is redistributed with shear deformation which suggests that no simple modification of classical rupture theories suffices to predict the rupture of hydrated soft biological tissue.

4.2 Modeling Failure in an Aortic Dissection Using the Phase-Field Approach

4.2.1 Ginzburg–Landau Type Phase-Field Model for Diffusive Cracks

We introduce a material body $\mathcal{B} \subset \mathbb{R}^3$ at time $t_0 \in \mathbb{R}$, the reference configuration, and denote $\mathbf{X} \in \mathcal{B}$ as the material point. The placement of the body at $t \in \mathbb{R}$ we refer to as spatial configuration $\mathcal{S} \subset \mathbb{R}^3$ so that a material point $\mathbf{X} \in \mathcal{B}$ is mapped to the spatial point $\mathbf{x} \in \mathcal{S}$ by the deformation map $\varphi(\mathbf{X}, t)$, subsequently considered as a primary field variable. Next, we let $\partial\mathcal{B} \subset \mathbb{R}^2$ be the surface of $\mathcal{B} \subset \mathbb{R}^3$. Finally, we introduce the crack phase-field $d(\mathbf{X}, t) \in [0, 1]$, an additional primary field variable, where $d = 0$ characterizes an intact material, while $d = 1$ the ruptured state of a material.

Let us now introduce the field equation for the crack phase-field in 1D and assume an infinitely long 1D bar with a crack at $x = 0$. The crack phase-field $d(x) \in [0, 1]$ characterizes the crack topology with

$$d(x) = \delta(x) : \begin{cases} 1 & \text{for } x = 0, \\ 0 & \text{otherwise,} \end{cases} \quad (13)$$

where $\delta(x)$ is the Kronecker delta function, see Fig. 7a. This sharp crack topology may be approximated by a diffusive crack topology by

$$d(x) = \exp(-|x|/l), \quad (14)$$

where l is the length-scale parameter regularizing the sharp crack topology. This makes the crack spread over the whole length of the bar, see Fig. 7b. Relation (14) is the solution of the homogeneous ordinary differential equation (Miehe et al. 2010)

$$d(x) - l^2 d''(x) = 0, \quad (15)$$

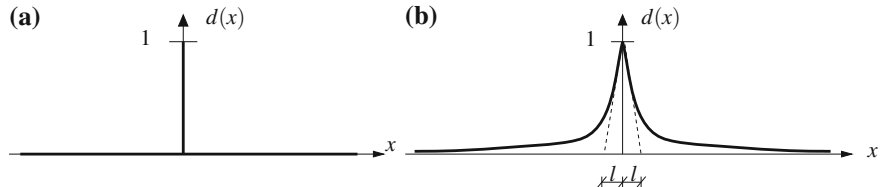


Fig. 7 **a** Sharp crack topology described by $d(x) = \delta(x)$ for vanishing length-scale parameter $l \rightarrow 0$; **b** diffusive crack topology $d(x) = \exp(-|x|/l)$ with length-scale parameter equal to l (Gultekin et al. 2016)

subjected to the Dirichlet-type boundary conditions $d(0) = 1$ and $d(\pm\infty) = 0$. An equivalent functional form may be given as

$$I(d) = \frac{1}{2} \int_{\mathcal{B}} (d^2 + l^2 d'^2) dx. \quad (16)$$

By scaling functional (16) with l we may define the crack surface density per unit length as

$$\gamma(d, d') = \frac{1}{2l} (d^2 + l^2 d'^2). \quad (17)$$

The multidimensional formulation of the cracking in solids may be achieved in a similar way to the 1D motivation. In particular, the analogue of Eq. (15) can be written as

$$d - l^2 \Delta d = 0 \quad \text{in } \mathcal{B} \quad \text{and} \quad \nabla d \cdot \mathbf{N} = 0 \quad \text{on } \partial \mathcal{B}, \quad (18)$$

where Δd signifies the Laplacian of the crack phase-field, and \mathbf{N} is the unit surface normal oriented outward in the reference configuration. For a detailed derivation see Güttekin (2014). The analogue of Eq. (17) in 3D is the volume-specific crack surface density

$$\gamma(d, \nabla d) = \frac{1}{2l} (d^2 + l^2 |\nabla d|^2). \quad (19)$$

4.2.2 Governing Equations of the Multifield Problem

As a point of departure we define the energy storage functional for the (elastic) anisotropic tissue as

$$E(\boldsymbol{\varphi}, d) = \int_{\mathcal{B}} \Psi(\mathbf{C}, \mathbf{H}_t; d) dV \quad (20)$$

in terms of the free-energy function Ψ for a degrading tissue, with

$$\Psi(\mathbf{C}, \mathbf{H}_t; d) = g(d) \Psi_0(\mathbf{C}, \mathbf{H}_t), \quad (21)$$

where Ψ_0 is the effective free-energy function of the hypothetical tissues as, e.g., provided in (7). A monotonically decreasing quadratic degradation function

$$g(d) = (1 - d)^2 \quad (22)$$

describes the degradation of the tissue with the evolving crack phase-field parameter d , with the following growth conditions:

$$g'(d) \leq 0 \quad \text{with} \quad g(0) = 1, \quad g(1) = 0, \quad g'(1) = 0. \quad (23)$$

The first condition ensures degradation, while the second and third conditions set the limits for the intact and the ruptured state, and the final condition ensures the saturation at $d \rightarrow 1$.

Time derivative of (20) gives the rate of energy storage functional

$$\mathcal{E}(\dot{\phi}, \dot{d}; \phi, d) = \int_{\mathcal{B}} (\mathbf{S} : \dot{\mathbf{E}} - f \dot{d}) dV, \quad (24)$$

with

$$\mathbf{S} = 2 \frac{\partial \Psi(\mathbf{C}, \mathbf{H}_i; d)}{\partial \mathbf{C}}, \quad f = - \frac{\partial \Psi(\mathbf{C}, \mathbf{H}_i; d)}{\partial d}, \quad (25)$$

where \mathbf{S} is the second Piola–Kirchhoff stress tensor and f is the energetic force which is work conjugate to the crack phase-field d . The external power functional can be described as

$$\mathcal{P}(\dot{\phi}) = \int_{\mathcal{B}} \rho_0 \bar{\gamma} \cdot \dot{\phi} dV + \int_{\partial \mathcal{B}_t} \bar{\mathbf{T}} \cdot \dot{\phi} dA, \quad (26)$$

where ρ_0 , $\bar{\gamma}$, and $\bar{\mathbf{T}}$ are the density, the prescribed body force, and the surface traction in the reference configuration, respectively.

Next, we define the crack energy functional D_c using the volume-specific crack surface density (19), i.e.,

$$D_c(d) = \int_{\mathcal{B}} g_c \gamma(d, \nabla d) dV, \quad (27)$$

where g_c denotes the critical fracture energy required to convert an uncracked tissue into a cracked tissue. The evolution of (27) yields the crack dissipation functional \mathcal{D} according to

$$\mathcal{D}(\dot{d}) = \int_{\mathcal{B}} g_c [\delta_d \gamma(d, \nabla d)] \dot{d} dV, \quad (28)$$

where $\delta_d \gamma$ denotes the variational derivative of the crack surface density γ (Miehe et al. 2010), with the explicit form

$$\delta_d \gamma = \frac{1}{l} (d - l^2 \Delta d). \quad (29)$$

According to the second law of thermodynamics the dissipation functional has to be nonnegative for all admissible deformation processes, i.e., $\mathcal{D} \geq 0$.

Finally, we provide the variational formulation based on the power balance which is obtained from the stated functionals (24), (26), and (28), i.e.,

$$\Pi(\dot{\phi}, \dot{d}) = \mathcal{E}(\dot{\phi}, \dot{d}) + \mathcal{D}(\dot{d}) - \mathcal{P}(\dot{\phi}) = 0. \quad (30)$$

On the basis of (30), a rate-type mixed variational principle can be constructed via a minimization principle for the quasi-static process, i.e.,

$$\{\dot{\phi}, \dot{d}\} = \text{Arg} \left\{ \inf_{\dot{\phi} \in \mathcal{W}_{\dot{\phi}}} \inf_{\dot{d} \in \mathcal{W}_{\dot{d}}} \Pi(\dot{\phi}, \dot{d}) \right\}, \quad (31)$$

with the admissible domains for the state variables

$$\mathcal{W}_{\dot{\phi}} = \{\dot{\phi} \mid \dot{\phi} = \mathbf{0} \text{ on } \partial \mathcal{B}_{\dot{\phi}}\}, \quad \mathcal{W}_{\dot{d}} = \{\dot{d} \mid \dot{d} = 0 \text{ on } \partial \mathcal{B}_{\dot{d}}\}. \quad (32)$$

The variation of the functional leads to the Euler–Lagrange equations which describe the multifield problem for the fracture of an anisotropic tissue, i.e.,

$$\text{Div}(\mathbf{F}\mathbf{S}) + \rho_0 \bar{\gamma} = \mathbf{0}, \quad (f - g_c \delta_d \gamma) \dot{d} = 0, \quad (33)$$

along with the loading–unloading conditions ensuring the principal of maximum dissipation during evolution of d . Thus,

$$\dot{d} \geq 0, \quad f - g_c \delta_d \gamma \leq 0, \quad (f - g_c \delta_d \gamma) \dot{d} = 0. \quad (34)$$

The first condition ensures the irreversibility of the evolution of the crack phase-field parameter. The second condition is an equality for evolving a crack, and it is negative for a stable crack. The third condition is the balance law for the evolution of the crack phase-field subject to the former conditions.

4.2.3 Constitutive Equations, Failure Criterion

For the numerical example provided in the next section, we use a simple constitutive equation. In particular, we use $A = 0$ and $B = 1$ in (10) so that $I_4^* = I_4$ and $I_6^* = I_6$, a case with perfectly aligned collagen fibers with the structure tensor given by (12). Hence, to describe the mechanical response of the intact aortic tissue the free-energy function Ψ_0 in (21) is specified as

$$\Psi_0 = \Psi_0^{\text{iso}}(J, I_1) + \Psi_0^{\text{ani}}(I_4, I_6), \quad (35)$$

where

$$\Psi_0^{\text{iso}}(J, I_1) = \bar{\kappa}(J - \ln J - 1) + \frac{\mu}{2}(I_1 - 2\ln J - 3), \quad (36)$$

is an isotropic function representing the mechanical behavior of the ground matrix, while

$$\Psi_0^{\text{ani}}(I_4, I_6) = \frac{k_1}{2k_2} \sum_{i=4,6} \{\exp[k_2(I_i - 1)^2] - 1\}, \quad (37)$$

is an exponential anisotropic free-energy function taking into account the contributions of the collagen fibers (Holzapfel et al. 2000), while $J = \det \mathbf{F} > 0$ denotes the volume ratio. In (36) $\bar{\kappa}$ denotes the penalty parameter whereas μ is the shear modulus. In the anisotropic terms k_1 and k_2 stand for a stress-like material parameter and a dimensionless parameter, respectively. The anisotropic functions should only contribute when the fibers are extended, that is when $I_4 > 1$ or $I_6 > 1$. If one or more of these conditions is not satisfied then the relevant part of the anisotropic function is omitted. If, for example, I_4 and I_6 are less than or equal to 1, then the tissue response is purely isotropic. Based on this constitutive descriptor it is straightforward to derive the related stress and elasticity tensors.

Finally, we provide a novel energy-based anisotropic failure criterion that portrays the tissue state at which the cracking starts and propagates. In order to describe anisotropic failure, we further elaborate on the equation for the evolution of d using (33)₂ with (29), and (25)₂ with (21), (22) for $\dot{d} \geq 0$, i.e.,

$$f - \frac{g_c}{l}(d - l^2 \Delta d) = 0, \quad f = 2(1 - d)\Psi_0. \quad (38)$$

We assume distinct failure processes for the ground matrix and the collagen fibers, i.e.,

$$2(1 - d)\Psi_0^{\text{iso}} - \frac{g_c^{\text{iso}}}{l}(d - l^2 \Delta d) = 0, \quad 2(1 - d)\Psi_0^{\text{ani}} - \frac{g_c^{\text{ani}}}{l}(d - l^2 \Delta d) = 0, \quad (39)$$

dual to the free-energy functions for the isotropic and the anisotropic parts, respectively, see (35). In (39) we have introduced the critical fracture energies g_c^{iso} and g_c^{ani} which relate to the isotropic ground matrix and the anisotropic fiber contribution, respectively. We now introduce the dimensionless crack driving function $\tilde{\mathcal{H}}$, which we additively decompose according to

$$\tilde{\mathcal{H}} = \tilde{\mathcal{H}}^{\text{iso}} + \tilde{\mathcal{H}}^{\text{ani}}, \quad \tilde{\mathcal{H}}^{\text{iso}} = \frac{\Psi_0^{\text{iso}}}{g_c^{\text{iso}}/l}, \quad \tilde{\mathcal{H}}^{\text{ani}} = \frac{\Psi_0^{\text{ani}}}{g_c^{\text{ani}}/l}, \quad (40)$$

where $\tilde{\mathcal{H}}^{\text{iso}}$ relates to the isotropic part and $\tilde{\mathcal{H}}^{\text{ani}}$ to the anisotropic part.

By superposing the isotropic and anisotropic failure processes (39), and with the use of (40), we obtain

$$d - l^2 \Delta d = (1 - d)\tilde{\mathcal{H}}. \quad (41)$$

The left-hand side of this relationship is the geometric resistance to crack growth whereas the right-hand side is the local source term for crack growth (Raina and Miehe 2016). To enforce the irreversibility condition and prevent healing effects, the dimensionless source term (40) is recast as

$$\mathcal{H}(t) = \max_{s \in [0, t]} [\langle \bar{\mathcal{H}}(s) - 1 \rangle], \quad (42)$$

with the Macaulay brackets $\langle (\bullet) \rangle = [(\bullet) + |(\bullet)|]/2$. Hence, d does not evolve for a dimensionless crack source term $\bar{\mathcal{H}}(s) < 1$. The specific choice for $\mathcal{H}(t)$ in (42) ensures irreversibility of the crack evolution.

4.3 Finite Element Simulation of Aortic Dissection

4.3.1 Finite Element Formulation

A staggered set of algebraic equations is obtained from the strong forms of the coupled set of equations by a Galerkin type finite element formulation. The weak form of the balance of static equilibrium is derived and consistently linearized along both the deformation map $\varphi(\mathbf{X}, t)$ and the crack phase-field $d(\mathbf{X}, t)$. A temporal and spatial discretization scheme is employed for φ and d . All field variables are discretized with isoparametric shape functions yielding a set of algebraic equations to be solved by a one-pass operator-splitting algorithm. A discrete time increment $\tau = t_{n+1} - t_n$ is considered, where t_{n+1} and t_n stand for the current and the previous time steps, respectively. The operator-splitting algorithm yields a decoupling within the time interval and is the composition of the mechanical subproblem and the crack growth subproblem according to

$$\text{ALGO}_{\text{CM}} = \text{ALGO}_{\text{C}} \circ \text{ALGO}_{\text{M}}. \quad (43)$$

This algorithm converts the nonconvex coupled problem into two convex subproblems. The algorithm of each subproblem is then obtained as

$$(M) : \begin{cases} \text{Div}(\mathbf{FS}) + \rho_0 \bar{\boldsymbol{\gamma}} = \mathbf{0}, \\ \dot{d} = 0, \end{cases} \quad \text{and} \quad (C) : \begin{cases} \dot{\varphi} = \mathbf{0}, \\ d - l^2 \Delta d - (1 - d) \mathcal{H} = 0. \end{cases} \quad (44)$$

The algorithm (M) is the mechanical predictor step to be solved for the frozen crack phase-field parameter $d = d_n$, while the algorithm (C) is the crack evolution step for the frozen deformation map φ .

The discrete residual vector \mathbb{R} and the (coupled) stiffness matrix \mathbb{K} have the forms

$$\mathbb{R} = \begin{bmatrix} \mathbb{R}_\varphi \\ \mathbb{R}_d \end{bmatrix}, \quad \mathbb{K} = \begin{bmatrix} \mathbb{K}_M & \mathbf{0} \\ \mathbf{0} & \mathbb{K}_C \end{bmatrix}. \quad (45)$$

Subsequently, we provide the discrete residual vector of each subproblem, i.e.,

$$\mathbb{R}_\varphi = \bigcup_{e=1}^{n_{el}} \sum_{i=1}^{n_{en}} \delta \hat{\mathbf{x}}^T \int_{\mathcal{B}_e^h} (\mathbf{B}^T \boldsymbol{\tau}_e - \mathcal{N}^i \rho_{0e} \bar{\boldsymbol{\gamma}}_e) dV - \bigcup_{e=1}^{n_{el}^t} \sum_{i=1}^{n_{sf}} \delta \hat{\mathbf{x}}^T \int_{\partial \mathcal{B}_e^h} \mathcal{N}^i \bar{\mathbf{T}}_e dA = \mathbf{0}, \quad (46)$$

$$\mathbb{R}_d = \bigcup_{e=1}^{n_{el}} \sum_{i=1}^{n_{en}} \delta \hat{d}^i \int_{\mathcal{B}_e^h} \{ \mathcal{N}^i [d_e - (1 - d_e) \mathcal{H}_e] + \nabla^T \mathcal{N}^i l_e^2 \nabla d_e \} dV = 0, \quad (47)$$

where $(\bullet)_e$ denotes the matrix form of the associated quantities, e.g., $\boldsymbol{\tau}_e$ is the 6×1 Kirchhoff stress matrix, on a typical element. In addition, \mathbf{B}^i is a 6×3 matrix associated with node i , and consisting of the partial derivatives $\mathcal{N}_{,j}^i$, $j = 1, 2, 3$ of the shape functions \mathcal{N}^i with respect to the spatial coordinates x_j . The nodal values of each element domain are characterized with a superimposed hat. \bigcup is the assembly operator, while n_{el} is the number of finite elements while n_{el}^t stands for the number of surface finite elements, n_{en} and n_{sf} denote the number of nodes per volume and surface element, respectively.

The element matrices \mathbb{K}_M and \mathbb{K}_C of each subproblem take on the following forms:

$$\mathbb{K}_M = \bigcup_{e=1}^{n_{el}} \sum_{i=1}^{n_{en}} \sum_{j=1}^{n_{en}} \delta \hat{\mathbf{x}}^T \mathbf{K}_{\varphi\varphi,e}^{ij} \Delta \hat{\mathbf{x}}^j, \quad \mathbb{K}_C = \bigcup_{e=1}^{n_{el}} \sum_{i=1}^{n_{en}} \sum_{j=1}^{n_{en}} \delta \hat{d}^i \mathbf{K}_{dd,e}^{ij} \Delta \hat{d}^j, \quad (48)$$

where \mathbb{K}_M is the stiffness matrix related to the mechanical predictor, while \mathbb{K}_C is the stiffness matrix describing the crack evolution. The components of the tangent matrices $\mathbf{K}_{\varphi\varphi,e}^{ij}$ and $\mathbf{K}_{dd,e}^{ij}$ for one element related to the nodes i, j can be given as

$$\mathbf{K}_{\varphi\varphi,e}^{ij} = \int_{\mathcal{B}_e^h} (\mathbf{B}^T \mathbf{D}_e \mathbf{B}^j + \nabla_x^T \mathcal{N}^i \boldsymbol{\tau}_e \nabla_x \mathcal{N}^j) dV, \quad (49)$$

$$\mathbf{K}_{dd,e}^{ij} = \int_{\mathcal{B}_e^h} [\mathcal{N}^i (1 + \mathcal{H}_e) \mathcal{N}^j + \nabla^T \mathcal{N}^i l_e^2 \nabla \mathcal{N}^j] dV, \quad (50)$$

where \mathbf{D}_e designates the matrix form of the elasticity tensor for a typical element. The operator-splitting algorithm is outlined in Table 4. It forms the basis for the numerical scheme in which the phase-field d is driven by the local history field $\mathcal{H}(t_{n+1})$. The phase-field model was implemented into the finite element analysis program FEAP (2008).

4.3.2 Simple Shear Test of a Thoracic Aortic Specimen

Finally, we illustrate the performance of the crack phase-field model applied to aortic fracture by means of finite element simulations to capture the experimental data obtained from a specimen extracted from the media of a human thoracic aorta. The performed simulations are based on data obtained from the specimen subjected to simple shear along the circumferential θ -direction (referred to as $z\theta$ mode) and the longitudinal z -direction (θz mode); the experimental data from specimen AVIII are displayed in Fig. 6c, d of this section.

Table 4 Operator-splitting algorithm for the multifield problem in $[t_n, t_{n+1}]$

1. Initialization	– At time t_n given: deformation map, phase-field, history field φ_n , d_n , \mathcal{H}_n
2. Update	– Update the prescribed loads $\bar{\gamma}$, $\bar{\varphi}$ and $\bar{\mathbf{T}}$ at current time t_{n+1}
3. Compute φ_{n+1}	– Determine φ_{n+1} from the minimization problem of elasticity $\bullet G_\varphi = \int_{\mathcal{B}} \text{sym}[\nabla_x(\delta\varphi)] : \tau dV - \int_{\mathcal{B}} \delta\varphi \cdot \rho_0 \bar{\gamma} dV - \int_{\partial\mathcal{B}} \delta\varphi \cdot \bar{\mathbf{T}} dA = 0$
4. Compute history	– Check crack initiation/propagation condition, update history $\bullet \mathcal{H}(t_{n+1}) \leftarrow \begin{cases} \mathcal{H}(t_n) & \text{if } \mathcal{H}(t_{n+1}) < \mathcal{H}(t_n) \\ \mathcal{H}(t_{n+1}) & \text{else} \end{cases}$
5. Compute d_{n+1}	– Determine d_{n+1} from the minimization problem of crack topology $\bullet G_d = \int_{\mathcal{B}} \delta d[d - (1-d)\mathcal{H}] dV + \int_{\mathcal{B}} \nabla(\delta d) \cdot l^2 \nabla d dV = 0$

The experiments are replicated computationally with respect to a monotonic shear load applied to the specimens with symmetric incisions; for the related geometries see Fig. 8a, c. The geometry of the specimen sheared along the θ -direction is discretized with 23 525 four-node tetrahedral elements, with a length-scale parameter $l = 0.167$ mm, see Fig. 8b, and the specimen sheared along the z -direction is discretized with 22 657 elements, with $l = 0.25$ mm, see Fig. 8d. Note that l is chosen to satisfy $l > 2h$ in order to resolve the crack surface properly, see Miehe et al. (2010). The finite element meshes are refined in the areas where the crack is expected to propagate in order to resolve the crack zone. With respect to the Dirichlet boundary conditions the nodes at $z = 0$ are constrained in three directions for the $z\theta$ mode, while those located at $\theta = 0$ are constrained in three directions for the θz mode. The elastic material parameters are obtained using a least-squares analysis. The critical fracture energies g_c^{iso} and g_c^{ani} are predicted for each mode by comparing the Cauchy stress versus the amount of shear curves of the simulation results with those of the experiments. A list of the parameters used is provided in Table 5.

Figure 9 shows the finite element results in terms of the Cauchy stress versus the amount of shear; they agree well with the anisotropic experimental response. The numerical results provided in Fig. 9 are obtained by considering the average of all nodal stresses at the edge $z = \theta = 3$ mm for the $z\theta$ mode, and at the edge $\theta = 3$, $z = 5$ mm for the θz mode. The onset of the cracks is observed at the two tips of the symmetrically incised region where the stress concentration, and, therefore, the energy of the intact tissue satisfies the failure condition. The two distinct crack patterns meet in the middle of the refined region at which the complete failure phenomenon manifests itself. This is accompanied by the sudden loss of the load-bearing capacity, as depicted in the corresponding curves of the Cauchy shear stress versus the amount of shear. Figure 10 illustrates the distributions of the crack phase-field d and the Cauchy shear stress $\sigma_{\theta z}$ at the locations A, B, C, and D (indicated in Fig. 9b).

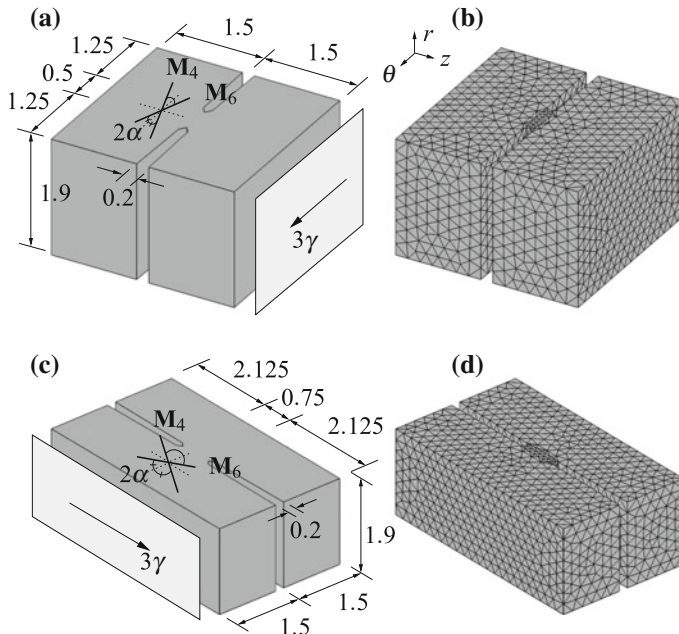


Fig. 8 **a, c** Geometries of the specimens sheared in the circumferential θ -direction ($z\theta$ mode) and in the longitudinal z -direction (θz mode) by the displacement 3γ (thickness times amount of shear). The structure of the media is characterized by two families of fibers, oriented in the directions M_4 and M_6 in the reference configuration, and they are symmetrically arranged with respect to the cylinder axis— α is the angle between the fibers and the circumferential direction; **b, d** finite element meshes. Dimensions are provided in millimeters (Gultekin et al. 2016)

Table 5 Elastic and crack phase-field parameters for anisotropic failure of aneurysmatic aortic specimens under simple shear along the circumferential (θ) and longitudinal (z) directions

Elastic	$\mu = 80.74 \text{ kPa}$ $k_1 = 62.04 \text{ kPa}$ $k_2 = 0.23$ $\alpha = 53.68^\circ$
Crack phase-field	$g_c^{\text{iso}} = 80 \text{ kPa mm}$ along the θ -direction $g_c^{\text{ani}} = 105 \text{ kPa mm}$ along the θ -direction $g_c^{\text{iso}} = 120 \text{ kPa mm}$ along the z -direction $g_c^{\text{ani}} = 240 \text{ kPa mm}$ along the z -direction

The parameters are according to (36), (37), (39), while α is the angle between the fibers (arranged in symmetrical spirals) and the circumferential direction of the media

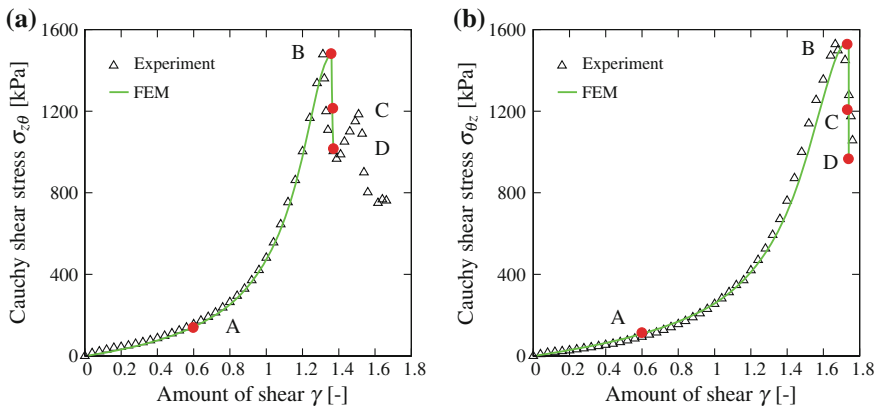


Fig. 9 Simple shear test data (triangles) and corresponding finite element results (solid curves): **a** Cauchy shear stress $\sigma_{z\theta}$ versus amount of shear γ for the $z\theta$ mode; **b** Cauchy shear stress $\sigma_{\theta z}$ versus γ for the θz mode (Gultekin et al. 2016)

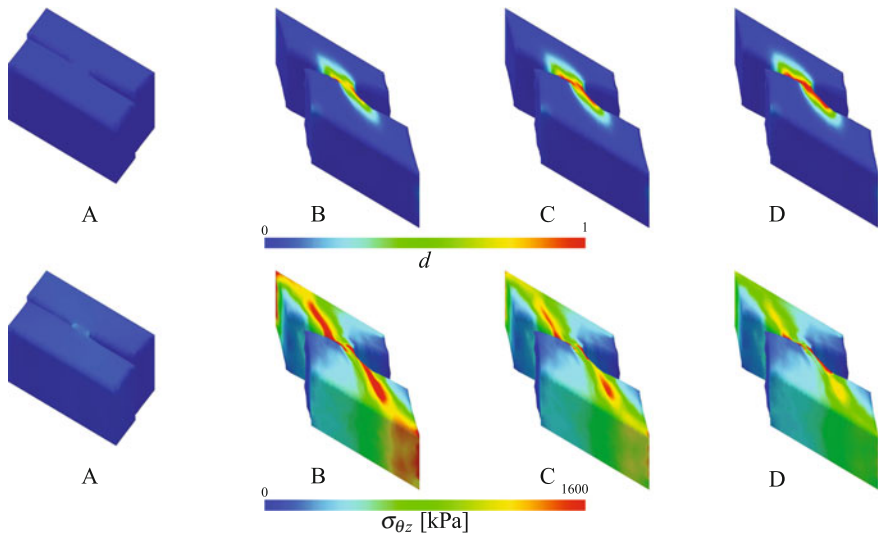


Fig. 10 Distributions of the numerical results of simple shear in the longitudinal z -direction (θz mode) with anisotropic failure at the locations A, B, C, and D according to Fig. 9b: (above) distribution of crack phase-field d ; (below) corresponding Cauchy shear stress $\sigma_{\theta z}$ (Gultekin et al. 2016)

5 Modeling Stress Softening and Permanent Deformation in Artery Walls

In cardiovascular treatments such as arterial clamping and balloon angioplasty the tissue is exposed to supraphysiological loading which may cause tissue damage. Consequently, some inelastic phenomena such as stress softening and permanent deformation may occur in the tissue. Figure 11 shows representative results of experimental data obtained from the intima of a thoracic aorta for tissue strips taken along the axial and circumferential directions (donor XII, see Weisbecker et al. 2012). Clearly seen in the stress–stretch response is the anisotropic behavior of the tissue and the softening during unloading from the primary loading path. As illustrated in the zoomed plots, Fig. 11b, c, a permanent deformation is observed whenever the load is completely removed. Stress softening and permanent deformation mainly occur in the first cycle of each load step.

In several studies continuum damage mechanics has been used to model damage-induced inelastic phenomena in arterial tissues (Rodríguez et al. 2006, 2008;

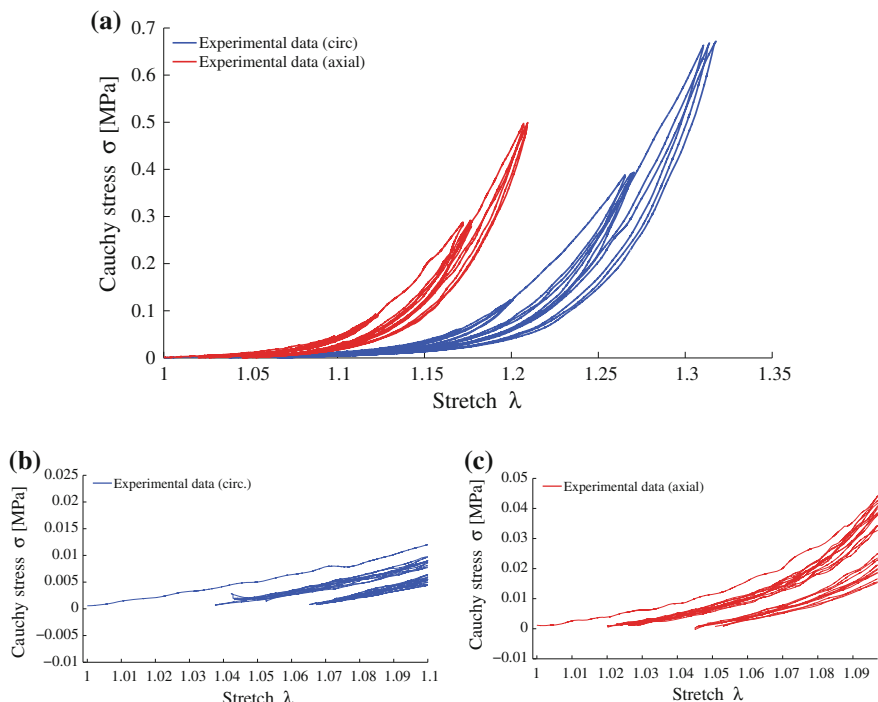


Fig. 11 **a** Representative experimental data from cyclic uniaxial tensile tests performed on the intima of a thoracic aorta (donor XII, see Weisbecker et al. 2012). The zoomed views—**b** tissue strip taken along the circumferential direction, and **c** along the axial direction—show permanent deformation after removing the stress (Fereidoonbehad et al. 2016)

Balzani et al. 2012; Maher et al. 2012; Marino and Vairo 2014; Schmidt et al. 2014). An alternative phenomenological approach is to model damage on the basis of pseudoelasticity, see, e.g., Ogden and Roxburgh (1999) and Dorfmann and Ogden (2004). The inherent simplicity of the pseudoelasticity approach makes it especially suitable for practical applications. Weisbecker et al. (2012) used that approach for the description of damage in soft collagenous tissues. In particular, an anisotropic model was proposed to account for the stress softening in aortic layers when loaded beyond the physiological range while permanent deformation was not accounted for. Subsequently, according to Fereidoonnehad et al. (2016), we briefly review a damage model for arterial tissue that takes into account both stress softening and permanent deformation. The constitutive model is an extension of the model of Weisbecker et al. (2012) to also take into account permanent deformation. We show that the model is able to capture special features such as nonlinearity, anisotropy, and damage-induced phenomena. Finally, we present finite element results of aortic clamping by considering the three aortic layers, residual stresses, nonsymmetric blood pressure after clamping, and patient-specific mechanical data.

5.1 Constitutive Model

5.1.1 Pseudoelastic Damage Model

We use here a multiplicative decomposition of the deformation gradient $\mathbf{F} = J^{1/3}\bar{\mathbf{F}}$, where $J = \det \mathbf{F} > 0$ is the volume ratio and $\bar{\mathbf{F}}$ is the modified deformation gradient ($\det \bar{\mathbf{F}} = 1$). Consequently, $\bar{\mathbf{C}} = \bar{\mathbf{F}}^T \bar{\mathbf{F}}$ denotes the modified right Cauchy–Green tensor (Holzapfel 2000).

By considering the pseudoelastic damage model, as introduced by Dorfmann and Ogden (2004), for the pseudo-energy function Ψ of an arterial layer, we write

$$\Psi = \Psi_{\text{vol}}(J) + \bar{\Psi}(\bar{\mathbf{C}}, \mathbf{M}_4, \mathbf{M}_6, \eta_s, \eta_{\text{in}}), \quad (51)$$

where $\Psi_{\text{vol}}(J)$ is the volumetric response and $\bar{\Psi}$ is the isochoric response of the damaged tissue, while \mathbf{M}_4 and \mathbf{M}_6 denote the directions of the collagen fiber families in the reference configuration, while η_s and η_{in} are two damage variables included to capture the stress softening and permanent deformation, respectively. The damage phenomenon is assumed to affect only the isochoric part of the deformation (Simo 1987).

Furthermore, the isochoric free-energy function of the undamaged tissue, say $\bar{\Psi}^0$, is decomposed into an energy stored in the ground matrix, say $\bar{\Psi}_g^0$, and an energy stored in the collagen fibers, say $\bar{\Psi}_{fi}^0$. Assuming that the softening phenomenon occurs only in the collagen fibers (Weisbecker et al. 2012), then the isochoric part of (51) may be represented as

$$\bar{\Psi} = \bar{\Psi}_g^0(\bar{I}_1) + \sum_{i=4,6} [\eta_{si} \bar{\Psi}_{fi}^0(\bar{I}_1, \bar{I}_i) + \phi_i(\eta_{si})] - [(1 - \eta_{in})N(\mathbf{C}^*) + \phi_{in}(\eta_{in})], \quad (52)$$

where $\bar{I}_1 = \text{tr}\bar{\mathbf{C}}$ is the first invariant of $\bar{\mathbf{C}}$ and $\bar{I}_i = \bar{\mathbf{C}} : \mathbf{M}_i \otimes \mathbf{M}_i$, $i = 4, 6$, are the modified pseudo-invariants, which are the analogues of (4)₂. The second part in (52) represents the energy of the softened fibers while the last part is the inelastic contribution related to the permanent set. In (52) ϕ_i and ϕ_{in} are dissipation functions and N is the inelastic energy dissipation characterizing the permanent set, i.e., a function of the modified right Cauchy–Green tensor at the peak deformation (deformation state at which $\bar{\Psi}^0$ is a maximum) of the loading history, say \mathbf{C}^* . Note that \mathbf{C}^* (and consequently N) is only updated on unloading from the maximum deformation state.

5.1.2 Stress Tensor and Thermodynamic Consistency

Let us consider the Clausius–Duhem inequality

$$\frac{1}{2} \mathbf{S} : \dot{\mathbf{C}} - \dot{\Psi} \geq 0, \quad (53)$$

where the material time derivative of Ψ is denoted by $\dot{\Psi}$. Differentiating (51) in view of (52), and substituting the result into inequality (53), we obtain

$$\begin{aligned} & \left(\frac{1}{2} \mathbf{S} - \frac{d\Psi_{\text{vol}}}{dJ} \frac{\partial J}{\partial \mathbf{C}} - \frac{\partial \bar{\Psi}}{\partial \bar{\mathbf{C}}} : \frac{\partial \bar{\mathbf{C}}}{\partial \mathbf{C}} \right) : \dot{\mathbf{C}} - \\ & - \sum_{i=4,6} \left(\bar{\Psi}_{fi}^0 + \frac{\partial \phi_i}{\partial \eta_{si}} \right) \dot{\eta}_{si} - \left(N - \frac{\partial \phi_{in}}{\partial \eta_{in}} \right) \dot{\eta}_{in} \geq 0, \end{aligned} \quad (54)$$

which must be fulfilled for arbitrary $\dot{\mathbf{C}}$. With standard arguments of continuum thermodynamics (Holzapfel 2000) we conclude that

$$\mathbf{S} = \mathbf{S}_{\text{vol}} + \bar{\mathbf{S}}, \quad \mathbf{S}_{\text{vol}} = 2 \frac{d\Psi_{\text{vol}}}{dJ} \frac{\partial J}{\partial \mathbf{C}}, \quad \bar{\mathbf{S}} = 2 \frac{\partial \bar{\Psi}}{\partial \bar{\mathbf{C}}} : \frac{\partial \bar{\mathbf{C}}}{\partial \mathbf{C}}, \quad (55)$$

where $\mathbf{S}_{\text{vol}} = p \mathbf{J} \mathbf{C}^{-1}$, with $p = d\Psi_{\text{vol}}/dJ$ (p is the hydrostatic pressure), and $\bar{\mathbf{S}}$ are the volumetric and isochoric parts of the second Piola–Kirchhoff stress tensor \mathbf{S} , respectively. The isochoric part $\bar{\mathbf{S}}$ is represented by

$$\begin{aligned} \bar{\mathbf{S}} = 2 \left\{ \frac{\partial \bar{\Psi}_g^0}{\partial \mathbf{C}} + \sum_{i=4,6} \left(\eta_{si} \frac{\partial \bar{\Psi}_{fi}^0}{\partial \mathbf{C}} + \frac{\partial \eta_{si}}{\partial \mathbf{C}} \bar{\Psi}_{fi}^0 + \phi'_i \frac{\partial \eta_{si}}{\partial \mathbf{C}} \right) \right. \\ \left. - \left[(1 - \eta_{in}) \frac{\partial N}{\partial \mathbf{C}} - \frac{\partial \eta_{in}}{\partial \mathbf{C}} N + \phi'_{in} \frac{\partial \eta_{in}}{\partial \mathbf{C}} \right] \right\}, \end{aligned} \quad (56)$$

where the prime denotes the derivative of the dissipative function (ϕ_i or ϕ_{in}) with respect to the damage variable (η_s or η_{in}).

Furthermore, the inequality (54) can be represented in the following simplified form:

$$-\sum_{i=4,6}\left(\bar{\Psi}_{\text{fi}}^0+\frac{\partial\phi_i}{\partial\eta_{si}}\right)\dot{\eta}_{si}-\left(N-\frac{\partial\phi_{\text{in}}}{\partial\eta_{\text{in}}}\right)\dot{\eta}_{\text{in}}\geqslant 0. \quad (57)$$

In order to satisfy (57), we assume that damage evolves with the deformation so that

$$\frac{\partial\Psi}{\partial\eta_{si}}=\bar{\Psi}_{\text{fi}}^0+\phi'_i=0, \quad \frac{\partial\Psi}{\partial\eta_{\text{in}}}=-N+\phi'_{\text{in}}=0, \quad (58)$$

which is in accordance with Dorfmann and Ogden (2004). Hence, the stress tensor (56) may then be presented as

$$\bar{\mathbf{S}}=\bar{\mathbf{S}}_g^0+\sum_{i=4,6}\eta_{si}\bar{\mathbf{S}}_{\text{fi}}^0-(1-\eta_{\text{in}})\mathbf{S}_{\text{in}}, \quad (59)$$

where the abbreviations

$$\bar{\mathbf{S}}_g^0=2\frac{\partial\bar{\Psi}_g^0}{\partial\mathbf{C}}, \quad \bar{\mathbf{S}}_{\text{fi}}^0=2\frac{\partial\bar{\Psi}_{\text{fi}}^0}{\partial\mathbf{C}}, \quad \mathbf{S}_{\text{in}}=2\frac{\partial N}{\partial\mathbf{C}} \quad (60)$$

have been introduced. It is now straightforward to derive the explicit form of the elasticity tensor, see Fereidoonnezhad et al. (2016).

5.1.3 Energy Functions and Damage Variables

Finally, we need specific forms of the energy functions and the damage variables. According to Sect. 2.2 we assume two collagen fiber families, symmetrically distributed at an angle α with respect to the circumferential direction of the aortic layer. By means of the analogue of (8) and (9) we have

$$\bar{\Psi}_g^0(\bar{I}_1)=\frac{c}{2}(\bar{I}_1-3), \quad \bar{\Psi}_{\text{fi},i}^0(\bar{I}_1,\bar{I}_i)=\frac{k_1}{2k_2}\left\{\exp\left[k_2(\bar{I}_i^*-1)^2\right]-1\right\}, \quad i=4,6, \quad (61)$$

where c , k_1 , k_2 are material parameters, and $\bar{I}_i^*=\text{tr}(\mathbf{H}_i\bar{\mathbf{C}})=\kappa\bar{I}_1+(1-3\kappa)\bar{I}_i$, where $\kappa\in[0,1/3]$ denotes again the dispersion parameter. This is the special case of transversely isotropic dispersion about \mathbf{M}_4 and \mathbf{M}_6 , as discussed in Sect. 2.3. In addition, the convex form

$$\Psi_{\text{vol}}(J)=\frac{1}{D}\left(\frac{J^2-1}{2}-\ln J\right) \quad (62)$$

is considered for the volumetric energy (numerically used as a penalty function), where $1/D$ is a penalty parameter. Moreover, we assume that the (anisotropic) inelastic energy dissipation N has the same form as the elastic free-energy function, with the related material parameters c^* , k_1^* , k_2^* , and κ^* .

Following Weisbecker et al. (2012) and assuming two mechanically equivalent collagen fiber families, the damage variable η_{si} may be specified as

$$\eta_{si} = 1 - \frac{1}{r_1} \operatorname{erf} \left[\frac{1}{m_1} \left(\bar{\Psi}_{fi}^{\max} - \bar{\Psi}_{fi}^0 \right) \right], \quad (63)$$

where $\operatorname{erf}(\bullet)$ is the error function of (\bullet) and $\bar{\Psi}_{fi}^{\max}$ denotes the maximum strain energy of the fiber family i obtained by the deformation history. The maximum material damage that can be induced under loading is characterized by $r_1 > 1$, while $m_1 > 0$ determines the dependence of the damage on the deformation. The damage induced in each fiber family can be characterized by the minimum value η_{si}^{\min} according to

$$\eta_{si}^{\min} = 1 - \frac{1}{r_1} \operatorname{erf} \left(\frac{1}{m_1} \bar{\Psi}_{fi}^{\max} \right). \quad (64)$$

During primary loading $\eta_{in} = 1$ and during unloading η_{in} is a decreasing function. It is convenient to set $\eta_{in} = 0$ at $\mathbf{C} = \mathbf{I}$ so that $0 \leq \eta_{in} \leq 1$. One possible expression, which satisfies the above restriction on the limiting values of η_{in} , is

$$\eta_{in} = \tanh \left[\left(\frac{\bar{\Psi}^0}{\bar{\Psi}^{\max}} \right)^{m_2} \right] / \tanh(1), \quad (65)$$

where m_2 is a parameter, and $\bar{\Psi}^{\max}$ is the maximum strain energy of the tissue obtained in the deformation history. With the particular forms of the energy functions, the inelastic dissipation, and the damage variables we are now able to provide explicit expressions for $\bar{\mathbf{S}}$, according to (59), and the elasticity tensor.

5.1.4 Material and Damage Parameters

The parameter identification was performed by the optimization toolbox MATLAB (R2012a, The MathWorks, Inc.). Thereby, the Cauchy stress in the loading direction was determined, then the lateral and through-the-thickness stretches were calculated using $J = 1$ together with the constraint that the stress in the lateral direction equals zero. With these stresses and stretches the parameter identification was performed by employing the nonlinear least-squares trust region algorithm to minimize the objective function

$$\chi = \sum_{i=1}^n (\sigma_i^{\exp} - \sigma_i^{\text{mod}})^2, \quad (66)$$

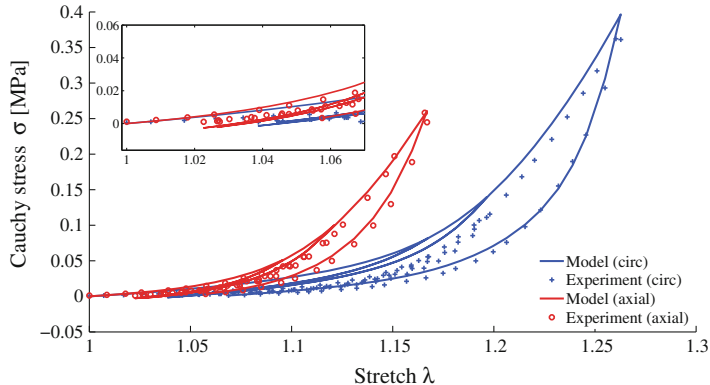


Fig. 12 Representative model fit for cyclic uniaxial tension data of the intima taken from a thoracic aorta (donor XII, see Weisbecker et al. 2012; compare also with Fig. 11 in this chapter). The inset shows the low stretch region to highlight the permanent set of deformation (Fereidoonnezhad et al. 2016)

where n is the number of considered data points, σ_i^{exp} are the Cauchy stresses determined experimentally and σ_i^{mod} are the corresponding values predicted by the model for both the circumferential and the axial directions. With the obtained parameters the lateral and the through-the-thickness stretches were updated and the parameter identification was repeated until the solution converged. The goodness of fit was evaluated by calculating the coefficient of determination $R^2 = 1 - S_{\text{err}}/S_{\text{tot}}$, where S_{err} and S_{tot} are the sums of squares of the differences between model/experiment and the mean of experiment/experiment, respectively (Holzapfel et al. 2015). The proposed constitutive model is able to reproduce the experimentally determined stress–stretch data in a good manner. A representative model fit for uniaxial data is shown in Fig. 12. The experimental data are for the intimal strips of a thoracic aorta (donor XII, see Weisbecker et al. 2012; compare also with Fig. 11 in this chapter), taken along the axial and circumferential directions. The related parameters for this sample from donor XII are $c = 0.024 \text{ MPa}$, $k_1 = 3.863 \text{ MPa}$, $k_2 = 0.001$, $\alpha = 47.9^\circ$, $\kappa = 0.18$, $c^* = 0.0021 \text{ MPa}$, $k_1^* = 0.03239 \text{ MPa}$, $k_2^* = 0.0028$, $\kappa^* = 0$, $r_1 = 1.79$, $m_1 = 0.004 \text{ MPa}$ and $m_2 = 2.0$. The parameters together with the coefficient of determination R^2 for the intima, media and adventitia of 14 human thoracic aortas and of 9 human abdominal aortas are summarized in the study of Fereidoonnezhad et al. (2016).

5.2 Aortic Clamping

Here, we briefly present finite element simulations of aortic clamping by considering residual stresses, a multilayer structure of the wall with layer-specific, anisotropic

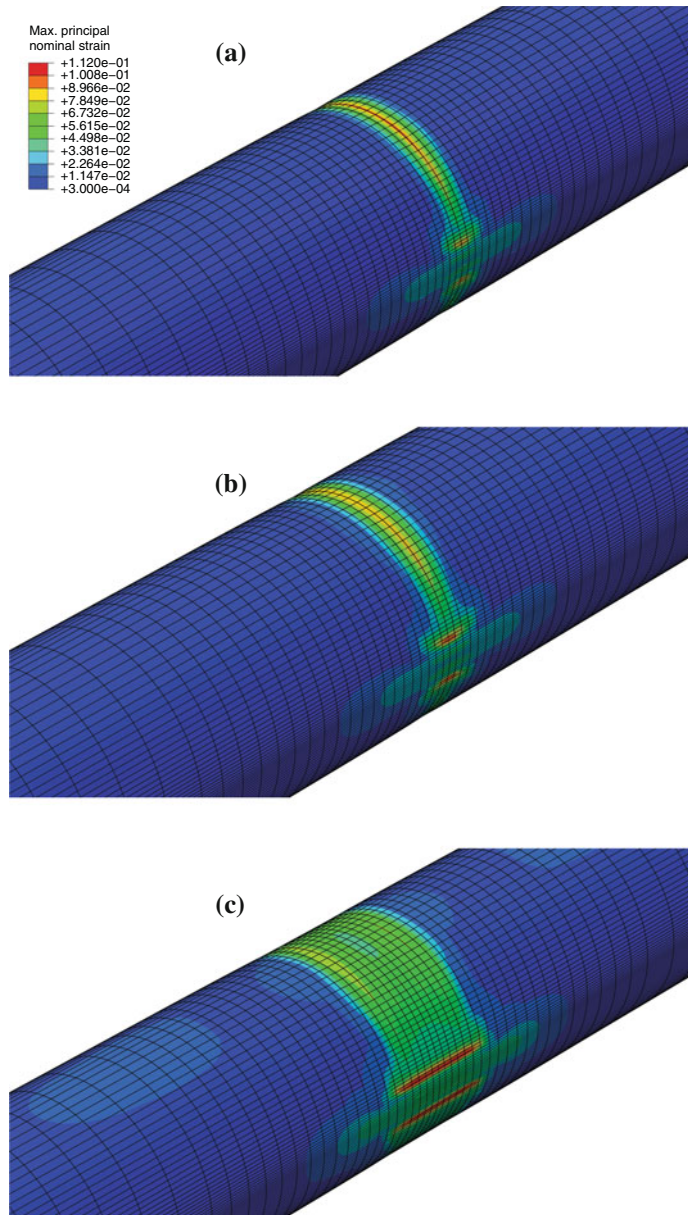


Fig. 13 Distributions of the maximum principal nominal strain with respect to the physiological configuration of the wall after unclamping for **a** a cylindrical clamp with 6 mm diameter, **b** a cylindrical clamp with 10 mm diameter, and **c** a flat clamp with 6 mm width. The values represent the damage-induced permanent strain in the aortic wall (Fereidoonnezhad et al. 2016)

and nonlinear responses. The 3D FE model was built in Abaqus/Standard (2013). For details on the opening angle and the geometry of the cylindrical segment, see Fereidoonnezhad et al. (2016). In total 9 elements were considered through the aortic wall thickness (3, 4, and 2 for adventitia, media, and intima, respectively). Eight-node linear brick elements (C3D8H) were assigned to the finite element mesh, with a total of 40 950 elements, and material parameters from a thoracic aorta (donor XI) were used (Fereidoonnezhad et al. 2016). The cylinder was axially stretched to 15% and the axial direction remained fixed for all nodes at the edges for the remainder of the simulation. The segment was pressurized with an internal mean aortic pressure of 13.3 kPa. The aortic clamp, idealized as a pair of rigid cylinders or a pair of rigid flat plates and modeled by 4-node 3D bilinear rigid quadrilateral elements (R3D4), were moved toward each other until the vessel became completely closed. The pressure drop due to clamping was simulated by a linear decay function to 90 % of the mean aortic pressure in the downstream (blood free) region, and increased with a linear function by 10 % in the upstream region; related values are based on experimental measurements (Attia et al. 1976). Contact, enforced with the penalty method, was defined between all contact surfaces and a friction coefficient of 0.1 was used. A surface to surface discretization method was chosen and the clamp surface was selected as the master surface while the outer surface of the adventitia was the slave surface.

The simulations were performed for three different types of clamp using the same inelastic properties for the aortic wall. The chosen geometries are: (i) cylindrical clamp with 6 mm diameter; (ii) cylindrical clamp with 10 mm diameter; (iii) flat clamp with 6 mm width. Figure 13 illustrates the distribution of the maximum principal nominal strains calculated with respect to the physiological configuration. The results show the damage-induced permanent strains in the aortic wall after unclamping. As can be seen from this figure there is no significant difference between the cylindrical clamps with 6 and 10 mm in diameter. Higher values for the permanent strains are observed for the flat clamp which implies that a higher injury is induced in the aortic wall using a flat clamp.

6 Concluding Remarks

This chapter was partly aimed at summarizing some of the recent findings on the microstructure and mechanics of human aortas in health and disease such as aneurysms and aortic dissections. We focussed attention on the continuum mechanical modeling of (i) the nonsymmetric collagen fiber dispersion occurring in aortic walls, a constitutive framework using a generalized structure tensor that incorporates a measure of fiber dispersion, then (ii) aortic dissection using the phase-field approach, and (iii) stress softening and permanent deformation as present in fibrous tissues that are exposed to supraphysiological loading causing tissue damage. The models are presented in a way that allows computational experts to implement them in a finite element program; we have implemented the described models into FEAP

and Abaqus/Standard. Finite element simulations were used to analyze simple shear of an aneurysmatic tissue loaded up to rupture, and to better understand aortic clamping using three different types of clamps. The reviewed models can also be extended to incorporate effects such as viscoelasticity and, in particular, muscle activation.

Acknowledgments I would like to thank many colleagues for their encouragement and perspective in the modeling of cardiovascular solid mechanics, in particular to Prof. *Ray W. Ogden*, FRS, FRSE, with whom I had the honor to fruitfully cooperate the last 20 years. I am also pleased to acknowledge the essential support and the helpful discussions of the many former and current doctoral and postdoctoral students who worked with me, performing experiments in the lab on cardiovascular tissues, producing images with microscopes, and elaborating on related models used for numerical simulations of cardiovascular tissues in health and disease. In particular, I would like to thank some of my current coworkers in Graz, i.e., Dr. *Anju Babu*, Ms. *Julia Brandstetter*, Mr. *Osman Gültekin*, Mr. *Daniel Haspinger*, Dr. *Kewei Li*, Dr. *Sae-Il Murtada*, Ms. *Justyna A. Niestrawska*, Ms. *Selda Sherifova*, Dr. *Gerhard Sommer*, and Ms. *Bettina Strametz*. Finally, I gratefully acknowledge funding from the National Institutes of Health (NIH), research grant no. NIH R01HL117063.

References

- Abaqus 6.13-4, Analysis user's guide. Dassault Systèmes Simulia Corp. (2013)
- Attia, R.R., Murphy, J.D., Snider, M., Lappas, D.G., Darling, R.C., Lowenstein, E.: Myocardial ischemia due to infrarenal aortic cross-clamping during aortic surgery in patients with severe coronary artery disease. *Circulation* **53**, 961–965 (1976)
- Balzani, D., Brinkhues, S., Holzapfel, G.A.: Constitutive framework for the modeling of damage in collagenous soft tissues with application to arterial walls. *Comput. Meth. Appl. Mech. Eng.* **213–216**, 139–151 (2012)
- Criado, F.J.: Aortic dissection: a 250-year perspective. *Tex. Heart Inst. J.* **38**, 694–700 (2011)
- Davies, R.R., Goldstein, L.J., Coady, M.A., Tittle, S.L., Rizzo, J.A., Kopf, G.S., Elefteriades, J.A.: Yearly rupture or dissection rates for thoracic aortic aneurysms: simple prediction based on size. *Ann. Thorac Surg.* **73**, 17–27 (2002)
- Dorfmann, A., Ogden, R.W.: A constitutive model for the Mullins effect with permanent set in particle-reinforced rubber. *Int. J. Solids Struct.* **41**, 1855–1878 (2004)
- FEAP - A finite element analysis program, Version 8.2 user manual. University of California at Berkeley, Berkeley, California (2008)
- Fereidoonnehzad, B., Naghdabadi, R., Holzapfel, G.A.: Stress softening and permanent deformation in human aortas: continuum and computational modeling with application to arterial clamping. *J. Mech. Behav. Biomed. Mater.* **61**, 600–616 (2016)
- Fleming, C., Whitlock, E.P., Beil, T.L., Lederle, F.A.: Screening for abdominal aortic aneurysm: a best-evidence systematic review for the U.S. preventive services task force. *Ann. Intern. Med.* **142**, 203–211 (2005)
- Gasser, T.C., Ogden, R.W., Holzapfel, G.A.: Hyperelastic modelling of arterial layers with distributed collagen fibre orientations. *J. R. Soc. Interface* **3**, 15–35 (2006)
- Gültekin, O.: A phase field approach to the fracture of anisotropic medium. Master's thesis, University of Stuttgart, Institute of Applied Mechanics (CE), Pfaffenwaldring 7, Stuttgart (2014)
- Gültekin, O., Dal, H., Holzapfel, G.A.: A phase-field approach to model fracture of arterial walls: theory and finite element analysis. *Comput. Meth. Appl. Mech. Eng.* (2016) (in press)
- Haslach Jr., H.W., Leahy, L.N., Fathi, P., Barrett, J.M., Heyes, A.E., Dumsha, T.A., McMahon, E.L.: Crack propagation and its shear mechanisms in the bovine descending aorta. *Cardiovasc. Eng. Technol.* **6**, 501–518 (2015)

- Holzapfel, G.A.: Nonlinear Solid Mechanics. A Continuum Approach for Engineering. Wiley, Chichester (2000)
- Holzapfel, G.A.: Arterial tissue in health and disease: experimental data, collagen-based modeling and simulation, including aortic dissection. In: Holzapfel, G.A., Ogden, R.W. (eds.) Biomechanical Modelling at the Molecular, Cellular and Tissue Levels. CISM Courses and Lectures, vol. 508 pp. 259–343. Springer, Wien (2009)
- Holzapfel, G.A., Gasser, T.C., Ogden, R.W.: A new constitutive framework for arterial wall mechanics and a comparative study of material models. *J. Elast.* **61**, 1–48 (2000)
- Holzapfel, G.A., Niestrawska, J.A., Ogden, R.W., Reinisch, A.J., Schriebl, A.J.: Modelling non-symmetric collagen fibre dispersion in arterial walls. *J. R. Soc. Interface* **12**, 20150188 (2015)
- Humphrey, J.D., Holzapfel, G.A.: Mechanics, mechanobiology, and modeling of human abdominal aorta and aneurysms. *J. Biomech.* **45**, 805–814 (2012)
- Humphrey, J.D., Taylor, C.A.: Intracranial and abdominal aortic aneurysms: similarities, differences, and need for a new class of computational models. *Annu. Rev. Biomed. Eng.* **10**, 221–246 (2008)
- Khan, I.A., Nair, C.K.: Clinical, diagnostic, and management perspectives of aortic dissection. *Chest* **122**, 311–328 (2002)
- Knipp, B.S., Deeb, G.M., Prager, R.L., Williams, C.Y., Upchurch Jr., G.R., Patel, H.J.: A contemporary analysis of outcomes for operative repair of type a aortic dissection in the united states. *Surgery* **142**, 524–528 (2007)
- Maher, E., Creane, A., Lally, C., Kelly, D.J.: An anisotropic inelastic constitutive model to describe stress softening and permanent deformation in arterial tissue. *J. Mech. Behav. Biomed. Mater.* **12**, 9–19 (2012)
- Marino, M., Vairo, G.: Influence of inter-molecular interactions on the elasto-damage mechanics of collagen fibrils: a bottom-up approach towards macroscopic tissue modeling. *J. Mech. Phys. Solids* **73**, 38–54 (2014)
- Miehe, C., Welschinger, F., Hofacker, M.: Thermodynamically consistent phase-field models of fracture: variational principles and multi-field FE implementations. *Int. J. Numer. Methods Eng.* **83**, 1273–1311 (2010)
- Niestrawska, J.A., Regitnig, P., Viertler, C., Cohnert, T.U., Holzapfel, G.A.: Mechanics and microstructure of healthy human aortas and AAA tissues: experimental analysis and modeling. Submitted (2016)
- Ogden, R.W., Roxburgh, D.G.: A pseudo-elastic model for the Mullins effect in filled rubber. *Proc. R. Soc. Lond. A* **455**, 2861–2877 (1999)
- Pal, S., Tsamis, A., Pasta, S., D'Amore, A., Gleason, T.G., Vorp, D.A., Maiti, S.: A mechanistic model on the role of radially-running collagen fibers on dissection properties of human ascending thoracic aorta. *J. Biomech.* **47**, 981–988 (2014)
- Pasta, S., Phillipi, J.A., Gleason, T.G., Vorp, D.A.: Effect of aneurysm on the mechanical dissection properties of the human ascending thoracic aorta. *J. Thorac. Cardiovasc. Surg.* **143**, 460–467 (2012)
- Pratt, B., Curci, J.: Arterial elastic fiber structure. Function and potential roles in acute aortic dissection. *J. Cell Sci.* **51**, 647–656 (2010)
- Raina, A., Miehe, C.: A phase-field model for fracture in biological tissues. *Biomech. Model. Mechanobiol.* **15**, 479–496 (2016)
- Rodríguez, J.F., Cacho, F., Bea, J.A., Doblaré, M.: A stochastic-structurally based three dimensional finite-strain damage model for fibrous soft tissue. *J. Mech. Phys. Solids* **54**, 864–886 (2006)
- Rodríguez, J.F., Alastrue, V., Doblaré, M.: Finite element implementation of a stochastic three dimensional finite-strain damage model for fibrous soft tissue. *Comput. Meth. Appl. Mech. Eng.* **197**, 946–958 (2008)
- Schmidt, T., Balzani, D., Holzapfel, G.A.: Statistical approach for a continuum description of damage evolution in soft collagenous tissues. *Comput. Meth. Appl. Mech. Eng.* **278**, 41–61 (2014)

- Schriefl, A.J., Zeindlinger, G., Pierce, D.M., Regitnig, P., Holzapfel, G.A.: Determination of the layer-specific distributed collagen fiber orientations in human thoracic and abdominal aortas and common iliac arteries. *J. R. Soc. Interface* **9**, 1275–1286 (2012)
- Schriefl, A.J., Wolinski, H., Regitnig, P., Kohlwein, S.D., Holzapfel, G.A.: An automated approach for 3D quantification of fibrillar structures in optically cleared soft biological tissues. *J. R. Soc. Interface* **10**, 20120760 (2013)
- Simo, J.C.: On a fully three-dimensional finite-strain viscoelastic damage model: formulation and computational aspects. *Comput. Meth. Appl. Mech. Eng.* **60**, 153–173 (1987)
- Sommer, G., Gasser, T.C., Regitnig, P., Auer, M., Holzapfel, G.A.: Dissection properties of the human aortic media: an experimental study. *J. Biomech. Eng.* **130**, 021007-1–021007-12 (2008)
- Sommer, G., Sherifova, S., Oberwalder, P.J., Dapunt, O.E., Ursomanno, P.A., DeAnda, A., Griffith, B.E., Holzapfel, G.A.: Mechanical strength of aneurysmatic and dissected human thoracic aortas at different shear loading modes. *J. Biomech.* (2016) (in press)
- Thubrikar, M.J., Agali, P., Robicsek, F.: Wall stress as a possible mechanism for the development of transverse intimal tears in aortic dissections. *J. Med. Eng. Technol.* **23**, 127–134 (1999)
- Tong, J., Cheng, Y., Holzapfel, G.A.: Mechanical assessment of arterial dissection in health and disease: advancements and challenges. *J. Biomech.* (2016) (in press)
- Vorp, D.A.: Biomechanics of abdominal aortic aneurysm. *J. Biomech.* **40**, 1887–1902 (2007)
- Weisbecker, H., Pierce, D.M., Regitnig, P., Holzapfel, G.A.: Layer-specific damage experiments and modeling of human thoracic and abdominal aortas with non-atherosclerotic intimal thickening. *J. Mech. Behav. Biomed. Mater.* **12**, 93–106 (2012)

Arterial and Atherosclerotic Plaque Biomechanics with Application to Stent Angioplasty Modeling

Brían L. O'Reilly, Claire Conway, J. Patrick McGarry
and Peter E. McHugh

Abstract This chapter provides a brief review of continuum mechanics in relation to application in vascular biomechanics. The initial focus is on arterial tissue, where fundamental constitutive representations, tissue anisotropy, tissue remodeling and damage modeling are overviewed. The focus then shifts to diseased tissue (atherosclerotic plaque tissue), where experimental mechanical characterization, and constitutive and damage modeling are reviewed. Conclusions are drawn on what has been achieved thus far, and the main challenges for the future in characterizing and modeling this complex tissue are identified. Finally, the application of the arterial mechanics in the computational modeling of the stent angioplasty procedure is considered, with future challenges identified.

1 Introduction

Mathematical modeling, both analytical and computational, is a vitally important component of soft tissue biomechanics. In the case of vascular biomechanics, as is of interest here, modeling can generate deep insight into the fundamental physical and mechanical behavior of the tissue, in both healthy and diseased states. In addition, modeling is vitally important for the analysis, design, and performance assessment of devices and implants used in surgical interventions of the vasculature. Of particular interest here is the stent angioplasty procedure, for the treatment of atherosclerosis, where a stent is introduced into the blocked region of a diseased artery and expanded to restore arterial lumen patency. All proper modeling investigations, not least in the present case of vascular biomechanics, are built on the generation and availability of accurate experimental data, for model development, calibration, and validation. This chapter summarises some of the most important mathematical modeling work performed in the vascular biomechanics domain over the past 20 years or so, focusing

B.L. O'Reilly · C. Conway · J.P. McGarry · P.E. McHugh (✉)
National University of Ireland, Galway, Ireland
e-mail: peter.mchugh@nuigalway.ie

on approaches that can be implemented computationally using the finite element method. Particular attention is paid to reviewing modeling work on diseased tissue.

The chapter starts with a brief review of the aspects of continuum mechanics that are most relevant to vascular biomechanics. The focus is then applied to arterial tissue, where fundamental constitutive representations, tissue anisotropy, tissue remodeling, and damage modeling are overviewed. The focus then shifts to diseased tissue (atherosclerotic plaque tissue), where experimental mechanical characterization, and constitutive and damage modeling are reviewed. Conclusions are drawn on what has been achieved thus far, and the main challenges for the future in characterizing and modeling this complex tissue are identified.

In the final section of the chapter, focus is applied to the computational modeling of stent angioplasty, where many of the modeling features described in the previous sections are implemented. The work reviewed in this section illustrates the practicalities of attempting to achieve an accurate numerical simulation of stent deployment, and points up challenges still to be overcome in relation to such modeling efforts. Finally, the reviewed work is used to generate recommendations for the improvement of regulatory body guidelines for the computational modeling of stent angioplasty as part of the medical device regulatory approval process.

2 Finite Deformation Kinematics: Strain and Stress Measures

Standard tensor and indicial notation is used throughout the following, and tensor/vector components are written with respect to the standard orthonormal base vectors \mathbf{e}_1 , \mathbf{e}_2 , and \mathbf{e}_3 . The right and left Cauchy–Green tensors are given below, respectively, where \mathbf{F} is the deformation gradient tensor

$$\mathbf{C} = \mathbf{F}^T \mathbf{F}, \quad \mathbf{B} = \mathbf{F} \mathbf{F}^T. \quad (1)$$

Hyperelasticity is a type of constitutive model characterized by the strain-energy density function W , which can be written as a function of \mathbf{F} . The gradient of the strain-energy density with respect to \mathbf{F} yields the nominal stress \mathbf{S}

$$\mathbf{S} = \frac{\partial W(\mathbf{F})}{\partial \mathbf{F}}. \quad (2)$$

The Cauchy (true) stress, σ , is defined as the force over the area in the current configuration, and is given by the following, where J is the Jacobian of the deformation (determinant of \mathbf{F}),

$$\sigma = \frac{1}{J} \mathbf{F} \frac{\partial W(\mathbf{F})}{\partial \mathbf{F}}, \quad J = |\mathbf{F}|. \quad (3)$$

In isotropic materials, W can be written in terms of the eigenvalues of \mathbf{C} . These eigenvalues are the squares of the principal stretches, λ_1 , λ_2 , and λ_3 , shown below

$$[\mathbf{C}] = \begin{bmatrix} \lambda_1^2 & 0 & 0 \\ 0 & \lambda_2^2 & 0 \\ 0 & 0 & \lambda_3^2 \end{bmatrix}. \quad (4)$$

Invariants of the strain can be defined to eliminate coordinate axes dependence in the constitutive expressions

$$I_1 = \lambda_1^2 + \lambda_2^2 + \lambda_3^2, \quad I_2 = \lambda_2^2 \lambda_3^2 + \lambda_3^2 \lambda_1^2 + \lambda_1^2 \lambda_2^2, \quad I_3 = \lambda_1^2 \lambda_2^2 \lambda_3^2. \quad (5)$$

The Jacobian determines volume change in a material and can be related to the third invariant as follows:

$$J = \sqrt{I_3}. \quad (6)$$

Using these relationships allows the Cauchy stress to be written in terms of the invariants, with implied summation over the three invariant indices $i = 1, 2, 3$

$$\boldsymbol{\sigma} = \frac{1}{J} \mathbf{F} \frac{\partial W(\mathbf{F})}{\partial \mathbf{F}} = \frac{1}{J} \mathbf{F} \left(\frac{\partial W}{\partial I_i} \frac{\partial I_i}{\partial \mathbf{F}} \right). \quad (7)$$

This leads to the general result for an isotropic hyperelastic material

$$\boldsymbol{\sigma} = \frac{2}{J} \left(\frac{\partial W}{\partial I_1} + I_1 \frac{\partial W}{\partial I_2} \right) \mathbf{B} - \frac{2}{J} \frac{\partial W}{\partial I_2} \mathbf{B}^2 + 2J \frac{\partial W}{\partial I_3} \mathbf{I}. \quad (8)$$

3 Arterial Tissue

3.1 Fundamental Representation

Arterial tissue has been extensively linked in studies with the characteristics of hyperelasticity. Significant focus has been applied to the representation of tissue anisotropy; models have been developed to capture the anisotropy that occurs due to the directionality of the collagen and elastin fibers in the different layers of the artery.

Arterial tissue consists of layers, where each layer makes a different contribution to the collective mechanical properties of the tissue, with each layer having its own fiber orientation characteristics. In the adventitial layer, for example, are helically distributed collagen fibers. The layered structure and the corresponding fiber orientations are illustrated in Fig. 1. The most popular constitutive model implemented in recent studies of arterial mechanics is the now commonly referred to as the Holzapfel–Gasser–Ogden (HGO) model, first presented by Holzapfel et al. (2000), and further

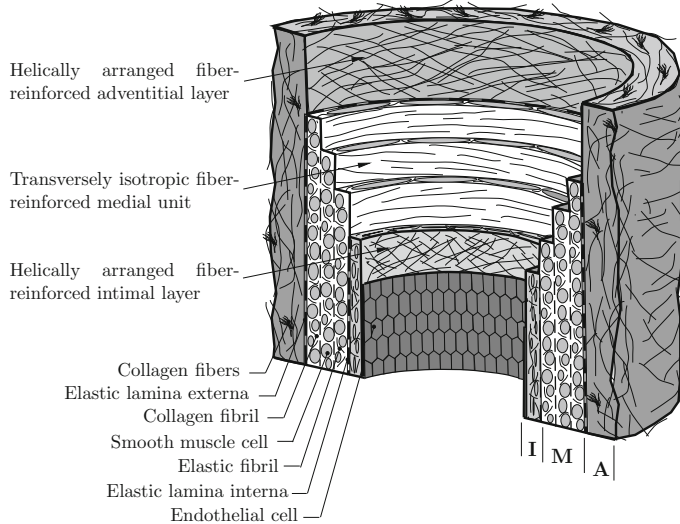


Fig. 1 Representative image of the cross-section along an arterial displaying the layers and collagen fiber orientations within the wall (Gasser et al. 2006). Reproduced with permission

elucidated in a series of papers, including Gasser et al. (2006). This model assumes material incompressibility and introduces a unit vector \mathbf{M} in order to define the orientation of a family of transversely isotropic aligned collagen fibers in the arterial tissue, and a related strain invariant I_4 , which represents the square of the stretch in the fiber direction, through the following

$$I_4 = \mathbf{M} \cdot (\mathbf{C}\mathbf{M}) = M_i C_{ij} M_j, \quad \mathbf{m} = \mathbf{F}\mathbf{M}, \quad m_i = F_{ij} M_j. \quad (9)$$

An illustration of the fiber angle γ is given in Fig. 2.

In the context of incompressibility in the material $J = 1$ and the general expression for the stress can be written as follows:

$$\boldsymbol{\sigma} = -p\mathbf{I} + 2 \left(\frac{\partial W}{\partial I_1} + I_1 \frac{\partial W}{\partial I_2} \right) \mathbf{B} - 2 \frac{\partial W}{\partial I_2} \mathbf{B}^2, \quad (10)$$

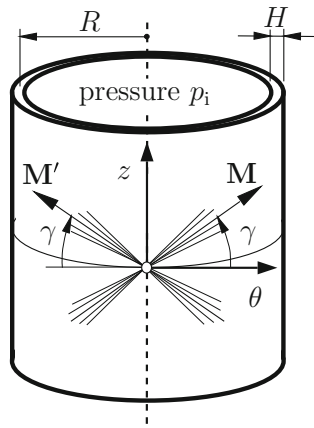
where p is a Lagrange multiplier that can be interpreted as a hydrostatic pressure.

For the present consideration of the HGO model it is useful to introduce isochoric (deviatoric) counterparts of the deformation gradient, deformation tensors, and invariants

$$\mathbf{F} = (J^{1/3}\mathbf{I})\bar{\mathbf{F}}, \quad \bar{\mathbf{C}} = \bar{\mathbf{F}}^T \bar{\mathbf{F}}, \quad \bar{\mathbf{B}} = \bar{\mathbf{F}} \bar{\mathbf{F}}^T, \quad (11)$$

$$\bar{I}_1 = J^{-2/3} I_1, \quad \bar{I}_4 = J^{-2/3} I_4. \quad (12)$$

Fig. 2 Representative image of the cross-section along an artery displaying the layers and collagen fiber orientations within the wall. γ is the angle between the fiber directions \mathbf{M} and \mathbf{M}' and the circumferential direction. Adapted from Gasser et al. (2006). Reproduced with permission



The original quantities and their isochoric counterparts are equal for the incompressible case, hence the isochoric quantities are used in the following for overall consistency.

\bar{I}_4 can be utilized to split the energy density function into a term describing the isotropic deformation of the ground substance (tissue matrix) and a second term describing the anisotropic deformation of the transversely isotropic family of aligned fibers, through the following equation

$$W = W_g(\bar{I}_1) + W_f(\bar{I}_4), \quad (13)$$

which can be more comprehensively expressed as

$$W_g(\bar{I}_1) = \frac{1}{2}\mu(\bar{I}_1 - 3), \quad W_f(\bar{I}_4) = \frac{k_1}{k_2}\{\exp[k_2(\bar{I}_4 - 1)^2] - 1\}. \quad (14)$$

The coefficients are as follows: μ is the shear modulus, k_1 is a stress-like parameter, and k_2 is a dimensionless parameter.

The exponential function in the strain-energy function captures the strong stiffening effects of the interior tensions in collagen fibers at higher strain levels. Using these expressions the relationship for the Cauchy stress is defined as

$$\boldsymbol{\sigma} = -p\mathbf{I} + \mu\mathbf{B} + 4k_1(\bar{I}_4 - 1)\exp[k_2(\bar{I}_4 - 1)^2]\overline{\mathbf{m}} \otimes \overline{\mathbf{m}}, \quad \overline{\mathbf{m}} = \overline{\mathbf{F}}\mathbf{M}. \quad (15)$$

Extending this framework to better represent arterial tissue structure is the inclusion of a second fiber family which is transversely symmetrical to the first fiber family (see Fig. 2), and identified by the unit vector \mathbf{M}' . For completeness, the two families are described below using the invariants \bar{I}_4 and \bar{I}_6

$$\bar{I}_4 = \mathbf{M} \cdot (\overline{\mathbf{C}}\mathbf{M}), \quad \bar{I}_6 = \mathbf{M}' \cdot (\overline{\mathbf{C}}\mathbf{M}'). \quad (16)$$

The strain-energy density can now be written as

$$W = W_g(\bar{I}_1) + W_f(\bar{I}_4, \bar{I}_6), \quad (17)$$

$$W_f(\bar{I}_4, \bar{I}_6) = \frac{k_1}{2k_2} \sum_{i=4,6} \{\exp[k_2(\bar{I}_i - 1)^2] - 1\}, \quad (18)$$

with $W_g(\bar{I}_1)$ given by (14)₁, and thus

$$\begin{aligned} \boldsymbol{\sigma} = & -p\mathbf{I} + \mu\mathbf{B} + 2k_1(\bar{I}_4 - 1)\exp[k_2(\bar{I}_4 - 1)^2]\bar{\mathbf{m}} \otimes \bar{\mathbf{m}} \\ & + 2k_1(\bar{I}_6 - 1)\exp[k_2(\bar{I}_6 - 1)^2]\bar{\mathbf{m}}' \otimes \bar{\mathbf{m}}', \end{aligned} \quad (19)$$

with $\bar{\mathbf{m}}' = \bar{\mathbf{F}}\mathbf{M}'$ and $\bar{\mathbf{m}}$ defined in (15)₂.

Going further, consider that, anatomically, individual fibers in a fiber family are not aligned, but are distributed around a mean direction (see Fig. 2). In the HGO model, this can be captured by introducing a generalized structure tensor \mathbf{H} to account for the dispersion around the mean \mathbf{M} and \mathbf{M}' vectors in the arterial tissue, written for the \mathbf{M} case as follows:

$$\mathbf{H} = \kappa\mathbf{I} + (1 - 3\kappa)\mathbf{M} \otimes \mathbf{M}, \quad \kappa = \frac{1}{4} \int_0^\pi \rho \sin^3 \Theta \, d\Theta, \quad (20)$$

where κ is a dispersion parameter and ρ is an orientation density function based on a π periodic von Mises distribution of fibers rotationally symmetric around \mathbf{M} . A graphical representation of this function is given in Fig. 3, while a three-dimensional representation is provided in Fig. 4.

\bar{I}_4 must then be modified to account for dispersion and is replaced with \bar{I}_4^* , defined as follows:

$$\bar{I}_4^* = \mathbf{H} : \bar{\mathbf{C}} = H_{ij}\bar{C}_{ij}, \quad (21)$$

which can also be simplified to the following:

$$\bar{I}_4^* = \kappa\bar{I}_1 + (1 - 3\kappa)\bar{I}_4. \quad (22)$$

This leads to the following expression for W_f

$$W_f(\bar{I}_1, \bar{I}_4) = \frac{k_1}{k_2} \{\exp[k_2(\bar{I}_4^* - 1)^2] - 1\} = \frac{k_1}{k_2} \{\exp[k_2(\kappa\bar{I}_1 + (1 - 3\kappa)\bar{I}_4 - 1)^2] - 1\}. \quad (23)$$

Repeating the process for \mathbf{M}' yields

$$\mathbf{H}' = \kappa\mathbf{I} + (1 - 3\kappa)\mathbf{M}' \otimes \mathbf{M}', \quad \bar{I}_6^* = \kappa\bar{I}_1 + (1 - 3\kappa)\bar{I}_6. \quad (24)$$

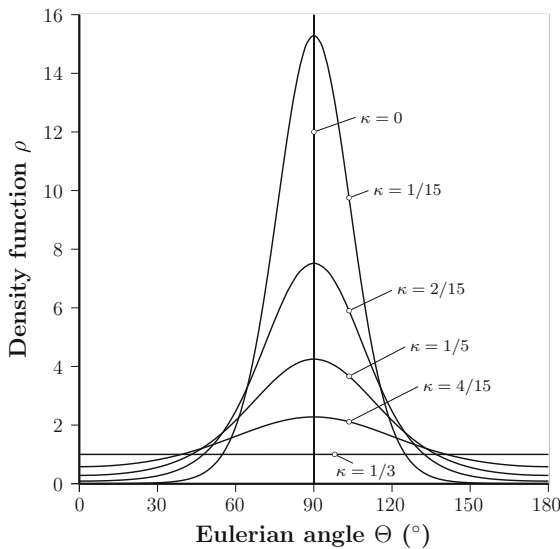


Fig. 3 A two-dimensional graphical representation of the (transversely isotropic) von Mises distribution of collagen fibers (Gasser et al. 2006). Reproduced with permission

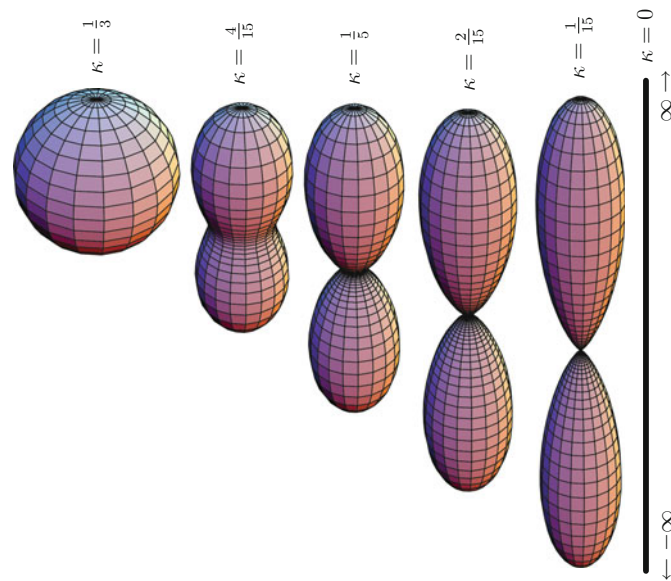


Fig. 4 A three-dimensional graphical representation of the (transversely isotropic) von Mises distribution of collagen fibers (Gasser et al. 2006). Reproduced with permission

and then finally

$$W = W_g(\bar{I}_1) + W_f(\bar{I}_1, \bar{I}_4, \bar{I}_6), \quad (25)$$

where

$$W_f(\bar{I}_1, \bar{I}_4, \bar{I}_6) = \frac{k_1}{2k_2} \sum_{i=4,6} \{\exp[k_2(\bar{I}_i^* - 1)^2] - 1\} \quad (26)$$

and $W_g(\bar{I}_1)$ is again given by (14)₁.

Figure 5 shows the analytical solution to the HGO model for the case of a thin-walled tube, showing the influence of the mean alignment and dispersion coefficient on the overall mechanical properties. From the figure it can be seen that higher fiber dispersion κ correlates with lower fiber family orientation angle dependence γ .

For the case of compressible or slightly compressible materials, a recent study by Nolan et al. (2014) has demonstrated that the full forms of the anisotropic invariants (I_4, I_6) must be used. If the isochoric forms of the anisotropic invariants (\bar{I}_4, \bar{I}_6) are used when material volume change is permitted ($J \neq 1$) then significant errors in the computed stress can emerge. An experimental study on ovine aortic tissue by Nolan and McGarry (2015) reveals significant material volume change and suggests that such tissue is compressible at a macroscopic continuum level. To fully characterize such phenomena, there is a need for further experimentation to be performed on muscular arterial tissue, including compressibility tests on healthy and diseased human arterial tissue.

Two other phenomena that are important in the modeling of arterial tissue and that have been addressed in the literature are remodeling and damage.

3.2 Remodeling

Remodeling of fiber directions in arterial layers has been considered by a number of authors in the field of biomechanics. These studies typically assume that the mechanical stimuli (stress or strain) on arterial tissue determine the local fiber orientations, for example:

- Fibers will reorient towards the plane of maximum and intermediate principal directions of the tensorial stimuli.
- In this plane, the angle of fiber alignment with respect to maximum principal stimulus is determined by magnitudes of two maximum principal stimuli. In the principal stress case, where γ is angle of fiber alignment with respect to the maximum principal stress, and σ_1 and σ_2 are the maximum and intermediate principal stresses, $\tan \gamma$ can be written as a function, M , of the principal stress ratio:

$$\tan \gamma = M(\sigma_2/\sigma_1). \quad (27)$$

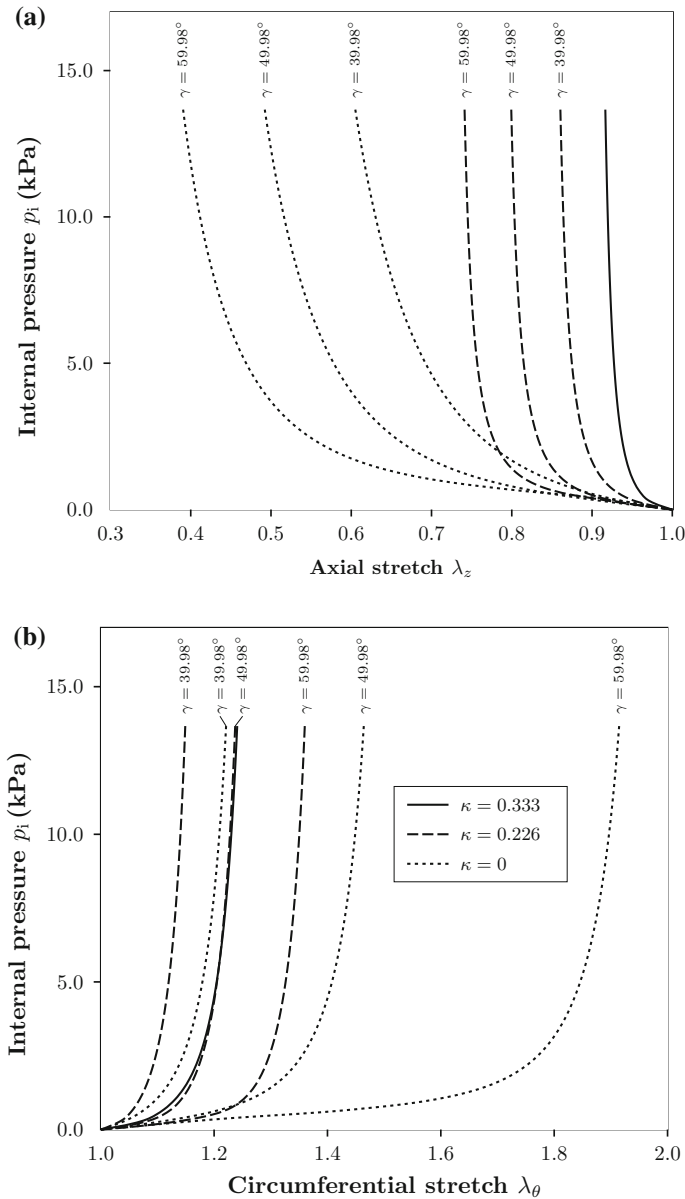


Fig. 5 Graphs depicting the influence of the mean fiber alignment and dispersion on the pressure response of the artery wall (Gasser et al. 2006). Reproduced with permission

Other approaches to the fiber remodeling have been discussed in more recent studies. Driessen et al. (2004) developed principal stress-based approaches for fiber remodeling using the principle discussed for dispersed fiber populations. Hariton et al. (2007) proposed a stress-based approach using the Holzapfel-type fibrous hyperelastic model discussed above (HGO without dispersion), where

$$\tan \gamma = M(\sigma_2/\sigma_1) = \sigma_2/\sigma_1. \quad (28)$$

Creane (2011) reviewed the topic of fiber remodeling and has developed a strain-based remodeling algorithm for dispersed fiber populations, based on the HGO model. This model uses an iterative method to create an optimal structure tensor for the fiber orientation for each fiber family (Creane 2011; Creane et al. 2012).

3.3 Damage-Induced Softening

Damage models are used to replicate the effects of stress softening in soft tissues. These types of models are needed to account for damage induced in soft tissues during supra-physiological loading, e.g., stenting procedure. This type of modeling uses a continuum approach and is distinct from microstructure and material separation modeling.

Most commonly, damage is modeled using a damage parameter, introduced into finite-deformation elasticity laws, to account for tissue softening in terms of a reduction in the mechanical properties and stress, which represents damage to collagen fibers and matrix in the tissue. A comprehensive review of this topic is given in Conway (2013). Analysis of this type can be classified under two major headings: continuum damage mechanics approach and pseudo-elasticity approach (Weisbecker et al. 2011).

3.3.1 Continuum Damage Mechanics Approach

A general form for a modified strain-energy density function, to account for damage, is given as (Miehe 1995)

$$W(\mathbf{C}, D) = (1 - D)W_0(\mathbf{C}), \quad (29)$$

where D is the damage parameter and W_0 is the undamaged strain-energy density function. There are two sub-categories to consider: discontinuous damage and continuous damage, as reviewed in Miehe (1995) and Peña and Doblaré (2009).

Discontinuous Damage

This form of damage is calculated by the accumulation of damage in the first loading cycle of a strain-controlled loading. In any subsequent load cycle, further damage may only be accumulated with strain energy exceeding the previous maximum strain energy achieved.

This is best described by the relationship below, where damage is governed by the quantity α , which represents the maximum undamaged strain-energy density achieved during the loading history (time: $0 \rightarrow t$) (Miehe 1995):

$$\alpha = \max W_0(\mathbf{C}(s)), \quad s \in (0, t). \quad (30)$$

During a typical loading history, involving loading, unloading, reloading, etc., there is no (further) damage accumulation when $W_0(\mathbf{C}) < \alpha$.

Continuous Damage

When determining this type of damage, the entire loading history is accounted for, and this type of damage can account for the continuous softening of a material over its lifespan. Damage is possible during loading in cycles of the same amplitude. The variable β is used to govern the continuous damage and monotonically increases with deformation through the following (Miehe 1995):

$$\beta = \int_0^t |\dot{W}_0(\mathbf{C}(s))| \, ds. \quad (31)$$

Comparison

Both discontinuous and continuous damage models are usually applied to only the isochoric (deviatoric) part of the deformation gradient tensor. In algebraic form, $W_0^{\text{ich}}(\mathbf{C})$.

The discontinuous model approach has been the more commonly applied of the two, arguably due to it being more physically relevant for soft tissues. For example, the well-known Mullins effect is well described by this model type; capturing this behavior is important because soft tissue loading and unloading curves have been observed to clearly exhibit the Mullins effect, as reviewed in Conway (2013). Studies that have used the soft tissue discontinuous modeling approach include: Hokanson and Yazdani (1997), Balzani et al. (2004, 2006, 2012), Rodríguez et al. (2006), Calvo et al. (2007), Alastraú et al. (2007), Brinkhues et al. (2009), Maher et al. (2011, 2012), Peña (2011).

Continuous damage modeling exhibits advantages in relation to the modeling of cyclic loading, for example, in relation to capturing hysteresis in arterial tissue cyclic stress-strain curves, and in relation to simulating the effects of preconditioning

loading histories performed prior to the testing proper. Studies in this domain include: Miehe (1995), Ehret and Itsikov (2009), Peña and Doblaré (2009), Martin and Sun (2013).

Very good predictive performance for cyclic loading has been achieved using discontinuous and continuous modeling combinations, for example in: Miehe (1995), Peña et al. (2009), Martin and Sun (2013). Figure 3 from Peña et al. (2009) compares combined discontinuous and continuous model predictions for aortic tissue response under cyclic loading (Fig. 6a) with predictions for a discontinuous only (Fig. 6b) and a continuous only (Fig. 6c). The superior performance of the combined model is evident in this case.

Continuum damage mechanics approaches have been developed and applied to soft tissue in a range of contexts; in anisotropic tissue models to represent matrix and fiber damage, to capture material rate dependence and permanent deformation on unloading, and in models that include arterial tissue residual stresses. Example studies include: Hokanson and Yazdani (1997), Volokh (2008) (isotropic damage models); Balzani et al. (2004, 2006, 2012), Brinkhues et al. (2009), Gasser (2011) (collagenous damage models); Calvo et al. (2007), Rodríguez et al. (2008), Gracia et al. (2009), Peña et al. (2009), Weisbecker et al. (2011) (matrix and fiber damage models); Peña (2011) (rate dependent material damage); Maher et al. (2011) (inelastic isotropic damage).

3.3.2 Pseudo-Elasticity Approach

The pseudo-elasticity approach is another discontinuous damage modeling approach, but its formulation is not classified under the heading of continuum damage mechanics. In the pseudo-elasticity approach, if one considers strain controlled loading, then damage accumulates during the first loading path, with no damage accumulation on unloading, and in any subsequent load cycle there is no further damage unless the previous maximum strain energy is exceeded.

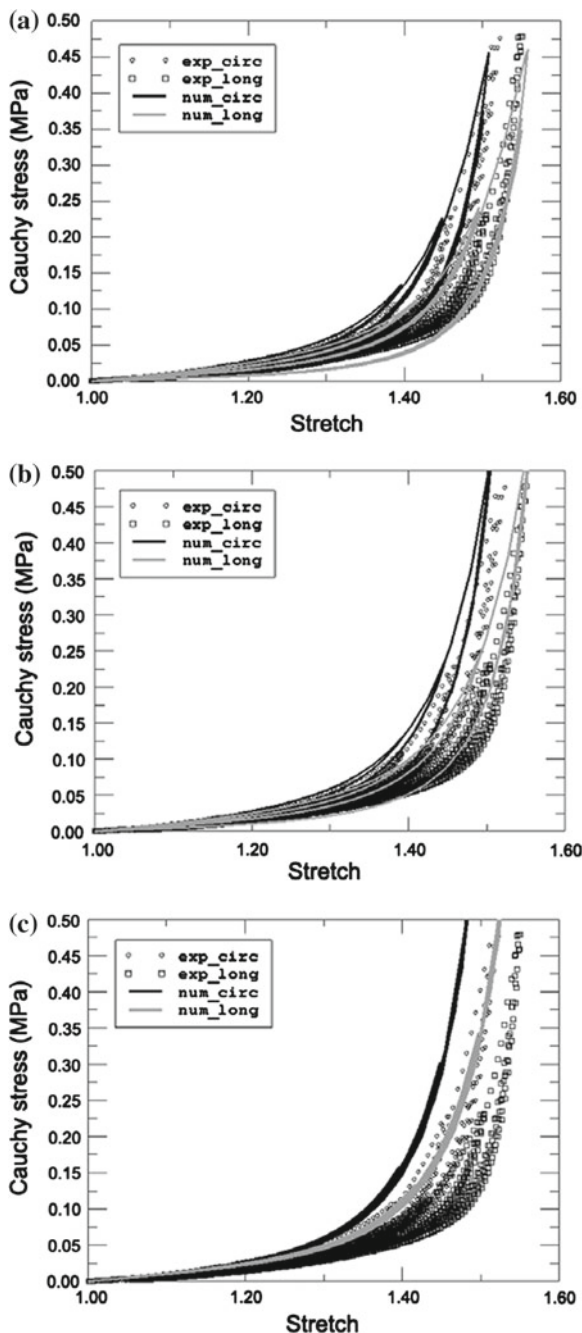
Ogden and Roxburgh (1999) developed a pseudo-elastic model that is widely used. This model was originally developed for modeling filled rubber elastomers that display the Mullins effect; this would later become the basis for the implementation of the Mullins effect in finite element software, i.e., Abaqus (2013).

The model can be described in terms of a modification of the strain-energy density to generate a pseudo-energy density

$$W(\mathbf{C}, \eta) = \eta W_0(\mathbf{C}) + \Phi(\eta), \quad (32)$$

where η is a damage parameter, W_0 is the undamaged strain-energy density and Φ is a damage function.

Fig. 6 Stress response of aortic tissue during cyclic biaxial tensile loading comparing experimental versus numerical models to capture damage. The different models used were mixed model (a), discontinuous model (b) and continuous (c) (from Peña et al. 2009). Reproduced with permission



Mullins Effect

The Mullins effect is important for arterial modeling as it is more physically relevant than pure hyperelasticity. The Mullins effect (see Fig. 7) is described by the loading and unloading curves following different loading paths, allowing for the formation of hysteresis loops in stress-strain curves during cyclic loading.

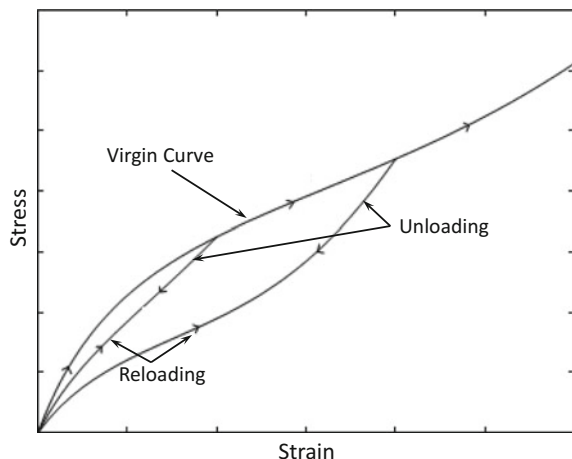
The Ogden and Roxburgh (1999) model assumes incompressibility. In simple tension, the stress is described by the following relationship, where λ is the principal stretch in the loading direction:

$$\sigma = \eta \lambda \frac{\partial W_0}{\partial \lambda}. \quad (33)$$

With reference to Fig. 7, on a virgin curve $\eta = 1$ and the loading follows the path $\sigma = \lambda \partial W_0 / \partial \lambda$. Upon unloading η becomes less than 1; there a softening effect and the material unloads along a lower stress path given by (33). As unloading progresses, the damage parameter reduces gradually to a minimum value $\eta = \eta_m < 1$ which, in turn, is determined by the original point of unload on the virgin curve. Upon reloading the material reloads along the softer curve with η gradually increasing, until the virgin curve is re-joined ($\eta = 1$), and further loading continues along the virgin curve. If a subsequent unloading event occurs, the process described above is repeated. An explicit form of η is given in Ogden and Roxburgh (1999) as follows, where r and m are model parameters, and W_0^m is the maximum value of the pseudo-energy function reached over the loading history:

$$\eta = 1 - \frac{1}{r} \operatorname{erf} \left[\frac{1}{m} (W_0^m - W_0) \right]. \quad (34)$$

Fig. 7 Stress/strain response of a material exhibiting an idealized Mullins effect. Adapted from Ogden and Roxburgh (1999). Reproduced with permission



The model is normally applied to the isochoric part of the deformation, but the framework can be extended to compressible materials.

Pseudo-elastic modeling approach developments include the representation of damage in anisotropic fibrous soft biological materials, better definitions of the hysteresis loops observed in cyclic loading and also the implementation of residual permanent deformation upon unloading. Example studies include: Ogden and Roxburgh (1999), Dorfmann and Ogden (2003, 2004), Franceschini et al. (2006), Ciarletta et al. (2008), Peña and Doblaré (2009), Peña et al. (2011), Weisbecker et al. (2012).

Important differences between the continuum damage mechanics and pseudo-elastic modeling approaches are that continuum damage mechanics allows for continuous and discontinuous softening, while pseudo-elastic model calibration from experimental data is typically easier since material parameters and damage model parameters can be fitted independently (Weisbecker et al. 2011).

4 Atherosclerotic Plaque

4.1 Introduction

Atherosclerotic plaque is an extremely complex structure with wide variations in both geometries and constituents. It is really a term for a wide range of geometries and structures that can change over time: soft lesions evolve to become hard calcified lesions. A schematic of the cross section of an atherosclerotic plaque is presented in Fig. 8. In this illustration, components such as lipid pools, calcifications and a fibrous cap are shown. In more advanced stages, stable lesions can continue to grow and also become highly calcified. Alternatively the fibrous caps can become unstable, leading to rupture and the formation of thrombus material, which can lead to embolism formation in the blood flow. A particularly dangerous situation is that of ‘vulnerable’ plaque, where the lesion can become unstable and the fibrous cap rupture early in lesion development; detection of early stage plaque vulnerability is still a major clinical challenge. For additional information on atherosclerosis please refer to Stary (1999).

The experimental characterization and modeling of plaque tissue is distinctly lacking in comparison to the extent of experimental characterization and modeling of healthy arterial tissue, and still represents a frontier for vascular mechanics and modeling. The importance of accuracy in the modeling of atherosclerotic plaque is paramount in the accurate prediction of the performance of vascular implants, such as vascular stents. Further to this, improvements in modeling capabilities for the prediction of implant performance could be very beneficial in the evolution of regulatory approval processes, for example, Food and Drug Administration (FDA 2010) requirements for the finite element modeling of stents as part of the medical device regulatory approval process.

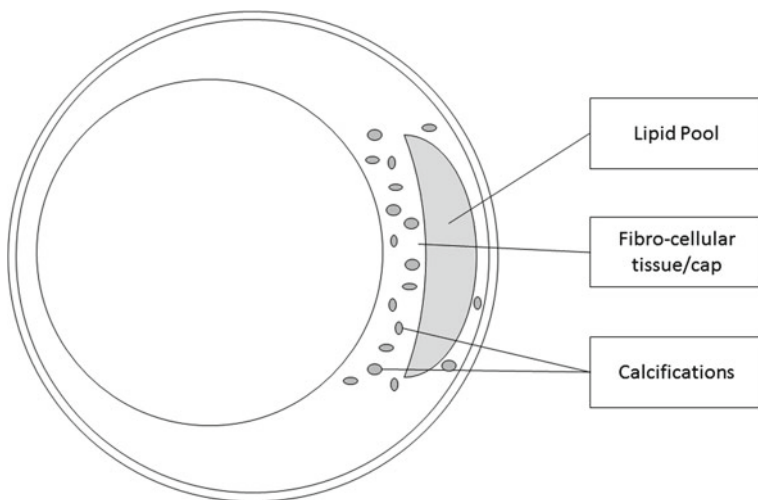


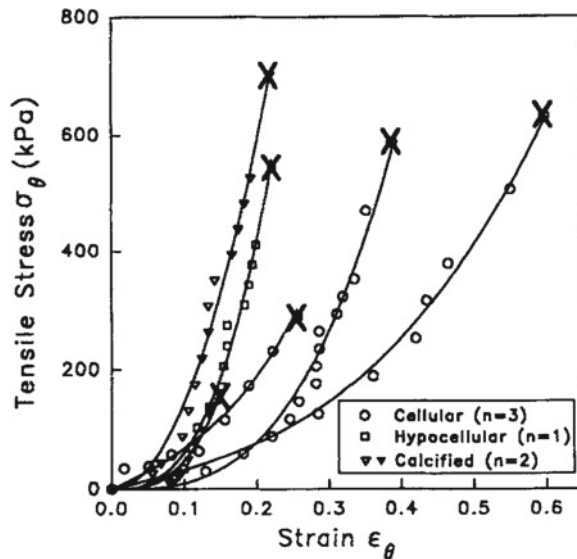
Fig. 8 Schematic of the cross section of an atherosclerotic plaque. Plaque constituents usually include lipid pools, a fibrous cap and calcifications

4.2 Experimental Mechanical Characterization and Testing

There are many challenges in the mechanical testing of atherosclerotic plaque tissue; it can be very soft and typically contains fluidic regions leading to issues in the handling and gripping of the tissue. There is difficulty in obtaining and isolating plaque tissue, and in particular for human tissue, for obvious reasons. Such difficulties present significant challenges in relation to trying to ensure material consistency for testing across different testing programmes and in relation to test reproducibility. The tissue is inherently highly heterogeneous and a broad range of structural variability exists, leading to a discussion of whether testing entire plaques or cut sections of a plaque is more appropriate. One major limitation to plaque tissue analysis, characterization and testing is the lack of a robust animal model of atherosclerotic plaque that is sufficiently representative of the disease in humans; the lack of such a model has significant implications for material availability, consistency and test reproducibility.

In the literature that is available, the main approach to experimental testing is macroscopic mechanical testing, focusing on compressive and tensile loading, and extracting overall mechanical response (stress-strain curves) and mechanical properties, including elastic modulus and ultimate strength (UTS), etc. Relatively speaking, there has been a limited focus on determining local/sub-structure tissue mechanical properties. Examples of studies focusing on macroscopic mechanical characterization include: Loree et al. (1994), Topoleski et al. (1997), Salunke et al. (2001), Walraevens et al. (2008), Maher et al. (2009, 2011), Teng et al. (2009), Lawlor et al. (2011), Mulvihill et al. (2013). Also reported in a number of these studies

Fig. 9 Data from Loree et al. (1994) tensile stress-strain curves for 6 fractured plaque specimens categorized by plaque type. Reproduced with permission



are macroscopic constitutive model fits to the experimental stress-strain data, using neo-Hookean and polynomial hyperelastic models for example.

The study of Loree et al. (1994) is an influential early study where the broad variation in mechanical response was clearly illustrated (see Fig. 9) as a function of plaque material type. Useful data on basic stress-strain curve shapes, and fracture stress and strain ranges, was reported; for example fracture stresses in the range 149–701 kPa, and strains in the range 15–60 %, were reported. These data have been used as the basis for a number of plaque constitutive model calibrations in subsequent studies, including Gastaldi et al. (2010), Conway et al. (2012, 2014), Morlacchi et al. (2013). The more recent study of Maher et al. (2009) also illustrates significant tissue type dependence and also significant differences between tensile and compressive loading response (see Fig. 10).

One difficulty, due to the heterogeneity and broad range of structural variability, is that a definitive and standardized tissue type categorization has not been established, and the tissue type descriptions reported in different studies are very much study dependent, where the authors have made efforts to come to terms with the nature of the tissue samples available in any given instance. This adds a layer of complexity and uncertainty to the interpretation of mechanical property data that is not present for traditional materials, where constituents, manufacturing route and mechanical properties generally adhere to well established standards. The Loree et al. (1994) and Maher et al. (2009) studies illustrate this point for plaque (Figs. 9 and 10); ‘cellular’, ‘hypocellular’ and ‘cholucent’ tissue types are identified, but these are quite subjectively defined as determined by the specific tissue at hand and the specific microscopy/characterization method employed. In the same vein, a recent study by Barrett et al. (2016) has proposed a number of calcified plaque sub-classifications.

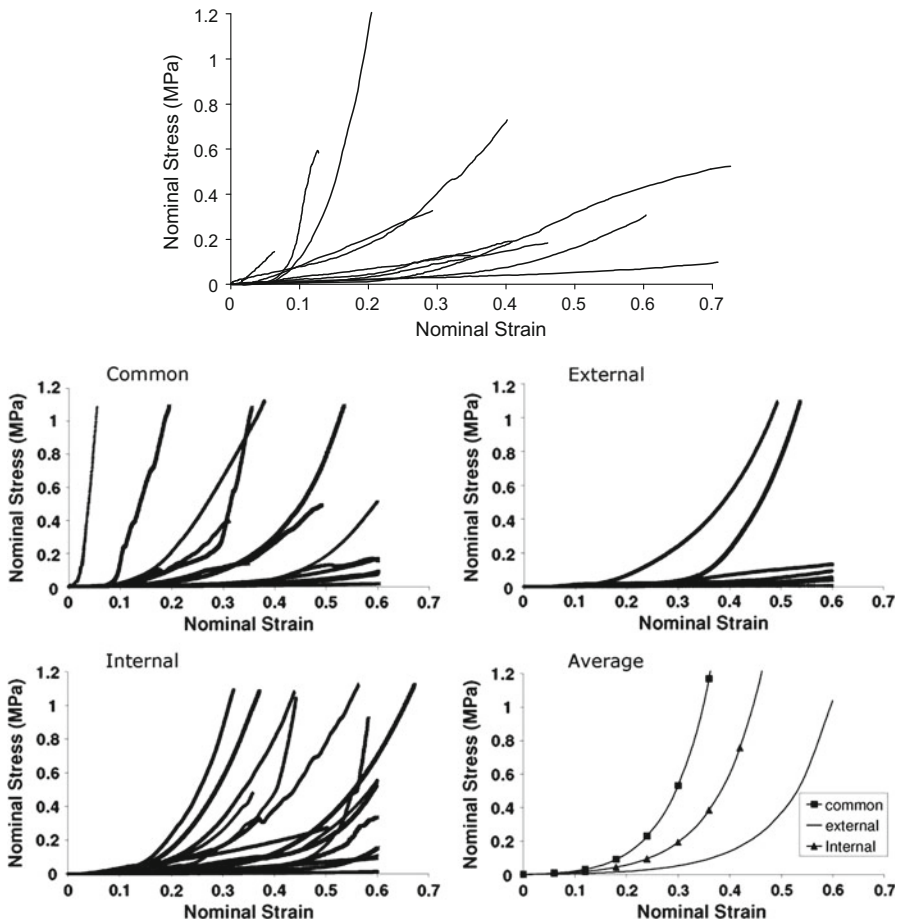


Fig. 10 Figures from Maher et al. (2009) for mechanical testing of carotid plaque: the *upper figure* shows tensile stress-strain response, and the group of *four figures* show compressive stress-strain response (unconfined compression), depending on tissue type. The average curves were obtained using a mean set of hyperelastic constants using a second order polynomial hyperelastic strain-energy function. Reproduced with permission

The relatively small number of studies focusing on plaque tissue sub-structure characterization includes those given in Table 1. A range of testing methods has been used, including tensile and compressive mechanical testing, rheometry and nano-indentation, to resolve the mechanical response and behavior of individual plaque constituents such as the fibrous cap, lipid core, calcifications, etc. Anisotropy of constituent layers in plaque has also been measured through tensile testing in axial and circumferential arterial directions (Holzapfel et al. 2004; Teng et al. 2009).

Nano- and micro-indentation presents very useful possibilities for determining constituents' mechanical behavior, since the necessity for extracting test samples of

Table 1 Experimental studies reporting on plaque tissue constituent mechanical characterization

Reference	Location	Method	Constituents	Data reported/model fit
Chai et al. (2013)	Carotid	Indentation	Fibrous cap	Reported: elastic moduli
			Intima	
			Lipid core	
Barrett et al. (2009)	Carotid	Indentation	Fibrous cap	Model fit: neo-Hookean
Ebenstein et al. (2009)	Carotid	Indentation	Calcification	Reported: reduced moduli
			Fibrous tissue	
			Hematoma (clot)	
Holzapfel et al. (2004)	Iliac	Tensile	Fibrous cap	Reported: stress-strain curves
			Fibrous intima	
			Fibrotic media	
Loree et al. (1994)	Synthetic	Rheometer	Lipid pools	Reported: storage and loss moduli
Lee et al. (1991)	Aorta	Cyclic compressive	Fibrous cap	Reported: elastic moduli

the different constituents can largely be avoided. Studies utilizing nano-indentation (for example, Barrett et al. 2009) have shown large variation in local constituent mechanical properties, similar to that seen at the macroscopic level for the tissue as a whole. While useful for determining material properties in the physiological loading regime, indentation is limited when response to higher (supra-physiological) loads is being explored, including tissue rupture behavior.

It should be emphasized that it is necessary to determine plaque tissue mechanical behavior in both the physiological loading and supra-physiological loading regimes; the former is obviously relevant, but the latter is also of significant importance due, for example, to the high local strains and stresses caused by vascular device deployment and implantation.

Overall, looking into the future, mechanical testing and characterization of plaque tissue at the sub-structural scale is vitally important, to address the unmet need for more accurate atherosclerotic plaque constitutive and damage models.

For more information on these topics, the reader is referred to recent comprehensive review articles on plaque testing and mechanical properties (Cardoso and Weinbaum 2014) and the special issue on ‘Plaque Mechanics’ in the Journal of

biomechanics (Gijsen and Migliavacca 2014) that includes, for example, Akyildiz et al. (2014), Chai et al. (2014), Holzapfel et al. (2014), Kolandaivelu et al. (2014), Walsh et al. (2014).

4.3 Computational Modeling of Atherosclerotic Plaque

Based on the experimental mechanical property data that is available, constitutive models for plaque have been developed and implemented in computational models of atherosclerotic arteries. Linear elastic plaque representations have been developed (typically found in earlier studies) based on measured elastic modulus data. As an advancement on this, plaque tissue stress-strain curves have been used to calibrate a range of hyperelastic models in the finite deformation kinematics regime, and this is the most common approach reported in the literature to date. The majority of studies have assumed material isotropy for individual plaque constituents or the plaque as a whole where homogeneity and effective properties have been assumed. Anisotropy in fibrous tissue has also been explored. Table 2 gives a summary listing of reported computational studies involving atherosclerotic artery representations, where the studies have been categorized by spatial dimension (2D-planar or 3D), arterial geometry (idealized or realistic/patient specific, as might be determined from medical imaging), representation of the diseased tissue structure (whether homogenized or multi-component/multi-phase), and material model(s) employed. An illustrative example is that of Cilla et al. (2012) shown in Figs. 11 and 12, where a lipid core is represented using a hyperelastic idealization. In addition to this, the reader is referred to the aforementioned reviews for further information (in particular Holzapfel et al. 2014), and also Morlacchi and Migliavacca (2013).

4.3.1 Plaque Tissue Inelasticity and Damage Modeling

A significant limitation in current atherosclerotic plaque computational modeling is the accurate modeling of plaque inelasticity and damage. Clearly, significant challenges exist in characterizing plaque inelasticity and damage experimentally, going beyond difficulties associated with elastic and hyperelastic property identification. The small number of experimental studies that have investigated plaque inelasticity have shown the existence of inelastic/non-recoverable deformation (Topoleski et al. 1997; Topoleski and Salunke 2000; Ebenstein et al. 2009; Maher et al. 2011) depending on plaque type. Intimately linked with tissue inelasticity is tissue damage, not least because damage can manifest itself as inelastic deformation, with damage leading to material softening and rupture, and it is very clear from clinical practice that plaque can experience damage and rupture as part of the angioplasty procedure for example. As a consequence, there is a clear need for the accurate characterization of these phenomena (inelasticity, damage, softening and rupture) for the development of more accurate atherosclerotic artery computational models, in particular for the

Table 2 Computational modeling studies involving representation of atherosclerotic plaque

Reference	Type	Geometry	Constituents	Material model
Lee et al. (1992)	2D	Idealized	Plaque	Linear elastic
			Lipid pool	
Cheng et al. (1993)	2D	Realistic—Digitized tracing	Plaque	Linear elastic
			Lipid pool	
			Calcification	
Petrini et al. (2003)	3D	Idealized	Plaque	Hyperelastic 3rd order polynomial
Chua et al. (2004)	3D	Idealized	Plaque	Linear elastic
Migliavacca et al. (2004)	3D	Idealized	Plaque * 3 types	Hyperelastic 3rd order polynomial
Holzapfel et al. (2005b)	3D	Realistic—MRI scan	Diseased intima	Anisotropic hyperelastic
			Lipid pool	
			Calcification	
Li et al. (2006)	2D	Realistic—MRI scan	Fibrous cap	Hyperelastic ogden $n = 2$
			Lipid pool	
Migliavacca et al. (2007)	3D	Idealized	Plaque	Hyperelastic 3rd order polynomial
Kiousis et al. (2007)	3D	Realistic—MRI scan	Lipid pool	Hyperelastic
Timmins et al. (2008)	3D	Idealized	Plaque(stiffness varied)	Hyperelastic 3rd order polynomial
Bluestein et al. (2008)	3D	Idealized	Plaque	Hyperelastic Mooney–Rivlin
			Lipid pool	
			Calcification	
Tang et al. (2009a)	2D	Realistic—MRI scan	Plaque	Hyperelastic modified Mooney–Rivlin
			Lipid pool	
			Calcification	
Tang et al. (2009b)	3D	Realistic—MRI scan	Plaque	Hyperelastic modified Mooney–Rivlin
			Lipid pool	
			Calcification	
Pericevic et al. (2009)	3D	Idealized	Plaque * 3 types	Hyperelastic polynomial $n = 2$
Gastaldi et al. (2010)	3D	Idealized	Plaque	Hyperelastic polynomial $n = 2$

(continued)

Table 2 (continued)

Reference	Type	Geometry	Constituents	Material model
Gu et al. (2010)	3D	Idealized	Plaque	Hyperelastic polynomial $n = 2$
Sadat et al. (2010)	2D	Realistic–MRI scan	Plaque	Hyperelastic ogden $n = 2$
			Lipid pool	
			Calcification	
Zahedmanesh et al. (2010)	3D	Idealized	Plaque	Hyperelastic ogden $n = 1$
Wenk et al. (2010)	3D	Idealized	Fibrous tissue	Hyperelastic fung
			Lipid pool	
Pant et al. (2011)	3D	Idealized	Plaque	Hyperelastic neo-Hookean
Grogan et al. (2011)	3D	Idealized	Plaque	Hyperelastic polynomial $n = 6$
Wong et al. (2012)	2D	Realistic–MRI scan	Lipid pool	Linear elastic
			Fibrous cap	
			Calcification	
Cilla et al. (2012)	3D	Idealized	Lipid pool	Hyperelastic neo-Hookean
			Plaque	
García et al. (2012)	3D	Idealized	Lipid pool	Hyperelastic neo-Hookean
			Plaque	
			Calcification	
Conway et al. (2012)	3D	Idealized/Population specific	Plaque	Hyperelastic polynomial $n = 2$
				Plastic (range of yield strengths)
Morlacchi et al. (2013)	3D	Realistic–CTA	Plaque	Hyperelastic polynomial $n = 6$
		Patient specific		Plastic (yield = 400 kPa)
Grogan et al. (2013)	3D	Idealized	Plaque	Hyperelastic polynomial $n = 2$
Morlacchi et al. (2014)	3D	Idealized	Plaque	Hyperelastic polynomial $n = 6$
			Calcification	

(continued)

Table 2 (continued)

Reference	Type	Geometry	Constituents	Material model
Iannaccone et al. (2014)	3D	Realistic	Fibrotic media	Anisotropic hyperelastic with continuum Damage model
			Lipid pool	
			Fibrous cap	
			Calcification	
Conway et al. (2014)	3D	Idealized/Population specific	Plaque	Hyperelastic polynomial $n = 2$, ogden $n = 1$ and $n = 6$, plasticity and pseudo-elasticity
			Lipid pool	
			Calcification	

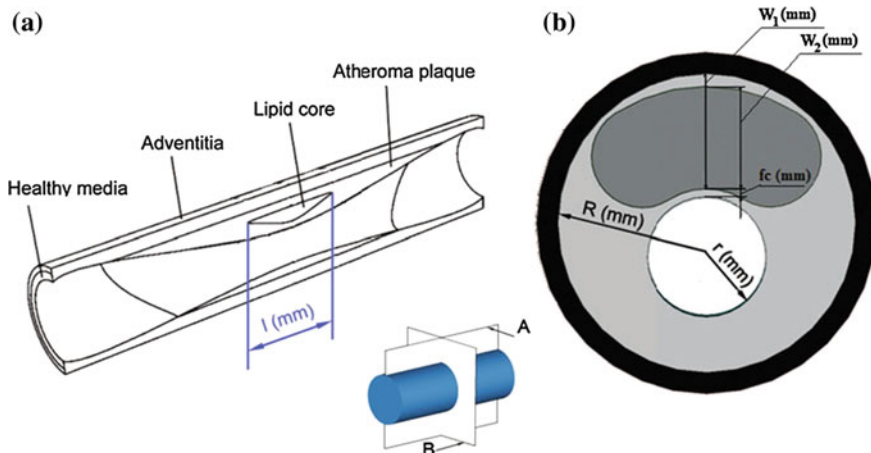


Fig. 11 Idealized geometry of an atherosclerotic arterial model (transversal section). Reproduced from Cilla et al. (2012) with permission

simulation of vascular interventions, such as balloon angioplasty, stent implantation and endarterectomy.

Inelasticity and Damage Modeling Approaches

Approaches reported in the literature for inelasticity and damage modeling include the following (Holzapfel et al. 2014).

The *fracture mechanics approach*, where plaque damage and rupture has been addressed as a crack initiation and growth problem, and some studies have used cohesive zone/interface debonding models to simulate material separation. Examples

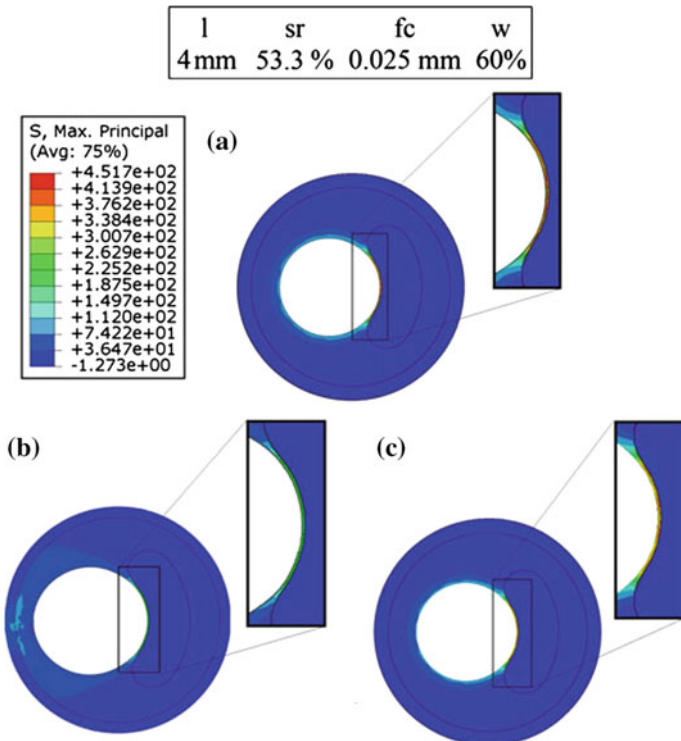


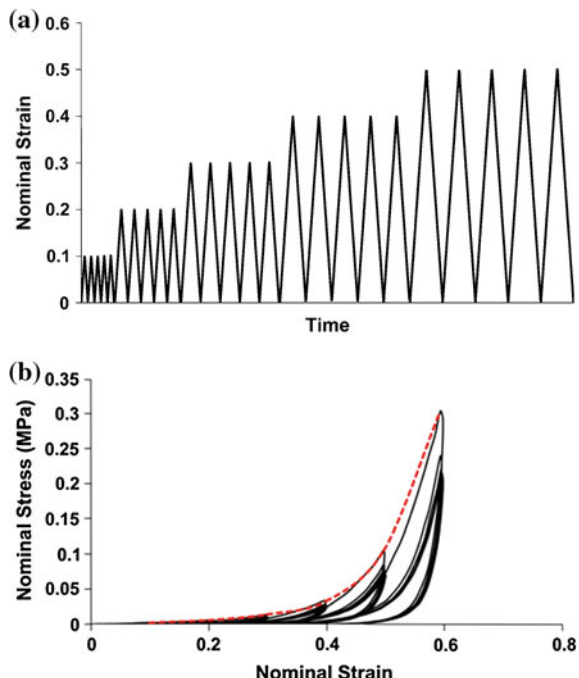
Fig. 12 Contour plots of the maximum principal stress with residual stresses included in (a) the longitudinal direction, (b) the longitudinal and circumferential directions, and (c) without either. Reproduced from Cilla et al. (2012) with permission

of studies in this category include: Versluis et al. (2006), Gasser and Holzapfel (2007), Ferrara and Pandolfi (2008), Nguyen and Levy (2010), Pei et al. (2013), McGarry et al. (2014), Máirtín et al. (2014). Most recently, Leng et al. (2015a, b) investigated the use of cohesive zone modeling to model the delamination of the plaque from the arterial wall.

The *continuum damage mechanics* approach, as described above in Sect. 3.3.1, where the plaque is simulated as a homogeneous continuum and with parameters introduced to represent permanent deformation (inelastic strain) and damage (damage parameter). Examples of studies in this category include Maher et al. (2011), Balzani et al. (2012), and Iannaccone et al. (2014).

The *pseudo-elasticity* and *elasto-plasticity* approaches have been used. The principle of the pseudo-elastic modeling approach has been described in Sect. 3.3.2, and has been used by Conway et al. (2014) to account for plaque damage in a computational

Fig. 13 Data on cyclic compression testing of atherosclerotic plaque samples (human carotid plaque) from Maher et al. (2011): incremental cyclic loading history (*upper figure*), and a typical stress–strain response (*lower figure* the dotted line represents the load envelope of the tissue). Reproduced with permission



model of stent angioplasty (see Sect. 5 below), motivated by the presence of the Mullins effect in experimental cyclic stress-strain data for plaque tissue (Maher et al. 2011) (see Fig. 13). In the elasto-plastic approach, to account primarily for tissue damage, the tissue has been idealized as an isotropic elastic-perfectly plastic material, where the plasticity is characterized by von Mises plasticity, with a yield stress determined from reported plaque stress–strain data. Examples of studies of this type are: Gastaldi et al. (2010), Conway et al. (2012, 2014), Morlacchi et al. (2013), where the Loree et al. (1994) data were used to identify a plaque yield stress of 400 kPa.

The continuum damage mechanics, pseudo-elasticity and elasto-plasticity modeling approaches are very useful phenomenological modeling approaches for attempting to incorporate plaque tissue damage into computational models. They are relatively easy to implement, as they are based on standard engineering mechanics modeling methods, and they do directly deal with the mechanical effects of damage in the tissue, viz., stress/load carrying capacity reduction (stress reduction/softening in the case of continuum damage mechanics and pseudo-elasticity, and stress limitation to the yield stress value in the case of elasto-plasticity). While attractive in terms of implementation, they are highly idealized and not physically based in terms of accounting directly for the microstructural deformation and failure mechanisms that are at play in the material, in particular given the structural heterogeneity of the material.

Plaque Rupture Stresses

In an attempt to characterize the mechanical strength of atherosclerotic plaque tissue, and to aid in assessing tissue rupture risk, significant attention has been paid in the literature to the identification of a ‘plaque rupture stress’. These efforts have typically involved diseased arterial tissue mechanical testing, backed up by computational modeling, where the modeling is used to calculate the local peak tissue stress at the point of macroscopic tissue rupture, thereby identifying the rupture stress value (see Cardoso and Weinbaum 2014; Gijsen and Migliavacca 2014). Using such an approach, a very widely quoted plaque rupture stress threshold of 300 kPa was established by Cheng et al. (1993); they also reported an average rupture stress of 545 ± 160 kPa. The measure of stress used here was the peak circumferential stress (PCS), the local stress component in the arterial circumferential direction.

In terms of using such data in computational models to assess tissue rupture risk, arguably the best stress component to use generally to compare with these values is the maximum principal stress, since it could be argued that it is more representative of a critically loaded condition in a soft predominantly elastic fibrous material, in comparison to von Mises stress, for example, which is more representative of a critically loaded condition in predominantly plastically deforming materials that fail through shape distortion deformation modes (such as ductile metals). Nonetheless, useful critical von Mises stress data has also been reported for vulnerable plaque as lying between 227 and 683 kPa (Li et al. 2006).

Not surprisingly, rupture stresses have been found to be highly variable, depending on the plaque type examined; for example 342 kPa for lipid dominant plaque and 618 kPa for calcified plaque (Mulvihill et al. 2013). Weinbaum and co-workers (Maldonado et al. 2012; Kelly-Arnold et al. 2013; Cardoso and Weinbaum 2014) have focussed on the very important topic of vulnerable cap rupture stress, finding that the high stress concentrations around micro-calcifications (increasing stresses up to $\times 15$) could significantly lower effective rupture stresses for such tissue (see Fig. 14), below the nominal value of 300 kPa, with a value of 107 kPa reported in Maldonado et al. (2012).

4.4 Discussion and Limitations

Undoubtedly, despite the practical difficulties in relation to tissue sourcing and testing, significant and important experimental and modeling work has been performed to characterize and represent the mechanical behavior of atherosclerotic plaque. Significant insights into the mechanical performance of the tissue have been established, and models have been developed that have proven practically useful in computational modeling investigations of vascular interventions such as stent angioplasty.

However, significant work remains to be done on a number of fronts. Although difficult it would be very beneficial if a universally accepted standard for plaque material type could be established. It is clear, however, that this will only be possible

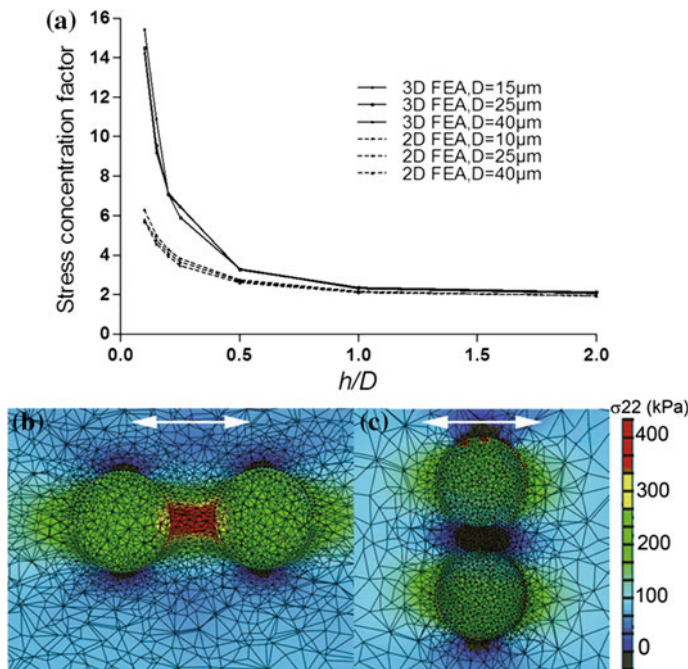


Fig. 14 **a** Illustrates the computational results for the analysis of stress concentrations caused by calcifications in a soft tissue matrix, and the relationship between the separation distance and the diameter, given by h and D , respectively. **b** and **c** show the finite element results for particles of h/D of 0.4 oriented along tensile and transverse loading axes, respectively (Kelly-Arnold et al. 2013). Reproduced with permission

when greater experimental characterization has been performed, but it would be hugely beneficial for the comparison of test data across different studies, and also for the development of constitutive models.

As indicated above, the modeling of plaque inelasticity and damage to date has primarily been phenomenological in nature, and while this is very useful for practical implementation in computational analysis and design studies, it is quite idealized and limited in its ability to accurately capture the details of material deformation and failure. Overall, improved and more physically based constitutive and damage model formulations are required (Holzapfel et al. 2014) that will be more physically accurate and representative in their mechanical performance predictions.

As part of this, multi-scale modeling (Gijsen and Migliavacca 2014) linking physically-based micromechanical modeling with macroscopic mechanical performance, to generate and calibrate more representative material constitutive and damage models, would be hugely beneficial. Current modeling efforts, where plaque tissue sub-structure has been modeled (e.g., Table 2), provide a roadmap for this, but focus needs to be given to more physically representative modeling of individual constituent behavior. In particular, focus needs to be applied to explicit representation of calcified particles and particle-matrix debonding as part of the damage process, the fluidic nature of the lipid pool, and matrix tissue anisotropy. The focus

of a number of recent studies on characterizing plaque calcification, and the effects of calcified particles on tissue mechanical response and rupture stresses, is particularly welcome in this regard (Maldonado et al. 2012; Kelly-Arnold et al. 2013; Cardoso and Weinbaum 2014; Barrett et al. 2016).

Further experimentation is required to more comprehensively characterize plaque tissue non-recoverable/plastic deformation, building on the limited work to date (Topoleski et al. 1997; Topoleski and Salunke 2000; Ebenstein et al. 2009; Maher et al. 2011), as this is essential for constitutive model development for use in computational modeling investigations of vascular interventions such as stent angioplasty, where tissue load-unload-reload behavior must be accurately captured.

Additionally, one area that has received little attention in the literature, in relation to experimental characterization and modeling, is plaque tissue loading rate dependence and viscoelasticity, although the existence of soft tissue viscoelasticity is well accepted. Indeed the tissue preconditioning cyclic loading that is widely utilized in mechanical testing programmes for soft tissue is largely intended to overcome tissue rate effects and viscoelasticity, and to produce stabilized stress-strain response curves for the testing programme proper. In relation to plaque tissue, Topoleski and Salunke (2000) report a significant time-dependent (stress-relaxation) response for the three plaque types that they considered (calcified, fibrous and atheromatous), indicating viscoelastic behavior, and they discuss the possibility that a plaque ‘opened during angioplasty may respond purely mechanically, reclosing after several days because of viscoelastic recovery in the tissue’. On this basis, further experimental work to obtain an accurate characterization of the rate dependence and viscoelasticity of plaque tissue would be extremely beneficial, with a view to accounting for such effects in constitutive and damage models. This would significantly enhance the capabilities of computational models, for example in relation to assessing the effects of balloon/stent deployment rate, and tissue strain recovery and stress relaxation over time.

In relation to future testing programmes, standardization of material storage, sample preparation and testing protocols would be very welcome, along the lines proposed by Walsh et al. (2014).

5 Applications in Stent Angioplasty

As is clear from the above sections, the development of tissue constitutive and damage models to enable the accurate computational modeling of vascular interventions, such as angioplasty, is of significant interest to the computational biomechanics community. This has, in part, been fueled by the industrial need for numerical simulation of medical device performance as part of medical device regulatory approval process, for example the US Food and Drug Administration (FDA 2010) requirements for the computational modeling of stent performance in angioplasty as part of their regulatory approval process.

While the literature on the computational modeling of stenting is vast, studies that have included explicit representations of plaque tissue sub-structure and constituents

are quite rate. This is surprising, given what is now known on the importance of having an accurate plaque tissue representation in computational models of this type, as reviewed in detail above. Examples of such studies include: Holzapfel et al. (2005b), García et al. (2012), Conway et al. (2014), Iannaccone et al. (2014), Morlacchi et al. (2014).

5.1 Stent Design Assessment—Population Specific Computational Modeling

As a practical application of the considerations discussed above, Conway et al. (2012, 2014) reported on the development of a computational test-bed for coronary angioplasty (using finite element analysis and the Abaqus software, Abaqus 2013) to facilitate stent mechanical performance assessment as part of the stent design process. In terms of overall arterial model geometry, the work proposed to bridge the gap between the use of highly idealized (straight or moderately curved cylindrical geometries) on the one hand, that have been extensively studied in the literature, and patient specific arterial geometries (generated from medical imaging) that have the limitation that they are by definition relevant for a particular individual, making generalizations difficult. Instead the population specific approach was taken where models for a range of geometrical population categories were created (covering variations in arterial curvature and stenosis level); this had the advantage of being more general than patient specific, yet more realistic than a single idealized arterial structure. The population specific arterial geometries are shown in Fig. 15, with the steps in the stent deployment simulation illustrated in Fig. 16.

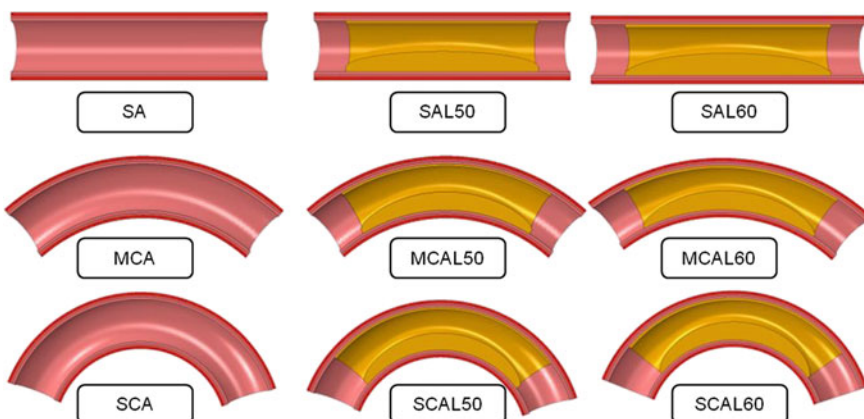
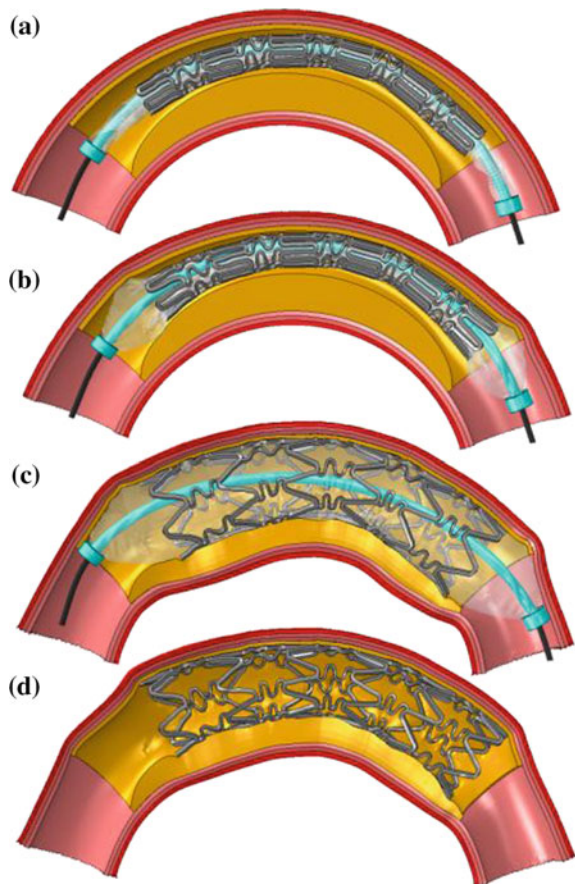


Fig. 15 The population-specific arterial geometries of Conway et al. (2012), covering three levels of curvature (straight artery SA, moderately curved artery MCA, severely curved artery SCA) and three stenosis levels (no stenosis, 50 % lesion L50, 60 % lesion L60). The curvature is quantified by the tortuosity index (TI), with values 0.0, 0.1, 0.3, reading from the *top* to the *bottom* row (Serruys 2008). Reproduced with permission

Fig. 16 Simulation of the steps in stent deployment simulation from Conway et al. (2012).
a Pre-deployment;
b mid-deployment;
c maximum balloon inflation;
d post balloon deflation and removal. Case considered is a severely curved artery with 60% lesion (SCAL60), and the Cypher-like stent.
Reproduced with permission



A second motivation of the work was to attempt to better inform regulatory body guidelines for medical device approval, in particular the FDA guidelines on computational modeling of stent performance in angioplasty (US Food and Drug Administration, FDA 2010). It is interesting to note that these guidelines are relatively imprecise in terms of prescribing details on the diseased artery model structure and the range of arterial geometries that should be considered in these analyzes to generate an accurate depiction of device performance *in vivo*.

Within the geometrical framework shown in Fig. 15 a three-layer arterial model (intima, media, adventitia) was implemented using the HGO model described above, with material constants as established in Holzapfel et al. (2005a,b). A wide range of stenotic (plaque) tissue representations were considered. In Conway et al. (2012) the tissue was represented as a homogeneous nonlinear elastic–plastic material with the nonlinear elasticity characterized by a Mooney–Rivlin polynomial hyperelastic model calibrated by Pericevic et al. (2009) to the Loree et al. (1994) experimental data; a range of plaque tissue types (cellular, hypocellular, calcified) with a range of

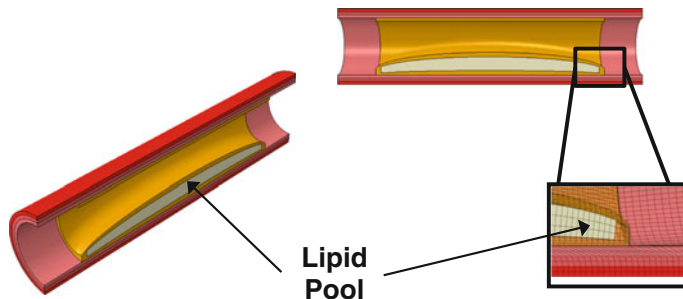


Fig. 17 Schematic diagram of SAL50 artery model (Fig. 15) with lipid pool, constituting 9.3 % of total atherosclerotic tissue volume (Conway et al. 2014). Reproduced with permission

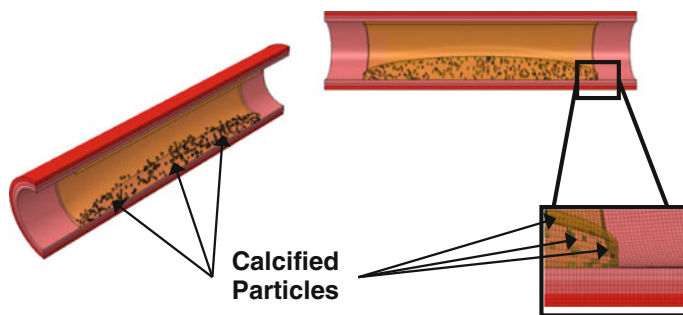


Fig. 18 Schematic diagram of SAL50 artery model (Fig. 15) with calcified particles, constituting 0.5 % of total atherosclerotic tissue volume (Conway et al. 2014). Reproduced with permission

plastic yield stresses (to represent plaque tissue damage) derived from the Loree et al. (1994) data were used. As test cases, the computational test-bed was applied to two stent geometries, based on the closed-cell Cypher stent and the open-cell Multi-Link stent. In Conway et al. (2014) particular focus was applied to the plaque representation to include multiple constituents and constituent combinations, including matrix tissue, lipid pool (Fig. 17) and calcified particles (Fig. 18). In addition, a range of matrix tissue representations was considered, ranging from very soft tissue (using a first-order Ogden hyperelastic model, calibrated from Maher et al. (2011) compressive stress-strain data) to significantly stiffer tissue (using the Mooney–Rivlin polynomial model calibration from Conway et al. 2012). Finally, two plaque (matrix) tissue damage representations were considered: elasto-plasticity (as per Conway et al. 2012) and pseudo-elasticity (using the Ogden and Roxburgh 1999 model, calibrated to the Maher et al. 2011 data—see Fig. 13). This computational test-bed formulation allowed for the effects of each of the modeling features and variations to be considered, and insight gained into their relative importance for the practical purpose of stent mechanical performance assessment, which in turn was assessed through the following measures: stented vessel recoil, stent scaffolding capability (related to radial strength) and tissue damage risk (related to peak tissue stress levels generated).

As detailed in Conway et al. (2012, 2014) the results generated were highly insightful. In relation to overall arterial geometry (Fig. 15), one surprising result was that arterial curvature had only a minor influence on the stent performance measures; relatively speaking, the stenosis level dominated the model predictions, controlling the differentiation between the performance of the two stents (with the open-cell design performing better for larger stenosis levels, and also for greater arterial tortuosity), leading to the suggestion that stenosis level could be critically important parameter in stent selection for the clinician.

Leading on from this, in addition to stenosis level (plaque size), the constitutive description of the plaque tissue, and its sub-structure details, were seen to be extremely influential in determining stent performance, and it was possible to infer relative importance across the range of plaque tissue modeling features considered. In this context, the choice of plaque tissue matrix properties was seen to dominate the results, indicating the importance of establishing clearly defined plaque tissue types, and achieving accurate experimental mechanical characterization that is tissue-type dependent. In relation to damage modeling, the elasto-plasticity approach was significantly more influential than the pseudo-elasticity approach, and this could be related to the significant peak stress limiting effect of the plasticity model on the loading and reloading path, relative to the pseudo-elastic model. This clearly indicates the need to accurately capture the stress softening effects of tissue damage in constitutive models. In relation to plaque tissue sub-structure representation, the presence of calcifications dominated over the presence of the lipid pool in determining stent performance, through increasing vessel recoil (reducing lumen gain) and increasing local tissue stresses (Fig. 19, and in particular Fig. 19f), with the lipid pool only being influential in very soft matrix tissue cases; this emphasizes the importance of having an accurate representation of calcified particles in the plaque tissue model, which is consistent with the recent enhanced focus on characterizing the mechanical effects of plaque tissue calcification, as noted above in Sect. 4.4 (Maldonado et al. 2012; Kelly-Arnold et al. 2013; Cardoso and Weinbaum 2014; Barrett et al. 2016).

One interesting observation was the degree to which plaque tissue is subjected to multi-axial stresses, including both tension and compression, indicating the need for experimental characterization of plaque tissue under multi-axial loading conditions to drive the development of sufficiently representative constitutive and damage models.

5.2 *Recommendations on Regulatory Body Guidelines*

The results of the Conway et al. (2012, 2014) studies are of value from the perspective of informing regulatory body guidelines on numerical simulation of stent performance as part of the medical device regulatory approval process. In the current FDA guidelines document (US Food and Drug Administration, FDA 2010) there is no specific requirement to include an atherosclerotic stenosis or to vary its geometry or constitutive representation in such numerical simulations. However, based on the

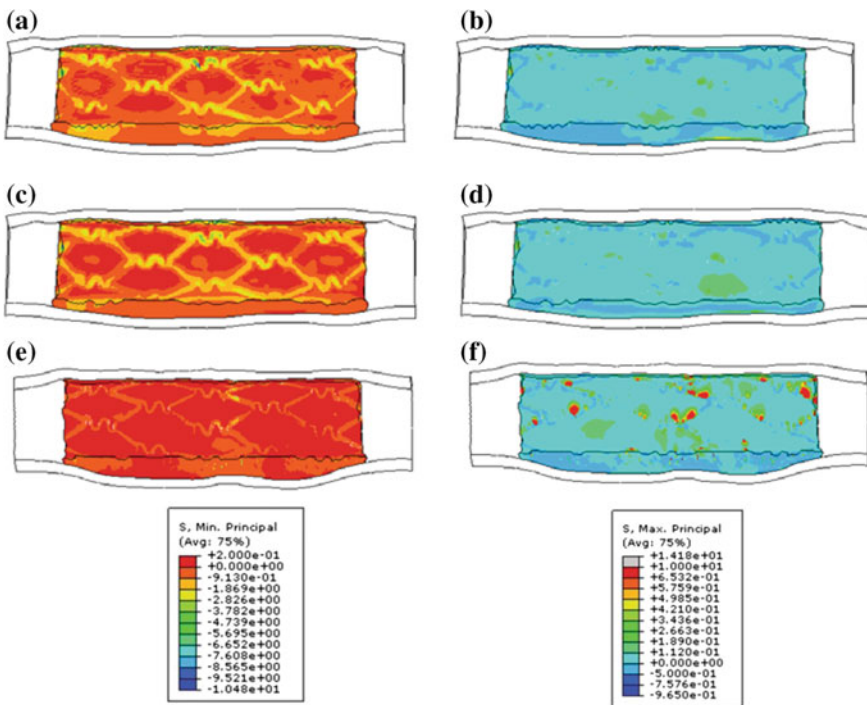


Fig. 19 Principal stress contour plots (MPa) in the plaque tissue at maximum balloon inflation, for the soft Ogden matrix tissue model and the Cypher-like stent (Conway et al. 2014). Minimum principal stresses (**a**, **c**, **e**); maximum principal stresses (**b**, **d**, **f**); lipid pool (**c**, **d**); calcifications (**e**, **f**). Reproduced with permission

present computational test-bed simulation results, it is strongly recommended that the guidelines on computational modeling of stent performance should be updated to:

- Require the inclusion of plaque tissue in such models and the assessment of stent performance over a range of plaque tissue volumes, consistent with the target diseased artery state.
- Require plaque tissue matrix elasticity to be varied over a range (stiff to compliant) that is consistent with the target diseased artery state, and that plaque tissue constituents such as calcifications (in particular) and lipid pools be included.
- Require plaque tissue damage to be represented in such models, perhaps using a plasticity representation (due in part to ease of implementation), until more physically representative models become established.
- Retain the representation of vessel curvature, adhering to the current guideline curvature levels as a minimum. While its influence was seen to be less influential in the test-bed simulations, its presence is nonetheless important to include when different stent designs are being compared.

6 Overall Conclusions

As this chapter has hopefully set out, outstanding progress has been made over (circa) the last twenty years in the characterization of the biomechanics of healthy and diseased vascular tissue, and in the use of such knowledge and data to develop mathematical models (analytical and computational) that can be of significant benefit in the analysis of vascular intervention procedures and in the analysis and design of vascular implants and devices. This has undoubtedly been fueled by rapid advances in imaging and characterization methodologies, and in computational power and simulation software development.

Nevertheless challenges still exist, in particular in relation to the plaque tissue, to more accurately characterize tissue mechanical behavior and quantify tissue mechanical properties, and from this to develop enhanced physically based constitutive and damage models. In relation to the latter, multi-scale modeling methods show promise, given that features and phenomena at different length scales in the material, such as micro- (and nano-) calcifications, calcified particle-matrix debonding, matrix tissue anisotropy and tissue inter-layer debonding, etc., can be explicitly represented, and their effects interrelated, in computational models.

Such developments will continue to enhance the power of computational models to be of significant importance in the analysis, design, and performance assessment of next generation vascular implants, such as biodegradable stents (Grogan et al. 2011, 2013; Boland et al. 2015; McHugh et al. 2015) and stents for peripheral and neural applications.

Acknowledgments The authors acknowledge funding from the Irish Research Council (IRC) under the Embark Initiative (C. Conway), the NUI Galway College of Engineering and Informatics (B. O'Reilly), the SFI/HEA Irish Centre for High-End Computing (ICHEC) and the Programme for Research in Third-Level Institutions (PRTLI) Cycle 5 and co-funded under the European Regional Development Fund (ERDF).

References

- Abaqus, Dassault Systèmes, Simulia, Providence, RI, USA (2013)
- Akyildiz, A.C., Speelman, L., Gijssen, F.J.: Mechanical properties of human atherosclerotic intima tissue. *J. Biomech.* **47**, 773–783 (2014)
- Alastrué, V., Rodríguez, J.F., Calvo, B., Doblaré, M.: Structural damage models for fibrous biological soft tissues. *Int. J. Solids Struct.* **44**, 5894–5911 (2007)
- Balzani, D., Schröder, J., Gross, D.: A simple model for anisotropic damage with applications to soft tissues. *PAMM* **4**, 236–237 (2004)
- Balzani, D., Schröder, J., Gross, D.: Simulation of discontinuous damage incorporating residual stresses in circumferentially overstretched atherosclerotic arteries. *Acta Biomater.* **2**, 609–618 (2006)
- Balzani, D., Brinkhues, S., Holzapfel, G.A.: Constitutive framework for the modeling of damage in collagenous soft tissues with application to arterial walls. *Comput. Methods Appl. Mech. Eng.* **213**, 139–151 (2012)

- Barrett, H.E., Cunnane, E.M., Kavanagh, E.G., Walsh, M.T.: On the effect of calcification volume and configuration on the mechanical behaviour of carotid plaque tissue. *J. Mech. Behav. Biomed. Mater.* **56**, 45–56 (2016)
- Barrett, S.R., Sutcliffe, M.P., Howarth, S., Li, Z.Y., Gillard, J.H.: Experimental measurement of the mechanical properties of carotid atherothrombotic plaque fibrous cap. *J. Biomech.* **42**, 1650–1655 (2009)
- Bluestein, D., Alemu, Y., Avrahami, I., Gharib, M., Dumont, K., Ricotta, J.J., Einav, S.: Influence of microcalcifications on vulnerable plaque mechanics using FSI modeling. *J. Biomech.* **41**, 1111–1118 (2008)
- Boland, E.L., Shine, R., Kelly, N., Sweeney, C.A., McHugh, P.E.: A review of material degradation modelling for the analysis and design of bioabsorbable stents. *Ann. Biomed. Eng.* **44**, 341–356 (2015)
- Brinkhues, S., Balzani, D., Holzapfel, G.A.: Simulation of damage hysteresis in soft biological tissues. *PAMM* **9**, 155–156 (2009)
- Calvo, B., Peña, E., Martínez, M.A., Doblaré, M.: An uncoupled directional damage model for fibred biological soft tissues. Formulation and computational aspects. *Int. J. Numer. Methods Eng.* **69**, 2036–2057 (2007)
- Cardoso, L., Weinbaum, S.: Changing views of the biomechanics of vulnerable plaque rupture: a review. *Ann. Biomed. Eng.* **42**, 415–431 (2014)
- Chai, C.-K., Akyildiz, A.C., Speelman, L., Gijssen, F.J., Oomens, C.W., van Sambeek, M.R., van der Lugt, A., Baaijens, F.P.: Local axial compressive mechanical properties of human carotid atherosclerotic plaques—characterisation by indentation test and inverse finite element analysis. *J. Biomech.* **46**, 1759–1766 (2013)
- Chai, C.-K., Speelman, L., Oomens, C.W., Baaijens, F.P.: Compressive mechanical properties of atherosclerotic plaques—Indentation test to characterise the local anisotropic behaviour. *J. Biomech.* **47**, 784–792 (2014)
- Cheng, G.C., Loree, H.M., Kamm, R.D., Fishbein, M.C., Lee, R.T.: Distribution of circumferential stress in ruptured and stable atherosclerotic lesions. A structural analysis with histopathological correlation. *Circulation* **87**, 1179–1187 (1993)
- Chua, S.N.D., MacDonald, B.J., Hashmi, M.S.J.: Finite element simulation of slotted tube (stent) with the presence of plaque and artery by balloon expansion. *J. Mater. Process. Technol.* **155**, 1772–1779 (2004)
- Ciarletta, P., Dario, P., Micera, S.: Pseudo-hyperelastic model of tendon hysteresis from adaptive recruitment of collagen type I fibrils. *Biomaterials* **29**, 764–770 (2008)
- Cilla, M., Peña, E., Martínez, M.A.: 3D computational parametric analysis of eccentric atheroma plaque: influence of axial and circumferential residual stresses. *Biomech. Model. Mechanobiol.* **11**, 1001–1013 (2012)
- Conway, C.: The development of a computational test-bed to assess coronary stent implantation. Ph.D. thesis, National University of Ireland, Galway (2013)
- Conway, C., Sharif, F., McGarry, J.P., McHugh, P.E.: A computational test-bed to assess coronary stent implantation mechanics using a population-specific approach. *Cardiovasc. Eng. Technol.* **3**, 374–387 (2012)
- Conway, C., McGarry, J.P., McHugh, P.E.: Modelling of atherosclerotic plaque for use in a computational test-bed for stent angioplasty. *Ann. Biomed. Eng.* **42**, 2425–2439 (2014)
- Creane, A.: Identification of potential clinical indicators of carotid plaque disruption using patient specific finite element modelling. Ph.D. thesis, Dublin City University (2011)
- Creane, A., Maher, E., Sultan, S., Hynes, N., Kelly, D.J., Lally, C.: A remodelling metric for angular fibre distributions and its application to diseased carotid bifurcations. *Biomech. Model. Mechanobiol.* **11**, 869–882 (2012)
- Dorfmann, A., Ogden, R.W.: A pseudo-elastic model for loading, partial unloading and reloading of particle-reinforced rubber. *Int. J. Solids Struct.* **40**, 2699–2714 (2003)
- Dorfmann, A., Ogden, R.W.: A constitutive model for the Mullins effect with permanent set in particle-reinforced rubber. *Int. J. Solids Struct.* **41**, 1855–1878 (2004)

- Driessen, N.J., Wilson, W., Bouten, C.V., Baaijens, F.P.: A computational model for collagen fibre remodelling in the arterial wall. *J. Theor. Biol.* **226**, 53–64 (2004)
- Ebenstein, D.M., Coughlin, D., Chapman, J., Li, C., Pruitt, L.A.: Nanomechanical properties of calcification, fibrous tissue, and hematoma from atherosclerotic plaques. *J. Biomed. Mater. Res. A* **91**, 1028–1037 (2009)
- Ehret, A.E., Itskov, M.: Modeling of anisotropic softening phenomena: application to soft biological tissues. *Int. J. Plast.* **25**, 901–919 (2009)
- FDA: Non-Clinical Engineering Tests and Recommended Labeling for Intravascular Stents and Associated Delivery Systems. Printable version (2010). <http://www.fda.gov/medicaldevices/deviceregulationandguidance/guidancedocuments/ucm071863.htm>
- Ferrara, A., Pandolfi, A.: Numerical modelling of fracture in human arteries. *Comput. Meth. Biomed. Eng.* **11**, 553–567 (2008)
- Franceschini, G., Bigoni, D., Regitnig, P., Holzapfel, G.A.: Brain tissue deforms similarly to filled elastomers and follows consolidation theory. *J. Mech. Phys. Solids* **54**, 2592–2620 (2006)
- García, A., Peña, E., Martínez, M.A.: Influence of geometrical parameters on radial force during self-expanding stent deployment. Application for a variable radial stiffness stent. *J. Mech. Behav. Biomed. Mater.* **10**, 166–175 (2012)
- Gasser, T.C.: An irreversible constitutive model for fibrous soft biological tissue: a 3-D microfiber approach with demonstrative application to abdominal aortic aneurysms. *Acta Biomater.* **7**, 2457–2466 (2011)
- Gasser, T.C., Holzapfel, G.A.: Modeling plaque fissuring and dissection during balloon angioplasty intervention. *Ann. Biomed. Eng.* **35**, 711–723 (2007)
- Gasser, T.C., Ogden, R.W., Holzapfel, G.A.: Hyperelastic modelling of arterial layers with distributed collagen fibre orientations. *J. R. Soc. Interface* **3**, 15–35 (2006)
- Gastaldi, D., Morlacchi, S., Nichetti, R., Capelli, C., Dubini, G., Petrini, L., Migliavacca, F.: Modelling of the provisional side-branch stenting approach for the treatment of atherosclerotic coronary bifurcations: effects of stent positioning. *Biomech. Model. Mechanobiol.* **9**, 551–561 (2010)
- Gijsen, F.J., Migliavacca, F.: Plaque mechanics. *J. Biomech.* **4**, 763–764 (2014)
- Gracia, L.A., Peña, E., Royo, J.M., Pelegay, J.L., Calvo, B.: A comparison between pseudo-elastic and damage models for modelling the Mullins effect in industrial rubber components. *Mech. Res. Commun.* **36**, 769–776 (2009)
- Grogan, J.A., O'Brien, B.J., Leen, S.B., McHugh, P.E.: A corrosion model for bioabsorbable metallic stents. *Acta Biomater.* **7**, 3523–3533 (2011)
- Grogan, J.A., Leen, S.B., McHugh, P.E.: Optimizing the design of a bioabsorbable metal stent using computer simulation methods. *Biomaterials* **34**, 8049–8060 (2013)
- Gu, L., Zhao, S., Muttyam, A.K., Hammel, J.M.: The relation between the arterial stress and restenosis rate after coronary stenting. *J. Med. Devices* **4**, 031005 (2010)
- Hariton, I., de Botton, G., Gasser, T.C., Holzapfel, G.A.: Stress-driven collagen fiber remodeling in arterial walls. *Biomech. Model. Mechanobiol.* **6**, 163–175 (2007)
- Hokanson, J., Yazdani, S.: A constitutive model of the artery with damage. *Mech. Res. Commun.* **24**, 151–159 (1997)
- Holzapfel, G.A., Gasser, T.C., Ogden, R.W.: A new constitutive framework for arterial wall mechanics and a comparative study of material models. *J. Elast.* **61**, 1–48 (2000)
- Holzapfel, G.A., Sommer, G., Regitnig, P.: Anisotropic mechanical properties of tissue components in human atherosclerotic plaques. *J. Biomech. Eng.* **126**, 657–665 (2004)
- Holzapfel, G.A., Sommer, G., Gasser, C.T., Regitnig, P.: Determination of layer-specific mechanical properties of human coronary arteries with nonatherosclerotic intimal thickening and related constitutive modeling. *Am. J. Physiol.-Heart Circ. Physiol.* **289**, H2048–H2058 (2005a)
- Holzapfel, G.A., Stadler, M., Gasser, T.C.: Changes in the mechanical environment of stenotic arteries during interaction with stents: computational assessment of parametric stent designs. *J. Biomech. Eng.* **127**, 166–180 (2005b)
- Holzapfel, G.A., Mulvihill, J.J., Cunnane, E.M., Walsh, M.T.: Computational approaches for analyzing the mechanics of atherosclerotic plaques: a review. *J. Biomech.* **47**, 859–869 (2014)

- Iannaccone, F., Debusschere, N., De Bock, S., De Beule, M., Van Loo, D., Vermassen, F., Segers, P., Verheghe, B.: The influence of vascular anatomy on carotid artery stenting: a parametric study for damage assessment. *J. Biomech.* **47**, 890–898 (2014)
- Kelly-Arnold, A., Maldonado, N., Laudier, D., Aikawa, E., Cardoso, L., Weinbaum, S.: Revised microcalcification hypothesis for fibrous cap rupture in human coronary arteries. *Proc. Nat. Acad. Sci.* **110**, 10741–10746 (2013)
- Kiousis, D.E., Gasser, T.C., Holzapfel, G.A.: A numerical model to study the interaction of vascular stents with human atherosclerotic lesions. *Ann. Biomed. Eng.* **35**, 1857–1869 (2007)
- Kolandaivelu, K., Leiden, B.B., Edelman, E.R.: Predicting response to endovascular therapies: dissecting the roles of local lesion complexity, systemic comorbidity, and clinical uncertainty. *J. Biomech.* **47**, 908–921 (2014)
- Lawlor, M.G., O'Donnell, M.R., O'Connell, B.M., Walsh, M.T.: Experimental determination of circumferential properties of fresh carotid artery plaques. *J. Biomech.* **44**, 1709–1715 (2011)
- Lee, R.T., Grodzinsky, A.J., Frank, E.H., Kamm, R.D., Schoen, F.J.: Structure-dependent dynamic mechanical behavior of fibrous caps from human atherosclerotic plaques. *Circulation* **83**, 1764–1770 (1991)
- Lee, R.T., Richardson, S.G., Loree, H.M., Grodzinsky, A.J., Gharib, S.A., Schoen, F.J., Pandian, N.: Prediction of mechanical properties of human atherosclerotic tissue by high-frequency intravascular ultrasound imaging. An in vitro study. *Arterioscler. Thromb.* **12**, 1–5 (1992)
- Leng, X., Chen, X., Deng, X., Sutton, M.A., Lessner, S.M.: Modeling of experimental atherosclerotic plaque delamination. *Ann. Biomed. Eng.* **43**, 2838–2851 (2015a)
- Leng, X., Chen, X., Deng, X., Sutton, M.A., Lessner, S.M.: Simulation of atherosclerotic plaque delamination using the cohesive zone model. In: Barthelat, F., Korach, C., Zavatieri, P., Prorok, B.C., Grande-Allen, K.J. (eds.) *Mechanics of Biological Systems and Materials*, vol. 7, pp. 81–88. Springer, Berlin (2015b)
- Li, Z.-Y., Howarth, S., Trivedi, R.A.: U-King-Im, J.M., Graves, M.J., Brown, A., Wang, L., Gillard, J.H.: Stress analysis of carotid plaque rupture based on in vivo high resolution MRI. *J. Biomech.* **39**, 2611–2622 (2006)
- Loree, H.M., Grodzinsky, A.J., Park, S.Y., Gibson, L.J., Lee, R.T.: Static circumferential tangential modulus of human atherosclerotic tissue. *J. Biomech.* **27**, 195–204 (1994)
- Maher, E., Creane, A., Sultan, S., Hynes, N., Lally, C., Kelly, D.J.: Tensile and compressive properties of fresh human carotid atherosclerotic plaques. *J. Biomech.* **42**, 2760–2767 (2009)
- Maher, E., Creane, A., Sultan, S., Hynes, N., Lally, C., Kelly, D.J.: Inelasticity of human carotid atherosclerotic plaque. *Ann. Biomed. Eng.* **39**, 2445–2455 (2011)
- Maher, E., Creane, A., Lally, C., Kelly, D.J.: An anisotropic inelastic constitutive model to describe stress softening and permanent deformation in arterial tissue. *J. Mech. Behav. Biomed. Mater.* **12**, 9–19 (2012)
- Máirtín, É.Ó., Parry, G., Beltz, G.E., McGarry, J.P.: Potential-based and non-potential-based cohesive zone formulations under mixed-mode separation and over-closure-Part II: Finite element applications. *J. Mech. Phys. Solids* **63**, 363–385 (2014)
- Maldonado, N., Kelly-Arnold, A., Vengrenyuk, Y., Laudier, D., Fallon, J.T., Virmani, R., Cardoso, L., Weinbaum, S.: A mechanistic analysis of the role of microcalcifications in atherosclerotic plaque stability: potential implications for plaque rupture. *Am. J. Physiol.-Heart Circ. Physiol.* **303**, H619–H628 (2012)
- Martin, C., Sun, W.: Modeling of long-term fatigue damage of soft tissue with stress softening and permanent set effects. *Biomech. Model. Mechanobiol.* **12**, 645–655 (2013)
- McGarry, J.P., Máirtín, É.Ó., Parry, G., Beltz, G.E.: Potential-based and non-potential-based cohesive zone formulations under mixed-mode separation and over-closure. Part I: Theoretical analysis. *J. Mech. Phys. Solids* **63**, 336–362 (2014)
- McHugh, P.E., Grogan, J.A., Conway, C., Boland, E.: Computational modeling for analysis and design of metallic biodegradable stents. *J. Med. Devices* **9**, 030946 (2015)
- Miehe, C.: Discontinuous and continuous damage evolution in Ogden-type large-strain elastic materials. *Eur. J. Mech.-A/Solids* **14**, 697–720 (1995)

- Migliavacca, F., Petrini, L., Massarotti, P., Schievano, S., Auricchio, F., Dubini, G.: Stainless and shape memory alloy coronary stents: a computational study on the interaction with the vascular wall. *Biomech. Model. Mechanobiol.* **2**, 205–217 (2004)
- Migliavacca, F., Gervaso, F., Prosi, M., Zunino, P., Minisini, S., Formaggia, L., Dubini, G.: Expansion and drug elution model of a coronary stent. *Comput. Meth. Biomed. Eng.* **10**, 63–73 (2007)
- Morlacchi, S., Migliavacca, F.: Modeling stented coronary arteries: where we are, where to go. *Ann. Biomed. Eng.* **41**, 1428–1444 (2013)
- Morlacchi, S., Colleoni, S.G., Cárdenes, R., Chiastri, C., Diez, J.L., Larrabide, I., Migliavacca, F.: Patient-specific simulations of stenting procedures in coronary bifurcations: two clinical cases. *Med. Eng. Phys.* **35**, 1272–1281 (2013)
- Morlacchi, S., Pennati, G., Petrini, L., Dubini, G., Migliavacca, F.: Influence of plaque calcifications on coronary stent fracture: a numerical fatigue life analysis including cardiac wall movement. *J. Biomech.* **47**, 899–907 (2014)
- Mulvihill, J.J., Cunnane, E.M., McHugh, S.M., Kavanagh, E.G., Walsh, S.R., Walsh, M.T.: Mechanical, biological and structural characterization of *in vitro* ruptured human carotid plaque tissue. *Acta Biomater.* **9**, 9027–9035 (2013)
- Nolan, D.R., Gower, A.L., Destrade, M., Ogden, R.W., McGarry, J.P.: A robust anisotropic hyperelastic formulation for the modelling of soft tissue. *J. Mech. Behav. Biomed. Mater.* **39**, 48–60 (2014)
- Nolan, D.R., McGarry, J.P.: On the compressibility of arterial tissue. *Ann. Biomed. Eng.* (2015) (in Press). doi:[10.1007/s10439-015-1417-1](https://doi.org/10.1007/s10439-015-1417-1)
- Nguyen, C.M., Levy, A.J.: The mechanics of atherosclerotic plaque rupture by inclusion/matrix interfacial decohesion. *J. Biomech.* **43**, 2702–2708 (2010)
- Ogden, R.W., Roxburgh, D.G.: A pseudo-elastic model for the Mullins effect in filled rubber. *Proc. R. Soc. Lond. A* **455**, 2861–2877 (1999)
- Pant, S., Limbert, G., Curzen, N.P., Bressloff, N.W.: Multiobjective design optimisation of coronary stents. *Biomaterials* **32**, 7755–7773 (2011)
- Pei, X., Wu, B., Li, Z.-Y.: Fatigue crack propagation analysis of plaque rupture. *J. Biomech. Eng.* **135**, 101003 (2013)
- Peña, E.: A rate dependent directional damage model for fibred materials: application to soft biological tissues. *Comput. Mech.* **48**, 407–420 (2011)
- Peña, E., Doblaré, M.: An anisotropic pseudo-elastic approach for modelling Mullins effect in fibrous biological materials. *Mech. Res. Commun.* **36**, 784–790 (2009)
- Peña, E., Martins, P., Mascarenhas, T.: Natal Jorge, R.M., Ferreira, A., Doblaré, M., Calvo, B.: Mechanical characterization of the softening behavior of human vaginal tissue. *J. Mech. Behav. Biomed. Mater.* **4**, 275–283 (2011)
- Pericevic, I., Lally, C., Toner, D., Kelly, D.J.: The influence of plaque composition on underlying arterial wall stress during stent expansion: the case for lesion-specific stents. *Med. Eng. Phys.* **31**, 428–433 (2009)
- Peña, E., Peña, J.A., Doblaré, M.: On the Mullins effect and hysteresis of fibered biological materials: a comparison between continuous and discontinuous damage models. *Int. J. Solids Struct.* **46**, 1727–1735 (2009)
- Petrini, L., Migliavacca, F., Dubini, G., Auricchio, F.: Numerical analysis of vascular stents exploiting shape-memory-alloy behavior. In: 16th AIMETA Congress of the Theoretical and Applied Mechanics, pp. 1–10 (2003)
- Rodríguez, J.F., Cacho, F., Bea, J.A., Doblaré, M.: A stochastic-structurally based three dimensional finite-strain damage model for fibrous soft tissue. *J. Mech. Phys. Solids* **54**, 864–886 (2006)
- Rodríguez, J.F., Alastrué, V., Doblaré, M.: Finite element implementation of a stochastic three dimensional finite-strain damage model for fibrous soft tissue. *Comput. Meth. Appl. Mech. Eng.* **197**, 946–958 (2008)
- Sadat, U., Li, Z.-Y., Young, V.E., Graves, M.J., Boyle, J.R., Warburton, E.A., Varty, K., O'Brien, E., Gillard, J.H.: Finite element analysis of vulnerable atherosclerotic plaques: a comparison

- of mechanical stresses within carotid plaques of acute and recently symptomatic patients with carotid artery disease. *J. Neurol. Neurosurg. Psychiatry* **81**, 286–289 (2010)
- Salunke, N.V., Topoleski, L.D., Humphrey, J.D., Mergner, W.J.: Compressive stress-relaxation of human atherosclerotic plaque. *J. Biomed. Mater. Res.* **55**, 236–241 (2001)
- Serruys, P.W., Onuma, Y., Morel, M.: CAAS 2D/3D QCA Bifurcation analysis approach. European Bifurcation Club, Prague (2008)
- Stary, H.C.: Atlas of Atherosclerosis: Progression and Regression, 1st edn. CRC Press, New York (1999)
- Tang, D., Teng, Z., Canton, G., Hatsukami, T.S., Dong, L., Huang, X., Yuan, C.: Local critical stress correlates better than global maximum stress with plaque morphological features linked to atherosclerotic plaque vulnerability: an in vivo multi-patient study. *Biomed. Eng. Online* **8**, 15 (2009a). doi:[10.1186/1475-925X-8-15](https://doi.org/10.1186/1475-925X-8-15)
- Tang, D., Yang, C., Kobayashi, S., Zheng, J., Woodard, P.K., Teng, Z., Billiar, K., Bach, R., Ku, D.N.: 3D MRI-based anisotropic FSI models with cyclic bending for human coronary atherosclerotic plaque mechanical analysis. *J. Biomech. Eng.* **131**, 061010 (2009b)
- Teng, Z., Tang, D., Zheng, J., Woodard, P.K., Hoffman, A.H.: An experimental study on the ultimate strength of the adventitia and media of human atherosclerotic carotid arteries in circumferential and axial directions. *J. Biomech.* **42**, 2535–2539 (2009)
- Timmings, L.H., Meyer, C.A., Moreno, M.R., Moore, J.E.: Effects of stent design and atherosclerotic plaque composition on arterial wall biomechanics. *J. Endovasc. Ther.* **15**, 643–654 (2008)
- Topoleski, L.D., Salunke, N.V.: Mechanical behavior of calcified plaques: a summary of compression and stress-relaxation experiments. *Z. Kardiol.* **89**, S085–S091 (2000)
- Topoleski, L.D., Salunke, N.V., Humphrey, J.D., Mergner, W.J.: Composition- and history-dependent radial compressive behavior of human atherosclerotic plaque. *J. Biomed. Mater. Res.* **35**, 117–127 (1997)
- Versluis, A., Bank, A.J., Douglas, W.H.: Fatigue and plaque rupture in myocardial infarction. *J. Biomech.* **39**, 339–347 (2006)
- Volokh, K.: Prediction of arterial failure based on a microstructural bi-layer fiber-matrix model with softening. *J. Biomech.* **41**, 447–453 (2008)
- Walraevens, J., Willaert, B., De Win, G., Ranftl, A., De Schutter, J., Vander Sloten, J.: Correlation between compression, tensile and tearing tests on healthy and calcified aortic tissues. *Med. Eng. Phys.* **30**, 1098–1104 (2008)
- Walsh, M.T., Cunnane, E.M., Mulvihill, J.J., Akyildiz, A.C., Gijsen, F.J., Holzapfel, G.A.: Uniaxial tensile testing approaches for characterisation of atherosclerotic plaques. *J. Biomech.* **47**, 793–804 (2014)
- Weisbecker, H., Pierce, D.M., Holzapfel, G.A.: Modeling of damage-induced softening for arterial tissue. In: Proceedings of the 2011 SCATH Joint Workshop on New Technologies for Computer/robot Assisted Surgery, Graz, pp. 1–4 (2011)
- Weisbecker, H., Pierce, D.M., Regitnig, P., Holzapfel, G.A.: Layer-specific damage experiments and modeling of human thoracic and abdominal aortas with non-atherosclerotic intimal thickening. *J. Mech. Behav. Biomed. Mater.* **12**, 93–106 (2012)
- Wenk, J.F., Papadopoulos, P., Zohdi, T.I.: Numerical modeling of stress in stenotic arteries with microcalcifications: a micromechanical approximation. *J. Biomech. Eng.* **132**, 091011 (2010)
- Wong, K.K., Thavornpattanapong, P., Cheung, S.C., Sun, Z., Tu, J.: Effect of calcification on the mechanical stability of plaque based on a three-dimensional carotid bifurcation model. *BMC Cardiovasc. Disord.* **12**, 7 (2012). doi:[10.1186/1471-2261-12-7](https://doi.org/10.1186/1471-2261-12-7)
- Zahedmanesh, H., Kelly, D.J., Lally, C.: Simulation of a balloon expandable stent in a realistic coronary artery-determination of the optimum modelling strategy. *J. Biomech.* **43**, 2126–2132 (2010)

Biomechanics of Myocardial Ischemia and Infarction

Colleen M. Witzenburg and Jeffrey W. Holmes

Abstract Each year, over seven million people suffer a myocardial infarction (heart attack). For those who survive the initial event, the mechanical properties of the scar tissue that gradually replaces the damaged muscle are a critical determinant of many life-threatening sequelae, such as infarct rupture and the development of heart failure. Thus, understanding the mechanics of healing infarct scar, its interaction with the rest of the heart, and the resulting changes in heart function are critical to devising effective therapies. Computational models play an essential role in understanding these potentially complex interactions. The first section of this chapter reviews the structure and mechanical properties of the normal heart and the methods used to study those properties. The second section discusses the structure and mechanical properties of healing post-infarction scar. The remaining sections review landmark analytical and computational models that provided insight into the functional consequences of myocardial infarction and potential therapies. Finally, we briefly consider emerging models of wound healing in the infarct region and growth and remodeling in the surviving myocardium that are beginning to predict the long-term effects of infarction and post-infarction therapies. In the future, multi-scale models that capture such remodeling in addition to the beat-to-beat mechanics of the heart hold great promise for designing novel therapies, not only for myocardial infarction but also for a wide range of cardiac pathologies.

1 Structure and Mechanical Properties of Myocardium

In order to assess changes in myocardial structure, mechanics, and function that result from ischemia and infarction, it is important to first understand the mechanics of the normal heart. Thus, this section reviews the basic anatomy and mechanical properties of heart tissue (myocardium), with an emphasis on the experimental testing methods used to determine myocardial mechanical properties.

C.M. Witzenburg · J.W. Holmes (✉)
University of Virginia, Charlottesville, VA, USA
e-mail: holmes@virginia.edu

1.1 Anatomy and Structure of the Heart

The heart is a muscular pump that circulates blood throughout the body. It is comprised of four chambers and four valves. Deoxygenated blood returning from the body through the veins first reaches the right atrium; it then flows through the tricuspid valve into the right ventricle, and is pumped through the pulmonary valve to the lungs. Oxygenated blood leaving the lungs enters the left atrium, flows across the mitral valve into the left ventricle (LV), and is pumped through the aortic valve into the network of arteries that carry blood throughout the body (West 1985).

The size and shape of the four heart chambers vary considerably, as does the pressure they typically generate during contraction. The atria are irregularly shaped with walls that are just 1–2 mm thick; normal atria experience peak pressures of roughly 10 mmHg (a little more than 1 kPa). By contrast, in adult humans the LV is shaped like a truncated ellipsoid with 10 mm thick walls and generates pressures exceeding 100 mmHg during contraction. The right ventricle is crescent-shaped in cross section, wrapping partially around the LV, with which it shares a common wall called the interventricular septum. The normal human right ventricular (RV) free wall is 3–4 mm thick. Pressures in the RV are roughly 1/5 those of the LV (West 1985).

The muscle cells (myocytes) in the heart are arranged end-to-end and coupled tightly to one another both electrically and mechanically. Although individual myocytes frequently branch and connect to two other myocytes rather than one, on gross inspection or in low-magnification micrographs of any small region of the left and right ventricles there is a clear preferred fiber orientation. Over the years, many anatomists and physiologists have studied the muscle fiber structure of the LV and sought to understand how this structure relates to heart mechanics and function; a compilation of drawings from several influential studies is reproduced in Fig. 1 from a review by Buckberg et al. (2008).

One central feature of the left ventricular muscle fiber structure is that the fiber orientation changes through the depth of the wall. Near the outer surface of the heart (epicardium), muscle fibers are oriented approximately 60° clockwise from the circumferential direction, while near the inner surface (endocardium), they are oriented approximately 60° counterclockwise from the circumferential direction (Fig. 1). One functional consequence of this arrangement is that as the heart contracts and relaxes, it also twists. Among early studies of heart structure, the work of Streeter and colleagues exerted a particularly strong influence on subsequent computational models, because these investigators carefully quantified both left ventricular shape and fiber orientation, and fitted these data with continuous functions that are straightforward to incorporate into analytical and finite element models of the heart (Streeter and Hanna 1973a,b).

In addition to the muscle fibers, connective tissue surrounding and linking the myocytes makes an important contribution to the mechanical properties of the heart (Fomovsky et al. 2010). Histologic sections taken parallel to the muscle fibers show large collagen fibers running parallel to the myocytes. These collagen fibers comprise

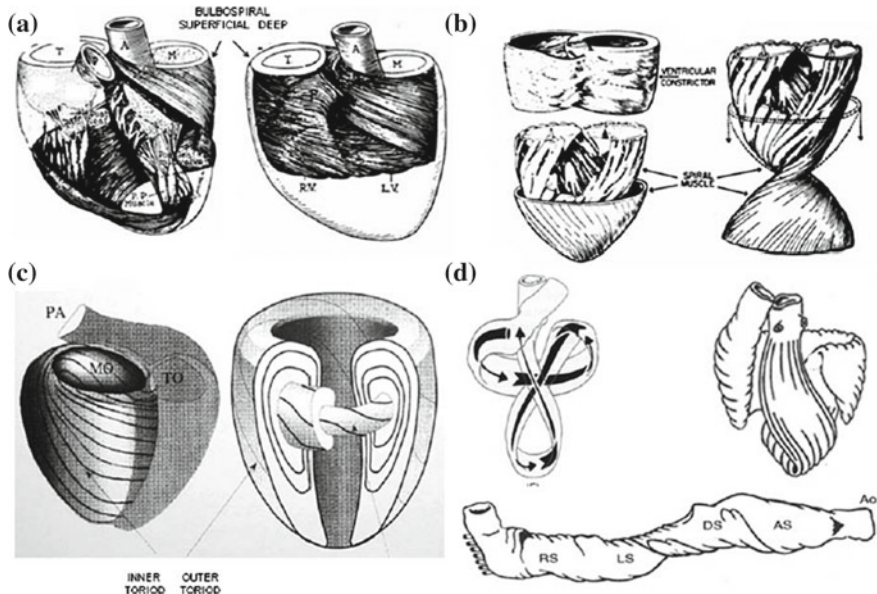


Fig. 1 Drawings from several classic studies of left ventricular fiber structure, reproduced from Buckberg et al. (2008): **a** McCallum (1900); **b** Rushmer et al. (1953); **c** Streeter (1979); **d** Torrent-Guasp (1967). These drawings illustrate the oblique angles of muscle fibers in the inner and outer layers of the heart wall, and the difference in fiber orientations between these layers

2–3 % of the tissue volume in normal hearts, and at low pressures they appear wavy or coiled whereas at high pressures they appear flat and unfolded. Therefore, at very low pressures or stresses these fibers likely contribute little to the mechanical properties of the heart, but as the heart is inflated to higher pressures and the collagen fibers straighten, they gradually bear more of the load (Fomovsky et al. 2010). For the passively inflated LV, this arrangement results in an exponential pressure-volume curve that becomes quite steep at high pressures. In addition to these large collagen fibers, histologic studies show layers of connective tissue that separate muscle fibers into parallel sheets approximately 4–5 myocytes thick (LeGrice et al. 2001), as well as small collagen struts that connect the myocytes and sheets to one another (Caulfield and Borg 1979). Recent experimental and modeling studies suggest that this laminar organization is an important determinant of left ventricular mechanics (Costa et al. 1999; Usyk et al. 2000). However, the overall contribution of extracellular matrix to heart mechanics remains an active and important area of investigation. Furthermore, while it is generally recognized that collagen and myocyte structure in other chambers—particularly the atria—differ from those in the LV (Ho et al. 2002; Zhao et al. 2012), much work remains to define these structures and incorporate them into models.

Muscle fibers and the surrounding extracellular matrix are arguably the most important determinants of the mechanical properties of myocardium, but there are

other important contributors that are not discussed in detail here. For example, a network of coronary blood vessels supplies blood to the heart and interacts dynamically with the surrounding myocardium. Compression of coronary vessels by the myocardium limits blood flow during systole (Lee and Smith 2012), while pressurization of the coronary tree alters the compliance of the heart (May-Newman et al. 1994). Many of the mechanical testing methods described below start by excising tissue, disconnecting it from its blood supply; obviously, such tests cannot capture the contributions of coronary blood flow to heart mechanics.

1.2 *Mechanical Testing of Myocardium*

The material properties that govern the response of normal and diseased tissues to mechanical loading are centrally important in the field of biomechanics. However, in the case of the heart, determining those material properties by appropriate testing is complicated by the geometry and architecture outlined above. Pressures in the individual chambers of the heart and deformation within its walls can be measured directly in an intact heart, but the corresponding stresses must be estimated using analytical or computational models and cannot be directly verified. Alternatively, pieces of myocardium can be excised and tested ex vivo; however, in practice cutting injury and contracture of the myocytes typically complicate such experiments. Consequently, experimentally determining the properties of fully relaxed, passive myocardium using the methods reviewed below has proven quite challenging. Yet understanding the passive response is only a beginning, as myocardial material properties vary throughout the cardiac cycle due to the cyclic contraction and relaxation of the individual myocytes.

1.2.1 **Passive Inflation of Arrested Hearts**

One of the most straightforward preparations for assessing heart mechanics is the isolated heart. Typically, the heart is perfused with a cold, oxygenated cardioplegia solution to block contraction while preserving cell viability. The heart is then excised along with a portion of the aorta, which is mounted onto a cannula. Fluid flowing into this cannula from the aorta toward the heart (retrograde perfusion) forces the leaflets of the aortic valve closed and flows into the coronary arteries through their ostia in the aortic root, providing control over myocardial temperature, oxygenation, and chemical environment. Often, a balloon is introduced into the left ventricular cavity to provide control over left ventricular volume, while a pressure transducer integrated in the balloon provides real-time pressure data.

Suga and Sagawa (1974) used a version of this isolated heart preparation to explore the pressure-volume behavior of the actively contracting heart. They perfused the coronary arteries of isolated hearts with warm, oxygenated blood and stimulated the hearts electrically to induce contraction at a regular rate. One of their simplest

experiments was to hold volume in the balloon constant during an entire contraction and measure the maximum pressure the heart could generate under specified conditions. Other studies included using a computer-controlled servopump to vary balloon volume over time in order to simulate the filling, emptying, and isovolumetric phases of a normal cardiac cycle. Many other physiologists have used similar approaches—particularly a version called the Langendorff preparation—to study aspects of heart physiology ranging from electrical activation to contraction to metabolism (Bell et al. 2011).

McCulloch et al. (1987) employed isolated, arrested canine hearts to study the passive material properties of myocardium. In addition to inserting a balloon into the left ventricular cavity, they placed a triangle of sutures on the epicardial surface and tracked the motion of these markers using video during inflation of the intracavitary balloon to simulate diastolic filling. Using the images of the markers, they computed regional strains on the epicardial surface during inflation. They found that principal strains during inflation differed substantially in magnitude, that the direction of principal epicardial stretch was close to the fiber direction, and that the LV twists as it inflates. These data suggested that passive myocardium was mechanically anisotropic and provided important validation data for emerging models of LV mechanics.

The major advantages of the isolated heart preparation for characterizing left ventricular mechanics are that: (i) the heart remains intact with its coronaries perfused; (ii) the boundary conditions—pressure applied to the inner wall of the LV and deformation constrained only at the mitral valve ring—are reasonably physiologic; (iii) the myocardium can be activated for study of time-varying material properties. The major disadvantages are that: (i) stresses in the LV wall cannot be measured directly; (ii) the range of stresses that can be applied along the different material axes (e.g., parallel vs. transverse to the fibers) is limited by the geometry of the heart.

1.2.2 Planar Biaxial Testing

Circumferential and longitudinal stresses in the wall of the inflated LV are tensile, while radial stresses are compressive on the endocardium and zero (or very small if the pericardium is intact) at the epicardial surface. Therefore, another common approach to determine the passive material properties of myocardium is biaxial testing in the circumferential-longitudinal plane (Fig. 2). Much of the early work in this area was done by Yin and colleagues (Demer and Yin 1983; Yin et al. 1987). They prepared samples for testing by slicing the LV wall into sheets 1–2 mm thick, and mounted them so that the test axes were aligned with the predominant fiber and crossfiber directions. Then, they subjected the myocardial samples to many combinations of stretch in the fiber and crossfiber directions while measuring the net forces imposed along each test axis. They found that passive myocardium was nonlinear, viscoelastic, and anisotropic, having greater stiffness along the fiber direction (Demer and Yin 1983). Furthermore, the two directions were mechanically coupled: stress in each

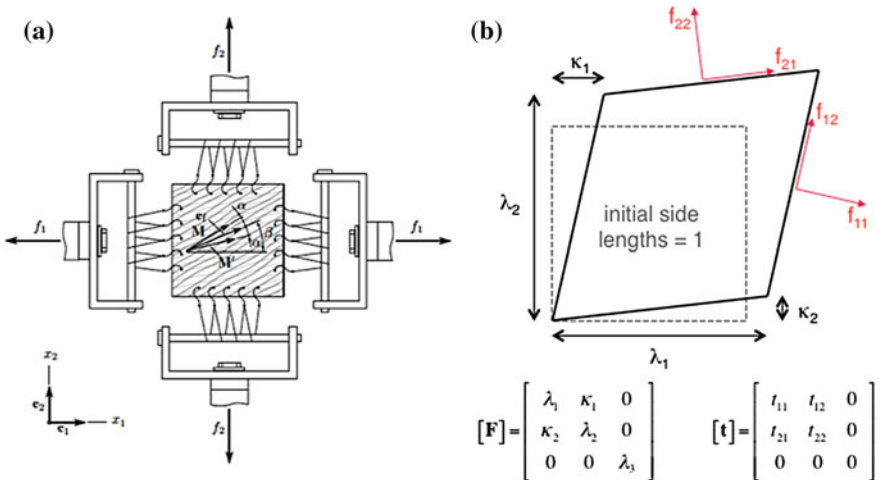


Fig. 2 Kinematics of planar biaxial testing of myocardium: **a** Schematic of typical test setup, showing force transducers that measure a single force in each test direction, reproduced by permission from Sommer et al. (2015). **b** Assuming a state of plane stress, in general there are five nonzero components of the deformation gradient \mathbf{F} and three independent, nonzero components of the Cauchy stress matrix ($t_{12} = t_{21}$, see text) related to the four force components f_{ij} applied to the sample edges. Computing three nonzero stresses from two net forces requires making additional assumptions (Fomovsky and Holmes 2010; Sommer et al. 2015)

test direction depended on stretch in both directions (Demer and Yin 1983; Yin et al. 1987).

One of the best biaxial testing studies on myocardium was published by Humphrey et al. (1990a, b). Following an approach suggested by Rivlin and Saunders (1951) for isotropic materials, Humphrey et al. (1990a, b) postulated a transversely isotropic strain-energy function for myocardium that depended on two invariants of the right Cauchy–Green tensor. They imposed combinations of stretches that held one invariant constant while changing the other. Then, they used the measured stresses and stretches to estimate the derivatives of the strain-energy function with respect to those invariants. Plotting the derivatives against the invariants allowed them to determine the form of the polynomial strain-energy function that best fit their experimental data. This elegant approach takes advantage of a major advantage of biaxial testing: it provides excellent control over the loading protocol, allowing application of any desired combination of fiber/crossfiber stretch or load. Other important advantages include the ability to align the test axes with the anatomic fiber and crossfiber directions, and the ability to directly compute stresses from experimentally measured forces. The major disadvantages of planar biaxial testing for characterizing the passive material properties of myocardium are the need for extensive dissection and the related difficulty of preventing contracture of the sample.

One important warning regarding biaxial testing is that in practice, the computation of stresses is not always straightforward. As shown in Fig. 2, if samples are thin

enough relative to their other dimensions so that plane stress is a reasonable assumption, only three independent components of the Cauchy stress matrix are nonzero (the Cauchy stress matrix is symmetric, $t_{12} = t_{21}$, per conservation of angular momentum). When the fiber axis is aligned with one of the test axes, there is little or no shear deformation, and the force components f_{12} and f_{21} and shear stresses $t_{12} = t_{21}$ vanish. Such biaxial tests are useful in identifying material parameters that affect resistance to stretch in the fiber or crossfiber direction, but do not provide information on the shear behavior of the myocardium. In theory, it should be possible to obtain additional information on shear behavior by intentionally orienting the fiber direction oblique to the test axes, but in practice most testing devices are not designed to separately measure the normal (f_{11} and f_{22}) and lateral (f_{12} and f_{21}) force components applied to the sample edges. Rather, most investigators introduce additional assumptions that may affect the accuracy of the computed stresses (Fomovsky and Holmes 2010; Sommer et al. 2015).

An increasingly popular approach is to map deformation across biaxial samples using large numbers of markers, and combine test data with sample-specific finite element models to extract material parameters. A major advantage of this approach is that it allows for more realistic variations in material properties across a sample. However, conceptually such approaches are more like model-based extraction of properties from isolated heart experiments—the results depend on the choice of the underlying constitutive model, and predict spatial variations in stress that are difficult to verify.

1.2.3 Extension and Torsion of Papillary Muscles

Humphrey et al. (1992) proposed an alternate approach to biaxial mechanical testing of myocardium that requires less dissection and is therefore less influenced by cutting injury. Taking advantage of prior theoretical work on torsion and extension of cylinders, they developed an analytical solution for the stresses in the central region of a papillary muscle induced by first stretching, then twisting the muscle. Papillary muscles connect the left (or right) ventricular walls to the mitral (or tricuspid) valves and surrounding valve rings. Dissecting them free requires cutting into myocardium at one end (where they connect to the wall) and severing the chordae tendinae at the other end (where they connect to the valve and surrounding valve ring). The resulting sample is relatively long and thin, with muscle fibers aligned parallel to its long axis. Although this process does induce some damage at one end, the damage appears to have little effect on behavior in the central region of the muscle. Accordingly, early cardiac physiologists often used papillary muscles for studies of basic cardiac muscle physiology.

During uniaxial extension of a papillary muscle, relating the applied axial load to measured axial stretch is straightforward and provides information about material properties along the muscle fiber axis. Humphrey et al. (1992) realized that by twisting the papillary muscle at different axial extensions and relating the applied moment to measured shear strains, they could also obtain information on shear properties.

Thus, they could experimentally determine coefficients for a transversely isotropic constitutive law that depended only on the first invariant of the right Cauchy–Green tensor and on the stretch in the fiber (axial) direction. Advantages of this approach include: (i) ease of dissection; (ii) excellent control over the loading protocol; (iii) known orientation of the test axes relative to the anatomic fiber and crossfiber directions; (iv) the ability to directly compute stresses from the measured axial force and moment. The primary disadvantages of this approach relate to the anatomic differences between papillary muscles and the myocardium within the ventricular walls that may limit use of information obtained from papillary muscles: (i) papillary muscles are enclosed in a fibrous sheath that may contribute significantly to the measured mechanics (Criscione et al. 1999); (ii) papillary muscles do not contain the laminar sheet structure identified elsewhere in the heart wall. Thus, although a transversely isotropic constitutive model may be appropriate for papillary muscles, the resulting parameters do not capture the orthotropic nature of the myocardium in the heart walls. One other potential benefit of papillary muscle testing is the ability to study active in addition to passive properties. The most important caveat with such studies is that the metabolic demands of cardiac muscle are quite high, even at rest; therefore, diffusion from a surrounding fluid bath is often insufficient to supply papillary muscles with adequate oxygen (Holmes et al. 2002). Testing the thinner right ventricular papillary muscles or even very small trabeculae dissected from the inner surface of the heart wall can help avoid confounding effects from hypoxia at the center of the muscles.

1.2.4 Shear Testing

Dokos et al. (2002) developed one final approach to material testing of passive myocardium designed to more fully characterize properties of the myocardium within and across the laminar sheets (LeGrice et al. 1995, 2001). They cut myocardium into cubes with the edges aligned with the local fiber, sheet (perpendicular to the fibers within the sheets), and sheet-normal (perpendicular to the sheet surfaces) directions. They then glued the top and bottom of each cube to parallel metal plates and sheared them while measuring both the shear and axial forces applied by their device. By applying shear in different directions to different faces of the cubes, these investigators were able to quantify the response to a much wider range of deformations than would be possible with any of the other tests discussed above, and clearly relate those tests to the anatomic structure of the tissue. Relative to the other methods discussed here, the obvious disadvantage of testing small cubes of myocardium is that it requires much more dissection.

1.3 *Mathematical Descriptions of Myocardial Properties*

Any mathematical description of passive myocardium must account for both its anisotropic nature and its nonlinear behavior. The most common approach is to

formulate a strain-energy function, a potential function with the property that its derivatives with respect to strains or stretches yield expressions for the components of the stress tensor. Polynomial, exponential, or pole-zero formulations for the strain-energy function are the most frequently used in cardiac mechanics. Some of these equations contain a large number of material coefficients; however, the testing methods described above allow the unique identification of only a handful of coefficients.

As described above, Humphrey et al. (1990a,b) used biaxial test data both to determine the functional form of a polynomial strain-energy function and to identify the material parameters in that formulation. They assumed myocardium was pseudoelastic, incompressible, transversely isotropic, and locally homogenous, and that the stress was a function of only the first, I_1 , and the fourth, I_4 , invariants of the right Cauchy–Green tensor \mathbf{C} . Their strain-energy function contained five material constants:

$$W = c_1(\sqrt{I_4} - 1)^2 + c_2(\sqrt{I_4} - 1)^3 + c_3(I_1 - 3) + c_4(I_1 - 3)(\sqrt{I_4} - 1) + c_5(I_1 - 3)^2. \quad (1)$$

In a subsequent study, Novak et al. (1994) used the same strain-energy function to quantify transmural mechanical differences across the heart wall and found that the orientation of the preferred direction changes through the wall, and that myocardium is stiffer near the endocardium and epicardium than at the midwall.

Guccione et al. (1991) employed a Fung-type exponential form in their finite element simulations of inflation, extension, and torsion of a thick-walled cylinder representing the passive canine LV:

$$W = \frac{C}{2} \exp [2b_1(E_{RR} + E_{FF} + E_{CC}) + b_2E_{FF}^2 + b_3(E_{CC}^2 + E_{RR}^2 + E_{CR}^2 + E_{RC}^2) + b_4(E_{RF}^2 + E_{FR}^2 + E_{FC}^2 + E_{CF}^2)] - \frac{C}{2}, \quad (2)$$

where C , b_1 , b_2 , b_3 , and b_4 are material constants, \mathbf{E} is the Green–Lagrange strain tensor, and the subscripts R, F, C refer to the radial, fiber, and crossfiber directions, respectively. They also treated the myocardium as pseudoelastic, transversely isotropic, and incompressible, and obtained best-fit values for the coefficients by minimizing the error between model-predicted epicardial strains and those reported by McCulloch et al. (1989) during passive inflation of isolated, arrested hearts. Based on the work of LeGrice et al. (1995, 2001) and Dokos et al. (2002) discussed in Sect. 1.2, Costa et al. (2001) extended the strain-energy function employed by Guccione et al. (1991) to model the myocardium as orthotropic rather than transversely isotropic.

Holzapfel and Ogden (2009) proposed an alternate exponential strain-energy function that accounts for the orthotropy of myocardium, and fitted their function to both the biaxial testing data of Yin et al. (1987) and the shear data of Dokos et al. (2002):

$$W = \frac{a}{2b} \{ \exp[b(I_1 - 3)] - 1 \} + \frac{a_F}{2b_F} \{ \exp[b_F(I_{4F} - 1)^2] - 1 \} \\ + \frac{a_S}{2b_S} \{ \exp[b_S(I_{4S} - 1)^2] - 1 \} + \frac{a_{FS}}{2b_{FS}} \{ \exp[b_{FS}I_{8FS}^2] - 1 \}, \quad (3)$$

where I_1 is the first invariant, I_{4F} is the fourth invariant associated with the fiber direction, I_{4S} is the fourth invariant associated with the sheet direction, and I_{8FS} is a coupling invariant involving both the sheet and fiber directions.

One other approach in the literature is the pole-zero formulation. Again treating myocardium as orthotropic and incompressible and guided by experimental results showing an extremely steep rise in stress approaching a limiting strain in each direction, the group at the University of Auckland developed a strain-energy function of the form

$$W = \frac{k_{FF}E_{FF}^2}{|a_{FF} - E_{FF}|^{b_{FF}}} + \frac{k_{NN}E_{NN}^2}{|a_{NN} - E_{NN}|^{b_{NN}}} + \frac{k_{SS}E_{SS}^2}{|a_{SS} - E_{SS}|^{b_{SS}}} \\ + \frac{k_{FN}E_{FN}^2}{|a_{FN} - E_{FN}|^{b_{FN}}} + \frac{k_{FS}E_{FS}^2}{|a_{FS} - E_{FS}|^{b_{FS}}} + \frac{k_{NS}E_{NS}^2}{|a_{NS} - E_{NS}|^{b_{NS}}}, \quad (4)$$

where the subscripts N, F, S refer to the normal, fiber and sheet directions (Nash and Hunter 2001). This function contains 18 material constants, making it impractical to identify all the coefficients through direct mechanical testing. Accordingly, Nash and Hunter (2001) suggested that some of the parameters might be estimated from histological data.

Most studies simply select one of these formulations based on convenience, familiarity, or ease of numerical implementation. However, a few studies have compared various features of these strain-energy functions. Holzapfel and Ogden (2009) discussed the stability of these strain-energy functions and identified all of those listed here as convex and strongly elliptic except for the polynomial form of Humphrey et al. (1990a). Schmid et al. (2006, 2008) fitted the data of Dokos et al. (2002) both directly and using a finite element model. They compared several strain-energy functions including the pole-zero formulation and the orthotropic exponential formulation of Costa et al. (2001). They fitted each function to the test data and compared goodness of fit, between-specimen variability of the fitted parameters, and the numerical stability of the optimization process. Overall, Schmid et al. (2006, 2008) concluded that the exponential function of Costa et al. (2001) provided the best balance between fitting the data well with fewer parameters and limiting between-specimen variability in parameter values.

2 Structure and Mechanical Properties of Myocardial Scar Tissue

Following interruption of the normal blood supply to a region of the heart, the affected myocytes stop contracting within the first minute (Tennant and Wiggers 1935) and begin to die within the first hour (Connelly et al. 1982). Due to the prevalence of coronary artery disease in Western societies, occlusion of coronary arteries long enough to induce myocyte death—termed myocardial infarction (MI)—is common, with over 7 million new infarctions per year worldwide (White and Chew 2008). Most patients now survive the initial infarction, and many reach the hospital quickly enough to undergo procedures such as thrombolysis or balloon angioplasty to reopen the occluded arteries, limiting the total amount of damage. However, the myocytes that die during the infarction cannot regenerate; instead, dead myocytes are gradually resorbed and replaced by a collagenous scar. Over the weeks and months following MI, the evolving structure and mechanical properties of the healing infarct scar are an important determinant of heart function as well as of the likelihood of a range of serious post-infarction complications such as infarct rupture, infarct expansion, and heart failure (Holmes et al. 2005). Accordingly, understanding the mechanical properties of the evolving scar—and how those properties affect growth, remodeling, and function of the heart—is an important and active area of cardiovascular biomechanics research.

2.1 *Myocardial Scar Structure*

The cellular and extracellular composition of a healing myocardial infarct evolves rapidly over the first days and weeks following the initial injury. Initially, white blood cells invade the damaged region, secreting proteolytic enzymes and removing debris through phagocytosis. These inflammatory cells also secrete growth factors that encourage invasion and proliferation of fibroblasts, the cells that deposit the extracellular matrix proteins that make up the scar tissue. Extracellular matrix (ECM) deposition by fibroblasts increases rapidly after the first few days, and ECM protein content continues to increase for the next several weeks. Although the maturing scar contains many different collagens, proteoglycans, and other ECM proteins, collagen is thought to account for most of the mechanical properties of post-infarction scar tissue; accordingly, this section will focus on changes in collagen content and structure. Several recent review articles provide more detail on the pathology of infarct healing and changes in other ECM components (Lindsey and Zamilpa 2012; Frangogiannis 2014; Richardson et al. 2015).

2.1.1 Collagen Content and Crosslinking

Collagen content begins to rise 4–7 days after infarction and typically reaches a plateau by 3–6 weeks, depending on the animal model. Whereas collagen occupies about 3 % of the area of a histologic section of normal myocardium, reported collagen area fractions range from roughly 30 % in the rat (McCormick et al. 1994; Fomovsky and Holmes 2010) to 60 % in the pig (Holmes et al. 1997) and dog (Clarke et al. 2015) following permanent coronary ligation. An alternate approach to measuring collagen content is to measure the concentration of the modified amino acid hydroxyproline and then estimate the percentage of collagen by weight assuming that the weight of collagen is 7.42 the times the weight of hydroxyproline; this method gives slightly lower estimates of about 25 % collagen by weight in mature rat infarcts (McCormick et al. 1994; Fomovsky and Holmes 2010) and 45 % in dogs (Jugdutt and Amy 1986). In addition to collagen content, the degree of crosslinking of the collagen molecules can affect tissue mechanical properties. Studies of crosslinking during infarct healing suggest that crosslink density initially rises with a similar time course to collagen, but may continue to rise even after collagen content plateaus (Vivaldi et al. 1987; Zimmerman et al. 2001; Fomovsky and Holmes 2010).

2.1.2 Collagen Alignment

Another potentially important determinant of scar mechanics is collagen fiber alignment. In some tissues such as tendon and ligament, highly aligned collagen results in a mechanically anisotropic tissue that resists tension much more effectively along the fiber axis than transverse to it. Early studies of infarct healing focused on collagen content rather than alignment, but more recent studies have revealed that the collagen fiber structure of healing infarct scars varies dramatically across different animal models. One reason that many early studies missed this variation is that the collagen fibers in healing infarcts lie in planes parallel to the epicardial surface, but histologic sections are typically cut perpendicular to the epicardial surface, making collagen fiber orientation difficult to visualize. Histologic sections cut parallel to the epicardial surface reveal highly aligned fibers following permanent coronary ligation in dogs (Whittaker et al. 1989; Clarke et al. 2015) and pigs (Holmes and Covell 1996); in these infarcts, the collagen fibers in the midwall are strongly aligned in the circumferential direction, while at the epicardium and endocardium fibers are oriented obliquely and are less strongly aligned (Holmes et al. 1997; Clarke et al. 2015). By contrast, Fomovsky and Holmes (2010) showed that following coronary ligation in rats, collagen fibers are randomly oriented (Fig. 3), resulting in scars that are not only structurally but also mechanically isotropic.

In a subsequent study, Fomovsky et al. (2012b) used liquid-nitrogen-cooled probes to create cryoinfarcts (well-defined regions of cell death) with controlled sizes, shapes, and locations on the rat LV. They found that infarcts in different locations on the LV experienced different patterns of stretch, which correlated with the collagen fiber structure observed three weeks later: infarcts that stretched similarly in

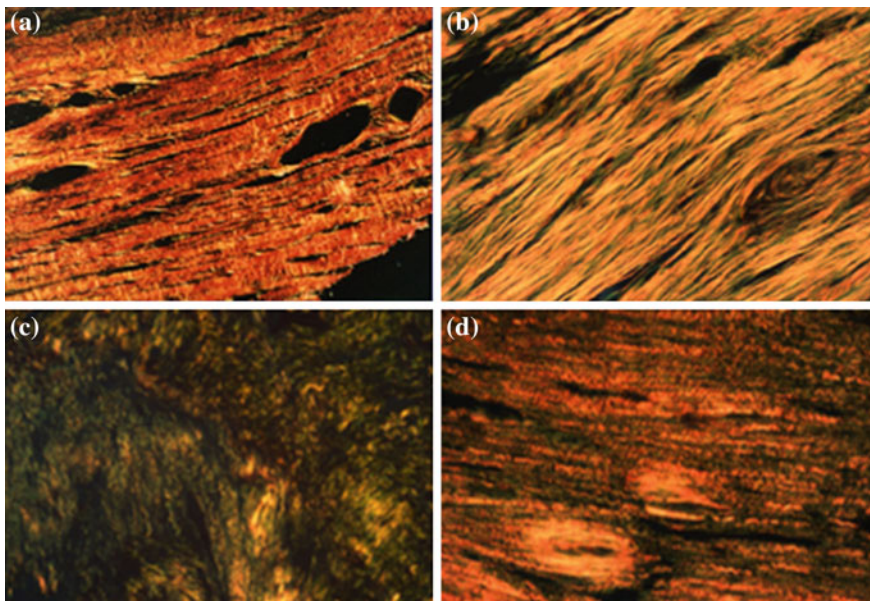


Fig. 3 Illustration of differences in collagen fiber alignment in histologic sections taken from the center of the infarct scar in different experimental models and imaged under polarized light: **a** pig, three weeks after ligation of a branch of the left circumflex (LCx) coronary artery (Holmes and Covell 1996); **b** dog, eight weeks after ligation of the left anterior descending (LAD) coronary artery (unpublished data from Clarke et al. 2015); **c** rat, three weeks after ligation of the LAD (unpublished data from Fomovsky and Holmes 2010); **d** rat, three weeks after cryoinfarction of the anterior wall at the mid-ventricle (unpublished data from Fomovsky et al. 2012b)

both the circumferential and longitudinal directions during healing formed scars with randomly oriented collagen fibers (similar to rat ligation infarcts), while those that stretched in only the circumferential direction contained circumferentially aligned collagen fibers (similar to pig ligation infarcts). Therefore, differences in mechanics during healing may explain the different collagen fiber structures reported in different animal models.

2.2 *Myocardial Scar Mechanics*

Within minutes after a region of the heart is deprived of blood flow, it stops contracting actively and begins to stretch and recoil passively as the stress in the heart wall rises and falls with each heartbeat. In some respects, the fact that the material properties of the healing scar vary little over the cardiac cycle makes studying infarct mechanics simpler than studying the mechanics of normal myocardium. However, because infarct composition, material properties, and volume all change as the scar forms and

remodels, comprehensive studies that measure infarct mechanics and composition at multiple time points are needed to understand not only the natural time course of healing but also the response of the heart to clinical post-infarction therapies. Given the clinical importance of myocardial infarction, surprisingly few such studies have been performed.

2.2.1 In Vivo Deformation

Some of the best early studies of infarct and scar mechanics used implanted measurement devices to track changes in local deformation over time. Tyberg et al. (1974) sutured strain gauges to the surface of the LV of dog hearts and plotted gauge length in the fiber direction against the pressure in the LV cavity. During normal contraction, these plots traced out counterclockwise loops very similar to the pressure-volume loops often employed to study cardiac physiology: segment length increased as the heart filled during diastole, remained nearly constant during isovolumetric contraction, decreased as the LV ejected blood into the aorta, and then remained nearly constant during isovolumetric relaxation (Fig. 4a). Following occlusion of the coronary artery supplying blood to the study region, the area inside the pressure-length loops rapidly decreased, reflecting the loss of active mechanical work by the muscle fibers; in some cases, the plots again traced out loops but in the opposite (clockwise) direction, suggesting that the ischemic segments were dissipating work done by the rest of the heart.

Tyberg et al. (1974) also reported an interesting shift in the end-diastolic dimensions of the regions they studied. They found that even when measured at an identical pressure at end diastole, segment lengths were significantly longer after 30 min of coronary occlusion. This finding was surprising, because it seems unlikely that the

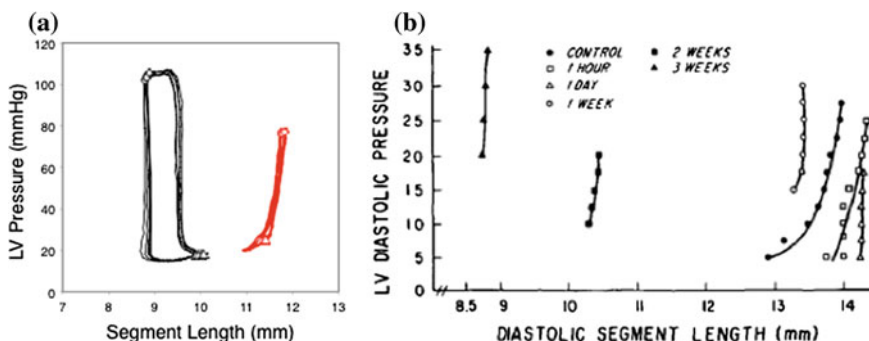


Fig. 4 **a** Pressure-circumferential segment length loops in an anesthetized dog at control (black) and 15 min after coronary ligation (red) show conversion from active shortening to passive stretching and recoil (data from the study of Fomovsky et al. 2012a). **b** Evolution of diastolic pressure-segment length curves in a healing canine infarct indicating substantial geometric remodeling of the healing scar (Theroux et al. 1977)

structure or composition of the ischemic region could change significantly in just 30 min. Some have postulated that a phenomenon called strain softening, observed in soft materials such as rubber, could play a role. However, Holmes et al. (2005) proposed a simpler alternative explanation that highlights the potential limitations of using *in situ* measurements to deduce information about material properties in the heart: occluding a coronary artery decreases blood flow, tissue volume, and wall thickness in the affected region of the heart. Holmes et al. (2005) estimated that this decrease in wall thickness due to loss of perfusion could increase stresses enough to explain the observation of Tyberg et al. (1974) of increased diastolic stretch at matched pressure.

Around the same time that Tyberg et al. (1974) performed their study of acute ischemia, Theroux et al. (1977) published a series of studies on longer term changes in regional segment lengths during healing of myocardial infarcts in dogs. This group used implanted sonomicrometers to measure segment lengths at multiple time points in the same animals. They reported that end-diastolic lengths increased slightly ($3 \pm 2\%$) immediately after injury (consistent with the study of Tyberg et al. 1974), remained elevated for about a week, but then decreased as much as 30 % by week 4 (Fig. 4b). A number of subsequent studies confirmed that infarcts can shrink in volume significantly as scar forms (Richardson et al. 2015), an important consideration when predicting the long-term effects of post-infarction therapies (Clarke et al. 2015).

Because the diastolic portion of their pressure-length curves had an exponential shape, Theroux et al. (1977) plotted lengths measured during filling (x-axis) against the natural log of the corresponding pressures (y-axis) in each dog at each time point and compared the slope of those curves as an index of regional stiffness. They found that the slope increased nearly 10 fold in the first day, then remained nearly constant over the next four weeks. However, as discussed in Sect. 1.2.1, the slopes of such curves depend not only on the changing passive material properties of the study region but also on the pressure and the geometry of the LV, which determine where the material is operating along its nonlinear stress-strain curve. Accordingly, *ex vivo* mechanical testing has provided the best information to date on changes in infarct material properties during healing, as reviewed in the next section.

Since these early studies, many groups have used implanted markers, sonomicrometers, ultrasound, and MRI to examine patterns of deformation in healing infarcts. Three broad themes emerge from these studies. First, in most animal models of permanent ligation of a coronary, strains drop to near zero in the infarct region and remain small throughout healing (Theroux et al. 1977; Holmes et al. 1994; Fomovsky and Holmes 2010). In studies with the resolution to distinguish these small strains statistically from zero, the circumferential and longitudinal strains are typically positive (indicating stretching of the scar during systole) and the radial strain is negative (indicating wall thinning in the infarct region). Unlike in the myocardium, where there are large variations in strain magnitude across the heart wall, in transmural infarcts the strains change little with depth (Villareal et al. 1991). The second broad trend is that when the occluded coronary artery is reopened before all of the downstream myocardium dies ('reperfused' infarcts), circumferential and longitudinal shortening often recover partially (Theroux et al. 1977; Kramer et al. 1997; Bogaert et al. 1999;

Kidambi et al. 2013). Finally, the third trend is that coupling to adjacent surviving myocardium can induce unexpected shears or other deformations in the infarct region that are tricky to interpret. For example, Holmes et al. (1994) measured large radial thickening strains in dense collagenous scars 3 weeks after infarction in pigs; although such strains normally indicate wall thickening due to active contraction, no surviving myocytes were apparent on histology in these scars.

One final point deserves mention regarding the interpretation of in vivo strains in healing infarcts. The convention in most cardiac mechanics studies is to compute deformation between end diastole, when muscle fibers in the heart wall are usually at their maximum length, and end systole, when they are at their minimum length. However, circumferential and longitudinal segment lengths in a passively deforming infarct typically reach their minimum length at the end of isovolumetric relaxation, when LV pressure is minimum, and their maximum at the end of isovolumetric contraction, when wall stress is greatest (Richardson et al. 2015). Therefore, infarct mechanics studies that compute strains from measurements taken only at end diastole and end systole likely neglect a substantial portion of the deformation.

2.2.2 Ex Vivo Mechanical Testing

Two of the approaches reviewed in Sect. 1.2 have also been employed for ex vivo testing of myocardial scar tissue: passive inflation of isolated arrested hearts and planar biaxial testing. Holmes et al. (1997) inflated isolated, arrested pig hearts three weeks following coronary ligation while tracking three-dimensional deformation in both the infarct scar and the remote myocardium. Consistent with the highly anisotropic collagen fiber structure shown in Fig. 3a, these scars stretched by as much as 40 % in the longitudinal direction but less than 15 % in the circumferential direction at a cavity pressure of 25 mmHg; by comparison, peak strains in the remote myocardium were approximately 30 % (longitudinal) and 35 % (circumferential) at the same cavity pressure. By contrast, Omens et al. (1997) measured epicardial strains during passive inflation of isolated arrested rat hearts 2 weeks after coronary ligation and reported greater infarct stretch in the circumferential direction than in the longitudinal direction. However, Fujimoto et al. (2007) reported equal circumferential and longitudinal infarct strains in passively inflated rat hearts 8 weeks after MI. Unfortunately, as discussed in Sect. 1.2.1, comparing infarct material properties across these studies would require constructing computational models to estimate circumferential and longitudinal wall stresses at each pressure.

To date, only two comprehensive biaxial testing studies have quantified the mechanics of healing myocardial scar tissue over time, and these studies reached very different conclusions. Gupta et al. (1994) studied anteroapical infarcts induced by coronary ligation in sheep. They reported average circumferential and longitudinal stresses at 15 % equibiaxial extension at 4 h, 1w, 2w, and 6w, and found that infarct anisotropy varied with time: longitudinal stresses were significantly higher at 1 week, while circumferential stresses were higher at six weeks. They also found that stresses in both directions peaked at 1–2 weeks and then decreased by six weeks, which was

unexpected given that they also reported a progressive increase in collagen content with time. By contrast, Morita et al. (2011) observed isotropic stretch under equibiaxial stress 8 weeks after MI in the same animal model. Fomovsky and Holmes (2010) conducted biaxial testing of rat anteroapical infarcts induced by coronary ligation and found that scars were mechanically isotropic at 1w, 2w, 3w, and 6w. Furthermore, the fitted material coefficient in their isotropic strain-energy function increased with time post-infarction, and correlated reasonably well with collagen content on a sample-by-sample basis. While the fact that different animal models develop post-infarction scars with different degrees of structural anisotropy (see Sect. 2.1.2) may explain differences in the levels of mechanical anisotropy reported by Gupta et al. (1994) and Fomovsky and Holmes (2010), it is more difficult to explain why collagen content and material properties were correlated in Fomovsky's study (Fomovsky and Holmes 2010) but decoupled in Gupta's (Gupta et al. 1994).

3 Analytical Models of Heart Function During Ischemia and Infarction

The primary function of the heart is to pump blood through the body. Therefore, the ultimate goal of studying the biomechanics of the normal and diseased heart is to understand the underlying basis for the heart's ability to perform this function, and how disease impairs pump function. Due to the complex geometry of the heart, measuring changes in tissue properties is usually necessary but not sufficient to quantitatively predict changes in overall pump function; researchers also typically employ a geometric or computational model to relate pressures and volumes inside the chambers of the heart to the stress and strain experienced by the myocardium that comprises those chambers. One of the most surprising things about the heart is that despite the complexity of its anatomy, geometry, and material properties, very simple analytical models can provide critical insight regarding heart function even in the setting of a myocardial infarction.

3.1 Normal Pump Function of the Left Ventricle

One of the most useful conceptual frameworks for analyzing pump function of the heart from an engineering perspective is the pressure-volume loop (Fig. 5). The idea of plotting volume against pressure to analyze the performance of a pump or engine is familiar to most engineers who have taken a course in thermodynamics. Pioneering physiologists such as Otto Frank applied this same idea to the heart over a century ago, plotting the internal pressure and volume of the LV against one another; in the 1970s and 1980s, Kiichi Sagawa and his colleagues at Johns Hopkins University

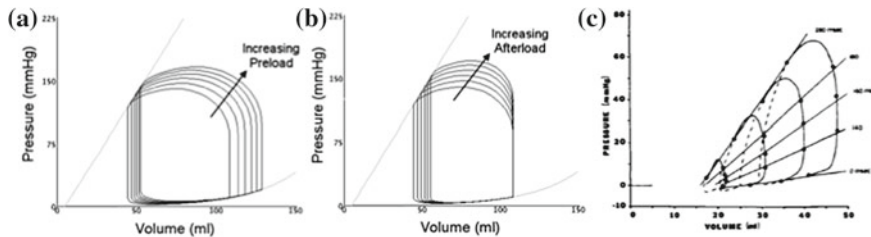


Fig. 5 **a** Simulated response of the isolated left ventricle to changes in filling pressure (preload) or, **b**, resistance to ejection (afterload). Simulations performed using the Heart Simulator developed by Kelsey et al. (2002) based on Santamore and Burkhoff (1991). **c** Connecting points at the same time in the cardiac cycle illustrates the concept of time-varying elastance in the canine right ventricle (Maughan et al. 1979, Fig. 4)

popularized this framework and applied it to myocardial infarction (Suga et al. 1973; Suga and Sagawa 1974; Sunagawa et al. 1983).

When viewing a pressure-volume (PV) loop for the LV (Fig. 5), the events of the cardiac cycle are as follows: (i) the mitral valve opens at the lower left corner of the loop and blood flows from the left atrium into the relaxed LV (filling phase), generating a large increase in volume but relatively small change in pressure; (ii) at the lower right corner, contraction begins and pressure rises but volume does not change because both the mitral valve and aortic valve are closed (isovolumetric contraction); (iii) at the upper right corner, the LV pressure exceeds aortic pressure, forcing the aortic valve open and allowing the LV to eject blood into the aorta (ejection); (iv) at the upper left corner, the aortic valve closes and the LV pressure drops as the muscle in the wall relaxes (isovolumetric relaxation). The area within the loop represents the mechanical work performed by the LV in ejecting blood into the circulation.

3.1.1 Diastolic Function

The portion of the cardiac cycle during which the heart is passively filling (bottom portion of the PV loop) is called diastole. The main factors that control how much the heart fills during this phase include the material properties of the myocardium, the geometry of the LV, and the upstream pressure in the pulmonary veins and left atrium. At high heart rates or when the material properties of the myocardium are altered, the time available before the next contraction can also become an important determinant of filling. In theory, the resistance to blood flow through the open mitral valve could affect the rate of filling, but this is usually significant only in the setting of pathologic narrowing (stenosis) of the valve.

Suga and Sagawa (1974) and Sunagawa et al. (1983) performed many of their studies on isolated, blood-perfused canine hearts. This experimental preparation allowed them to separately vary factors that influence pump function and explore their impact individually. As one example, when they increased the upstream

pressure but held heart rate and the resistance to ejection through the aorta constant, the LV not only filled to higher volumes and pressures, but also ejected a larger volume of blood (stroke volume) with each contraction (Fig. 5a). This fundamental property of the heart is often called the Frank–Starling mechanism. At the level of individual myocytes, this property arises because increased diastolic stretch alters both the overlap between actin and myosin filaments and the binding of calcium to the myofilaments, increasing the active force generated by each cell during the subsequent contraction.

Another central experimental finding illustrated in Fig. 5a is that the lower right corners of PV loops with different filling pressures appear to lie along a single exponential curve. These points indicate pressures and volumes at the end of diastole when the heart muscle is fully relaxed, and the curve connecting them is termed the end-diastolic pressure-volume relationship (EDPVR). It is typically modeled using a simple equation that includes a volume intercept to account for the fact that even a completely unloaded, arrested LV has a nonzero cavity volume:

$$P_{ED} = A \{ \exp [B(V_{ED} - V_0)] - 1 \}. \quad (5)$$

In part, the exponential shape of the diastolic pressure-volume relationship reflects the exponential stress–strain relationships measured in mechanical tests of the passive myocardium discussed in Sect. 1.2. However, one key point that may seem obvious to a mechanics audience has caused considerable confusion over the years among physicians and physiologists, because of the fact that many diseases alter the size and shape of the heart: both changes in material properties of the myocardium and changes in LV geometry will alter the EDPVR. One simple illustration of this concept is to imagine a pressurized, thin-walled elastic sphere. A force balance on one half of the sphere reveals that the force arising from the pressure pushing against the hemisphere must be balanced by the force associated with the stress in its wall; setting these two forces equal and simplifying yields an equation often termed Laplace's law. Thus,

$$Pr^2\pi = \sigma 2r\pi h \rightarrow \sigma = \frac{Pr}{2h}, \quad (6)$$

where h = wall thickness and r = radius. This equation shows clearly that at a given pressure the wall stress increases as radius increases and decreases as the wall thickens; thus, deformation will depend not only on material properties but also on geometry. While this simple equation is not appropriate for computing stresses in the thick-walled, elliptical LV, the same basic concepts apply to the heart: dilation (increased radius) shifts the EDPVR rightward (lower pressure at any volume), while wall thickening shifts the EDPVR leftward.

3.1.2 Systolic Function

When Sagawa and colleagues varied the resistance to ejection through the aorta in their isolated heart preparation and held heart rate and diastolic pressure constant, they saw that the LV ejected less blood against high resistance and more blood against low resistance, as expected (Fig. 5b). They also found that the upper left corners of the loops—indicating the pressure and volume at the end of systole for each beat—traced out a straight line. Although there are a few exceptions, this end-systolic pressure-volume relationship (ESPVR) is approximately linear in most animal models and under most loading conditions; e.g., inflating the LV to different diastolic volumes and then clamping the aorta to measure the maximum pressure generated during ‘isovolumetric’ beats yields basically the same relationship as connecting the upper left corners of normal, ejecting beats (Suga et al. 1973).

The linearity of the ESPVR is perhaps the single most remarkable finding in cardiac physiology: a complex structure composed of mechanically nonlinear and anisotropic materials generates a maximum pressure that is linearly proportional to cavity volume! The slope of the ESPVR, which Sagawa et al. (1988) termed the end-systolic elastance, E_{ES} , provides a very useful index of the ‘contractility’ of the heart. Drugs that increase calcium cycling and force of contraction in individual myocytes also increase E_{ES} , indicating that the heart can generate more isovolumetric pressure at a given volume or eject more blood against a given aortic resistance. The simple equation Sagawa et al. (1988) used to describe the ESPVR is

$$P_{ES} = E_{ES}(V_{ES} - V_0), \quad (7)$$

where V_0 is a volume intercept at which no active pressure is generated by contraction.

Sagawa and his colleagues made one more discovery about the behavior of the LV that has proved invaluable in modeling heart function. When they varied filling pressures (preload) and resistance to ejection (afterload) to generate a range of PV loops, then connected PV points acquired at identical times after electrically stimulating the heart, they found that these isochronal points were connected by a family of lines (Fig. 5c). The slope of these lines increased as the LV contracted, reached a maximum at end systole (hence E_{ES} is also often called E_{max}), and then decreased again as the muscle in the LV relaxed. In other words, the LV can be reasonably modeled as a single chamber or compartment with a time-varying stiffness (Suga et al. 1973):

$$P(t) = E(t)(V(t) - V_0). \quad (8)$$

This is now known as the time-varying elastance model, and together with an experimentally measured curve for the time-varying slope $E(t)$, it provides a remarkably accurate prediction of PV loops for a given LV across a wide range of hemodynamic loading conditions. As we will see in the next section, the time-varying elastance framework also forms the basis for an influential analytical model of LV function in the setting of infarction.

3.2 Functional Impact of Myocardial Infarction

There are many different mechanisms by which a myocardial infarction can impair the pump function of the heart either directly or indirectly (Holmes et al. 2005); the related mechanics and physiology are discussed in detail in review articles by Holmes et al. (2005) and Richardson et al. (2015). This chapter focuses on the use of computational models in understanding and simulating these mechanisms and their effects on heart function; as an introduction, the mechanisms are reviewed briefly here. (i) The first mechanism by which infarction could impair function is particularly dramatic: if post-infarction necrosis weakens the infarct too much in the first few days before sufficient new collagen is deposited, the heart can rupture, leading to sudden death. (ii) A more common mechanism in the first few days after infarction is that the damaged region stretches passively as the rest of the heart contracts, reducing pressure generation and ejection from the LV and wasting mechanical energy; this mechanism and analytical models that capture it are discussed in detail in Sect. 3.2.1. (iii) Over time, as collagenous scar forms in the damaged region, systolic stretching becomes less problematic, but the stiff scar can limit LV filling during diastole; this mechanism is discussed in Sect. 3.2.2. (iv) A more subtle mechanism by which the infarct impairs LV function is that it is physically coupled to adjacent noninfarcted myocardium. Therefore, stretching, thinning, and outward bulging (dyskinesis) of the infarct can reduce thickening and inward motion in the borderzone, resulting in a region of functional depression that is bigger than the actual infarct. Anatomically detailed finite element models are needed to capture these three-dimensional interactions, as discussed in Sect. 4 of this chapter.

In addition to direct effects on function, myocardial infarction triggers a process of growth and remodeling that gradually alters function indirectly. (v) In the infarct region, collagen deposition can increase stiffness, affecting both systolic and diastolic function; in addition, gradual thinning of the infarct is common in most settings and acts to increase wall stress in the infarct and adjacent borderzone. (vi) In the surviving muscle, infarction triggers lengthening of individual myocytes with modest increases in cross-sectional area; at the chamber level, this is reflected in an increased cavity volume with relatively modest changes in wall thickness, a geometric change that increases wall stresses throughout the LV. Computational modeling of growth and remodeling following myocardial infarction is a young but exciting field, and is discussed in Sect. 5 of this chapter.

3.2.1 Systolic Function

The slope of the ESPVR provides a measure of the contractility of the heart. Therefore, it seems reasonable to expect that myocardial infarction will decrease this slope. Yet when Sunagawa et al. (1983) actually performed this experiment by ligating different coronary arteries in the isolated dog heart preparation, they found something unexpected: the slope of the ESPVR, E_{ES} , changed little, while the intercept, V_0 ,

increased in proportion to the size of the infarct! They also constructed a simple compartmental model that explained these apparently paradoxical results. The notation in the original paper is somewhat confusing, and has been modified here to improve clarity.

Sunagawa et al. (1983) knew that within a few seconds after coronary ligation, the ischemic region would stop contracting and begin passively stretching and recoiling with each beat. Accordingly, they modeled the LV as consisting of two compartments: a normally contracting compartment described by the usual time-varying elastance model, and a passive ischemic compartment where pressure and volume were related according to the EDPVR at all times. They assumed that the two compartments always operated at the same pressure but could contain different volumes, and computed the ESPVR for the two-compartment model using a weighted average of the end-systolic volumes that would be expected if the entire LV were contracting normally or the entire LV were ischemic. In the normal compartment

$$P_{\text{ES}} = E_{\text{ES}}(V_{\text{ES}} - V_0) \rightarrow V_{\text{ES},n} = (1 - R)V_{\text{ES}} = (1 - R) \left(\frac{P_{\text{ES}}}{E_{\text{ES}}} + V_0 \right), \quad (9)$$

and in the ischemic compartment

$$P_{\text{ES}} = A \{ \exp [B(V_{\text{ES}} - V_0)] - 1 \} \rightarrow V_{\text{ES},i} = R V_{\text{ES}} = R \left[\frac{1}{B} \ln \left(\frac{P_{\text{ES}}}{A} + 1 \right) + V_0 \right], \quad (10)$$

yielding the overall ESPVR, i.e.

$$V_{\text{ES}} = V_{\text{ES},n} + V_{\text{ES},i} = (1 - R) \left(\frac{P_{\text{ES}}}{E_{\text{ES}}} + V_0 \right) + R \left[\frac{1}{B} \ln \left(\frac{P_{\text{ES}}}{A} + 1 \right) + V_0 \right], \quad (11)$$

where R is the size of the ischemic region as a fraction of the LV. Figure 6 shows the predictions of this model for pressures and volumes typical of the experiments of Sunagawa et al. (1983), compared to original data from the paper. The key feature of the acutely infarcted heart that is captured by this simple model is the exponential nature of the EDPVR. Normally, diastolic pressures do not exceed 15–20 mmHg in the dog, but when the ischemic compartment is exposed to systolic pressures, it moves to a very steep portion of the EDPVR. At these high pressures, the slope of the EDPVR is very similar to the slope of the normal ESPVR, but the volumes are much larger. Thus, a weighted average of the behavior of the two compartments predicts a shift toward larger volumes (increased V_0) without much change in slope (unchanged E_{ES}).

The work of Sunagawa et al. (1983) is a wonderful example of the adage that a model should be as simple as possible, but not simpler. In this case, representing the complex, infarcted LV using two compartments—essentially two balloons

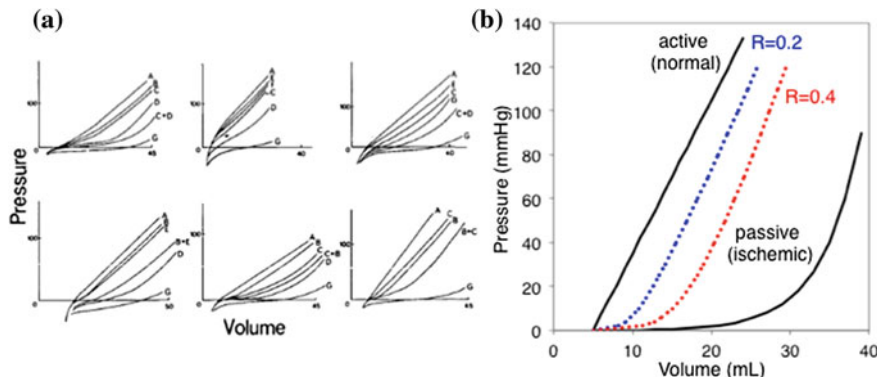


Fig. 6 **a** End-systolic pressure-volume relationships measured in six isolated dog hearts following coronary occlusions affecting different sized regions (Fig. 5 of Sunagawa et al. 1983, letters indicate which coronary branches were occluded). **b** Predictions of the two-compartment model of Sunagawa et al. (1983) (described in the text) for two different infarct sizes

connected by a straw—provides an accurate and useful analysis, as long as the exponential nature of the passive myocardium is incorporated. By contrast, simplifying the EDPVR by using a straight line—which is a fairly common and reasonable simplification in compartmental models operating in the range of diastolic pressures experienced by a normal heart—completely changes the behavior, resulting in an erroneous predicted decrease in E_{ES} during ischemia. Even a sophisticated finite element model would make similarly errant predictions if the ischemic region were assumed to be linearly elastic.

3.2.2 Diastolic Function

Three years before Sunagawa et al. (1983) published their compartmental model, Bogen et al. (1980) published a more complex analytical model that predicted similar pressure-volume behavior. They modeled the LV wall as a thin membrane with two sets of nonlinearly elastic material properties, simulating the myocardium as a softer, highly nonlinear material at end diastole, and a stiffer, less nonlinear material at end systole. Bogen et al. (1980) then assigned different material properties to one region of the simulated LV to represent infarcts at different stages of healing following infarction. Although representing the thick-walled LV as a thin-walled membrane did produce some unphysiologic predictions such as a sudden jump in stress at the infarct border, the model produced realistic diastolic and systolic pressure-volume behavior for both baseline and acute infarction cases.

More importantly, the model of Bogen et al. (1980) produced a fundamental insight about the impact of infarct stiffness on LV function that has since been verified in more sophisticated finite element models and experiments: stiffening the infarct improves systolic function by limiting bulging of the infarct, but impairs diastolic

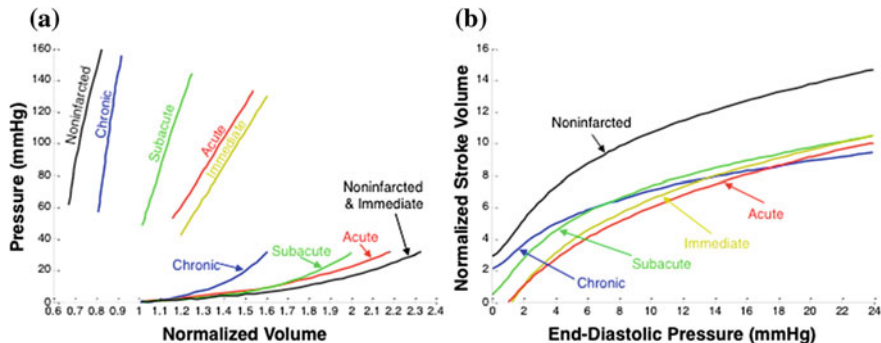


Fig. 7 **a** Predicted changes in end-systolic (ESPVR) and end-diastolic (EDPVR) pressure-volume relationships as the passive material properties of a large (41 % of LV) infarct region are increased to simulate different stages of infarct healing (replotted from Bogen et al. 1980); the ESPVR and EDPVR both shift left as infarct stiffness is increased. **b** Model ventricular function curves showing the net stroke volume pumped by the LV at different filling pressures in the presence of a moderate (25 %) infarct; stiffening the infarct yields little change in pump function at most filling pressures

function by restricting filling. As Bogen et al. (1980) increased the simulated stiffness of the infarct region in their model, the predicted ESPVR shifted to the left, reflecting an improved ability to eject blood against a given aortic resistance (Fig. 7a). At the same time, the predicted EDPVR shifted to the left, reflecting the fact that stiffening part of the LV reduces the overall chamber compliance. In order to understand the relative impact of these two effects, Bogen et al. (1980) plotted a ventricular function curve, showing the total stroke volume that would be expected at each filling pressure if afterload (resistance to ejection) were kept constant. Surprisingly, they found that the diastolic and systolic effects of infarct stiffening offset almost exactly, yielding no change in predicted pump function at most filling pressures across the entire range of infarct properties tested (Fig. 7b). This remarkable prediction has held up extremely well over more than three decades. More sophisticated finite element models (discussed in Sect. 4) have confirmed this prediction, and multiple experimental studies using surgical reinforcement or injection of polymers have shown that stiffening or reinforcing the infarct reduces diastolic and systolic volumes without changing stroke volume or cardiac output (Clarke et al. 2014; Richardson et al. 2015).

3.2.3 Coupling to the Circulation and Reflex Compensation

In vivo, the heart is coupled to the circulatory system, which regulates resistance to ejection from the ventricles during systole as well as the pressures driving filling during diastole. Therefore, understanding the physiology and mechanics of the heart in vivo often requires coupling models of the heart to models of the circulation. One of the most influential circulation models is the windkessel model, which incorporates the resistance of the peripheral arteries and capacitance of the aorta (Westerhof et al.

1969). This simple model explains how the arteries buffer pulses of flow from the LV during systole to provide continuous flow to the body. Building on the windkessel concept, Westerhof et al. (1969) developed more sophisticated circuit models of the circulation that better reflected the interaction between the heart and circulation on both the arterial and venous sides. Such lumped-parameter approaches form the basis for most mathematical models of the circulation. These lumped-parameter representations of the circulation are easily coupled not only to time-varying elastance models of heart mechanics but also to sophisticated finite element models (see, e.g., Kerckhoff et al. 2007; Wall et al. 2012; Moyer et al. 2015).

The pressure in the systemic arteries is the driving force for blood flow through the body, and is determined by the balance between cardiac output and resistance to flow. The body senses changes to mean arterial pressure (MAP) through arterial baroreceptors and acts through compensatory reflexes to maintain MAP. During myocardial ischemia, reduced cardiac output should produce a fall in MAP; however, the circulation rapidly compensates by (i) increasing heart rate, (ii) increasing calcium cycling and the force the surviving myocardium can generate (contractility), and (iii) constricting peripheral blood vessels. Using a time-varying elastance model of the left and right ventricles coupled to a lumped-parameter model of the circulation, Burkhoff and Tyberg (1993) investigated the potential role of reflex hemodynamic compensation in generating pulmonary edema, one of the most serious consequences of acute left ventricular dysfunction. They found that even a large acute drop in left ventricular function caused relatively modest changes in pulmonary venous pressures if the parameters of the circulatory model were unaltered. Next, they simulated different reflex compensations that might be expected following a drop in LV function and found that only venoconstriction (a reduction in venous capacitance) substantially increased pulmonary venous pressures. Thus, they concluded that pulmonary edema was not a direct result of reduced left ventricular function, but rather a consequence of the reflex venoconstriction. Their work demonstrates both the power of mathematical modeling to provide new insights in cardiovascular physiology and the importance of the circulation in determining the consequences of changes in heart mechanics and function.

One of the most important long-term risks following myocardial infarction is the risk of developing heart failure. Here again, interaction of the heart, circulation, and hemodynamic reflexes likely plays an important role. Most standard post-infarction treatments primarily modulate the circulatory system or reflex compensations rather than the heart itself. Angiotensin converting enzyme (ACE) inhibitors, angiotensin receptor blockers, and a number of other drugs dilate arteries and veins. Beta blockers directly oppose reflex compensations, reducing both cardiac contractility and heart rate. Assessing the impact of even one of these drugs can be difficult as they often affect more than one cardiac or circulatory parameter. For example, Maurer et al. (2009) studied the effect of a common beta blocker, carvedilol, on patients with systolic heart failure. In patients who responded to carvedilol, Maurer et al. (2009) attributed 56 % of the increase in ejection fraction to heart rate reduction, 28 % to altered contractility, and 16 % to the reduction in total peripheral resistance using

multiple linear regression. In such situations, models can play an important role in estimating the relative importance of multiple simultaneous changes.

4 Finite Element Models of Ischemia and Infarction

Despite the success of the analytical models reviewed above in explaining global pressure-volume behavior in the infarcted heart, these simple models cannot accurately represent distributions of stresses and strains through the wall, mechanical interactions at the infarct border, or the effects of therapies such as polymer injection that perturb mechanics locally. Therefore, some questions related to the biomechanics of myocardial ischemia and infarction require anatomically realistic, detailed finite element models. Many investigators have developed and published finite element models of the heart over the past several decades; this review focuses on a few of these models selected for their historical value (Sect. 4.1) or as examples of particularly interesting applications of modeling to answer physiologic questions (Sect. 4.2) and design novel therapies (Sect. 4.3).

4.1 Early Models

One of the earliest modeling studies exploring interactions at the infarct border was published by Janz and Waldron (1978). They constructed an axisymmetric model of a rat LV based on geometry measured from a longitudinal (apex-base) slice through a fixed heart. They simulated a thinned, infarcted region at the apex of the model, and explored how stretches varied from the infarct into the adjacent normal myocardium during simulated passive inflation (diastole). When they simulated stiff chronic infarcts, circumferential stretch was low in the infarct and gradually increased with distance from the center of the infarct, reaching a normal (noninfarcted) value only in elements a substantial distance away from the infarct border. This simple result has potentially important physiologic consequences: because active force generation in cardiac muscle depends on diastolic sarcomere length (the Frank–Starling mechanism, discussed in Sect. 3.1.1), active contraction in normal myocardium near the infarct border could be impaired because diastolic prestretch is below normal.

Over the next two decades, most models of the ischemic or infarcted LV were conceptually similar, employing an axisymmetric elliptical geometry composed of a nonlinearly elastic passive material, then adding features such as active contraction or the presence of appropriately oriented fibers. Bovendeerd et al. (1996) published one of the last of this early class of models, integrating many of the most important features now common to modern models of the infarcted heart. Their model included muscle fibers with an orientation that varied through the wall, as described by Streeter and co-workers (Sect. 1.1), active stress generation in the direction of the fibers that depended on local diastolic prestretch, and a realistic infarct geometry

based on the perfusion territory of a branch of the left anterior descending coronary artery. They also simulated the full cardiac cycle rather than just end diastole and end systole, and—perhaps most importantly—compared their model predictions to hemodynamic data and epicardial surface strains measured in dogs during coronary occlusion. Bovendeerd et al. (1996) achieved an excellent match to experimentally measured fiber strains, then used their model to explore the impact of both transmural and non-transmural ischemia on regional work in the infarct borderzone.

4.2 *Understanding Coupling to Adjacent Myocardium*

Both models discussed in the previous section showed that the functional impact of a myocardial infarction could extend well beyond the infarct, into the surrounding myocardium near the infarct border. A number of groups subsequently used detailed finite element models of ischemia and infarction to explore this concept further. Mazhari and McCulloch (2000) and Mazhari et al. (2000) combined experiments and anatomically detailed finite element models of regional ischemia in the dog to ask whether the gradual transition from impaired to normal function across the infarct border implies a transition in local myocyte contractility. They found that they could reproduce measured distributions of fiber and crossfiber strain across the infarct border for a range of pressures and for different ischemic region locations even if they assumed a sudden step in contractility at the border of the ischemic region. In other words, mechanical interactions between the ischemic region and the surrounding myocardium are sufficient to create gradients in function that extend well beyond the infarct, even if the borderzone is composed of functionally normal myocytes.

Herz et al. (2005) applied similar models of regional ischemia to develop strategies for identifying and quantifying regional ischemia using three-dimensional echocardiography. Stress echocardiography is a common clinical test in which the heart is imaged using ultrasound both before and during elevation of cardiac energy consumption imposed by exercise or infusion of a drug such as dobutamine. Cardiologists typically evaluate the resulting images visually, looking for changes in inward motion or wall thickening (wall motion abnormality, WMA) that indicate compromised regional function due to a coronary stenosis that limits the increase in blood flow that would normally occur in response to stress. Herz et al. (2005) used finite element models to examine the relationship between the size of the simulated ischemic region and the size of the WMA as detected by various quantitative measures of endocardial motion. They found that with an appropriate choice of threshold, they could use quantitative wall motion measures to estimate the size of ischemic regions larger than about 10 % of the LV. However, small ischemic regions did not produce detectable wall motion abnormalities, because as the surrounding adjacent normal myocardium moved inward, it carried the ischemic region with it. Later, Herz et al. (2010) confirmed in animal experiments that most small ischemic regions induced no detectable WMA. Thus, whereas Mazhari and McCulloch (2000) and Mazhari

et al. (2000) showed that mechanical coupling to the ischemic region can cause dysfunction in surrounding myocardium, Herz et al. (2010) showed that coupling to the surrounding myocardium can also mask dysfunction in the ischemic region.

One final aspect of mechanical coupling that is of interest is the increase in wall stresses in the borderzone caused by the infarct. Myocytes generating higher stresses consume more oxygen and are energetically less efficient, so elevated wall stresses can be particularly disruptive in regions near an infarct where blood flow, systolic function, or both are already compromised. In addition, some investigators hypothesize that increased wall stress is a stimulus for growth and remodeling in myocardium, so elevated wall stress in the borderzone could contribute to the post-infarction remodeling that often leads to heart failure. Yet one of the central challenges of cardiac mechanics research is that it is virtually impossible to directly measure forces or stresses in the intact heart wall. Therefore, finite element models are an important tool for estimating wall stresses based on other, directly measurable quantities such as cavity pressure and regional strains. For example, Walker et al. (2005) constructed finite element models of the infarcted LV using geometry and regional strains measured by MRI in individual sheep with healed, large infarctions. They found that the presence of a healed infarct substantially increased stresses in the adjacent myocardium, particularly in the crossfiber direction. These studies set the stage for subsequent models of novel therapies intended to work partly or primarily by reducing wall stress following infarction.

4.3 Modeling and Designing Novel Therapies

One of the most exciting applications of finite element modeling of the heart is the design of novel post-infarction therapies. Drug and device therapies for heart disease are usually developed through trial-and-error. As one example, many years ago a series of studies tested the idea that lowering blood pressure might reduce remodeling of the heart following infarction. These studies culminated in a definitive clinical trial that showed that while lowering blood pressure did improve survival, one of the classes of antihypertensives—ACE inhibitors—conferred added benefit through an independent and previously unknown mechanism (Cohn et al. 1991). By contrast, current state-of-the-art finite element models are beginning to allow researchers to screen potential therapies computationally, testing a much wider range of ideas before beginning experimental trials of the most promising candidates.

Wall et al. (2006) published one of the earliest studies to harness the potential of model-based approaches in designing therapies. They used a finite element model of the infarcted sheep heart to simulate the effects of polymer injection into the infarct or adjacent borderzone, considering a range of potential polymer material properties, injection volumes, and injection patterns. They found that the volume of polymer injected was the most important determinant of how much the injection reduced wall stress, and that even relatively small volumes injected into the borderzone could substantially reduce elevated wall stresses by locally thickening the

heart wall. Importantly, some of the predicted effects were counterintuitive, such as the finding that stiffer polymers reduce wall stress when injected into the border, but actually exacerbate elevated borderzone stresses when injected into the infarct. Finally, some of the results confirmed predictions from earlier analytical models: injecting a stiff polymer into the infarct reduced both systolic and diastolic volumes, but produced no net improvement in the simulated ventricular function curve.

Fomovsky et al. (2011, 2012a) also published a series of studies illustrating the power of finite element models for designing post-infarction therapies. They returned to the original prediction by Bogen et al. (1980) that stiffening an infarct reduces diastolic and systolic volumes but does not improve overall pump function. Fomovsky et al. (2011) noted that prior analytical and finite element models of infarct stiffening typically treated the infarct as isotropic, whereas healing infarcts are often anisotropic (Sect. 2). Accordingly, they used a finite element model of the canine LV following a large anteroapical infarction to explore the functional impact of a wide range of both isotropic and anisotropic infarct material properties (Fig. 8a). They varied the ratio of coefficients controlling circumferential and longitudinal infarct stiffness in their Fung-type strain energy function from 60:1 to 1:60 and computed the predicted stroke volume at matched diastolic and systolic pressures for each choice of parameters. Surprisingly, they found that a scar that is much stiffer in the longitudinal direction than the circumferential direction—something that has never been observed in any animal model—provided the best predicted pump function (Fig. 8b). Unlike isotropic stiffening, selective stiffening in the longitudinal direction shifted the ESPVR to the left without altering diastolic function. Fomovsky et al. (2012a) then tested this prediction experimentally by selectively reinforcing acute canine infarcts in the longitudinal direction, and confirmed that anisotropic reinforcement provided the predicted improvement in pump function (Fig. 8c). This series of studies illustrates the promise of finite element modeling for identifying novel and potentially unexpected approaches by allowing exploration of a much larger parameter space than could ever be tested experimentally.

5 Models of Myocardial Infarct Healing

The studies by Wall et al. (2006) and Fomovsky et al. (2011, 2012a) reviewed in the previous section are excellent examples of the power of current models to predict the immediate effects of a novel therapy. Yet because the heart can grow and remodel in response to chemical or mechanical changes in its environment, predicting the short-term response is only half the battle. ACE inhibitors have modest acute effects on heart function, but improve survival over the long term by limiting growth and remodeling in the noninfarcted regions of the ventricle. Beta blockers—another class of drug given to most patients following infarction—actually depress heart function acutely, yet improve survival in the long term. The long-term effects of therapies on the healing infarct region are also important: e.g., steroids and other anti-inflammatory drugs were once tested as treatments to reduce infarct size, but ultimately abandoned

because they interfered with scar formation and increased the risk of dilation and rupture.

These examples illustrate the need to accurately predict not just short-term but also long-term effects of therapies on infarct healing and myocardial growth and remodeling. Predicting growth and remodeling is one of the newest and most exciting emerging areas within the field of biomechanics. This section focuses on early models of infarct healing, in keeping with the overall theme of the chapter. However, ongoing work on myocardial growth and remodeling in response to changes in hemodynamic loading will also prove important to developing new treatments for myocardial infarction, since the geometry and material properties of both the infarct region and the remaining undamaged myocardium ultimately determine long-term outcomes following myocardial infarction.

5.1 Inflammation and Cell–Cell Signaling

As discussed in Sect. 2, healing following myocardial infarction involves a series of different cell types that infiltrate the damaged region, remove damaged myocytes, and deposit scar tissue. The recruitment and activity of these cells are regulated in large part through a series of secreted factors called cytokines; therefore, modulating cell–cell signaling through cytokines is one potentially important approach to modulating infarct healing. Accordingly, Jin et al. (2011) developed a system of differential equations representing the infiltration and removal/death of key cell types as well as communication among these cell populations through some of the major known cytokines. Their model suggests that interactions among the different cell types involved in infarct healing can produce unexpected results in response

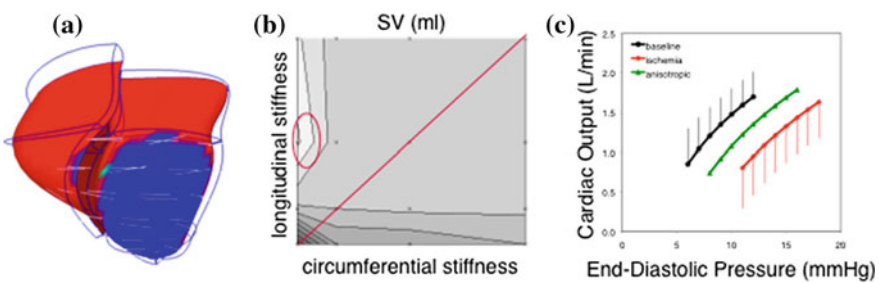


Fig. 8 **a** Finite element model of anteroapical infarction in the dog employed by Fomovsky et al. (2011). **b** Varying material parameters controlling circumferential and longitudinal infarct stiffness revealed that infarcts with high longitudinal and low circumferential stiffness (*circle*) had the best predicted pump function, while isotropic stiffening (*diagonal line*) had little effect across physiologically plausible values. **c** A subsequent experimental study confirmed that selective reinforcement in the longitudinal direction improved the cardiac output curve in infarcted canine hearts (Fomovsky et al. 2012a)

to potential therapies. As one example, increasing the level of TGF- β —which is generally considered a pro-fibrotic cytokine—actually reduced the predicted level of collagen deposition, by increasing the recruitment of macrophages that produce the collagen-degrading enzyme MMP-9.

5.2 Collagen Deposition and Alignment

Rouillard and Holmes (2012) developed an agent-based model (ABM) of infarct healing focused more narrowly on predicting the evolution of collagen alignment. The ABM tracked each fibroblast in the healing infarct as it migrated into the infarct, reorganized existing collagen, and deposited new collagen. The model considered two mechanisms by which fibroblast orientation could determine collagen orientation: fibroblasts deposited collagen fibers aligned with the cell, as has been shown in culture under some circumstances (Canty et al. 2006), and reoriented nearby collagen fibers, as has been demonstrated in collagen gels (Lee et al. 2008). At each time step, each cell selected an orientation and direction of motion from a probability distribution constructed by integrating multiple local factors known to influence fibroblast orientation in vitro: the prior direction (persistence), the spatial gradient of chemokines produced by inflammatory cells in the healing infarct (chemotaxis), the orientation of nearby collagen fibers (contact guidance), and the principal direction of stretch. The model also made a number of simplifications, such as attributing collagen degradation to fibroblasts rather than including other cell types that produce many of the collagen-degrading enzymes, and simulating the chemokine gradient as constant in time rather than varying over the course of the healing process.

Nevertheless, the ABM of Rouillard and Holmes (2012) was able to reproduce much of the data on scar structure reviewed under Sect. 2, including isotropic collagen orientation in ligation-induced rat infarcts and in cryoinfarcts stretching biaxially during healing, aligned collagen in rat cryoinfarcts stretching circumferentially during healing, and transmural gradients in collagen fiber orientation and alignment strength in healing pig infarcts, see Fig. 9. This last prediction was particularly interesting, because it shed new light on previously published but unexplained data. Experiments in healing pig infarcts revealed that during the first three weeks of healing the infarct experiences nearly uniaxial circumferential stretch; thus the direction of principal stretch conflicted with the orientation of the preexisting matrix in the epicardial (outer) and endocardial (inner) layers of the wall. The ABM predicted that these two conflicting cues would produce a relatively weak alignment signal in the inner and outer layers of the scar, and that collagen would gradually become more circumferential over time due to ongoing collagen turnover. By contrast, at the midwall the initial circumferential fiber orientation and the ongoing circumferential stretch would act synergistically, producing very high alignment in the circumferential direction. Remarkably, these predictions—achieved without tuning any of the parameters affecting cell and collagen orientation in the model—agreed very closely with published measurements (Fig. 9).

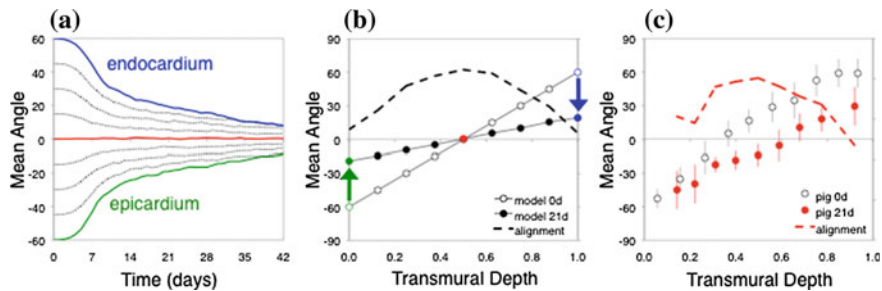


Fig. 9 Simulations of transmural variation in healing pig infarcts (data replotted from Rouillard and Holmes 2012): **a** Predicted mean angle in all transmural layers gradually converges toward 0° (circumferential), the direction of principal strain. **b** After 21 days of simulated healing, mean angles show some transmural variation, but less than in normal myocardium prior to infarction (0d); predicted alignment is strongest in the midwall, where preexisting matrix orientation and strain both promote circumferential alignment, and weakest at the epicardium and endocardium, where matrix and mechanical cues conflict. **c** Published data from Holmes et al. (1997) show a similar trend (data replotted from Holmes et al. 1997). Note alignment in panels **b** and **c** is plotted on an arbitrary scale

Models such as the one by Rouillard and Holmes (2012) represent a first step toward predicting the effects of therapeutic interventions on infarct healing. Their ABM could be used to predict an intervention with clear, known effects on one of the guidance cues (such as surgical reinforcement that alters stretch). However, the ABM is not currently able to predict the effects of drugs that alter intracellular signaling within fibroblasts or the cell–cell cytokine interactions modeled by Jin et al. (2011). Furthermore, changes in infarct healing may in turn influence scar mechanics, ventricular remodeling, systemic levels of hormones involved in reflex control of hemodynamics, etc. Ultimately, multi-scale models that represent intracellular signaling, cell–cell communication, scar formation, scar mechanics, ventricular mechanics and remodeling, and systemic hemodynamics and reflexes will be needed to fully predict the long-term effects of individual interventions.

6 Conclusions

Several themes are apparent from the experiments and models reviewed above. First, understanding the mechanics of myocardial infarction relies on high-quality data on the structure and mechanical properties of healing infarcts. Yet only a handful of studies have carefully quantified these properties in multiaxial mechanical tests, and those studies produced conflicting data; clearly, more fundamental testing data are needed in order to understand the evolution of infarct mechanical properties and possible differences across species. The second broad theme is that computational models are essential in understanding the functional impact of myocardial infarction, because that impact depends not only on infarct mechanical properties but also

on interactions between the infarct and the surviving myocardium, and between the infarcted heart and the circulation. One clear, significant success of infarct biomechanics research to date is that current models are accurate enough to suggest novel, unexpected therapeutic approaches that work as predicted when tested experimentally. A critical future direction for infarct biomechanics is extending such models to incorporate the effects of drug and device therapies on wound healing in the infarct and on growth and remodeling in the rest of the heart. The final lesson apparent from the work reviewed here is that models do not always have to be complicated in order to provide useful insight. The analytical models of Sunagawa et al. (1983) and Bogen et al. (1980) captured essential features of the mechanics and physiology of the infarcted heart that remain relevant today, more than 30 years later.

References

- Bell, R.M., Mocanu, M.M., Yellon, D.M.: Retrograde heart perfusion: the Langendorff technique of isolated heart perfusion. *J. Mol. Cell Cardiol.* **50**, 940–950 (2011)
- Bogaert, J., Maes, A., Van de Werf, F., Bosmans, H., Herregods, M.C., Nuyts, J., Desmet, W., Mortelmans, L., Marchal, G., Rademakers, F.E.: Functional recovery of subepicardial myocardial tissue in transmural myocardial infarction after successful reperfusion: an important contribution to the improvement of regional and global left ventricular function. *Circulation* **99**, 36–43 (1999)
- Bogen, D.K., Rabinowitz, S.A., Needleman, A., McMahon, T.A., Abelmann, W.H.: An analysis of the mechanical disadvantage of myocardial infarction in the canine left ventricle. *Circ. Res.* **47**, 728–741 (1980)
- Bovendeerd, P.H., Arts, T., Delhaas, T., Huyghe, J.M., van Campen, D.H., Reneman, R.S.: Regional wall mechanics in the ischemic left ventricle: numerical modeling and dog experiments. *Am. J. Physiol.* **270**, H398–H410 (1996)
- Buckberg, G., Hoffman, J.I.E., Mahajan, A., Saleh, S., Coghlan, C.: Cardiac mechanics revisited: the relationship of cardiac architecture to ventricular function. *Circulation* **118**, 2571–2587 (2008)
- Burkhoff, D., Tyberg, J.V.: Why does pulmonary venous pressure rise after onset of LV dysfunction: a theoretical analysis. *Am. J. Physiol.* **265**, H1819–H1828 (1993)
- Canty, E.G., Starborg, T., Lu, Y., Humphries, S.M., Holmes, D.F., Meadows, R.S., Huffman, A., O'Toole, E.T., Kadler, K.E.: Actin filaments are required for fibropositor-mediated collagen fibril alignment in tendon. *J. Biol. Chem.* **281**, 38592–38598 (2006)
- Caulfield, J.B., Borg, T.K.: The collagen network of the heart. *Lab. Invest.* **40**, 364–372 (1979)
- Clarke, S.A., Ghanta, R.K., Ailawadi, G., Holmes, J.W.: Cardiac restraint and support following myocardial infarction. In: Franz, T. (ed.) *Cardiovascular and cardiac therapeutic devices*, pp. 169–206. Springer, Berlin (2014)
- Clarke, S.A., Goodman, N.C., Ailawadi, G., Holmes, J.W.: Effect of scar compaction on the therapeutic efficacy of anisotropic reinforcement following myocardial infarction in the dog. *J. Cardiovasc. Transl. Res.* **8**, 353–361 (2015)
- Cohn, J.N., Johnson, G., Ziesche, S., Cobb, F., Francis, G., Tristani, F., Smith, R., Dunkman, W.B., Loeb, H., Wong, M., Bhat, G., Goldman, S., Fletcher, R.D., Doherty, J., Hughes, C.V., Carson, P., Cintron, G., Shabetai, R., Haakenson, C.: A comparison of enalapril with hydralazine-isosorbide dinitrate in the treatment of chronic congestive heart failure. *N. Engl. J. Med.* **325**, 303–310 (1991)
- Connelly, C., Vogel, W.M., Hernandez, Y.M., Apstein, C.S.: Movement of necrotic wavefront after coronary artery occlusion in rabbit. *Am. J. Physiol.* **243**, H682–H690 (1982)

- Costa, K.D., Takayama, Y., McCulloch, A.D., Covell, J.W.: Laminar fiber architecture and three-dimensional systolic mechanics in canine ventricular myocardium. *Am. J. Physiol.* **276**, H595–H607 (1999)
- Costa, K.D., Holmes, J.W., McCulloch, A.D.: Modeling cardiac mechanical properties in three dimensions. *Phil. Trans. R. Soc. Lond. A* **359**, 1233–1250 (2001)
- Criscione, J.C., Lorenzen-Schmidt, I., Humphrey, J.D., Hunter, W.C.: Mechanical contribution of endocardium during finite extension and torsion experiments on papillary muscles. *Ann. Biomed. Eng.* **27**, 123–130 (1999)
- Demer, L.L., Yin, F.C.P.: Passive biaxial mechanical properties of isolated canine myocardium. *J. Physiol.* **339**, 615–630 (1983)
- Dokos, S., Smaill, B.H., Young, A.A., LeGrice, I.J.: Shear properties of passive ventricular myocardium. *Am. J. Physiol. Heart Circ. Physiol.* **283**, H2650–H2659 (2002)
- Fomovsky, G.M., Holmes, J.W.: Evolution of scar structure, mechanics, and ventricular function after myocardial infarction in the rat. *Am. J. Physiol. Heart Circ. Physiol.* **298**, H221–H228 (2010)
- Fomovsky, G.M., Thomopoulos, S., Holmes, J.W.: Contribution of extracellular matrix to the mechanical properties of the heart. *J. Mol. Cell Cardiol.* **48**, 490–496 (2010)
- Fomovsky, G.M., Macadangdang, J.R., Ailawadi, G., Holmes, J.W.: Model-based design of mechanical therapies for myocardial infarction. *J. Cardiovasc. Transl. Res.* **4**, 82–91 (2011)
- Fomovsky, G.M., Clark, S.A., Parker, K.M., Ailawadi, G., Holmes, J.W.: Anisotropic reinforcement of acute anteroapical infarcts improves pump function. *Circ. Heart Fail.* **5**, 515–522 (2012a)
- Fomovsky, G.M., Rouillard, A.D., Holmes, J.W.: Regional mechanics determine collagen fiber structure in healing myocardial infarcts. *J. Mol. Cell Cardiol.* **52**, 1083–1090 (2012b)
- Frangogiannis, N.G.: The inflammatory response in myocardial injury, repair, and remodelling. *Nat. Rev. Cardiol.* **11**, 255–265 (2014)
- Fujimoto, K.L., Tobita, K., Merryman, W.D., Guan, J., Momoi, N., Stoltz, D.B., Sacks, M.S., Keller, B.B., Wagner, W.R.: An elastic, biodegradable cardiac patch induces contractile smooth muscle and improves cardiac remodeling and function in subacute myocardial infarction. *J. Am. Coll. Cardiol.* **49**, 2292–2300 (2007)
- Guccione, J.M., McCulloch, A.D., Waldman, L.K.: Passive material properties of intact ventricular myocardium determined from a cylindrical model. *J. Biomech. Eng.* **113**, 42–55 (1991)
- Gupta, K.B., Ratcliffe, M.B., Fallert, M.A., Edmunds Jr., L.H., Bogen, D.K.: Changes in passive mechanical stiffness of myocardial tissue with aneurysm formation. *Circulation* **89**, 2315–2326 (1994)
- Herz, S.L., Ingrassia, C.M., Homma, S., Costa, K.D., Holmes, J.W.: Parameterization of left ventricular wall motion for detection of regional ischemia. *Ann. Biomed. Eng.* **33**, 912–919 (2005)
- Herz, S.L., Hasegawa, T., Makaryus, A.N., Parker, K.M., Homma, S., Wang, J., Holmes, J.W.: Quantitative three-dimensional wall motion analysis predicts ischemic region size and location. *Ann. Biomed. Eng.* **38**, 1367–1376 (2010)
- Ho, S.Y., Anderson, R.H., Sánchez-Quintana, D.: Atrial structure and fibres: morphologic bases of atrial conduction. *Cardiovasc. Res.* **54**, 325–336 (2002)
- Holmes, J.W., Covell, J.W.: Collagen fiber orientation in myocardial scar tissue. *Cardiovasc. Pathobiol.* **1**, 15–22 (1996)
- Holmes, J.W., Yamashita, H., Waldman, L.K., Covell, J.W.: Scar remodeling and transmural deformation after infarction in the pig. *Circulation* **90**, 411–420 (1994)
- Holmes, J.W., Nuñez, J.A., Covell, J.W.: Functional implications of myocardial scar structure. *Am. J. Physiol. Heart Circ. Physiol.* **272**, H2123–H2130 (1997)
- Holmes, J.W., Hünlich, M., Hasenfuss, G.: Energetics of the Frank–Starling effect in rabbit myocardium: economy and efficiency depend on muscle length. *Am. J. Physiol.* **283**, H324–H330 (2002)
- Holmes, J.W., Borg, T.K., Covell, J.W.: Structure and mechanics of healing myocardial infarcts. *Annu. Rev. Biomed. Eng.* **27**, 223–253 (2005)
- Holzapfel, G.A., Ogden, R.W.: Constitutive modelling of passive myocardium: a structurally based framework for material characterization. *Phil. Trans. R. Soc. Lond. A* **367**, 3445–3475 (2009)

- Humphrey, J.D., Strumpf, R.K., Yin, F.C.P.: Determination of a constitutive relation for passive myocardium: I. A new functional form. *J. Biomech. Eng.* **112**, 333–339 (1990a)
- Humphrey, J.D., Strumpf, R.K., Yin, F.C.P.: Determination of a constitutive relation for passive myocardium: II. Parameter estimation. *J. Biomech. Eng.* **112**, 340–346 (1990b)
- Humphrey, J.D., Barazotto, R.L., Hunter, W.C.: Finite extension and torsion of papillary muscles: a theoretical framework. *J. Biomech.* **25**, 541–547 (1992)
- Janz, R.F., Waldron, R.J.: Predicted effect of chronic apical aneurysms on the passive stiffness of the human left ventricle. *Circ. Res.* **42**, 255–263 (1978)
- Jin, F.-Y., Han, H.-C., Berger, J., Dai, Q., Lindsey, M.L.: Combining experimental and mathematical modeling to reveal mechanisms of macrophage-dependent left ventricular remodeling. *BMC Syst. Biol.* **5**, 60 (2011)
- Jugdutt, B.I., Amy, R.W.M.: Healing after myocardial infarction in the dog: changes in infarct hydroxyproline and topography. *J. Am. Coll. Cardiol.* **7**, 91–102 (1986)
- Kelsey, R., Botello, M., Millard, B., Zimmerman, J.: An online heart simulator for augmenting first-year medical and dental education. *Proc. AMIA Symp.* 370–374 (2002)
- Kerckhoffs, R.C.P., Neal, M.L., Gu, Q., Bassingthwaite, J.B., Omens, J.H., McCulloch, A.D.: Coupling of a 3D finite element model of cardiac ventricular mechanics to lumped systems models of the systemic and pulmonic circulation. *Ann. Biomed. Eng.* **35**, 1–18 (2007)
- Kidambi, A., Mather, A.N., Swoboda, P., Motwani, M., Fairbairn, T.A., Greenwood, J.P., Plein, S.: Relationship between myocardial edema and regional myocardial function after reperfused acute myocardial infarction: an MR imaging study. *Radiology* **267**, 701–708 (2013)
- Kramer, C.M., Rogers, W.J., Theobald, T.M., Power, T.P., Geskin, G., Reichek, N.: Dissociation between changes in intramyocardial function and left ventricular volumes in the eight weeks after first anterior myocardial infarction. *J. Am. Coll. Cardiol.* **30**, 1625–1632 (1997)
- Lee, J., Smith, N.P.: The multi-scale modelling of coronary blood flow. *Ann. Biomed. Eng.* **40**, 2399–2413 (2012)
- Lee, E.J., Holmes, J.W., Costa, K.D.: Remodeling of engineered tissue anisotropy in response to altered loading conditions. *Ann. Biomed. Eng.* **36**, 1322–1334 (2008)
- LeGrice, I.J., Smaill, B.H., Chai, L.Z., Edgar, S.G., Gavin, B., Hunter, P.J., Gavin, J.B.: Laminar structure of the heart: ventricular myocyte arrangement and connective tissue architecture in the dog. *Am. J. Physiol.* **269**, 571–582 (1995)
- LeGrice, I.J., Hunter, P.J., Young, A., Smaill, B.H.: The architecture of the heart: a data-based model. *Phil. Trans. R. Soc. Lond. A* **359**, 1217–1232 (2001)
- Lindsey, M.L., Zamilpa, R.: Temporal and spatial expression of matrix metalloproteinases and tissue inhibitors of metalloproteinases following myocardial infarction. *Cardiovasc. Ther.* **30**, 31–41 (2012)
- Maughan, W.L., Shoukas, A.A., Sagawa, K., Weisfeldt, M.L.: Instantaneous pressure-volume relationship of the canine right ventricle. *Circ. Res.* **44**, 309–15 (1979)
- Maurer, M.S., Sackner-Bernstein, J.D., El-Khoury Rumbarger, L., Yushak, M., King, D.L., Burkhoff, D.: Mechanisms underlying improvements in ejection fraction with carvedilol in heart failure. *Circ. Heart Fail.* **2**, 189–196 (2009)
- May-Newman, K., Omens, J.H., Pavlec, R.S., McCulloch, A.D.: Three-dimensional transmural mechanical interaction between the coronary vasculature and passive myocardium in the dog. *Circ. Res.* **74**, 1166–1178 (1994)
- Mazhari, R., McCulloch, A.D.: Integrative models for understanding the structural basis of regional mechanical dysfunction in ischemic myocardium. *Ann. Biomed. Eng.* **28**, 979–990 (2000)
- Mazhari, R., Omens, J.H., Covell, J.W., McCulloch, A.D.: Structural basis of regional dysfunction in acutely ischemic myocardium. *Cardiovasc. Res.* **47**, 284–293 (2000)
- McCallum, J.B.: On the muscular architecture and growth of the ventricles of the heart. *Johns Hopkins Hospital Reports.* **9**, 307–335 (1900)
- McCormick, R.J., Musch, T.I., Bergman, B.C., Thomas, D.P.: Regional differences in LV collagen accumulation and mature cross-linking after myocardial infarction in rats. *Am. J. Physiol.* **266**, H354–H359 (1994)

- McCulloch, A.D., Smaill, B.H., Hunter, P.J.: Left ventricular epicardial deformation in isolated arrested dog heart. *Am. J. Physiol.* **252**, H233–H241 (1987)
- McCulloch, A.D., Smaill, B.H., Hunter, P.J.: Regional left ventricular epicardial deformation in the passive dog heart. *Circ. Res.* **64**, 721–733 (1989)
- Morita, M., Eckert, C.E., Matsuzaki, K., Noma, M., Ryan, L.P., Burdick, J.A., Jackson, B.M., Gorman, J.H., Sacks, M.S., Gorman, R.C.: Modification of infarct material properties limits adverse ventricular remodeling. *Ann. Thorac Surg.* **92**, 617–624 (2011)
- Moyer, C.B., Norton, P.T., Ferguson, J.D., Holmes, J.W.: Changes in global and regional mechanics due to atrial fibrillation: insights from a coupled finite-element and circulation model. *Ann. Biomed. Eng.* **43**, 1600–1613 (2015)
- Nash, M.P., Hunter, P.J.: Computational mechanics of the heart. *J. Elasticity* **61**, 113–141 (2001)
- Novak, V.P., Yin, F.C.P., Humphrey, J.D.: Regional mechanical properties of passive myocardium. *J. Biomech. Eng.* **27**, 403–412 (1994)
- Omens, J.H., Miller, T.R., Covell, J.W.: Relationship between passive tissue strain and collagen uncoiling during healing of infarcted myocardium. *Cardiovasc. Res.* **33**, 351–358 (1997)
- Richardson, W.J., Clark, S.A., Holmes, J.W.: Physiological implications of myocardial scar structure. *Compr. Physiol.* **5**, 1877–1909 (2015)
- Rivlin, R.S., Saunders, D.W.: Large elastic deformations of isotropic materials. VII. Experiments on the deformation of rubber. *Phil. Trans. R. Soc. Lond. A* **243**, 251–288 (1951)
- Rouillard, A.D., Holmes, J.W.: Mechanical regulation of fibroblast migration and collagen remodelling in healing myocardial infarcts. *J. Physiol.* **590**, 4585–4602 (2012)
- Rushmer, R.F., Crystal, D.K., Wagner, C.: The functional anatomy of ventricular contraction. *Circ. Res.* **1**, 162–170 (1953)
- Sagawa, K., Maughan, L., Suga, H., Sunagawa, K.: Cardiac contraction and the pressure-volume relationship. Oxford University Press, New York (1988)
- Santamore, W.P., Burkhoff, D.: Hemodynamic consequences of ventricular interaction as assessed by model analysis. *Am. J. Physiol.* **260**, H146–57 (1991)
- Schmid, H., Nash, M.P., Young, A.A., Hunter, P.J.: Myocardial material parameter estimation - a comparative study for simple shear. *J. Biomech. Eng.* **128**, 742–750 (2006)
- Schmid, H., O'Callaghan, P., Nash, M.P., Lin, W., LeGrice, I.J., Smaill, B.H., Young, A.A., Hunter, P.J.: Myocardial material parameter estimation: a non-homogeneous finite element study from simple shear tests. *Biomech. Model. Mechanobiol.* **7**, 161–173 (2008)
- Sommer, G., Haspinger, D.C., Andrä, M., Sacherer, M., Viertler, C., Reginig, P., Holzapfel, G.A.: Quantification of shear deformations and corresponding stresses in the biaxially tested human myocardium. *Ann. Biomed. Eng.* **43**, 2334–2348 (2015)
- Streeter, D.D.: Gross morphology and fiber geometry of the heart. In: Berne, R.M. (ed.) *Handbook of physiology: the cardiovascular system*, pp. 61–112. Williams & Wilkins, Baltimore (1979)
- Streeter, D.D., Hanna, W.T.: Engineering mechanics for successive states in canine left ventricular myocardium. I. Cavity and wall geometry. *Circ. Res.* **33**, 639–655 (1973a)
- Streeter, D.D., Hanna, W.T.: Engineering mechanics for successive states in canine left ventricular myocardium. II. Fiber angle and sarcomere length. *Circ. Res.* **33**, 656–664 (1973b)
- Suga, H., Sagawa, K.: Instantaneous pressure-volume relationships and their ratio in the excised, supported canine left ventricle. *Circ. Res.* **35**, 117–126 (1974)
- Suga, H., Sagawa, K., Shoukas, A.A.: Load independence of the instantaneous pressure-volume ratio of the canine left ventricle and effects of epinephrine and heart rate on the ratio. *Circ. Res.* **32**, 314–322 (1973)
- Sunagawa, K., Maughan, W.L., Sagawa, K.: Effect of regional ischemia on the left ventricular end-systolic pressure-volume relationship of isolated canine hearts. *Circ. Res.* **52**, 170–178 (1983)
- Tenant, R., Wiggers, C.J.: The effect of coronary occlusion on myocardial contraction. *Am. J. Physiol.* **112**, 351–361 (1935)
- Theroux, P., Ross, J., Franklin, D., Covell, J.W., Bloor, C.M., Sasayama, S.: Regional myocardial function and dimensions early and late after myocardial infarction in the unanesthetized dog. *Circ. Res.* **40**, 158–165 (1977)

- Torrent-Guasp, F.: On morphology and cardiac function. 4th communication. Rev. Española Cardiol. **20**, 2–13 (1967)
- Tyberg, J.V., Forrester, J.S., Wyatt, H.L., Goldner, S.J., Parmley, W.W., Swan, H.J.: An analysis of segmental ischemic dysfunction utilizing the pressure-length loop. Circulation **49**, 748–754 (1974)
- Usyk, T., Mazhari, R., McCulloch, A.D.: Effect of laminar orthotropic myofiber architecture on regional stress and strain in the canine left ventricle. J. Elasticity **61**, 143–164 (2000)
- Villareal, F.J., Lew, W.Y., Waldman, L.K., Covell, J.W.: Transmural myocardial deformation in the ischemic canine left ventricle. Circ. Res. **68**, 368–381 (1991)
- Vivaldi, M.T., Eyre, D.R., Kloner, R.A., Schoen, F.J.: Effects of methylprednisolone on collagen biosynthesis in healing acute myocardial infarction. Am. J. Cardiol. **60**, 424–425 (1987)
- Walker, J.C., Ratcliffe, M.B., Zhang, P., Wallace, A.W., Fata, B., Hsu, E.W., Saloner, D., Guccione, J.M.: MRI-based finite-element analysis of left ventricular aneurysm. Am. J. Physiol. Heart Circ. Physiol. **289**, H692–H700 (2005)
- Wall, S.T., Walker, J.C., Healy, K.E., Ratcliffe, M.B., Guccione, J.M.: Theoretical impact of the injection of material into the myocardium: a finite element model simulation. Circulation **114**, 2627–2635 (2006)
- Wall, S.T., Guccione, J.M., Ratcliffe, M.B., Sundnes, J.S.: Electromechanical feedback with reduced cellular connectivity alters electrical activity in an infarct injured left ventricle: a finite element model study. Am. J. Physiol. Heart Circ. Physiol. **302**, H206–H214 (2012)
- West, J.B.: Best and Taylor's physiological basis of medical practice, 11th edn. Williams and Wilkins, Baltimore (1985)
- Westerhof, N., Bosman, F., De Vries, C.J., Noordergraaf, A.: Analog studies of the human systemic arterial tree. J. Biomech. **2**, 121–143 (1969)
- White, H.D., Chew, D.P.: Acute myocardial infarction. Lancet **372**, 570–584 (2008)
- Whittaker, P., Boughner, D.R., Kloner, R.A.: Analysis of healing after myocardial infarction using polarized light microscopy. Am. J. Pathol. **134**, 879–893 (1989)
- Yin, F.C.P., Strumpf, R.K., Chew, P.H., Zeger, S.L.: Quantification of the mechanical properties of noncontracting canine myocardium under simultaneous biaxial loading. J. Biomech. **20**, 577–589 (1987)
- Zhao, J., Butters, T.D., Zhang, H., Pullan, A.J., LeGrice, I.J., Sands, G.B., Smaill, B.H.: An image-based model of atrial muscular architecture: effects of structural anisotropy on electrical activation. Circ. Arrhythm. Electrophysiol. **5**, 361–370 (2012)
- Zimmerman, S.D., Thomas, D.P., Velleman, S.G., Li, X., Hansen, T.R., McCormick, R.J.: Time course of collagen and decorin changes in rat cardiac and skeletal muscle post-MI. Am. J. Physiol. Heart Circ. Physiol. **281**, H1816–H1822 (2001)

Fiber-Network Modeling in Biomechanics: Theoretical and Analytical Approaches

Rohit Y. Dhume and Victor H. Barocas

Abstract Network problems arise in all aspects of bioengineering, including biomechanics. For decades, the mechanical importance of highly interconnected networks of macromolecular fibers, especially collagen fibers, has been recognized, but models at any scale that explicitly incorporate fiber-fiber interactions into a mechanical description of the tissue have only started to emerge more recently. The purpose of this chapter is to provide the reader with the basic tools to develop next-generation, fiber-based models of tissue mechanics, a goal that is pursued in three steps. First, we provide a brief introduction to the mathematical language for describing networks in general. Second, existing single-scale mechanical network models are reviewed, including a short discussion of how the different models differ in approach based on the biophysics of their specific problems. Third, and finally, we describe a multiscale approach in which individual network problems at the small scale are coupled to a macroscopic finite element scheme. This approach is general and can be applied with any microstructural model but has significant computational demands, so it should be used only when the value of the scale coupling is great.

1 Introductory Remarks

Networks of all sorts are ubiquitous in nature (Fig. 1). Macromolecular networks such as the actin of the cytoskeleton form the basis for the cells shape and ability to deform the tissue around it. Fiber networks of collagen and elastin are critical to the maintenance of tissue integrity and elasticity. Beyond mechanical networks, systems biology has recognized the essential role of complex metabolic networks in determining cell behavior, neural networks produce complex functions through

R.Y. Dhume · V.H. Barocas (✉)
University of Minnesota, Twin Cities, Minnesota, MN, USA
e-mail: baroc001@umn.edu

R.Y. Dhume
e-mail: dhume001@umn.edu

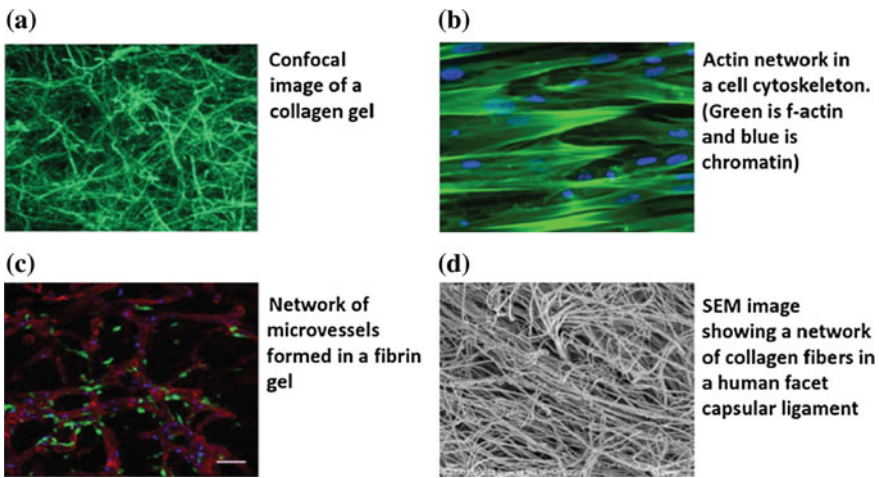


Fig. 1 Examples of networks in nature. Image **a** courtesy V. Lai; for more information, see Lai et al. (2012), Image **b** courtesy P. Alford; for more information, see Win et al. (2014), Image **c** courtesy R. Tranquillo; for more information, see Morin et al. (2013). **a** Confocal image of a collagen gel. **b** Actin network in a cell cytoskeleton. (Green is f-actin and blue is chromatin). **c** Network of microvessels formed in a fibrin gel. **d** SEM image showing a network of collagen fibers in a human facet capsular ligament

the interactions of relatively simple components, and vascular/capillary networks distribute blood and oxygen throughout the body.

In light of the importance of bionetworks, our purpose in this document is three-fold. First, we will present a brief description of the mathematical tools necessary to describe networks in the abstract, as well as some common features of fiber networks. Second, we will present a review of recent work using network-based models to explore the mechanics of biological materials; this review will describe a wide range of networks and tissues, focusing primarily on the techniques and network features rather than attempting to describe the biological ramifications in full detail. Finally, we will present a multiscale approach that can be used to describe a macroscopic tissue in terms of the microstructure and microstructural response at specific points.

The sections are organized to represent a hierarchy of demands if one is to develop accurate network-based computational models of the mechanical behavior of large tissues. For any model to succeed, it is obviously necessary that one have a mathematical statement of the physical problem at hand. One must, e.g., define a node and a connection within the network and specify how they behave and interact. These definitions, with our understanding of how to extract information from the mathematical structures so formed, are the emphasis area for the first section. Subsequently, we review how the network approach has been used. Many investigators have developed network-based models of various forms and to describe various tissues. Having established the methodology of the first section, we will discuss in

the second section how different models were created and how they behave. The third and final section addresses a critical issue in the use of such models: how can we model a large piece of tissue, which may contain millions of fibers, varying in composition, density, diameter, and orientation as a function of position within the tissue, in a way that is computationally tractable and still realistic? To put the issue another way, one must be able to communicate information between the large and small scales efficiently and consistently. We will present a method we use, based on volume averaging concepts previously used in other disciplines, to couple the two scales.

2 Mathematical Fundamentals

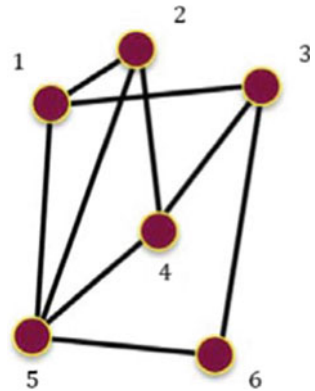
In the next section, we discuss some basic mathematical concepts related to networks. For further detail, the reader is referred to the excellent review by Boccaletti et al. (2006).

2.1 Terminology and Basic Concepts

A network consists of two fundamental entities. *Nodes* are points, possibly but not necessarily in a physically realizable space, that are connected to each other by *links*. Both nodes and links may have properties that are independent of the network topology but may be important in other contexts. For example, the surface chemistry of a fiber might be very important in some interaction of a fiber network with a cell entrapped in it, but the fiber network's topology does not depend on fiber chemistry. At its most basic level, the network is defined by which nodes are connected by which links, and by which links are connected to which nodes. A simple example is given in Fig. 2. The network contains six nodes and nine links. The nodes have been numbered 1–6. The links could also be numbered, but that is not necessary for most of this chapter, so for the time being, we will leave them unnumbered and will refer to them simply as L_{ij} for the link from node i to node j .

We can make certain observations about this network. First, we observe that the graph is *undirected*, meaning that a link from node i to node j is also a link from node j to node i . Directedness is a property of some networks but not others, depending on what they represent. In a neural network, e.g., it is possible that neuron i stimulates neuron j , but neuron j does not stimulate neuron i . Likewise, in a metabolic network, it is possible that enzyme i synthesizes (or degrades) enzyme j , but enzyme j does not affect enzyme i . In these cases, the directed network could be represented by arrows showing which way the links act. For mechanical networks, however, the effect of a link is normally symmetric. That is, if displacing node i leads to a force on node j (by stretching the connection between them), then displacing node j leads to a force on node i as well. Thus, it is common to use undirected graphs, such as that in Fig. 2, to model mechanical networks.

Fig. 2 An example of a simple network



We next observe that although each link in the network connects exactly two nodes, each node in the network can have any number of links attached to it. The number of connections for a given node is that node's *degree* or *nodal degree*. In Fig. 2, nodes 1–4 are all of degree three, node 5 is of degree four, and node 6 is of degree two.

The *adjacency matrix* of the network is a compact representation of all of the connections. For an unweighted, undirected network such as in Fig. 2, the adjacency matrix is constructed by setting

$$A_{ij} = A_{ji} = \begin{cases} 0, & i = j \\ 1, & i \neq j \text{ and nodes } i \text{ and } j \text{ are connected} \\ 0, & i \neq j \text{ and nodes } i \text{ and } j \text{ are not connected.} \end{cases} \quad (1)$$

Since the links are undirected, the matrix $[A]$ must be symmetric by construction (that is, if i connects to j , then j connects to i). If one is interested in using the adjacency matrix to understand the topology of the network, then it is most convenient to set all of the diagonal elements to zero (that is, a node is not connected to itself).

The adjacency matrix has trace zero, so its eigenvalues must sum to zero, and the spectral properties of the adjacency matrix have been used in a variety of ways to characterize network topology in biological contexts (Larremore et al. 2012; Speck-Planche et al. 2012; Hwang et al. 2014). For the network in Fig. 2, the adjacency matrix $[A]$ is

$$[A] = \begin{bmatrix} 0 & 1 & 1 & 0 & 1 & 0 \\ 1 & 0 & 0 & 1 & 1 & 0 \\ 1 & 0 & 0 & 1 & 0 & 1 \\ 0 & 1 & 1 & 0 & 1 & 0 \\ 1 & 1 & 0 & 1 & 0 & 1 \\ 0 & 0 & 1 & 0 & 1 & 0 \end{bmatrix}. \quad (2)$$

When one is interested in interactions among the nodes and/or in some quantity transported via the links, then it is often more convenient to consider the so-called Laplacian matrix [L] rather than the adjacency matrix. The Laplacian matrix is defined by

$$L_{ij} = L_{ji} = \begin{cases} n_i & i = j \\ -1 & i \neq j \text{ and nodes } i \text{ and } j \text{ are connected,} \\ 0 & i \neq j \text{ and nodes } i \text{ and } j \text{ are not connected,} \end{cases} \quad (3)$$

where n_i is the degree of node i . The Laplacian matrix, also called the Kirchhoff matrix, is attractive in that it measures not only connectivity but also transport, thus providing a representation similar to what one would derive from a network of resistors (following Kirchhoff's laws) or a heat- or mass-transport problem in which conservation laws apply to nodes and transport is via links (i.e., a discrete analogue of the Laplacian operator). For the network of Fig. 2, the Laplacian matrix [L] is

$$[L] = \begin{bmatrix} 3 & -1 & -1 & 0 & -1 & 0 \\ -1 & 3 & 0 & -1 & -1 & 0 \\ -1 & 0 & 3 & -1 & 0 & -1 \\ 0 & -1 & -1 & 3 & -1 & 0 \\ -1 & -1 & 0 & -1 & 4 & -1 \\ 0 & 0 & -1 & 0 & -1 & 2 \end{bmatrix}. \quad (4)$$

2.1.1 Eigenvalues of the Laplacian Matrix

It is readily seen that the matrix [L] is singular because each of its rows sums to zero, a necessary result since there are n_i links coming out of node i , so there will be n_i elements of value -1 in a row. Thus, [L] always has an eigenvalue 0 corresponding to the eigenvector of all 1's. If we think about this in light of the transport analogy, the significance of this eigenvalue becomes clear: if all of the nodes have the same (concentration, temperature, voltage), then there is no (diffusion, heat flow, current) along any links, and the result is that the system does not change.

Our understanding of the Laplacian matrix's meaning is enhanced by recognizing that in a system that has equal weight connections among nodes, the temporal evolution of some nodal quantity (concentration, etc.) is given by

$$\frac{\partial c_i}{\partial t} = - \sum_{j=1}^N L_{ij} c_j, \quad (5)$$

where c_i is the concentration of interest at node i . In this problem, the eigenvalues of [L] represent (inverse) time scales over which the system relaxes from a perturbation, and the corresponding eigenvectors represent perturbations that relax at

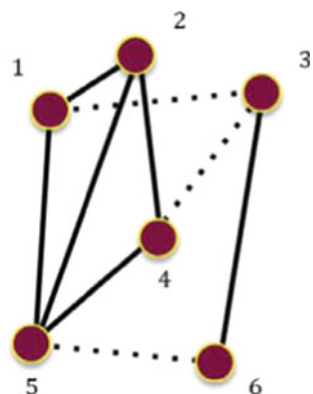
different rates. The uniform perturbation (i.e., all concentrations increased by the same amount) relaxes with rate zero because the shifted concentration is neutrally stable. The largest eigenvalue of $[L]$ represents the fastest-relaxing mode. In Fig. 2, above, e.g., the largest eigenvalue of $[L]$ is 5.68, corresponding to the eigenvector $[-0.42, 0.08, 0.42, -0.42, 0.62, -0.28]^T$. Notice that the values at nodes 3 and 5 are positive, and those at nodes 1, 4, and 6 are negative, creating large differences (and thus high transport rates) along the links connecting nodes 3 or 5 to 1, 4, or 6. Node 2, which connects to both positive and negative valued nodes, is assigned a value near zero.

It is also possible for $[L]$ to have more than one eigenvector corresponding to a zero eigenvalue. To put it another way, the nullity of $[L]$, that is the dimension of the null space of $[L]$, may be greater than one. What does that mean? The question is answered best by considering the consequences of a second eigenvector in the null space of $[L]$ in terms of the conductivity or flow problem. The second eigenvector means that there is another nontrivial solution to $[L][x] = [0]$ beyond the uniform solution mentioned in the previous paragraph. If we think in terms of conductivity, we know that if one node has a higher voltage (temperature, pressure) than another to which it is connected, there must be flow between them. Thus, the only way that the second eigenvector could exist would be if the network was not completely connected. For example, if the three dotted connections in Fig. 3 were removed, $[L]$ would become

$$[L] = \begin{bmatrix} 2 & -1 & 0 & 0 & -1 & 0 \\ -1 & 3 & 0 & -1 & -1 & 0 \\ 0 & 0 & 1 & 0 & 0 & -1 \\ 0 & -1 & 0 & 2 & -1 & 0 \\ -1 & -1 & 0 & -1 & 3 & 0 \\ 0 & 0 & -1 & 0 & 0 & 1 \end{bmatrix}, \quad (6)$$

which still has a zero eigenvalue with eigenvector all ones, $[1, 1, 1, 1, 1, 1]^T$, but also has a second eigenvector, $[0, 0, 1, 0, 0, 1]^T$, with eigenvalue zero (note that

Fig. 3 Example network with three links removed



$[1, 1, 0, 1, 1, 0]^T$ is also an eigenvector since it is a linear combination of the other two). This result arises because the cluster 1-2-4-5 and the cluster 3-6 are not connected to each other. The nullity of $[L]$ is thus the number of unconnected clusters in the network. Although most mechanical network problems involve a single network with all nodes connected, it is important to be aware of the possibility of the network becoming disconnected, particularly if damage or digestion is to be considered.

2.1.2 Weighted Laplacian Matrix

All of the above analysis was for unweighted networks, but it is easily extended to weighted networks by replacing the 1's in $[A]$ and the -1 's in $[L]$ with the weight of the connection, and by redefining n_i to be the sum of the weights of all of the links coming out of node i rather than just the number of links. That is

$$w_{ij} = \begin{cases} 0 & \text{nodes } i \text{ and } j \text{ are not connected} \\ \omega & \text{nodes } i \text{ and } j \text{ are connected by a link of weight } \omega, \end{cases} \quad (7)$$

$$n_i = \sum_{j=1}^N w_{ij}, \quad (8)$$

$$L_{ij} = L_{ji} = \begin{cases} n_i & i = j \\ -w_{ij} & i \neq j. \end{cases} \quad (9)$$

In the context of a transport problem, the weights of $[L]$ represent different conductivities between nodes. That is, the weighted graph has some connections that are stronger than the others. All of the previous analysis applies to weighted as well as to unweighted graphs.

Suppose, e.g., that we make the dotted connections in Fig. 3 of lower weight. This modified network would correspond to thinner vessels in a fluid transport network or to greater resistance in an electrical network. Taking the solid lines to be of weight 3, e.g., and the dotted lines to be of weight 1, we get

$$[L] = \begin{bmatrix} 7 & -3 & -1 & 0 & -3 & 0 \\ -3 & 9 & 0 & -3 & -3 & 0 \\ -1 & 0 & 5 & -1 & 0 & -3 \\ 0 & -3 & -1 & 7 & -3 & 0 \\ -3 & -3 & 0 & -3 & 10 & -1 \\ 0 & 0 & -3 & 0 & -1 & 4 \end{bmatrix}, \quad (10)$$

and the eigenvector of the new Laplacian with the largest eigenvalue is $[0.42, -0.04, -0.15, 0.42, -0.78, 0.13]^T$. Note that nodes 3 and 6, which are now less well connected to the rest of the network, have smaller terms in the eigenvector.

2.1.3 Aside: Network Partitioning

Although the primary emphasis in the chapter is on mechanical network models, we divert our attention briefly to the problem of network partitioning. Often, one has a single network, and one would like to subdivide that network into two or more distinct smaller networks in some natural and automatic way. Such problems arise, e.g., in the segmentation of images (e.g., Kamenskiy et al. 2012), the identification of metabolic pathways (e.g., Hao et al. 2012), or the definition of social groups (e.g., Naug 2008; Molloy et al. 2014; Feng and Bhanu 2015). Two simple algorithms are described here, the first because of its natural connection to the previous section, and the second because we have used it in a mechanical context previously.

The random walker approach involves a series of steps. First, the user manually identifies seed points within different regions of the image/network. That is, one identifies specific nodes as being in distinct subnetworks from each other. The method was developed for image segmentation (Grady 2006), so this step would involve the user selecting some points from the image in, say, the heart, and others in the lungs. Next, the algorithm solves the linear problem of steady conduction through a resistor network weighted according to the network's Laplacian matrix, with stronger connections being represented by lower resistances (i.e., greater conductances). The problem is solved with all of the seed node values set to zero except for one, which is set to unity. That is, the following problem is solved once for each seed node,

$$x_i = 1 \quad \text{node } i \text{ is the target seed node,} \quad (11)$$

$$x_i = 0 \quad \text{node } i \text{ is a non target seed node,} \quad (12)$$

$$L_{ij}x_j = 0 \quad \text{node } i \text{ is not a seed node.} \quad (13)$$

Finally, each non-seed node j is assigned to the segment containing the seed node that yielded the largest x_j value. This approach is simple, fast, and robust to noise, but it requires manual identification of the subnetworks and may require that the user select multiple seed points in each region to achieve proper segmentation.

A very popular alternative approach is based on the concept of *betweenness*. The betweenness of a link in the network is defined as the number of shortest paths between any two network nodes that include the link in question. Thus, to calculate the betweenness, one constructs the shortest path between every pair of nodes and counts how many times each link lies on the path, with fractional occurrences being counted when multiple shortest paths exist between the same pair of nodes. If we consider the unweighted network of Fig. 2, e.g., there are two shortest paths (both of length 2) between nodes 3 and 5, so each of them would be counted as half of a path. Newman (2001, 2004) developed an algorithm in which the connection of maximum betweenness is removed, after which the process is repeated until the network has been divided into subnetworks. The method can be applied to weighted networks by appropriate weighting of the calculated betweenness values (Newman 2004). Although this approach is much slower, it is extremely robust and does not require a priori specification of seed points. We have applied this approach to segmenting

images based on the deformation gradient jump between finite elements (Witzenburg et al. 2015) as a prelude to solving complicated inverse mechanics problems.

2.2 The Mechanical Problem

We now have in hand the essential machinery to analyze a network problem, and we turn to mechanics, specifically to the network that would be known as a truss in most engineering concepts: a collection of units (henceforth called ‘fibers’ in this text but potentially referring to any long, thin piece of connecting material) that can support tensile or compressive loads, joined at nodes that allow free rotation. Thus, the force balance at node k is

$$\sum_{j=1}^{n(k)} f_i^{(j)} = 0, \quad (14)$$

where $n(k)$ is the degree of node k , j is a summation variable, $f^{(j)}$ is the tension in fiber j coming off from node k , and i is the coordinate index (i can go from 1 to 2 in 2-D or from 1 to 3 in 3-D). If one assumes an elastic network, the force on a fiber depends only on its stretch ratio, so we can replace the above expression with

$$\sum_{j=1}^{n(k)} \left(\frac{x_i^j - x_i^k}{|x_i^j - x_i^k|} \right) f \left(\frac{|x_i^j - x_i^k|}{l_{jk}} \right) = 0. \quad (15)$$

The first term is the unit vector pointing from node k to node j . It gives the direction of the force due to stretch in the connection between nodes k and j . The second term is the scalar force, which depends on the distance from node k to node j , divided by the rest length l_{jk} of the fiber connecting the two nodes.

Three immediate observations must be made. First, the solution to the problem is trivially that all of the fibers are at their rest length and there is no tension anywhere in the network. This result is, of course, uninteresting, but it is the solution to the problem as described. The reason that it is not the correct solution is that boundary conditions must be imposed also. For example, one might specify that certain nodes in the network are fixed and that others must move (e.g., to stretch or shear the network), or one might specify that some are fixed and others are subject to some external load. Regardless, something must be done to force the system away from the trivial equilibrium.

Second, and perhaps most importantly, we observe that because position, displacement, and force are vector, not scalar, quantities, the mechanical network has two (in 2-D) or three (in 3-D) pieces of information associated with each node, not just one. As a result, even a very simple network such as that of Fig. 4a becomes the considerably more complicated Fig. 4b when one treats each component as a scalar. Thus, the adjacency and Laplacian matrices for this system, if one thinks in terms of

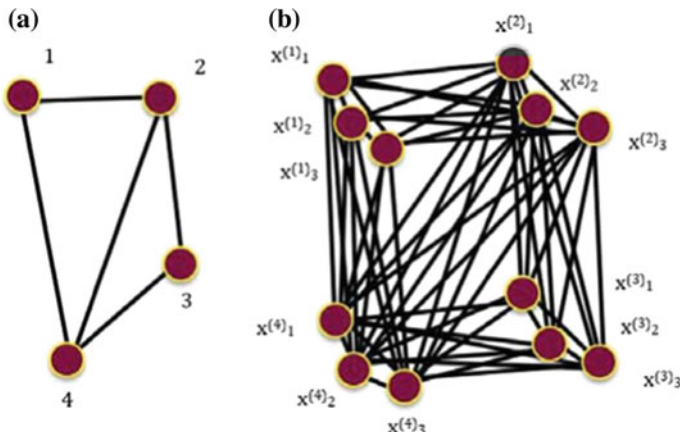


Fig. 4 Even a simple 2-D network (a) can become complicated in 3-D (b)

scalar quantities at each node, will be 12×12 , not 4×4 . Of course, the adjacency of all three components is the same at a given node, so the 4×4 adjacency matrix contains all of the information, but the weightings are not the same for all connections at the same node, as we will explore in the next section.

Third, even if the force function is linear, the system is *kinematically nonlinear* because of the fact that movement of the nodes causes both tension in the fibers and a change in the direction of the forces acting on the nodes (because the fiber direction changes). Thus, even the simplest network problems are nonlinear and can prove quite challenging computationally.

2.2.1 The Maxwell Limit

Because of the importance of mechanical structures in bearing loads, trusses (i.e., connections of beams with free rotation at intersections) and frames (no rotation at intersections) have been studied for over a century. The landmark analysis of Maxwell (1864) argued that a truss with N nodes and C rigid connections has $3N$ degrees of freedom (X , Y , and Z position of each node) and C constraints (one translational direction restricted by each connection). For the truss to be stable, it must have only six degrees of freedom, representing the three translations and the three rotations of the frame as a rigid body. Thus, Maxwell concluded that for a truss to be stable, it must satisfy $C \geq 3N - 6$; by similar arguments, a two-dimensional network must satisfy $C \geq 2N - 3$. For large networks, N and C are both much greater than 6, and we may use $C > 3N$ as a global stability limit (or $C > 2N$ for a two-dimensional network). Since each connection adds to the degree of two different nodes, this limit is equivalent to requiring that the average nodal degree n be greater than 6 for a three-dimensional network and be greater than 4 for a two-dimensional network. In

biological systems, there may well exist networks with lower degrees of connectivity; such a network has zero stiffness in its rest state but can achieve finite stiffness as its fibers become aligned in the direction of the pull, producing a large toe region in the stress-strain curve even if the individual fibers are linear in their mechanical response (Stylianopoulos and Barocas 2007a).

2.2.2 Non-affinity of Fiber Networks Under Load

The final topic for this section is that of affinity versus nonaffinity (Fig. 5). We begin with a definition of affinity. Suppose that a fibrous material undergoes a macroscopic deformation defined by the deformation gradient F_{ij} . Further suppose that each individual fiber is characterized by a vector v_i that defines its length and direction. Then, if for every fiber in the network, the initial fiber vector v_i^0 and the final fiber vector v_i^1 are related by $v_i^1 = F_{ij}v_j^0$, then we say that the fibers are deforming affinely with respect to the macroscopic deformation, or that the system is affine. We may state that requirement in an alternative manner by requiring that the same deformation gradient F_{ij} applies at the microscopic as well as the macroscopic scale.

The affine assumption is an extremely powerful assumption because *it eliminates the need to consider microscale interactions*. Since every fiber's deformation is defined perfectly by the macroscopic deformation gradient F_{ij} , each fiber can be evaluated independently, and the total stress (or strain energy) at a point can be determined from the sum of independent fiber contributions. This assumption was made by Lanir (1983), who argued that it is 'intuitively justified by the multiplicity of interconnections (attachments) between the different fibers.' Modern tissue mechanics theory, which owes much to Lanir (1983), thus often involves the affine assumption, as can be seen in many of the other chapters of this volume and throughout the field (see, e.g., Martufi and Gasser 2013; Amini et al. 2014; Fata et al. 2014). The affine assumption is, of course, a considerable simplification. We have found, e.g., that in simple two-dimensional networks (Chandran and Barocas 2006), the average rotation of the fibers is predicted very well by an affine model, but the fiber stretch

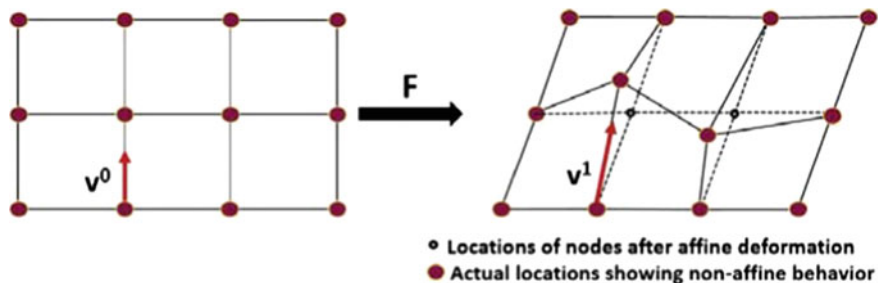


Fig. 5 Example of nonaffine deformation in a network. The vector shown does not satisfy $v_i^1 = F_{ij}v_j^0$

is overpredicted by a considerable amount, and some fibers may be in compression (or may buckle) even though the network as a whole is in tension. Nevertheless, for tissue-level studies, the affine model is often convenient, and the simplification it introduces may be deemed acceptable in exchange for much more solution of the problem.

In the subsequent sections, we provide a brief review of network-explicit modeling approaches to biomechanical problems, meaning those problems in which the individual fibers/fibrils/filaments are modeled, and the affine assumption is not imposed on individual fibers. These models, which focus on the small scale, provide a view of the range of problems that can be done using a network-based approach. After that review, we will present a theoretical framework for coupling a network-explicit, nonaffine microscale model with a larger scale continuum model.

3 Single-Scale Fiber Models in Biomechanics

In this section, we look at different network modeling approaches that have been utilized to model tissues over the past few decades. We start out with a brief review of some of the well known and still widely used affine models. Then, we proceed on to discuss a few nonaffine network models beginning with ones that use homogeneous, hyperelastic networks, followed by a section discussing evolving network models (e.g., viscoelastic networks).

3.1 Affine Models

In the latter half of the twentieth century, several constitutive models were proposed to predict and understand the behavior of various biological tissues. Many of these models borrowed the idea behind their construction from polymer science. These models were passive and assumed the tissue to deform in an affine manner. They did not model the various network components and their interactions individually as some of the more recent models (discussed later in this section) have done. These constitutive models have played a major role in our understanding and modeling of biological tissue over the last few decades, so we begin our network review with a brief discussion of a few of the more well known and still widely used continuum models.

3.1.1 Fung et al. (1979)

This constitutive equation was developed by Fung et al. (1979) to model the mechanics of arteries and to match their nonlinear stress-strain curve obtained from experimental testing. The strain energy as proposed by Fung et al. (1979) is given by

$$W = \frac{C}{2} \exp(a_1 E_{\theta\theta}^2 + a_2 E_{zz}^2 + 2a_4 E_{\theta\theta} E_{zz}), \quad (16)$$

where $E_{\theta\theta}$ and E_{zz} are components of the Green–Lagrange strain tensor, C is a material constant with units of stress, and a_1 , a_2 , and a_4 are nondimensional material constants. Fung et al. (1979) ignored the radial stress in comparison to stress in the other two directions, and the tissue was assumed to be incompressible (i.e., $E_{rr} = f(E_{\theta\theta}, E_{zz})$). There have been several modifications and generalizations to this model (Kas'yanov and Rachev 1980; Deng et al. 1994; Humphrey 1995; Ateshian and Costa 2009).

Although the model of Fung et al. (1979) was a major advance and was perhaps the first tissue constitutive model to account for anisotropy (i.e., $a_1 \neq a_2$) and cross-directional coupling (via a_4), theoretical and practical challenges, especially in 3-D, have made it less popular today than fiber-based models except in limited cases.

3.1.2 Holzapfel et al. (2000)

Holzapfel et al. (2000) assumed the tissue to be a composite reinforced by fiber families oriented in different directions. The strain energy was split into two parts, the contribution from the nonfibrous, isotropic matrix (e.g., neo-Hookean) and that from the fiber families. A general form of this equation is given as

$$W = W_{\text{iso}} + W_{\text{aniso}}, \quad (17)$$

$$W_{\text{aniso}} = \sum_{i=1}^n \frac{k_1^{(i)}}{2k_2^{(i)}} \{\exp[k_2^{(i)}(\mathbf{a}_i \cdot \mathbf{Ca}_i - 1)^2 - 1]\}. \quad (18)$$

Here, n is the number of fiber families, $k_1^{(i)}$ and $k_2^{(i)}$ are material parameters for the i th family, \mathbf{C} is the right Cauchy–Green tensor and \mathbf{a}_i is the direction vector of the i th family. The term $\mathbf{a}_i \cdot \mathbf{Ca}_i$ represents the square of the stretch experienced along the direction of the fibers. Future modifications to this model included parameters to consider the amount of fibers present and their distribution around a primary orientation direction (e.g., Driessens et al. 2005).

The constitutive equations described above were developed to fit experimental data (mainly in the physiological range) and thus one must exercise caution when applying these models to deformations lying outside of the experimental range of data. The strain energy also depends strongly on the fitting parameters, and for models with multiple free parameters, these values might not be unique. One must also properly constrain the possible values of the free parameters while fitting the data else it can result in the energy being undefined (e.g., the model of Takamizawa and Hayashi 1987) or in the strain-energy function being non-convex.

The form of Eqs. (17) and (18), and similar forms such as the four-fiber-family model of Baek et al. (2007) and the fiber orientation-based models of Sacks (2003) and others (Annaidh et al. 2012; Avril et al. 2013; Nagel et al. 2014; Trajkovski

et al. 2014), have proven extremely successful. They have been implemented in finite element codes such as Abaqus (Hibbit et al. 2007) and FEBio (Maas et al. 2012), making them available to the general user, another significant advantage. In general, methods of this type are the models of choice for fitting experimental data and constructing finite element models of the tissue. The advantages of simple structure, easy use, and rapid computation often outweigh the loss of ability to capture microstructural interactions or nonaffine behavior.

3.1.3 Arruda and Boyce (1993)

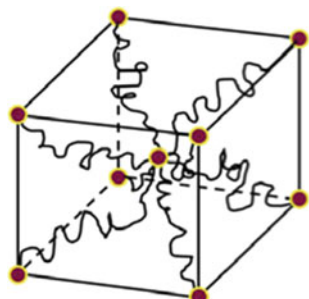
This constitutive model, developed by Arruda and Boyce (1993), uses a statistical mechanics approach to model polymer materials. It was based upon the already existing three-chain and four-chain models for rubber and rubber-like materials (Flory and Rehner 1943; Treloar 1946; Wang and Guth 1952). The earlier models predicted the behavior of rubber rather well but did not capture the large-strain behavior shown by other amorphous polymers (e.g., polycarbonate) in their plastic region. The model of Arruda and Boyce (1993) also improved upon some of the issues seen with the previous models, e.g., the inherent anisotropy of the four-chain model.

The model of Arruda and Boyce (1993) has a cubic representative volume element (RVE) with eight chains (representing polymer macromolecules), connected to a common node at the center, extending along the main diagonals to the corners of the cube (Fig. 6). The assumption of hyperelasticity allows stresses in the network to be calculated directly from the strain energy. Use of non-Gaussian statistics in modeling the chains results in a ‘lockout’ length, at which the chains are fully extended, and the material response shows a highly nonlinear strain hardening behavior. The strain energy developed in the original paper was given by

$$W = nk_B T N \left(\frac{\lambda_{\text{chain}}}{N} \beta + \ln \frac{\beta}{\sinh \beta} \right), \quad (19)$$

where n is the number of chains, k_B is the Boltzmann’s constant, T is the absolute temperature, N is the number of segments that make up one chain and β is the

Fig. 6 A RVE in the model of Arruda and Boyce (1993)



inverse Langevin function, i.e., $\beta = L^{-1}(\lambda_{\text{chain}}/N)$, with $L(x) = \coth(x) - 1/x$, which limits the chain extension.

In our opinion, the model of Arruda and Boyce (1993) is more important as a conceptual advance than it is useful as a tissue constitutive equation. The expression does not handle anisotropy well, and the model does not lend itself easily to incorporation of a complicated distribution of fiber orientations and/or properties. It does, however, account explicitly for finite fiber extensibility, an issue largely ignored by other models, and it recognizes that fibers are connected to form a network. This second idea, that fibers are connected and interact with each other when the tissue is deformed, is central to all of the work in the next section.

3.2 Homogeneous Hyperelastic Network Models

The next class of models to be discussed includes models that account explicitly for the presence of a fibrous or filamentous network via an initially homogeneous (often periodic) network of hyperelastic fibers. These models tend to be highly tissue-specific and represent tissues with a distinctive matrix architecture. In such models, three important factors influence the mechanics:

1. Network geometry.
2. Constitutive equation of individual components.
3. Interaction between different components.

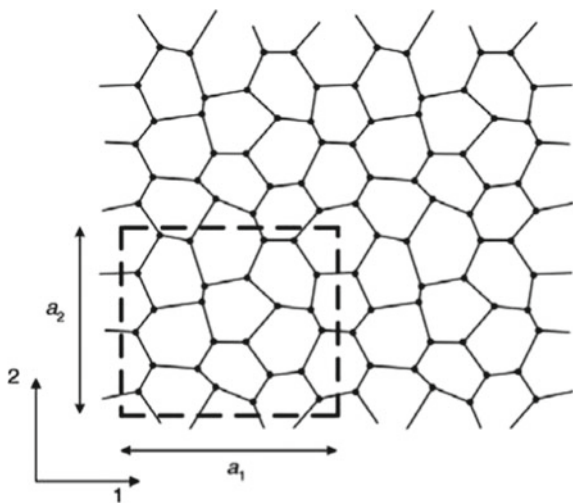
The specific handling of these factors determines the behavior of each model.

3.2.1 Lens Capsule

Burd (2008) developed a model of a type IV collagen network to predict the behavior of the lens capsule in the eye. This model used an irregular hexagonal network of fibers to represent collagen IV embedded in a neo-Hookean matrix. The choice of fiber structure was informed by histological studies and theoretical models on the mechanisms of collagen IV assembly (Yurchenco and Ruben 1987; Inoue and Leblond 1988; Barnard et al. 1992). Burd (2008) used periodic boundary conditions, wherein the performance of the entire network was determined from the response of the network within a repeating unit cell (Fig. 7). Periodic boundary conditions eliminate the possibility of any adverse boundary effects creeping into the simulation due to improper sizing of the representative volume, but they assume that the network structure is infinite and repetitive and so it is not the optimal choice to model random networks.

Burd (2008) experimented with two different types of constitutive equations for the collagen fibers; one was linearly elastic, and the other included a strain energy defined so that the incremental stiffness of the fibers approached a constant value for increasing values of strain. The matrix surrounding the fibers was neo-Hookean.

Fig. 7 The 2-D network used by Burd (2008). The dashed rectangle shows the periodic cell whose repeated translation forms the infinite network shown. Image reprinted from Burd (2008) with permission from Springer



Burd (2008) assumed that collagen networks primarily assemble into 2-D sheets and that the surrounding matrix is incompressible. Previously existing models for the lens capsule (e.g., Fisher 1969) were based on constitutive equations developed for the entire tissue and did not consider the geometric effects of the network structure, and they did not capture the geometric nonlinearity of the network which was captured by the model of Burd (2008). The model of Burd (2008) was able to match both uniaxial and biaxial experimental data even though it used a simple neo-Hookean model for the matrix. Interestingly, Pedrige et al. (2007) have had success of late using a fiber-composite type model to describe mechanics of the lens capsule, demonstrating that different models may all work well for the same tissue depending on one's goal. It remains difficult if not impossible, however, to relate specific model parameters to biological changes, such as those seen in Alport syndrome (Gyoneva et al. 2013).

3.2.2 Lung Tissue

The lung undergoes very large deformations without failure and recovers its original shape. Like most other tissues, the lung has as its major extracellular matrix (ECM) constituents collagen, elastin, microfibrils (e.g., fibrillin and fibulin), and proteoglycans (Setnikar 1955; Yuan et al. 2000). Among these fibers, collagen and elastin dominate (Fung 1993). Collagen is a stiff and nonlinear fiber, and it provides the structural framework of the alveolar walls. Elastin is very flexible and can stretch to almost twice its length without failure, which gives the lung its resilient and elastic nature. However, the mechanics of lung tissue depend not only on its underlying constituents, but also on their organization. Keeping this in mind, many models have been proposed for the lung which use fibrous networks to represent tissue.

The models described below all aimed to develop an accurate numerical representation of the lung tissue and thereby to predict its behavior under normal physiological conditions and under extreme (failure) conditions. The interactions between the different fibers found within the lung ECM were modeled by Black et al. (2008) via a regular hexagonal network. Fibers were represented by springs whose elastic energy was given as

$$E_s = \frac{1}{2}k\Delta l^2 + \frac{1}{3}b\Delta l^3. \quad (20)$$

This form of energy results in the springs being nonlinear with a quadratic force-displacement relationship. The elastic constant k was assumed to include the effects of both elastin and collagen, and the parameter b accounted for the nonlinear effect of collagen. This choice of strain energy introduces nonlinearity to the system but it is not optimal in that the energy becomes negative for sufficiently large negative values of Δl , destroying the convexity of the mechanical system. Thus, Eq. (20) can be used for sufficiently small compressions and appropriate values of b and k , but care must be exercised because the constitutive equation is not universally valid.

Regular hexagonal structures with pin joints are intrinsically unstable because they violate the Maxwell constraint. To stabilize the network, Black et al. (2008) added a constraint on the rotation at each joint (effectively changing the network from a truss to a frame) by introducing a rotational energy term in the total elastic energy of the network given by

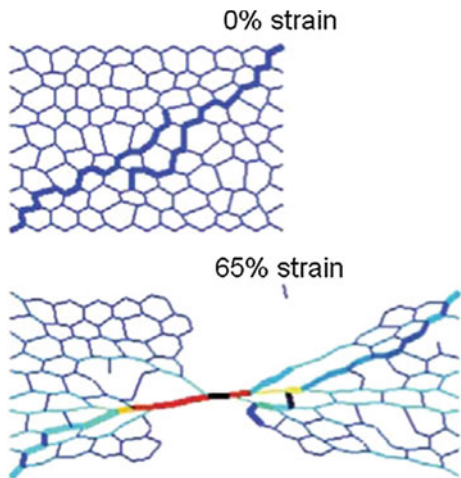
$$E_r = \frac{1}{2}r\Delta\theta^2, \quad (21)$$

where $\Delta\theta$ is the angular rotation of a fiber. The simulated annealing method of Kirkpatrick et al. (1983) was used to determine the response of this network model to an imposed strain. Values for k , b , and r were obtained by matching the simulation to experimental data.

The advantages of this model are that it is easy to implement and matches the experimental data well, but the actual structure of the networks in the lung ECM can be more irregular in nature and might not be properly represented by a regular hexagonal network. Also, introducing a rotational energy penalty term in the elastic energy to stabilize the network alters the low strain behavior of the network which is dominated by fiber reorientation into the direction of stress.

A follow-up by the same group (Ritter et al. 2009) investigated the role of the network structure in the failure mechanics of lung tissue. It is well known that elastin, an important component of lung ECM can strain up to 200 % before failure, but lung tissue fails at much lower strains (Fung 1993). To match these experimental findings and to understand better the role of proteoglycans in the lung ECM, Ritter et al. (2009) modeled lung tissue with a ‘zipper’ network model (Fig. 8). In this network, elastin fibers did not percolate through the network but overlapped from opposite sides in a zipper-like manner. These elastin fibers were connected to each other via a network of proteoglycans. The reasoning behind this construction was that elastin and collagen

Fig. 8 The ‘zipper’ network used by Ritter et al. (2009). Thick lines represent elastin fibers and thin lines are proteoglycans. Image reprinted from Ritter et al. (2009) with permission from Proc. Natl. Acad. Sci. USA



are load-bearing fibrous proteins embedded in a gel made up of proteoglycans, which are necessary for the stability of the ECM. Each elastin and proteoglycan fiber were represented by a linear spring with a torsional spring at the pin joints to constrain rotation of fibers. The net elastic energy in the network was given by

$$E = \frac{1}{2}k\Delta l^2 + \frac{1}{3}r\Delta\theta^2. \quad (22)$$

This model used linear springs and a very simplified structure for the tissue network, but an important point to be noted from the results are that the properties of a network can vary greatly from those of its constituent fibers. In this case, Ritter et al. (2009) noticed that the strain at failure for the tissue was much lower than that of an individual elastin fiber, a result attributed to the presence of the proteoglycan fibers in the network. The stress at failure was dependent on elastin fibers since these fibers bore majority of the load (Fig. 8). The predictions of this model could be improved by using nonlinear fibers and accounting for the presence of collagen.

The same group has also developed several similar models to study lung tissue mechanics and diseases (e.g., fibrosis). They have looked at mechanics of the network with variation in fiber properties (Oliveira et al. 2014) and effects of network failure in lung tissue (Suki et al. 2012). However, these models use the same network model with small variations and thus will not be discussed here.

Another model of lung tissue by Maksym et al. (1998) started with a similar regular 2-D structure. Irregularity was added to the network by randomly perturbing the node positions. Maksym et al. (1998) assumed each of their fibers to be a parallel combination of a collagen and elastin fibril. Elastin was represented by a linear spring element while collagen was represented by a string. As an individual pair was stretched, the collagen string element was initially flaccid and provided no force as long as the stretched length was less than a predetermined contour length. Beyond

this threshold length, the string became taut, and the unit became much stiffer. The force–displacement relations were of the form

$$F = \begin{cases} k_{\text{elas}}(l - l_0) & l \leq l_k \\ k_{\text{elas}}(l - l_0) + k_{\text{col}}(l - l_k) & l \geq l_k. \end{cases} \quad (23)$$

Variability was added to the parameters l_k , k_{elas} , and k_{col} by selecting values using a distribution function (e.g., Gaussian distribution or a power law distribution). The model used a variation on the simulated annealing method (Kirkpatrick et al. 1983) to find the equilibrium positions of the nodes.

The model of Maksym et al. (1998) is a highly simplified representation of lung ECM, and it does not capture the nonlinear behavior of each fiber well. The combination of linear spring and string will lead to a sudden change in slope of the stress–strain curve when the collagen fibers start extending, whereas the experimental data predict a more gradual increase in stiffness. However, this model is computationally inexpensive and shows the heterogeneous load distribution within the network at large strains and the formation of preferred pathways for stress transmission. Understanding the formation of these pathways could be used to develop accurate bulk failure models for lung tissue.

3.2.3 Red Blood Cell Cytoskeleton

The red blood cell (erythrocyte) cytoskeleton is a remarkable structure. It provides a structural framework for the cell and can undergo and recover from large deformations fairly easily. An erythrocyte has a life span of 120 days, during which it circulates through the body around a million times, squeezing through narrow blood vessels. These extraordinary mechanical properties arise due to the unique structure of its cell membrane.

The red blood cell (RBC) cytoskeleton is primarily composed of a spectrin network tethered to a phospholipid bilayer at sites mediated by ankyrin, band3, and protein 4.2, as shown in Fig. 9. The spectrin fibers connect with each other at junction complexes composed of actin. This network allows the cell to be flexible and undergo significant changes in shape while also providing a resilient lipid base that helps the cell recover its original shape when under no load. However, it is believed that this network is not stationary and it is constantly evolving. With the evolving spectrin network, it is possible to explain the large deformations and plastic behavior exhibited by the cell. Certain experiments have also shown that under physiological conditions, spectrin filaments exist in a dynamic equilibrium between two states, tetramers and dimers (Bennet 1985; Mohandas and Evans 1994; Li et al. 2007).

The following models aim to study the behavior of the erythrocyte cell membrane and to understand better how its structure allows such remarkable mechanical behavior. The real cell membrane has a complex topography and many different components but these models make assumptions to simplify the system to only its major

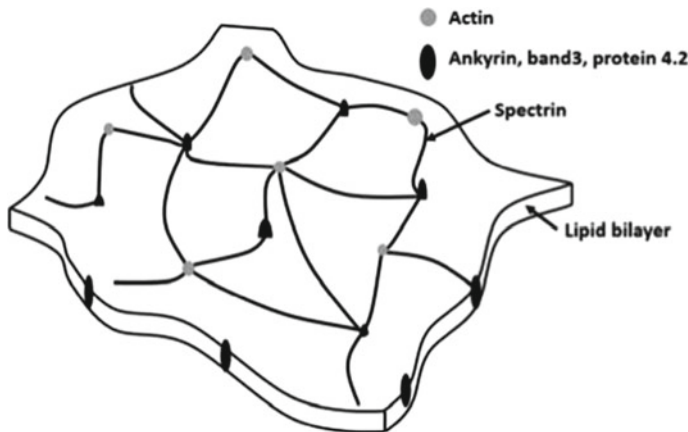


Fig. 9 Arrangement of the components of the RBC cytoskeleton (Hansen et al. 1996)

contributors. A few of the models assume static networks while others incorporate the effect of network evolution. The goal of all the models is to identify those unique features of the erythrocyte cytoskeletal network that allows its extreme deformation and resilient behavior.

A cytoskeleton model developed by Hansen et al. (1996) assumed the network to be made up of spectrin tetramers connected to each other at actin junctions. Hansen et al. (1996) used images of the RBC cytoskeleton to obtain certain topological parameters of the network structure (e.g., the average number of spectrin molecules per actin junction, and the distribution of spectrin dimer lengths). These parameters were then used to create simulated networks that were structurally different but had similar parameter values. All the fibers in the network were modeled by an appropriately selected constitutive equation. Thus, this model accounted for two essential properties of the RBC cytoskeleton, the network topology and the elasticity of individual spectrin molecules. Networks were created using Delaunay triangulation with each edge representing a spectrin tetramer and each node corresponding to an actin junction. By controlling the standard deviation of nodal degree and the standard deviation of mean fiber length, the Delaunay networks were modified to match the network parameters measured from images. Hansen et al. (1996) assumed a linear force–displacement relationship for the spectrin tetramers. Cauchy stresses in the network were calculated from the reaction forces on the boundary nodes as

$$\sigma_{11} = \frac{1}{2} \left(\frac{\sum F_1^R}{L^R} - \frac{\sum F_1^L}{L^L} \right), \quad \sigma_{12} = \frac{1}{2} \left(\frac{\sum F_2^R}{L^R} - \frac{\sum F_2^L}{L^L} \right), \quad (24)$$

$$\sigma_{21} = \frac{1}{2} \left(\frac{\sum F_1^T}{L^T} - \frac{\sum F_1^B}{L^B} \right), \quad \sigma_{22} = \frac{1}{2} \left(\frac{\sum F_2^T}{L^T} - \frac{\sum F_2^B}{L^B} \right), \quad (25)$$

where the superscripts R, L, T and B denote the right, left, top, and bottom face of the 2-D network, respectively, while σ_{ij} are the components of the 4×4 Cauchy stress tensor and F_1 and F_2 are the forces on the boundary nodes in the x and y direction, respectively. The forces from opposite boundaries (top and bottom, left and right) were averaged since normally, the forces on both sides, following this method of calculation, need not be equal.

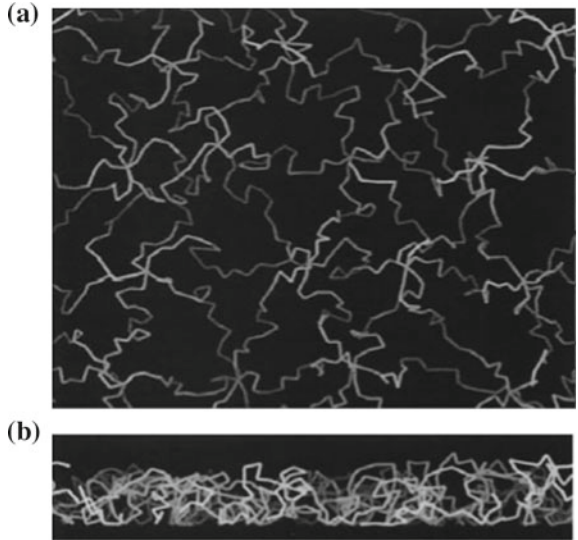
The model of Hansen et al. (1996) is relatively easy to implement and not very computationally demanding, especially with the assumption of a 2-D network. Another advantage of this model is that the network generation procedure can be easily modified to include spectrin hexamers (by connecting the three nodes of a Delaunay triangle with a Y-shaped element), thus allowing the creation of networks made entirely of spectrin tetramers or hexamers or any combination of the two. Such an approach is, however, sensitive to the sample size and boundary effects. Also, the Cauchy stress tensor calculated from reaction forces will not necessarily be symmetric since the forces on the top–bottom and left–right boundaries will not always be the same. This network also does not take into account the entropic elastic effects of spectrin and is entirely based on an enthalpic approach.

A different approach at modeling the cytoskeleton can be seen in the work by Li et al. (2007). A molecular dynamics approach was used to model the cytoskeletal network. This approach modeled the filaments and other nonfilamentous components of the network as spheres that interacted with each other through appropriately chosen potential energy functions. The chosen functions could be complex N -body potentials or simple pair potentials like the Lennard-Jones (LJ) potential.

The method of Li et al. (2007) has the advantage that it can accurately model interactions between fibers (e.g., due to steric effects and contact). It also captures well the effect of temperature on the system behavior. Also, the use of the LJ potential to describe spectrin–actin bonding leads to continuously evolving bonds, which can break and reform as the distance between the spheres changes. The string of spheres used to represent spectrin filaments can be thought of as a network of nodes with nodal degree 2. The nodal degree of these nodes, however, changes as the spheres in one filament interact with spheres representing other filaments and nonfilamentous material. However, due to the small time scale and large number of degrees of freedom, simulations can only be run for a very short amount of time. The choice of potentials greatly affects the forces that the fibers experience.

Another cytoskeleton model proposed by Boal (1994) (see Fig. 10 therein) took into account the entropic effects using freely jointed chains in a 3-D network. In this model, each spectrin tetramer was represented by a self-avoiding chain of n_{seg} segments, each of which was composed of a straight flexible tether connected to $n_{\text{seg}} + 1$ vertices represented by spherical beads of diameter a . The ends of these chains were connected to junction vertices with a coordination of 6 to form a network, in the same way that spectrin tetramers are joined by actin and protein 4.2. The chain midpoints were constrained to lie on the computational bilayer defined by the plane $z = 0$, similar to the way spectrin is attached to the lipid bilayer by ankyrin. All other chain segments could undergo free motion above the bilayer plane. In order to ensure a nonintersecting chain, a minimum length of a and a maximum length of $\sqrt{2}a$ were

Fig. 10 Example of the network used by Boal with $n_{\text{seg}} = 20$. **a** Viewed normal to the bilayer **b** Viewed along the bilayer. Notice that no elements are allowed to cross the bilayer (below $z = 0$). Image reprinted from Boal (1994) with permission from Elsevier



imposed on the tethers. These lengths were enforced in the simulation by use of an intervertex potential V given by

$$V(r) = V_{\text{attractive}}(r) + V_{\text{repulsive}}(r), \quad (26)$$

where the repulsive potential $V_{\text{repulsive}}$ was defined for all vertices as

$$V_{\text{repulsive}}(r) = \begin{cases} \infty & \text{for } 0 < r \leq a \\ 0 & \text{for } r > a, \end{cases} \quad (27)$$

and the attractive potential $V_{\text{attractive}}$ was defined only for nearest neighbor vertices as

$$V_{\text{attractive}}(r) = \begin{cases} \infty & \text{for } r > \sqrt{2}a \\ 0 & \text{for } r \leq \sqrt{2}a. \end{cases} \quad (28)$$

The model used a Monte Carlo algorithm to simulate and propagate the network using periodic boundary conditions in the X and Y directions. At each step, the beads were moved by a predetermined finite step size (in the published simulation a step size of $0.1a$ was used), and the new configuration was accepted or rejected based on a Boltzmann weight. The simulation generated a set of configurations which were used to calculate the ensemble averages of macroscopic observables like the simulation box lengths L_x and L_y and its area A_{xy} . Network elastic constants can be determined using these ensemble averages via fluctuations as

$$\beta K_A = \frac{\langle A_{xy} \rangle}{\langle A_{xy}^2 \rangle - \langle A_{xy} \rangle^2}, \quad (29)$$

where $\beta = 1/(k_B T)$, K_A is the area compression modulus of the network and $\langle \bullet \rangle$ denotes an ensemble average. The shear modulus μ is determined from (see Boal 1994 for the derivation)

$$(\beta K_A)^{-1} - (\beta \mu)^{-1} = 4\langle A \rangle \left(\frac{\langle L_x L_y \rangle}{\langle L_x \rangle \langle L_y \rangle} - 1 \right). \quad (30)$$

This model assumes the network to be composed entirely of spectrin tetramers, and needs a considerable amount of computing power and time to obtain the large number of configuration snapshots needed to make the ensemble averages meaningful (as evident from their simulation taking 1 year to complete on a 40 MHz processor). It considers the effect of steric interactions and entropic effects on the network behavior, however, which is a significant advantage. Boal's results were different from networks composed only of Gaussian springs, showing that steric effects at the small length scales are important. Another possible drawback is that this model is dependent on the chosen interparticle potential functions.

Li et al. (2005) modeled the cytoskeleton with a 2-D network formed on the surface of a 3-D volume. This model captured the mechanical contribution of the lipid bilayer as well as the mechanics of the fiber network underlying it. This approach of modeling the entire RBC was based on a previously developed model by Discher et al. (1994).

In the model of Li et al. (2005), the network nodes are formed at actin junctions and network edges represent spectrin fibers, as seen in earlier models. The entire network is made up of triangular elements which form the surface of a three-dimensional enclosed volume. Assuming that the triangles tessellate the entire surface of the enclosed volume, the surface area and the volume of the cell can be calculated by knowing the coordinates of the vertices of each element ($\mathbf{x}_n, \mathbf{x}_m, \mathbf{x}_l$):

$$A^{(i)} = \frac{|(\mathbf{x}_m - \mathbf{x}_l) \times (\mathbf{x}_n - \mathbf{x}_l)|}{2}, \quad V_{\text{total}} = \sum_i \frac{\mathbf{x}^{(i)} \cdot \mathbf{n}^{(i)} A^{(i)}}{3}. \quad (31)$$

Here, $\mathbf{x}^{(i)} = (\mathbf{x}_n + \mathbf{x}_m + \mathbf{x}_l)/3$ is the center of mass of the triangular element i , and $\mathbf{n}^{(i)}$ is the normal to the element pointing toward the exterior of the cell.

The approach of Li et al. (2005) to simulate this system uses coarse grained molecular dynamics which balances the forces on the nodes (i.e., $f_n^{\text{int}} + f_n^{\text{ext}} = 0$) to obtain their equilibrium positions. The forces in the previous equation are obtained from an energy term defined as

$$W_{\text{total}} = W_{\text{in-plane}} + W_{\text{bending}} + W_{\text{surfacearea}} + W_{\text{cellvolume}}. \quad (32)$$

This energy term includes the contribution from in-plane stretching of the spectrin network along with constraints on the curvature of the bilayer and cell volume and surface area which are of the form

$$W_{\text{cellvolume}} = k_v(V_{\text{total}} - V_{\text{desired}})^2, \quad (33)$$

$$W_{\text{surfacearea}} = k_a(A_{\text{total}} - A_{\text{desired}})^2, \quad (34)$$

$$W_{\text{bending}} = \sum_{\text{adjacent } i,j} \{k_{\text{bend}}[1 - \cos(\theta_{ij} - \theta_0)]\}, \quad (35)$$

where the constants k_v , k_a and k_{bend} include appropriate scaling terms. The bending energy is calculated by summing over adjacent triangular elements where θ_0 is the ideal curvature angle between the normals of adjacent elements.

These terms act as a feedback control system, increasing the energy of the system if any of the properties (curvature, volume, or area) deviate from the desired value. Forces acting on nodes can be obtained from this energy density function. The forces f_{WLC} due to worm-like chain (WLC) fibers are given by

$$f_{\text{WLC}} = -\frac{k_{\text{B}}T}{L_p} \left[\frac{1}{4(1-x)^2} - \frac{1}{4} + x \right], \quad (36)$$

where L_0 is the contour length, L is the chain end-to-end distance, and L_p is the persistence length.

This model is able to track the shape evolution of the full cell and predict the equilibrium shape of the surface of the cell. It also reasonably models experiments where the cytoskeleton undergoes large deformations without failure (e.g., in an optical tweezer stretching experiment).

3.2.4 Other Models

All the previous network approaches described here represented fibers as either linear or nonlinear springs or modeled them as molecules interacting with each other through potential energy functions. Another popular approach (van Dillen et al. 2008; Zagar et al. 2011; Ma et al. 2013; Nair et al. 2014; Wang et al. 2014; Zagar et al. 2015) discretizes fibers into beams (e.g., the beam of Timoshenko 1921), allowing them to be solved using traditional finite element methods and commercially available FE software. Such models generally perform better than the models using truss (line) elements to represent fibers in cases where the fibers are short and stiff (i.e., persistence length is greater than contour length). This is because beam elements account for the shear and bending along the fiber, whereas in a line element only axial loads can be considered and bending (if any) needs to be accounted for in other ways.

One of the models using a discrete-fiber network approach by Ma et al. (2013) simulated ECM remodeling and long-range stress transmission due to contractile

activity of cells. The model of Ma et al. (2013) used confocal microscope images of a cell and its surrounding environment to generate their network. A similar study published later by Nair et al. (2014) used networks that were generated by uniformly distributing fibers in the computational domain. Crosslinks were formed at the intersection of two fibers. This method of generating random fibers offers the advantage of being simple to implement but it does not translate easily to three dimensions.

Fibers were represented by flexible Timoshenko beam elements. This led to the following expression for the total strain energy

$$W = \frac{1}{2} \sum_{i=1}^{N_{\text{fibers}}} \int \left[EI \left(\frac{\partial \psi}{\partial s} \right)^2 + EA \left(\frac{\partial u}{\partial s} \right)^2 + \lambda GA \left(\frac{\partial v}{\partial s} - \psi \right)^2 \right], \quad (37)$$

where E is the Young's modulus, G is the shear modulus, I is the second moment of area of fibers, $\partial u/\partial s$ is the axial strain, $\partial v/\partial s$ is the rotation of the fiber and ψ is the rotation of the plane perpendicular to the normal axis of the fiber (i.e., fiber bending).

To simulate cells and cell contractility in the network, all the fibers lying inside the area enclosed by the cell were removed, and those fibers that terminated on the boundary were fixed to nodes generated on the cell boundary. An isotropic inward displacement was applied on this boundary to mimic the effect of cell contraction.

Another study using the discrete-fiber network model used a more complex method of generating random networks. Zagar et al. (2011) derived a scaling relation for the nonlinear behavior of actin networks to study the mechanics of cell cytoskeletons. In their work, Zagar et al. (2011) used 3-D isotropic networks of athermal filaments generated using the algorithm introduced by Huisman et al. (2007). An attractive force field with a $1/r^2$ dependence set in motion filaments of initial length l_0 in a periodic box. The filaments were also assumed to be moving in a viscous fluid which provided a drag force. Crosslinks between fibers were formed when two filaments got within a predetermined cut off distance of each other. The number of filaments in the box was determined by the concentration of the filament material.

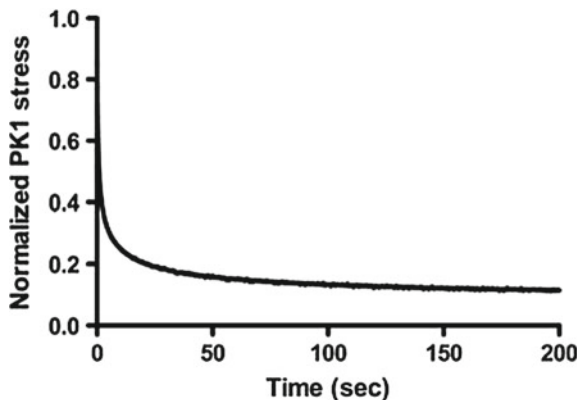
3.3 Evolving Network Models

In this section we briefly discuss network models which account for the variations in network properties over time, including viscoelasticity, network remodeling, and failure.

3.3.1 Viscoelastic Network Models

Biological networks are viscoelastic in nature. For example, Fig. 11 shows the viscoelastic response observed in a collagen gel. Several studies numerically modeling

Fig. 11 Viscoelastic relaxation behavior observed in a collagen gel



viscoelastic networks have aimed at understanding and modeling the behavior of the cell cytoskeleton. Besides providing structure to the cell, the cytoskeleton of a cell plays a very important role in cell functions such as locomotion, force sensing, and remodeling of the external environment. The viscoelastic response of the cytoskeleton has been seen in various experimental studies (e.g., Bausch et al. 1998; Janmey and Weitz 2004; Mizuno et al. 2007). Different factors can contribute to the viscoelasticity seen in microfilament networks such as sliding of entangled fibers, the bending-stretching transitions in rigidly cross-linked networks, and the intrinsic viscoelastic nature of the microfilament itself.

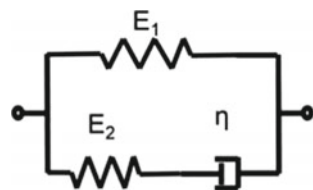
One of the methods used to model viscoelastic networks assumes the network to exist in a volume filled with a viscous fluid. An example of this is the model developed by Bottino (1998) to represent the actin cytoskeleton of an amoeboid cell. This model uses the immersed boundary method (Peskin and McQueen 1989). The network is represented by N points P_i in a 2-D domain Ω connected by elastic links similar to several other models described previously. The fluid surrounding the network is modeled using the incompressible Navier–Stokes equation

$$\rho \left(\frac{\partial \mathbf{u}}{\partial t} + \mathbf{u} \cdot \nabla \mathbf{u} \right) = -\nabla p + \mu \nabla^2 \mathbf{u} + \mathbf{F}, \quad (38)$$

where ρ is the fluid density, \mathbf{u} is the fluid velocity, p is the pressure, μ is the fluid viscosity, and \mathbf{F} contains the forces acting on the fluid due to the immersed network.

Forces arise in the network as the nodes are carried along at local fluid velocities $\mathbf{u}(P_i, t)$ leading to stretching of the interconnecting links. By varying the stiffness of the links over time, Bottino (1998) achieved different network properties, e.g., a simple fluid behavior when the stiffness of every link, $K_{ij}(t) = 0$, a memory network when $K_{ij}(t) = K_{ij}(0)$ and even network failure by dropping the stiffness of ‘ruptured’ links. The force \mathbf{F} transmitted to the fluid from the immersed network is calculated from the net forces acting on a small part of network enclosed by a rectangular area $\Delta A = [x_1, x_2] \times [y_1, y_2]$ due to the network lying outside this envelope.

Fig. 12 Spring-dashpot representation of a SLS



Thus,

$$\mathbf{F} = \int_{x_1}^{x_2} [\mathbf{T}_y(x, y_2) - \mathbf{T}_y(x, y_1)] dx + \int_{y_1}^{y_2} [\mathbf{T}_x(x_2, y) - \mathbf{T}_x(x_1, y)] dy, \quad (39)$$

where \mathbf{T}_x and \mathbf{T}_y are tractions on the surfaces with normals in the x and y directions, respectively.

This method of modeling networks has the advantage that it can be used to model two-phase flow and account for the interaction between the network fibers and surrounding matrix. Another advantage is that with appropriate modifications (e.g., if the viscous fluid is replaced by a viscoplastic solid model), matrix failure due to high local stresses within the matrix can be modeled. Two possible modes of failure within a network, failure of fibers and failure of the non-fibrillar matrix, can then be considered. The potential pitfall of this method, however, is that it can become computationally expensive as the fiber density of the networks is increased and especially in the context of a 3-D multiscale approach as discussed in Sect. 4.

Another possible method of simulating viscoelastic networks, and the approach that we have used in our rigidly cross-linked network models, represents fibers with an appropriate constitutive equation (e.g., a Standard Linear Solid (SLS), as shown in Fig. 12). 3-D networks are generated using either Delaunay or Voronoi tessellations. Network parameters such as its fiber density, alignment, etc., are selected based on the tissue being modeled. Networks are deformed by applying displacement boundary conditions on the nodes lying on the faces of the network. Internal nodes are allowed to equilibrate and find new positions such that the forces on these nodes are minimized. Nodal forces arise due to fibers stretching and are evaluated using the constitutive equations selected to represent fibers. An advantage of using such a model is that it allows simple simulation of networks with multiple types of fibers and/or fibers whose properties vary over time since only the parameters defining the constitutive equation need to be changed. This model can also be used to simulate network failure (Wang and Sastry 2000). However, the calculation of stresses is based only on the fiber network and does not consider the matrix material surrounding the fibers. This can be modified to include the matrix material such that the non-fibrillar matrix component (e.g., neo-Hookean) is stretched in parallel to the fiber network and its contribution to the overall stress is added to that calculated from the fiber network (Stylianopoulos and Barocas 2007a; Lake and Barocas 2011; Lake et al. 2012). This method simplifies the simulation while slightly compromising on the accuracy of the results (see the discussion in Zhang et al. 2013a,b).

4 A Multiscale Approach to the Network Problem

In this final section, we address a fundamental challenge in network modeling of tissue mechanics. As seen in Sect. 3, there are numerous biological systems in which the network problem is interesting and important, and the high-level view offered by the affine assumption is not always sufficient. Solving network problems, however, is extremely demanding computationally, and the sheer size of the network problem rapidly becomes prohibitive. A single migrating cell, e.g., may contain thousands or even millions of actin filaments, and even a relatively dilute collagen gel contains millions of collagen fiber segments per cubic millimeter. Thus, if one wishes to account for network effects within a large system, some approximate scheme is required. The scheme presented here represents an intermediate step between the affine assumption and the fully explicit network model. Details may be found in Chandran and Barocas (2007), Stylianopoulos and Barocas (2007b), Chandran et al. (2008) and Sander et al. (2009).

4.1 Basic Assumptions

In the modeling framework, certain assumptions about the tissue properties are made. These assumptions are essential for the framework to be theoretically sound, and, although the methods described will still produce results even if the assumptions are violated, caution must necessarily be taken in their interpretation.

4.1.1 The Microscopic Network

It is assumed that the tissue consists of a network that contains fibers connected at freely rotating joints (i.e., a truss network). This assumption is not formally necessary, but we will develop the theory for this case. In this assumption, we use the term ‘fiber’ in its general sense and do not distinguish among fibers, fibrils, filaments, etc.

It is also assumed that the network is at all times at mechanical equilibrium, so the sum of the forces on any point is zero and the divergence of the stress anywhere within an individual fiber is zero. In extremely rapid situations (e.g., traumatic injury), the inertia of the system would require a different theoretical approach.

The fiber network contains two types of nodes, *interior nodes* and *boundary nodes*. It is required that the network be large enough that boundary artifacts are negligible (typically having a network length scale at least ten times the connection length scale; see Shasavari and Picu (2012) for more discussion of this matter).

Finally, it is assumed that the random networks in the model are *statistically homogeneous*, that is any random network generated according to the problem specifications exhibits, to within reasonable error, the same macroscopic properties as any other network so generated even though the fine details of the two networks

may differ. This assumption is closely related to the previous one. Our experience is that about 500 fibers is typically sufficient for a two-dimensional problem and 1000–2000 fibers is typically sufficient for a three-dimensional problem, depending on the nature of the specific networks under study.

4.1.2 Displacement of the Representative Volume Element

The central construct of our multiscale approach is a RVE at each integration point in the macroscopic finite element model. The networks within the RVE are constructed as described above, but two additional restrictions on the RVE must be considered.

First, it is assumed that the RVE is small compared to the continuum (macroscopic) scale. Of course, if the RVE is not small, then there is minimal benefit in constructing a multiscale model since there are not really multiple scales. Nevertheless, it is important to recognize that the RVE represents a region of finite size, and one should always confirm that the RVE dimensions are significantly smaller than the finite element dimensions.

Second, we assume that because the network is sufficiently large, the displacement of the boundaries for each RVE is given by the macroscopic displacement field around the corresponding integration point. That is, all nonaffinity arises from motion of the *interior* nodes in the RVE, whereas the *boundary* nodes of the RVE track the macroscopic displacement field.

Those assumptions create the framework for the first step in the computation, passing displacement information from the macroscopic (FE) to the microscopic (RVE) scale.

4.2 The Multiscale Algorithm

4.2.1 Equilibrating the Microscopic Network

The system is assumed to be quasistatic, so mechanical equilibrium of the micronetwork for each RVE is obtained by solving the force balance on all nodes simultaneously, in conjunction with the boundary conditions obtained from the macroscopic scale:

Find a set of $x_i^{(k)}$ values such that

$$\sum_{j=1}^{n^{(k)}} f_i^{(j)} = 0 \quad k \text{ is an interior node,} \quad (40)$$

$$x_i^{(k)} = x_i^{(k),\text{macro}} \quad k \text{ is a boundary node,} \quad (41)$$

where the superscript k refers to node number, the superscript j refers to fiber number on each node, and the subscript i is the index and runs from 1 to 3 in three dimensions. This problem is fairly straightforward and can be solved by a zero-finding method (e.g., Newton iteration) or a minimization scheme (minimizing the system energy instead of balancing the nodal forces). Once the nodal positions and fiber forces have been determined, the next step is to compute the average stress within the RVE.

4.2.2 Average Cauchy Stress Within the RVE

Before continuing, we note one more important assumption underlying our method. Although the fine detail is essential for defining the material behavior, it is assumed that the average Cauchy stress varies slowly enough with respect to the macroscopic scale that the integrals calculated via the integration points are accurate, and that the average Cauchy stress is sufficient to represent the stress state of the tissue at the large scale. That is, although $\sigma_{ij,k}$ might be quite large, if we consider the volume-averaged stress $\langle \sigma_{ij} \rangle$, then $\langle \sigma_{ij} \rangle_{,k}$ is not too large.

The average Cauchy stress within the material is defined as

$$\langle \sigma_{ij} \rangle = \frac{1}{V_\omega} \int_\omega \sigma_{ij} dV, \quad (42)$$

where ω is the RVE, and V_ω is its volume. It is convenient to introduce a factor of $x_{i,j}$, which is just the derivative of x with respect to itself and thus the identity, so

$$\langle \sigma_{ij} \rangle = \frac{1}{V_\omega} \int_\omega \sigma_{ik} x_{j,k} dV. \quad (43)$$

Integration of the above by parts yields

$$\langle \sigma_{ij} \rangle = \frac{1}{V_\omega} \int_\omega (\sigma_{ik} x_j)_{,k} dV - \frac{1}{V_\omega} \int_\omega \sigma_{ik,k} x_j dV. \quad (44)$$

The first term can be converted to a surface integral by the divergence theorem, and the second term is zero because $\sigma_{ik,k} = 0$ under the assumption of mechanical equilibrium, so we write

$$\langle \sigma_{ij} \rangle = \frac{1}{V_\omega} \int_{\partial\omega} \sigma_{ik} x_j n_k dA, \quad (45)$$

where $\partial\omega$ is the boundary of ω , and n_k is its unit outward normal. Noting that $\sigma_{ik} n_k$ is the traction vector f_i on the surface, and assuming that the fiber diameter is sufficiently small that x and f do not vary significantly over the area of intersection between a given fiber and the boundary, we can replace the integral with a sum over boundary nodes so that

$$\langle \sigma_{ij} \rangle = \frac{1}{V_\omega} \sum_{\substack{\text{boundary} \\ \text{nodes } b}} f_i^{(b)} x_j^{(b)}. \quad (46)$$

That is, the average Cauchy stress within the RVE is calculated from boundary node forces and positions. It can be shown that if all forces in the network are along the fibers, the above construction gives a symmetric average Cauchy stress tensor.

The averaged Cauchy stress for each RVE is calculated and passed up to the macroscopic problem.

4.2.3 The Macroscopic Averaged Cauchy Stress Balance

If one wishes to allow the averaging volume to deform, as ours does, one must recognize that the volume-averaged Cauchy stress can change because of local variations or because of changes in the RVE shape with position. This result, which derives directly from Leibniz's Rule for differentiation of an integral, is derived elsewhere (Chandran and Barocas 2006) and can be written as

$$\langle \sigma_{ij} \rangle_{,j} = \frac{1}{V_\omega} \int_{\partial\omega} (\sigma_{ij} - \langle \sigma_{ij} \rangle) u_{k,j} n_k dA, \quad (47)$$

where u_k is the displacement of the RVE boundary. The term on the right-hand side accounts for changes in the average due to correlations between boundary motion and stress. It is calculated from the RVE solution once the average stress $\langle \sigma_{ij} \rangle$ has been determined. This extra term, while theoretically important, is usually small (<5% change in result) and can be time-consuming to compute, so it is often convenient to omit it in preliminary calculations.

4.2.4 The Coupling Loop

The problem is solved in fully coupled form using Newton iteration. An initial guess is made of the macroscopic displacements, from which each RVE's boundary displacements are determined. The individual RVE problems are solved (usually in parallel on a high-performance computational platform), and the averaged stresses are calculated. We also calculate the Jacobian matrix for the large nonlinear problem analytically by calculating the derivative of the averaged stress with respect to the macroscopic nodal positions. The key to the Jacobian calculation is to recognize that changes in the macroscopic nodal positions lead to changes in the boundary node positions in the RVE, which in turn lead to interior node position changes as the system reequilibrates:

$$\frac{\partial \langle \sigma_{ij} \rangle}{\partial x_k^{\text{macro}}} = \left(\frac{\partial \langle \sigma_{ij} \rangle}{\partial f_m^{\text{boundary}}} \right) \left(\frac{\partial f_m^{\text{boundary}}}{\partial x_p^{\text{boundary}}} \right)_{\substack{\text{mechanical} \\ \text{equilibrium}}} \left(\frac{\partial x_p^{\text{boundary}}}{\partial x_p^{\text{macro}}} \right). \quad (48)$$

The first term is readily derived from Eq. (48) above, and the third term is likewise straightforward because the boundary nodes are required to move affinely with the macroscopic displacement field. The second term, however, is somewhat more complicated, and is best evaluated by breaking it down further,

$$\begin{aligned} \left(\frac{\partial f_m^{\text{boundary}}}{\partial x_p^{\text{boundary}}} \right)_{\substack{\text{mechanical} \\ \text{equilibrium}}} &= \left(\frac{\partial f_m^{\text{boundary}}}{\partial x_q^{\text{interior}}} \right) \left(\frac{\partial x_q^{\text{interior}}}{\partial x_p^{\text{boundary}}} \right) \\ &= \left(\frac{\partial f_m^{\text{boundary}}}{\partial x_q^{\text{interior}}} \right) \left[- \left(\frac{\partial f_r^{\text{interior}}}{\partial x_q^{\text{interior}}} \right)^{-1} \left(\frac{\partial f_r^{\text{interior}}}{\partial x_p^{\text{boundary}}} \right) \right]. \end{aligned} \quad (49)$$

The last expansion arises because when a boundary node moves, that causes an imbalance in the interior forces $\partial f^{\text{interior}} / \partial x^{\text{boundary}}$, which must be corrected by moving the interior nodes $(\partial f^{\text{interior}} / \partial x^{\text{interior}})^{-1}$. The net effect of these two terms is the differential change in interior node position required $\partial x^{\text{interior}} / \partial x^{\text{boundary}}$ to remove the force imbalance generated by boundary node motion. The quantity $\partial f^{\text{interior}} / \partial x^{\text{interior}}$ is calculated already as part of the Jacobian calculation for the network mechanics problem, so it does not require significant additional computation.

Thus, a full Newton loop is possible between the macroscopic and microscopic scales. The RVE problems are solved, and the average stress balance of Eq. (49) checked for each macroscopic finite element basis function. If it is not converged, a Newton update step is performed, and the RVE calculations are repeated for the new nodal positions. The new average stresses are passed back to the macroscopic scale, and the process repeats until all macroscopic and microscopic calculations have converged. Figure 13 provides a schematic of the process.

4.3 More Advanced Models and Future Directions

The methods described in this section work very well for simple models of a single component network, but their potential value is not in such simple problems. Rather, it is in their ability to address issues on the single-fiber level and the continuum level simultaneously. For example, failure of a tissue can be modeled at the continuum scale (Ionescu et al. 2006), but then it is not obvious how to introduce changes in tissue architecture into the model parameters. By modifying the microstructure in the multiscale model, however, one can change the macroscopic behavior of the tissue by changing only the structural and not the biomechanical parameters (Hadi et al. 2012b). This approach, especially if combined with more realistic models of the tissue, has potential to produce some new and interesting results. Of course, defining

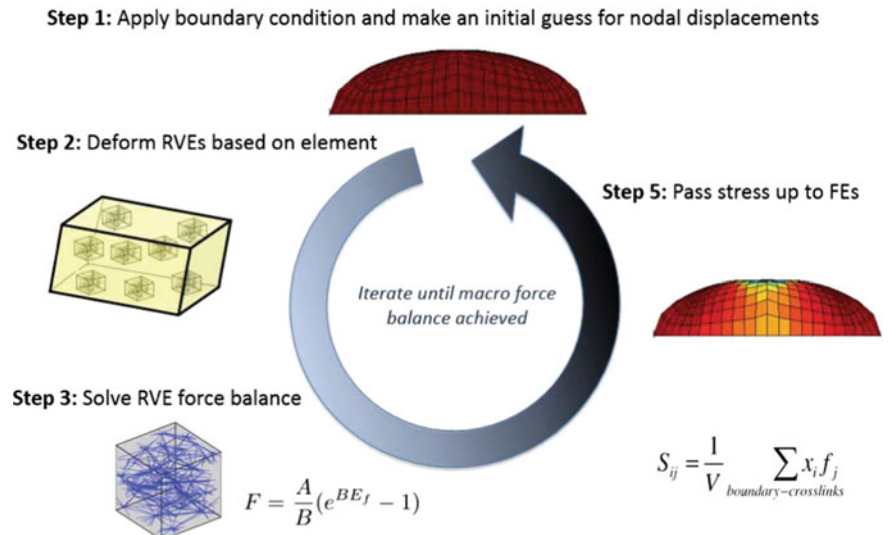


Fig. 13 Flow chart of the multiscale finite element procedure

what a realistic model is is by no means trivial and has numerous challenges, including determining what components need to be considered, how they will be arranged, and how different RVEs should be populated to account for variability within the tissue. Nevertheless, it is our hope that as imaging methods continue to improve, more and more information will become available about tissue architecture in health and disease.

Similar comments could be made about tissue remodeling. A model in which individual fibers change in response to degradation (Hadi et al. 2012a) or synthesis could potentially provide a great deal of insight into the detailed mechanisms of remodeling and how they translate from the microscopic to the macroscopic scale. Cell-driven compaction can also be modeled (Aghvami et al. 2013), and models of a cell in which the cytoskeleton is represented by a fiber network are also possible (Lai et al. 2013). Even more than the failure problem, the mathematical modeling of interactions between the cell and the ECM, or of the mechanics of the intracellular matrix, remains a challenge from the biophysical standpoint and from a numerical standpoint, but such problems could be studied within the context of the methods described in this section if sufficient resources and information were available.

References

- Aghvami, M., Barocas, V.H., Sander, E.A.: Multiscale mechanical simulations of cell compacted collagen gels. *J. Biomech. Eng.* **135**, 71004 (2013)
- Amini, R., Voycheck, C.A., Debski, R.E.: A method for predicting collagen fiber realignment in non-planar tissue surfaces as applied to glenohumeral capsule during clinically relevant deformation. *J. Biomech. Eng.* **136**, 031003 (2014)

- Annaidh, A.N., Bruyere, K., Destrade, M., Gilchrist, M.D., Maurini, C., Ottenio, M., Giuseppe, S.: Automated estimation of collagen fiber dispersion in the dermis and its contribution to the anisotropic behavior of skin. *Ann. Biomed. Eng.* **40**, 1666–1678 (2012)
- Arruda, E.M., Boyce, M.C.: A three-dimensional constitutive model for the large stretch behavior of rubber elastic materials. *J. Mech. Phys. Solids* **41**, 389–412 (1993)
- Ateshian, G.A., Costa, K.D.: A frame-invariant formulation of Fung elasticity. *J. Biomech.* **42**, 781–785 (2009)
- Avril, S., Badel, P., Gabr, M., Sutton, M.A., Lessner, S.M.: Biomechanics of porcine renal arteries and role of axial stretch. *J. Biomech. Eng.* **135**, 081007-1–081007-10 (2013)
- Baek, S., Gleason, R.L., Rajagopal, K.R., Humphrey, J.D.: Theory of small on large: potential utility in computations of fluid-solid interactions in arteries. *Comput. Meth. Appl. Mech. Eng.* **196**, 3070–3078 (2007)
- Barnard, K., Burgess, S.A., Carter, D.A., Woolley, D.M.: Three-dimensional structure of type IV collagen in the mammalian lens capsule. *J. Struct. Biol.* **108**, 6–13 (1992)
- Bausch, A.R., Ziemann, F., Boulbitch, A.A., Jacobson, K., Sackmann, E.: Local measurements of viscoelastic parameters of adherent cell surfaces by magnetic bead microrheometry. *Biophys. J.* **75**, 2038–2049 (1998)
- Bennet, V.: The membrane skeleton of human erythrocytes and its implications for more complex cells. *Annu. Rev. Biochem.* **54**, 273–304 (1985)
- Black, L.D., Allen, P.G., Morris, S.M., Stone, P.J., Suki, B.: Mechanical and failure properties of extracellular matrix sheets as a function of structural protein composition. *Biophys. J.* **94**, 1916–1929 (2008)
- Boal, D.H.: Computer simulation of a model network for the erythrocyte cytoskeleton. *Biophys. J.* **67**, 521–529 (1994)
- Boccaletti, S., Latora, V., Moreno, Y., Chavez, M., Hwang, D.U.: Complex networks: structure and dynamics. *Phys. Rep.* **424**, 175–308 (2006)
- Bottino, D.C.: Modeling viscoelastic networks and cell deformation in the context of the immersed boundary method. *J. Comput. Phys.* **147**, 86–113 (1998)
- Burd, H.J.: A structural constitutive model for the human lens capsule. *Biomech. Model Mechanobiol.* **8**, 217–231 (2008)
- Chandran, P.L., Barocas, V.H.: Affine versus non-affine fibril kinematics in collagen networks: theoretical studies of network behavior. *J. Biomech. Eng.* **128**, 259–270 (2006)
- Chandran, P.L., Barocas, V.H.: Deterministic material-based averaging theory model of collagen gel micromechanics. *J. Biomech. Eng.* **129**, 137–147 (2007)
- Chandran, P.L., Sylianopoulos, T., Barocas, V.H.: Multiscale modeling for the poro-elastic behavior of collagen networks. *SIAM J. Multiscale Model. Simul.* **7**, 22–43 (2008)
- Deng, S.X., Tomioka, J., Debes, J.C., Fung, Y.C.: New experiments on shear modulus of elasticity of arteries. *Am. J. Physiol.* **266**, H1–H10 (1994)
- Discher, D.E., Boal, D.H., Boey, S.K.: Phase transitions and anisotropic responses of planar triangular nets under large deformation. *Phys. Rev. E* **55**, 521–529 (1994)
- Driessens, N.J.B., Bouten, C.V.C., Baaijens, F.P.T.: A structural constitutive model for collagenous cardiovascular tissues incorporating the angular fiber distribution. *J. Biomech. Eng.* **127**, 494–503 (2005)
- Fata, B., Zhang, W., Amini, R., Sacks, M.S.: Insights into regional adaptations in the growing pulmonary artery using a meso-scale structural model: effects of ascending aorta impingement. *J. Biomech. Eng.* **136**, 021009 (2014)
- Feng, L., Bhanu, B.: Understanding dynamic social grouping behaviors of pedestrians. *IEEE J. Sel. Top. Signal Process.* **9**, 317–329 (2015)
- Fisher, R.F.: Elastic constants of the human lens capsule. *J. Physiol.* **201**, 1–19 (1969)
- Flory, P.J., Rehner, J.J.: Statistical mechanics of crosslinked polymer networks I. Rubberlike elasticity. *J. Chem. Phys.* **11**, 512 (1943)
- Fung, Y.C.: *Biomechanics: Mechanical Properties of Living Tissues*. Springer, Berlin (1993)

- Fung, Y.C., Fronek, K., Patitucci, P.: Pseudoelasticity of arteries and the choice of its mathematical expression. *Am. J. Physiol.* **237**, H620–H631 (1979)
- Grady, L.: Random walks for image segmentation. *IEEE Trans. Pattern Anal. Mach. Intell.* **28**, 1768–1783 (2006)
- Gyoneva, L., Segal, Y., Dorfman, K.D., Barocas, V.H.: Mechanical response of wild-type and alport murine lens capsules during osmotic swelling. *Exp. Eye Res.* **113**, 87–91 (2013)
- Hadi, M.F., Sander, E.A., Barocas, V.H.: Multiscale model predicts tissue-level failure from collagen fiber-level damage. *J. Biomech. Eng.* **134**, 091005 (2012a)
- Hadi, M.F., Sander, E.A., Ruberti, J.W., Barocas, V.H.: Simulated remodeling of loaded collagen networks via strain-dependent enzymatic degradation and constant-rate fiber growth. *Mech. Mater.* **44**, 72–82 (2012b)
- Hansen, J.C., Skalak, R., Chien, S., Hoger, A.: An elastic network model based on the structure of the red blood cell membrane skeleton. *Biophys. J.* **70**, 146–166 (1996)
- Hao, T., Ma, H.W., Zhao, X.M., Goryanin, I.: The reconstruction and analysis of tissue specific human metabolic networks. *Mol. BioSyst.* **8**, 663–670 (2012)
- Hibbit, Karlsson, Sorensen. ABAQUS/Standard Analysis User's Manual. Hibbit, Karlsson, Sorensen Inc., USA (2007)
- Holzapfel, G.A., Gasser, T.C., Ogden, R.W.: A new constitutive framework for arterial wall mechanics and a comparative study of material models. *J. Elast.* **61**, 1–48 (2000)
- Huisman, E.M., van Dillen, T., Onck, P.R., van der Giessen, E.: Three-dimensional cross-linked F-actin networks: relation between network architecture and mechanical behavior. *Phys. Rev. Lett.* **99**, 208103 (2007)
- Humphrey, J.D.: Mechanics of arterial wall: review and directions. *Crit. Rev. Biomed. Eng.* **23**, 1–162 (1995)
- Hwang, S., Lee, D.S., Kahng, B.: Blind and myopic ants in heterogeneous networks. *Phys. Rev. E* **90**, 052814-1–052814-9 (2014)
- Inoue, S., Leblond, C.P.: Three-dimensional network of cords: the main component of basement membranes. *Am. J. Anat.* **181**, 341–358 (1988)
- Ionescu, I., Guilkey, J.E., Berzins, M., Kirby, R.M., Weiss, J.A.: Simulation of soft tissue failure using the material point method. *J. Biomech. Eng.* **128**, 917–924 (2006)
- Janmey, P.A., Weitz, D.A.: Dealing with mechanics: mechanisms of force transduction in cells. *Trends Biochem. Sci.* **29**, 364–370 (2004)
- Kamenskiy, A.V., Mactaggart, J.N., Pipinos, I.I., Bikhchandani, J., Dzenis, Y.A.: Three-dimensional geometry of the human carotid artery. *J. Biomech. Eng.* **134**, 064502 (2012)
- Kas'yanov, V.A., Rachev, A.I.: Deformation of blood vessels upon stretching, internal pressure, and torsion. *Mech. Comput. Mater.* **16**, 76–80 (1980)
- Kirkpatrick, S., Gelatt, C.D., Vecchi, M.P.: Optimization by simulated annealing. *Science* **220**, 671–680 (1983)
- Lai, V.K., Frey, C.R., Kerandi, A.M., Lake, S.P., Tranquillo, R.T., Barocas, V.H.: Microstructural and mechanical differences between digested collagenfibrin co-gels and pure collagen and fibrin gels. *Acta. Biomat.* **8**, 4031–4042 (2012)
- Lai, V.K., Hadi, M.F., Tranquillo, R.T., Barocas, V.H.: A multiscale approach to modeling the passive mechanical contribution of cells in tissues. *J. Biomech. Eng.* **135**, 71007 (2013)
- Lake, S.P., Barocas, V.H.: Mechanical and structural contribution of non-fibrillar matrix in uniaxial tension: a collagen-agarose co-gel model. *Ann. Biomed. Eng.* **39**, 1891–1903 (2011)
- Lake, S.P., Hadi, M.F., Lai, V.K., Barocas, V.H.: Mechanics of a fiber network within a non-fibrillar matrix: model and comparison with collagen-agarose co-gels. *Ann. Biomed. Eng.* **40**, 2111–2121 (2012)
- Lanir, Y.: Constitutive equations for fibrous connective tissues. *J. Biomech.* **16**, 1–12 (1983)
- Larremore, D.B., Shew, W.L., Restrepo, J.G.: Predicting criticality and dynamic range in complex networks: effects of topology. *Phys. Rev. E* **106**, 058101-1–058101-4 (2012)
- Li, J., Dao, M., Lim, C.T., Suresh, S.: Spectrin-level modeling of the cytoskeleton and optical tweezers stretching of the erythrocyte. *Biophys. J.* **88**, 3707–3719 (2005)

- Li, J., Lykotrafitis, G., Dao, M., Suresh, S.: Cytoskeletal dynamics of human erythrocyte. *Proc. Natl. Acad. Sci. USA* **104**, 4937–4942 (2007)
- Ma, X., Schickel, M.E., Stevenson, M.D., Sarang-Sieminski, A.L., Gooch, K.J., Ghadiali, S.N., Hart, R.T.: Fibers in the extracellular matrix enable long-range stress transmission between cells. *Biophys. J.* **104**, 1410–1418 (2013)
- Maaß, S.A., Ellis, B.J., Ateshian, G.A., Weiss, J.A.: Febio: finite elements for biomechanics. *J. Biomech. Eng.* **134**, 1–10 (2012)
- Maksym, G.N., Fredberg, J.J., Bates, J.H.: Force heterogeneity in a two-dimensional network model of lung tissue. *Appl. Physiol.* **85**, 1223–1229 (1998)
- Martufi, G., Gasser, C.T.: Review: the role of biomechanical modeling in the rupture risk assessment for abdominal aortic aneurysms. *J. Biomech. Eng.* **135**, 021010 (2013)
- Maxwell, J.C.: On the calculation of the equilibrium and stiffness of frames. *Philos. Mag.* **27**, 294–299 (1864)
- Mizuno, D., Tardin, C., Schmidt, C.F., MacKintosh, F.C.: Nonequilibrium mechanics of active cytoskeletal networks. *Science* **315**, 370–373 (2007)
- Mohandas, N., Evans, E.: Mechanical properties of the red cell membrane in relation to molecular structure and genetic defects. *Annu. Rev. Biophys. Biomol. Struct.* **23**, 787–818 (1994)
- Molloy, L.E., Gest, S.D., Feinberg, M.E., Osgood, D.W.: Emergence of mixed-sex friendship groups during adolescence: developmental associations with substance use and delinquency. *Dev. Psychol.* **50**, 2449–2461 (2014)
- Morin, K.T., Smith, A.O., Davis, G.E., Tranquillo, R.T.: Aligned human microvessels formed in 3-d fibrin gel by constraint of gel contraction. *Microvasc. Res.* **190**, 12–22 (2013)
- Nagel, T.M., Hadi, M.F., Claeson, A.A., Nuckley, D.J., Barocas, V.H.: Combining displacement field and grip force information to determine mechanical properties of planar tissue with complicated geometry. *J. Biomech. Eng.* **136**, 114501-1–114501-5 (2014)
- Nair, A., Baker, B.M., Trappmann, B., Chen, C.S., Shenoy, V.B.: Remodeling of fibrous extracellular matrices by contractile cells: predictions from discrete fiber network simulations. *Biophys. J.* **107**, 1829–1840 (2014)
- Naug, D.: Structure of the social network and its influence on transmission dynamics in a honeybee colony. *Behav. Ecol. Sociobiol.* **62**, 1719–1725 (2008)
- Newman, M.E.J.: Scientific collaboration networks. II. Shortest paths, weighted networks, and centrality. *Phys. Rev. E* **64**, 016132 (2001)
- Newman, M.E.J.: Analysis of weighted networks. *Phys. Rev. E. Stat. Nonlin. Soft Matter Phys.* **70**, 056131 (2004)
- Oliveira, C.L.N., Bates, J.H.T., Suki, B.: A network model of correlated growth of tissue stiffening in pulmonary fibrosis. *New J. Phys.* **16**, 065022 (2014)
- Pedrini, R.M., David, G., Dziezyc, J., Humphrey, J.D.: Regional mechanical properties and stress analysis of the human anterior lens capsule. *Vis. Res.* **47**, 1781–1789 (2007)
- Peskin, C.S., McQueen, D.M.: A three-dimensional computational method for blood flow in the heart. I. Immersed elastic fibers in a viscous incompressible fluid. *J. Comput. Phys.* **81**, 372–405 (1989)
- Ritter, M.C., Jesudason, R., Majumdar, A., Stamenović, D., Buczek-Thomas, J.A., Stone, P.J., Nugent, M.A., Suki, B.: A zipper network model of the failure mechanics of extracellular matrices. *Proc. Natl. Acad. Sci. USA* **106**, 1081–1086 (2009)
- Sacks, M.S.: Incorporation of experimentally derived fiber orientation into a structural constitutive model for planar collagenous tissues. *J. Biomech. Eng.* **125**, 280–287 (2003)
- Sander, E.A., Stylianopoulos, T., Tranquillo, R.T., Barocas, V.H.: Image-based multiscale modeling predicts tissue-level and network-level fiber reorganization in stretched cell-compacted collagen gels. *Proc. Natl. Acad. Sci. USA* **106**, 17675–17680 (2009)
- Setnikar, I.: Origin and significance of the mechanical property of the lung. *Arch. Fisiol.* **55**, 349–374 (1955)
- Shasavari, A., Picu, R.C.: Model selection for athermal cross-linked fiber networks. *Phys. Rev. E. Stat. Phys.* **86**, 011923 (2012)

- Speck-Planche, A., Kleandrova, V.V., Luan, F., Cordeiro, M.N.D.S.: A ligand-based approach for the in silico discovery of multi-target inhibitors for proteins associated with HIV infection. *Mol. Biosyst.* **8**, 2188–2196 (2012)
- Stylianopoulos, T., Barocas, V.H.: Multiscale, structure-based modeling for the elastic mechanical behavior of arterial walls. *J. Biomech. Eng.* **129**, 611–618 (2007a)
- Stylianopoulos, T., Barocas, V.H.: Volume-averaging theory for the study of the mechanics of collagen networks. *Comput. Method Appl. Mech. Eng.* **196**, 2981–2990 (2007b)
- Suki, B., Jesudason, R., Sato, S., Parameswaran, H., Araujo, A.D., Majumdar, A., Allen, P.G., Bartolák-Suki, E.: Mechanical failure, stress redistribution, elastase activity and binding site availability on elastin during the progression of emphysema. *Pulm. Pharmacol. Ther.* **25**, 268–275 (2012)
- Takamizawa, K., Hayashi, K.: Strain energy density function and uniform strain hypothesis for arterial mechanics. *J. Biomech.* **20**, 7–17 (1987)
- Timoshenko, S.P.: On the correction factor for shear of the differential equation for transverse vibrations of bars of uniform cross-section. *Philos. Mag.* **41**, 744–746 (1921)
- Trajkovski, A., Omerovic, S., Hribernik, M., Prebil, I.: Failure properties and damage of cervical spine ligaments, experiments and modeling. *J. Biomech. Eng.* **136**, 031002-1–031002-19 (2014)
- Treloar, L.: The elasticity of a network of long-chain molecules. III. *Trans. Faraday Soc.* **42**, 83–94 (1946)
- van Dillen, T., Onck, P.R., Van der Giessen, E.: Models for stiffening in cross-linked biopolymer networks: a comparative study. *J. Mech. Phys. Solids* **56**, 2240–2264 (2008)
- Wang, M.C., Guth, E.: Statistical theory of networks of nongaussian flexible chains. *J. Chem. Phys.* **20**, 1144 (1952)
- Wang, C.W., Sastry, A.M.: Structure, mechanics and failure of stochastic fibrous networks: part II - network simulations and applications. *J. Eng. Mater. Technol.* **122**, 460–468 (2000)
- Wang, H., Abhilash, A.S., Chen, C.S., Wells, R.G., Shenoy, V.B.: Long-range force driven transmission in fibrous matrices enabled by tension-driven alignment of fibers. *Biophys. J.* **107**, 2592–2603 (2014)
- Win, Z., Steucke, K.E., Sevcik, E.N., Hald, E.S., Alford, P.W.: Smooth muscle architecture within cell-dense vascular tissue influences functional contractility. *Integr. Biol.* **6**, 1201–1210 (2014)
- Witzenburg, C.M., Dhume, R.Y., Lake, S.P., Barocas, V.H.: Automatic segmentation of mechanically inhomogeneous tissues based on deformation gradient jump. *IEEE Trans. Med. Imaging* (2015) (in press). doi:[10.1109/TMI.2015.2453316](https://doi.org/10.1109/TMI.2015.2453316)
- Yuan, H., Kononov, S., Cavalcante, F.S.A., Lutchen, K.R., Ingenito, E.P., Suki, B.: Effects of collagenase and elastase on the mechanical properties of lung tissue strips. *J. Appl. Physiol.* **89**, 3–14 (2000)
- Yurchenco, P.D., Ruben, G.C.: Basement membrane structure in situ: evidence for lateral associations in the type IV collagen network. *J. Cell Biol.* **105**, 2559–2568 (1987)
- Zagar, G., Onck, P.R., Van der Giessen, E.: Elasticity of rigidly cross-linked networks of athermal filaments. *Macromolecules* **44**, 7026–7033 (2011)
- Zagar, G., Onck, P.R., van der Giessen, E.: Two fundamental mechanisms govern the stiffening of cross-linked networks. *Biophys. J.* **108**, 1470–1479 (2015)
- Zhang, L., Lake, S.P., Barocas, V.H., Picu, R.C.: Cross-linked fiber network embedded in an elastic matrix. *Soft Matter* **9**, 6398–6405 (2013a)
- Zhang, L., Lake, S.P., Lai, V.K., Picu, C.R., Barocas, V.H., Shephard, M.S.: A coupled fiber-matrix model demonstrates highly inhomogeneous microstructural interaction in soft tissues under tensile load. *J. Biomech. Eng.* **135**, 011008 (2013b)

Author Index

A

Ateshian, Gerard A., 1

Holzapfel, Gerhard A., 157

B

Barocas, Victor H., 271

M

McGarry, J. Patrick, 193

McHugh, Peter E., 193

McMeeking, Robert M., 53

C

Conway, Claire, 193

D

Deshpande, Vikram S., 53

Dhume, Rohit Y., 271

O

O'Reilly, Brían L., 193

Ogden, Ray W., 83

H

Holmes, Jeffrey W., 233

W

Witzenburg, Colleen M., 233

Subject Index

A

Abdominal aorta, 158, 162–165, 187
Abdominal aortic aneurysm, 162–164, 166–168
Abluminal layer, 166
Actin concentration, 73
Actin distribution, 72
Actin junctions, 290
Actin networks, 295
Adipocyte, 166
Adjacency matrix, 274
Adventitia, 157, 163–166, 168, 169, 187, 189
Affine deformation, 281
Affine model, 281, 282
Agarose disk, 21, 44
Agent-based model (ABM), 263
Aggregate modulus, 14, 16, 17, 20
Amount of shear, 170, 171, 179–181
Anatomy of the heart, 233, 234
Aneurysm, 157, 158, 162, 164
Angioplasty, 220
Angiotensin converting enzyme (ACE) inhibitor, 257, 260, 262
Angiotensin receptor blocker, 257
Angular momentum balance, 5
Animal model, 208, 244, 245, 247, 249, 252, 261
Anteroapical infarct, 248, 249, 261
Aorta, 157
Aortic clamping, 157, 159, 183, 187, 190
Aortic dissection, 157, 158, 168–170, 177, 189
Aortic valve, 234, 236, 250
Apparent density, 3, 4, 6, 9, 43
Apparent stress, 4, 5
Arrested heart, 236, 241, 248
Arruda–Boyce model, 284

Arterial tissue, 195

Articular cartilage, 1, 2, 6, 17, 19, 20, 29–32, 37, 40–42, 44, 46
Atherosclerosis, 169
Atherosclerotic plaque, 207, 208, 212
Atrium, 234, 250
Average Cauchy stress, 300, 301
Axial load, 116

B

Balance law, 175
Balloon angioplasty, 159, 182, 243
Beta blocker, 257, 262
Betweenness, 278
Biaxial stretching test, 158, 163, 165, 167
Bio-chemo-mechanical model, 53, 54, 67, 68
Biphasic-CLE model, 41
Biphasic mixture, 1, 6, 9, 42
Blood cell, 243
Blood flow, 236, 245, 247, 250, 257, 259, 260
Blood supply, 236, 243
Blood vessel, 157, 236, 257
Body force, 4, 5, 9, 43, 174
Boundary condition, 11–15, 17, 20, 22, 23, 28, 34–36, 237
Boundary nodes, 298

C

Calcification, 164, 166, 168
Cardiac muscle, 239, 240, 258
Cardiac output, 256, 257, 261
Cardiac physiology, 246, 252
Cauchy stress tensor, 91, 99, 101, 103, 104, 107, 121, 133, 134, 150, 197

- Cayley–Hamilton theorem, 90
 Cell model, 75, 76
 Cell–cell signaling, 262
 Cells on grooved substrates, 77
 Cells on patterned substrates, 69
 Chambers of the heart, 236, 249
 Chemical kinetics, 59
 Chemical potential, 70
 Chemical reaction, 1, 2, 5, 45, 47
 Chemotaxis, 263
 Chondrocyte, 45, 75
 Circular cylindrical tube, 84
 Circular symmetry, 115
 Clausius–Duhem inequality, 184
 Coefficient of determination, 165, 167, 187
 Cohesive zone model, 215, 216
 Collagen, 2, 3, 40, 41, 45
 Collagen alignment, 158, 244, 263
 Collagen fiber, 157–159, 162–164, 166, 168–170, 175, 176, 183, 185, 186, 189, 234, 235, 244, 245, 248, 263
 Compliant substrate, 74
 Computational model, 212, 216–218, 220, 226, 233, 234, 236, 248, 249, 253, 264, 272
 Concentration parameter, 131
 Confined compression, 1, 21, 22, 24–27, 29–33
 Confined compression modulus, 38
 Constitutive model, 158–160, 162, 163, 183, 187, 194, 195, 209, 212, 219, 220, 224, 282–284
 Continuum damage mechanics, 182
 Continuum mechanics, 2, 46
 Contractile stress-fibers, 72
 Coronary artery, 236, 243, 245–247, 253, 258
 Coronary ligation, 244, 246, 248, 249, 254
 Coronary occlusion, 246, 255, 258
 Crack dissipation functional, 174
 Crack energy functional, 174
 Crack evolution step, 159, 177
 Crack phase-field, 157, 159, 172–175, 177, 179–181
 Crack surface density, 173, 174
 Crack zone, 179
 Creep problem, 23, 24, 27, 28
 Critical fracture energy, 174, 176
 Cross-linked network model, 297
 Crossfiber direction, 237–241, 260
 Cytokine, 262, 263
 Cytoskeleton, 55, 57, 61, 293
 Cytoskeleton model, 71, 290, 291
 Cytoskeleton polymerization, 75
- D**
 Damage mechanics, 202
 Damage model, 183, 202–204, 207, 211, 215, 219, 220, 224, 226
 Damage variable, 183, 185, 186
 Darcy’s law, 9, 10, 17, 43, 44
 Deformation function, 88
 Deformation gradient, 7, 10, 88, 160, 183, 281
 Deformed configuration, 88
 Deoxygenated blood, 234
 Diastolic function, 250, 253, 255, 261
 Diffusion velocity, 5, 7, 45
 Diffusive crack, 172
 Dimensionless pressure, 123, 138
 Dimensionless reduced axial load, 123, 138
 Directed network, 273
 Dirichlet boundary condition, 173, 179
 Discrete-fiber network, 294, 295
 Disease progression, 158
 Dispersion model, 157, 158
 Dispersion parameter, 130, 132, 137, 158, 162, 168, 185, 198
 Dissipation function, 184
 Donnan’s law, 43
 Dynamic loading, 22, 27, 28, 30–32, 44
 Dyskinesis, 253
- E**
 Echocardiography, 259
 Effective free-energy function, 173
 Ehlers–Danlos syndrome, 169
 Elastance model, 252, 254, 257
 Elasticity tensor, 176, 178, 185
 Elastin, 2, 3, 45, 158, 169, 170
 Electrical potential, 13, 43
 Electrically neutral, 1, 13
 Element matrix, 159, 178
 End-diastolic pressure-volume relationship (EDPVR), 251, 254–256
 End-systolic pressure-volume relationship (ESPVR), 252–254, 256, 261
 Endocardium, 234, 237, 241, 264
 Energetic force, 174
 Energy balance, 2, 3, 11–13
 Entropy inequality, 3, 7
 Epicardial strain, 241, 248
 Epicardial surface, 237, 244, 258
 Epicardium, 234, 264
 Equilibrium equation, 92, 115

Euler–Lagrange equation, 175
 Eulerian principal axes, 91
 Extension, inflation of an artery, 113
 Extracellular ligand, 70
 Extracellular matrix, 59, 235, 243, 286

F

Failure criterion, 157, 159, 175, 176
 False lumen, 169
 Fiber bundle, 163
 Fiber diameter, 164
 Fiber direction, 237, 239, 240, 242, 246
 Fiber dispersion, 127, 128, 130, 158–160,
 189
 Fiber dispersion – effect on artery response,
 137
 Fiber dispersion in two dimensions, 135
 Fiber orientation, 234, 235, 244, 263
 Fiber orientation dispersion data, 147
 Fiber remodeling, 200
 Fibroblast, 243, 263
 Fibronectin, 56, 58, 65, 69, 72
 Fick’s law, 43, 44
 Filling phase, 250
 Finite element mesh, 179, 180, 189
 Finite element method, 169
 Finite element model, 189, 234, 239, 242,
 253, 255–261, 299
 Finite element simulation, 177, 178, 187,
 190, 241
 First Piola–Kirchhoff stress tensor, 93
 Fluid flux, 9, 12, 13, 20–22, 24–28, 33–35
 Fluid perfusion velocity, 16
 Fluid velocity, 13, 14, 19
 Focal adhesion model, 69
 Focal adhesions, 56, 57, 60, 69, 78
 Frank–Starling mechanism, 251, 258
 Free-energy function, 159, 161, 173, 175,
 176, 183, 186
 Friction coefficient, 189
 Frictional drag, 9, 44
 Fung model, 282
 Fung-type exponentials, 111

G

Gel time constant, 18, 19, 24, 38
 General invariant formulation, 102
 Generalized invariants, 132, 149
 Generalized structure tensor, 129, 132, 142,
 144, 148, 159, 161, 189, 198
 Goodness of fit, 187
 Green–Lagrange strain tensor, 160

Ground matrix, 34, 37, 157, 161, 175, 176,
 183
 Growth and remodeling, 1, 45, 233, 253,
 260, 262, 265
 Growth factor, 243

H

Heart failure, 233, 243, 257, 260
 Heart mechanics, 234–236, 257
 Heart wall, 235, 240, 241, 245, 247, 248,
 260
 Heaviside unit step function, 23, 33
 Hemodynamic loading, 252, 262
 HGO model, 162, 195, 196, 198, 200, 202,
 222, 283
 Holzapfel-type model, 202
 Homogeneous biaxial deformation, 108
 Homogeneous deformations, 108
 Hooke’s law, 10
 Hydrated biological tissue, 1, 25, 37
 Hydraulic permeability, 13, 20, 30, 31
 Hydrogel, 20, 44, 45
 Hyperelastic network models, 285
 Hypertension, 169
 Hypoxia, 240

I

Incompressibility constraint, 89, 114
 Incompressible fluid, 27, 42
 Incompressible solid, 27, 42
 Inelastic energy dissipation, 184, 186
 Inelastic phenomena, 157, 159, 182
 Infarct mechanics, 245, 248, 264
 Infarct scar, 233, 243–245, 248
 Inflammatory cell, 243, 263
 In-plane dispersion parameter, 144
 In-plane orientation density, 142
 Integrins, 56, 69, 72
 Intensity plot, 163, 164, 166, 168
 Interior nodes, 298
 Intermediate filaments, 55
 Interstitial fluid, 1, 6, 8, 13, 17, 20, 23, 43
 Interstitial fluid pressure, 1, 13, 23–27, 29,
 32, 33, 35–37, 39, 41, 43
 Intervertebral disc, 6, 20
 Intima, 157, 163–166, 168, 169, 182, 187,
 189
 Intimal tear, 168
 Ischemia, 233, 247, 255, 259
 Isolated heart, 236, 237, 239, 250, 252
 Isometric network, 65
 Isometric tension, 60

Isotropic elastic material, 98
 Isotropic function, 98
 Isovolumetric contraction, 246, 248, 250
 Isovolumetric relaxation, 246, 248, 250

J

Jump condition, 12, 13

K

Kinematics, 88, 194
 Kirchhoff matrix, 275
 Kronecker delta function, 172

L

Lagrange multiplier, 7, 161
 Lagrangian principal axes, 91
 Lamé coefficient, 11
 Laplace transform, 38
 Laplace's law, 251
 Laplacian, 173
 Laplacian matrix, 275
 Left Cauchy–Green tensor, 90
 Length-scale parameter, 158, 172, 179
 Lens capsule, 285
 Ligament, 244
 Linear momentum balance, 4, 8, 9
 Links, 273
 Luminal layer, 164, 166, 168
 Lumped-capacitance model, 257
 Lung, 234, 286, 287

M

Macromolecular networks, 271
 Marfan syndrome, 169
 Mass balance, 2–7, 10–13, 15, 45, 46
 Mass transport, 1
 Master surface, 189
 Material parameter identification, 151
 Material symmetry, 97
 Matrix, 83
 Mechanical predictor step, 159, 177, 178
 Media, 157, 163–166, 168, 169, 178, 180, 187, 189
 Micropost deflection, 62, 63
 Micropost stiffness, 63
 Microscopic network, 298, 299
 Microstructure, 157, 158, 162, 169, 189
 Microtubules, 55
 Minimization principle, 175
 Mitral valve, 234, 237, 250

Mitochondria, 55
 Mixed model, 205
 Mixed variational principle, 175
 Mixture constituent, 2, 3, 5, 8, 43–45
 Mixture model, 44, 46, 47
 Mixture theory, 1, 2, 6, 9, 43–46
 MMP-9, 262
 Momentum balance, 2–5, 8–10, 12–14, 43
 Mooney–Rivlin model, 223
 MRI, 247, 260
 Mullins effect, 206
 Multi-field problem, 158, 173, 175, 179
 Multi-scale algorithm, 299
 Multi-scale model, 219, 233, 264, 299, 302
 Muscle activation, 190
 Muscle fiber, 234, 235, 239, 246, 248, 258
 Muscular pump, 234
 Myocardial infarction, 233, 243, 246, 249, 250, 253, 257, 259, 262, 264
 Myocardial ischemia, 257, 258
 Myocardium, 233, 235–242, 244, 245, 247–251, 253, 255, 257–260, 262, 264
 Myocyte, 234–236, 243, 248, 251–253, 259, 262

N

Natural configuration, 95
 Navier–Stokes equation, 296
 Neo-Hookean matrix, 285
 Neo-Hookean model, 111, 209, 286
 Network model, 271, 278, 282, 287, 288, 295, 298
 Network partitioning, 278
 Nodal degree, 274
 Nodes, 273
 Nominal strain, 188, 189
 Nominal stress tensor, 92, 99
 Non-affine model, 282
 Non-homogeneous uniaxial extension, 139, 152
 Non-polar material, 5
 Non-symmetric fiber dispersion, 140

O

Objectivity, 97
 Ogden model, 223
 Operator-splitting algorithm, 159, 177, 178
 Orientation density function, 128
 Orientation density normalization, 128, 130, 135, 142
 Orthotropy, 104, 111

Orthotropy of myocardium, 241
Osmotic loading, 6, 45
Osmotic swelling, 17, 43
Osteoblasts, 77
Out-of-plane dispersion parameter, 143
Out-of-plane orientation density, 142
Oxygenated blood, 234, 236

P
Papillary muscle, 239, 240
PDMS posts, 56
Peeling test, 169, 170
Penalty parameter, 176, 186
Permanent deformation, 157–159, 182, 183, 189
Permeability tensor, 9
Permeation, 1, 13, 43
Permeation experiment, 6, 13, 17–21
Phase-field model, 172, 178
Planar biaxial testing, 237, 238, 248
Planar Cauchy stress, 136
Plane strain, 101, 104, 107
Plaque rupture stress, 218
Poisson's ratio, 37, 38
Polar decomposition theorem, 90
Polar material, 6
Porous filter, 13–17, 20, 24
Porous indenter, 21, 22, 24–28
Porous matrix, 43
Porous media, 6, 9, 17, 43, 44, 46
Post-infarction necrosis, 253
Post-infarction scar, 233, 243, 249
Post-infarction therapy, 233, 246, 247, 260, 261
Preferred direction, 85, 100, 109
Pressure, 116, 122
Pressure-volume behavior, 236, 255, 258
Principal invariants, 90, 91
Principal stretches, 91
Probability density, 159
Proteoglycans, 2, 40, 243
Proteolytic enzyme, 243
Pseudo-elastic damage model, 159
Pseudo-elasticity, 204
Pseudoelastic damage model, 183
Pulmonary edema, 257
Pulmonary valve, 234
Pure homogeneous strain, 108

Q
Quasi-static process, 175

R
Red blood cell cytoskeleton, 289
Reduced axial load, 116, 118, 122
Reference configuration, 88, 159, 172–174, 180, 183
Reflex compensation, 256, 257
Regulatory body guidelines recommendations, 224
Representative volume element (RVE), 60, 299
Residual stress, 85, 93, 105, 117, 121, 157, 159, 183, 187
Residual stress model, 121
Residual vector, 159, 177
Residually stressed configuration, 95
Right and left stretch tensors, 90
Right Cauchy–Green tensor, 90, 160, 183, 184, 238, 240, 241
Rotation tensor, 10
Rotationally symmetric dispersion, 133

S
Saturation condition, 6, 8
Scar mechanics, 244–246, 264
Scar structure, 243, 263
Scar tissue, 233, 243, 248, 262
Second law of thermodynamics, 174
Second Piola–Kirchhoff stress tensor, 93, 97, 150, 174, 184
Second-harmonic generation, 158, 162, 163, 165–167
Sharp crack, 158, 172
Shear deformation of cells, 75
Shear modulus, 37
Shear testing, 240, 242
Sheet direction, 240, 242
Sheet-normal direction, 240
Signaling proteins, 59
Simple shear test, 157, 178, 181
Slave surface, 189
Soft biological tissue, 25, 33, 45, 171
Solid matrix, 1, 6, 10, 12, 13, 16, 30–33, 37, 40–46
Solute transport, 1, 43, 44
Spectral decompositions, 90
Spectrin network, 289
Spectrin tetramers, 290, 293
Steady-state permeation, 15, 16
Stenosis, 250, 259
Stent computational modeling, 221
Stent design, 221
Stiff substrate, 63, 74
Stiffness matrix, 177, 178

Strain cycling of cells, 66, 67
 Strain-energy function, 94, 105, 106, 134, 137, 150, 238, 241, 242, 249
 Stress-fiber alignment, 69, 77
 Stress-fiber concentration, 60, 74, 78
 Stress-fiber contraction, 60
 Stress-fiber model, 59
 Stress-fiber network, 65, 69, 78
 Stress-fiber polymerization, 59, 65, 67, 78
 Stress-fiber tension, 60, 61, 72
 Stress relaxation, 22, 25–27, 30, 31, 36, 40, 41
 Stress softening, 157–159, 182, 183, 189, 202
 Stress tensors, 106
 Stroke volume, 251, 256, 261
 Structural parameters, 162, 164, 165, 167
 Structural stability, 169
 Structure of the heart, 234
 Structure tensor, 100, 158–162, 175, 189
 Supra-physiological loading, 182, 189
 Surface traction, 174
 Symmetry group, 98
 Symmetry transformation, 97
 Systolic function, 252, 253, 255, 260

T

Tangent matrix, 178
 Tendon, 244
 TGF- β , 262
 Thermodynamics, 249
 Thin-walled tube, 117
 Thoracic aorta, 158, 170, 171, 178, 182, 187, 189

Time increment, 177
 Timoshenko beam elements, 295
 Tissue damage, 182, 189
 Traction vector, 5, 12
 Transient permeation, 18, 20
 Transversely isotropic, 100, 238, 240, 241
 Transversely isotropic dispersion, 130
 Tricuspid valve, 234
 Two preferred directions, 103

U

Ultimate shear stress, 171
 Ultrasound, 247, 259
 Unconfined compression, 1, 33, 36–41, 44
 Unconfined compression modulus, 37
 Unconnected clusters, 277

V

Valve ring, 237, 239
 Vascular tissue, 6, 20
 Ventricle, 234, 245, 250, 256, 257, 262
 Viscoelastic network models, 295
 Volume fraction, 6
 Volume ratio, 176, 183
 von Mises distribution, 131, 145, 146, 158, 159

W

Waviness, 164
 Weighted networks, 277
 Windkessel model, 256
 Wound healing, 233, 264